

# Aeroelasticity of Large Wind Turbines

## Proefschrift

ter verkrijging van de graad van doctor  
aan de Technische Universiteit Delft,  
op gezag van de Rector Magnificus, Prof. dr. ir. J.T. Fokkema,  
voorzitter van het College voor Promoties,  
in het openbaar te verdedigen op woensdag 19 november 2008 om 12:30 uur

door

Jessica Gabriëlle HOLIERHOEK

ingenieur Luchtvaart en Ruimtevaart  
geboren te Leiderdorp.

Dit proefschrift is goedgekeurd door de promotor:

Prof. dr. ir. Th. van Holten

Samenstelling promotiecommissie:

Rector Magnificus

Prof. dr. ir. Th. van Holten

Prof. dr. ir. G.A.M. van Kuik

Prof. dr. ir. G.J.W. van Bussel

Prof. ir. O.H. Bosgra

Prof. dr. J. Arbocz

ir. H Snel

voorzitter

Technische universiteit Delft, promotor

Technische universiteit Delft

Technische universiteit Delft

Technische universiteit Delft

Technische universiteit Delft

Energieonderzoek Centrum Nederland

ISBN 978-90-9023627-8

Printed by: PrintPartners Ipskamp, Enschede

Copyright ©2008 Jessica Holierhoek. All rights reserved. No part of this publication may be reproduced, stored in a retrieval system, or transmitted in any form or by any means, electronic, mechanical, photocopying, recording or otherwise, without prior written permission from the author.

# Preface

During my studies I already knew that I wanted to do a PhD after graduation. I feel very lucky that I got the chance to do a PhD and especially that I had the opportunity to do the research in a field that is not only very challenging but also, in my eyes, of great importance. The world is being destroyed at a very rapid rate by people. In order to save this planet, a lot of changes are necessary. In my opinion wind energy is one of the opportunities to prolong the earth's life, but it can only play a small part, many other measures will have to be taken. I am grateful that I have had a chance to contribute a very tiny bit towards a better future.

This dissertation is the result of (too) many years of hard work. During those years, my life has completely changed. Starting right after graduation, in the years that followed I have lost my mother, become a mother, have had the joy of experiencing being a teacher to students and have learned about the uncertainties in life and the fragility of the human body, but I did manage to finish it. Some people thought I would never finish this dissertation, but I am extremely glad to prove all these skeptics to be wrong.

Most of the research I have done has been performed as a part of several different projects which were funded by NOVEM and the European Commission (ENK-CT 2001-00524). These funds made it possible to do the research and my promotor, Theo van Holten, was kind enough to grant me some extra time in order to expand the research and write this dissertation.

My goal with this dissertation has been to write something that other people can work with to continue the aeroelastic research of wind turbines. I hope it is a good starting point for anyone interested in this subject, something that I have missed during my research. There are a few good books on aeroelasticity of helicopters, but on wind turbines the information in books is very limited. The aerodynamics in most wind energy books are reasonably well described, though somewhat inaccurate, but aeroelasticity is hardly touched on. This dissertation has been written for people with different technical backgrounds. Aerodynamics, dynamics and aeroelasticity are explained for those that lack in the background in those areas.

Of course many people have to be thanked for making all this possible.

My promotor, Theo van Holten, for giving me guidance and commenting on the chapters enabling me to improve them greatly.

My friends, Kajsa, Gillian, Annemie, Dennis and Karen and my many colleagues at Delft University as well as all those other friends for helping with all kinds of things and their support.

My family for their support and in particular my father Kees Holierhoek and aunt Jeanne Holierhoek for their help. I regret that my mother and grandparents could not be witness to the finish, of course they are also thanked.

Sara, for her support and her energy, for being a wonderful daughter and for behaving well or sleeping when I needed to do my work.

My colleagues at ECN for encouraging me to finish this work.

Most importantly, Hossein, for his support, his incredible patience, but also the necessary pressure he put on this project and especially everything he has done to enable me to work all the necessary extra hours and get this all done. Kheli mammunaam azizaam!

# Contents

<b>List of Symbols</b>	<b>xiii</b>
<b>Summary</b>	<b>xix</b>
<b>Samenvatting</b>	<b>xxiii</b>
<b>1 Introduction</b>	<b>1</b>
1.1 Wind Energy . . . . .	1
1.2 Goal of this Dissertation . . . . .	4
1.3 Outline . . . . .	5
<b>2 Dynamics</b>	<b>7</b>
2.1 Newtonian Dynamics . . . . .	7
2.1.1 Conventional Notations . . . . .	8
2.1.2 Vector and Matrix Notations . . . . .	17
2.2 Lagrange's Equations . . . . .	28
2.2.1 Hamilton's Principle and Lagrange's Equations for particles . . . . .	28
2.2.2 Lagrange's Equations for Rigid Body Systems . . . . .	33
<b>3 Horizontal Axis Wind Turbine Aerodynamics</b>	<b>37</b>
3.1 Blade Element - Momentum Method . . . . .	38
3.1.1 Momentum Theory . . . . .	38
3.1.2 Betz Limit . . . . .	44
3.1.3 Rotor Disc Theory . . . . .	44
3.1.4 Blade Element theory . . . . .	47

---

3.1.5	Blade Element and Momentum Theory . . . . .	49
3.1.6	Turbulent Wake state . . . . .	51
3.1.7	Dynamic Inflow . . . . .	53
3.1.8	Tip Loss Corrections . . . . .	54
3.1.9	Dynamic stall . . . . .	58
3.2	Alternatives for Blade Element Momentum Theory . . . . .	61
3.2.1	Global flow . . . . .	61
3.2.2	Blade Flow . . . . .	63
<b>4</b>	<b>Aeroelastic Instability</b>	<b>67</b>
4.1	Aeroelasticity . . . . .	67
4.2	Helicopters and Wind Turbines . . . . .	69
4.3	Blade Instabilities . . . . .	71
4.3.1	Blade Edgewise Instability and Blade Flapwise Instability . . . . .	72
4.3.2	Stall Flutter . . . . .	75
4.3.3	Flap-Lag Flutter, Including Flap-Lag-Stall Flutter . . . . .	76
4.3.4	Pitch-Lag Instability . . . . .	79
4.3.5	Pitch-Flap Flutter and Divergence . . . . .	80
4.4	Rotor Tower Instabilities . . . . .	80
4.4.1	Lead-Lag and Sideways Tower Instability . . . . .	80
4.4.2	Whirl Flutter . . . . .	81
4.4.3	Advancing Lead-Lag Mode Coupled with Tower Modes Instabilities . . . . .	85
<b>5</b>	<b>Hamiltonian Dynamics for Rigid Body Simulations</b>	<b>87</b>
5.1	Background . . . . .	88
5.2	The Core of the Method . . . . .	89
5.2.1	Energy Matrix . . . . .	91
5.2.2	Derivatives of Kinetic and Potential Energy . . . . .	97
5.3	Additional Modelling Features . . . . .	99
5.3.1	Pitch Setting / Fixed Angles . . . . .	99
5.3.2	Controlled rotations . . . . .	100

---

5.4	Generalised Forces . . . . .	103
5.4.1	Automated Calculation of the Generalised Forces due to Aerodynamics	103
5.4.2	Structural Damping . . . . .	106
5.4.3	Generator Control . . . . .	106
<b>6</b>	<b>WOBBE; a Nonlinear Rigid Body Simulation Tool</b>	<b>109</b>
6.1	General Overview . . . . .	110
6.2	Subroutines and Functions . . . . .	115
6.2.1	WOBBEB, branch.f . . . . .	115
6.2.2	INITL, initl3.f . . . . .	116
6.2.3	VECMAT, vecmat.f . . . . .	117
6.2.4	DIRECT, direct.f . . . . .	117
6.2.5	ENERGY, energy.f . . . . .	117
6.2.6	TRAFI, trafin.f, TRAFTOT, traftot.f . . . . .	118
6.2.7	TRNSLAT, transl.f . . . . .	119
6.2.8	INTGRD, integrd.f . . . . .	119
6.2.9	DIVPAG (imsl), RK4 (rk4.f), STIFFX (stiffx.f), SIMPR (simpr.f) . .	120
6.2.10	DERIVS (derivs2.f), DERIVSN (derivsn.f) . . . . .	120
6.2.11	NRGDTDQ, nrgdtdq.f . . . . .	121
6.2.12	EXOMEGA, exomega.f . . . . .	122
6.2.13	LUDCMP, ludcmp.f, LUBKSB, ludcmp.f . . . . .	122
6.2.14	OMEGA, omega.f . . . . .	122
6.2.15	GENFO3, genfo3.f . . . . .	122
6.2.16	FRCAIR, frcair.f . . . . .	123
6.2.17	VELOC, veloc.f . . . . .	124
6.2.18	WALKBK, walk.f . . . . .	125
6.2.19	CALCAPR, calcapr.f . . . . .	125
6.2.20	PRTIP, calcapr.f . . . . .	125
6.2.21	WALK2, walk.f . . . . .	126
6.2.22	LINCL, Lincl.f . . . . .	126
6.2.23	AERO, aero.f . . . . .	127

6.2.24	CLCDCM, clcdcm.f . . . . .	127
6.2.25	CLxxx, clxxx.f . . . . .	128
6.2.26	HISTORY history.f . . . . .	128
6.2.27	DFRIDR, dfrid.f . . . . .	128
6.2.28	V, v3c.f . . . . .	129
6.2.29	T, t.f . . . . .	129
6.2.30	JACOBN (jacobn.f), JCBNIMSL (jcbnimsl.f) . . . . .	130
6.2.31	DPDOTDP, dpdotdp.f . . . . .	131
6.2.32	Linalg.f . . . . .	131
<b>7</b>	<b>Multi-Body Modelling of Large Wind Turbines</b>	<b>133</b>
7.1	Superelements . . . . .	133
7.2	Calculation of the Superelement Properties . . . . .	136
7.3	Elements used in a Model of a Wind Turbine . . . . .	141
<b>8</b>	<b>Verification and Validation of WOBBE</b>	<b>147</b>
8.1	Verification of WOBBE . . . . .	148
8.1.1	Verification by Results Comparison . . . . .	148
8.1.2	Euler-Bernoulli Beam . . . . .	152
8.1.3	Structural Dynamics for Branched Systems . . . . .	156
8.2	Benchmarking . . . . .	156
8.2.1	LMH64-5 . . . . .	159
8.2.2	STABCON Benchmark . . . . .	160
8.3	Validation of WOBBE . . . . .	165
8.3.1	Measurements for Validation . . . . .	165
8.3.2	Model of the NM80 in WOBBE . . . . .	170
8.3.3	Comparison of Measurements and Simulation Results . . . . .	171
8.4	Alterations to WOBBE due to Validation . . . . .	174
8.5	Summary of Verification and Validation . . . . .	175
<b>9</b>	<b>Calculation of Model Properties</b>	<b>177</b>
9.1	Stiffness Calculation . . . . .	178

---

9.2	Structural Pitch Calculation . . . . .	186
<b>10</b>	<b>Investigation into the Possibility of Flap-Lag-Stall Flutter</b>	<b>193</b>
10.1	Classical Flap-Lag Equations . . . . .	194
10.1.1	Derivation of the Equations of Motion . . . . .	194
10.1.2	Stability Calculations . . . . .	200
10.2	Flap-Lag-Stall Instability as Derived in STABTOOL . . . . .	202
10.2.1	Equations of Motion for Three DOF Model in Stall . . . . .	202
10.2.2	Multi-blade Effects . . . . .	204
10.2.3	Stability of the Isolated Blade . . . . .	206
10.2.4	Effect of Linearisations . . . . .	208
10.3	Helicopter Flap-Lag Instability and Wind Turbine Flap-Lag-Stall Instability	211
10.4	Flap-Lag Coincidence . . . . .	212
10.5	Simplified Blade Damping Model . . . . .	218
10.5.1	Derivation of the Damping Coefficients . . . . .	218
10.5.2	Difference Between Two Instabilities: Flap-Lag Flutter and Negative Damping of Edgewise Mode . . . . .	221
10.5.3	Flap-Lag Coincidence and the Possibility of Flap-Lag-Stall . . . . .	222
<b>11</b>	<b>Conclusions and Recommendations</b>	<b>231</b>
11.1	Conclusions . . . . .	231
11.2	Recommendations . . . . .	233
	<b>Bibliography</b>	<b>235</b>
<b>A</b>	<b>Unsteady Aerodynamics</b>	<b>247</b>
<b>B</b>	<b>Introduction to Elasticity</b>	<b>249</b>
<b>C</b>	<b>Introduction to Linear Vibrations</b>	<b>257</b>
<b>D</b>	<b>Post-Processing Methods</b>	<b>265</b>
D.1	Fast Fourier Transform . . . . .	265
D.1.1	Fourier Transformation . . . . .	265

D.1.2	Determination of Natural Frequencies using FFT . . . . .	266
D.1.3	Determination of Damping using FFT . . . . .	271
D.2	Logarithmic Decrement . . . . .	273
D.3	System Identification . . . . .	275
D.3.1	Constant Steady State . . . . .	276
D.3.2	Periodic Steady State . . . . .	277
<b>E</b>	<b>Controlled Rotations vs the Flywheel Approach</b>	<b>279</b>
E.1	Shortcomings of the Flywheel approach . . . . .	279
E.2	Verification of the Controlled Rotations . . . . .	280
<b>F</b>	<b>WOBBE Flow Diagrams</b>	<b>285</b>
F.1	Explanation of Terms Used in Flow Diagrams . . . . .	285
F.2	Subroutines . . . . .	285
F.2.1	Main Program . . . . .	285
F.2.2	INITL . . . . .	288
F.2.3	ENERGY . . . . .	290
F.2.4	TRAFOTOT . . . . .	293
F.2.5	DERIVS/DERIVSN . . . . .	293
F.2.6	NRGDTDQ . . . . .	296
F.2.7	EXOMEGA . . . . .	296
F.2.8	GENFO3 . . . . .	296
F.2.9	CLCDCM . . . . .	302
F.2.10	V . . . . .	302
<b>G</b>	<b>Energy Matrix Calculations</b>	<b>305</b>
G.1	Reduction in Number of Calculations . . . . .	305
G.2	Results . . . . .	309
<b>H</b>	<b>Rotating beam</b>	<b>313</b>
<b>I</b>	<b>Derivation of the Equations Governing the Flap-Lag Instability</b>	<b>317</b>
I.1	Governing Equations for an Isolated Blade with 3 Degrees of Freedom . . . . .	317

---

I.1.1	Model Description . . . . .	317
I.1.2	Using Vector and Matrix Notations to Determine the Equations of Motion . . . . .	318
I.2	Neglecting Drag Forces . . . . .	326
I.3	Drag-stall . . . . .	326
	<b>Index</b>	<b>330</b>



# List of Symbols

$a$	- Induction factor $a = \frac{v_i}{V_W}$	[-]
$a_T$	- Induction factor in the transition point	[-]
$a'$	- Tangential induction factor $a' = \frac{U_{Ti}}{\Omega r}$	[-]
$[A]$	- Energy or mass matrix	[kgm <sup>2</sup> ]
$A_d$	- Actuator disc area	[m <sup>2</sup> ]
$A_R$	- Rotor swept area	[m <sup>2</sup> ]
$(c_{i_x}, c_{i_y}, c_{i_z})$	- Row indicating the direction of the rotation axis in local frame	[-]
$c_d$	- 2D Drag coefficient: $\frac{d}{\frac{1}{2}\rho V^2 c}$	
$c_{d_\alpha}$	- $\frac{dc_d}{d\alpha}$	[-]
$C_{Dax}$	- Non-dimensional axial force: $\frac{D_{ax}}{\frac{1}{2}\rho V^2 A_R}$	[-]
$C_{Dax1}$	- Non-dimensional axial force for $a = 1$	[-]
$C_{DaxT}$	- Non-dimensional axial force at transition point between momentum theory and turbulent wake state	[-]
$c_l$	- 2D Lift coefficient: $\frac{l}{\frac{1}{2}\rho V^2 c}$	[-]
$c_{l_\alpha}$	- $\frac{dc_l}{d\alpha}$	[-]
$c_m$	- 2D Moment coefficient: $\frac{m}{\frac{1}{2}\rho V^2 c^2}$	[-]
$C_p$	- Power coefficient: $C_p = \frac{P}{\frac{1}{2}\rho U_W^3 A_d}$	[-]
$c_{xx}$	- Damping in-plane	[kg/s]
$c_{xy}$	- Damping coupling	[kg/s]
$c_{yx}$	- Damping coupling	[kg/s]
$c_{yy}$	- Damping out-of-plane	[kg/s]
$C_{xy}, C_{yz}, C_{x\bar{z}}$	- Products of inertia	[kgm <sup>2</sup> ]
$D_{ax}$	- Axial force	[N]
$\mathbf{D}$	- Angular momentum	[kgm <sup>2</sup> /s]
$E$	- Modulus of elasticity	[N/m <sup>2</sup> ]
$\{\underline{\mathbf{E}}_i\}$	- Row of unit vectors defining reference frame $i$	[-]
$\mathbf{F}$	- Force	[N]
$\mathbf{F}_{aero}$	- Aerodynamic force	[N]
$F_x$	- Force in-plane	[N]
$F_y$	- Force out-of-plane	[N]
$g$	- Gravitational acceleration	[m/s <sup>2</sup> ]

$\mathbf{g}$	- Gravitational acceleration vector	$[m/s^2]$
$G$	- Modulus of elasticity in shear	$[N/m^2]$
$h$	- Height	$[m]$
$H_d$	- Total head downstream of the disc	$[N/m^2]$
$H_u$	- Total head upstream of the disc	$[N/m^2]$
$\mathbf{i}$	- Unit vector defining $x$ direction	$[-]$
$I_x$	- Area moment of inertia with respect to $x$ axis	$[m^4]$
$I_p$	- Polar moment of inertia	$[m^4]$
$I_{xx}$	- Mass moment of inertia about the $x$ axis	$[kgm^2]$
$I_{yy}$	- Mass moment of inertia about the $y$ axis	$[kgm^2]$
$I_{zz}$	- Mass moment of inertia about the $z$ axis	$[kgm^2]$
$\mathbf{I}$	- Momentum	$[kgm/s]$
$\mathbf{j}$	- Unit vector defining $y$ direction	$[-]$
$[J]$	- Jacobian	
$[J_{cg}]$	- Inertia matrix about the c.g. of the element	$[kgm^2]$
$\mathbf{k}$	- Unit vector defining $z$ direction	$[-]$
$k$	- Partitioning factor	$[-]$
$k$	- Spring stiffness	$[N/m]$
$k$	- Spring stiffness	$[Nm/rad]$
$m$	- Mass	$[kg]$
$\mathbf{M}$	- Moment	$[Nm]$
$M_\beta$	- Moment about the flap hinge	$[Nm]$
$M_\varepsilon$	- Moment about $\varepsilon$ axis	$[Nm]$
$M_\zeta$	- Moment about the lead-lag hinge	$[Nm]$
$N$	- Number of degrees of freedom	
$NT$	- Number of degrees of freedom plus controlled rotations	
$p_\infty$	- Pressure in far wake and far before disc	$[N/m^2]$
$p_d^+$	- Pressure just in front of disc	$[N/m^2]$
$p_d^-$	- Pressure just behind the disc	$[N/m^2]$
$p_i$	- Hamilton's generalised momentum of element $i$ : $p_i = \frac{\partial T}{\partial \dot{q}_i}$	$[kgm^2/s]$
$P$	- Power	$[Watt]$
$q$	- Distributed force	$[N/m]$
$q_i$	- Generalised Lagrangian coordinate	$[-]$ or $[m]$
$Q$	- Torque	$[Nm]$
$Q_i$	- Generalised force for DOF $i$	$[Nm]$ or $[N]$
$r$	- Local radial position	$[m]$
$\mathbf{r}$	- Position vector	$[m]$
$R$	- Blade radius	$[m]$
$[R_i]$	- Rotation transformation matrix for $q_i$	$[-]$
$T$	- Kinetic energy	$[J]$
$[T_{RB}]$	- Transformation matrix from in-plane to principal directions	$[-]$
$u_i$	- Induced velocity	$[m/s]$

---

$u_p$	- Dimensionless velocity in perpendicular direction: $\frac{V_p}{\Omega r}$	[-]
$u_t$	- Dimensionless velocity in tangential direction: $\frac{V_t}{\Omega r}$	[-]
$U_\infty$	- Undisturbed wind velocity	[m/s]
$U_d$	- Velocity of wind at rotor swept area: $U_d = (1 - a)V_\infty$	[m/s]
$U_{eff}$	- Local velocity at the blade elements	[m/s]
$U_{Ti}$	- Tangential induced velocity	[m/s]
$U_W$	- Velocity of the wind in the far wake	[m/s]
$v$	- Vertical deflection	[m]
$V$	- Potential energy	[J]
$V$	- Total velocity	[m/s]
$V_e$	- Elastic energy	[J]
$V_g$	- Potential energy due to gravitational forces	[J]
$\mathbf{V}$	- Velocity	[m/s]
$\mathbf{V}_{cg}$	- Velocity of the centre of gravity	[m/s]
$W$	- Work done	[J]
$x$	- x coordinate, distance	[m]
$y$	- y coordinate, distance	[m]
$z$	- z coordinate, distance	[m]

### Greek symbols

$\alpha$	- Angle of attack	[rad]
$\beta$	- Flapping angle	[rad]
$\gamma$	- Lock number $\gamma = \frac{\rho c_{l\alpha} c^* R^4}{I}$	[-]
$\gamma$	- Shear strain	[-]
$\delta$	- A small increment	
$\varepsilon$	- Normal strain	[-]
$\zeta$	- Lead-lag angle	[rad]
$\theta$	- Pitch angle	[rad]
$\theta_{aero}$	- Aerodynamic pitch angle	[rad]
$\theta$	- Angle of twist per unit length	[rad]
$\kappa$	- Curvature	[1/m]
$\lambda$	- Tip speed ratio: $\lambda = \frac{\Omega R}{U_\infty}$	[-]
$\lambda_i$	- $\frac{u_i}{\Omega r}$	[-]
$\lambda_r$	- Local speed ratio: $\lambda_r = \frac{\Omega r}{U_\infty}$	[-]
$\mu$	- Non-dimensional radial position: $\mu = \frac{r}{R}$	[-]
$\mu$	- $\mu = \frac{U}{\Omega r}$	[-]
$\nu$	- Kinematic viscosity	[m <sup>2</sup> /s]
$\nu$	- Poisson's ratio	[-]
$\nu_\beta$	- Non-dimensionalised rotating flap frequency	[-]
$\rho$	- Air density	[kg/m <sup>3</sup> ]

---

$\rho$	- Radius	[m]
$\rho$	- Radius of curvature	[m]
$\sigma$	- Normal stress	[N/m <sup>2</sup> ]
$\tau$	- Shear stress	[N/m <sup>2</sup> ]
$\phi$	- Local flow angle	[rad]
$\phi$	- Angle of twist	[rad]
$\psi$	- Azimuthal angle	[rad]
$\omega_i$	- Total rotational velocity vector of element $i$	[rad/s]
$\Omega$	- Rotational velocity	[rad/s]

### Subscripts

$cg$	- Centre of gravity
$hg$	- Hinge connecting the <i>next</i> element
$nc$	- Nonconservative
$rot$	- Corresponding to rotation
$st$	- Hinge connecting the <i>previous</i> element
$tip$	- Corresponding to tip
$trans$	- Corresponding to translation
$x$	- Corresponding to $x$ -direction
$y$	- Corresponding to $y$ -direction
$z$	- Corresponding to $z$ -direction
$0$	- Equilibrium state
$\times$	- Operator matrix form of row, changes cross product to matrix product

### Superscripts

*	- Representative value at $\frac{3}{4}R$
'	- Slope

### Notations

$(\dot{\quad})$	- Time derivative: $\frac{d}{dt}$
$(\ddot{\quad})$	- Second time derivative: $\frac{d^2}{dt^2}$
$(\quad)'$	- Derivative with respect to azimuth: $\frac{d}{d\psi}$
$\mathbf{a}$	- Vector
$(\underline{a})$	- Row $(a_1, a_2, \dots, a_n)$
$\{\underline{a}\}$	- Column $(a_1, a_2, \dots, a_n)^T$
$\frac{\partial}{\partial q_i}$	- Partial derivative w.r.t. $q_i$ keeping all other values for $\{\underline{q}\}$ and all values

$\frac{\partial^p q}{\partial q_i}$  of  $\{\underline{q}\}$  constant  
- Partial derivative w.r.t.  $q_i$  keeping all other values of  $\{\underline{q}\}$  and all values of  $\{\underline{p}\}$  constant



# Summary

Over the years it has become clear that renewable energy is an absolute necessity and wind energy is one alternative source of energy that can replace part of the non-renewable energy generation. Generating the energy from the wind by slowing the wind down must however still be further developed before it becomes economically viable. As the wind velocity and therefore the possible energy to be gained from the wind is higher at greater height, wind turbines have been getting larger and larger over the years. Another reason for the increase in size is the placement at sea, where the wind is stronger and there is more space available, but at sea installation and maintenance becomes very expensive and therefore it is beneficial to have less machines that are larger rather than many smaller turbines. Increasing the size of the turbines has resulted in a price reduction for the electricity per kWh, but it has created new possible aeroelastic problems.

For example, in practice the larger blade designs have resulted in a flap frequency that is closer to the lead-lag frequency than was the case for the smaller blades. If these frequencies are close together, it could result in unexpected aeroelastic instabilities. The aeroelastic stability of wind turbines can be investigated by simulating models of the turbines under different conditions: wind condition, pitch angle setting and rotational velocity will influence the aeroelastic stability. The development and use of one fully nonlinear aeroelastic tool is described. This tool, WOBBE, has been developed especially for large wind turbines, but it can also be used for smaller turbines as well as many other systems with bending and torsional degrees of freedom, e.g. helicopters.

The calculations in WOBBE are performed using nonlinear dynamics combined with nonlinear aerodynamics. The somewhat arbitrary process of linearising is therefore not necessary. The importance of performing fully nonlinear calculations is shown by discussing the differences between the results from a linear programme and WOBBE. The combination of using linearised tools to identify the possible problem areas and nonlinear tools to zoom in on these possible unstable conditions seems to be a logical approach of the aeroelastic analysis during the design.

WOBBE simulates multi-body systems, where the rigid bodies are interconnected with hinges, springs and dampers. The aerodynamic forces acting on this system are calculated using the blade element momentum method. The calculations of the motions are performed using Hamilton's generalised momenta and the generalised coordinates as state variables. If

there are any unknown or unexpected instabilities for the given setting, these will also show up in the simulations, as the method does not focus solely on expected instabilities.

The modelling method that is used is very important. Using so-called superelements, the correct frequencies will show up in the results using only a few elements. The minimum number of superelements that needs to be used in a model in order to produce reliable results has been investigated. From this investigation it can be concluded that one needs to include at least one superelement more than the number of frequencies in one direction that need to be modelled with enough accuracy. The method used to calculate the stiffnesses of the springs has also been investigated. For a structure that does not have a uniform bending stiffness, the average bending stiffness needs to be determined over half the length of the superelement to find the values of the springs in that half of the superelement. The structural pitch can also be modelled in several ways. Different methods have been looked at in an attempt to find out which method would be the best method. This investigation did however not show one method being distinctively better than the others.

After verification and benchmarking, the programme WOBBE has also been validated. Measurements were performed on an NM-80 wind turbine and the results from these measurements were compared to the results from WOBBE using a model with 27 degrees of freedom. In order to compare the calculations to the measurements, linear identification has been used to extract the frequencies and the damping of the different modes from the simulation results. A large drawback for WOBBE showed up during the validation. The code is not a fast code and a small increase in the number of degrees of freedom results in a large increase in the calculation time. Next to this, it is necessary to run at least two simulations before the linear identification gives good results; first a simulation has to be run to determine the steady state, second a simulation has to be run with a small initial deflection from this steady state. The results from this simulation are used for the identification. If the initial deflection is too large or too small, a new simulation needs to be run using a smaller or larger initial deflection, respectively. This entire process takes up a lot of computation time. This has limited the validation of the tool, the simulations for the validation were performed for only three wind speeds.

Finally the possibility of flap-lag-stall flutter occurring on large wind turbines has been investigated using WOBBE. The upscaling of wind turbines has resulted in the flap frequency coming closer to the lead-lag frequency. Therefore instabilities that concern these two frequencies being close to each other, become realistic possibilities. The investigations have shown that flap-lag-stall flutter is not likely to occur on large wind turbines. In the cases that flap-lag-stall flutter could occur, negative damping of the first edgewise mode would also show up and be more critical. Flap-lag flutter was found to occur without negative damping of the first edgewise mode in cases that concern unrealistic blade configurations and the operation was not near or in stall.

The tool WOBBE would be an even more useful tool for aeroelastic analysis, if the computation time is further reduced. There are several possibilities for this, therefore further development of the code could decrease or eliminate this problem. It is also possible and

recommended to further extend the programme by adding translational degrees of freedom. This would increase the use for helicopter analysis.



# Samenvatting

Het is de afgelopen jaren duidelijk geworden dat groene energie noodzakelijk is. Windenergie is een alternatieve bron van energie die een deel van de niet-duurzame energie kan vervangen. Energie maken van de wind door de wind te vertragen moet echter nog verder ontwikkeld worden om deze vorm van energiewinning economisch leefbaar te maken. Aangezien de windsnelheid en daarom ook de energie die uit de wind gewonnen kan worden, op grotere hoogte hoger is, worden windturbines steeds groter. Een andere reden voor de grotere turbines is het plaatsten van turbines op zee, waar de wind sterker is en er meer vrije ruimte beschikbaar is. Installatie en onderhoud zijn echter erg kostbaar en daarom is het voordeliger om enkele grotere turbines te plaatsen in plaats van meerdere kleinere. Het vergroten van de windturbines heeft geresulteerd in een kostenreductie voor de elektriciteit per kWh, maar het heeft ook de mogelijkheid van nieuwe aeroelastische problemen gecreëerd.

In de praktijk is bijvoorbeeld gebleken dat de bladontwerpen geresulteerd hebben in een klapproefrequentie die dicht bij de zwaai-frequentie is gekomen dan het geval was voor kleinere bladen. Dit kan resulteren in onverwachte aeroelastische instabiliteiten. De aeroelastische stabiliteit van windturbines kan onderzocht worden door modellen van de turbines te simuleren onder verschillende condities: de windconditie, spoedhoekinstelling en de rotatiesnelheid zullen effect hebben op de aeroelastische stabiliteit. De ontwikkeling en het gebruik van een volledig niet-lineair aeroelastisch programma wordt beschreven. Dit programma, WOBBE, is speciaal ontwikkeld voor grote windturbines, maar het kan ook gebruikt worden voor kleinere turbines en voor veel andere systemen die over buigings- en torsie-vrijheidsgraden beschikken, zoals helikopters.

De berekeningen in WOBBE worden gedaan door gebruik te maken van niet-lineaire dynamica gecombineerd met niet-lineaire aerodynamica. Het enigszins arbitraire proces van lineariseren is daardoor niet nodig. Het belang van volledig niet-lineair rekenen wordt geïllustreerd door te kijken naar de verschillen tussen resultaten behaald met een lineair programma en de resultaten van WOBBE. Het lijkt een logische aanpak om tijdens het ontwerp met een gelineariseerd programma de mogelijke probleemgebieden te identificeren om vervolgens met niet-lineaire codes in te zoomen op deze mogelijk instabiele condities.

WOBBE simuleert multi-body systemen, waar de starre lichamen onderling verbonden zijn met scharnieren, veren en dempers. De aerodynamische krachten die op het systeem werken, worden berekend door gebruik te maken van de blad-element-impuls methode (BEM). De

berekeningen van de bewegingen worden uitgevoerd met Hamilton's gegeneraliseerde impuls en de gegeneraliseerde coördinaten als toestandsvariabelen. Als er onbekende of onverwachte instabiliteiten zijn voor de gegeven instellingen, dan zullen deze in de simulaties naar boven komen, omdat de methode niet alleen focust op verwachte instabiliteiten.

De modelleermethode die gebruikt wordt, is zeer belangrijk. Wanneer zogenoemde superelementen worden gebruikt, komen de correcte frequenties al bij gebruikmaking van slechts enkele elementen in het model tevoorschijn in de resultaten. Het minimum aantal superelementen dat nodig is in een model om betrouwbare resultaten te genereren, is onderzocht. Hieruit is gebleken dat men één superelement meer in het model moet hebben dan het aantal frequenties dat men in een richting met redelijke accuratie moet modelleren. De methode die gebruikt wordt om de stijfheid van de veren te berekenen, is ook onderzocht. Voor een constructie die niet een uniforme buigstijfheid heeft, moet de gemiddelde stijfheid over een half superelement worden bepaald om de stijfheden te berekenen van de veren in die helft van het superelement. De structurele wrong kan ook op verschillende manieren worden gemodelleerd. Verschillende methoden zijn onderzocht in een poging uit te vinden welke methode de beste is. Hier kwam echter geen duidelijke winnaar uit te voorschijn.

Na verificatie en benchmarking is het programma WOBBE ook gevalideerd. De resultaten van metingen aan de NM-80 windturbine zijn vergeleken met de resultaten van WOBBE voor een model met 27 graden van vrijheid. Om de berekeningen te kunnen vergelijken met de metingen is lineaire identificatie gebruikt. Daarmee zijn de frequenties en de dempingswaarden van de verschillende modes bepaald. Een groot nadeel van WOBBE werd tijdens de validatie duidelijk. De code is niet een snelle code en een kleine toename in het aantal vrijheidsgraden resulteert in een grote toename van de benodigde rekentijd. Daarnaast is het noodzakelijk om minstens twee simulaties te draaien, voordat de lineaire identificatie goede resultaten kan geven. De eerste simulatie is nodig om de evenwichtssituatie te bepalen, de tweede simulatie moet beginnen met een kleine initiële uitwijking van deze evenwichtssituatie. Als deze initiële uitwijking te groot of te klein blijkt te zijn, dient er een nieuwe simulatie gedaan te worden met respectievelijk een kleinere of grotere beginuitwijking. Dit hele proces kost veel rekentijd. Hierdoor is de validatie van het programma beperkt gebleven: slechts drie windsnelheden zijn gesimuleerd ten behoeve van de validatie.

Tenslotte is de mogelijkheid van het optreden van 'flap-lag-stall' flutter bij grote windturbines onderzocht aan de hand van WOBBE. Het groter maken van de windturbines heeft erin geresulteerd dat de klapfrequentie dicht bij de zwaai-frequentie is komen te liggen. Instabiliteiten die op kunnen treden indien deze twee frequenties dicht bij elkaar zijn, worden daarmee realistische mogelijkheden. Het onderzoek heeft aangetoond dat 'flap-lag-stall' flutter kan optreden, maar dat negatieve demping van de eerste zwaai mode dan ook op zal treden en kritischer zal zijn. Een klap-zwaai instabiliteit werd wel gevonden zonder negatieve demping van de eerste zwaai mode, maar desbetreffende bladconfiguratie is verre van realistisch. Bovendien was er geen sprake van overtrek.

Het programma WOBBE zou een nog veel nuttiger gereedschap voor aeroelastische analyse kunnen zijn, als de rekentijd verder wordt gereduceerd. Door verdere ontwikkeling van de

code zou dit probleem kunnen worden verminderd of geëlimineerd, en daartoe bestaan wel degelijk mogelijkheden. Het is ook mogelijk en aan te raden om het programma verder uit te breiden met translatie vrijheidsgraden. Dit zou de mogelijkheden voor helikopter analyse vergroten.



# Chapter 1

## Introduction

*Whatever is produced in haste goes hastily to waste.*

- Saadi

The current generation in Western society is living in more prosperity and luxury than ever before. This has resulted in consumption increasing rapidly, giving rise to a huge growth in the total energy demand. Obviously, this consumption philosophy cannot be sustained for a long time, provided we want to leave a fruitful and pleasant planet earth behind for future generations. The main sources of energy currently used, are fossil fuels that are not renewable, at some point the reserves of these fuels will run out. Therefore alternatives have to be implemented before this occurs.

The energy from the wind has been used for over three thousand years and for over a century there have been wind turbines that generate electricity. The past decades electrical energy generating wind turbines have been getting a lot more attention from politicians, businesses and consumers, as it is probably one of the necessary solutions. In this period, the amount of energy produced from the wind in the world has increased exponentially and this trend is still being continued. This dissertation has been written to contribute to the continuation of the successful development of this alternative source of energy.

This chapter starts with a section further discussing the necessity of wind energy and why aeroelastic analysis of wind turbines is of importance. This is followed by the description of the goal of this dissertation. Finally a short outline is given of the structure of this dissertation.

### 1.1 Wind Energy

Over the years it has become painfully clear that renewable energy is a necessity. People are not willing, or maybe not able, to reduce their energy consumption. Actually, as shown

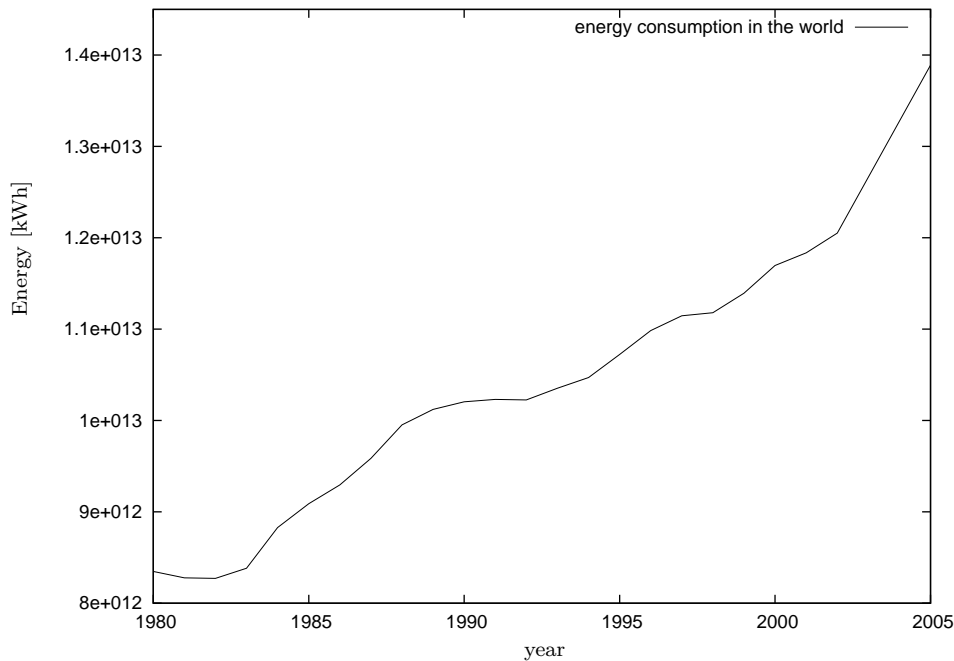


Figure 1.1: World wide energy consumption over the past 25 years shows a steep increase [source: Energy Information Administration]

in figure 1.1, the consumption is still increasing rapidly and as more and more countries are further developing, it will not stop increasing at this high rate any time soon. The effect of greenhouse gasses is already noticeable and therefore alternatives for the fossil fuels are necessary. Next to this, there is the fact that the fossil fuels will at some point run out, there are only limited reserves available, which strongly increases the need for alternative sources of energy.

Wind energy is one alternative source of energy that can replace part of the non-renewable energy generation. Only a part, because the wind cannot be controlled neither be predicted very well. This means that there will be times when the wind is not strong enough to generate any energy and it also means that the connection to the grid becomes very difficult if a large part of the necessary energy would be provided by wind turbines.

Especially in wind-rich countries, like most countries of Europe, wind energy is a very useful alternative for a part of the currently fossil fuel generated energy. Generating the energy from the wind by slowing the wind down must however still be further developed in order to make it not only environmentally friendly, but also economically viable. As the wind velocity and therefore the possible energy to be gained from the wind is higher at greater height, wind turbines are getting larger and larger. Another reason for the increase in size is the placement at sea. The wind is stronger at sea and there is more free space, but installation and maintenance becomes very expensive and therefore it is beneficial to have less machines that are larger (especially since noise is not a real problem at sea) rather than many smaller



Figure 1.2: Two examples of broken wind turbines, source: youtube.com

turbines. Therefore the incentive to reduce the cost of the generated electricity has led to larger and larger wind turbines. In 1990 the average wind turbine that was installed would be around 500 kW and have a diameter between 30 and 50 meters [76], while currently the turbine rotors have diameters of around 90 meters producing 3 MW.

Increasing the size of the turbines has resulted in a price reduction for the electricity per kWh, but it has created new possible aeroelastic problems. Due to the fact that the energy generated by a wind turbine will depend on the volume of wind that passes the rotor each second, a higher velocity at greater altitude from the ground or sea and a larger rotor swept area will increase the power of the turbine. However, the costs of a turbine will roughly depend on its mass, thus on the radius cubed ( $R^3$ ), while the rotor swept area will depend on its radius squared ( $R^2$ ). Scaling the turbine would therefore result in the cost going up by  $(\frac{R_{new}}{R_{old}})^3$ , while the energy will only go up roughly by  $(\frac{R_{new}}{R_{old}})^2$ , the so-called square-cube law. For this reason the larger blades are usually designed such that the increase in mass is less than  $(\frac{R_{new}}{R_{old}})^3$ . In practice the larger blade designs have resulted in a flap frequency that is closer to the lead-lag frequency than was the case for the smaller blades [138]. This could result in unexpected aeroelastic instabilities. For example Moeller reports [95] that 0.5% of the LM Glasfiber 19 m blades were damaged within eight to nine months. These blades were installed on 600 kW turbines in different places in the world. Severe edgewise vibrations produced longitudinal cracks. The changes in wind turbine designs due to the increase in size could result in other not yet known instabilities, therefore it is important to thoroughly investigate the aeroelastic stability of each new design.

It is required that wind turbines become more reliable and incidents such as shown in figure 1.2 must be prevented. Not only for economical and environmental reasons but also for public opinion. There are many people in favour of wind energy, but there is also a relevant number of opponents. And incidents as shown in this picture will not do the public opinion any good.

Incidents can occur for many different reasons, for example lightning, extreme weather conditions, design faults or human error. Neglecting the investigation of the aeroelastic stability of wind turbines can result in incidents that should have been prevented. Therefore it is important to thoroughly investigate the aeroelastic stability and not to neglect it during the design process.

## 1.2 Goal of this Dissertation

The aeroelastic stability of wind turbines can be investigated by simulating models of the turbines under different conditions. Wind condition, pitch angle setting and rotational velocity will influence the aeroelastic stability. This dissertation describes the development and use of one fully nonlinear aeroelastic tool that has been developed especially for large wind turbines, but it can also be used for many other systems with bending and torsional degrees of freedom, e.g. helicopters [89]. This tool is called WOBBE [104]. The calculations are performed using nonlinear dynamics and nonlinear aerodynamics. This is important, because linearising is always a somewhat arbitrary process where experience is used to determine which terms can and cannot be left out of the equations. The importance of performing fully nonlinear calculations will be shown by discussing the differences between the results from linear programmes and WOBBE. The combination of using linearised tools to investigate the possible problem areas and nonlinear tools to zoom in on these possible unstable conditions seems to be a logical approach of the aeroelastic analysis during the design.

WOBBE simulates multi-body systems, where the rigid bodies are interconnected with hinges, springs and dampers. The aerodynamic forces acting on this system are calculated by the programme. The blade element momentum method is used for these calculations. The calculations of the motions are performed using Hamilton's generalised momenta and the generalised coordinates as state variables. WOBBE has been developed purely to perform simulations to determine the aeroelastic (in)stability of the system, not to determine the stresses in the components of the turbine. If there are any unknown or unexpected instabilities for the given setting, these will also show up in the simulation, as the method does not focus solely on expected instabilities. Next to the fact that WOBBE performs the simulations fully nonlinear, this is another advantage of the programme.

The way to model a wind turbine is very important. If the model is incorrect, the results will never be of any use (garbage in, garbage out). Using so-called superelements [94, 119, 120], the correct frequencies will show up in the results using only a few elements. This can easily be tested by simulating a beam for which the theoretical eigenfrequencies are known. Using WOBBE, this test has been performed and as a result, superelements have been chosen for the models used in this programme. WOBBE is a useful tool to perform the final check in the design process. Due to the fact that the equations of motion do not need to be derived, it is also a useful tool to investigate the detail necessary to perform reliable simulations. The user can easily change the complexity of the model and perform new simulations without

much preparation time. The minimum number of superelements that needs to be used in a model in order to produce reliable results has been investigated, resulting in some guidelines concerning the model. The method used to calculate the stiffnesses of the springs has also been investigated. The structural pitch can also be modelled in several ways. Different methods have been looked at in an attempt to find out which method would be the best method.

The programme has been validated. Measurements were performed on an NM-80 wind turbine and the results from these measurements were compared to the results from WOBBE. This validation process is described in the dissertation and is of great importance. Without validation the programme could only be used to signal trends. Being validated, it can actually be used in the determination of the stability of wind turbines.

Finally the possibility of flap-lag-stall flutter occurring on large wind turbines has been investigated using WOBBE. As discussed in the previous section, the upscaling of wind turbines has resulted in the flap frequency coming closer to the lead-lag frequency. Therefore instabilities that concern these two frequencies being close to each other, become realistic possibilities.

## 1.3 Outline

Figure 1.3 shows the structure of this dissertation. As shown in this figure, chapters 2, 3 and 4 deal with background information concerning dynamics, aerodynamics and aeroelasticity respectively. The next two chapters explain the theory behind the simulation programme WOBBE and the structure of the programme. The method to model wind turbines is discussed in chapter 7. The verification and validation of the programme is described in chapter 8. The calculation methods for the model properties are discussed in chapter 9. Chapter 10 deals with the possibility of flap-lag-stall flutter. Finally the last chapter gives the conclusions and the recommendations for further improvements to the tool.

The appendices are also shown in figure 1.3. The figure shows for every appendix which chapter is supported by the appendix.

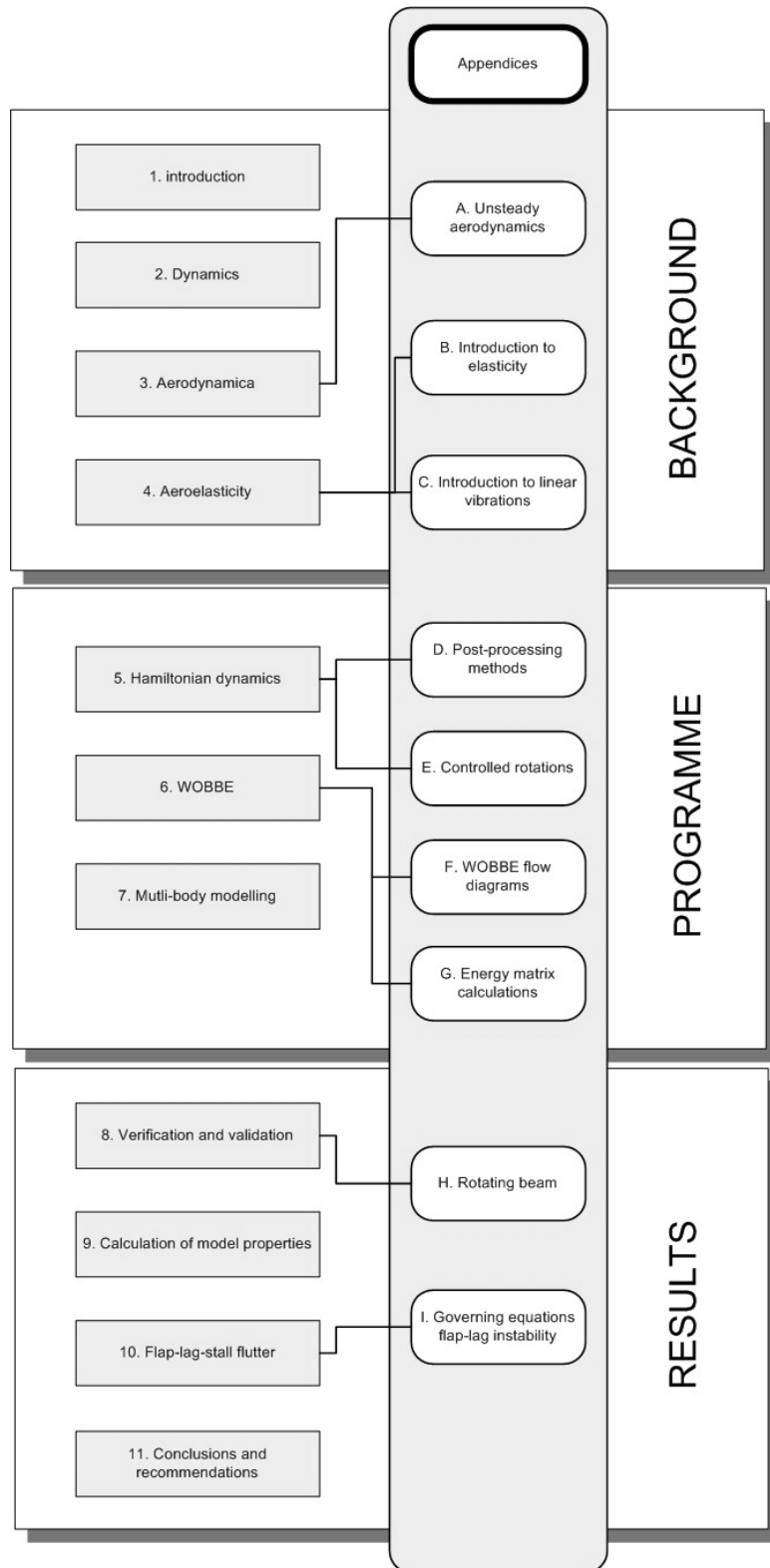


Figure 1.3: The structure of this dissertation

# Chapter 2

## Dynamics

*"Give me but one firm spot on which to stand, and I will move the earth."*<sup>1</sup>

- Archimedes

In order to investigate aeroelastic stability of wind turbines it is necessary to determine the equations of motion of the system. These equations of motion come in many different forms. Some of the more common methods of deriving the equations of motion are described in this chapter. This chapter will only give a limited introduction into the field of the dynamics, the dynamics field is much more extensive than can be discussed here. This chapter is limited to rigid body dynamics and only two methods to derive the equations of motion are described. First the Newtonian dynamics are described. Both a conventional method and an alternative method using matrix notations for the vector products are explained. The second section discusses Lagrange's equations, which are used in chapter 5 to derive an alternative set of equations that describes the motion.

### 2.1 Newtonian Dynamics

The procedure needed to find the equations of motion for dynamic systems is derived in this section. First the conventional notations will be used. The second part shows the matrix notations, a method that is especially well suited to use in combination with symbolic manipulation software. It is also very suitable for simulation tools.

There are many good books describing dynamics in conventional notations e.g. [4, 90]. The vector and matrix notations are partly described by Ginsberg [38] and a full treatment of the method is given by Th. van Holten *et al.* in [66].

---

<sup>1</sup>on the action of a lever

### 2.1.1 Conventional Notations

#### Particles

Sir Isaac Newton has stated three laws with which he laid out the foundation for current mechanics [98]. These three laws are valid when the speed is significantly smaller than the speed of light and they concern point masses. Newton's first law states that an object can only accelerate if a force acts on this object. The second law states that the acceleration of this object is proportional to the force:

$$\mathbf{F} = m\mathbf{a} \quad (2.1)$$

The third law states that action equals reaction. This law is very important and useful when deriving equations of motion as will be shown further on in the section.

Newton's second law (equation 2.1) is the basic equation used to derive equations of motion. First, from this equation it is possible to derive the work-energy principle. Multiplying Newton's 2<sup>nd</sup> law with an infinitesimal distance  $d\mathbf{r}$  gives:

$$\mathbf{F} \cdot d\mathbf{r} = m\mathbf{a} \cdot d\mathbf{r} \quad (2.2)$$

The right hand side can be rewritten:

$$m\mathbf{a} \cdot d\mathbf{r} = m\mathbf{a} \cdot \frac{d\mathbf{r}}{dt}dt = m\frac{d\mathbf{V}}{dt} \cdot \mathbf{V}dt = \frac{1}{2}m\frac{d\mathbf{V} \cdot \mathbf{V}}{dt}dt = \frac{1}{2}md(V^2) \quad (2.3)$$

The path integral of this equation gives:

$$\int_1^2 \mathbf{F} \cdot d\mathbf{r} = \frac{1}{2}m(V_2^2 - V_1^2) \quad (2.4)$$

where 1 indicates the initial position and 2 the final position. The kinetic energy of a particle is defined as:

$$T = \frac{1}{2}mV^2 \quad (2.5)$$

And the work done by the force is defined as:

$$W_{1 \rightarrow 2} = \int_1^2 \mathbf{F} \cdot d\mathbf{r} \quad (2.6)$$

This results in the work-energy principle:

$$T_2 = T_1 + W_{1 \rightarrow 2} \quad (2.7)$$

stating that the kinetic energy at time 2 is equal to that at time 1 plus the work done between the two moments in time.

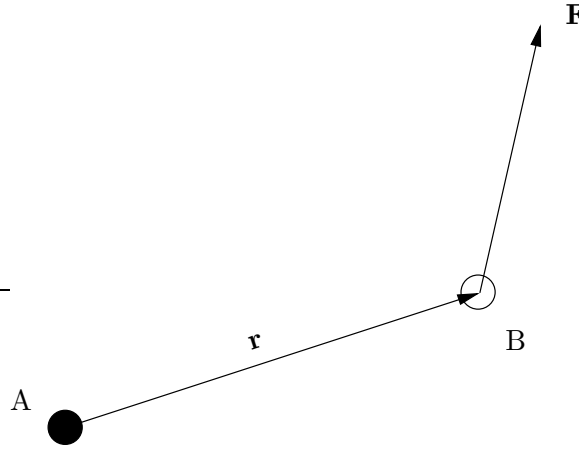


Figure 2.1: A point mass in point B with a force acting on it and the arm to reference point A.

From equation 2.1 it is also possible to derive the linear impulse-momentum principle. If the force acting on the particle is a known function of time, the second law of Newton can be integrated in time:

$$\int_{t_1}^{t_2} \mathbf{F} dt = \int_{t_1}^{t_2} m \mathbf{a} dt = [m\mathbf{V}]_1^2 = m(\mathbf{V}_2 - \mathbf{V}_1) \quad (2.8)$$

where the momentum of a particle moving along a (possibly curved) line is defined as  $m\mathbf{V}$ . The term  $\int_{t_1}^{t_2} \mathbf{F} dt$  is called the impulse. This equation therefore shows that the difference in momentum between  $t_2$  and  $t_1$  is equal to the impulse acting on the particle. It is often used for forces that result in a large acceleration in a short time interval or when the force is known as a function of time.

Now looking at the moment of a force acting on a particle at a certain distance from a reference point, the angular momentum principle can be derived.

The moment due to the force about reference point A, as shown in figure 2.1, is:

$$\mathbf{M}_A = \mathbf{r}_{BA} \times \mathbf{F} \quad (2.9)$$

Using equation 2.1, this can be written as:

$$\mathbf{M}_A = \mathbf{r}_{BA} \times m\mathbf{a} = \mathbf{r}_{BA} \times m \frac{d\mathbf{V}}{dt} \quad (2.10)$$

It is possible to take the time derivative on the right hand side outside the cross-product:

$$\mathbf{M}_A = \frac{d}{dt}(\mathbf{r} \times m\mathbf{V}) - m \frac{d\mathbf{r}}{dt} \times \mathbf{V} = \frac{d}{dt}(\mathbf{r} \times m\mathbf{V}) - \mathbf{V} \times m\mathbf{V} = \frac{d}{dt}(\mathbf{r} \times m\mathbf{V}) \quad (2.11)$$

The angular momentum of a particle is defined as:

$$\mathbf{D}_A = \mathbf{r} \times dm\mathbf{V} \quad (2.12)$$

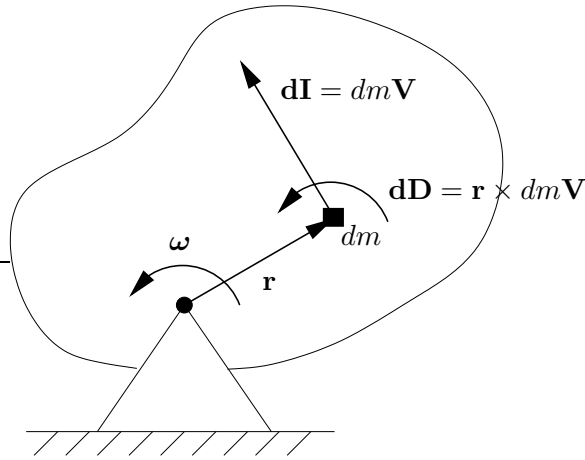


Figure 2.2: Angular momentum, two dimensional

therefore

$$\mathbf{M}_A = \frac{d}{dt} \mathbf{D}_A \quad (2.13)$$

This expression can be integrated over time resulting in:

$$(\mathbf{D}_A)_2 = (\mathbf{D}_A)_1 + \int_{t_1}^{t_2} \sum \mathbf{M}_A dt \quad (2.14)$$

A particle can be a mass element that is part of a rigid body. The momentum of such a mass element  $dm$  with place vector  $\mathbf{r}$  is defined as:

$$d\mathbf{I} = dm\mathbf{V} = dm\dot{\mathbf{r}} \quad (2.15)$$

The angular momentum  $d\mathbf{D}$  of a mass element  $dm$  that is part of a rigid body rotating about a fixed point is defined as:

$$d\mathbf{D} = \mathbf{r} \times dm\dot{\mathbf{r}} \quad (2.16)$$

In figure 2.2 an example is given of the angular momentum of a mass element that is part of a two-dimensional rigid body. The angular momentum of the mass element is a vector perpendicular to the page, pointing towards the reader. The velocity of the mass element can be written as:

$$\dot{\mathbf{r}} = \boldsymbol{\omega} \times \mathbf{r} \quad (2.17)$$

The angular momentum becomes:

$$d\mathbf{D} = \mathbf{r} \times dm\dot{\mathbf{r}} = \mathbf{r} \times dm(\boldsymbol{\omega} \times \mathbf{r}) \quad (2.18)$$

The angular momentum of a mass element as defined in equation 2.16 can be differentiated in time:

$$\frac{d}{dt}d\mathbf{D} = \dot{\mathbf{r}} \times dm\dot{\mathbf{r}} + \mathbf{r} \times dm\ddot{\mathbf{r}} \quad (2.19)$$

The first term is a cross product of one vector with itself. This is always equal to zero. The second term can be rewritten using Newton, resulting in a cross product of the position times the force acting on the mass element. This is the same as the moment about the rotation point:

$$\frac{d}{dt}d\mathbf{D} = \mathbf{r} \times \mathbf{F} = d\mathbf{M}_0 \quad (2.20)$$

This shows that the derivative of the angular momentum of the mass element with respect to time is equal to the moment about the rotation point.

### Rigid bodies

When looking at a rigid body, Newton's second law must be valid for all particles. The forces acting on particle  $i$  are external forces  $\mathbf{F}_i$  as well as internal forces exerted by the other particles on particle  $i$ :  $\mathbf{f}_{ij}$ . Therefore:

$$\mathbf{F}_i + \sum_{\substack{j=1 \\ j \neq i}}^N \mathbf{f}_{ij} = m_i \mathbf{a}_i \quad (2.21)$$

where  $N$  is the total number of particles in the rigid body. Taking the sum over all particles leads to:

$$\sum_{i=1}^N \mathbf{F}_i + \sum_{i=1}^N \sum_{\substack{j=1 \\ j \neq i}}^N \mathbf{f}_{ij} = \sum_{i=1}^N m_i \mathbf{a}_i \quad (2.22)$$

As a consequence of Newton's third law, the summation of  $\mathbf{f}_{ij}$  becomes zero, resulting in:

$$\sum_{i=1}^N \mathbf{F}_i = \sum_{i=1}^N m_i \mathbf{a}_i \quad (2.23)$$

This equation can be rewritten as:

$$\sum_{i=1}^N \mathbf{F}_i = \frac{d^2}{dt^2} \left( \sum_{i=1}^N m_i \mathbf{r}_{i/O} \right) \quad (2.24)$$

where  $\mathbf{r}_{i/O}$  is the position of mass element  $i$  relative to an inertial point  $O$ . The right hand side term is related to the position of the centre of mass:

$$m\mathbf{r}_{\text{cg}/O} = \sum_{i=1}^N m_i \mathbf{r}_{i/O} \quad (2.25)$$

where  $\mathbf{r}_{\text{cg}/O}$  is the position of the centre of gravity of the rigid body relative to an inertial point  $O$ . This gives:

$$\sum_{i=1}^N \mathbf{F}_i = m\mathbf{a}_{\text{cg}} \quad (2.26)$$

with  $m$  the total mass of the rigid body. This equation shows that the sum of all forces acting on a rigid body must be equal to the acceleration of the centre of gravity times the mass of the rigid body. Note that this is a vector equation, so it must be satisfied in all three directions.

Similar to the derivation given above for the acceleration of a body, it is possible to derive an equation for the resultant moment and the rotation using Newton's second law. The moment about a point A due to the forces acting on a particle  $i$  must be equal to:

$$(\mathbf{M}_A)_i = \mathbf{r}_{i/A} \times \left[ \mathbf{F}_i + \sum_{\substack{j=1 \\ j \neq i}}^N \mathbf{f}_{ij} \right] = \mathbf{r}_{i/A} \times m_i \mathbf{a}_i \quad (2.27)$$

The acceleration of particle  $i$  can be written as:

$$\mathbf{a}_i = \mathbf{a}_A + \frac{d}{dt} \mathbf{v}_{i/A} \quad (2.28)$$

This gives:

$$(\mathbf{M}_A)_i = \mathbf{r}_{i/A} \times m_i \mathbf{a}_A + \mathbf{r}_{i/A} \times m_i \frac{d}{dt} \mathbf{v}_{i/A} = m_i \mathbf{r}_{i/A} \times \mathbf{a}_A + \frac{d}{dt} (\mathbf{r}_{i/A} \times m_i \mathbf{V}_{i/A}) \quad (2.29)$$

In this equation  $m_i \mathbf{V}_{i/A}$  is the momentum of the particle relative to point A, therefore  $\mathbf{r}_{i/A} \times m_i \mathbf{V}_{i/A}$  is the angular momentum of the particle about point A. Taking the sum over all particles, whereby all internal forces are cancelled, gives:

$$\mathbf{M}_A = \sum_{i=1}^N (\mathbf{r}_{i/A} \times \mathbf{F}_i) = \sum_{i=1}^N (m_i \mathbf{r}_{i/A} \times \mathbf{a}_A) + \sum_{i=1}^N \frac{d}{dt} (\mathbf{r}_{i/A} \times m_i \mathbf{V}_{i/A}) \quad (2.30)$$

This equation can be written as:

$$\mathbf{M}_A = \sum_{i=1}^N (\mathbf{r}_{i/A} \times \mathbf{F}_i) = m\mathbf{r}_{\text{cg}/A} \times \mathbf{a}_A + \dot{\mathbf{D}}_A \quad (2.31)$$

with  $\mathbf{D}_A$  the angular momentum of the rigid body about point A. This equation can be further reduced if the term  $\mathbf{r}_{cg/A} \times \mathbf{a}_A$  becomes zero. This will be the case when point A is chosen in the centre of gravity or when the acceleration of point A is equal to zero. A third option would be that the acceleration of point A is parallel to  $\mathbf{r}_{cg/A}$  in which case the cross-product will also become zero. This will only occur instantaneously and is therefore not a useful option. The most commonly used expression is the equation when using the centre of gravity as reference point:

$$\mathbf{M}_{cg} = \dot{\mathbf{D}}_{cg} \quad (2.32)$$

This is another vector equation that must be satisfied in all three directions. Therefore there are now six equations available (three from equation 2.26 and three from equation 2.32) for six degrees of freedom: three translations and three rotations. With these equations it is therefore possible to determine the motion of the rigid body.

The angular momentum for a three dimensional body, as used in equation 2.32, is defined as the volume integral of equation 2.18:

$$\mathbf{D} = \iiint \mathbf{r} \times dm\dot{\mathbf{r}} \quad (2.33)$$

The rotational velocity can be written as:

$$\boldsymbol{\omega} = (p, q, r) \quad (2.34)$$

This gives:

$$\mathbf{D} = \iiint \mathbf{r} \times dm\dot{\mathbf{r}} = (p, q, r)[J] \quad (2.35)$$

where the integration is over all mass elements of the body. In this equation [J] can be derived by calculating the cross-products in equation 2.18 and rewriting the expression. Using the identity:

$$\mathbf{a} \times (\mathbf{b} \times \mathbf{c}) = (\mathbf{a} \cdot \mathbf{c})\mathbf{b} - (\mathbf{a} \cdot \mathbf{b})\mathbf{c} \quad (2.36)$$

gives

$$\begin{aligned} d\mathbf{D} &= \mathbf{r} \times dm\dot{\mathbf{r}} = (x, y, z) \times dm((p, q, r) \times (x, y, z)) \\ &= ((x, y, z) \cdot (x, y, z))dm(p, q, r) - ((x, y, z) \cdot (p, q, r))dm(x, y, z) \\ &= (x^2 + y^2 + z^2)dm(p, q, r) - (px + qy + zr)dm(x, y, z) \\ &= (p(y^2 + z^2) - qxy - rxz, q(x^2 + z^2) - pxy - rxy, r(x^2 + y^2) - pxz - qyz)dm \\ &= (p, q, r) \begin{bmatrix} y^2 + z^2 & -xy & -xz \\ -xy & x^2 + z^2 & -yz \\ -xz & -yz & x^2 + y^2 \end{bmatrix} dm \end{aligned} \quad (2.37)$$

The volume integral gives the expressions for the inertia matrix that is defined as:

$$[J] = \begin{bmatrix} I_x & -C_{xy} & -C_{xz} \\ -C_{xy} & I_y & -C_{yz} \\ -C_{xz} & -C_{yz} & I_z \end{bmatrix} \quad (2.38)$$

Where the moments of inertia are defined as:

$$\begin{aligned} I_x &= \iiint (y^2 + z^2) dm \\ I_y &= \iiint (x^2 + z^2) dm \\ I_z &= \iiint (x^2 + y^2) dm \end{aligned} \quad (2.39)$$

and the products of inertia are defined as:

$$\begin{aligned} C_{xy} &= \iiint xy dm \\ C_{xz} &= \iiint xz dm \\ C_{yz} &= \iiint yz dm \end{aligned} \quad (2.40)$$

Similar as shown for the mass element the angular momentum of a body can also be differentiated in time:

$$\frac{d}{dt} \mathbf{D} = \iiint \mathbf{M}_0 = \mathbf{M}_{ext} \quad (2.41)$$

Where  $\mathbf{M}_{ext}$  is the sum of all external moments on the body about the rotation point, because using Newton's third law means that all internal moments will cancel each other out. This shows the use of the angular momentum; for bodies that are fixed in one point, the angular momentum can be used to derive the equation of motion in a rather simple manner.

A mass element has a kinetic energy. The kinetic energy of a *particle* has already been defined in equation 2.5. This means that for a mass element that is part of a body the kinetic energy is:

$$dT = \frac{1}{2} dm \dot{\mathbf{r}} \cdot \dot{\mathbf{r}} \quad (2.42)$$

Using equation 2.5, one can find for the kinetic energy of the complete body with a *fixed point of rotation*:

$$T = \iiint \frac{1}{2} dm \dot{\mathbf{r}} \cdot \dot{\mathbf{r}} = \frac{1}{2} (p, q, r) [J] \begin{Bmatrix} p \\ q \\ r \end{Bmatrix} \quad (2.43)$$

with

$$\boldsymbol{\omega} = (p, q, r) \quad (2.44)$$

gives:

$$T = \frac{1}{2} \mathbf{D} \cdot \boldsymbol{\omega} \quad (2.45)$$

If a body does not have a fixed point of rotation, the kinetic energy must be determined in a different way. The kinetic energy of all particles in the rigid body is again:

$$T = \iiint \frac{1}{2} dm \dot{\mathbf{r}} \cdot \dot{\mathbf{r}} \quad (2.46)$$

Now take one reference point A to which the velocity of every particle is referred and use the fact that the body is assumed to be rigid. Chasles' theorem [21] states that the motion of a rigid body can be conveyed as a superposition of a translation that follows a point on the rigid body and a rotation about that point. The point can be any point on the rigid body. This gives:

$$\mathbf{V} = \mathbf{V}_A + \boldsymbol{\omega} \times \mathbf{r}_A \quad (2.47)$$

The kinetic energy then becomes

$$T = \frac{1}{2} \iiint \{ \mathbf{V}_A \cdot \mathbf{V}_A dm + \mathbf{V}_A \cdot (\boldsymbol{\omega} \times \mathbf{r}_A) dm + (\boldsymbol{\omega} \times \mathbf{r}_A) \cdot (\boldsymbol{\omega} \times \mathbf{r}_A) dm \} \quad (2.48)$$

The first term in the integral gives the energy due to the translation of the reference point A and all particles following this translation. The second term shows the interaction of the motions of the reference point and of the centre of gravity relative to this reference point. By choosing the centre of gravity as the reference point, this term becomes zero. Then using the scalar triple product:

$$(\mathbf{a} \times \mathbf{b}) \cdot \mathbf{c} = \mathbf{a} \cdot (\mathbf{b} \times \mathbf{c}) \quad (2.49)$$

the last term can be rewritten as:

$$T = \frac{1}{2} m \mathbf{V}_{cg} \cdot \mathbf{V}_{cg} + \frac{1}{2} \iiint \boldsymbol{\omega} \cdot [\mathbf{r}_{-g} \times (\boldsymbol{\omega} \times \mathbf{r}_{-g})] dm \quad (2.50)$$

where  $\mathbf{r}_{-g}$  represents the distance between a mass element  $dm$  and the centre of gravity. This gives:

$$T = \frac{1}{2} m \mathbf{V}_{cg} \cdot \mathbf{V}_{cg} + \frac{1}{2} \mathbf{D}_{cg} \cdot \boldsymbol{\omega} \quad (2.51)$$

In this equation the first term is the translational part of the kinetic energy and the second term is the rotational part. The work-energy principle discussed at the beginning of this section also holds for the rigid body:

$$T_2 = T_1 + W_{1 \rightarrow 2} \quad (2.52)$$

Using Chasles' theorem this the work done can be derived to be [38]:

$$\int_1^2 \sum \mathbf{F} \cdot d\mathbf{r}_B + \int_1^2 \sum \mathbf{M}_B \cdot d\boldsymbol{\theta} \quad (2.53)$$

where B is an arbitrary point on the rigid body. Therefore the work done is split into two parts. The first part is due to the resultant of the external forces in moving point B on the rigid body. The second part is due to the rotation about point B. This part of the work is therefore done by the moment of the external forces about point B.

In some cases the work done by an external force depends on the begin and end point only, e.g. gravitational forces or spring forces. The work done is independent of the path taken to get from point 1 to point 2. Therefore there is no total work done on an arbitrary closed path. Forces that comply with this property are called conservative forces. The function describing the work done by these conservative forces due to the change in position is called the potential energy and is defined as:

$$W_{1 \rightarrow 2} = V_1 - V_2 \quad (2.54)$$

Therefore the potential energy depletion is equal to the work done by the conservative forces. The most common sources of potential energy are gravitation and springs. Looking at the work done by a gravitational force, the potential energy due to gravity can be defined as:

$$V = -m\mathbf{g} \cdot \mathbf{r} \quad (2.55)$$

For elastic springs the conservative force in the spring due to an elongation is:

$$\mathbf{F}_s = -k\boldsymbol{\epsilon} \quad (2.56)$$

where  $\boldsymbol{\epsilon}$  is the elongation of the spring. If the spring is linear, the stiffness  $k$  stays constant. Using this to calculate the work done by this force gives the following expression for the potential energy in a spring:

$$V_s = \frac{1}{2}k\boldsymbol{\epsilon} \cdot \boldsymbol{\epsilon} \quad (2.57)$$

Often torsional springs are also used. In that case the spring exerts a moment and not a force on the system:

$$\mathbf{M}_s = -k_\alpha \boldsymbol{\alpha} \quad (2.58)$$

where  $\boldsymbol{\alpha}$  is the deformation angle. In that case the potential energy becomes:

$$V_s = \frac{1}{2}k_\alpha \boldsymbol{\alpha} \cdot \boldsymbol{\alpha} \quad (2.59)$$

In general, the conservative force is always the negative of the gradient of the potential energy function:

$$\mathbf{F}_{conservative} = -\nabla V \quad (2.60)$$

The work done by the conservative forces can be separated from the work done by all forces resulting in another notation of the work-energy principle:

$$T_2 + V_2 = T_1 + V_1 + W_{1 \rightarrow 2}^{NC} \quad (2.61)$$

where  $W_{1 \rightarrow 2}^{NC}$  is used for all work done by the nonconservative external forces.

More on these and other possible governing equations can be found in all dynamics books (e.g. [4, 38]).

## 2.1.2 Vector and Matrix Notations

Next to the conventional method described in the previous section, it is also possible to use the same governing equations, but applying strict vector notations and coordinates defined in different rotating reference frames. This makes it important to uphold a clear distinction between a vector (a physical concept) and a row (a notation) as explained below. The method described in this section includes using matrix notations for cross products. The method actually changes the derivation of the equations of motion of complex 3-D systems into a straightforward "bookkeeping" effort. All this makes it simpler to translate into computer code. Making efficient use of different reference frames can also simplify the code generation.

### Position vectors

A vector has a length and a direction. To give an expression for a vector it is divided into components. The vector is a combination of  $x$  times the unit vector  $\mathbf{i}$  in the  $x$ -direction,  $y$  times the unit vector  $\mathbf{j}$  in the  $y$ -direction and  $z$  times the unit vector  $\mathbf{k}$  in the  $z$ -direction. A choice must be made defining the directions of these unit vectors. Here, only right-handed Cartesian coordinate systems will be used, but these coordinate systems can be in many different directions and they can be rotating or standing still. Using the vector and matrix notations for dynamics, it is important to realise that a vector remains the same vector independent of the chosen reference frame. It is always the same "arrow" just decomposed in different directions.

When looking at systems consisting of combinations of rigid bodies (e.g. figure 2.3), the possibility of using different reference frames becomes extremely useful. The position vector of a point in this system relative to the reference point can be written as a combination of different parts in different reference frames. For each rigid element of the system a reference frame can be defined that will rotate with the same rotational velocity as the element. Therefore the reference frame will not rotate relative to this body. This way setting up the position vector will be rather simple as shown below.

First the notation used throughout the rest of this dissertation must be explained. **Vectors** are given as **bold symbols**:  $\mathbf{a}$ , while **Underlined** symbols are used for **rows** ( $\underline{a}$ ) and

**columns:**  $\{\underline{a}\}$ . This last category therefore **does not** have a physical meaning, it is simply an enumeration of numbers. Quite often vectors are denoted as only a row or a column, as was done in the previous section, but due to the use of different reference frames in this method, that notation cannot be used here. A vector is always a combination of a row or column with a set of unit vectors.

Now, looking at an example of a position vector using different reference frames, the position vector of point A relative to point O in figure 2.3 can be written as:

$$\mathbf{r}_{\mathbf{AO}} = \mathbf{r}_0 + \mathbf{r}_1 + \mathbf{r}_2 + \mathbf{r}_3 = (r_{x0}, r_{y0}, r_{z0})\{\underline{\mathbf{E}}_0\} + (r_{x1}, r_{y1}, r_{z1})\{\underline{\mathbf{E}}_1\} \\ + (r_{x2}, r_{y2}, r_{z2})\{\underline{\mathbf{E}}_2\} + (r_{x3}, r_{y3}, r_{z3})\{\underline{\mathbf{E}}_3\} \quad (2.62)$$

where  $\{\underline{\mathbf{E}}_i\}$  is a column of unit vectors defining reference frame  $i$ :

$$\{\underline{\mathbf{E}}_i\} = \begin{Bmatrix} \mathbf{i}_i \\ \mathbf{j}_i \\ \mathbf{k}_i \end{Bmatrix} \quad (2.63)$$

In general a position vector can be written as:

$$\mathbf{r} = (\underline{r}_1)\{\underline{\mathbf{E}}_1\} + (\underline{r}_2)\{\underline{\mathbf{E}}_2\} + \dots + (\underline{r}_n)\{\underline{\mathbf{E}}_n\} \quad (2.64)$$

where the discussed notation has been used, the underlined symbols  $(\underline{r}_i)$  are not vectors, but only rows.

Rotation transformation matrices can be set up to transform the vector components from one reference frame to another.

For example, the unit vectors of the  $\psi$ -reference frame figure 2.4 can be written as:

$$\begin{aligned} \mathbf{i}_\psi &= \mathbf{i}_H \\ \mathbf{j}_\psi &= \mathbf{j}_H \cos \psi + \mathbf{k}_H \sin \psi \\ \mathbf{k}_\psi &= -\mathbf{j}_H \sin \psi + \mathbf{k}_H \cos \psi \end{aligned} \quad (2.65)$$

This can be summarised in a rotation transformation matrix between the two reference frames:

$$\{\underline{\mathbf{E}}_\psi\} = [R_\psi]\{\underline{\mathbf{E}}_H\} \quad (2.66)$$

This rotation transformation matrix therefore is:

$$\{\underline{\mathbf{E}}_\psi\} = [R_\psi]\{\underline{\mathbf{E}}_H\} = \begin{bmatrix} 1 & 0 & 0 \\ 0 & \cos \psi & \sin \psi \\ 0 & -\sin \psi & \cos \psi \end{bmatrix} \{\underline{\mathbf{E}}_H\} \quad (2.67)$$

Once all rotation transformation matrices in a system are known, the position vector (or any other vector) can be written as one single row in one reference frame by determining:

$$\mathbf{r} = \left( (\underline{r}_1) + (\underline{r}_2)[R_{2-1}] + (\underline{r}_3)[R_{3-2}][R_{2-1}] + \dots + (\underline{r}_n)[R_{n-(n-1)}] \dots [R_{2-1}] \right) \{\underline{\mathbf{E}}_1\} \quad (2.68)$$

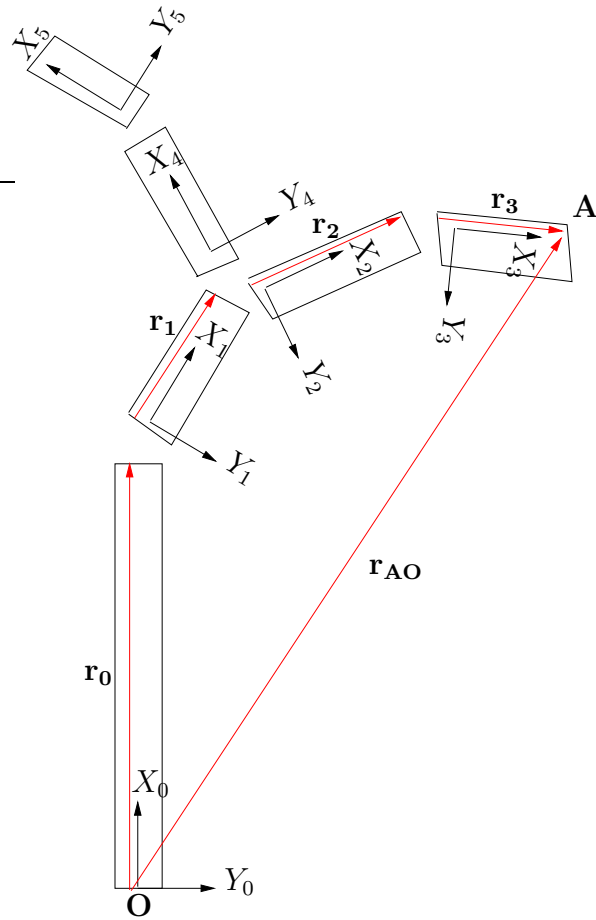


Figure 2.3: Different elements with different reference frames. A summation of vectors in these frames result in the vector from point 0 to point A.

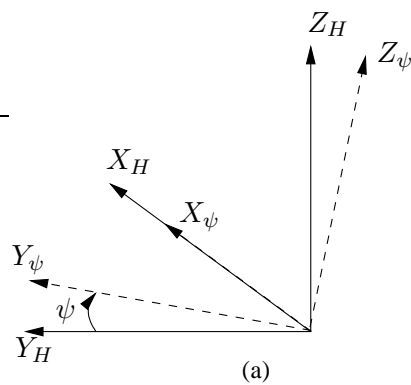


Figure 2.4: The non-rotating (inertial) reference frame  $\{\underline{E}_H\}$  and the rotating reference frame  $\{\underline{E}_\psi\}$ .

or

$$\mathbf{r} = \left( (\underline{r}_1)[R_{2-1}]^{-1} + (\underline{r}_2) + (\underline{r}_3)[R_{3-2}] + \cdots + (\underline{r}_n)[R_{n-(n-1)}] \cdots [R_{3-2}] \right) \{\underline{\mathbf{E}}_2\} \quad (2.69)$$

and similarly for all other reference frames.

The rotation transformation matrices are orthonormal, meaning that the inverse of the matrix is equal to the transposed matrix. To prove this, start with the transformation matrix from reference frame  $i + 1$  to reference frame  $i$ :

$$\{\underline{\mathbf{E}}_{i+1}\} = [R_i]\{\underline{\mathbf{E}}_i\} \quad (2.70)$$

Transposing this equation results in:

$$(\underline{\mathbf{E}}_{i+1}) = (\underline{\mathbf{E}}_i)[R_i]^T \quad (2.71)$$

Now multiplying both sides of this equation by both sides of equation 2.70 gives:

$$\{\underline{\mathbf{E}}_{i+1}\}(\underline{\mathbf{E}}_{i+1}) = [R_i]\{\underline{\mathbf{E}}_i\}(\underline{\mathbf{E}}_i)[R_i]^T \quad (2.72)$$

The left side of this equation can be worked out:

$$\{\underline{\mathbf{E}}_{i+1}\}(\underline{\mathbf{E}}_{i+1}) = \begin{pmatrix} \mathbf{i} \\ \mathbf{j} \\ \mathbf{k} \end{pmatrix} (\mathbf{i} \ \mathbf{j} \ \mathbf{k}) = \begin{bmatrix} 1 & 0 & 0 \\ 0 & 1 & 0 \\ 0 & 0 & 1 \end{bmatrix} = [I] \quad (2.73)$$

Therefore the same must be true for the two terms on the right-hand side of the equation:

$$\{\underline{\mathbf{E}}_i\}(\underline{\mathbf{E}}_i) = [I] \quad (2.74)$$

Meaning that

$$[I] = [R_i][I][R_i]^T = [R_i][R_i]^T \quad (2.75)$$

From this it can be concluded that:

$$[R_i]^T = [R_i]^{-1} \quad (2.76)$$

This proves the orthonormality of the rotation transformation matrices. This is a very useful property for the transformation matrices which will very often be used. It means that given:

$$\{\underline{\mathbf{E}}_{i+1}\} = [R_i]\{\underline{\mathbf{E}}_i\} \quad (2.77)$$

the following must be true:

$$\{\underline{\mathbf{E}}_i\} = [R_i]^T\{\underline{\mathbf{E}}_{i+1}\} \quad (2.78)$$

And going back to equation 2.69, this then becomes:

$$\mathbf{r} = \left( (\underline{r}_1)[R_{2-1}]^T + (\underline{r}_2) + (\underline{r}_3)[R_{3-2}] + \cdots + (\underline{r}_n)[R_{n-(n-1)}] \cdots [R_{3-2}] \right) \{\underline{\mathbf{E}}_1\} \quad (2.79)$$

## Velocity vectors

The velocity vector of a point can be found by differentiating the position vector, provided that this position vector gives the position of the point relative to an inertial point. It is possible to determine the derivatives of each part in the sum of the elements in different reference frames. It is also possible to first determine the position vector decomposed in one single reference frame and take the time derivative of that result. To illustrate both options, first the second option used on the position vector in equation 2.64 gives:

$$\begin{aligned}\mathbf{r} &= \left( (\underline{r}_1) + (\underline{r}_2)[R_{2-1}] + (\underline{r}_3)[R_{3-2}][R_{2-1}] + \cdots + (\underline{r}_n)[R_{n-(n-1)}] \cdots [R_{2-1}] \right) [R_{1-0}]\{\underline{\mathbf{E}}_0\} \\ &= (a, b, c)\{\underline{\mathbf{E}}_0\}\end{aligned}\quad (2.80)$$

The velocity can then be determined:

$$\dot{\mathbf{r}} = (\dot{a}, \dot{b}, \dot{c})\{\underline{\mathbf{E}}_0\} \quad (2.81)$$

where  $\{\underline{\mathbf{E}}_0\}$  is the inertial reference frame. To find the expression for the velocity vector, each element of the row  $(a, b, c)$  has to be differentiated with respect to time. This can be a laborious task.

The first option is usually the most efficient for computer programmes. The time derivative of the position vector given in equation 2.64 then becomes:

$$\dot{\mathbf{r}} = (\dot{r}_1)\{\underline{\mathbf{E}}_1\} + (r_1)\{\dot{\underline{\mathbf{E}}}_1\} + (\dot{r}_2)\{\underline{\mathbf{E}}_2\} + (r_2)\{\dot{\underline{\mathbf{E}}}_2\} + \cdots + (\dot{r}_n)\{\underline{\mathbf{E}}_n\} + (r_n)\{\dot{\underline{\mathbf{E}}}_n\} \quad (2.82)$$

where  $\{\dot{\underline{\mathbf{E}}}_i\}$  is the column with the time derivatives of the three unit vectors and  $(\dot{r}_i)$  is the time derivative of the row in local coordinates  $(\underline{r}_i)$ . Often a rigid body is assumed for which a reference frame is chosen that rotates with this body, whereby the time derivative  $(\dot{r}_i)$  will be zero.

Now assume that the reference frame is rotating with:

$$\boldsymbol{\omega}_i = (p_i, q_i, r_i)\{\underline{\mathbf{E}}\} \quad (2.83)$$

The vector of point P on an object rotating with this same velocity is:

$$\underline{R} = (x, y, z)\{\underline{\mathbf{E}}\} \quad (2.84)$$

Differentiating this equation will result in the velocity for point P:

$$\dot{\underline{R}} = (\dot{x}, \dot{y}, \dot{z})\{\underline{\mathbf{E}}\} + (x, y, z)(\{\dot{\underline{\mathbf{E}}}\}) \quad (2.85)$$

where  $(\dot{x}, \dot{y}, \dot{z})$  is equal to  $(0, 0, 0)$ , because the point does not move relative to the reference frame that is fixed to the object.  $\{\dot{\underline{\mathbf{E}}}\}$  is a column with the time derivatives of the unit vectors. The unit vectors have a constant length, but the direction changes due to the angular velocity of the object. As shown in figure 2.5 the velocities are:

$$\begin{aligned}\dot{\mathbf{i}} &= 0\mathbf{i} + r_i\mathbf{j} - q_i\mathbf{k} \\ \dot{\mathbf{j}} &= -r_i\mathbf{i} + 0\mathbf{j} + p_i\mathbf{k} \\ \dot{\mathbf{k}} &= q_i\mathbf{i} - p_i\mathbf{j} + 0\mathbf{k}\end{aligned}\quad (2.86)$$

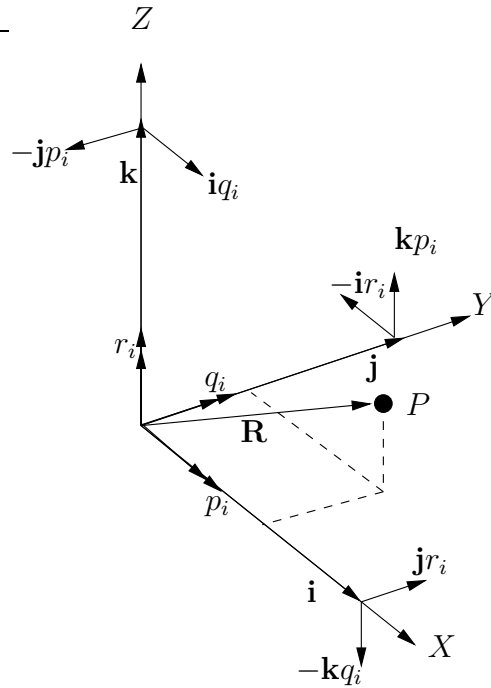


Figure 2.5: Angular velocity in matrix notation

This can be written as a matrix multiplication:

$$\begin{Bmatrix} \dot{\mathbf{i}} \\ \dot{\mathbf{j}} \\ \dot{\mathbf{k}} \end{Bmatrix} = \begin{bmatrix} 0 & r_i & -q_i \\ -r_i & 0 & p_i \\ q_i & -p_i & 0 \end{bmatrix} \begin{Bmatrix} \mathbf{i} \\ \mathbf{j} \\ \mathbf{k} \end{Bmatrix} \quad (2.87)$$

In short this can be written as

$$\{\dot{\mathbf{E}}\} = [\Omega_{\times}]\{\mathbf{E}\} \quad (2.88)$$

$[\Omega_{\times}]$  is called the rotation operator. The elements of the rotation vector  $\boldsymbol{\omega}$  are placed in such a way in the matrix that operation on  $\{\mathbf{E}\}$  results in  $\{\dot{\mathbf{E}}\}$ . As can be seen in equation 2.87, the rotation operator has the following property:

$$[\Omega_{\times}]^T = -[\Omega_{\times}] \quad (2.89)$$

For many systems the degrees of freedom and therefore the corresponding rotational velocities will follow each other according to a definite hinge order. To give an example of the simplicity of the calculation of the time derivatives of the unit vectors in the reference frames, an example can be given for a hinged rotor blade shown in figure 2.6. This rotor blade is set at a fixed pitch angle  $\theta$  and is free to rotate about the flap hinge with the flap angle  $\beta$ . The reference frame attached to this blade would have the following rotational

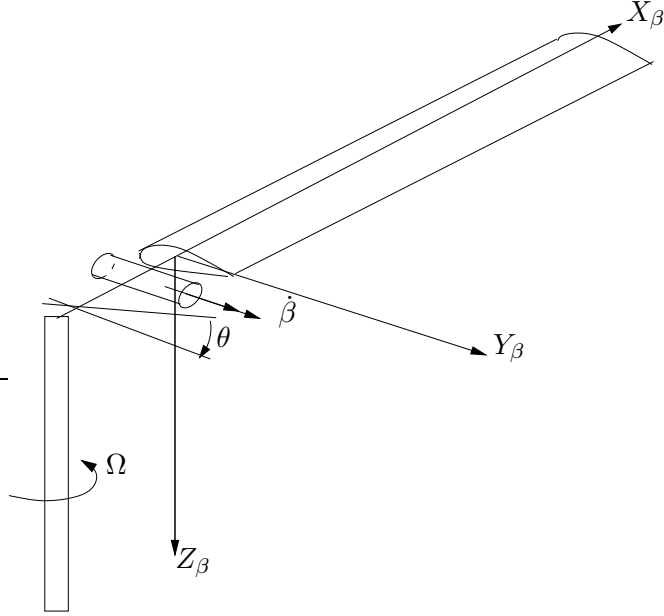


Figure 2.6: A rotating blade with flapping degree of freedom

velocity:

$$\begin{aligned}\boldsymbol{\omega}_\beta &= (0, 0, -\Omega)\{\underline{\mathbf{E}}_\psi\} + (0, \dot{\beta}, 0)\{\underline{\mathbf{E}}_\beta\} = \left( (0, 0, -\Omega)[R_\theta]^T[R_\beta]^T + (0, \dot{\beta}, 0) \right)\{\underline{\mathbf{E}}_\beta\} \\ &= (p_\beta, q_\beta, r_\beta)\{\underline{\mathbf{E}}_\beta\}\end{aligned}\quad (2.90)$$

using  $\{\underline{\mathbf{E}}_\beta\} = [R_\beta][R_\theta]\{\underline{\mathbf{E}}_\psi\}$ . The rotation vector  $\boldsymbol{\omega}_\beta = (p_\beta, q_\beta, r_\beta)\{\underline{\mathbf{E}}_\beta\}$  can be used to set up the rotation operator matrix  $[\Omega_{\times\beta}]$ :

$$[\Omega_{\times\beta}] = \begin{bmatrix} 0 & r_\beta & -q_\beta \\ -r_\beta & 0 & p_\beta \\ q_\beta & -p_\beta & 0 \end{bmatrix}\quad (2.91)$$

Once the rotation operator matrices of the rigid elements are known, the velocity can be determined. For the centre of gravity of the rotor blade in figure 2.6 the velocity becomes:

$$\mathbf{v}_{cg} = (r_{cg}, 0, 0)[\Omega_{\times\beta}]\{\underline{\mathbf{E}}_\beta\}\quad (2.92)$$

For cases where the expression for the position vector is given in several parts in different reference frames, it is possible to calculate the the velocity components in one single reference frame. For example, for point A in figure 2.3, the velocity expressed in components of  $\{\underline{\mathbf{E}}_3\}$

becomes:

$$\begin{aligned}
\dot{\mathbf{r}}_{\mathbf{A0}} &= \dot{\mathbf{r}}_0 + \dot{\mathbf{r}}_1 + \dot{\mathbf{r}}_2 + \dot{\mathbf{r}}_3 \\
&= (r_{x1}, r_{y1}, r_{z1})\{\dot{\mathbf{E}}_1\} + (r_{x2}, r_{y2}, r_{z2})\{\dot{\mathbf{E}}_2\} + (r_{x3}, r_{y3}, r_{z3})\{\dot{\mathbf{E}}_3\} \\
&= \left( (r_{x1}, r_{y1}, r_{z1})[\Omega_{\times 1}][R_{2-1}]^T[R_{3-2}]^T + \right. \\
&\quad \left. (r_{x2}, r_{y2}, r_{z2})[\Omega_{\times 2}][R_{3-2}]^T + (r_{x3}, r_{y3}, r_{z3})[\Omega_{\times 3}] \right) \{\mathbf{E}_3\}
\end{aligned} \tag{2.93}$$

This method can easily and efficiently be implemented into a computer programme. It is also very useful when using symbolic manipulation programmes, e.g. Maple. If the method described so far is consequently used, the art of deriving the equations of motion almost changes into simple bookkeeping work.

Similar to the determination of the velocity vector, the acceleration vector can be determined as the time derivative of the velocity vector or the second derivative w.r.t. time of the position vector:

$$\ddot{\mathbf{r}} = (\ddot{r}_1)\{\mathbf{E}_1\} + 2(\dot{r}_1)\{\dot{\mathbf{E}}_1\} + (r_1)\{\ddot{\mathbf{E}}_1\} \cdots + (\ddot{r}_n)\{\mathbf{E}_n\} + 2(\dot{r}_n)\{\dot{\mathbf{E}}_n\} + (r_n)\{\ddot{\mathbf{E}}_n\} \tag{2.94}$$

In this case  $\{\ddot{\mathbf{E}}_i\}$  must also be determined. This will become:

$$\begin{aligned}
\{\ddot{\mathbf{E}}_i\} &= [\dot{\Omega}_{\times i}]\{\mathbf{E}_i\} + [\Omega_{\times i}](\{\dot{\mathbf{E}}_i\}) \\
&= \begin{bmatrix} 0 & \dot{r} & -\dot{q} \\ -\dot{r} & 0 & \dot{p} \\ \dot{q} & -\dot{p} & 0 \end{bmatrix} \{\mathbf{E}_i\} + \begin{bmatrix} 0 & r & -q \\ -r & 0 & p \\ q & -p & 0 \end{bmatrix} \begin{bmatrix} 0 & r & -q \\ -r & 0 & p \\ q & -p & 0 \end{bmatrix} \{\mathbf{E}_i\}
\end{aligned} \tag{2.95}$$

with these expressions the equations of motion can be derived using the equations found in section 2.1.1:

$$\mathbf{F}_i = m\mathbf{a}_{\mathbf{cg}}$$

and

$$\mathbf{M}_{\mathbf{cg}} = \dot{\mathbf{D}}_{\mathbf{cg}}$$

To be able to use these equations, one must express the forces and moments in the same reference frame as the acceleration and the angular momentum respectively. This can again be achieved by using rotation transformation matrices. For example if one has:

$$\mathbf{M}_{\mathbf{cg}} = (M_x, M_y, M_z)\{\mathbf{E}_i\} \tag{2.96}$$

and

$$\dot{\mathbf{D}}_{\mathbf{cg}} = (D_x, D_y, D_z)\{\mathbf{E}_{i-2}\} \tag{2.97}$$

then one must transform either of these to expressions to the other reference frame. Of course it is also possible to transform both expressions to some other reference frame  $\{\underline{\mathbf{E}}_n\}$ , any frame will do as long as it is the same for both vectors. In this example one can, for instance, calculate the components of the moment in the reference frame in which the angular momentum is already known:

$$\begin{aligned}\mathbf{M}_{\mathbf{cg}} &= (M_x, M_y, M_z)\{\underline{\mathbf{E}}_i\} = (M_x, M_y, M_z)[R_{i-(i-1)}][R_{(i-1)-(i-2)}]\{\underline{\mathbf{E}}_{i-2}\} \\ &= (M_{x_{i-2}}, M_{y_{i-2}}, M_{z_{i-2}})\{\underline{\mathbf{E}}_{i-2}\}\end{aligned}\quad (2.98)$$

After this coordinate transformation, it is possible to equate the different components of the vectors:

$$\begin{aligned}M_{x_{i-2}} &= \dot{D}_x \\ M_{y_{i-2}} &= \dot{D}_y \\ M_{z_{i-2}} &= \dot{D}_z\end{aligned}\quad (2.99)$$

## Energy

In the next section Lagrange's equations will be derived. These equations are very useful to find the equations of motion of systems. As described in the next section, the kinetic and potential energy of the system must be determined in order to be able to use the Lagrangian method. Recall that the kinetic energy of a rigid body is (equation 2.51):

$$T = \frac{1}{2}m\mathbf{v}_{cg} \cdot \mathbf{v}_{cg} + \frac{1}{2}\mathbf{D}_{cg} \cdot \boldsymbol{\omega}$$

The kinetic energy of the complete system is the sum of the energies of the rigid bodies:

$$T = \sum_{i=1}^N \left( \frac{1}{2}m\mathbf{v}_{cg} \cdot \mathbf{v}_{cg} + \frac{1}{2}\mathbf{D}_{cg} \cdot \boldsymbol{\omega} \right)\quad (2.100)$$

If the velocities of the centres of gravity of all rigid bodies have been determined, this expression can be used to calculate the total kinetic energy of the system. Notice that, to be able to calculate the dot product, the velocity of each element should be decomposed in a reference frame of choice but not be a summation of different parts that are decomposed in different reference frames. It is however not necessary to state the velocity of each rigid body in the same reference frame. The velocities must be calculated relative to the inertial reference frame, but they can be expressed in any reference frame. The calculations can even become shorter by using the reference frame attached to the rigid element, so different frames for each element. When the rotation part of the kinetic energy is calculated, it is always easiest to use the local reference frame. Because it is attached to the element, the inertia matrix will be constant in this frame. It is possible to transform an inertia matrix to another reference frame, but it is simpler to transform the total rotation to the local reference frame of the element.

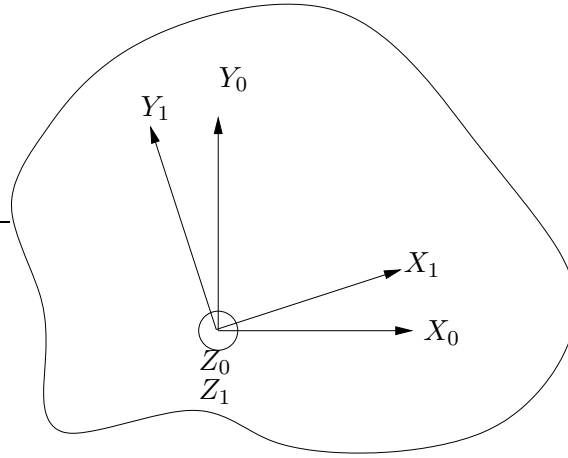


Figure 2.7: Two different reference frames on the rigid body.

To find the expression for the transformation of an inertia matrix, figure 2.7 shows a body and two different reference frames.  $[J_0]$  is the inertia matrix of the body w.r.t. reference frame 0 and the inertia w.r.t. reference frame 1 needs to be determined. The two reference frames are defined as:

$$\{\underline{\mathbf{E}}_1\} = [R]\{\underline{\mathbf{E}}_0\} \quad (2.101)$$

Where  $[R]$  is the transformation matrix. This transformation matrix can consist of several transformations, it could be that  $[R] = [\alpha][\beta][\gamma]$ . The angular velocity of the body can be written as:

$$\boldsymbol{\omega} = (p, q, r)\{\underline{\mathbf{E}}_0\} = (\underline{\mathbf{E}}_0) \begin{Bmatrix} p \\ q \\ r \end{Bmatrix} \quad (2.102)$$

The rotation is about the origin, thus the origin of the reference frame does not move. This means that the angular momentum can be written as:

$$\mathbf{D} = (p, q, r)[J_0]\{\underline{\mathbf{E}}_0\} \quad (2.103)$$

The kinetic energy for this body with a *fixed point of rotation* is:

$$T = \frac{1}{2}\mathbf{D}\boldsymbol{\omega} = \frac{1}{2}(p, q, r)[J_0] \begin{Bmatrix} p \\ q \\ r \end{Bmatrix} \quad (2.104)$$

For reference frame 1 the angular velocity of the body would be:

$$\boldsymbol{\omega} = (p, q, r)[R]^T\{\underline{\mathbf{E}}_1\} = (\underline{\mathbf{E}}_1)[R] \begin{Bmatrix} p \\ q \\ r \end{Bmatrix} \quad (2.105)$$

The angular momentum can be written using this expression as:

$$\mathbf{D} = (p, q, r)[R]^T[J_1]\{\mathbf{E}_1\} \quad (2.106)$$

Resulting in the following expression for the kinetic energy:

$$T = \frac{1}{2}\mathbf{D}\boldsymbol{\omega} = \frac{1}{2}(p, q, r)[R]^T[J_1][R] \begin{Bmatrix} p \\ q \\ r \end{Bmatrix} \quad (2.107)$$

As the kinetic energy must be independent of the reference frame the following must be true:

$$[J_0] = [R]^T[J_1][R] \quad (2.108)$$

Similarly of course:

$$[R][J_0][R]^T = [J_1] \quad (2.109)$$

This expression is valid only for inertia matrices about the same point, but with different directions for the axes. When the components of the rotational velocity are known relative to a different reference frame than the inertia matrix, it is possible to use these expressions to transform the inertia matrix. However, the equations are exactly the same as one would use to transform the rotational velocity to the reference frame of the inertia matrix, as is shown in the derivation. Because the velocity is a vector with three components, it takes less calculations to start here and transform these, rather than do the matrix multiplications given in equation 2.109.

Similar to the expressions derived in the previous section, the potential energy of a system, in the case of linearly elastic springs and gravitational acceleration is:

$$V = \sum_{i=1}^N \frac{1}{2}k_i q_i^2 + \sum_{i=1}^N -m_i \mathbf{g} \cdot \mathbf{r}_{cgi} \quad (2.110)$$

Here again the matrix and vector notations can be used in the calculation of the gravitational part of the potential energy. The position vectors relative to an inertial point must first be determined. Once more it is important to start from a point with zero velocity, but it is not necessary to express everything in the inertial reference frame. The gravitational acceleration will be known in the inertial reference frame, but it is possible to transform both the position vector and the gravitational acceleration vector to another reference frame. When these two are expressed in the same reference frame, the dot product can be determined. It is however not necessary to use the same reference frame for each element, again, as long as both the position vector of element  $i$  and the gravitational acceleration vector are expressed in the same reference frame, the answer will be correct. For example, if the position vector is expressed in  $\{\mathbf{E}_3\}$  while the gravitational acceleration is usually expressed in  $\{\mathbf{E}_0\}$  the product can be calculated as:

$$\begin{aligned} V_g &= -m\mathbf{g} \cdot \mathbf{r} = -m(0, 0, g)\{\mathbf{E}_0\} \cdot (r_x, r_y, r_z)\{\mathbf{E}_3\} \\ &= -m \left( (0, 0, g)[R_{1-0}]^T[R_{2-1}]^T[R_{3-2}]^T \right) \cdot (r_x, r_y, r_z) \\ &= -m(0, 0, g) \cdot ((r_x, r_y, r_z)[R_{3-2}][R_{2-1}][R_{1-0}]) \end{aligned} \quad (2.111)$$

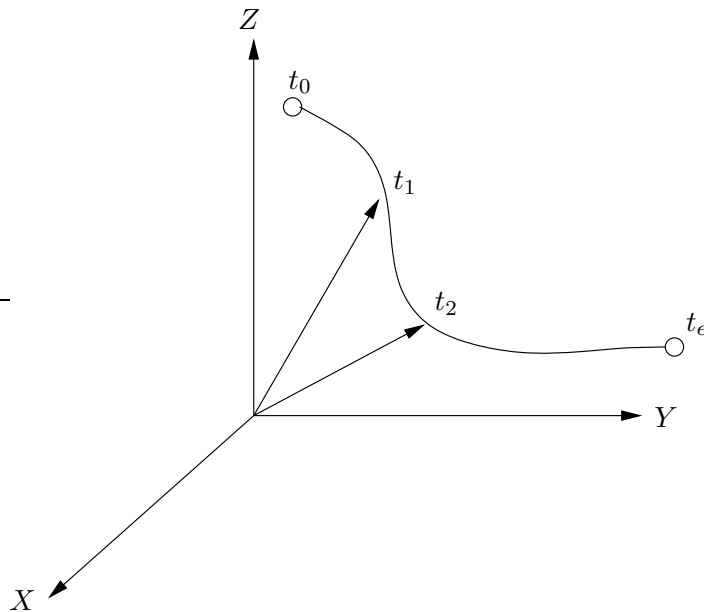


Figure 2.8: The path of a particle

In this example an inertial reference frame has been used where the  $z$ -axis is directed toward the centre of the earth.

## 2.2 Lagrange's Equations

Using Hamilton's generalised momentum it is possible to find the equations of motion according to Lagrange's equations as shown by e.g. van Holten in [66]. These equations are extremely effective when analysing systems with multiple rigid bodies that are connected, because the internal forces do not need to be calculated when using Lagrange's equations in this section. First Hamilton's principle is discussed and used to derive Lagrange's equations for particles. The extension of these equations to rigid body systems is discussed in the second part of this section.

### 2.2.1 Hamilton's Principle and Lagrange's Equations for particles

To derive Hamilton's principle, a moving particle with forces acting on it, is looked at. In figure 2.8 the path of a particle under the influence of a force is drawn in the so-called configuration space. The configuration space is the space with all possible positions that a physical system may attain, including the possible external constraints. Suppose that the particle will follow a slightly different path between the starting point  $(\mathbf{r}_0, t_0)$  and the end point  $(\mathbf{r}_e, t_e)$ , as depicted in figure 2.9. This means that two particles will travel two different routes from point A to point B, both starting at time  $t_0$  and both arriving together at time

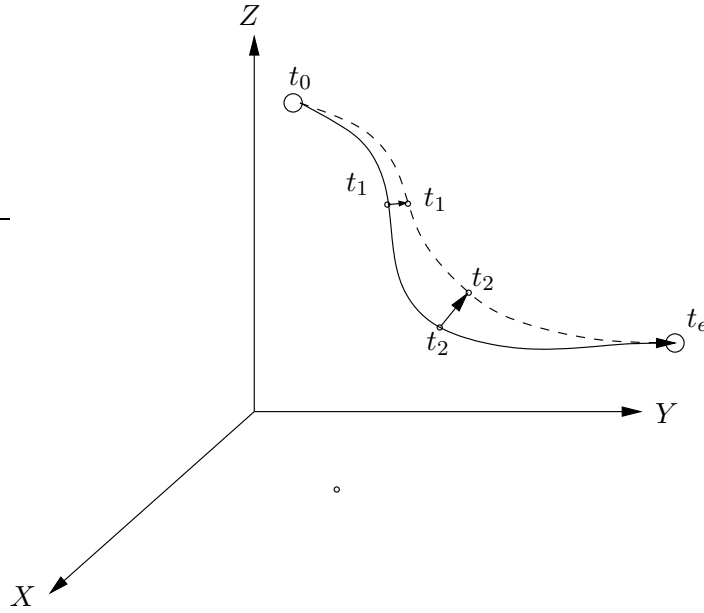


Figure 2.9: A variational path of a particle

$t_e$ . The forces acting on the particles will be different, as will the velocities at every time instant. The differences in the forces, velocities and place vectors between the two different paths are assumed to be small.

The difference in position at a certain time is called the virtual displacement  $\delta \mathbf{r}$ . The velocity along the original path is defined as:

$$\mathbf{V} = \lim_{t_2 \rightarrow t_1} \frac{\mathbf{r}_2 - \mathbf{r}_1}{t_2 - t_1} \quad (2.112)$$

The velocity along the new alternative path has a different value:  $\mathbf{V} + \delta \mathbf{V}$ :

$$\mathbf{V} + \delta \mathbf{V} = \lim_{t_2 \rightarrow t_1} \frac{(\mathbf{r}_2 + \delta \mathbf{r}_2) - (\mathbf{r}_1 + \delta \mathbf{r}_1)}{t_2 - t_1} = \mathbf{V} + \lim_{t_2 \rightarrow t_1} \frac{\delta \mathbf{r}_2 - \delta \mathbf{r}_1}{t_2 - t_1} = \mathbf{V} + \frac{d}{dt}(\delta \mathbf{r}) \quad (2.113)$$

Thus:

$$\delta \mathbf{V} = \frac{d}{dt}(\delta \mathbf{r}) \quad (2.114)$$

It appears from equation 2.114 that in this case  $\delta$  and  $\frac{d}{dt}$  are interchangeable operators (commutative). This expression relates the variation of the velocity to the virtual displacement.

The variation of the kinetic energy  $\delta T$  can similarly be related to the virtual displacement. At a certain moment in time the kinetic energy of the particle along the original path is:

$$T = \frac{1}{2} m \mathbf{V} \cdot \mathbf{V} \quad (2.115)$$

At the same time, but on the alternative path the kinetic energy will be:

$$T + \delta T = \frac{1}{2}m[(\mathbf{V} + \delta\mathbf{V}) \cdot (\mathbf{V} + \delta\mathbf{V})] = T + m\mathbf{V} \cdot \delta\mathbf{V} \quad (2.116)$$

To get the last expression in this equation a linearisation was done, therefore this is only valid for small virtual displacements. The term  $\delta T$  can be written as:

$$\delta T = m\mathbf{V} \cdot \delta\mathbf{V} = m\mathbf{V} \frac{d}{dt}(\delta\mathbf{r}) = m\frac{d}{dt}(\mathbf{V} \cdot \delta\mathbf{r}) - m\mathbf{a} \cdot \delta\mathbf{r} \quad (2.117)$$

According to Newton the following is true along the original path of the particle at every moment in time (see section 2.1.1):

$$\mathbf{F} - m\mathbf{a} = 0 \quad (2.118)$$

Thus the following must also be true:

$$\mathbf{F} \cdot \delta\mathbf{r} - m\mathbf{a}\delta\mathbf{r} = 0 \quad (2.119)$$

The virtual work is defined by:

$$\delta W = \mathbf{F} \cdot \delta\mathbf{r} \quad (2.120)$$

This is the work that the force  $F$  would do if the particle was moved to the corresponding point of the alternative path. This corresponding point is the point on the alternative route at the same moment in time. Combining Eqs. 2.117, 2.119 and 2.120 gives:

$$\delta W + \delta T - m\frac{d}{dt}(\mathbf{V} \cdot \delta\mathbf{r}) = 0 \quad (2.121)$$

This equation can be integrated from  $t_0$  to  $t_e$ . The third term in equation 2.121 becomes zero after the integration because at  $t_0$  and at  $t_e$  the two different paths go through the same point, thus for these times  $\delta\mathbf{r} = 0$ . Therefore the integration becomes:

$$\int_{t_0}^{t_e} (\delta W + \delta T) dt = 0 \quad (2.122)$$

Equation 2.122 is known as Hamilton's principle. It is applicable for particles, rigid bodies but also for continuous deformable media. This equation shows that, if the path of a particle is disturbed, the virtual work done plus the difference in the kinetic energy on average over the entire path is equal to zero.

If all the forces on the particle are assumed to be conservative, meaning that they depend on the place only and thus can be derived from a potential function  $V(x, y, z)$  and the system is holonomic [38], the virtual work due to the virtual displacement of the particle will be equal to the reduction in potential energy. A constraint in a system is defined as holonomic if the constraint can be expressed as a function of the coordinates and the time, it must be

independent of the velocities. A system is holonomic if all constraints are holonomic. If the system is nonholonomic, the constraint forces will do work for arbitrary changes in the path. So for a holonomic system with only conservative forces, Hamilton's principle becomes:

$$\int_{t_0}^{t_e} (\delta W + \delta T) dt = \int_{t_0}^{t_e} (\delta T - \delta V) dt = 0 \quad (2.123)$$

or using the action integral  $I$ :

$$I = \int_{t_0}^{t_e} (T - V) dt \quad (2.124)$$

the expression can be written as:

$$\delta I = 0 \quad (2.125)$$

Therefore out of all variational paths between initial and final positions, the true path is that path for which the action integral  $I$  is stationary. In other words: the actual path of a particle in a conservative force field differs from all other possible paths by the fact that the above mentioned integral has an extreme value (minimum or maximum) for this path. It is as if the particle 'knows' at every moment in time to move in a certain way in order to get the action integral to be minimal over the entire path.

The path of the element can be described using a set of generalised coordinates  $q_i(t)$ . The number of generalised coordinates is equal to the number of degrees of freedom, e.g. a particle that is free to move in three directions will have three degrees of freedom and can be described using three generalised coordinates. This could be Cartesian coordinates for example or polar coordinates. The position of the particle will be a function of the generalised coordinates and of the time. To find the true path of the element,  $q_i(t)$  must be chosen such that

$$\delta I = \int_{t_0}^{t_e} \delta L dt = 0 \quad (2.126)$$

where  $L$  is the Lagrangian function defined as  $L = T(q_i, \dot{q}_i) - V(q_i)$  thus a function of  $q_i$  and  $\dot{q}_i$ :

$$\delta L = \sum_i \left[ \frac{\partial L}{\partial q_i} \delta q_i + \frac{\partial L}{\partial \dot{q}_i} \delta \dot{q}_i \right] \quad (2.127)$$

Thus

$$\int_{t_0}^{t_e} \delta L dt = \sum_i \left[ \int_{t_0}^{t_e} \frac{\partial L}{\partial q_i} \delta q_i dt + \int_{t_0}^{t_e} \frac{\partial L}{\partial \dot{q}_i} \delta \dot{q}_i dt \right] \quad (2.128)$$

Using partial integration this can be written as:

$$\int_{t_0}^{t_e} \delta L dt = \sum_i \left[ \int_{t_0}^{t_e} \left\{ \frac{\partial L}{\partial q_i} - \frac{d}{dt} \frac{\partial L}{\partial \dot{q}_i} \right\} \delta q_i dt + \frac{\partial L}{\partial \dot{q}_i} \delta q_i \Big|_{t_0}^{t_e} \right] \quad (2.129)$$

The last part of this expression is equal to zero, because  $\delta q_i(t_0) = \delta q_i(t_e) = 0$  as the path was chosen as such. This means that the integral in the last expression must be equal to zero, for an arbitrary  $\delta q_i(t)$ . The only possible solution is:

$$\frac{d}{dt} \frac{\partial L}{\partial \dot{q}_i} - \frac{\partial L}{\partial q_i} = 0 \quad (i = 1 \dots N) \quad (2.130)$$

These are Lagrange's equations in a conservative force field. Using the fact that the kinetic energy depends on  $\dot{q}_i$  and  $q_i$  and the potential energy only depends on  $q_i$  the equation can be written as:

$$\frac{d}{dt} \frac{\partial T}{\partial \dot{q}_i} - \frac{\partial T}{\partial q_i} + \frac{\partial V}{\partial q_i} = 0 \quad (i = 1 \dots N) \quad (2.131)$$

These equations found are valid in conservative force fields only. To determine the equations in the case of nonconservative forces, first rewrite equation 2.122 by splitting up the virtual work in a term for the contribution of nonconservative forces:  $\delta W_{nc}$ , and the contribution of conservative forces expressed as the negative of the potential energy  $\delta V$ . This gives:

$$\int_{t_0}^{t_e} (\delta W_{nc} - \delta V + \delta T) dt = 0 \quad (2.132)$$

where the virtual work is:

$$\delta W_{nc} = \mathbf{F}_{nc} \cdot \delta \mathbf{r} \quad (2.133)$$

This means that the virtual work is the work done if the point mass would be moved to the corresponding point, at the same moment in time, of the disturbed path.

The virtual displacement  $\delta \mathbf{r}$  can be related to the variations of the generalised coordinates  $\delta q_i$ , so the following can be written:

$$\delta \mathbf{r}_j = \sum_i \frac{\partial \mathbf{r}_j}{\partial q_i} \delta q_i \quad (i = 1 \dots N) \quad (2.134)$$

Using this:

$$\begin{aligned} \delta W_{nc} &= \mathbf{F}_{ncj} \cdot \delta \mathbf{r}_j \\ &= \sum_{gen\ coord\ i} \left( \mathbf{F}_{ncj} \frac{\partial \mathbf{r}_j}{\partial q_i} \right) \delta q_i \\ &= \sum_{gen\ coord\ i} Q_i \cdot \delta q_i \end{aligned} \quad (2.135)$$

The generalised force  $Q_i$  is defined as:

$$Q_i = \mathbf{F}_{ncj} \frac{\partial \mathbf{r}_j}{\partial q_i} \quad (2.136)$$

This is the formal definition of the generalised force  $Q_i$ . According to equation 2.135 the method to find the generalised force is rather simple: vary one of the generalised coordinates  $\delta q_i$  and analyse the work that is done by all nonconservative forces (and moments) due to the variation. This virtual work  $\delta W_{nc_i}$  can be divided by  $\delta q_i$  resulting in the generalised force. Similar to the derivation of Lagrange's equation in a conservative force field, the complete equation of Lagrange can now be derived using:

$$\int_{t_0}^{t_e} [\delta L + \delta W_{nc}] dt = \int_{t_0}^{t_e} [\delta L + \sum_i Q_i \delta q_i] dt \quad (2.137)$$

Using the same method as before leads to:

$$\frac{d}{dt} \frac{\partial T}{\partial \dot{q}_i} - \frac{\partial T}{\partial q_i} + \frac{\partial V}{\partial q_i} = Q_i \quad (2.138)$$

This is the complete version of Lagrange's equation.

Lagrange's equations are very useful for the derivation of the equations of motion. The equations for rigid bodies and systems of rigid bodies are derived in the next section. This next section also illustrates that using these equations is less complicated than using the Newtonian dynamics described in section 2.1.1.

## 2.2.2 Lagrange's Equations for Rigid Body Systems

The equations found in the previous section can be extended from particles to rigid bodies. Equation 2.132 for the entire body is the summation over all mass elements:

$$\int_{t_0}^{t_e} (\delta W_{nc} - \delta V + \delta T) dt = 0 \quad (2.139)$$

Where  $\delta V$  and  $\delta T$  are integrated over the entire body. The work done by the nonconservative forces for a rigid body is:

$$\delta W_{nc} = \sum_{\text{all masses } j} \mathbf{F}_{nc_j} \cdot \delta \mathbf{r}_j \quad (2.140)$$

Notice that due to Newton's third law, action is reaction, the work done by internal forces does not contribute to the total sum of work done by nonconservative forces. Each internal force will act on two particles, but in opposing directions giving two equal but opposite contributions to the work done.

Using equation 2.134 the virtual work for a rigid body becomes:

$$\begin{aligned} \delta W_{nc} &= \sum_{\text{all masses } j} \mathbf{F}_{nc_j} \cdot \delta \mathbf{r}_j \\ &= \sum_{\text{gen coord } i} \left( \sum_{\text{all masses } j} \mathbf{F}_{nc_j} \frac{\partial \mathbf{r}_j}{\partial q_i} \right) \delta q_i \\ &= \sum_i Q_i \cdot \delta q_i \end{aligned} \quad (2.141)$$

Similar to the generalised force for a particle, the generalised force  $Q_i$  for a rigid body is defined as:

$$Q_i = \sum_{\text{all masses } j} \mathbf{F}_j \frac{\partial \mathbf{r}_j}{\partial q_i} \quad (2.142)$$

Using the same method as used for a particle in the previous section, the same equation is found for the rigid body or a system of rigid bodies:

$$\frac{d}{dt} \frac{\partial T}{\partial \dot{q}_i} - \frac{\partial T}{\partial q_i} + \frac{\partial V}{\partial q_i} = Q_i \quad (2.143)$$

This is the complete version of Lagrange's equation. When using this for a system of rigid bodies the energies in the equation are for the complete system.

Lagrange's equations are very useful for the derivation of the equations of motion. Using these equations is less complicated than using the Newtonian dynamics described in section 2.1.1, because the reaction forces within the system do not need to be determined when using Lagrange's equations.

The kinetic and potential energy must be determined when using Lagrange's equations. In general, as described in the first section of this chapter, the kinetic energy of a system is defined as:

$$T = \sum \left( \frac{1}{2} m_i \mathbf{v}_{cg,i} \cdot \mathbf{v}_{cg,i} + \frac{1}{2} (p_i, q_i, r_i) [J_{cg,i}] (p_i, q_i, r_i)^T \right) \quad (2.144)$$

and the potential energy is:

$$V = \sum \left( -m_i \mathbf{g} \cdot \mathbf{r}_{cg,i} + \frac{1}{2} k_i q_i^2 \right) \quad (2.145)$$

As described in section 2.1.2, the kinetic energy and the potential energy of a system can be calculated using vector or matrix notations. The generalised forces can also be determined using vector notations. The generalised forces must be determined for all degrees of freedom taking into account all nonconservative forces acting on the system (e.g. aerodynamic forces, friction forces).

If the degree of freedom used in Lagrange's equation is a rotation and not a translation, the generalised force must be a moment. This is immediately apparent when looking at the units. For a rotation as a generalised coordinate, the resulting moment due to all external forces about the hinge corresponding to this generalised coordinate has to be used. The component in the direction of this coordinate gives the generalised 'force'  $Q_i$  that is needed in Lagrange's equations.

An example of using Lagrange's equations combined with the vector and matrix notations to find the equations of motion of a system is given in appendix I. The example in the appendix is a clear illustration of the simplicity and effectiveness of using Lagrange and the matrix notation.

The programme described in chapters 5 and 6 uses Lagrange's equations to find the time derivative of Hamilton's generalised momenta. Hamilton's generalised momenta are defined as:

$$p_i = \frac{\partial T}{\partial \dot{q}_i} \quad (2.146)$$

In the programme, the generalised momenta and the angles corresponding to the degrees of freedom are used as state variables, which results in a set of equations with only first order time derivatives to be solved. Using the methods to find the equations of motion as described in this chapter, the equations of motion that are found, include first and second order derivatives w.r.t. time of the state variables which are the generalised coordinates, in which case a set of second order differential equations has to be solved. The details of the calculations in the programme are given in chapters 5 and 6.

There are many other methods that can be used to derive equations of motion. Ginsberg [38] gives a clear description of alternative methods such as Hamilton's canonical equations, Gibbs-Appell equations and Kane's formulation. The interested reader is therefore referred to Ginsberg's "Advanced Engineering Dynamics".



## Chapter 3

# Horizontal Axis Wind Turbine Aerodynamics

*"Who has seen the wind? Neither you nor I: But when the trees bow down their heads, the wind is passing by. "*

- Christina Rossetti

Wind turbines transform the kinetic energy of the air into electrical energy. To do this, the turbines must decelerate the air particles. The amount of deceleration and the mass of the air that is being decelerated determines the amount of energy that is captured by the wind turbine. In this dissertation the concentration is on the aeroelastic stability of wind turbines. Aeroelasticity (see chapter 4) concerns the stability of motions due to the combination of aerodynamic, elastic and inertia forces, where the aerodynamics play an important role. It is clear that for different research fields on wind energy, knowledge and understanding of aerodynamics is important.

As Leishman states, wind turbine aerodynamics are extremely complicated [81]. There are still many challenges left in this field e.g. understanding and predicting the unsteady loads on the blades as well as accurately predicting rotor performance and wake interaction of turbines in a wind turbine park setting. Also the environmental effects are complicated, e.g. atmospheric turbulence, the ground boundary layer effects and wind shear . However there is a basic aerodynamic theory that gives reasonable results for many conditions [43]. This is the Blade Element - Momentum (BEM) method which is discussed first in this chapter. It is a combination of blade element theory and momentum theory. The latter originated from the field of ship propellers, but has been further developed to be used for aeroplane propellers and helicopters. A wind turbine is very similar to a helicopter, though a turbine takes energy from the wind and decreases the velocity whereas a helicopter will, in most flight situations, increase the velocity and add energy to the air. Due to the similarities between helicopters and wind turbines, the BEM method can also be used for wind turbines. It is also used in the programme WOBBE, discussed in chapters 5 and 6. Most aeroelastic

codes for wind turbines also use BEM, because its calculations are relatively simple and the results, as mentioned above, have proven to be quite reasonable in most cases. Some examples of other aeroelastic codes using BEM are HAWCSTAB [44], PHATAS [83], GAST [123] and TURBU Offshore [32].

The second section of this chapter gives examples of other more complex methods than BEM that can be used to calculate the aerodynamic forces and the flow of the air particles. It gives examples of more complex methods that can be used to determine the global flow and of methods that determine the local flow.

## 3.1 Blade Element - Momentum Method

The blade element - momentum method (BEM) is described in probably all books and articles dealing with the aerodynamics of wind turbines and helicopters, e.g. [18, 73, 80, 130, 133]. Especially Hansen [47] and Eggleston and Stoddard [31] give very clear descriptions of this method, specifically with respect to wind turbines. As mentioned in this chapter's introduction, this method is currently still used in most aeroelastic codes. This is because it is relatively simple and therefore not very time consuming while the results are quite reasonable for aeroelastic analysis. BEM is based on the consideration of the flow field around a rotor as two separated flows that are united by boundary conditions. The local flow field around the rotor is regarded as a separated box within the global flow field. The pressures, velocity and the continuity form the boundary conditions between the two.

The global flow field is determined using momentum theory. The forces on the rotor blades representing the local flow, are calculated using the blade element method. The global flow field is described in sections 3.1.1 - 3.1.3. The blade flow is described in section 3.1.4. Corrections and additions to the BEM method in order to obviate some of the limitations in the method are given in sections 3.1.6 - 3.1.9.

As mentioned before, alternatives to the Blade Element - Momentum method are shortly described in section 3.2. These methods are more complex and can give better predictions especially for cases where BEM brakes down. The largest drawback of these alternative methods is the time consumption due to the complexity of the calculations [131].

### 3.1.1 Momentum Theory

Axial momentum theory is the classical analysis method to determine the global flow. The roots of this method lie in ship propeller theory as developed in the second half of the nineteenth century by Rankine, R.E. Froude, W. Froude and Lanchester [33, 34, 79, 118]. It has become widely used for aeroplane propellers, helicopters and wind turbines. The momentum theory looks at the idealised flow in a stream tube that encloses an actuator disc, as shown in figure 3.1. The energy and momentum in the control volume are used. In

case of axial flow, with no rotational motion, it is possible to derive the thrust and power by applying continuity, momentum balance and Bernoulli's equation to the flow.

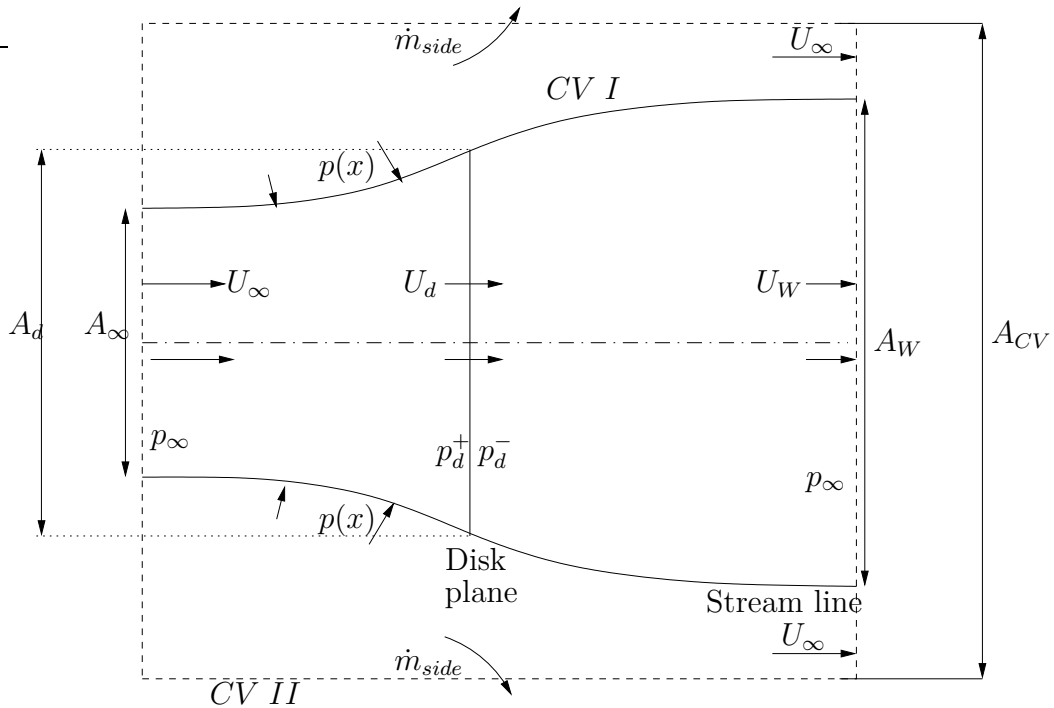


Figure 3.1: The stream tube around an actuator disc. The pressures and the local wind velocities at the disc, in the far wake and far upstream are shown.

The actuator disc is assumed to be homogeneous and infinitely thin. It exerts a force opposite to the free stream velocity on the stream. A physical approximation of the actuator disc would be a rotor with a large number of very thin and dragless blades that rotate such that the speed of the tip is much higher than the wind speed and that all vorticity is shed by tip vortices.

For helicopters and propellers the thrust force exerted by the disc will usually increase the velocity of the air flow, but for wind turbines the velocity is reduced. The thrust on the disc corresponds to a pressure difference between the two sides of the disc, as illustrated in figure 3.1. Far upwind from the disc the wind velocity is  $U_\infty$  and the static pressure is  $p_\infty$ . When modeling a wind turbine the pressure goes up to  $p_d^+$  just in front of the disc. The actuator disc causes a step pressure difference resulting in a pressure drop to  $p_d^-$  just downstream of the disc. The velocity at the disc will be reduced and is called  $U_d$ . The stream tube will have a larger cross sectional area due to the smaller velocity. In the far wake the cross sectional area is again larger. The velocity is further reduced to  $U_W$ . The pressure in the far wake has returned to the value far upstream:  $p_\infty$ . The flow is assumed to be steady.

To find expressions for the different velocities, first conservation of mass is used. The mass

flow must be the same at every cross section of the stream tube (*CV I*):

$$\rho A_\infty U_\infty = \rho A_d U_d = \rho A_W U_W \quad (3.1)$$

where  $\rho$  is the air density,  $A_\infty$  is the area of the stream tube far upstream,  $A_d$  the actuator disc area and  $A_W$  is the area of the stream tube in the far wake. The flow is assumed to be incompressible, therefore the air density is the same everywhere. This assumption is valid for low Mach-numbers (velocity is small relative to the speed of sound).

The flow  $\dot{m}_{side}$  can also be calculated using the conservation of mass, but this time on *CVII*. This alternative control volume is very large, close to infinite such that the pressure on this control volume is equal to  $p_\infty$  everywhere. *CVII* has the shape of a cylinder and is illustrated in figure 3.1. Using conservation of mass for *CVII* gives:

$$A_{CV} U_\infty = \dot{m}_{side} + (A_{CV} - A_W) U_\infty + A_W U_W \quad (3.2)$$

Therefore:

$$\dot{m}_{side} = A_W (U_\infty - U_W) \quad (3.3)$$

The change in momentum must be equal to the sum of all external forces. The overall change of momentum must therefore be equal to the thrust  $T$ , because there are no other resulting forces in axial direction on *CVII*. This gives:

$$\dot{m}_{side} U_\infty + (A_{CV} - A_W) U_\infty^2 + A_W U_W^2 - A_{CV} U_\infty^2 = \frac{T}{\rho} \quad (3.4)$$

Using equation 3.3 this gives for the thrust:

$$T = \rho A_W U_W (U_\infty - U_W) \quad (3.5)$$

Using the conservation of mass (equation 3.1) this can be written as:

$$T = \rho U_d A_d (U_\infty - U_W) \quad (3.6)$$

Bernoulli's equation for incompressible flow can be used for the flow upstream of the disc and again for the part of the flow downstream of the disc. It cannot be used across the disc, because there is a discontinuity in total pressure caused by the disc. Bernoulli's equation states that under steady conditions and when no work is done the total pressure is constant:

$$\frac{1}{2} \rho V^2 + p + \rho g h = const \quad (3.7)$$

A horizontal flow is assumed, therefore the gravity term drops from the equation. The total pressure upstream can be calculated far upstream and equalised to the total pressure just upstream of the disc:

$$p_\infty + \frac{1}{2} \rho U_\infty^2 = p_d^+ + \frac{1}{2} \rho U_d^2 \quad (3.8)$$

The total pressure downstream of the disc can be calculated in the far wake and equalised to the total pressure just downstream of the disc:

$$p_\infty + \frac{1}{2}\rho U_W^2 = p_d^- + \frac{1}{2}\rho U_d^2 \quad (3.9)$$

By subtracting equation 3.9 from equation 3.8, an equation is found for the pressure difference over the disc.

$$p_d^+ - p_d^- = \frac{1}{2}\rho(U_\infty^2 - U_W^2) \quad (3.10)$$

The thrust on the disc must be equal to the pressure difference over the disc times the area of the disc:

$$T = (p_d^+ - p_d^-)A_d \quad (3.11)$$

Combining this with equation 3.10 gives:

$$T = \frac{1}{2}\rho A_d(U_\infty^2 - U_W^2) = \frac{1}{2}\rho A_d(U_\infty + U_W)(U_\infty - U_W) \quad (3.12)$$

Now there are two different expressions for the thrust: equation 3.6 and the equation above. These two must be equivalent, therefore:

$$\rho U_d A_d (U_\infty - U_W) = \frac{1}{2}\rho A_d (U_\infty + U_W)(U_\infty - U_W) \quad (3.13)$$

which gives:

$$U_d = \frac{1}{2}(U_\infty + U_W) \quad (3.14)$$

Now defining the induction factor  $a$  as:

$$a = \frac{U_\infty - U_d}{U_\infty} \quad (3.15)$$

the velocity at the disc can be written as:

$$U_d = U_\infty(1 - a) \quad (3.16)$$

Combining equation 3.14 with equation 3.16 gives for the velocity in the far wake:

$$U_W = U_\infty(1 - 2a) \quad (3.17)$$

Since  $aU_\infty$  is the reduction in velocity between far upstream and at the disc, equation 3.17 shows that at the disc the velocity has already been reduced by half of the total reduction.

The power extracted from the wind can be written as the energy per second that is removed by the disc. Because the pressure everywhere outside  $CVII$  is equal to  $p_\infty$ , only kinetic energy has to be looked at. The change in kinetic energy per second is:

$$\frac{\Delta KE}{t} = \frac{1}{2}\dot{m}_{side}U_\infty^2 + \frac{1}{2}\rho(A_{CV} - A_W)U_\infty^3 + \frac{1}{2}\rho A_W U_W^3 - \frac{1}{2}\rho A_{CV}U_\infty^3 \quad (3.18)$$

This can be written as:

$$\frac{\Delta KE}{t} = \frac{1}{2}\rho A_W U_W(U_W^2 - U_\infty^2) \quad (3.19)$$

Using the continuity equation (equation 3.1) this gives:

$$\frac{\Delta KE}{t} = \frac{1}{2}\rho A_d U_d(U_W^2 - U_\infty^2) \quad (3.20)$$

Using the equation for the thrust, equation 3.12, this results in:

$$\frac{\Delta KE}{t} = -TU_d \quad (3.21)$$

The power output of the actuator disc is:

$$P = -\frac{\Delta KE}{t} = TU_d \quad (3.22)$$

Using the induction factor, the expressions for the thrust and power can be rewritten. By combining equations 3.12 and 3.17, the thrust on the rotor or axial force ( $D_{ax}$ ) can be written as:

$$T = D_{ax} = \frac{1}{2}\rho U_\infty^2 A_d [4a(1 - a)] \quad (3.23)$$

This can also be used to calculate a non-dimensional coefficient:

$$C_{D_{ax}} = \frac{D_{ax}}{\frac{1}{2}\rho U_\infty^2 A_d} = 4a(1 - a) \quad (3.24)$$

If  $C_{D_{ax}}$  is known, the induction factor can be calculated using

$$a = \frac{1}{2} - \frac{1}{2}\sqrt{1 - C_{D_{ax}}} \quad (3.25)$$

As an extra illustration of the conditions in the flow, figure 3.2 shows the velocity, dynamic pressure, static pressure and total pressure against the axial distance from the disc. These plots summarise the effects of a wind turbine on the global flow.

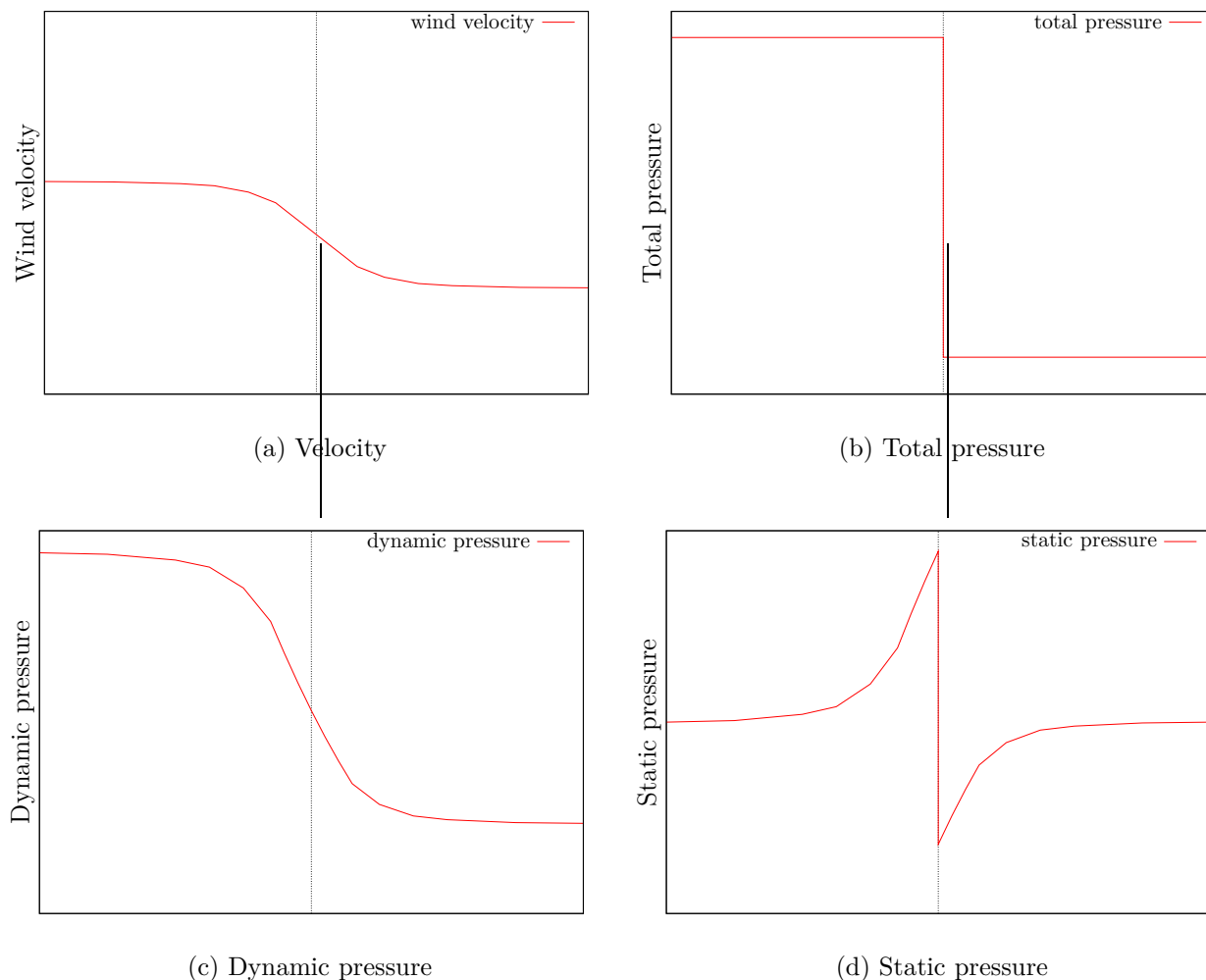


Figure 3.2: The velocity (a), total pressure (b), dynamic pressure (c) and static pressure (d) according to the momentum theory. The velocity is reduced by  $aU_\infty$  to  $U_d$  at the disc and by  $2aU_\infty$  to  $U_W$  in the far wake. The total pressure is reduced from  $p_\infty + \frac{1}{2}\rho U_\infty^2$  upstream of the disc to  $p_\infty + \frac{1}{2}\rho U_W^2$  downstream of the disc. The dynamic pressure far upstream is  $\frac{1}{2}\rho U_\infty^2$ , it is reduced to  $\frac{1}{2}\rho U_d^2$  at the disc and to  $\frac{1}{2}\rho U_W^2$  in the far wake. The static pressure increases from  $p_\infty$  far upstream of the disc to  $p_d^+$  just upstream of the disc. Just downstream of the disc it has been reduced to  $p_d^-$ . It increases again to  $p_\infty$  in the far wake.

### 3.1.2 Betz Limit

Betz [6, 7] has applied the momentum method to the wind turbine situation. His most famous outcome was the limit he calculated, the so-called Betz limit which determines the maximum power coefficient that can theoretically be achieved. This limit was however predicted earlier by Lanchester [5, 79, 77], but in practice the limit is mostly attributed to and named after Betz. This is due to the fact that Betz published his result in a journal whereas Lanchester published his result in the transactions of his institute.

One might expect the maximum power to be obtained at a maximum thrust, but, as shown below, this is not the case. The power coefficient is defined as:

$$C_p = \frac{P}{\frac{1}{2}\rho U_\infty^3 A_d} \quad (3.26)$$

This definition can be rewritten using equations 3.16, 3.22 and 3.23:

$$C_p = \frac{P}{\frac{1}{2}\rho U_\infty^3 A_d} = \frac{D_{ax}(1-a)U_\infty}{\frac{1}{2}\rho U_\infty^3 A_d} = 4a(1-a)^2 \quad (3.27)$$

Therefore the maximum power coefficient can be determined by first calculating the derivative of  $C_p$  to  $a$ :

$$\frac{dC_p}{da} = 4(1-a)(1-3a) \quad (3.28)$$

The maximum will occur when this derivative is equal to zero, thus when  $a = \frac{1}{3}$ . Substituting this value back into equation 3.27 gives a maximum power coefficient of:

$$C_{p_{max}} = \frac{16}{27} \approx 0.59 \quad (3.29)$$

This limit on the maximum power coefficient is not caused by the design of the wind turbine, but by the fact that the wind flowing through the area of the actuator disc has already been slowed down and therefore the area of the stream tube far upstream was smaller than the area of the actuator disc. This means that there are two opposing effects when the axial force increases. The higher force takes out more energy from the air per kilogram of air, but at the same time the amount of air flowing through the disc is further reduced, so there are less kilograms of air from which to take the energy. According to van Kuik [75] the maximum power coefficient is slightly higher than  $\frac{16}{27}$  due to the edge forces. In practice the Betz-limit is not reached in real wind turbines, because there is a finite number of blades on a wind turbine and due to the drag force that is acting on the blades [133].

### 3.1.3 Rotor Disc Theory

A wind turbine generates power from the torque acting on the shaft by using a generator. The generator transforms the torque into electrical energy. The air passing through the rotor

swept area exerts the torque on the shaft, therefore the air will be accelerated in the opposite direction. The velocity of the wind will gain a component parallel to the rotor movement. This change in velocity will completely take place in the thickness of the disc. The rotor disc theory is used to determine the change in velocity in this direction. It is described in most wind turbine literature, e.g. [18, 47]. The velocity of the air relative to the disc will increase in the tangential direction due to the induced tangential velocity. At the middle of the disc thickness, the tangential induced velocity will be  $a'\Omega r$  and will therefore depend on the radial position. The velocity at the end of the disc thickness will be  $2a'\Omega r$ . To determine the value of  $a'$  an annular ring will be considered. It is assumed that the torque acting on that part of the rotor that is within this ring causes the tangential velocity change of the air in this same ring or annulus.

The change of the angular momentum of the air that passes through the annulus must be equal to the torque acting on this ring or annulus:

$$\delta Q = 2\Omega a' r^2 \rho U_\infty (1 - a) \delta A_r \quad (3.30)$$

with  $\delta A_r = 2\pi r \delta r$  the area of the annulus. The power delivered by the ring is:

$$\delta P = \Omega \delta Q \quad (3.31)$$

This power is gained by slowing down the wind in the annulus, therefore:

$$\delta P = 2\rho U_\infty^3 a (1 - a)^2 \delta A_r \quad (3.32)$$

Substituting equation 3.30 into equation 3.32 results in the following relation:

$$U_\infty^2 a (1 - a) = \Omega^2 r^2 a' \quad (3.33)$$

By defining the local speed ratio as  $\lambda_r = \frac{\Omega r}{U_\infty}$  the equation can be rewritten as:

$$a(1 - a) = \lambda_r^2 a' \quad (3.34)$$

Using this equation, the power delivered by the annulus can be written as:

$$\delta P = \frac{1}{2} \rho U_\infty^3 2\pi \delta r 4a' (1 - a) \lambda_r^2 \quad (3.35)$$

The terms before the 4 in this equation are equal to the total available power in the ring, therefore the other terms determine the efficiency of the wind turbine blade element:

$$\eta_r = 4a' (1 - a) \lambda_r^2 \quad (3.36)$$

The radial derivative of the power coefficient can be calculated using:

$$\frac{d}{dr} C_p = \frac{4\pi \rho U_\infty^3 (1 - a) a' \lambda_r^2 r}{\frac{1}{2} \rho U_\infty^3 \pi R^2} = \frac{8(1 - a) a' \lambda_r^2 r}{R^2} \quad (3.37)$$

This can be rewritten by using the non-dimensional radial position  $\mu = \frac{r}{R}$ :

$$\frac{d}{d\mu}C_p = 8(1-a)a'\lambda^2\mu^3 \quad (3.38)$$

with  $\lambda$  the tip speed ratio:  $\lambda = \frac{\Omega R}{U_\infty}$ .

To find the maximum power coefficient, the expression for  $a'\lambda_r^2$  as found in equation 3.34 can be substituted into the blade element efficiency in equation 3.36:

$$\eta_r = 4a(1-a)^2 \quad (3.39)$$

The maximum power coefficient will occur when

$$\frac{d\eta_r}{da} = 0 \quad (3.40)$$

Therefore the maximum power will occur for a uniform distribution of  $a$ , with  $a = \frac{1}{3}$ . In momentum theory the same value is found for the induction factor  $a$  for which the power is maximum. Uniform distribution of the induction factor is one of the assumptions in the momentum theory. The tangential induction factor does depend on the radial position and for the maximum power this would be:

$$a' = \frac{a(1-a)}{\lambda^2\mu^2} \quad (3.41)$$

Substituting these values into equation 3.38 and integrating from 0 to 1 gives the maximum power coefficient. Its value is again  $C_{p,max} = \frac{16}{27}$ , the same as found using the momentum theory with the non-rotating wake.

The kinetic energy of the wake is increased due to the angular momentum of the wake. It is balanced by a loss of static pressure:

$$\Delta p_r = \frac{1}{2}\rho(2\Omega a' r)^2 \quad (3.42)$$

Using the expression for  $a'$  in equation 3.41 gives:

$$\Delta p_r = \frac{1}{2}\rho U_\infty^2 \left[ 2 \frac{a(1-a)}{\lambda\mu} \right]^2 \quad (3.43)$$

This pressure creates a radial pressure gradient that balances the centrifugal force on the rotating wake. If the wake would not expand, this radial pressure gradient would remain constant further down stream and it would be superimposed on the pressure as found using the momentum theory. It would therefore not affect the change of axial momentum. In reality the wake does expand, but for tip speed ratios  $\lambda > 1.5$ , this does not have a significant effect and can be neglected. Burton *et al.* notice that most books adopt Glauert's assumption that the kinetic energy of the wake rotation is drawn from the kinetic energy of the flow (see [41]), while for propellers Glauert had concluded that the effect of wake rotation was only significant for  $\lambda < 1.5$  and he accounted for this effect by a reduction in the static pressure in the wake [40].

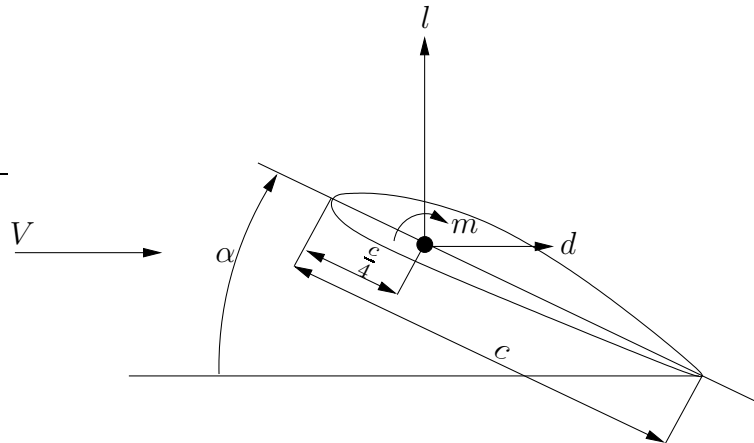


Figure 3.3: The aerodynamic forces acting on a blade element (2D).

### 3.1.4 Blade Element theory

Rotor aerodynamics are usually separated: the global flow field, as discussed in the previous sections, is analysed separately from the local flow field about the aerofoils. The boundary conditions form the connection between the two. After all, the global flow field determines part of the inflow conditions for the blades and therefore the forces acting on the blades. These forces in their turn determine the global flow.

The blade element theory described in this section can be used to calculate the blade flow. It is originated by W. Froude [34] and developed further by Drzewiecki [29].

Since the early days of flight, different aerofoils have been designed and tested. The 2 dimensional properties of the aerofoils can be tested in a wind tunnel. From these measurements lift- drag- and moment coefficients are determined for different angles of attack  $\alpha$ . These coefficients are defined as:

$$c_l = \frac{l}{\frac{1}{2}\rho V^2 c} \quad (3.44)$$

$$c_d = \frac{d}{\frac{1}{2}\rho V^2 c} \quad (3.45)$$

$$c_m = \frac{m}{\frac{1}{2}\rho V^2 c^2} \quad (3.46)$$

where  $l$  is the lift force per meter span,  $d$  the drag force per meter span,  $m$  the moment per meter span and  $c$  is the chord of the blade. These forces are illustrated in figure 3.3. The drag force is defined in the same direction as the local velocity and the lift force is perpendicular to the local velocity.

The values of these coefficients against angle of attack  $\alpha$  for an aerofoil at a certain Reynolds

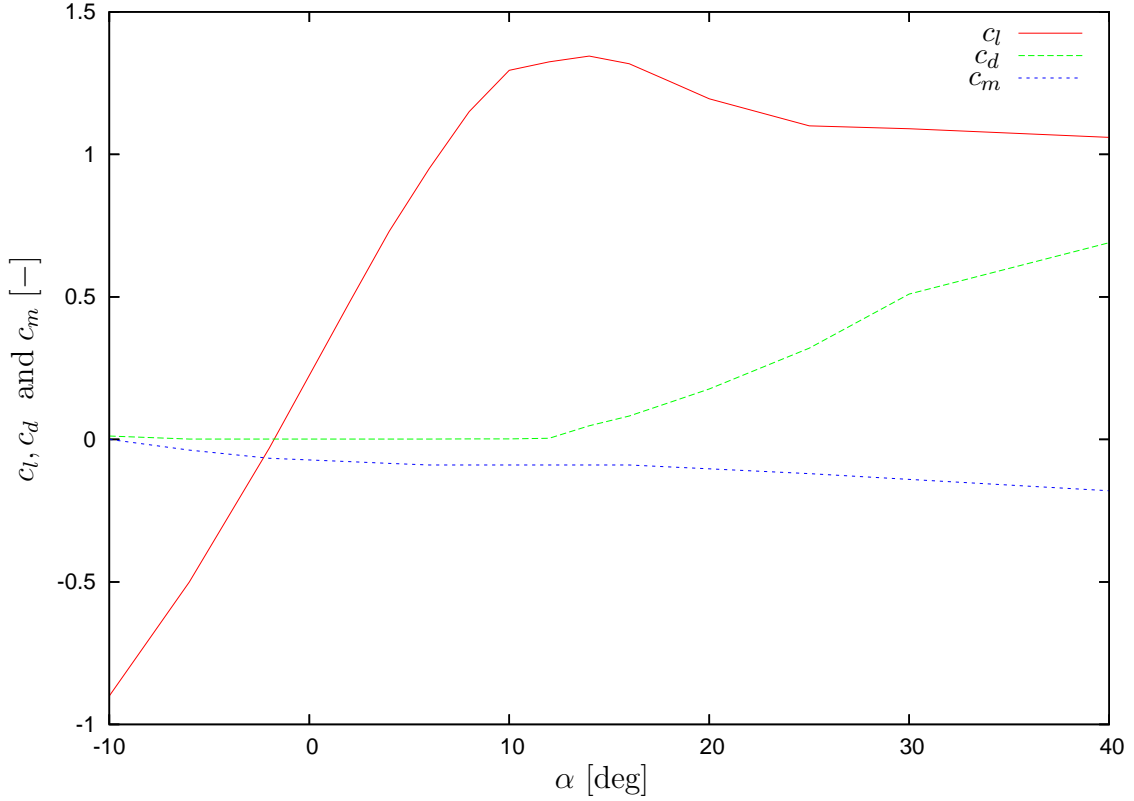


Figure 3.4: An example of a lift coefficient, drag coefficient and moment coefficient against the angle of attack.

<sup>1</sup> and Mach number can be found in the literature describing the results of measurements. The coefficients for a given Reynolds number and Mach number are a function of the angle of attack only. This angle is determined by the local velocity and the position of the blade as shown in figure 3.3. An example of the different coefficients as a function of the angle of attack is given in figure 3.4. This graph is valid for a certain Reynolds and Mach number and for one particular aerofoil.

It is possible to calculate the force distribution on the blade by determining the velocities along the blade and from this the angles of attack and determine the corresponding lift-drag- and moment coefficients. By integrating over the radius, the total force and moment are determined, assuming the 2D measurements can be used for 3D reality:

$$L = \int_0^R \frac{1}{2} \rho V^2 c_l c dr \quad (3.47)$$

$$D = \int_0^R \frac{1}{2} \rho V^2 c_d c dr \quad (3.48)$$

---

<sup>1</sup> $Re = \frac{\rho U d}{\mu}$  describing the ratio between inertia force on a volume and the viscous force. For high Reynolds numbers the viscous forces are relatively low.

$$M = \int_0^R \frac{1}{2} \rho V^2 c_m c^2 dr \quad (3.49)$$

However, when looking at a finite wing of an aircraft, the 2-D coefficients must be corrected for 3-D effects. Prandtl developed the first practical theory for predicting the properties of finite wings. This method is still used [3]. Prandtl stated that it is possible to look at the aerodynamics on a wing in two stages. First the section of a wing can be looked at as part of an infinite wing as a starting point and then the correction due to the finiteness of the wing can be added.

What causes the difference between 2D and 3D flow around aerofoils? Assume a lifting line: the lift on a wing is caused by the circulation about the wing sections. A pressure difference between the top surface and the bottom surface causes the lift. When a wing is finite, the air can flow from below the wing to above the wing, resulting in a vortex, as illustrated in figure 3.5 a. This is however only part of the story. The strength of the circulation causing the lift, will not be constant along the span, for finite wings. Therefore the distribution of the circulation is represented by infinitely many horseshoe vortices that are superimposed. As illustrated in figure 3.5 b, the vortices result in a downwash. This creates an effective angle of attack that is smaller than the angle of attack for an infinite wing. At the same time the lift force will also be turned slightly, resulting in an induced drag. The 2-D coefficients for the lift, drag and moment that have been determined from measurements, need to be corrected for this difference in the angle of attack.

Prandtl derived equations for the downwash, but also stated that the theory was unusable for unsteady or yawed flow, because in those cases his theory resulted in infinite downwash. His theory however can also be used in these two cases, the singularities were the results of a misinterpretation. As described by van Holten in [57], it is possible to use a definition of the induced velocity that does not lead to this singularity.

However, when looking at the calculations for a wind turbine or a helicopter, the induced velocity is usually calculated using the momentum theory described in section 3.1.1. Using the momentum to calculate the induced velocity is equivalent to the lifting line theory described here.

### 3.1.5 Blade Element and Momentum Theory

The combination of the blade element theory and the momentum theory is called the blade element - momentum theory (BEM). The blade element theory, as discussed above, is used to calculate the local forces based in the local velocity vector. The momentum theory, as discussed in section 3.1.1, is used to calculate the induced velocity that is the result of the local forces. The induced velocity in turn has its influence on the local forces as calculated using blade element theory. The connection between the two methods is therefore formed by the forces and the induced velocity. BEM is very often used in aeroelastic codes for wind turbines and helicopters and is also used in the programme WOBBE that is described in chapters 5 and 6.

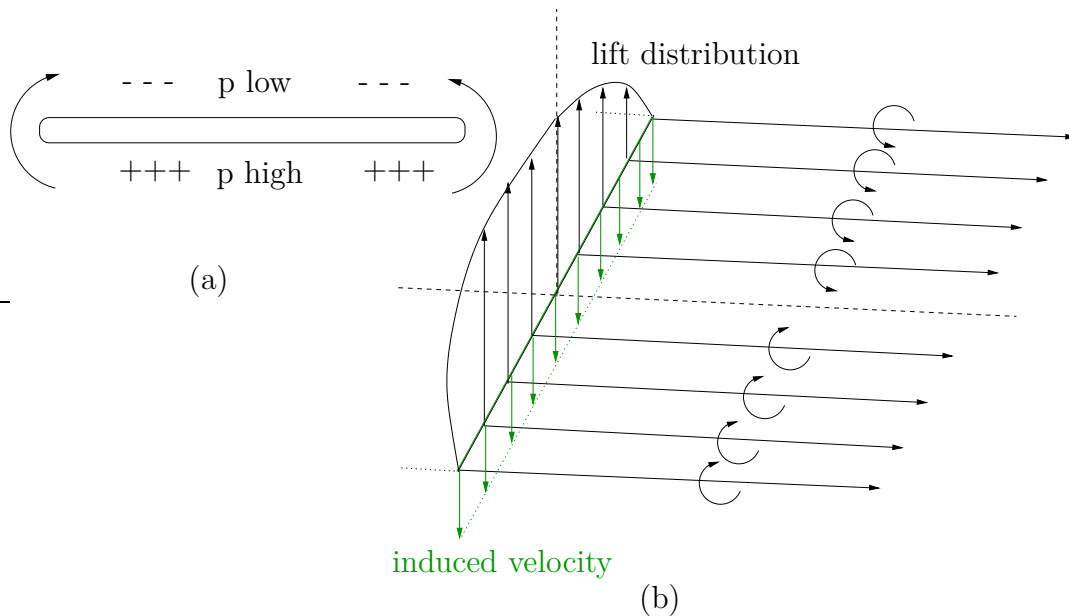


Figure 3.5: The effect of the finiteness of the wing, (a): The pressure difference between top and bottom results in a strongly 3D flow, (b): The change in lift along the width of the wing results in vortices. These vortices result in an induced velocity.

Glauert [30] applies the momentum method to annuli, not the complete rotor plane. The forces acting on the blade elements (see 3.1.4) in one annulus result in the induced velocity in this annulus. The induced velocity is calculated using the momentum theory. This so-called strip theory relates the rotor performance to the geometry of the rotor. Three assumptions are needed:

1. Individual stream tubes or strips can be analysed independently of the rest of the flow (annular independence). This condition is met as long as the circulation distribution over the blade is relatively uniform, so when most vorticity is shed at the root and the tip.
2. The spanwise flow can be neglected, therefore it is possible to use 2D aerofoil data.
3. The flow conditions do not vary in the circumferential direction. This excludes among other wind shear and yawed flow.

In the programme WOBBE, described in chapters 5 and 6, the blade element momentum theory used is not based on using strips, but a constant induction factor over the rotor plane has been assumed. It is clear that both methods are invalid, after all the different strips will not be completely independent, there will always be some redistribution of the forces, but assuming the induction factor constant over the entire rotor swept area is also an incorrect assumption.

To determine the forces on a blade, an iteration will always be needed, because of the coupling between the global and local flow. The angle of attack depends on the induction factor, therefore the forces depend on the induction factor, but the induction factor in turn depends on the forces.

For aeroelastic analysis, it is very important to take the motions due to deformations of the blade into account when determining the aerodynamic forces. The coupling between the aerodynamic forces and the deformations is the cause of aeroelastic instabilities.

The changing forces due to the deformations will result in flow conditions that vary in the circumferential direction as well as changes of momentum in the global flow. Therefore the assumption of steady conditions as used in BEM is not valid for aeroelastic calculations of wind turbines. As mentioned in the previous sections, there are also other limitations to the BEM theory. Therefore there are several corrections and additions to the BEM theory. These are discussed in the next sections. Corrections are needed for high disc loading (turbulent wake state); when the induction factor gets above 0.4 the momentum method is no longer valid. Corrections are also needed due to the limited number of blades (Prandtl's tip correction). Finally methods exist that can model parts of the unsteadiness in the flow. This includes dynamic stall models and dynamic inflow models. The extent of the unsteadiness of the flow is given by the reduced frequency  $k = \frac{\omega b}{U_\infty} = \frac{\omega c}{2U_\infty}$ . Leishman states that only if this frequency is below  $O(0.01)$ , a steady or quasi-steady flow can be assumed [81].

### 3.1.6 Turbulent Wake state

Wind turbines can operate in different states. Usually wind turbines will operate in the windmill state. The induction factor is then approximately between 0 and 0.4 (as defined for wind turbines, so negative values for helicopters) and the axial momentum theory is valid. If the induction factor is less than 0, e.g. for an ascending helicopter, the state is called the propeller state and the momentum theory is also valid. When the induction factor is between approximately 0.4 and 1.0 the state is called the turbulent wake state. These and other possible states for helicopters and wind turbines are described by Lock and Wilson [84, 141].

According to the momentum theory, described in section 3.1.1, for heavily loaded wind turbines with a high induction factor  $a$ , the wind behind the turbine should show a reversal of the flow. A reversal of flow cannot actually happen in practice. For one, the flow would have to come to a stop ( $U = 0$ ) somewhere which makes continuity impossible. Therefore the momentum theory is clearly no longer valid in these cases. The stream in the wake will, instead of coming to a stop, become turbulent. This causes air from outside the wake to mix with the wake and in doing so it will re-energise the air that has been slowed down by the rotor. This operating condition is called the turbulent wake state. It will usually occur for low wind speeds, because wind turbines are usually heavily loaded for low wind speeds. Especially fixed speed turbines will operate under high disc loading conditions at low wind

speeds. The wind turbine will reduce the wind velocity by a relatively large proportion. For tip speed ratios ( $\lambda = \frac{R\Omega}{U_\infty}$ , where  $R$  is the radius of the turbine) that are above the design value, (e.g. low wind speed), the air particles will meet with a less permeable disc than for low tip speed ratios. Air that cannot pass through the disc will move radially outwards. This will cause a low pressure downstream, while the air stagnation in front of the disc will cause a high pressure upstream resulting in a much larger thrust acting on the disc than predicted by the momentum theory. If  $C_{Dax}$  goes above a certain transition point, the wake will become turbulent. Glauert has proposed an empirical formula to predict the induction factor for heavily loaded turbines [39]. This is based on measurements he performed. This empirical method from Glauert to describe the turbulent wake state is a reasonable model of rotor thrust behaviour for induction factors above 0.4 and it is often used in aeroelastic wind turbine codes. Glauert proposes the following parabola [18]:

$$C_{Dax} = C_{Dax1} - 4(\sqrt{C_{Dax1}} - 1)(1 - a) \quad (3.50)$$

where  $C_{Dax1}$  is the value for  $C_{Dax}$  when  $a = 1$ . From measurements it appears that the value for  $C_{Dax1}$  is somewhere between 1.6 and 2. The value of  $C_{DaxT}$  in the transition point is then found by equalising the two derivatives of  $C_{Dax}$  with respect to  $a$  determined from equation 3.50 for the turbulent wake state and equation 3.24 for the momentum theory:

$$\frac{d}{da} \left( C_{Dax1} - 4(\sqrt{C_{Dax1}} - 1)(1 - a) \right) = \frac{d}{da} (4a(1 - a)) \quad (3.51)$$

which gives:

$$4(\sqrt{C_{Dax1}} - 1) = 4 - 8a \quad (3.52)$$

This means that:

$$a_t = 1 - \frac{1}{2}\sqrt{C_{Dax1}} \quad (3.53)$$

The value of  $C_{Dax}$  in the transition point can then be found by substituting this expression in either equation 3.50 or equation 3.24, both resulting in the same expression:

$$C_{DaxT} = -C_{Dax1} + 2\sqrt{C_{Dax1}} \quad (3.54)$$

For values of  $C_{Dax}$  that are higher than  $C_{DaxT}$ , equation 3.50 can be used to calculate the induction factor. For values of  $C_{Dax}$  that are lower than  $C_{DaxT}$ , momentum theory can be used as given in equation 3.25. This results in a correlation as shown in figure 3.6.

Wind turbines operating near their optimum should be operating close to  $a = \frac{1}{3}$ , so not in the turbulent wake state. However, for lower wind speeds, as mentioned before, they will often operate at higher induction factors. The maximum will be somewhere around 0.6.

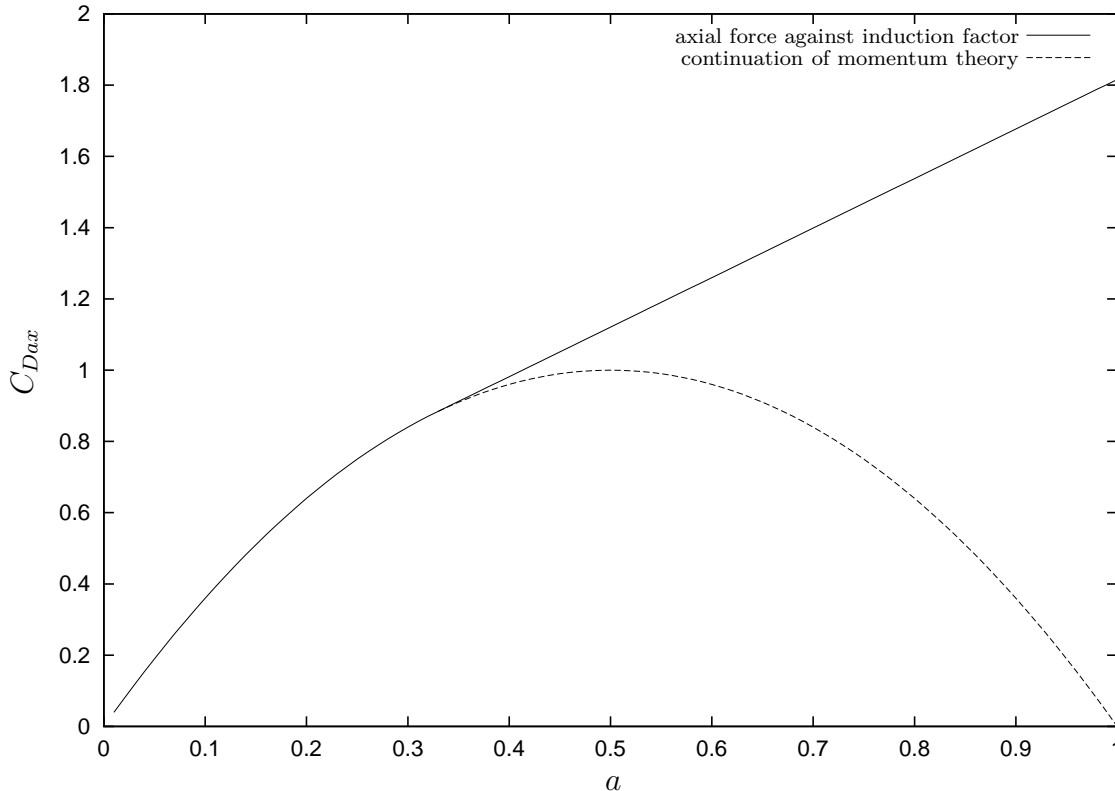


Figure 3.6: The axial force coefficient  $C_{Dax}$  plotted against the induction factor  $a$  using momentum theory and Glauert to estimate the turbulent wake state for a value of  $C_{Dax1} = 1.816$ . This results in  $a_t = 0.326$  and  $C_{DaxT} = 0.879$ . The unrealistic values for the momentum theory for higher induction factors are also illustrated.

### 3.1.7 Dynamic Inflow

The BEM method is derived for time-independent flows. However, there can be different possibilities that would cause the flow and therefore the induction factor to change in time, e.g. changes in the wind velocity or changes in deformation of the blades causing altering aerodynamic forces. It is not realistic to assume that the stream will instantaneously adapt to this change. When thinking of a vortex model, it is clear that it will take some time to change to the new induction value. This can be modelled using a dynamic inflow model. Using these models can have a large effect on aeroelastic results as shown by e.g. Crews *et al.* [25] and Ormiston [99]. The dynamic inflow model will act on a relatively long time-scale, while the unsteady aerodynamics discussed in section 3.1.9 as well as the blade vibrations of a wind turbine blade are on a much shorter time-scale.

Different variants of the dynamic inflow model exist, see for example Pitt and Peters [114]. The tool discussed in chapters 5 and 6 includes a model for dynamic inflow [10, 73]. This model is based on using the equations for  $C_{Dax}$  for both wind mill state and turbulent wake

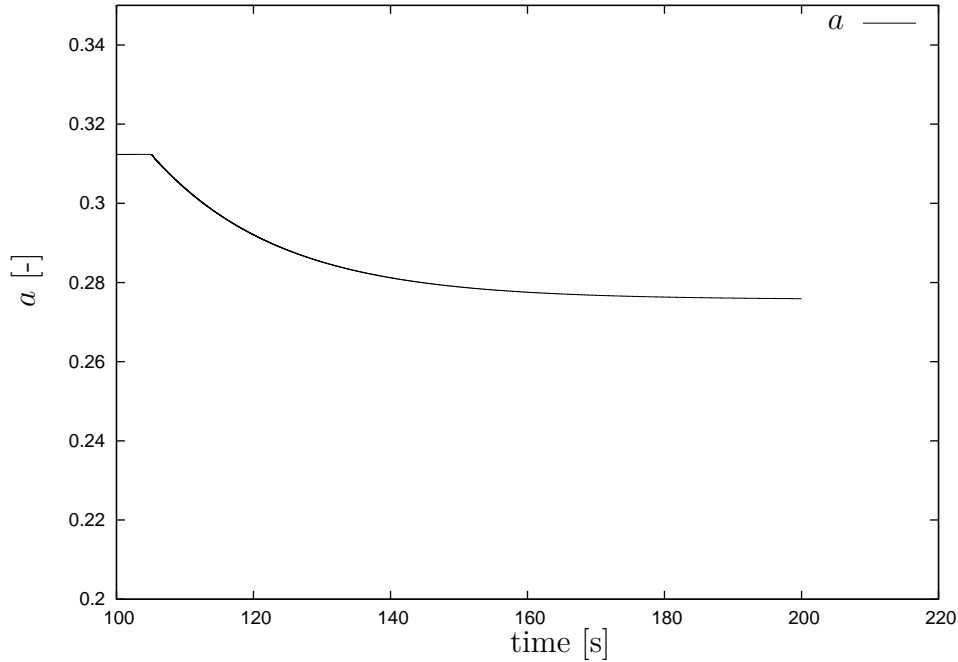


Figure 3.7: An example of dynamic inflow. This graph shows the resulting induction factor from a simulation of an isolated blade at constant wind speed with a sudden step change in pitch setting at 105 s.

state and adding a time derivative term. This gives:

$$a + \tau_w \dot{a} = \begin{cases} 0.5 - 0.5\sqrt{1 - C_{Dax}} & \text{for } C_{Dax} \leq C_{DaxT} \\ \frac{(C_{Dax} - C_{Dax1})}{4(\sqrt{C_{Dax1}} - 1)} + 1 & \text{for } C_{Dax} > C_{DaxT} \end{cases} \quad (3.55)$$

Here  $C_{DaxT}$  is the axial force coefficient in the transition point between momentum theory and turbulent wake state.  $\tau_w$  is a characteristic time constant, e.g.  $4\frac{R}{U_\infty}$  [106].

The dynamic inflow will result in slowly adjusting values for  $a$  and  $a'(r)$ . An example of the resulting induction factor  $a$  plotted against the time is given in figure 3.7. This shows a case where the undisturbed wind velocity is constant, but there is a step change in the pitch angle at  $t = 105$  s. The plot for  $\dot{a}$  for the same simulation is given in figure 3.8. Both plots illustrate the delay that is present in obtaining the induction factor after a step change. These results were obtained using the programme described in chapter 6.

### 3.1.8 Tip Loss Corrections

The actuator disc model used to derive the momentum equations assumes an infinite number of blades. Wind turbines will have only two or three blades, therefore not every air particle passing through the rotor swept area will be strongly affected by the pressure fields of the

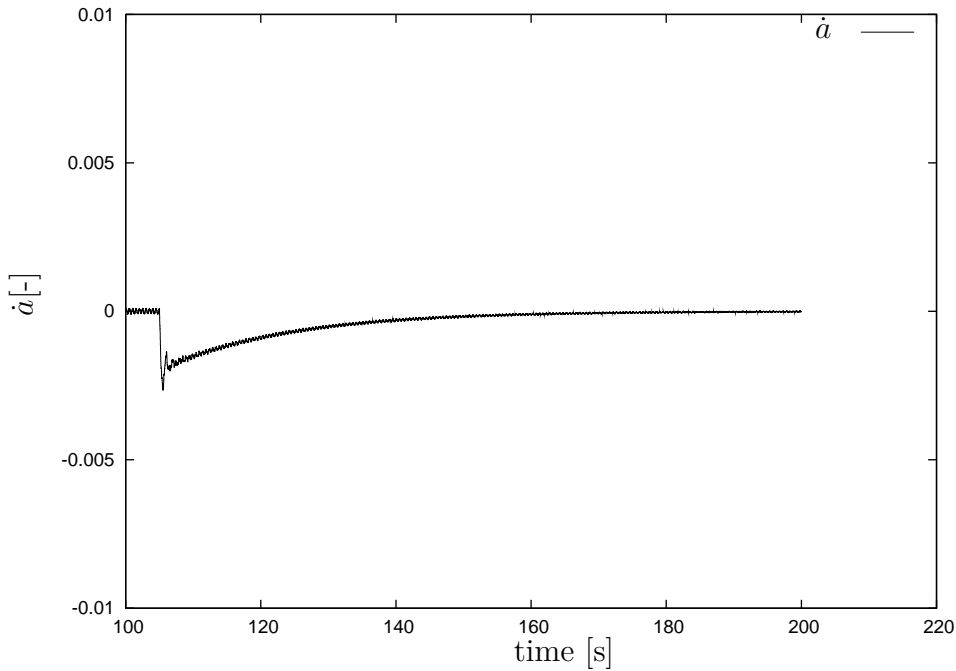


Figure 3.8: An example of dynamic inflow. This graph shows the time derivative of the induction factor from a simulation of an isolated blade at constant wind speed with a sudden step change in pitch setting at 105 s.

blades of the wind turbine. To compensate for this fact, so-called tip-loss corrections can be used. These corrections will reduce the induction factor in the outer annuli and therefore the aerodynamic forces acting near the tip. Because the correction mainly affects the forces near the tip they are called tip corrections. In this section several tip-correction methods will be discussed shortly. The most widely used is Prandtl's tip-loss correction. Prandtl has developed an analytical formula for the tip loss function. Prandtl derived a simple analytical model replacing the vortex sheets that are impermeable with material sheets that move at the same speed as the vortex sheets in the wake. This way they would have no effect on the wake flow. The model was further simplified by Prandtl by replacing the helicoidal sheets with a number of discs that are at the same distance from each other as the normal distance between the vortex sheets. The discs move with the wake velocity:  $U_\infty(1 - a)$ . The distance between the discs must be much smaller than the radius of the disc. The free-stream air will move at a higher velocity and will follow the paths as illustrated in figure 3.9. The wider the discs are apart, the more the free-stream will penetrate between the discs. Therefore at some radial distance  $r$  the velocity will be slightly higher than the wake velocity, but lower than the free-stream velocity. The average velocity at  $r$  is written as  $U_\infty(1 - af(r))$ , where  $f(r)$  is the tip-loss function.

The function that Prandtl found, based on this wake-disc model is [6, 18]:

$$f(r) = \frac{2}{\pi} \arccos\left[e^{-\pi\left(\frac{R_W-r}{d}\right)}\right] \quad (3.56)$$

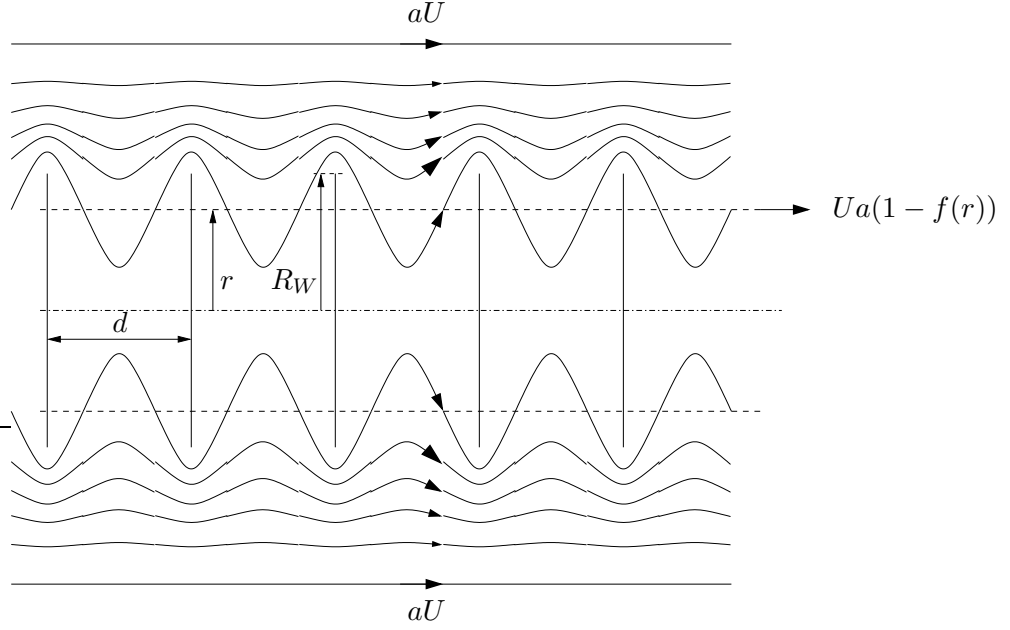


Figure 3.9: Prandtl's tip correction is based on a wake-disc model. The discs move with the wake velocity, the flow is illustrated relative to these moving discs. The velocities are also given relative to the moving discs. The discs are at the same distance from each other as the normal distance between the vortex sheets.

where  $R_W - r$  is the distance measured from the wake edge. The distance  $d$  is taken to be the normal distance between successive helicoidal vortex sheets by Glauert [40]. For  $N$  blades this would be [18]:

$$d = \frac{2\pi R_W}{N} \sin \phi_s = \frac{2\pi R_W U_\infty (1 - a)}{N W_S} \quad (3.57)$$

with  $\phi_s$  the helix angle of the vortex sheets which is equal to the flow angle.  $W_S$  is the resultant velocity (excluding radial terms) at the edge of the disc. According to Glauert [40] one can state that

$$\frac{R_W}{W_S} \approx \frac{r}{W} \quad (3.58)$$

With  $W$  the local velocity due to the wind speed, the induced velocity and the rotation:

$$W = \sqrt{[U_\infty(1 - a)]^2 + (\Omega r)^2} \quad (3.59)$$

This approximation given by Glauert is easier to use in combination with the blade element momentum method. Using this gives:

$$\frac{\pi}{d} = \frac{N W_S}{2 R_W U_\infty (1 - a)} = \frac{N W}{2 r U_\infty (1 - a)} \quad (3.60)$$

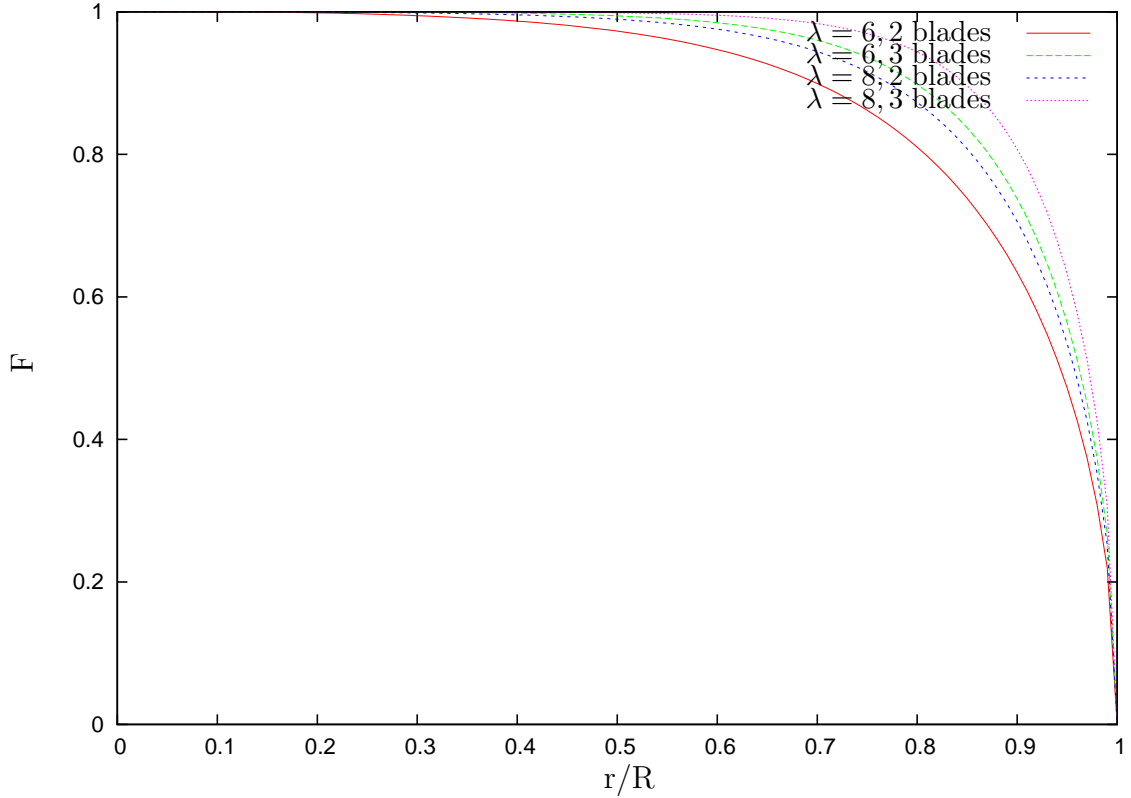


Figure 3.10: Prandtl's correction factor  $F$  along the blade radius for two values of  $\lambda$  and for 2 and 3 bladed turbines

The exponent in Prandtl's correction function therefore becomes:

$$-\pi \left( \frac{R_W - r}{d} \right) = -\frac{N}{2} \left( \frac{R_W - r}{d} \right) \sqrt{1 + \frac{(\Omega r)^2}{[U_\infty(1-a)]^2}} \quad (3.61)$$

This results in the following equation for the tip-loss factor:

$$f(\mu) = \frac{2}{\pi} \arccos \left[ e^{-\left(\frac{N}{2}\right)(1-\mu)/\mu} \sqrt{1 + (\lambda\mu)^2 / (1-a)^2} \right] \quad (3.62)$$

where  $\mu$  is the non-dimensional radial position  $\frac{r}{R}$  and  $\lambda$  is the tip speed ratio:  $\lambda = \frac{\Omega R}{U_\infty}$ .

Prandtl's tip loss correction factor against radial position is shown for two and three blades and for two different tip speed ratios in figure 3.10.

Prandtl's tip correction can be used in several ways. The problem is that it is a correction of the momentum theory while it is used in the blade element momentum theory. Therefore any method used will result in an inconsistency in the blade element momentum theory. It is obvious that the aerodynamic force should be reduced according to Prandtl's tip correction factor, but there are two main ways to do this. These methods are illustrated in figure

3.11. Figure a. in figure 3.11 shows the flow situation for an element that is not close to the tip. Prandtl's tip correction will not have much effect here. Figure b. in this same figure shows the first method to use the correction near the tip. The forces are multiplied by the correction factor. Then an angle of attack is attained that corresponds to the low aerodynamic forces. This is achieved by changing the induced velocity such that the angle of attack corresponds to corrected aerodynamic forces. This means that the induced velocity is strongly increased around the tip, while all aerodynamic forces acting on this part of the blade strongly decrease. Therefore the forces that should cause the induced velocity are much smaller than the forces that are needed to cause the induced velocity that is assumed. The induced velocity is assumed much higher in order to get the low aerodynamic forces determined by the angle of attack. This is the inconsistency that cannot be avoided, when applying the correction factor to the blade element momentum theory.

The second option (c. in figure 3.11) is to multiply the uncorrected force by Prandtl's correction and ignore the fact that these corrected forces do not correspond to the local velocities anymore. The induction factor can be adjusted to the new force, but the angle of attack close to the tip will not correspond to the angle of attack that would correspond to the assumed forces at the section. Again there is an inconsistency in the theory. Using Prandtl's tip correction it is no longer possible to have a system where the local flow and the local forces correspond according to blade element momentum theory. This is because for both options discussed above the correction is used in the blade element theory as part of the blade element momentum theory, while Prandtl's tip correction is a correction of the momentum method.

Using the BEM method without any correction results in a lift force near the tip that is too high. Another method, which has only limited applicability, is using the effective radius which is used to correct performance calculations of helicopters. Prandtl derived the following equation for the effective radius factor  $B$  [80, 117, 134]:

$$B = 1 - \frac{\sqrt{2c_T}}{N} \quad (3.63)$$

where  $N$  is the number of blades. For helicopter rotors the effective radius factor will be in the range of 0.95 to 0.98.

Other tip-corrections that can be used include the tip loss correction of Wilson and Lissaman and the tip loss correction of de Vries as described by Shen *et al.* in [126, 127]. Shen *et al.* also describe an alternative method that removes the inconsistency described above by correcting the lift and drag coefficients near the tip. This way the angle of attack and the induced velocity correspond correctly to the forces acting on the outer parts of the blades.

### 3.1.9 Dynamic stall

Next to the dynamic inflow effect discussed in section 3.1.7, another dynamic effect that plays an important role and should be included in aeroelastic simulations is dynamic stall.

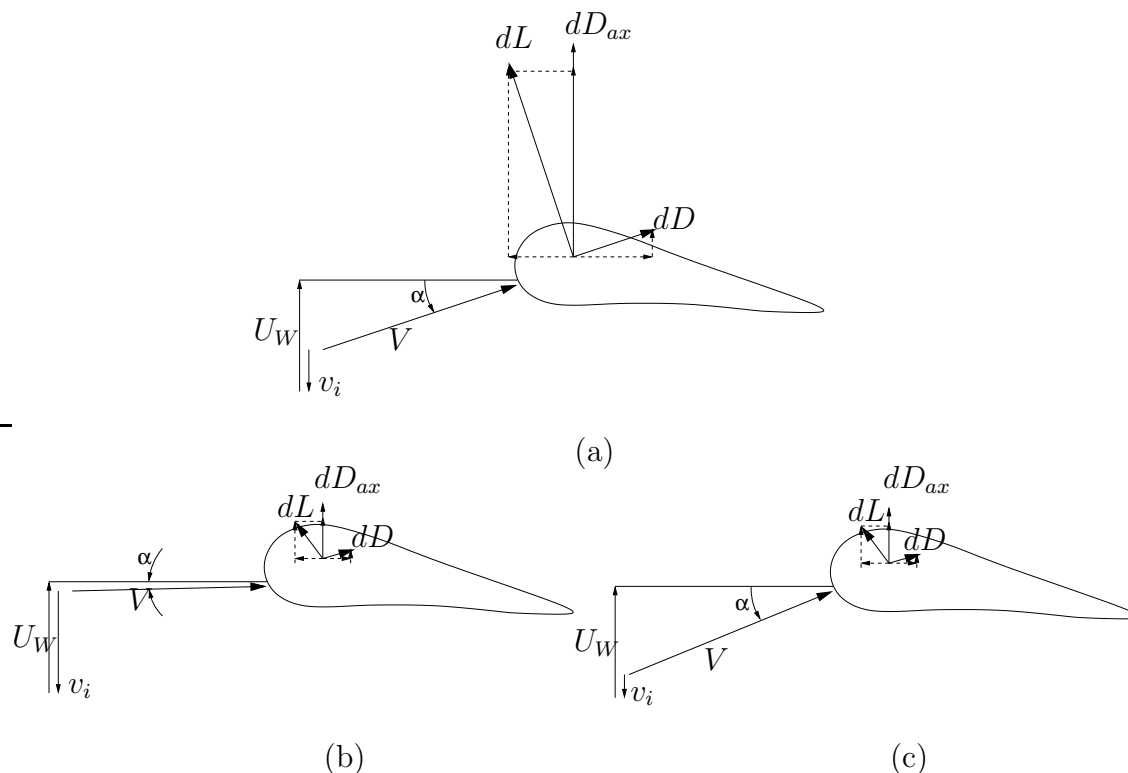


Figure 3.11: Applying Prandtl's tip correction: (a) the situation far away from the tip, no tip correction applied. (b) Near the tip, option 1: adjust the induced velocity in such a way that the angle of attack corresponds to the corrected lift and drag forces. The axial force no longer corresponds to the induced velocity. (c) Near the tip, option 2: calculate the induced velocity using the corrected aerodynamic forces. These no longer correspond to the angle of attack, but they do correspond to the induced velocity.

The time-scale of this unsteady phenomenon is much shorter than the dynamic inflow effects.

In section 3.1.4 the lift- and drag coefficients have been discussed as depending on the angle of attack and Reynolds and Mach number only. However, dynamic effects will change the values of these coefficients. The value of the coefficients at a certain angle of attack while the angle of attack is increasing will be different than the static value and different than the value at the same angle of attack, but for decreasing angle of attack. The same is true for the drag coefficient. The lift-curve will show a hysteresis. The name dynamic stall can be misleading, as there can also be a significant unsteady effect when the flow is fully attached. The dynamic stall phenomenon is illustrated in figure 3.12. This phenomenon can result in unsteady aerodynamic forces that are considerably in excess of what would be expected or predicted under steady conditions. Unsteady aerodynamics can therefore have a large influence on the aeroelastic stability of a wind turbine. The dynamic stall problem cannot be looked at isolated from the rest of the flow. The shed vortices in the wake are coupled to the dynamic stall. Determining the precise character of this unsteady behaviour is not yet

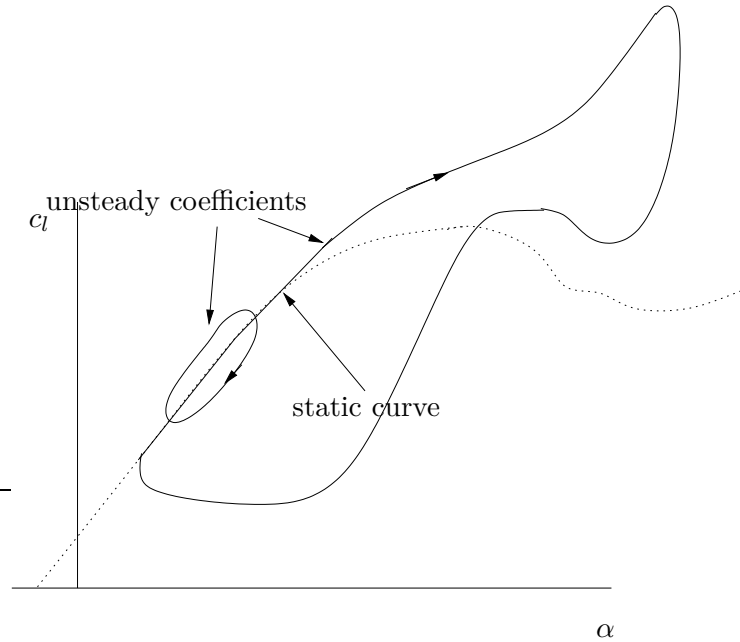


Figure 3.12: The static and dynamic values of the lift coefficient against the angle of attack. Two examples of possible loops are illustrated.

possible, but several engineering models do exist.

In this section one model for unsteady aerodynamics will be described, as this model is later used in the aeroelastic tool WOBBE discussed in chapters 5 and 6. This method was developed by Snel in 1997 [129]. It is inspired by Truong's work on a dynamic stall model based on a Hopf bifurcation [139] and it is primarily based on mathematical reasoning as opposed to physical reasoning. Snel expects the set of equations for this model will not need any further tuning for different airfoils as this is often a drawback for other dynamic stall models, such as ONERA's model [113]. Wind tunnel experiments of two airfoils making a periodic pitch motion have been used as a starting point. An attempt is made to identify the type of terms needed to reproduce the observed behaviour.

The steady lift coefficient that corresponds to the angle of attack is corrected with a first and a second order term,  $\Delta c_{l1}$  and  $\Delta c_{l2}$  respectively:

$$c_{l,dyn} = c_{l,steady} + \Delta c_{l1} + \Delta c_{l2} \quad (3.64)$$

The first correction term describes the forcing frequency response. In this model the behaviour of the angle of attack is not used as a forcing term, but a derived airfoil specific quantity: the time derivative of the difference between the potential flow lift coefficient ( $c_{l,pot} = 2\pi \sin(\alpha - \alpha_0)$ ) and the airfoil steady lift coefficient.

The second term,  $\Delta c_{l2}$ , is described using the reduced Strouhal frequency. This correction term introduces the higher frequency dynamics, thus a second order differential equation

is used for this term. The coefficients for this equation were determined by performing many numerical experiments and comparing the results with measurements. As one of the coefficients in the equation for the second order correction factor  $\Delta c_{l2}$  depends on this factor, an iterative process is used to calculate  $\Delta c_{l2}$ .

The full details of the model are described in appendix A.

The unsteady aerodynamic model results in a changing loop. The lift coefficient reached at a certain angle of attack when this is increasing will be higher than the lift coefficient reached at this same angle of attack when the angle is decreasing. This effect is very important as it has a considerable effect on the aerodynamic damping of the system.

## 3.2 Alternatives for Blade Element Momentum Theory

The blade element - momentum theory as described in the previous sections, is a relatively simple method that is often used in aeroelastic tools. However, most assumptions on which BEM is based are never actually met. Alternatives for the BEM theory that do not show these limitations, are therefore necessary and are discussed in this section. These alternatives can also be used to further improve the BEM theory. Better models of the aerodynamics can result in better predictions of the performance of the wind turbine as well as improved calculations of the structural loads. This can result in cost reductions, but before this can be achieved a better understanding of the (unsteady) aerodynamics is necessary.

Similar to the BEM theory, the discussion will be split into two parts, one describing the global flow and one describing the local flow around the blade. The boundary conditions (equal velocity and pressure at the boundary) will connect these two [130], except for the vortex wake/lifting line methods, where no patching between global and local flow is necessary.

### 3.2.1 Global flow

The most meticulous way to analyse the flow field is using the Navier-Stokes equations. The incompressible Navier-Stokes equations are valid when assuming uniform density and an incompressible flow. For wind turbines the Mach number is usually low enough to enable the assumption of incompressibility. Note however that Leishman states that, strictly speaking, the product of the Mach number of the flow with the reduced frequencies of the unsteady effects should also be small for the assumption of incompressibility to be correct [81]. There can be situations where this assumption will not be valid, but the effect of this will, most of the time, be limited and does not weigh against the increase in calculation costs [80].

The Navier-Stokes equations using Cartesian coordinates 1, 2 and 3 are [130]:

$$\frac{\partial u_j}{\partial x_j} = 0 \quad (3.65)$$

$$\frac{\partial u_i}{\partial t} + u_j \frac{\partial u_i}{\partial x_j} = -\frac{1}{\rho} \frac{\partial p}{\partial x_i} + \nu \frac{\partial^2 u_i}{\partial x_j^2} + f_i \quad i = 1, 2, 3 \quad (3.66)$$

Derivations of these equations can be found in many books, e.g. [3, 140].

Equation 3.65 is the continuity equation, while equation 3.66 is Newton's law of conservation of momentum in the direction of the three Cartesian coordinates. In this equation the accelerations are put on the left hand side of the equation, while the force terms (pressure, viscous and external) are given on the right hand side of the equation.

Solutions to the Navier-Stokes equations must satisfy certain boundary conditions, such as the no-slip and the no transparency boundary conditions for solid surfaces. The no-slip condition implies that the relative tangential velocity at the surface is equal to zero. The velocity perpendicular to the surface must also be equal to zero because the flow cannot go through the surface (no transparency). All in all there are four scalar equations and four unknowns. However the equations are nonlinear and they cannot be solved in closed analytical form.

To solve this problem, one can neglect the viscous forces as they will be much smaller than the accelerations in the flow. The Reynolds number of a wind turbine of 2 MW will typically be of the order of magnitude of  $6 \times 10^6$  [131] and will not vary much along the blade. This high Reynolds number indicates that the accelerations in the flow are of much higher importance than the viscous forces. Neglecting these viscous forces, results in the Euler equations [130]:

$$\frac{\partial u_j}{\partial x_j} = 0 \quad (3.67)$$

$$\frac{\partial u_i}{\partial t} + u_j \frac{\partial u_i}{\partial x_j} = -\frac{1}{\rho} \frac{\partial p}{\partial x_i} + f_i \quad i = 1, 2, 3 \quad (3.68)$$

Neglecting the viscous forces means that it is no longer possible to impose the no-slip boundary condition, only the no-transparency condition is left. This implies that there cannot be any vorticity generated except by external forces. This is not in agreement with reality where there is clearly vorticity being generated. This vorticity is generated on the blade surface as a result of the no-slip condition. In the real flow about a blade the gradient of the velocity close to the blade becomes so high that the viscous forces are of the same order of magnitude as the pressure forces and accelerations. This layer close to the blade is called the boundary layer. Euler's equations clearly cannot be used in this boundary layer.

The methods discussed above are so-called Computational Fluid Dynamics methods or CFD. One large drawback for these methods is the necessary computational time, the calculations are very complex and will take a long time even on the fastest currently available systems.

Another problem is the grid generation. This is, even after thirty years of research, still a bottleneck of CFD. Generating a grid is time-consuming, tedious and it requires specialized training though steps are being taken to solve this problem [69]. Another problem is the necessity of a turbulence model, the turbulence model can have an important effect on the end result.

A special class of Euler solutions are the vortex wake methods. These are usually combined with lifting line or lifting surface models for the rotor representation. The assumption here is an incompressible potential flow where all vorticity is concentrated in the vortex filaments. The strengths of these filaments is determined by the aerodynamic lift distribution. By applying the Biot-Savart law, the induced velocities can be calculated. An example of such a method can be found in [36].

An advantage of vortex wake methods is its ability to easily calculate unsteady situations for the inflow or yawed conditions. The method also has some disadvantages. There is a mathematical problem that can prevent convergence of the results for reduced element size. The vortices will introduce singularities in the flow. Therefore the results at these locations and at a certain cut-off length around these locations will not be obtainable. Reducing the element size will therefore at some point not lead to convergence. Also the CPU time that these methods need is very large ( $10^4$  times larger than BEM). An example of a free wake method used for aeroelastic stability calculations is given by Riziotis and Voutsinas in [122].

The CPU time needed for vortex wake methods can be reduced by using a prescribed wake. For example one can assume the wake to be a conical wake and prescribe the exact shape of the wake, but this adds the uncertainty of the correctness of the prescription. Due to this uncertainty the advantage over the momentum theory is in this case no longer evident.

Another method uses the asymptotic acceleration potential method. This is in fact also an Euler solver. It was first developed for helicopters [58] and later expanded to wind turbines [19]. The main disadvantage of this method is the linearisation; it assumes small perturbations of the main flow. This assumption is valid for helicopters, but assuming this for wind turbines is more doubtful. Due to the linearisation, the calculation is faster than the other methods discussed in this section, but concerning calculation time, it can still not compete with the momentum theory.

All the methods above can be used to further improve momentum methods, especially for situations in which the momentum methods are less reliable, such as yawed flow.

### 3.2.2 Blade Flow

Next to alternatives for the momentum method for the global flow, there are also alternative methods for the blade element theory, discussed in section 3.1.4, for the flow in the vicinity of the rotor.

The lifting line method has already been described in section 3.1.4, where it is used as part

of the blade element method. For vortex wake methods, lifting line theory is also often used such that the vorticity created by the presence of the wing in the flow is added to the global flow. The strength of the bound vortex can be calculated using:

$$\Gamma = \frac{cC_l(\alpha)V_{eff}}{2} \quad (3.69)$$

Where the lift coefficient  $C_l$  is taken from 2D measurements or 2D theory. This means that the induced velocity must be calculated only due to 3D effects. That part of the vorticity effects that are not due to 3D effects also have their effect in the measurements or 2D theoretical analysis and must therefore not be taken into account.

A more detailed representation of the blade can be accomplished by using the lifting surface theory. An significant difference with the lifting line method is that, when this method is used, the 2D measurements or theoretical values can no longer be used. The flow is aligned with the surface along the blades camber surface. Of course extra detail in the method leads to a longer computational time. Another disadvantage that the lifting surface theory has over the lifting line theory is the performance for separated flow. Using lifting line, it is possible to use the experimental data for the lift coefficient. For lifting surface theory, the assumption of inviscid flow is not as easily corrected for separated flow. Another disadvantage of both methods is the fact that viscous drag is not included, while drag is important to predict the turbine's shaft torque (and therefore the power output) correctly. It can also have an important effect on the aeroelastic stability of a turbine.

Better methods can be obtained by including viscous effects. In that case, it is possible to include the viscous drag and enable calculations in separated flow. However, because there will at least be a part of the flow around the blade that is turbulent, it is important to somehow try to determine the transition point where the flow changes from laminar to turbulent. Modelling the turbulence is also a fundamental problem in the analysis. One relatively simple method is the 3D boundary layer method [132]. The flow is separated into an inviscid potential flow part and a thin viscous boundary layer on the blade surface. In this method the pressure change perpendicular to the blade surface (the direction of axis  $x_2$ ) is neglected resulting in the following equation for the momentum in this direction:

$$\frac{\partial p}{\partial x_2} = 0 \quad (3.70)$$

The diffusion in the directions along the surface are much smaller than the convection, therefore the viscous terms containing these derivatives can be neglected, resulting in two momentum equations in the directions parallel to the surface:

$$\frac{\partial u_i}{\partial t} + u_j \frac{\partial u_i}{\partial x_j} = -\frac{1}{\rho} \frac{\partial p}{\partial x_i} + \nu \frac{\partial^2 u_i}{\partial x_2^2} \quad i = 1, 3, \quad j = 1, 2, 3 \quad (3.71)$$

The outer flow field is assumed not to contain vorticity. This results in a known pressure gradient along the surface in the boundary layer, which is used to solve the equations. When

separation occurs, the boundary layer equations and the outer flow equations must be solved simultaneously, but when the separation region becomes large, the method is no longer valid.

The methods discussed here can be an alternative for the blade element method discussed in the first part of this chapter. They can possibly give better results in cases where BEM breaks down, but at the cost of more calculation time.



# Chapter 4

## Aeroelastic Instability

*"The fundamental concept in social science is Power, in the same sense in which Energy is the fundamental concept in physics. "*

- Bertrand Russell

With the increasing size of the wind turbines, aeroelastic problems have been experienced on some turbines. Aeroelastic problems can be devastating to the wind turbine, therefore it is crucial to make sure that wind turbines are designed such that they do not suffer from instabilities. To be able to investigate ways to prevent instabilities, some knowledge of aeroelasticity is a necessity. In this chapter a short introduction will be given in aeroelasticity followed by a short description of the differences and similarities between helicopters and wind turbines concerning aeroelasticity. The third section of this chapter discusses the possible blade instabilities of wind turbines. Finally the last section discusses some combined instabilities of structure and blades. The mechanism behind the different instabilities is explained and some aspects to keep in mind are discussed. This chapter does not go into detail concerning the different instabilities, it is only an introduction.

### 4.1 Aeroelasticity

Aeroelasticity is traditionally concerned with the combination of aerodynamic forces together with elastic forces and dynamic forces where there is significant mutual interaction between these forces [28, 144]. Collar illustrated this by forming a triangle of these three disciplines as illustrated in figure 4.1 [24]. However for wind turbines, the controls have become important players as well. Pitch and especially generator control have substantial influence on the aeroelastic stability of the wind turbine, for this reason it makes sense to add the control forces to the triangle, as illustrated in the figure.

The interaction of the forces is strong in wind turbines, helicopters and aeroplanes for example. Looking at the aerodynamic forces on these structures, they depend on the relative

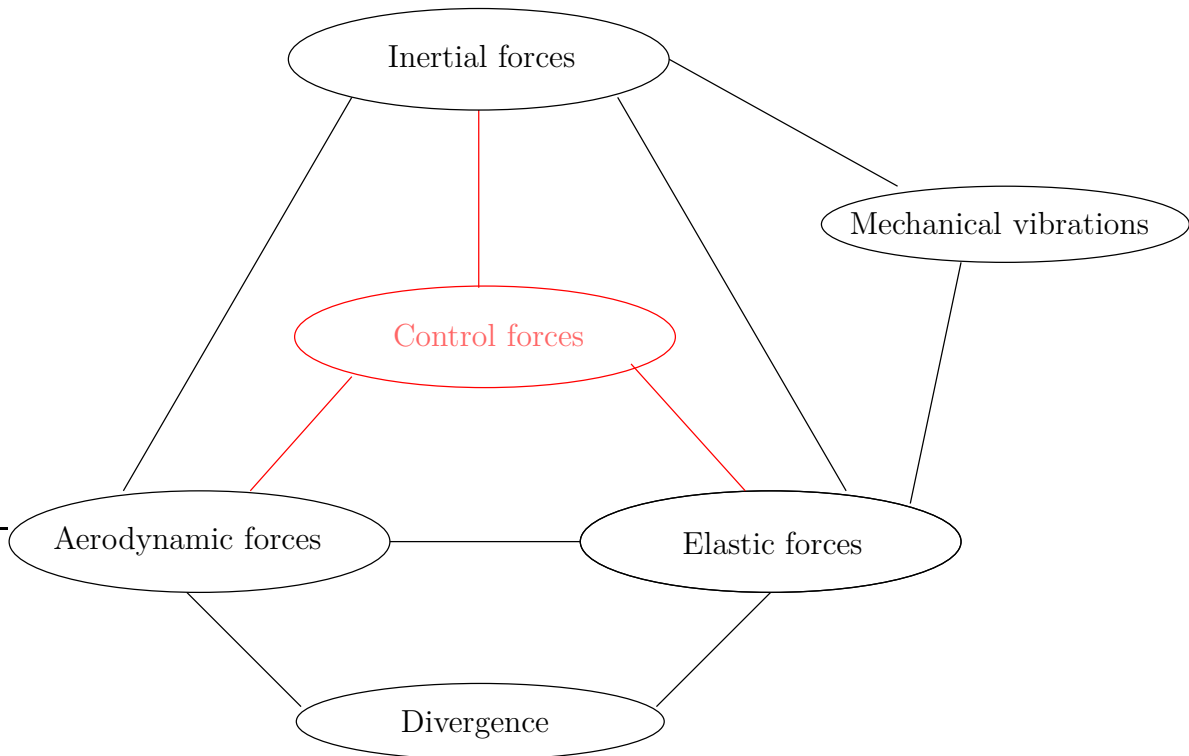


Figure 4.1: The triangle of disciplines [24], but with the addition of control forces.

velocities of the air passing the structure. If the structure is deformed, the change in shape due to the elastic bending will affect the aerodynamic forces, e.g. due to a changed angle of twist. The time derivatives of the deformations will result in a change of the relative velocity of the air passing the structure, therefore changing the aerodynamic force. In turn the aerodynamic forces influence the deformation and the velocity of the structure. The inertia forces play an important role in the correlation between the aerodynamic and elastic forces and the resulting accelerations. The structure can start to oscillate due to the changing forces. When this vibration has an increasing amplitude, the structure is unstable.

If a structure is elastic, it will respond to periodic forcing functions by vibrating in discrete geometric patterns [133]. These geometric patterns are called the mode shapes of the structure. Each mode will have a corresponding mode frequency. The vibration in the mode shape will occur at this modal frequency. Wind turbines and helicopters are flexible structures that will vibrate when forces act on the structure. Their response will be in the mode shapes and at the modal frequencies of the structures.

The mode shapes depend mainly on the distribution of mass, the distribution of stiffness and the boundary conditions such as clamped or hinged connections. The rotational motion of the blades also has an effect on the modal shapes and frequencies, because the centrifugal and Coriolis forces in a way change the stiffnesses of the blades. The aerodynamic damping forces can also have a significant effect on the mode shapes and frequencies.

When a wind turbine is designed, it is important to look at the damping of all modes (e.g. first blade flap mode, first blade edgewise mode, etc.) but also to look at the natural frequencies of the blade and the structure. The avoidance of resonant oscillations is a very important aspect in blade design. In order to avoid aeroelastic problems, it is essential to keep the tower and the natural blade frequencies well separated from the exciting frequencies, such as the rotation frequency  $\Omega$  and integer multiples of this frequency, often noted as 1P, 2P etc. The blade passing frequency is especially critical, the natural frequencies of the blade should not be close to this frequency. During the design it is also important to try to optimise the aerodynamic damping of the blade modes. The first blade modes are most critical, because the structural damping increases with frequency, therefore for high frequencies the structural damping will prevent instability occurring for that mode, even if these higher modes have negative aerodynamic damping.

If the aerodynamic damping of a mode is negative, this can result in an oscillation with increasing amplitude if the absolute value of the negative aerodynamic damping is higher than the structural damping of the mode. A coincidence of one of the natural frequencies with one of the exciting frequencies is, in that case, not a necessity for an instability. This is discussed in more detail in section 4.3.1.

Next to the combination of all three forces, aerodynamic, inertia and elastic, there are other related technical fields that are also important to look at, but are not part of the field of aeroelasticity. Two combinations of only two of the three types of forces are also shown in figure 4.1. First there are mechanical vibrations which are a combination of inertia forces and elastic forces. Second there is divergence which is caused by a bad combination of aerodynamic forces and elastic forces [35].

One must distinguish between aeroelastic instabilities and resonance. Resonance is the case where there is a forcing frequency that is close to one of the natural frequencies and energy can be added to the vibration. Information about resonance responses of large wind turbines can be found in e.g. [136]. In this chapter the focus is on the aeroelastic instabilities, not on the resonance problems.

In the previous chapters dynamic forces and aerodynamic forces have been discussed. The elastic forces are shortly discussed in appendix B. A short introduction to linear vibrations is given in appendix C.

## 4.2 Helicopters and Wind Turbines

In some ways wind turbines are very similar to helicopters. The lift generating rotating blades of both devices are flexible and/or attached to the hub using hinges. One important difference is the direction of the gravity forces. Due to the different position of the blades for horizontal axis wind turbines, the influence of gravity on the turbine is more important for turbines than for helicopters. The gravity forces on the blades not only cause important fatigue loads but they are also associated with at least one instability, see section 4.4.3.

Another important difference between helicopters and wind turbines is the direction of the aerodynamic forces and the angles of attack during operation as discussed below.

From the early beginnings of the helicopter technology, it became clear that one of the problems for designing safe helicopters is flutter. When flutter occurs, the blades will vibrate with increasing amplitude. This can lead to destruction of the blades, loss of control of the helicopter or if the problem does damp out the vibration will exacerbate fatigue damage. This results in a much shorter life of the construction. Therefore it is important to prevent flutter.

In the next sections several possible instabilities for wind turbines are described. Most instabilities are originally known from helicopter analysis. As horizontal axis wind turbines are rather similar to helicopters, the knowledge and experience from helicopters is a valuable source of information for anyone dealing with aeroelasticity of wind turbines. For most wind turbine designs, the rotor shows more similarities to a hingeless helicopter rotor rather than an articulated rotor. In most wind turbines there are no hinges that will remove the lead-lag and flap moments, but there is a bearing for the pitch-setting. In contrast with the articulated helicopter rotor, the hingeless rotor does not have dampers in the lead-lag directions. This makes the field of aeroelasticity more important as it becomes possible for the usually badly damped lead-lag mode to result in instabilities.

The conditions in the flow around a wind turbine at zero yaw are rather similar to the flow conditions for a helicopter in descending vertical flight. There are of course a few important differences. When the lifting line theory is used, one can look at blade elements to calculate the forces on the structure. Blade elements for helicopter blades and wind turbine blades are illustrated in figure 4.2. The figure also shows some of the main differences in the local flow of a helicopter and a wind turbine. A blade element of a wind turbine is illustrated at the top and a blade element of a climbing helicopter at the bottom. The different angles are also shown: the angle of attack  $\alpha$ , the local flow angle  $\phi$  and the aerodynamic pitch angle  $\theta$ . The figure clearly illustrates some of the differences. Under normal operating conditions, the pitch angle of a wind turbine is defined positive in the opposite direction compared to the pitch angle for a helicopter. The most fundamental difference is the direction of the resulting force in the direction of the plane of rotation. On a wind turbine the aerodynamic forces result in a torque that causes the rotation of the blade, while on a helicopter the torque must be provided by an engine. Less obvious from the figure is the difference in the angle of attack during operation. A wind turbine will often operate near stall, especially a stall regulated turbine, while a helicopter will not operate in stall that often.

Other differences between wind turbines and helicopters, according to Eggleston and Stoddard, are the larger planform area of wind turbines and the larger twist of the blades. The chordwise location of the blade mass axis of a wind turbine is usually aft which also differs from helicopters. Another difference during operation is the torque of the wind turbine that continually changes. On top of that, for variable speed turbines the rotor speed is also not constant in contrast with helicopters [31].

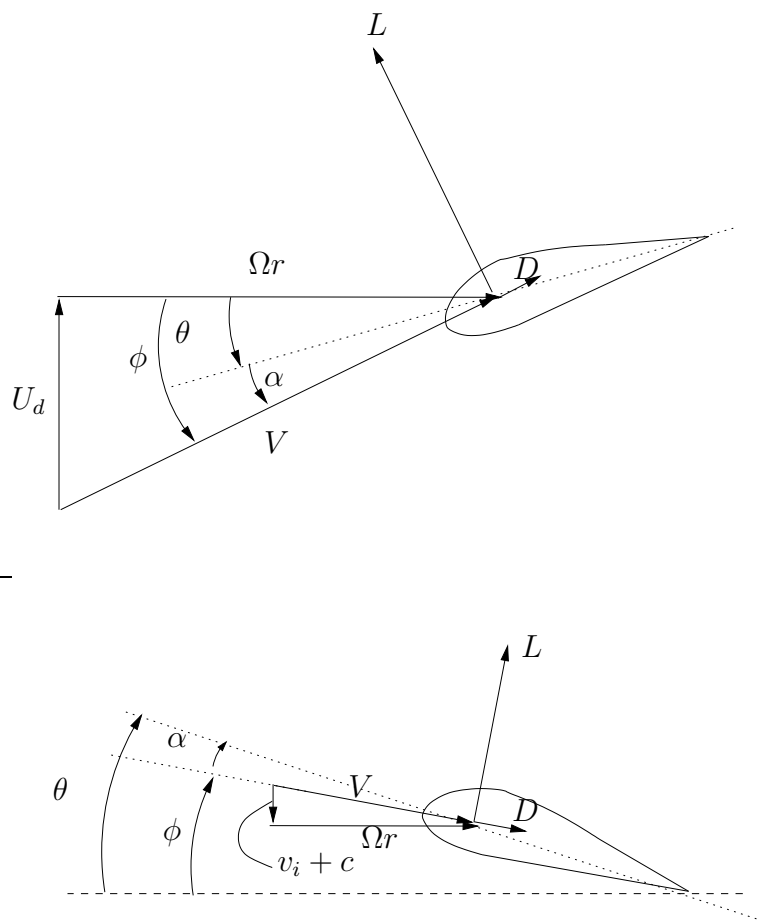


Figure 4.2: The flow angles, lift and drag on a wind turbine blade element (top) and on a helicopter blade element (bottom).

Looking at differences in non-dimensional parameters; the Lock number ( $\gamma = \frac{\rho c_{l\alpha} c R^4}{I}$ ) differs, for wind turbines it is significantly lower than for helicopters. Another important difference is the non-dimensional rotating flap- and edgewise frequencies of wind turbines, which are much higher than the frequencies of helicopters.

In [108] a literature survey is given on instabilities in wind turbines and helicopters. The instabilities that could be of importance with respect to wind turbines are discussed in the next two sections.

### 4.3 Blade Instabilities

In this section different possible blade instabilities are discussed. The first three instabilities discussed are single degree of freedom instabilities. These are discussed in the first two sections. The other instabilities entail two or three degrees of freedom and are discussed in

the last three sections.

### 4.3.1 Blade Edgewise Instability and Blade Flapwise Instability

In the development of ever larger wind turbines, problems were encountered by some manufacturers. In 1994 Stiesdal reported problems with edgewise vibrations on a stall regulated wind turbine with a 37 meter rotor diameter [135]. This problem had not been evident on earlier wind turbines but with the increase in size, it quickly became an important issue for wind turbines. Damage and even loss of blades was reported by Møller in 1997 [95]. Another example of a blade that suffered from this instability was the Aerpac APX40T blade. These blades were mounted on 600 kW turbines with a 37 meter rotor diameter. They showed a severe instability at high winds [2]. As described by Anderson *et al.*, this problem was solved by Aerpac by installing a mechanical damper inside the blades.

The vibrations of the APX40T blades were caused by negative damping of the first edgewise mode. This resulted in divergent oscillations of the blades at their first edgewise eigenfrequency during high wind operation. The problem is aggravated by the fact that the phase difference between the three APX40T blades in this vibration is such that there is a zero net oscillatory torque on the rotor shaft. Therefore it is not possible for the power train to supply any damping to this instability. The frequency of the first edgewise mode is not the cause of the problem, as mentioned before, it is due to the negative damping of the corresponding eigenmode. Therefore the shape of the eigenmode has a strong influence on the stability. An out-of-plane component in the first edgewise mode will have a stabilising effect on the stability of this mode. Because the mode shape is determined by the stiffness and mass distribution, these distributions have significant effect on the instability [111].

The reason for this instability can be illustrated using figure 4.3. This figure shows a 2D sketch of the flow on a wind turbine at a cross-section of the blade. Looking only at the significant effects, the effects of changing the in-plane and out-of-plane velocities on the aerodynamic forces are sketched in this picture. The linearised changes are drawn in two phases: first the new larger force due to the change in the total velocity  $W$  is drawn ( $dL = \frac{1}{2}\rho W^2 C_{lc}$ ), assuming the same lift- or drag coefficient as for the original flow. The tilting of this force is also included in the picture. Second, the change due to the difference in angle of attack is drawn as a second arrow. This change corresponds to the slope of the lift- or drag coefficient.

The change in in-plane velocity  $\Delta\Omega r$  is a result of the blade moving to the left. Therefore force changes in this direction result in negative damping, while force changes in the negative  $X$ -direction correspond to positive damping. The forces corresponding to this change in velocity are shown in green in the figure. It illustrates that the lift force increases due to the increase in the total velocity. The component in the in-plane direction increases, therefore this gives negative damping. However, the change in angle of attack has an opposing effect. Assuming the angle of attack to be in the range with a positive lift slope, the change in lift coefficient reduces the lift force. Therefore in total the change in lift force has two opposing

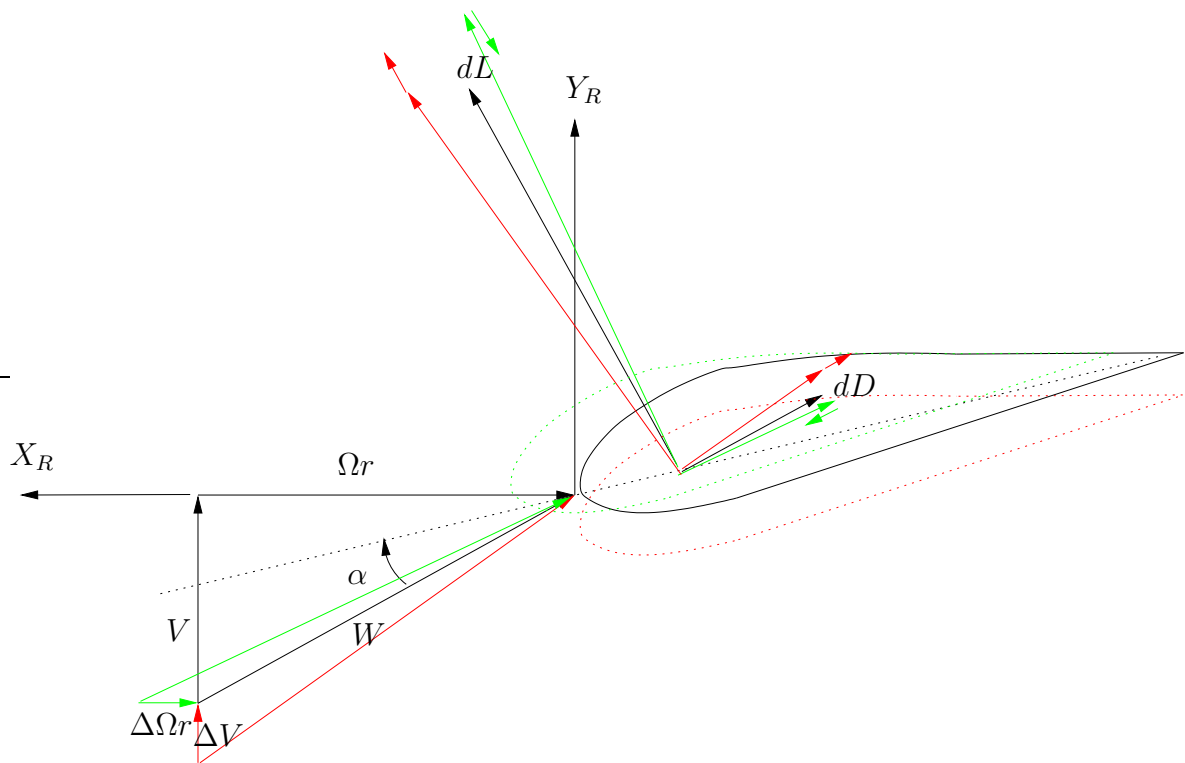


Figure 4.3: The aerodynamic forces acting on an element due to the local wind velocity. The effect of changes in the wind speed and rotational speed of the rotor on the aerodynamic forces is illustrated. The changes due to the increase in total velocity are shown as an increase in the force and added to this is the change due to the increased or decreased angle of attack as a small extra vector. The changes in velocities correspond to the in-plane and out-of-plane movements of the aerofoil in the directions as shown.

effects.

The drag force is also shown in the figure. The increase in drag force due to the change in total velocity is in the opposite direction of the motion, therefore this provides positive damping. The change in the drag force due to the change in the drag coefficient however, will be destabilising; it reduces the stabilising drag force.

This discussion illustrates that there are several opposing effects. Therefore it is possible for the damping to be positive or negative. It depends on the aerofoil characteristics and the local velocities. When the destabilising changes are larger than the stabilising forces, the edgewise instability could occur. However, the motion looked at here is purely in-plane, while the first edgewise mode will always have some out-of-plane motion as well. The effect of out-of-plane motion can also be looked at using figure 4.3 and is illustrated using red vectors.

If the blade moves downwards, the velocity change of the airflow is shown in the figure. This change increases the angle of attack. The total velocity  $W$  is again increased. The change in total velocity as well as the change in angle of attack both result in an increase in lift (again assuming the angle of attack to be in the range where the slope of the coefficient is positive). As illustrated in the figure, this change results in a change of the out-of-plane force that opposes the downwards motion, therefore this is a stabilising force. The component of the drag force in the out-of-plane direction also opposes the downwards motion. For this reason the out-of-plane motion is usually very well damped. Adding out-of-plane motion to the first edgewise mode can increase the damping, as the out-of-plane motion is a strongly damped motion under most circumstances.

In chapter 10 the edgewise blade instability is investigated further and equations for the damping coefficients are derived.

The blade flapwise instability is another single degree of freedom instability. It is possible for the damping of the flap mode to become negative. Recall that the discussion given above assumes the angle of attack to be in the range where the lift slope is positive. When the blade is stalled, the slope can become negative, changing the stabilising effect of the larger angle of attack to a destabilising effect.

This instability is not likely to occur on helicopters. According to Horvay it can only occur for helicopters when the flapping frequency is a multiple of half the rotor frequency:  $\omega_\beta = k \cdot \frac{1}{2}\Omega$  and for negative damping of the flapping mode [68]. The flapping motion of a helicopter blade is usually strongly damped and negative damping will occur only for extremely high advance ratios that are not realistic.

The flapwise instability might however be a realistic problem for wind turbines. Over a quarter of a century ago Lundsager already reported increased loads and severe vibrations in flapwise direction for the Nibe turbines, when they were operating in stall [85]. The Nibe A and Nibe B turbines had a diameter of 40 meters. A few years later, measurements conducted by ECN on their 25 m test turbine with the 20-WPX-THR blades appeared to validate the possibility of a flapwise instability when the blade is operating in stall [26]. An

important factor here was the fact that the flapping frequency was very close to  $3P$  as well as close to the drive train natural frequency, further deteriorating the instability.

Wind turbines often operate in stall, especially active and passive stall regulated wind turbines, which makes the possibility of the flapwise instability relevant, especially when taking into account that the flapwise mode will also include some in-plane motion that is badly damped. However, using detailed models with nonlinear unsteady aerodynamics, it has been shown by Petersen *et al.* in [111] that this instability will not occur on small or medium sized stall regulated wind turbines. In theory it is possible for stall regulated wind turbines to suffer from this instability, especially when the structural pitch angle is large or the frequency  $\omega_\beta = k \cdot \frac{1}{2}\Omega$ , but good design can easily prevent this instability.

### 4.3.2 Stall Flutter

The classical form of stall flutter also involves a single degree of freedom, this time it is the torsion degree of freedom. The mechanism behind this instability can easily be explained. Assume a gust that increases the angle of attack  $\alpha$  while the blade was already in stall. The forces will then decrease with an increasing angle of attack. If the aerodynamic centre is in front of the centre of twist, the smaller forces result in a decrease of the torsional deformation. This in turn reduces the angle of attack. For a smaller angle of attack in stall the force will again increase resulting in a cycle that can become unstable. In helicopters this instability can occur during high speed flight and maneuvering. This instability is not likely to occur during normal operations in wind turbines due to their much higher stiffness in torsion. However, when there is a flexible pitch control system or a pitch link failure it is possible to occur [31]. It is necessary to check for this instability in wind turbines, because a pitch link failure is not allowed to lead to a complete destruction of the wind turbine. Actually, the origins of the simulation tool discussed in chapters 5 and 6 also lie in the possibility of this instability as described by van Holten in [60] (see also section 5.1). Stall flutter has also been observed on a test turbine of ECN, the FLEXTEETER with a diameter of 25 m [14]. Therefore it is a possibility that must be checked.

For helicopters it is also possible that the torsion frequency is almost the same as the frequency of an aerodynamic forcing function resulting in the instability. This can occur when the wake vorticity gives harmonic forcing that could match the pitching frequency. For wind turbines the wake is convected away from the turbine much faster. Therefore this type of harmonic forcing will not occur in wind turbines.

In practice this instability will result in a limit cycle oscillation in both wind turbines and helicopters. On a helicopter there are large differences in angle of attack across the rotor plane due to the fact that on one side the velocity of the helicopter reduces the local velocity on the blade and on the other side the local velocity is increased. These sides are called the retreating side and advancing side respectively. The angle of attack on the advancing side will be much smaller than on the retreating side and this variation in aerodynamic forces will result in a limit cycle oscillation [28].

### 4.3.3 Flap-Lag Flutter, Including Flap-Lag-Stall Flutter

Flap-lag flutter is a known blade instability for hingeless and articulated helicopter rotors [100, 102]. It has been observed on some hingeless rotor blades when operating at high thrust or high pitch levels. It is an unstable oscillation that is caused by the coupling of the flap and lead-lag motion. It is a mild instability when compared to e.g. classical blade flutter, but it can become destructive within a few cycles. Several different investigations have taken place to find out if this instability can occur on wind turbines, resulting in different conclusions.

According to Eggleston and Stoddard [31] it is only likely to occur in wind turbines when there is:

- substantial lead-lag motion. This will only occur at high load levels.
- substantial steady coning angle
- substantial flapping motion. This will occur when the stiffness is low or the loads are high.
- a small difference between the flap and lead-lag frequency:  $\frac{\omega}{\Omega} \approx 1.15$  for both.

The instability is caused by a coupling of two changing moments. First, there is the in-plane Coriolis moment due to the flapping velocity. Second, there is the change of the flapping centrifugal moment due to the difference of the in-plane velocity by the lead-lag velocity. It was concluded by Ormiston [102] that the instability can only occur when  $\Omega < \omega_\beta < \sqrt{2}\Omega$ . For helicopters this range holds realistic values for the blade flapping frequency. However for wind turbines the frequency will be higher unless the wind turbine is large and there is a hinge in flapping direction. If the flap frequency is outside this range, the instability could occur when the damping of the flap mode is strongly reduced when entering the turbulent wake state or when the turbine is allowed to overspeed. The stability can easily be resolved by adding mechanical damping. A more detailed discussion of this instability and the derivation of the equations governing this instability is given in the chapter 10.

Chaviaropoulos [22] has investigated the possibility of flap-lag flutter in wind turbines. However, in his work he does not look at frequency coincidence but uses typical values for the dimensionless flap and lag frequency, 4 and 7 respectively. Both frequencies are also doubled to look at the effect, but this has little effect on the instability. It is shown that the edgewise mode is unstable for the complete range of the reduced rotational speed  $\kappa = \frac{\Omega c}{V}$ . The flap mode is only unstable in a small range of  $\kappa$ . The results also show that especially thin aerofoils are sensitive to this instability, due to the large difference between the linear inviscid lift coefficient and the viscous lift coefficient for the NACA 63-2XX aerofoils used:

$$\Delta C_L(\alpha) = C_{L_\alpha}(\alpha_0) * (\alpha - \alpha_0) - C_L(\alpha) \quad (4.1)$$

with  $\alpha_0$  the angle of attack for which  $C_L(\alpha) = 0$ . The derivative of  $\Delta C_L$  with respect to an instantaneous change in angle of attack,  $di$ , which is due to the movement of the aerofoil,

is written as  $\frac{d\Delta(C_L)}{di}|^{ref} = \Delta C_{Li}$ , where *ref* is used to denote a reference equilibrium state. The derivative of the drag coefficient with respect to *di* is noted as:  $\frac{d(C_D)}{di}|^{ref} = C_{Di}$ . Note that this notation is easily confused with the induced drag, but in this case it is used for the derivative of the drag coefficient.

The values of  $\Delta C_{Li}$  as well as the values of  $C_{Di}$  are also destabilising factors that are larger for thin aerofoils. An increased value for  $\Delta C_L$  results in a more unstable lead-lag mode and flap mode. Increasing  $C_{Di}$  has little effect on the lead-lag mode, but strongly destabilises the flap mode. When  $C_{Di}$  is increased, it results in a more stable flap motion, but the lead-lag instability is worsened. The instabilities occur mainly for small values of the reduced rotational speed  $\kappa$ . These low values will occur close to the tip, where the aerofoils are thin. It is not really clear if it is a coupled instability that shows up, or that it is a combination of two unstable modes, without the coupling being important. Because there is a relatively large frequency difference in the model between the flap and lead-lag mode, the suggestion is given that the latter is closest to the truth. The equations derived in section 10.5.1 and the good correspondence of these with the discussed results, strengthens this suggestion.

During the Dutch STABTOOL projects, it was concluded that even though the flap frequency of large wind turbines is much higher than the interval found by Ormiston and Hodges [102], this instability could still be the cause of problems on large stall regulated wind turbines. As described in earlier sections, large wind turbines have shown some unexpected instabilities. Because there were no stability problems on smaller turbines it was assumed that these instabilities were scale dependent. Investigating the natural frequencies of several blades that are of different sizes showed that the manufacturers scale their turbines up in such a way that the difference between the flap frequency and the lag frequency becomes smaller [138, 67]. The frequencies for different rotor blade lengths and the corresponding extrapolations are shown in figures 4.4 and 4.5.

The actual difference between the lead-lag frequency and the flap frequency becomes even smaller if one also takes into account the clamping stiffness and multi-blade effects (discussed in more detail in section 10.2.2). This will result in the lag frequency being smaller than calculated and therefore even closer to the flap frequency, as illustrated in figure 4.6.

The change in relative stiffness has an influence on the flap-lag instability. Therefore, this was expected to be the root of the problem for large wind turbines. As discussed earlier, it has been shown that the flap-lead-lag instability will only occur if the non-dimensionalised rotating flap eigenfrequency is between  $1 < \nu_\beta < \sqrt{2}$  [102]. For wind turbines, the flap frequency will be much higher than this (e.g for the turbine used in section 8.3 it is appr. 3.5). There must be some reason why this instability does seem to occur in wind turbines even if the natural frequencies are much higher than the rotational frequency of the blades.

In [56] this instability has been investigated using a simple model of a single blade. Calculations showed that operating the blade in or even near stall is the cause of the problem. Helicopters rarely operate near or in the stalled region, the onset of stall is a hard boundary for helicopters that severely limits its performance. Therefore this instability had not yet

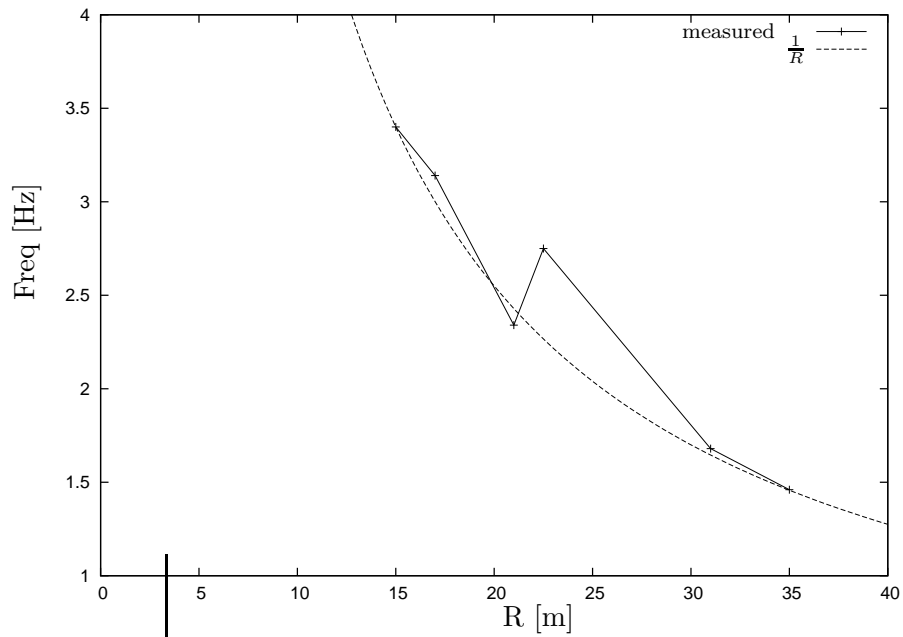


Figure 4.4: Comparison of measured first lead/lag frequency with  $R^{-1}$  extrapolation

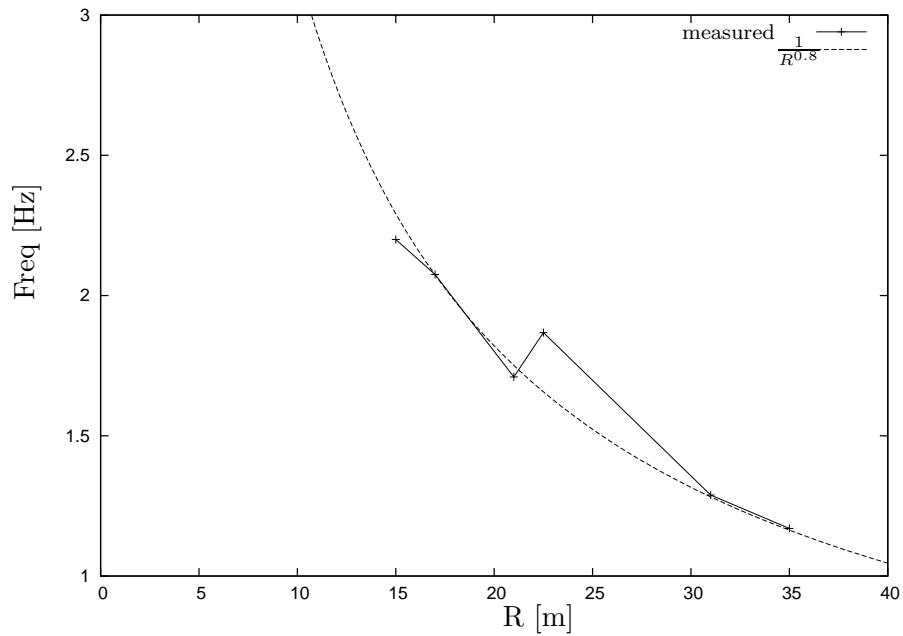


Figure 4.5: Comparison of measured first flap frequency with  $R^{-0.8}$  extrapolation

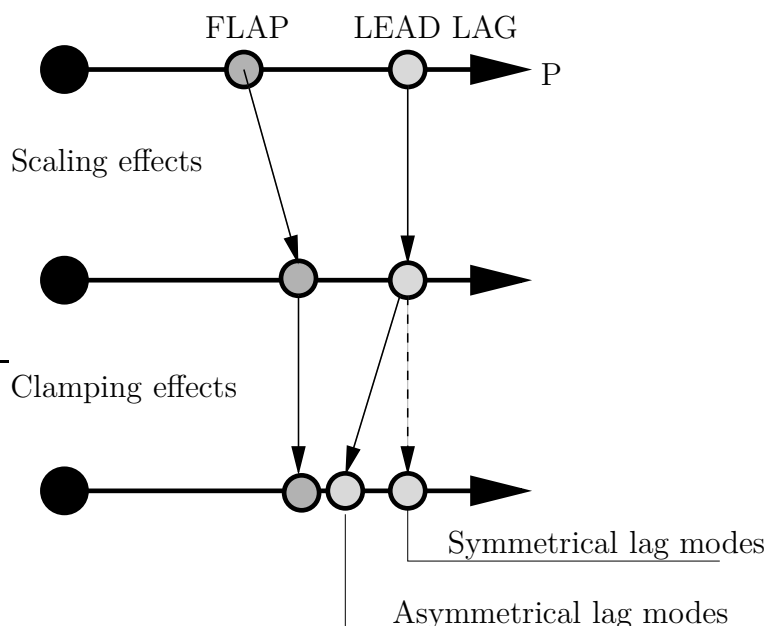


Figure 4.6: The flap and lag frequencies approaching each other due to scaling and clamping

been analysed as such. As mentioned before, wind turbines often operate with a considerable amount of flow separation and blade stall [70], especially the stall regulated and active stall regulated turbines. In [56] it is shown that it is possible that the instability will also occur in other frequency ranges for the non-dimensionalised rotating flap eigenfrequency when operating in or near stall. Therefore especially stall regulated turbines can be at risk concerning this instability. The differences between the results obtained by Ormiston and Hodges in [102] and the results obtained for a simple model of a wind turbine in [56] are looked at in more detail in chapter 10.

#### 4.3.4 Pitch-Lag Instability

The pitch-lag instability is an oscillation that is usually seen as a complication and aggravation of the flap-lag instability. In general it will be a limit cycle oscillation. The frequency of the oscillation of the blades relative to the rotating hub is equal to the fundamental lag mode. The coupling between the lead-lag motion and the pitch can lead to this instability. Due to the coupling of the pitch and lag motion, a lagging motion induces a change in the aerodynamic lift. This causes the blade to flap resulting in a Coriolis force that will induce more lag motion.

For articulated helicopter rotors the coupling between the pitch and lag motion can only be artificial coupling, but for hingeless blades and wind turbine blades this coupling is due to the structural coupling between lead-lag and pitch. The coupling results in a change of the blade pitch when the blade is bent.

According to Bramwell, the instability is only possible for articulated helicopter blades, when the blade pitch increases when the blade moves forward in the lead-lag motion [13]. For wind turbines the instability could occur when the stiffness in lead-lag direction is very low or if the blade has a large twist. Also when the coning angle is very large, the instability could occur [31].

### 4.3.5 Pitch-Flap Flutter and Divergence

Pitch-flap flutter and pitch-flap divergence are very similar to the classical flutter and divergence of fixed wing aeroplanes. Of course the centrifugal action on the helicopter blade is not part of the classical flutter of fixed wing aircraft. Due to the centrifugal forces, the flap stiffness is effectively increased.

Pitch-flap flutter is a destructive combination of torsional oscillation with a flapping oscillation. In the case of divergence, it can result in twisting off of the blade. The mechanism can easily be explained. If the blade flaps, the changes in aerodynamic force act in the aerodynamic centre, but the inertial forces act in the centre of gravity. If the aerodynamic centre is not coinciding with the centre of gravity, the flapping motion will result in a moment about the pitch axis. These moments can be proportional to the acceleration, velocity or displacement. Therefore there are different phase angles and a destructive interference is possible.

Divergence is only possible when the torsional stiffness is very low. For a wind turbine this could be the case when there is a pitch-link failure whereby  $k_\theta \approx 0$  and divergence can occur.

The combination of an aft position of the blade centre of gravity and the flap motion can result in limit cycle behaviour. In helicopters this instability is prevented by mass balancing the blades: weights that do not carry any load are added close to the leading edge along the full length of the blades. The instability is very sensitive to the flap frequency. A small increase in the flap stiffness can strongly reduce the requirements for the pitch.

## 4.4 Rotor Tower Instabilities

This section describes the instabilities that include coupling with the tower structure. The concentration is on instabilities that are of importance for wind turbines, but when possible the corresponding helicopter instability is also discussed.

### 4.4.1 Lead-Lag and Sideways Tower Instability

Wind turbines can suffer from an instability that is a combination of the lead-lag motion of the blades and a bending motion of the tower. This is somewhat similar to the ground

resonance that can occur for helicopters. Ground resonance for helicopters is a purely mechanical instability, the aerodynamic forces do not play an important role in the instability; it could also occur in a vacuum. The engine that gives the constant angular velocity, is the source of energy. The theory behind ground resonance was only developed between 1942 and 1947 by Coleman [23]. The name given to the instability can be somewhat confusing because it is a mechanical instability and not a resonance problem [28].

Helicopter ground resonance is caused by the displacement of the centre of gravity of the rotor due to the asymmetrical lead-lagging of the blades. This lead-lagging motion results in the collective c.g. moving in circles. These circles can be in the same direction as the rotor rotation or in the opposite direction. This first is called progressive, the other is called the regressive mode. The rotation of the centre of gravity about the rotation axis gives rise to inertia forces that result in oscillatory forces on the fuselage and chassis. Under certain circumstances, the regressing mode can result in the ground resonance instability. This can only occur for lead-lag frequencies that are smaller than the rotational frequency of the rotor.

For wind turbines this instability is a destructive instability. The instability occurs due to coupling of the asymmetric edgewise mode with the sideways tower bending mode. The nacelle will move in fore/aft and sideways directions. Power fluctuations can be caused by this instability and therefore there is a risk for the generator to cause the instability to be amplified even more due to the controls. This instability has been observed on several turbines [67].

#### 4.4.2 Whirl Flutter

Classical whirl flutter is well known to occur on tilt rotors [72], conventional turboprop aircraft [121] and helicopters. It was initially discovered analytically by Taylor and Browne in 1938 [137], but only became of importance in 1960 and onwards. It is an instability in the combined yaw and tilt direction, resulting in whirling rotor plane. Depending on the direction of this whirling motion, in the same direction or the opposite direction of the rotor rotation, this whirl mode is called a forward whirl or backward whirl respectively.

The source of this instability are the aerodynamic forces. It occurs at high inflows that are typical for cruising flight of V/STOL aircraft. Initially something (e.g. a gust) will result in a change of the angle of attack on the blades of the propeller which in turn results in a yawing moment. A sideslip angle due to this yawing moment produces a pitching moment. This can result in a whirling motion of the propeller or rotor. The moments are in the same direction as the backward whirl, therefore for rigid blades only the backward whirl mode can cause the problem. For flexible or hinged blades, it becomes possible for the forward whirl mode to become unstable [121].

Using the lifting line theory (see section 3.1.4), it is possible to look at a 2D blade element for the analysis of the mechanism behind the whirl instability. The flow around a propeller that is moving horizontally with a speed  $V$  and is pitched over an angle  $\theta$ , is shown in

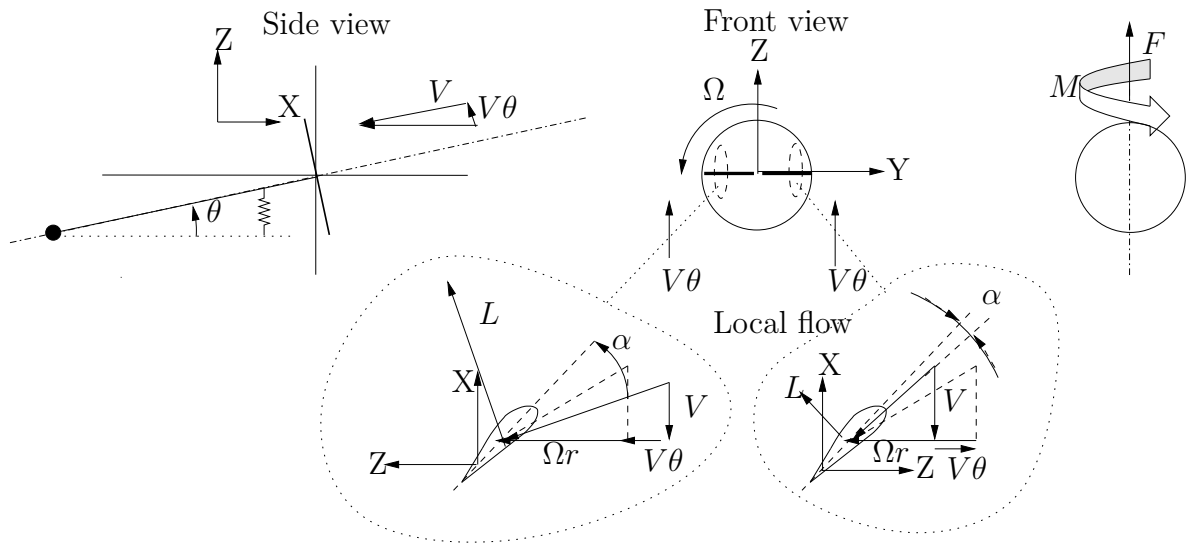


Figure 4.7: The whirl motion of a propeller. The flow contains a component parallel to the rotor plane, which influences the local flow around the blades differently for different azimuth angles.

figure 4.7. This shows the effect of the pitch angle. It introduces an extra velocity in the propeller plane: the velocity of the aircraft has a component in this plane due to the pitch angle. Assuming a small angle, the linearised velocity becomes  $V\theta$ . This velocity results in a difference in aerodynamic forces between the up-going and down-going side. When the blade is going down, the velocity increases the angle of attack as well as the total velocity and therefore also the lift force. On the other hand, the total velocity, angle of attack and lift are reduced on the up-going side. Therefore there is a resulting moment acting on the propeller as illustrated. It is a yawing moment that is the consequence of the pitch angle. There is also a resulting force upwards. This is due to the change in the lift force, on one side the force increase has a component in the positive  $z$ -direction. On the side where the force is reduced, the force is in the negative  $z$ -direction, therefore the force change also has a component in the positive  $z$ -direction, as illustrated in figure 4.7. Notice that this force can cause divergence, as it is in the direction that would result in further increase of the pitch angle if the stiffness of the connection to the aircraft is not high enough. This force is effectively a negative spring force.

When the propeller is at a yaw angle, the situation is very similar to the tilt angle discussed above. The yaw angle results in a moment and a force. The force is again effectively a negative spring. The moment is in the pitch direction. The pitching and yawing velocities also give rise to aerodynamic moments and forces. Again the local velocities at the blade elements change, now due to the velocity of the propeller itself. A pitching-up motion of the propeller results in larger forces at the top of the propeller plane and smaller forces at the bottom. Therefore a pitch-up velocity results in a pitch-down moment, providing damping. It also results in a force in the direction of the positive  $y$ -axis. A similar derivation can

be found for the yawing velocity which also results in a moment that provides damping to the yaw motion. Bielawa has derived the complete set of equations of motion for this simplified model of a propeller [8]. The moments and forces combined show that, above a certain velocity, whirl flutter will occur when the connection of the propeller to the aircraft is flexible. The instability will only occur in the backward whirl mode, when the pitch angle and the yawing velocity are in phase. The moments due to the pitch angle and yaw angle can then act as negative dampers. These moments are the source of the whirl flutter instability.

Whirl flutter can have a rapid onset. There is a critical velocity, the so-called whirl flutter velocity, above which the instability will occur. At the limit, the aerodynamic and structural damping are taking the exact same amount of energy out of the system as the yaw moment due to pitch and pitch moment due to yaw are putting into the system. For higher speeds the destabilising moments will become dominant and the instability occurs. This instability can put a limit on the maximum velocity for aircraft with flexible mounting of the engine-propeller combination [1].

An investigation into the possibility of this instability on wind turbines can be found in [16]. It was found that it is very unlikely that this instability occurs on wind turbines, the stiffness of the shaft or tower-top had to be reduced by such a degree before the instability occurred, that it is not likely to become a problem with any of the current wind turbines or larger up-scaled turbines.

However, in wind turbines there is an instability that is known that also involves the whirling motion of the rotor. When this instability occurs, a point on the rotor hub moves in a sort of spiral with a divergent character. Whirl flutter is an important instability to keep in mind. A clear description of the mechanism behind the instability is given by Petersen *et al.* in [112]. In this report two different types of whirl are distinguished, the so-called local blade whirl and the global rotor whirl. The local blade whirl is caused by the dynamic effects of unsymmetrical edgewise modes of the three blades (illustrated in section 10.2.2). In these modes, the resulting moment about the shaft is zero, but the resulting in-plane force due to inertia is not equal to zero. It can be shown that the resulting forces for the two unsymmetrical modes will follow an ellipse shaped rotation in the rotor plane when expressed in the rotating reference frame. For each of these two modes, this can be divided into two forces making a circular motion, one forward (same direction as the rotation of the blades) and one backward.

The tower, nacelle and shaft combination can also result in a whirl movement of the hub centre, again a forward and a backward whirl motion are possible. These whirl modes are the so-called global rotor whirl modes. These whirl modes are a combination of the tilt and yaw movements, including parts due to the bending flexibility of the shaft. The coupling between tilt and yaw is mainly due to dynamics. If a turbine yaws, the gyroscopic effect will give rise to a tilt movement and vice versa, resulting in an ellipse shaped path for the hub centre. According to Petersen *et al.* the second backward rotor whirl mode was the cause of a problem on a stall regulated turbine with 19 m blades. When the frequency of this mode is contained in the interval between the backward and forward local blade whirl modes, it

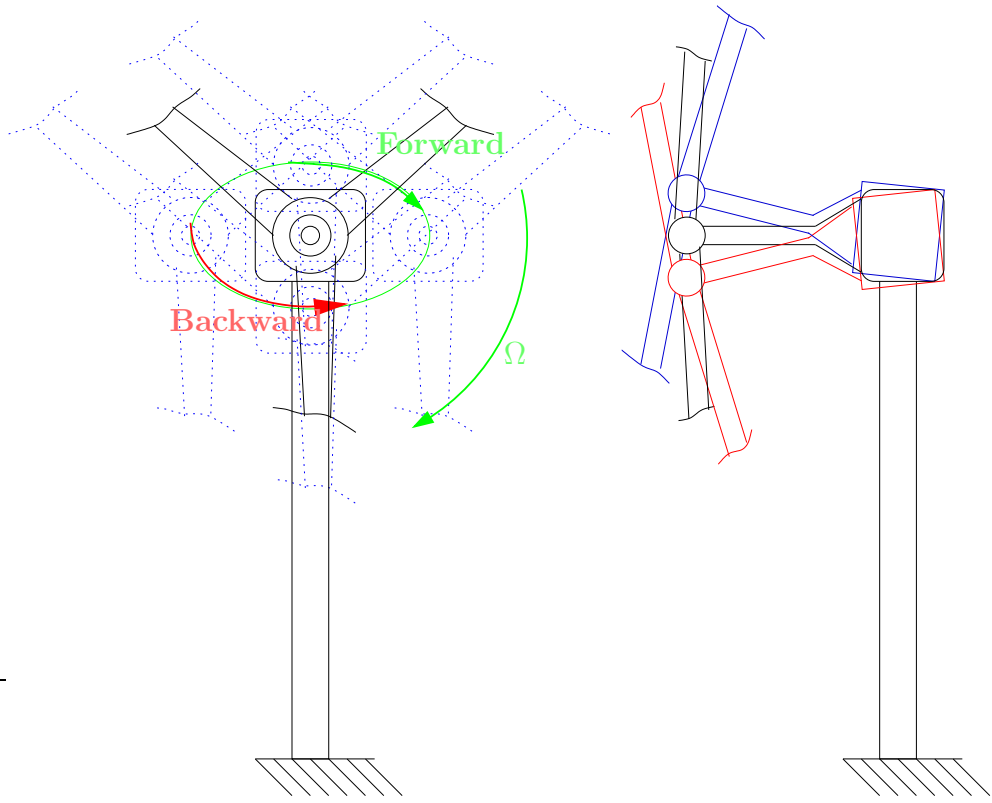


Figure 4.8: The whirl motion of a wind turbine, view from front and from the side. The rotor centre moves along an ellipse.

is possible for energy to be transported from the forward local blade whirl to the second backward rotor whirl and through to the backward local blade whirl. This illustrates that the instability is not a case of simple resonance.

To prevent this instability from occurring, it is important to keep the frequency of the second backward global whirl mode out of the range between the backward local blade whirl and forward local blade whirl referred to the stationary coordinates. At the same time it is important to have as much difference as possible between this second backward global whirl mode and the blade whirl frequencies. In the case discussed in [112], changing the shaft stiffness in order to change the frequency of the second backward global whirl mode was enough to prevent the instability. The small shift in frequency of 0.2 Hz that was achieved by doing so, was enough to eliminate the whirl instability, the second backward whirl mode frequency goes up from 3.4 to 3.6 Hz. It is then no longer in the interval between the two blade whirl modes and energy exchange becomes impossible.

The analysis performed in [112] uses a simplified model. For example, the blades are assumed infinitely stiff in the flapwise direction. Flapwise flexibility of the blades could have further effect on the instability. It is clear that this is a complex instability best checked using an advanced aeroelastic code. Though the example used in the report was of a stall regulated turbine, other types of wind turbines are also sensitive to this instability.

### 4.4.3 Advancing Lead-Lag Mode Coupled with Tower Modes Instabilities

As described in [108], this instability originates from the coupling between the lead-lag advancing blade mode and either the second tower bending mode or the tower torsion mode. The instability was never a problem for helicopters, but under the influence of gravity, it can become a problem for wind turbines. The KEWT prototype wind turbine ("Kosten Effectieve Wind Turbine" or cost effective wind turbine) suffered from this instability [107, 109]. During tests of the KEWT, the tower vibrated violently during the increase of the angular velocity  $\Omega$ . There were two different values of  $\Omega$  at which vibrations became visible. First there would be a violent vibration when the angular velocity was equal to half the tower torsion mode frequency. The torsion mode of the tower and the edgewise blade modes were clearly excited. It was the advancing lead-lag mode that coupled with the torsion mode. The torsion mode results in large, mainly sideways displacements of the rotor centre.

When the angular velocity was increased further, violent vibrations would again show up at a value of  $\Omega$  that was half the second tower bending mode's frequency. In this case the second tower bending mode and again the edgewise blade modes were excited. The second tower fore-aft tower mode results in large vertical displacements of the rotor centre.

Both instabilities result in very large tower motions, while the advancing lead-lag mode increases much slower than the tower motions. They also both occur at rotational velocities that are equal to half the frequency that is coupling with the edgewise mode. The gravita-

tional acceleration results in a 1P excitation of the edgewise mode in the rotating reference frame. If this excitation is transformed to the fixed reference frame it shows that the tower will experience a 2P excitation. The tower response at 2P is felt by the blade as 1P and 3P. These can both be transmitted to the tower again at 2P. So there are two important conditions that result in the instability: the excitation by the gravity force and the frequency change from rotating to non-rotating frame.

The energy source for these instabilities is the gravity combined with the generator. Because the velocity is kept constant by the generator control, the generator becomes a source of energy enabling this instability to occur. One might be tempted to think that stiffening the tower would solve the problem, but this actually worsens the instability [59]. In the case of the KEWT the solution to the instability is to either stiffen the blades or decrease the tower mass over blade mass ratio.

## Chapter 5

# Hamiltonian Dynamics for Rigid Body Simulations

*"Math is hard. Let's go shopping."*<sup>1</sup>

- Barbie

To investigate the aeroelastic stability of rotating systems like helicopters and wind turbines it can be very useful to have a tool that can perform fully non-linear simulations in the time domain. The complex interactions that take place make it almost impossible to trust any model simulation where the dynamics have been linearised. As will be shown in chapter 10, angles that one would expect to remain small enough for linearisation, can however not always be linearised (in the case in section 10.2.1 the angle  $\theta$ ). By using Hamilton's generalised momenta combined with the generalised coordinates as variables, it is possible to derive a set of equations that describe the motions of the system. A system consisting of rigid bodies can be simulated using these equations. The rigid bodies can be interconnected by hinges, springs and dampers. The bodies can be airfoils generating lift and drag forces or elements without any aerodynamic properties. By using these equations that result from an alternative formulation of the equations of motion in terms of Hamilton's generalised momenta, it is possible to simulate the motions fully nonlinear. It is not necessary to derive the equations of motion in their standard form  $[M]\{\ddot{\underline{x}}\} = \{\underline{F}(x, \dot{x})\}$  and  $\{\underline{\dot{D}}\} = \{\underline{M}(x, \dot{x})\}$ . If  $N$  is the number of degrees of freedom, a set of  $2N$  first order differential equations can be derived that constitutes the complete set of equations of motion. The derivation of the equations can easily be completely automated.

The results of the fully nonlinear simulations can be used to investigate e.g. the aeroelastic stability of the system.

---

<sup>1</sup>In 1992 Mattel put a talking Barbie on the market that among others spoke these two sentences. More information about this Barbie and the actions taken by an action group can be found on the internet: <http://www.sniggle.net/barbie.php>

In this chapter the theory of the method is explained in more detail. This theory has been applied in the development of the code called WOBBE. First in this chapter the reason for developing the programme WOBBE is described. After this the core of the method is discussed. Then all extra added features necessary for wind turbines and helicopters are described in the final section.

**NOTE:** the same notation will be used in this chapter as has been used in previous chapters. **Vectors** are given as **bold symbols**: **a**. **underlined** symbols are used for **rows** (a) and **columns**: {a}. This last category therefore does not have a certain direction, as a vector does, it is simply an enumeration of numbers without a physical meaning.

The next chapter gives a detailed description of the code WOBBE that is based on the theory described in this chapter.

## 5.1 Background

The foundation for this method was laid by Th. van Holten in 1984 and first presented in 1987 [60]. The method was developed in 1984 while testing the NEW ECS 45. The NEW ECS 45 was a wind turbine with a rotor diameter of 45 meters, which at that time was the largest wind turbine. During the development the option of hydraulics failure resulting in possible pitch motion of the blade was overlooked. Just before final assembly it was realised that this failure could become a serious problem. If the blade is free to pitch, flutter can occur. Therefore it was necessary to quickly check if there was a realistic risk of flutter occurring in this case. In case of a failure, a mechanical brake at the shaft will immediately be activated, because feathering the blade is not an option in the case of a pitch linkage failure. However, the rotor would need some time to come to a complete halt. During these few cycles, flutter can occur. It was decided that flutter occurring under these circumstances must be prevented from becoming so severe that the blades would fail before the rotor comes to a stop. The mechanism behind the possible flutter was rather complex with many variables influencing the system and not many angles that could be linearised, e.g. the azimuth angle and the pitch angle both do not remain small during this failure. It would have been a time consuming job to formulate the equations of motions for this system. At that time van Holten developed a method that would enable computer simulation without too much preliminary work. By formulating the analytical expressions for the kinetic and potential energy and the generalised forces, it was possible to shift the rest of the work to a computer. The necessary derivatives can be calculated numerically by a computer programme. A set of first order differential equations can then be integrated in time, resulting in a simulation in the time domain. For the case of the NEW ECS 45 turbine, the simulations in the time domain showed that flutter would occur in the case of a pitch linkage failure. However, it would not grow further after two cycles and the blades would not fail.

In 1990 his theory was elaborated in order to eliminate all analytical preliminary work [61]. This version of the programme could do all the work involved in deriving the governing

equations. In this programme all vectors are expressed in the inertial frame, therefore the inertia matrices were also transformed to this reference frame by the programme. It was expected that time could be saved by reformulating the programme and calculate all terms in their local reference frames. This work was performed by K. van Overbeek in 2000 [103, 104]. She further improved the method and programmed the core of WOBBE, a tool based on the method described in the next sections. Since 2000 the theory has been further developed in order to incorporate other options into the method and automate the calculation of the aerodynamic forces as described in the fourth section of this chapter.

The main advantage of the method incorporated in the programme WOBBE is the fact that the user does not need to do any preliminary work. The code can handle different kinds of models branched or unbranched, with as many degrees of freedom as the user wants. In 2000 there were very few computer programs that can combine generating and solving the equations of motion [92]. The available literature about these programmes was also rather limited. It must be noted that since then further developments have taken place and more and more codes that are able to do dynamic simulations have become available, e.g. Simpack [125].

The other advantage of the method described in this chapter is the fact that the dynamics can be kept completely nonlinear. Therefore, if many angles do not remain small, this is not a problem when using WOBBE. Time simulations can be run without any linearisations. The problem with the NEWECS 45 turbine illustrates that it is not always possible to only use linearised simulation tools.

Of course the method also has disadvantages. For one it is very difficult to draw conclusions from fully nonlinear results. Also the simulation becomes very slow, if 'many' degrees of freedom are used, where many is a rather small number when comparing to other tools. For the tool described in the next chapter, up to 15 elements is no problem, but the calculation time increases rapidly when more elements are added. When long simulations are needed to enable the user to draw conclusions from the simulations, this is an unfavourable combination.

## 5.2 The Core of the Method

Figure 5.1 summarises the method in a simple scheme. The key of this method is that knowing the values of the generalised momenta  $\{\underline{p}\}$  and the generalised coordinates  $\{\underline{q}\}$  at a certain moment in time, it is possible to determine the time derivatives of these variables. Integration of these will give the generalised momenta and generalised coordinates at the next time step. Therefore the state variables are  $\{\underline{p}\}$  and  $\{\underline{q}\}$ .

How can  $\{\dot{\underline{q}}\}$  and  $\{\dot{\underline{p}}\}$  be calculated? First the equation to determine  $\dot{q}_i$ , the time derivatives of the generalised coordinates, will be derived here. Assume a rigid body model for which

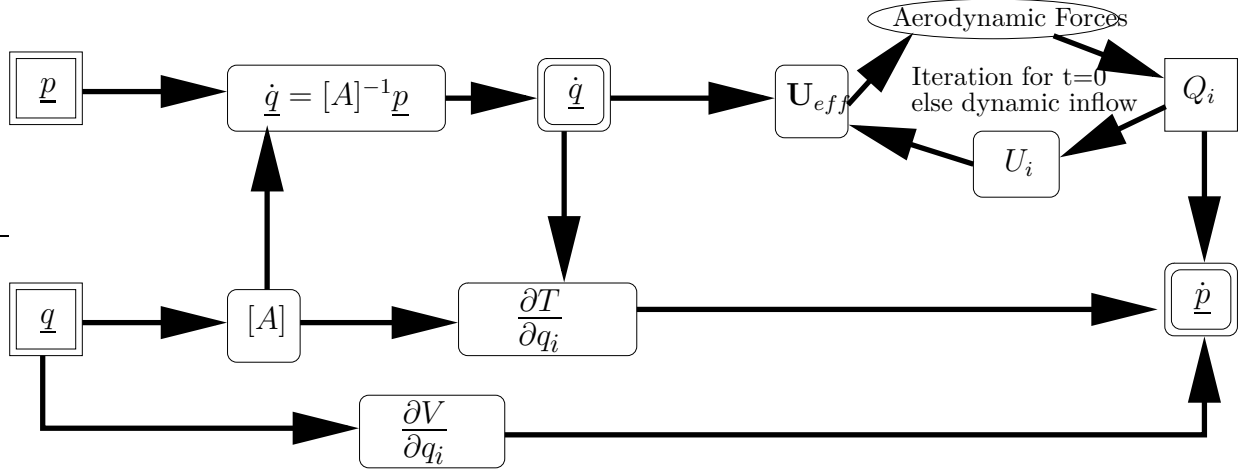


Figure 5.1: Flow diagram showing how to use Hamilton's generalised momenta  $\underline{p}$  to simulate motions of rigid bodies.  $\underline{q}$  are the generalised coordinates,  $[A]$  is the energy matrix,  $T$  the kinetic energy,  $V$  the potential energy,  $U_i$  the induced velocity,  $U_{eff}$  the resulting local velocity and  $Q_i$  are the generalised forces.

the kinetic energy of the system  $T$  is a homogeneous quadratic function of the velocities:

$$T = \frac{1}{2} \sum_{i=1}^N \sum_{j=1}^N \dot{q}_i A_{ij} \dot{q}_j \quad (5.1)$$

where  $N$  is the number of degrees of freedom of the system. This equation can be written as:

$$T = \frac{1}{2} (\dot{\underline{q}}) [A] \{\dot{\underline{q}}\} \quad (5.2)$$

Section 5.2.1 describes when the kinetic energy is a homogeneous quadratic function of the velocities. The matrix  $[A]$  in Equation 5.2 is called the mass or the energy matrix and its components will be discussed below. Using equation 5.2 to determine Hamilton's generalised momenta results in:

$$p_i = \frac{\partial T}{\partial \dot{q}_i} = \frac{\partial \frac{1}{2} (\dot{\underline{q}}) [A] \{\dot{\underline{q}}\}}{\partial \dot{q}_i} \quad (5.3)$$

Equation 5.3 gives:

$$\{\underline{p}\} = [A] \{\dot{\underline{q}}\} \quad (5.4)$$

$\{\dot{\underline{q}}\}$  can therefore be determined from:

$$\{\dot{\underline{q}}\} = [A]^{-1} \{\underline{p}\} \quad (5.5)$$

As will be described below, the matrix  $[A]$  can be determined if  $\{\underline{q}\}$  is known. Therefore this equation can be solved for  $\{\underline{\dot{q}}\}$ .

The time derivatives of  $\{\underline{p}\}$  can be determined from Lagrange's equations. Lagrange's equations are :

$$\frac{d}{dt} \frac{\partial T}{\partial \dot{q}_i} - \frac{\partial T}{\partial q_i} + \frac{\partial V}{\partial q_i} = Q_i, \quad i = 1, 2, \dots, n \quad (5.6)$$

Substituting  $p_i = \frac{\partial T}{\partial \dot{q}_i}$  into these equations results in an expression for  $\dot{p}_i$ :

$$\dot{p}_i = \frac{\partial T}{\partial q_i} - \frac{\partial V}{\partial q_i} + Q_i \quad (5.7)$$

where  $Q_i$  is the generalised force for  $q_i$ .

Note that despite  $\{\underline{p}\}$  and  $\{\underline{q}\}$  being the state variables, all partial derivatives with respect to  $q_i$  are for all other values of  $q_j$  with  $j \neq i$  kept constant and all values of  $\{\underline{\dot{q}}\}$  kept constant, not for the values of  $\{\underline{p}\}$  kept constant.

For the systems modelling wind turbines and helicopters the generalised force is mainly the resulting moment due to the dampers and the aerodynamic forces about the same axes as the  $i^{\text{th}}$  degree of freedom. Every term in equation 5.7 can be determined, if necessary by numerical differentiation. These terms will depend on  $\{\underline{q}\}$  and  $\{\underline{\dot{q}}\}$  as will be shown below. This results in a system of  $2N$  first order differential equations: equations 5.5 and 5.7. This system constitutes the complete set of equations of motion.

Once the time derivatives in equation 5.5 and 5.7 are known, the generalised coordinates  $\{\underline{q}\}$  and the generalised momenta  $\{\underline{p}\}$  can be determined by integration. The behaviour in time of the generalised coordinates will show the (in)stability of the system. Though due to the nonlinearity of these time series, some post-processing might be needed to get insight into the stability, especially if the model includes many degrees of freedom and therefore many different frequencies. More about post-processing can be found in appendix D.

### 5.2.1 Energy Matrix

The energy or mass matrix plays an important role in the method described in this chapter. This section will illustrate the calculations that need to be performed by the programme in order to determine the energy matrix.

First it was assumed that the kinetic energy is a homogenous quadratic function of the velocities of the generalised coordinates. This is a possible limitation of the method. Recall equation 2.144 from section 2.2 that described the kinetic energy for a system consisting of  $N$  rigid bodies:

$$T = \sum_{k=1}^N \left( \frac{1}{2} m_k \mathbf{v}_{cg,k} \cdot \mathbf{v}_{cg,k} + \frac{1}{2} (p_k, q_k, r_k) [J_{cg,k}] \begin{Bmatrix} p_k \\ q_k \\ r_k \end{Bmatrix} \right)$$

In this equation  $\mathbf{v}_{\text{cg},\mathbf{k}}$  denotes the velocity of the c.g. of element  $k$ ,  $m_k$  is the mass of this element and  $(p_k, q_k, r_k)\{\underline{\mathbf{E}}_{\mathbf{k}}\} = \boldsymbol{\omega}_{\mathbf{k}}$  is the total rotation of element  $k$ . The matrix  $[J_{\text{cg}k}]$  in this equation is the inertia matrix of element  $k$  about its c.g. and relative to its local reference frame.

This equation shows that as long as *all* velocities are included in  $\{\underline{\dot{q}}\}$ , the kinetic energy will in fact be a homogeneous quadratic function of the velocities  $\{\underline{\dot{q}}\}$ . In practice this means that all rotations and translations that should be taken into account in the kinetic energy must be included in the generalised coordinates. For example when looking at a helicopter blade the rotational velocity  $\Omega$  must be taken into account and therefore the azimuth angle must be one of the generalised coordinates. For a constant rotational speed, this angle will not be a degree of freedom, but the solution to this problem will be given in section 5.3.2. Another example might be a case where it is important to include the rotational velocity of the earth. This must then be taken into account in the kinetic energy and the coordinate belonging to the rotation must be used as a generalised coordinate. If this is done, the kinetic energy will indeed be a homogeneous quadratic function of the angular velocities  $\{\underline{\dot{q}}\}$ . The theory described in this chapter will focus on rotations as generalised coordinates. The option of translational generalised coordinates is not taken into account, but it is possible and not complicated to add this option to the theory.

In order to determine the matrix  $[A]$ , recall that (equation 5.1):

$$T = \frac{1}{2} \sum_{i=1}^N \sum_{j=1}^N \dot{q}_i A_{ij} \dot{q}_j$$

Thus

$$A_{ij} = \frac{\partial^2 T}{\partial \dot{q}_i \partial \dot{q}_j} \quad (5.8)$$

with the kinetic energy shown above. Therefore the energy or mass matrix  $[A]$  can be calculated as follows. Each element of the energy matrix  $[A]$  consists of the sum of two parts: a part describing the rotation energy and a part describing the translation energy, both of all elements.

To determine the rotational part recall that:

$$T_{\text{rot}} = \frac{1}{2} \sum_{k=1}^N (p_k, q_k, r_k) [J_{\text{cg},k}] \begin{Bmatrix} p_k \\ q_k \\ r_k \end{Bmatrix}$$

where  $(p_k, q_k, r_k)$  are the components of the total rotation vector of element  $k$  expressed in its local reference frame (see also 2.1.2). Using the notation  $(p_k, q_k, r_k) = (\underline{\omega}_k)$  and

$\begin{Bmatrix} p_k \\ q_k \\ r_k \end{Bmatrix} = \{\underline{\omega}_k\}$ , the derivative with respect to  $\dot{q}_i$  becomes:

$$\frac{\partial T}{\partial \dot{q}_i} = \frac{1}{2} \sum_{k=1}^N \left\{ \frac{\partial (\underline{\omega}_k)}{\partial \dot{q}_i} [J_{\text{cg},k}] \{\underline{\omega}_k\} + (\underline{\omega}_k) [J_{\text{cg},k}] \frac{\partial \{\underline{\omega}_k\}}{\partial \dot{q}_i} \right\} \quad (5.9)$$

Recall that  $\underline{\omega}_k$ , the total angular velocity of element  $k$ , will only have first order  $\dot{q}_i$  terms. Therefore  $\frac{\partial^2 \underline{\omega}_k}{\partial \dot{q}_i \partial \dot{q}_j} = 0$ . Thus for a system consisting of  $N$  elements, the part of an element of the energy matrix that concerns the rotation energy is:

$$A_{ijrot} = \left( \frac{\partial^2 T_{rot}}{\partial \dot{q}_i \partial \dot{q}_j} \right) = \left( \frac{\partial \underline{\omega}_1}{\partial \dot{q}_i} \right) [J_{cg1}] \left\{ \frac{\partial \underline{\omega}_1}{\partial \dot{q}_j} \right\} + \left( \frac{\partial \underline{\omega}_2}{\partial \dot{q}_i} \right) [J_{cg2}] \left\{ \frac{\partial \underline{\omega}_2}{\partial \dot{q}_j} \right\} + \dots \\ \dots + \left( \frac{\partial \underline{\omega}_N}{\partial \dot{q}_i} \right) [J_{cgN}] \left\{ \frac{\partial \underline{\omega}_N}{\partial \dot{q}_j} \right\} \quad (5.10)$$

In equation 5.10  $\underline{\omega}_k$  is the total angular velocity vector of element  $k$  expressed in its local reference frame, which is equal to that of the previous element plus the extra term due to its own degree of freedom. Using the vector notation  $\underline{\omega}_k$  for the total rotation, the following expressions can be derived:

$$\begin{aligned} \underline{\omega}_1 &= \dot{q}_1 (c_{1x}, c_{1y}, c_{1z}) \{\underline{\mathbf{E}}_1\} = (p_1, q_1, r_1) \{\underline{\mathbf{E}}_1\} \\ \underline{\omega}_2 &= \dot{q}_1 (c_{1x}, c_{1y}, c_{1z}) \{\underline{\mathbf{E}}_1\} + \dot{q}_2 (c_{2x}, c_{2y}, c_{2z}) \{\underline{\mathbf{E}}_2\} \\ &= (p_1, q_1, r_1) [R_2]^T + \dot{q}_2 (c_{2x}, c_{2y}, c_{2z}) \{\underline{\mathbf{E}}_2\} = (p_2, q_2, r_2) \{\underline{\mathbf{E}}_2\} \\ &\vdots \\ \underline{\omega}_k &= \dot{q}_1 (c_{1x}, c_{1y}, c_{1z}) \{\underline{\mathbf{E}}_1\} + \dot{q}_2 (c_{2x}, c_{2y}, c_{2z}) \{\underline{\mathbf{E}}_2\} + \dots + \dot{q}_k (c_{kx}, c_{ky}, c_{kz}) \{\underline{\mathbf{E}}_k\} \\ &= (p_{k-1}, q_{k-1}, r_{k-1}) [R_k]^T \{\underline{\mathbf{E}}_k\} + \dot{q}_k (c_{kx}, c_{ky}, c_{kz}) \{\underline{\mathbf{E}}_k\} = (p_k, q_k, r_k) \{\underline{\mathbf{E}}_k\} \end{aligned} \quad (5.11)$$

In these equations:

- $\{\underline{\mathbf{E}}_k\}$  is a column of unit vectors:  $\begin{Bmatrix} \mathbf{i} \\ \mathbf{j} \\ \mathbf{k} \end{Bmatrix}$ , defining the local reference frame that rotates with element  $k$ .
- $[R_k]$  is the rotation transformation matrix:  $\{\underline{\mathbf{E}}_k\} = [R_k] \{\underline{\mathbf{E}}_{k-1}\}$
- The row  $(c_{kx}, c_{ky}, c_{kz})$  indicates the direction of the local rotation axis of element  $k$ :  $(0,0,1)$  would for instance indicate a rotation about the z-axis of  $\{\underline{\mathbf{E}}_{k-1}\}$ .

The partial derivatives of  $\underline{\omega}_k$  with respect to the angular velocities  $\dot{q}_i$  can be determined. Starting from  $\dot{q}_1$  and giving the results in the local reference frames:

$$\begin{aligned} \frac{\partial \underline{\omega}_1}{\partial \dot{q}_1} &= (c_{1x}, c_{1y}, c_{1z}) \{\underline{\mathbf{E}}_1\} \\ \frac{\partial \underline{\omega}_2}{\partial \dot{q}_1} &= (c_{1x}, c_{1y}, c_{1z}) [R_2]^T \{\underline{\mathbf{E}}_2\} \\ &\vdots \\ \frac{\partial \underline{\omega}_N}{\partial \dot{q}_1} &= (c_{1x}, c_{1y}, c_{1z}) [R_2]^T [R_3]^T \dots [R_N]^T \{\underline{\mathbf{E}}_N\} \end{aligned} \quad (5.12)$$

What can be noticed from equation 5.12 is that the derivative  $\frac{\partial \boldsymbol{\omega}_1}{\partial \dot{q}_1}$  is actually the exact same vector as  $\frac{\partial \boldsymbol{\omega}_k}{\partial \dot{q}_1}$ . The only difference is that the components of the last one must be transformed to reference frame  $k$  as it will be multiplied with  $[J_{cgk}]$  which is given relative to the axes of reference frame  $k$ .

For the other angular velocities  $\dot{q}_i$ , similar expressions can be derived and a matrix can be set up showing the recurrent relationship that can be used in a computer programme. Note that for  $i > k$   $\frac{\partial \boldsymbol{\omega}_k}{\partial \dot{q}_i} = \frac{\partial \boldsymbol{\omega}_k}{\partial \dot{q}_i} \{\mathbf{E}_k\}$  will be zero. All the derivatives are expressions in the local reference frames:

$$\begin{aligned} \frac{\partial \boldsymbol{\omega}_1}{\partial \dot{q}_1} &= (c_{1x}, c_{1y}, c_{1z}) & \frac{\partial \boldsymbol{\omega}_1}{\partial \dot{q}_2} &= 0 & \dots & \frac{\partial \boldsymbol{\omega}_1}{\partial \dot{q}_N} &= 0 \\ \frac{\partial \boldsymbol{\omega}_2}{\partial \dot{q}_1} &= \frac{\partial \boldsymbol{\omega}_1}{\partial \dot{q}_1} [R_2]^T & \frac{\partial \boldsymbol{\omega}_2}{\partial \dot{q}_2} &= (c_{2x}, c_{2y}, c_{2z}) & \dots & \frac{\partial \boldsymbol{\omega}_2}{\partial \dot{q}_N} &= 0 \\ \vdots & & \vdots & & \ddots & \vdots & \\ \frac{\partial \boldsymbol{\omega}_N}{\partial \dot{q}_1} &= \frac{\partial \boldsymbol{\omega}_{N-1}}{\partial \dot{q}_1} [R_N]^T & \frac{\partial \boldsymbol{\omega}_N}{\partial \dot{q}_2} &= \frac{\partial \boldsymbol{\omega}_{N-1}}{\partial \dot{q}_2} [R_N]^T & \dots & \frac{\partial \boldsymbol{\omega}_N}{\partial \dot{q}_N} &= (c_{Nx}, c_{Ny}, c_{Nz}) \end{aligned} \quad (5.13)$$

Equation 5.13 also shows that this part of the energy matrix will only depend on  $\{q\}$ . To calculate the parts of the energy matrix that result from the rotation energy, the inertia matrices need to be known, as well as the generalised coordinates and the directions of the degrees of freedom. The inertia matrices of the elements need to be known about their own c.g. and relative to their local reference frame.

To determine the translation part of  $[A]$ , recall that  $\mathbf{v}_{cgi}$  is a first order expression in  $\dot{q}_k$ . Therefore  $\frac{\partial^2 \mathbf{v}_{cgi}}{\partial \dot{q}_i \partial \dot{q}_j} = 0$ , very similar to the rotational part described above. This means that the translation part of the energy matrix also depends on  $\{q\}$  only and not on the velocities. The part of the energy matrix concerning the translation energy becomes:

$$A_{ijtrans} = m_1 \frac{\partial \mathbf{v}_{cg1}}{\partial \dot{q}_i} \cdot \frac{\partial \mathbf{v}_{cg1}}{\partial \dot{q}_j} + m_2 \frac{\partial \mathbf{v}_{cg2}}{\partial \dot{q}_i} \cdot \frac{\partial \mathbf{v}_{cg2}}{\partial \dot{q}_j} + \dots + m_N \frac{\partial \mathbf{v}_{cgN}}{\partial \dot{q}_i} \cdot \frac{\partial \mathbf{v}_{cgN}}{\partial \dot{q}_j} \quad (5.14)$$

Now, for systems that consist of rigid elements that are interconnected by hinges, as shown in figure 5.2, the velocity of the centre of gravity of element  $k$  can be written as:

$$\begin{aligned} \mathbf{v}_{cgk} &= \mathbf{v}_{hg_{k-1}} + \boldsymbol{\omega}_k \times \mathbf{dr} = \mathbf{v}_{hg_{k-1}} + (x_{cgk}, y_{cgk}, z_{cgk}) \begin{bmatrix} 0 & r_k & -q_k \\ -r_k & 0 & p_k \\ q_k & -p_k & 0 \end{bmatrix} \{\mathbf{E}_k\} \\ &= \left( (v_{xhg_{k-1}}, v_{yhg_{k-1}}, v_{zhg_{k-1}}) [R_k]^T - (p_k, q_k, r_k) \begin{bmatrix} 0 & z_{cgk} & -y_{cgk} \\ -z_{cgk} & 0 & x_{cgk} \\ y_{cgk} & -x_{cgk} & 0 \end{bmatrix} \right) \{\mathbf{E}_k\} \\ &= \left( (v_{xhg_{k-1}}, v_{yhg_{k-1}}, v_{zhg_{k-1}}) [R_k]^T - (p_k, q_k, r_k) [R_{\times cgk}] \right) \{\mathbf{E}_k\} \end{aligned} \quad (5.15)$$

where  $\mathbf{dr}$  is the vector between the hinge and the centre of gravity of the element, as illustrated for element 5 in figure 5.2.  $\mathbf{v}_{hg(k-1)}$  is the velocity of the hinge that connects element  $k-1$  to element  $k$ . This is also shown in figure 5.2.

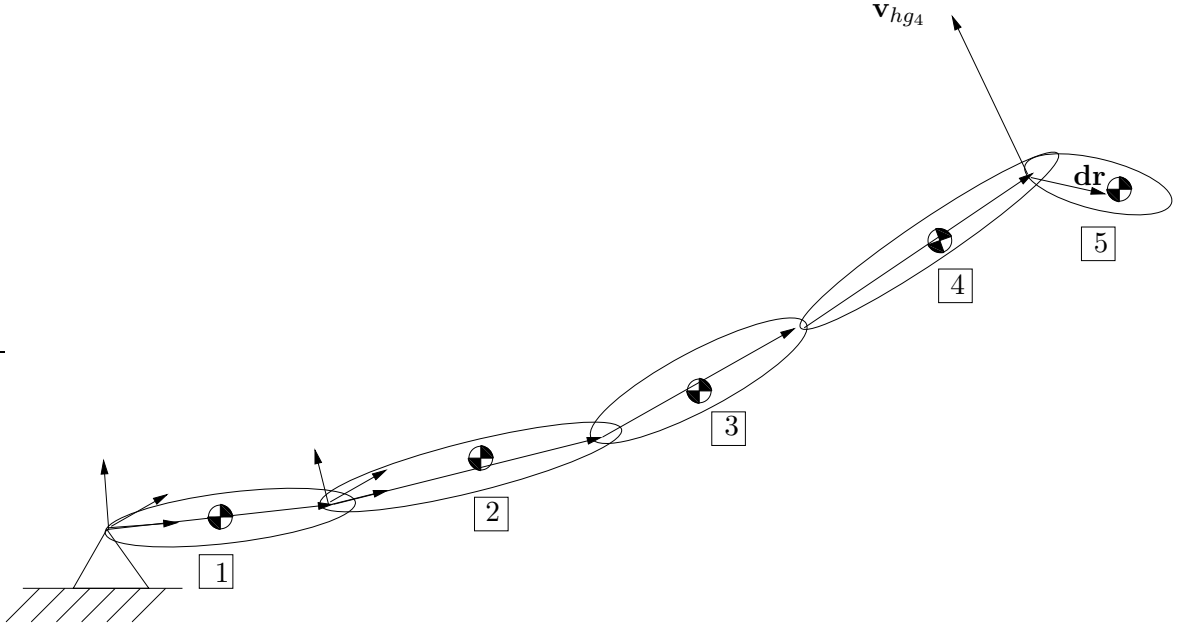


Figure 5.2: A multi-body system as can be simulated using WOBBE, a programme based on Hamiltonian dynamics

The derivatives of the velocity with respect to the angular velocities are needed. Using equation 5.15 the derivatives become:

$$\frac{\partial \mathbf{v}_{cgk}}{\partial \dot{q}_i} = \frac{\partial \mathbf{v}_{hgk-1}}{\partial \dot{q}_i} + \frac{\partial \boldsymbol{\omega}_k}{\partial \dot{q}_i} \times \mathbf{dr} \quad (5.16)$$

This equation shows that the results given in equation 5.13 can be used again to determine the derivatives needed for the translation energy, but the derivatives of the velocities of the hinges have not yet been derived. The velocities of the hinges can be expressed as:

$$\begin{aligned} \mathbf{v}_{hg1} &= \boldsymbol{\omega}_1 \times \mathbf{R}_{hg1} = -(p_1, q_1, r_1) \begin{bmatrix} 0 & z_{hg1} & -y_{hg1} \\ -z_{hg1} & 0 & x_{hg1} \\ y_{hg1} & -x_{hg1} & 0 \end{bmatrix} = -(p_1, q_1, r_1) [R_{\times hg1}] \{\underline{\mathbf{E}}_1\} \\ \mathbf{v}_{hg2} &= \mathbf{v}_{hg1} + \boldsymbol{\omega}_2 \times \mathbf{R}_{hg2} = -(p_1, q_1, r_1) [R_{\times hg1}] \{\underline{\mathbf{E}}_1\} - (p_2, q_2, r_2) [R_{\times hg2}] \{\underline{\mathbf{E}}_2\} \\ &\vdots \end{aligned} \quad (5.17)$$

Partial differentiation leads to:

$$\begin{aligned} \frac{\partial \mathbf{v}_{hg1}}{\partial \dot{q}_1} &= -(c_{x1}, c_{y1}, c_{z1}) [R_{\times hg1}] \{\underline{\mathbf{E}}_1\} \\ \frac{\partial \mathbf{v}_{hg2}}{\partial \dot{q}_1} &= -(c_{x1}, c_{y1}, c_{z1}) [R_{\times hg1}] \{\underline{\mathbf{E}}_1\} - (c_{x1}, c_{y1}, c_{z1}) [R_2]^T [R_{\times hg2}] \{\underline{\mathbf{E}}_2\} \\ &\vdots \end{aligned} \quad (5.18)$$

Using a similar notation as used for the total rotation vectors,  $\mathbf{v}_{hgk} = \underline{v}_{hgk} \{\mathbf{E}_k\}$ , and summarising the results found, the derivatives become:

for  $k < j$ :

$$\frac{\partial \mathbf{v}_{hgk}}{\partial \dot{q}_j} = \frac{\partial \underline{v}_{hgk}}{\partial \dot{q}_j} \{\mathbf{E}_k\} = 0 \quad (5.19)$$

for  $k = j$ :

$$\frac{\partial \mathbf{v}_{hgk}}{\partial \dot{q}_j} = \frac{\partial \underline{v}_{hgk}}{\partial \dot{q}_j} \{\mathbf{E}_k\} = (c_{x_k}, c_{y_k}, c_{z_k}) [R_{\times hgk}] \{\mathbf{E}_k\} \quad (5.20)$$

and for  $k > j$ :

$$\begin{aligned} \frac{\partial \mathbf{v}_{hgk}}{\partial \dot{q}_j} &= \frac{\partial \underline{v}_{hgk}}{\partial \dot{q}_j} \{\mathbf{E}_k\} \\ &= \left( \frac{\partial \underline{v}_{hgk-1}}{\partial \dot{q}_j} [R_k]^T - (c_{x_k}, c_{y_k}, c_{z_k}) [R_{j+1}]^T [R_{j+2}]^T \dots [R_k]^T [R_{\times hgk}] \right) \{\mathbf{E}_k\} \\ &= \left( \frac{\partial \underline{v}_{hgk-1}}{\partial \dot{q}_j} [R_k]^T - \frac{\partial \omega_k}{\partial \dot{q}_j} [R_{\times hgk}] \right) \{\mathbf{E}_k\} \end{aligned} \quad (5.21)$$

The contributions to the energy matrix due to translation can now be calculated if the mass, hinge distances and the distances to the centres of gravity are known.

All expressions needed to calculate the elements of the energy matrix are now known. Note that the expressions given so far are only valid for unbranched systems, for simplicity reasons. If a system is branched, the element before element  $k$  can have another index than  $k - 1$ . For this reason, in case of a branched system,  $k - 1$  should be replaced by *prior*( $k$ ) where *prior*( $k$ ) is the index of the element before element  $k$ .

Note also that for both the translation as for the rotation part it is not necessary to determine contributions for element  $k$  if  $k$  is smaller than  $j$ , because in that case the derivatives will become zero. Therefore, using this and the symmetry of the matrix, it is possible to rewrite equations 5.10 and 5.14 to become:

$$\begin{cases} A_{ij} = \sum_{k=j}^N \left\{ \frac{\partial \omega_k}{\partial \dot{q}_i} [J_{cgk}] \frac{\partial \omega_k}{\partial \dot{q}_j} + m_k \frac{\partial v_{cgk}}{\partial \dot{q}_i} \cdot \frac{\partial v_{cgk}}{\partial \dot{q}_j} \right\} & ; i < j \\ A_{ij} = A_{ji} & ; i > j \end{cases} \quad (5.22)$$

The energy matrix plays an important part in this method, see figure 5.1. The calculation of the energy or mass matrix will take up a large part of the calculation time. It needs to be calculated many times during a simulation, because it also plays an important role in the calculation of the derivatives of the kinetic energy as discussed next.

### 5.2.2 Derivatives of Kinetic and Potential Energy

Recall that, to determine the time derivative  $\dot{p}_i$  of the generalised momenta, the partial derivatives of both the kinetic and potential energy with respect to the generalised coordinates must be determined (equation 5.7):

$$\dot{p}_i = \frac{\partial T}{\partial \dot{q}_i} - \frac{\partial V}{\partial q_i} + Q_i$$

These derivatives will be determined numerically by determining the energies for different values of  $q_i$ .

#### Kinetic Energy

The kinetic energy can be determined using the energy matrix and the angular velocities:

$$T = \frac{1}{2}(\dot{\underline{q}})[A]\{\dot{\underline{q}}\} \quad (5.23)$$

This equation shows that the kinetic energy can only be determined once  $(\dot{\underline{q}})$  and  $[A]$  have been calculated. The derivatives of the kinetic energy  $\frac{\partial T}{\partial q_i}$  can for example be determined by calculating the energies for  $q_i^* = q_i + h$  and for  $q_i^* = q_i - h$ . This results in respectively  $T^+$  and  $T^-$ . The derivative is then determined by:

$$\frac{\partial T}{\partial q_i} = \frac{T^+ - T^-}{2h} + O(h^2) \quad (5.24)$$

Where the higher order terms  $O(h^2)$  are assumed to be unimportant.

Another option is to use the analytical derivative of the kinetic energy. The only term in equation 5.23 that depends on  $q_i$  is the energy matrix  $[A]$ . The terms  $\frac{\partial \omega_k}{\partial \dot{q}_j}$  and  $\frac{\partial \mathbf{v}_{cgk}}{\partial \dot{q}_j}$  depend on  $q_i$  through the rotation transformation matrix. The analytical derivative of these two terms can be determined by changing the rotation transformation matrix  $[R_i]$  by its derivative, e.g.

$$[R_i] = \begin{bmatrix} 1 & 0 & 0 \\ 0 & \cos q_i & \sin q_i \\ 0 & -\sin q_i & \cos q_i \end{bmatrix} \Rightarrow \frac{\partial [R_i]}{\partial q_i} = \begin{bmatrix} 0 & 0 & 0 \\ 0 & -\sin q_i & \cos q_i \\ 0 & -\cos q_i & -\sin q_i \end{bmatrix} \quad (5.25)$$

When the matrix  $[R_i]$  in the equations for  $\frac{\partial \omega_k}{\partial \dot{q}_j}$  and  $\frac{\partial \mathbf{v}_{cgk}}{\partial \dot{q}_j}$  is substituted by the matrix  $\frac{\partial [R_i]}{\partial q_i}$ , the derivatives  $\frac{\partial^2 \omega_k}{\partial \dot{q}_j \partial q_i}$  and  $\frac{\partial^2 \mathbf{v}_{cgk}}{\partial \dot{q}_j \partial q_i}$  are calculated. These can be used to determine the analytical derivative of  $[A]$ :

$$\begin{aligned} \frac{\partial A_{ij}}{\partial q_l} = \sum_{k=j}^N \left\{ \frac{\partial \omega_k}{\partial \dot{q}_i} [J_{cgk}] \frac{\partial^2 \omega_k}{\partial \dot{q}_j \partial q_l} + \frac{\partial^2 \omega_k}{\partial \dot{q}_i \partial q_l} [J_{cgk}] \frac{\partial \omega_k}{\partial \dot{q}_j} + \right. \\ \left. + m_k \frac{\partial \mathbf{v}_{cgk}}{\partial \dot{q}_i} \cdot \frac{\partial^2 \mathbf{v}_{cgk}}{\partial \dot{q}_j \partial q_l} + m_k \frac{\partial^2 \mathbf{v}_{cgk}}{\partial \dot{q}_i \partial q_l} \cdot \frac{\partial \mathbf{v}_{cgk}}{\partial \dot{q}_j} \right\} \quad (5.26) \end{aligned}$$

The analytical derivative of the kinetic energy becomes:

$$\frac{\partial T}{\partial q_i} = \frac{1}{2}(\dot{q}) \frac{\partial[A]}{\partial q_i} \{\dot{q}\} \quad (5.27)$$

### Potential Energy

The potential energy must also be determined to be able to solve equation 5.7. The partial derivative  $\frac{\partial V}{\partial q_i}$  can be numerically determined from the calculated potential energy.

The potential energy can be split up into two parts: the elastic energy, stored in the ideal torsional springs and the potential energy due to gravity forces. Often simulations will be run without taking gravity forces into account. In these cases the derivative can easily be determined analytically using:

$$V_{el} = \sum_{i=1}^N \frac{1}{2} k_i q_i^2 \quad (5.28)$$

therefore the derivatives simply become:

$$\frac{\partial V_{el}}{\partial q_i} = k_i q_i \quad (5.29)$$

If the gravitational forces cannot be neglected, then the calculation becomes more complicated. Due to the gravitation a term must be added to the result of equation 5.29 to find the derivative of the total potential energy. This part of the potential energy can be determined by using:

$$V_{grav} = \sum_{i=1}^N -m_i \mathbf{g} \cdot \mathbf{r}_{cgi} \quad (5.30)$$

The derivative can then be determined by calculating the potential energy for the two different values of  $q_i^*$ , similar to the calculation of  $\frac{\partial T}{\partial q_i}$ . During this calculation, time can be saved by only determining those parts that actually change with the change in  $q_i$ . This means only the elements behind this degree of freedom, including element  $i$  itself. All other elements will remain in exactly the same position if  $q_i$  is changed, therefore these elements will not have an influence on  $\frac{\partial V}{\partial q_i}$ .

Another option is using interim results that were found during the calculation of the energy matrix,  $\frac{\partial \mathbf{v}_{cgi}}{\partial \dot{q}_i}$ :

$$\frac{\partial V_{grav}}{\partial q_i} = \frac{\sum_{i=1}^N -m_i \mathbf{g} \cdot \mathbf{r}_{cgi}}{\partial q_i} = \sum_{i=1}^N -m_i \mathbf{g} \cdot \frac{\partial \mathbf{r}_{cgi}}{\partial q_i} = \sum_{i=1}^N -m_i \mathbf{g} \cdot \frac{\partial \mathbf{v}_{cgi}}{\partial \dot{q}_i} \quad (5.31)$$

where the last term has already been calculated during the determination of  $[A]$ . So all that is then left to calculate is the components of  $\mathbf{g}$  in the local reference frame  $\{\mathbf{E}_i\}$  by using the rotation transformation matrices.

## 5.3 Additional Modelling Features

The Hamiltonian method discussed so far in this chapter is convenient to create a useful, complete and nonlinear tool for the analysis of wind turbines and helicopters. However, to achieve this, it is necessary to add some extra possibilities to the basic method. These will be described in the following sections.

### 5.3.1 Pitch Setting / Fixed Angles

The models used in the theory described so far require the hinges to be set in the principal directions: the most flexible and the stiffest direction, otherwise cross-coupling cannot be taken into account. The stiffest and most flexible directions are often at a certain angle. It is necessary to be able to put this in the model.

Another reason why the option of fixed angles must be added to the programme, is the pitch setting of the blades. Nowadays most modern wind turbines are often so-called pitch regulated variable speed turbines. These use the pitch setting to control the angle of attack of the blade.

An engineering solution to model a fixed angle in a tool based on the method described in this chapter would be to add a degree of freedom with a very high stiffness and a generalised force that exactly counteracts the moment in the spring due to the pitch setting:

$$Q_{fix} = K(\theta - \theta_{fix}) \quad (5.32)$$

where  $K$  is the very large spring stiffness in the direction of the added degree of freedom,  $\theta$  is the added degree of freedom and  $\theta_{fix}$  has the value that the angle  $\theta$  should have. However, this will introduce a very high frequency in the system as well as an unnecessary extra degree of freedom resulting in longer calculation times. Next to that the angle will never remain exactly constant.

There are other options to add a constant angle such as a pitch setting [48]. An extra angle would mean that an extra rotation transformation matrix must be added. For example, looking at figure 5.3, reference frame 2 is the local reference frame for element 2 and reference frame 3' is rotated about the  $x_2$ -axis with a constant angle  $\theta_3$  simulating a pitch setting. The local reference frame for element 3 is rotated about the  $z_{3'}$ -axis with an angle  $q_3$ , where  $q_3$  is one of the degrees of freedom of the system. To determine the rotational velocity of element three in its local reference frame, the following expression must be used:

$$\begin{aligned} \omega_3 &= (0, 0, \dot{q}_1)\{\mathbf{E}_1\} + (0, \dot{q}_2, 0)\{\mathbf{E}_2\} + (0, 0, \dot{q}_3)\{\mathbf{E}_3\} = \\ &= \left( (0, 0, \dot{q}_1)[q_2]^T + (0, \dot{q}_2, 0) \right) [\theta_3]^T [q_3]^T + (0, 0, \dot{q}_3) \{\mathbf{E}_3\} \end{aligned} \quad (5.33)$$

where  $[q_i]$  and  $[\theta_i]$  are the rotational transformation matrices. Note that the first transformation matrix  $[\theta_3]$  is constant throughout the simulation. This example shows that a fixed

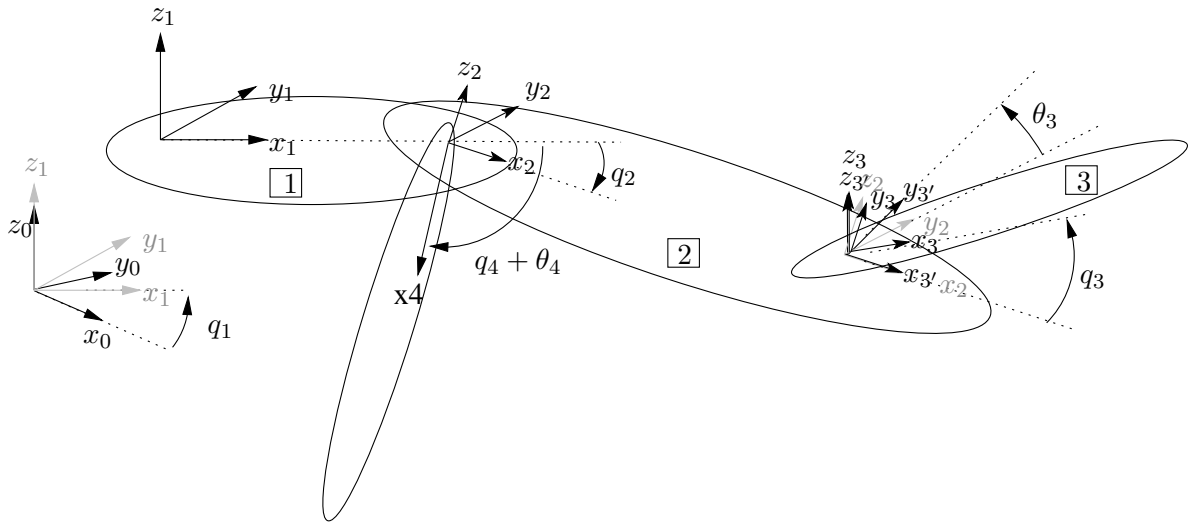


Figure 5.3: Multi body model with a fixed angle before element 3

angle can easily be incorporated in the method by adding an extra rotational transformation matrix. Obviously care must be taken not to change the order of the matrices and use the transposed matrix when necessary.

In variable pitch regulated wind turbines, the pitch setting of the blades will actually not remain constant during operation with varying wind speeds. A controller will adjust the pitch setting, depending on the torque available for the generator. In case a model of the controller is available, it is also possible to model the variable pitch using this "fixed pitch angle". This means that the rotation transformation matrices for the pitch angles must now change every time the pitch setting is changed. Otherwise the calculation remains exactly the same. Note that the pitch setting is only used at the root of the blade, other fixed angles that model the structural pitch, will always remain constant (in current blades).

If this "fixed angle-approach" is used, the velocities of the pitch setting are neglected. However, the velocity with which the pitch setting changes, is small and it is about an axis that has a relatively low inertia. The velocity will also have very little effect on the aerodynamics, therefore this quasi-steady approach does not lead to large errors.

### 5.3.2 Controlled rotations

The method described so far in this chapter is based on degrees of freedom. However, in many models some controlled rotations are desired. For example: the constant rotational velocity of a wind turbine. It is sometimes possible, as an engineering solution, to simulate a constant rotation by putting a flywheel in the model. This flywheel element would have a relatively large inertia about the rotating axes, but no mass and no inertia about the other axes. This way it would keep the rotational velocity approximately constant. However, this

method has a few drawbacks. First of all, the rotation will not be exactly constant. Second, the large inertia introduces a relatively large and constant term in the kinetic energy that will be taken into account when determining  $\frac{\partial T}{\partial q_i}$  numerically and will decrease the accuracy of this calculation. This is because there are large differences between the relatively small changes in the kinetic energy due to the change  $h$  in  $q_i$  (see section 5.2.2) and the large total kinetic energy itself, which is mainly due to the large inertia of the flywheel. Third, variation of this velocity according to a given function is impossible. Fourth, the velocity that one wants to keep constant, is calculated by solving equation 5.5 for every step, increasing the calculation time unnecessarily. And finally the fifth drawback is that this method cannot be used if there is a degree of freedom before the constant rotation that has a component in the direction of this constant rotation. In that case the flywheel will have unwanted (and incorrect!) effects on the results. This fifth drawback is illustrated by an example in appendix E.

For these reasons another way is needed to model controlled rotations. To simulate models that include one or more controlled rotations, extra elements can be created that do not have a real degree of freedom. These so-called dummy elements should be treated as normal elements when aerodynamic forces, the kinetic energy and the potential energy are calculated. This way the aerodynamic forces acting on the dummy element will be taken into account and the kinetic energy will remain a homogeneous quadratic function of the velocities. However, when the velocities are calculated by solving equation 5.5:

$$\underline{\dot{q}} = [A]^{-1} \underline{p}$$

the controlled velocities are already known and must not be solved using this equation. The controlled velocity must be removed from  $\{\underline{\dot{q}}\}$  and all elements of the  $[A]$ -matrix that correspond to this velocity must be removed from the energy matrix. The values of the generalised momenta must be corrected for the known velocity. The following shows an example for a system that has  $(N-1)$  degrees of freedom. Assuming that the complete system undergoes an extra controlled rotation with a velocity  $\Omega$ , therefore the first element in  $\{\underline{\dot{q}}\}$  becomes the known value  $\Omega$ :

$$\begin{bmatrix} p_1 \\ p_2 \\ p_3 \\ \vdots \\ p_n \end{bmatrix} = \begin{bmatrix} A_{11} & A_{12} & \dots & A_{1n} \\ A_{21} & A_{22} & \dots & A_{2n} \\ A_{31} & A_{32} & \dots & A_{3n} \\ \vdots & \vdots & \ddots & \vdots \\ A_{n1} & A_{n2} & \dots & A_{nn} \end{bmatrix} \begin{bmatrix} \Omega \\ \dot{q}_2 \\ \dot{q}_3 \\ \vdots \\ \dot{q}_n \end{bmatrix} \quad (5.34)$$

The velocity  $\Omega$  is known, therefore this can not be determined by this equation. All terms with  $\Omega$  can be taken to the left hand side of the equation. In this case the first equation  $p_1 = A_{11}\Omega + A_{12}\dot{q}_2 \dots$  has become redundant. The equation that should be solved for  $\underline{\dot{q}}$  in

this case becomes:

$$\begin{bmatrix} p_2 - A_{21}\Omega \\ p_3 - A_{31}\Omega \\ \vdots \\ p_n - A_{n1}\Omega \end{bmatrix} = \begin{bmatrix} A_{22} & A_{23} & \dots & A_{2n} \\ A_{32} & A_{33} & \dots & A_{3n} \\ \vdots & \vdots & \ddots & \vdots \\ A_{n2} & A_{n3} & \dots & A_{nn} \end{bmatrix} \begin{bmatrix} \dot{q}_2 \\ \dot{q}_3 \\ \vdots \\ \dot{q}_n \end{bmatrix} \quad (5.35)$$

This example could for instance represent the system depicted in figure 5.3 but adding a constant rotational velocity. E.g. element 1 rotates about the  $z$ -axis with  $\Omega$  rad/s, before rotating in the direction of the degree of freedom  $q_1$ . The extra dummy element will be added and becomes element 1. The original first element will therefore become element 2 etc. This way the energy matrix will become a  $5 \times 5$  matrix for the 4 degrees of freedom system in figure 5.3. Only in those parts of the calculations where  $\{\underline{\dot{q}}\}$  is solved, the matrix must be reduced to a  $4 \times 4$  matrix in the manner shown in equation 5.35. By solving this equation for  $\{\underline{\dot{q}}\}$  the angular velocities of the generalised coordinates can be found. For controlled rotations that are not before the first D.O.F., similar equations can be derived.

Another option is to let the rotational velocity be a function of one or more other rotational velocities. A good example of this would be the rotational velocity of the generator that is equal to the velocity of the shaft times the gear ratio. When the generator must be added, the equations to calculate the velocity change differently from the case discussed above, because the controlled velocity is not yet known. It has to be calculated at the same time as all other velocities. The matrix  $[A]$  must be changed. The row at the position of the generator will change into a row that corresponds to the equation that couples the velocity of the generator to the velocity of the shaft:

$$0 = \dot{q}_{shaft} * N_{gear} - \dot{q}_{gen} \quad (5.36)$$

For example, the matrix for a wind turbine with one tower element (1), a generator (2), a shaft (3) and two blade elements (4,5) will become:

$$\begin{aligned} \begin{Bmatrix} p_1 \\ p_2 \\ p_3 \\ p_4 \\ p_5 \end{Bmatrix} &= \begin{bmatrix} A_{11} & A_{12} & A_{13} & A_{14} & A_{15} \\ A_{12} & A_{22} & A_{23} & A_{24} & A_{25} \\ A_{13} & A_{23} & A_{33} & A_{34} & A_{35} \\ A_{14} & A_{24} & A_{34} & A_{44} & A_{45} \\ A_{15} & A_{25} & A_{35} & A_{45} & A_{55} \end{bmatrix} \begin{Bmatrix} \dot{q}_1 \\ \dot{q}_2 \\ \dot{q}_3 \\ \dot{q}_4 \\ \dot{q}_5 \end{Bmatrix} \Rightarrow \\ &\begin{Bmatrix} p_1 \\ 0 \\ p_3 \\ p_4 \\ p_5 \end{Bmatrix} = \begin{bmatrix} A_{11} & A_{12} & A_{13} & A_{14} & A_{15} \\ 0 & -1 & N & 0 & 0 \\ A_{13} & A_{23} & A_{33} & A_{34} & A_{35} \\ A_{14} & A_{24} & A_{34} & A_{44} & A_{45} \\ A_{15} & A_{25} & A_{35} & A_{45} & A_{55} \end{bmatrix} \begin{Bmatrix} \dot{q}_1 \\ \dot{q}_2 \\ \dot{q}_3 \\ \dot{q}_4 \\ \dot{q}_5 \end{Bmatrix} \end{aligned} \quad (5.37)$$

which can be solved to find the velocities. This way the inertia of the generator will be taken into account correctly.

## 5.4 Generalised Forces

One of the terms in equation 5.7 is the generalised force due to nonconservative forces. For wind turbines and helicopters the aerodynamics acting on the blades must be taken into account as generalised forces. If there are dampers present, the corresponding damping forces must also be included as generalised forces. All these generalised forces can also be calculated automatically, deriving the equations by hand is not necessary. The calculations needed for the aerodynamic forces are described next, followed by the calculation for damping. Finally it is also possible to include the torque of the generator, as calculated by some external programme, as a generalised force instead of using a constant rotational speed  $\Omega$ . This option is discussed last in this section.

### 5.4.1 Automated Calculation of the Generalised Forces due to Aerodynamics

Using the method described in this chapter, it is possible to create a programme that will fully automatically calculate the generalised forces due to aerodynamics. Using the blade element momentum method (see section 3.1), and specifying which elements generate lift and drag according to given lift-, drag- and moment coefficient curves, the forces can be determined.

Assuming the lifting line theory (see chapter 3), the lift- and drag forces as well as the aerodynamic moment about the aerodynamic centre can be determined. The lift- and drag forces acting on a small part of the blade can be calculated using the following equations:

$$dL = \frac{1}{2}\rho V^2 c_l c dx \quad (5.38)$$

$$dD = \frac{1}{2}\rho V^2 c_d c dx \quad (5.39)$$

In these equations  $V$  is the total velocity (neglecting the component in the direction of the local  $z$  axis) at the small blade element and  $c$  is the chord in that same point. The lift  $dL$  is the aerodynamic force perpendicular to the total velocity at the cross section, the drag  $dD$  is in the direction of the velocity as shown in figure 5.4. The moment about the quarter chord point can be calculated as follows:

$$dM = \frac{1}{2}\rho V^2 c_m c dx^2 \quad (5.40)$$

For every part of every element these forces and moments can be determined once the lift-drag- and moment coefficients and the local velocities are known. The coefficients depend on the angle of attack, which in turn depends on the direction of the local velocity of the air.

To calculate the velocity of the air relative to the blade at every cross-section, first the velocities at the two hinges (one connecting the rigid body element to the element in front of it and one connecting to the one behind it) must be determined. As one element is a rigid body, the velocity of the *structure* can then be calculated at every point along the radius within this element by linear interpolation between these two hinges.

The velocities of the structure are easily calculated, as the partial derivatives  $\frac{\partial \mathbf{v}_{h_j}}{\partial \dot{q}_i}$  have already been determined during the calculation of the energy matrix (see equations 5.19, 5.20 and 5.21). The velocities at the hinge of an element can then be calculated as follows:

$$\mathbf{v}_{h_j} = \sum_{i=1}^j \frac{\partial \mathbf{v}_{h_j}}{\partial \dot{q}_i} \dot{q}_i = (v_{x_{h_j}}, v_{y_{h_j}}, v_{z_{h_j}}) \{\underline{\mathbf{E}}_j\} \quad (5.41)$$

Equation 5.41 can be used because there is no constant term in the velocity, every term depends on  $\dot{q}_i$ , where  $\{\underline{\dot{q}}\}$  contains time derivatives of the generalised coordinates as well as those of controlled rotations. The summation in equation 5.41 goes up to  $j$ , because all other elements will be located behind element  $j$  or on another branch, therefore  $\frac{\partial \mathbf{v}_{h_j}}{\partial \dot{q}_i} = 0$  for  $i > j$ .

To determine the velocity at the root of the element  $\mathbf{v}_{st_j}$ , the velocity of the hinge of the previous element  $\mathbf{v}_{h_{prior(j)}}$  can be used and transformed to the local reference frame:

$$\mathbf{v}_{st_j} = (v_{x_{h_{prior(j)}}}, v_{y_{h_{prior(j)}}}, v_{z_{h_{prior(j)}}}) [R_j]^T \{\underline{\mathbf{E}}_j\} \quad (5.42)$$

Equations 5.41 and 5.42 give the velocities at both hinges of element  $j$  in the local reference frame  $\{\underline{\mathbf{E}}_j\}$ .

The velocities at every point between the two hinges of element  $j$  are now known. Linear interpolation between these two points will result in the exact velocity in a point on this line. This is not the velocity of the air relative to the aerofoil. The effect of wind and induced velocity have not yet been taken into account. The local velocity of the air at the rotor swept area will be (see section 3.1.1):

$$U_d = (1 - a)U_\infty \quad (5.43)$$

This velocity must be added to the negative of the velocity of the structure. Therefore the wind velocity must be transformed to the local reference frames of all elements.

$$\begin{aligned} \mathbf{U}_d &= (U_{x_0}, U_{y_0}, U_{z_0}) \{\underline{\mathbf{E}}_0\} = (U_{x_0}, U_{y_0}, U_{z_0}) [R_1]^T \{\underline{\mathbf{E}}_1\} \\ &= (U_{x_0}, U_{y_0}, U_{z_0}) [R_1]^T \dots [R_N]^T \{\underline{\mathbf{E}}_N\} \end{aligned} \quad (5.44)$$

The velocity of the air relative to the aerofoil therefore becomes:

$$\mathbf{V} = \left[ -\frac{\mathbf{v}_{h_j} - \mathbf{v}_{st_j}}{l_{rb}} \cdot (x - x_{0_j}) - \mathbf{v}_{st_j} \right] + \mathbf{U}_d \quad (5.45)$$

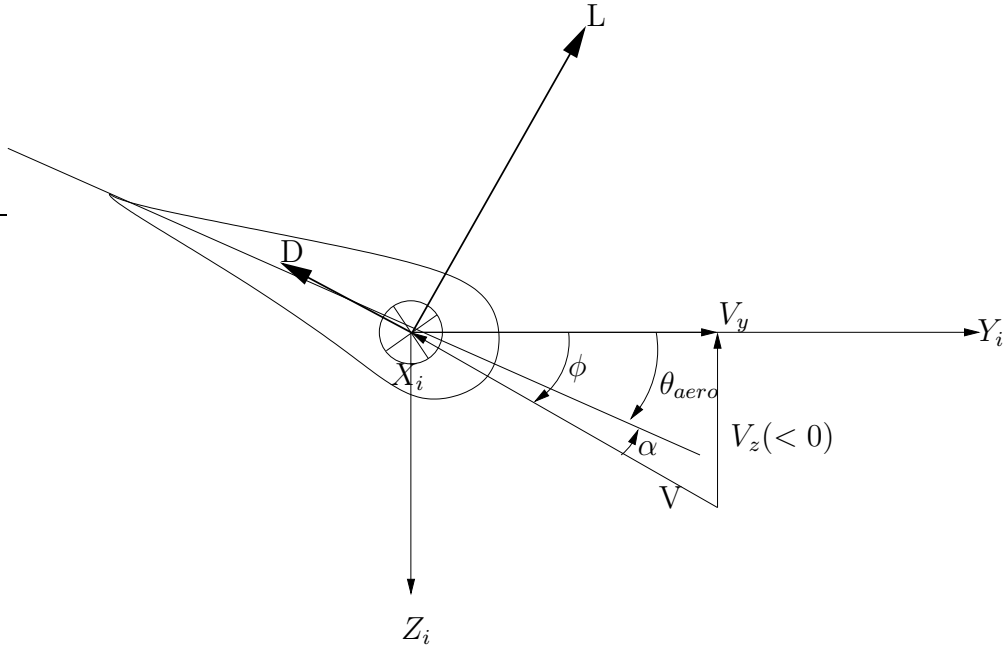


Figure 5.4: Definition of the angles in the local flow.

where  $l_{rb}$  is the length of the rigid body,  $x$  the radial distance from the rotor centre and  $x_0$  the radial distance of the root of the element till the rotor centre.

Once the velocity is known, the angle of attack  $\alpha$  can be calculated, see figure 5.4:

$$\alpha = \phi - \theta_{aero} \quad (5.46)$$

Where  $\phi$  is the angle between the projection of the velocity vector on the local  $yz$ -plane and the  $y$  axis of the **local** reference frame, as shown in the figure. The twist of the chord, relative to the local reference frame, is given as  $\theta_{aero}$ .

The generalised forces must be calculated by determining the work done by the aerodynamic forces and moments for a small deformation  $\delta \mathbf{q}_i$  and dividing this work by the magnitude of this small deformation:

$$Q_i = \frac{\delta W}{\|\delta \mathbf{q}_i\|} \quad (5.47)$$

The work done by the aerodynamic forces can be determined by calculating the moments about the hinge (for every hinge) or by using:

$$dQ_i = \mathbf{dF}_{aero j} \frac{\partial \mathbf{r}_j}{\partial q_i} = \mathbf{dF}_{aero j} \frac{\partial \mathbf{v}_j}{\partial \dot{q}_i} \quad (5.48)$$

and

$$dQ_i = \mathbf{dM}_{ac j} \frac{\partial \mathbf{q}_j}{\partial q_i} = \mathbf{dM}_{ac j} \frac{\partial \boldsymbol{\omega}_j}{\partial \dot{q}_i} \quad (5.49)$$

It is possible to include the effect of the induced velocity. The total axial force acting on the wind turbine or on each annulus can be determined when the aerodynamic forces are known. From this the induced velocity can be calculated, as described in 3.1. The influence of the aerodynamic forces on the induced velocity and vice versa result in the necessity of an iteration to find the correct induced velocity and aerodynamic forces. However, it is possible to prevent this iteration by using a dynamic inflow model, as discussed in 3.1.7.

### 5.4.2 Structural Damping

Next to the aerodynamic forces that usually result in damping there is another form of damping called structural damping. The structure will resist the rate of strain. The damping can be inserted as an extra term in the generalised forces. The most simple form would be:

$$Q_i = Q_{i-aero} - c\dot{q}_i \quad (5.50)$$

In this equation  $c$  is the damping coefficient due to structural damping. However the structural damping is usually given as a fraction of the critical damping (see appendix C) and therefore for each eigenfrequency. For higher frequencies the structural damping will become much higher than for the low frequencies. Including the structural damping into the generalised forces necessitates further analysis to find the values of  $c$  for the different generalised coordinates. This is rather complicated as the generalised coordinates do not directly correspond to the different mode shapes. Including structural damping in a linear code is less complex, for the nonlinear code it might be more practical to add the structural damping to the damping that is found by post-processing the resulting time series for simulations without structural damping. For example, if a damping of 10 % has been found for one mode and the structural damping is known to be 3 %, assuming the total damping to be 13 % is a realistic conclusion.

### 5.4.3 Generator Control

When using the method described in this chapter to simulate wind turbines, it is also possible to include a generator in the model. The torque that is created by the generator must be subtracted from the generalised force about the degree of freedom that models the rotational degree of freedom of the wind turbine axis. So instead of using a controlled rotation to simulate the constant rotational velocity, it is possible to model the rotation as a degree of freedom that is controlled by a generator through the generalised force. The torque from the generator is a non-conservative internal force. Therefore the other generalised forces will not be corrected, only the one corresponding to the ' $\Omega$ '-degree of freedom. For all other generalised coordinates that are before the generator, the reaction torque (opposed to the generator torque) will cancel the contribution of the generator torque to the generalised forces.

---

The method described in this chapter has been used to create a tool called WOBBE. This tool is described in detail in the next chapter.



## Chapter 6

# WOBBE; a Nonlinear Rigid Body Simulation Tool

*"An author is a fool who, not content with boring those he lives with, insists on boring future generations."*<sup>1</sup>

- Charles de Montesquieu

The theory described in the previous chapter has been used to develop a simulation tool called WOBBE. It is programmed in FORTRAN 77/Fortran 90. The tool uses the method described in the previous chapter and performs fully nonlinear time simulations of rigid body models representing wind turbines or helicopters. The dynamics and aerodynamics are calculated automatically.

This chapter will give a general overview of the structure of WOBBE using flow diagrams of the programme as well as short explanations of the calculations performed in the different subroutines. The first section describes the general composition of the programme, clarifying which calculations are performed in which part of the programme. The second section shortly describes every subroutine or function separately. For the more important subroutines, detailed descriptions of the calculations performed in these subroutines as well as flow diagrams are given in appendix F.

---

<sup>1</sup>"The passion of most of the French is to be taken for wits, and the passion of those who would be thought wits, is to write books. And yet there is nothing so badly imagined: nature seems to have provided, that the follies of men should be transient, but they by writing books render them permanent. A fool ought to content himself with having wearied those who lived with him: but he is for tormenting future generations; he is desirous that his folly should triumph over oblivion, which he ought to have enjoyed as well as his grave; he is desirous that posterity should be informed that he lived, and that it should be known for ever that he was a fool." Taken from: Charles Louis de Secondat, Baron de Montesquieu, The Complete Works of M. de Montesquieu (London: T. Evans, 1777), 4 vols. Vol. 3. Chapter: LETTER LXVI.: Rica to \* \* \*.

## 6.1 General Overview

This section describes in general which subroutine is called when and which part of the calculations are performed in the subroutine. However, the basic linear algebra routines that perform multiplications of matrices etc. are not mentioned in this summary. The subroutines in WOBBE are described in slightly more detail in the next section for every subroutine separately and for the important subroutines a detailed description and flow diagram can be found in appendix F.

Recall that the method described in chapter 5 uses the generalised momenta  $p_i = \frac{\partial T}{\partial \dot{q}_i}$  and the generalised coordinates  $q_i$  as the state variables. The time derivatives of the state variables can be calculated using equation 5.5:

$$\{\dot{q}\} = [A]^{-1}\{p\}$$

where  $[A]$  is the energy or mass matrix and equation 5.7:

$$\dot{p}_i = \frac{\partial T}{\partial q_i} - \frac{\partial V}{\partial q_i} + Q_i$$

Once the energy or mass matrix  $[A]$  is determined, the time derivatives of the generalised coordinates can be calculated. Once these derivatives are known, the second equation can be used to determine the time derivatives of the generalised momenta. The details of this method have been discussed in the previous chapter.

Figure 6.1 shows a general overview of all important subroutines and the main results provided by each subroutine. It also shows how these results are used to run the simulation. The flow diagram does not show the details of the calculation of the aerodynamic forces, it only shows subroutine FRCAIR. A more detailed description of this calculation is shown in figure 6.2. This figure illustrates which subroutines are called in order to calculate the aerodynamic forces.

As shown in figure 6.1, a run with WOBBE starts in the main programme, called WOBBER. The first subroutine that is called is the INITL-subroutine where the default values of variables are calculated after which the input file is read. The input file is a so-called 'namelist' in FORTRAN. This means that the input can be changed without the need of recompiling the programme. The input file gives the masses, inertias and size of the different elements, all in local reference frames. It also specifies the spring stiffnesses, the directions of the degrees of freedom and the springs as well as the aerodynamic properties of the blade (chord, pitch angles, thickness, aerofoils). The input file will also contain variables that will tell the programme whether or not to use Prandtl's tip correction, dynamic stall and/or dynamic inflow. The initial conditions must also be given in the input file, this means that the values of the generalised coordinates and their time derivatives should be given in the namelist. When there are controlled rotations in the model, these are also given in the namelist, with the values for mass, inertia length and velocity. In that case the dummy elements are added in the INITL subroutine, as described in section 5.3.2.

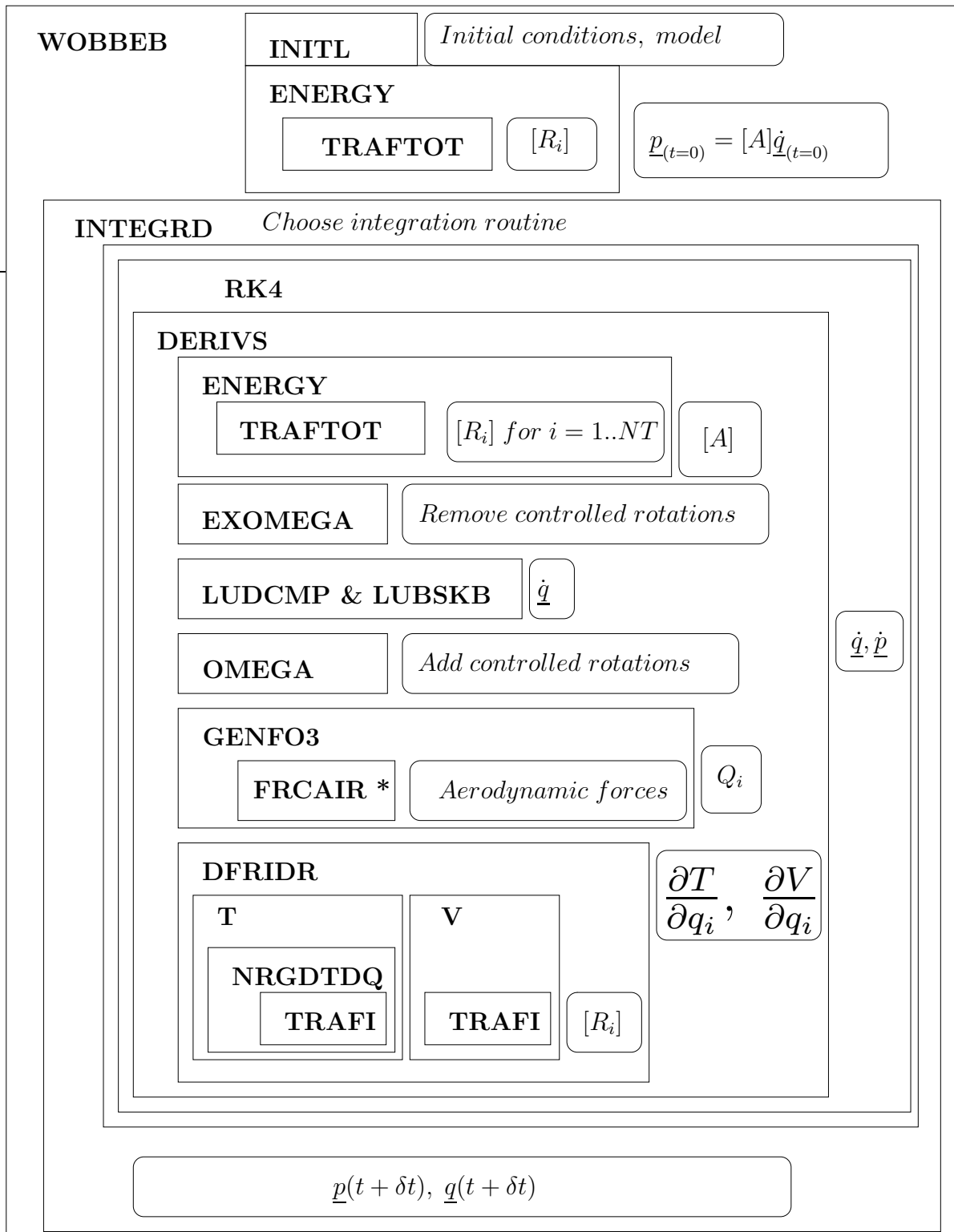


Figure 6.1: A flow diagram with the names of the subroutines in WOBBE. The part indicated with \* includes other subroutine calls.

After setting up the model in INITL, the programme will call the subroutine ENERGY. The energy matrix for  $t = 0$  is calculated and used to determine the generalised momenta at this time:  $\{\underline{p}_{(t=0)}\}$ :

$$\{\underline{p}_{(t=\tau_0)}\} = [A_{(t=\tau_0)}]\{\underline{\dot{q}}_{(t=\tau_0)}\} \quad (6.1)$$

In order to calculate the energy or mass matrix  $[A]$ , it is necessary to determine all rotation transformation matrices. Therefore in ENERGY the subroutine TRAFOT is called. This routine will calculate all rotation transformation matrices  $[R_i]$ .

Once the generalised momenta  $\{p\}$  at  $t = 0$  are known, the calculation of the time derivatives of the generalised momenta as well as of the generalised coordinates is the next step to be taken. The choice of the integration routine determines the calculations needed to calculate the derivatives. When using Runge-Kutta's fourth order only the time derivatives are calculated, whereas when using one of the implicit routines, the Jacobian must also be calculated. The integration subroutine is chosen in the INTEGRD subroutine, based on the input provided by the user. The different integration options all have different subroutines that are called from INTEGRD. But all integration routines use the the same subroutines either DERIVS or DERIVSN to calculate  $\{\underline{\dot{q}}\}$  and  $\{\underline{\dot{p}}\}$ . There are very few differences between these two routines, DERIVSN was written only because the IMSL implicit integration subroutine DIVPAG needs a slightly different setup of this subroutine.

In DERIVS(N), the time derivatives are calculated at every time step using equations 5.5 and 5.7:

$$\{\underline{\dot{q}}\} = [A]^{-1}\{p\}$$

and

$$\dot{p}_i = \frac{\partial T}{\partial q_i} - \frac{\partial V}{\partial q_i} + Q_i$$

First  $\{\underline{\dot{q}}\}$  must be calculated using equation 5.5, because this result is needed before it is possible to calculate  $\{\underline{\dot{p}}\}$ . In order to determine  $\{\underline{\dot{q}}\}$ , the energy matrix  $[A]$  must be calculated using the subroutine ENERGY. In this subroutine all rotation transformation matrices need to be calculated by TRAFOT.

Once the energy matrix is known, the LU-decomposition is determined using LUDCMP and the values for  $\{\underline{\dot{q}}\}$  are calculated using LUBSKB. The LU decomposition is basically a modified form of Gaussian elimination.

However, if there are any controlled rotations in the system, the corresponding known velocities must first be removed from equation 5.5, as described in section 5.3.2. The energy matrix must be reduced, the known velocities taken out of the column of velocities and the generalised momenta must be corrected by deducting the terms that contain the known velocities. These actions are performed in the subroutine EXOMEGA, before the LU-decomposition takes place. The LU-decomposition will then be performed on this reduced energy matrix.

If the model includes controlled rotational velocities, these must be appended to the calculated velocities  $\{\underline{\dot{q}}\}$  once these are known. All velocities, the calculated and the controlled velocities, have to be taken into account for the calculation of the kinetic energy as well as the generalised forces. The subroutine OMEGA will append the velocities of the controlled elements to the column of velocities. This column can then be used for the calculation of the generalised forces using the subroutine GENFO3.

The GENFO3 subroutine first calls FRCAIR for every rigid body that generates aerodynamic forces. In FRCAIR the aerodynamic forces and moments acting on one element are determined. Once these aerodynamic forces are known, the generalised forces are determined using the method described in 5.4.1. The very first time during a simulation that the generalised forces are calculated, an iteration will take place to calculate the induced velocity, as described in 5.4.1.

When the generalised forces are known in DERIVS(N), the next step that is taken in the programme is to calculate the derivatives  $\frac{\partial T}{\partial q_i}$  and  $\frac{\partial V}{\partial q_i}$ . For both derivatives a subroutine called DFRIDR is used combined with the function T or the function V respectively. The derivatives are calculated by determining the kinetic or potential energy for one slightly higher value for  $q_i$  and one slightly lower value, keeping all values for  $\{\underline{\dot{q}}\}$  constant, and this is repeated for all degrees of freedom.

As described in more detail in appendix G, it is possible to reduce the number of calculations by only calculating the changed parts of the kinetic energy. Many terms that are used in the calculation of the kinetic energy will remain the same for different values of  $q_i$  and do not need to be calculated. The subroutine NRGDTDQ takes this into account and thereby reduces the calculation time drastically. Within this routine, only the changed rotation transformation matrix is calculated using TRAFI. The unchanged rotation transformation matrices are called from memory. The output of NRGDTDQ is only that part of the kinetic energy that has changed due to the change in  $q_i$ .

The potential energy is due to the spring energy and, when included, gravitational energy. The spring energy in spring  $i$  is the only one that will depend on  $q_i$ , therefore only this is part of the elastic energy is calculated. The potential energy due to the gravitational forces is determined numerically by changing the values of  $q_i$ . Here the calculation is again limited to the calculation to those parts of the energy that actually changes due to a different value of  $q_i$ .

Now all terms needed to solve equation 5.7 are known. This means that both the derivatives of the generalised momenta as the derivatives of the generalised coordinates are determined and these can be integrated. The calculation will then continue by going through the same process but with new values for  $\{\underline{q}\}$  and  $\{\underline{p}\}$  in the chosen integration routine. If the integration is complete over one time step (e.g. after the four steps taken in RK4), the simulation will return to the main part of the programme and the results are stored in the output files. As long as the end time of the simulation has not been reached, the programme will go back into the loop through INTEGRD.

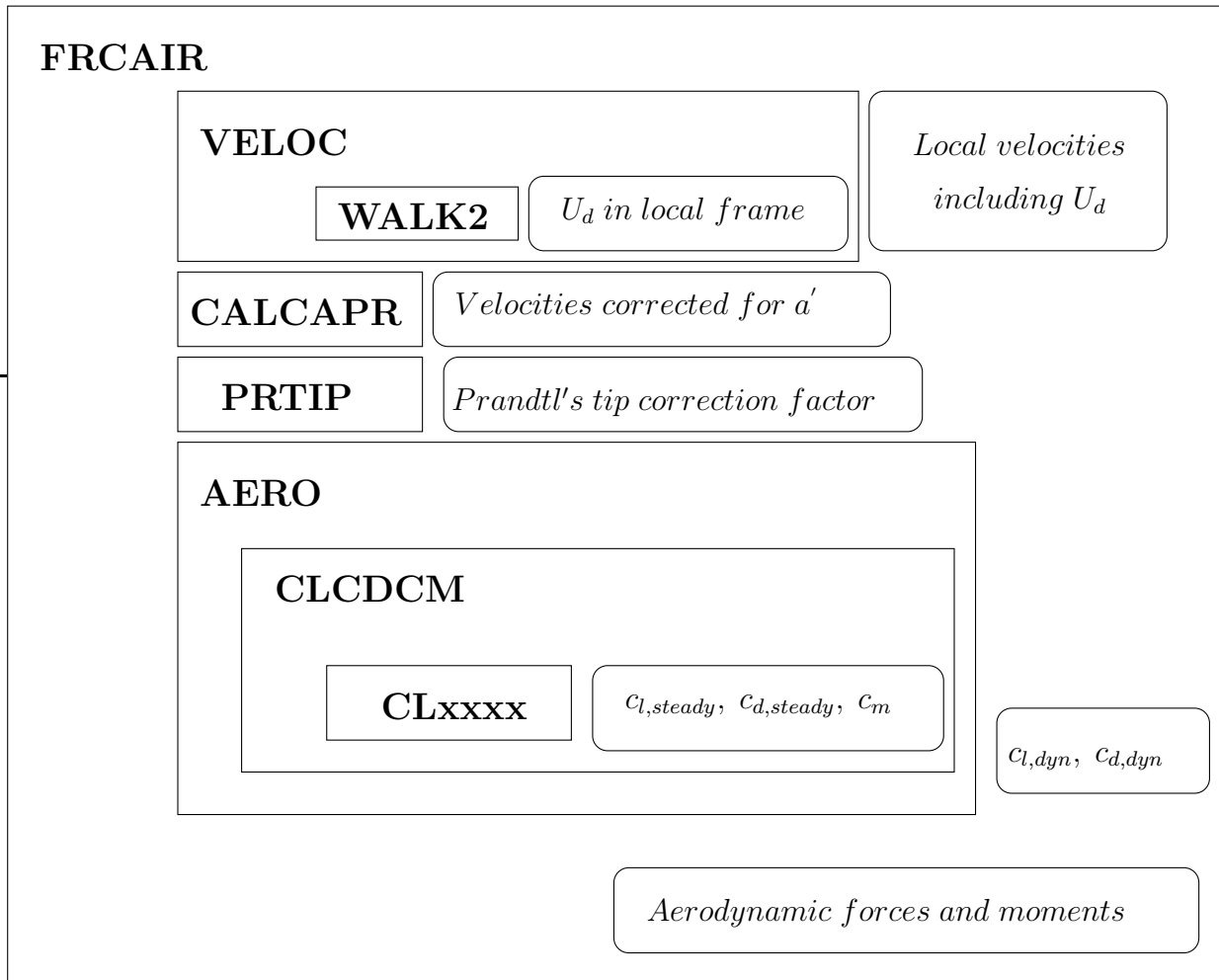


Figure 6.2: A flow diagram of the FRCAIR subroutine and the subroutines it calls to calculate the aerodynamic forces.

So far the details of the calculations of the aerodynamic forces have not yet been discussed. Figure 6.2 shows the subroutines that are called from FRCAIR in order to calculate the aerodynamic forces. The first step is to calculate the velocity of the structure at the beginning and end of the rigid body. The subroutine VELOC determines the velocity using the equations 5.41 and 5.42. The local wind velocity  $U_a$  is added to the negative of the velocity of the structure using the WALK2 subroutine that will transform the components of the wind velocity to the local reference frame. VELOC then returns this resulting velocity in the local reference frame. Using CALCAPR, this velocity is corrected for the tangential induced velocity. When applicable, Prandtl's tip correction is calculated using PRTIP.

Once the angle of attack has been calculated, the subroutine AERO is called. This subroutine will calculate the (dynamic) lift-, drag- and moment coefficients. First the steady coefficients must be determined. Therefore it will first call the subroutine CLCDCM. This subroutine

is linked to all available lift-, drag- and moment-curves, stored in subroutines CLxxxx. For the calculated angle of attack the corresponding coefficients are given. With this the forces and moments can be calculated in FRCAIR.

The general overview is now described, it is illustrated where all the subroutines fit in the overall programme. The next section gives short descriptions of every subroutine or function.

## 6.2 Subroutines and Functions

WOBBE contains many subroutines and two functions. Short descriptions of the different subroutines/functions are given in this section. For every subroutine or function the name of the file in which the subroutine is stored is also given in the title. It is stated behind the name of the subroutine. For some subroutines flow diagrams are given in appendix F.

### 6.2.1 WOBEB, branch.f

The file branch.f contains the main programme WOBEB. The B has been added at the end of the name to show it is able to handle branched systems [103]. In this file the simulation starts. This file is also where the instructions are given to store the results in the output file and the programme finishes here, as shown in figure F.1.

Entering this main file, the first thing that happens is calling the subroutine INITL. As described in 6.2.2, this subroutine will read the input and do all initial calculations and create the actual model within WOBBE. The generalised coordinates and their velocities at the start of the simulation are given in the input file and therefore are known after returning from the INITL subroutine. Next, the main programme will call the subroutine ENERGY (see section 6.2.5) to determine the energy or mass matrix  $[A]$ . This matrix is needed to calculate the starting values of the generalised momenta  $\{\underline{p}\}$ . Note that these are not known at the first time step, because the generalised coordinates  $\{\underline{q}\}$  and their time derivatives  $\{\underline{\dot{q}}\}$  are given as starting conditions in the input, not the generalised momenta  $\{\underline{p}\}$ . For all other time steps the generalised momenta are state variables determined by integration while the angular velocities  $\{\underline{\dot{q}}\}$  are unknowns that need to be determined.

The subroutine ENERGY will give the energy matrix  $[A]$ . Multiplication of this matrix with the rotational velocities results in the generalised momenta at the first time step.

$$\{p_{(t=T_0)}\} = [A_{(t=T_0)}]\{\underline{\dot{q}}_{(t=T_0)}\} \quad (6.2)$$

After these initial calculations, this main file opens all output files. The user can determine in the input which output to be stored and in which file. Depending on the input these include files to store

- the generalised coordinates

- the time derivatives of the generalised coordinates
- the power, the thrust coefficient, the induction factor and its time derivative
- the angles of attack
- the positions of the hinges relative to a chosen reference point and a chosen reference frame
- a restart file with variables needed to start a subsequent simulation

At each time step the calculation will return to this main file of the programme. The user can specify how often the results should be stored (e.g. every 5 time steps or every time step) and which results ( $q_1 \dots q_N$ ,  $\dot{q}_i$ ,  $a$ ,  $\dot{a}$ ,  $C_T$ ,  $P$ , ...). Therefore, if the user has specified the results to be saved at the current time step, then all desired results are stored. Otherwise the programme will go on with the calculation without storing the results in an output file. There is one exception, the output to the file with the time derivatives of the generalised coordinates is not stored from the main file, but in the file that calculates the derivatives (DERIVS or DERIVSN, see 6.2.10). A trigger is set in the main file to store only those values that the user wants. This trigger is taken to DERIVS(N) using a common block.

In order to reduce the time it takes to run a simulation, the results that must be stored in the output file are first stored in a matrix for every 100 steps and then all these steps are written to the output file in one go. This way the time spent in opening and closing the output files is reduced, which gives a small reduction of the total time needed to run a simulation. This reduction depends mainly on the hardware that is used to run the simulation.

To perform the integration, the subroutine INTGRD is called from the main programme where the different calls to different integration routines are given. The calculation will return to the main part of the programme once the new values of the generalised coordinates and the generalised momenta have been calculated.

More information and a flow diagram are shown in appendix F.2.1.

## 6.2.2 INITL, initl3.f

INITL is the first subroutine that is called from the main file WOBBEB. INITL's flow diagram is shown in figure F.2.

First the default settings are loaded, most variables will get a default value. To run a simulation, WOBBE of course needs an input model. The model is given in a so-called namelist [20]. After setting the default values, the input data is read from the namelist overwriting the default values. Then the output files are opened. If there are any controlled rotations in the model, the corresponding dummy elements are added to the model. As described in section 5.3.2, the elements behind the controlled rotation need to be renumbered, the numbers given by the user in the input file do not yet include extra numbers for the dummy

elements with controlled rotations. The method used for this renumbering is illustrated in the flow diagram in figure F.2. The dummy elements corresponding to the controlled rotations can have length, inertia, mass etc. if this is defined in the input. All properties are sorted according to the new numbers and the properties of the dummy elements are added to the model.

The INITL subroutine also performs many calculations that need to be performed only once during a simulation. This means i.a. the rotation transformation matrices of the fixed angles and the rotor swept area.

More details are given in appendix app:initl.

### 6.2.3 VECMAT, vecmat.f

This subroutine determines the operator matrices of the vectors given in the input. The operator matrices can be used to calculate the cross-products (see also 2.1.2):

$$\mathbf{a} \times \mathbf{xyz}_{\text{input}} = (a_x, a_y, a_z)\{\underline{\mathbf{E}}_i\} \times (x, y, z)\{\underline{\mathbf{E}}_i\} = \begin{bmatrix} 0 & z & -y \\ -z & 0 & x \\ y & -x & 0 \end{bmatrix} (a_x, a_y, a_z)\{\underline{\mathbf{E}}_i\} \quad (6.3)$$

Within one model in WOBBE there usually are several degrees of freedom and just as many rigid bodies. For every rigid body the local vector from the hinge that connects it to the previous body to the hinge connection with the following body is translated into an operator matrix. These operator matrices are stored in a three dimensional array.

### 6.2.4 DIRECT, direct.f

This subroutine sets up the unit vector that corresponds to the local axis about which the hinge is situated. The axis is indicated using a direction number which is given as input by the user. The variable DOFDIR is used for this direction definition: DOFDIR = 1 denotes a degree of freedom about the  $x$ -axis, DOFDIR = 2 about the  $y$ -axis and DOFDIR = 3 about the  $Z$ -axis. The corresponding direction vectors become:  $(1, 0, 0)\{\underline{\mathbf{E}}_i\}$ ,  $(0, 1, 0)\{\underline{\mathbf{E}}_i\}$  and  $(0, 0, 1)\{\underline{\mathbf{E}}_i\}$  respectively.

This subroutine is called for every degree of freedom from the INITL subroutine. In the INITL subroutine the resulting rows DIRECT are stored in an array DIRVEC.

### 6.2.5 ENERGY, energy.f

The subroutine ENERGY calculates the energy- or mass matrix  $[A]$ . Its flow diagram is shown in figure F.3 and the subroutine is described in more detail in the appendix F.2.3. This subroutine is only used when necessary: in many parts of the programme it is possible

to reduce the number of calculations, because large parts of the matrix have already been calculated and remain unchanged. To be more specific, this is the case when calculating the kinetic energy to find  $\frac{\partial T}{\partial q_i}$  and when doing calculations to determine the Jacobian matrix. In those cases another subroutine is used: NRGDTDQ, see section 6.2.11

If a new time step has been reached, the subroutine ENERGY must be used to determine the new energy matrix. As described in section 6.2.1, when the programme has just started a simulation, the energy matrix must be determined in order to calculate the generalised momenta for the starting time.

The energy matrix  $[A]$  is calculated using the equations given in section 5.2.1. First the routine will determine the rotation transformation matrices for the complete system. For this the subroutine TRAFTOT is called. Then the different components of the energy matrix can be calculated as illustrated in the flow diagram (figure F.3) and described in F.2.3.

### 6.2.6 TRAFI, trafin.f, TRAFTOT, traftot.f

The subroutines TRAFI and TRAFTOT determine the different rotation transformation matrices. The flow diagram for TRAFTOT is shown in figure F.4. The subroutine TRAFI determines one rotation transformation matrix, while the subroutine TRAFTOT determines all rotation transformation matrices corresponding to degrees of freedom and the controlled rotations at once.

When the calculation for a new time step begins, the values of all rotation transformation matrices can be changed, therefore they must all be recalculated. During the calculation of  $\frac{\partial T}{\partial q_i}$ ,  $\frac{\partial V}{\partial q_i}$  and the Jacobian only one degree of freedom will have changed, therefore only this rotation transformation matrix needs to be calculated. All other rotation transformation matrices remain unchanged compared to last performed calculation. In this case the subroutine TRAFI is used.

Because in the majority of the multiplications the transposed matrices are needed, these transposed matrices are the matrices that are calculated. There are three different types of matrices, one for rotations about the  $x$ -axis, one for rotations about the  $y$ -axis and one for rotations about the  $z$ -axis. The rotation transformation matrices are defined as:

$$\{\underline{\mathbf{E}}_i\} = [R_j]^T \{\underline{\mathbf{E}}_j\} \quad (6.4)$$

where  $i$  is the element before element  $j$ . Defining positive angles in the direction of the positive axes, the three different options are depicted in figure 6.3. The rotation transformation matrices that correspond to these three situations are (see section 2.1.2) :

$$\text{about } x \text{ axis: } [R_j] = \begin{bmatrix} 1 & 0 & 0 \\ 0 & \cos q_j & \sin q_j \\ 0 & -\sin q_j & \cos q_j \end{bmatrix} \Rightarrow [R_j]^T = \begin{bmatrix} 1 & 0 & 0 \\ 0 & \cos q_j & -\sin q_j \\ 0 & \sin q_j & \cos q_j \end{bmatrix} \quad (6.5)$$

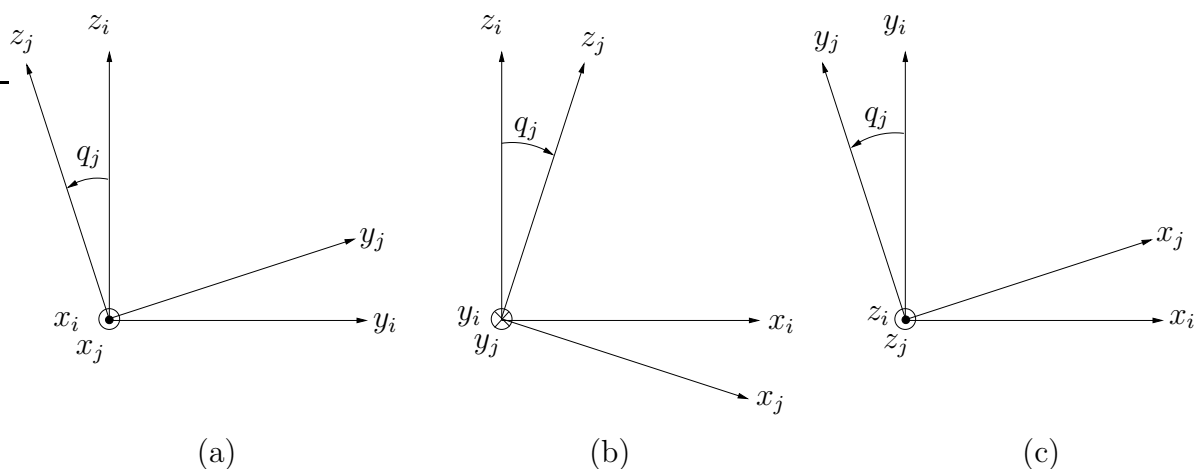


Figure 6.3: Three different rotations that are possible in WOBBE: (a) about the  $x$  axis, (b) about the  $y$  axis and (c) about the  $z$  axis, all showing positive angles.

$$\text{about } y \text{ axis: } [R_j] = \begin{bmatrix} \cos q_j & 0 & -\sin q_j \\ 0 & 1 & 0 \\ \sin q_j & 0 & \cos q_j \end{bmatrix} \Rightarrow [R_j]^T = \begin{bmatrix} \cos q_j & 0 & \sin q_j \\ 0 & 1 & 0 \\ -\sin q_j & 0 & \cos q_j \end{bmatrix} \quad (6.6)$$

$$\text{about } z \text{ axis: } [R_j] = \begin{bmatrix} \cos q_j & \sin q_j & 0 \\ -\sin q_j & \cos q_j & 0 \\ 0 & 0 & 1 \end{bmatrix} \Rightarrow [R_j]^T = \begin{bmatrix} \cos q_j & -\sin q_j & 0 \\ \sin q_j & \cos q_j & 0 \\ 0 & 0 & 1 \end{bmatrix} \quad (6.7)$$

### 6.2.7 TRNSLAT, transl.f

In the subroutine TRNSLAT the positions of the hinges in the model are calculated. This subroutine is only called if the user has specified that the positions are to be given as an output. This can be useful for post-processing of the results.

### 6.2.8 INTGRD, integrd.f

In the subroutine INTGRD the correct subroutine is called for the chosen integration method. Currently several integration methods can be used, i.a. Runge-Kutta fourth order and two implicit integration routines as described in the next section. The integration method determines which integration subroutine is called. Each integration subroutine is only a kind of interface between the main programme and the subroutines that calculate derivatives.

The next section shortly describes the different subroutines that can be called from the INTGRD subroutine.

### 6.2.9 DIVPAG (imsl), RK4 (rk4.f), STIFFX (stiffx.f), SIMPR (simpr.f)

There are 5 subroutines used to perform the integration: DIVPAG, RK4, STIFF, STIFFX and SIMPR. All but one of these routines come from Numerical Recipes [116]. Only DIVPAG comes from the IMSL. Because DIVPAG comes from the IMSL, it is not exactly known which calculations are performed in this subroutine, only the name of the method used is known.

Subroutine RK4 is called when the fourth order Runge-Kutta method with a constant time step is used. The semi-implicit integration routine taken from [116] is used through a call to STIFFX. In the STIFFX routine the Jacobian is first calculated. Then the SIMPR routine will be called. This uses the semi-implicit midpoint rule to perform the integration. When Gear's method is used the IMSL routine DIVPAG is called.

### 6.2.10 DERIVS (derivs2.f), DERIVSN (derivsn.f)

DERIVS and DERIVSN are two subroutines that are very similar. They both calculate the time derivatives of the state variables: the generalised coordinates:  $\{\underline{q}\}$  and the generalised momenta:  $\{\underline{p}\}$ .

DERIVSN is only used when DIVPAG is used as the integration routine. This IMSL subroutine needed another call sign than the original version of this subroutine DERIVS. For this reason some adjustments had to be made which resulted in a new subroutine that is very similar to DERIVS. As the differences are very small, both subroutines are discussed in this section and one flow diagram representing both routines is shown in figure F.5.

Knowing the generalised coordinates, the energy matrix is determined using ENERGY. However if the DERIVS(N) subroutine is called during the calculation of the Jacobian, only those parts of the energy matrix that have changed need to be calculated. In this case another subroutine is used: NRGDTDQ. Both ENERGY and NRGDTDQ will result in the energy matrix  $[A]$ .

If there are one or more controlled rotations present in the model (see section 5.3.2), these must be taken into account. The subroutine EXOMEGA will remove the generalised momenta of the controlled rotation from the column  $\{\underline{p}\}$  and correct the remaining values as described in section 5.3.2. The energy matrix is also reduced in this subroutine by removing the rows and columns corresponding to the controlled rotation(s).

The time derivatives of the generalised coordinates,  $\{\underline{\dot{q}}\}$  are now calculated by solving the equation 5.4:

$$\{\underline{p}\} = [A]\{\underline{\dot{q}}\}$$

for  $\{\underline{\dot{q}}\}$ . This equation is solved by LU-decomposition. The subroutines LUDCMP and LUBKSB are used to perform this calculation.

Once the time derivatives of the generalised coordinates are known, the time derivative of the generalised momenta can be determined using equation 5.7:

$$\dot{p}_i = \frac{\partial T}{\partial q_i} - \frac{\partial V}{\partial q_i} + Q_i$$

The calculated  $\{\dot{q}\}$  does not yet include any controlled rotational velocities, as these were already known and taken out of the equation. For this reason, when present, the controlled velocities are appended to the angular velocity vector using the subroutine OMEGA. The subroutine GENFO3 is then called to determine the generalised forces  $Q(i)$ .

As shown in equation 5.7, the derivatives of the kinetic energy and the potential energy with respect to the generalised coordinates are needed to calculate  $\{\dot{p}\}$ . These derivatives are calculated by numerical differentiation in the subroutine DFRIDR. This originally used Ridder's method [103], but because that resulted in calculations that were extremely slow, it has been turned into an almost empty routine that calls the functions T or V and calculates the derivatives without checking the accuracy of the solution.

Once these derivatives have been calculated all terms are known and  $\{\dot{p}\}$  can be calculated.

### 6.2.11 NRGDTDQ, nrgdtdq.f

The subroutine NRGDTDQ calculates either the kinetic energy or the energy matrix, but only during the calculation of the derivative of the kinetic energy  $\frac{\partial T}{\partial q_i}$  or the Jacobian. In those cases the calculation can be limited to those parts of the mass matrix that have changed. This is described in more detail in appendix G.

The NRGDTDQ subroutine can be called from the part of the programme where  $\frac{\partial T}{\partial q_i}$  is calculated. In this case all results obtained during previous calculations that are still valid are used, but the output of the routine is the new value of that part of the kinetic energy that changes due to the change in  $q_i$ , not the mass or energy matrix  $[A]$ .

When the Jacobian is calculated, the partial derivatives used, have another definition than until now. In Lagrange the partial derivatives with respect to  $q_i$  mean that all other generalised coordinates  $q_j$  and **all** time derivatives  $\dot{q}_l$  remain constant, only  $q_i$  changes. During the calculation of the Jacobian, either  $p_i$  or  $q_i$  is changed and all other values of both  $p_j$  and  $q_j$  remain constant, but their time derivatives will change. This is noted as  $\frac{\partial^{pq}}{\partial q_i}$ . This alternative definition for the partial derivative is **only** used in the calculation of the Jacobian. The Jacobian is discussed in more detail in section 6.2.30. When the call comes from the calculation of the Jacobian, there are two different situations: 1. NRGDTDQ is called to determine the complete mass matrix  $[A]$  in order to calculate the new values of  $\{\dot{q}\}$  to find  $\frac{\partial^{pq} \dot{q}_j}{\partial q_i}$  or 2. to determine the new value of the changed kinetic energy when calculating  $\frac{\partial T}{\partial q_i}$  to find  $\frac{\partial^{pq} \dot{p}_j}{\partial q_i}$ . The output of the subroutine in each of these two cases is different, the mass matrix or the changed energy respectively. The calculation for the complete mass matrix within the calculation of the Jacobian is illustrated in figures F.6 and F.7.

The calculation needed for  $\frac{\partial T}{\partial q_i}$  is similar to the calculation performed in the ENERGY subroutine, only limited to the changed elements of the mass matrix and the corresponding kinetic energy.

### 6.2.12 EXOMEGA, exomega.f

The subroutine EXOMEGA is only called if the model includes one or more controlled rotations. In case of a controlled rotation, the velocity of the corresponding coordinate has a given value or prescribed function of time. Therefore the energy matrix used to calculate  $\{\dot{q}\}$  must be reduced by removing the rows and columns corresponding to this rotation. The generalised momenta must also be corrected as described in 5.3.2. Finally the generalised momentum/momenta that correspond to the controlled rotation(s) must be removed from the column  $\{p\}$ . The calculations performed in this subroutine are illustrated in figure F.8.

### 6.2.13 LUDCMP, ludcmp.f, LUBKSB, ludcmp.f

The subroutines LUDCMP and LUBKSB are used to solve the equation that gives  $\{\dot{q}\}$ . LUDCMP results in the LU decomposition of the energy or mass matrix  $[A]$  and LUBKSB uses the back substitution to find the actual solution. The LU decomposition is basically a modified form of Gaussian elimination. These routines are both standard routines which are taken from numerical recipes in FORTRAN [116].

### 6.2.14 OMEGA, omega.f

As described in section 6.2.10, the rotational velocity  $\{\dot{q}\}$  that has been calculated from the LU decomposition of the energy matrix times the generalised momenta, does not include the controlled rotational velocities. These velocities do influence the kinetic energy as well as the aerodynamic forces, therefore it is important to include these controlled rotational velocities in the column of velocities. Subroutine OMEGA is used for this. It adds the rotational velocities of the dummy elements in the correct places and gives the complete column of velocities as an output.

### 6.2.15 GENFO3, genfo3.f

The generalised forces  $Q_i$  are calculated in the subroutine GENFO3. Its flow diagram can be found in figure F.9 and a more detailed description is given in F.2.8.

The only generalised forces that are currently calculated are due to the aerodynamic forces acting on the blades of wind turbines or helicopters. There is also the possibility to include some kind of structural damping according to equation 5.50, but, as discussed in section

5.4.2, further research is needed into the damping values. At this moment it is not clear how to determine the values that need to be used to model realistic structural damping. For this reason the discussion in this section is limited to the aerodynamic forces. These aerodynamic forces and the aerodynamic moments are calculated in FRCAIR.

The generalised forces can then be determined by taking the sum of the different elements. When the induced velocity has to be taken into account, this is also calculated in this subroutine. The total force in axial direction is used to calculate the induction factor using equation 3.25.

At the start of a simulation the value of the induction factor is not yet known and an iteration process is used to find the value of the induction factor at the start of the simulation. The time derivative of the induction factor as used in the dynamic inflow model is also calculated in this subroutine.

If an external generator model is coupled to the programme, the generalised force due to the generator will also be calculated in this subroutine.

Next to the generalised forces, the power is also calculated in this subroutine. This is not needed for the simulation, but can be a useful output when analysing a wind turbine. The power, induction factor and its time derivative are therefore stored in an output file.

### 6.2.16 FRCAIR, frcair.f

In the subroutine FRCAIR the aerodynamic forces and moments acting on a rigid body element are calculated. It is possible to use different aerodynamic models: a linear  $c_l - \alpha$  relation or  $c_l - \alpha$ -curves for different aerofoils.

Every force-generating rigid body element is divided into subelements. These are used for numerical integration of the aerodynamic forces over one rigid body element.

The VELOC subroutine is used to calculate the local velocities. Then, for every subelement, the aerodynamic force is determined. When the effect of induced velocity is taken into account, the tangential induced velocity is determined using CALCAPR. For this calculation it is necessary to know the distance from the point where the velocity is calculated to the rotating axis in the hub. The subroutine WALKBK is used for this calculation. The induced tangential velocity will be calculated in the rotating reference frame perpendicular and parallel to the shaft. It must be transformed to the local reference frame. Subroutine WALK2 is used for this, resulting in the induced tangential velocity that is expressed in the local reference frame. The angle of attack  $\alpha$  can be calculated. Once  $\alpha$  is known, the lift-, drag- and moment-coefficients are calculated. Depending on the model used, the function LINCL or the subroutine AERO is called. These functions/subroutines will give the coefficients. Knowing the velocity, the coefficients and the representative chord, the forces and moment on the subelement are calculated.

When the effect of Prandtl's tip correction is to be included, the correction factor for the

subelement is determined using CALCAPR (see section 3.1.8).

The calculation of the forces is performed for every subelement resulting in a term related to the total force acting on the element as well as a term related to the bending moment and a term for the aerodynamic moment. These forces and moments on subelements have been multiplied with factors that correlate to the relative position in the rigid body such that the resulting terms can be multiplied with the derivative at the root of the rigid body  $\frac{\partial \mathbf{v}_{st,j}}{\partial \dot{q}_i}$  or at the tip of the rigid body,  $\frac{\partial \mathbf{v}_{hg,j}}{\partial \dot{q}_i}$  to find the generalised moments as described in equation 5.48.

### 6.2.17 VELOC, veloc.f

The subroutine VELOC calculates the local velocity of the air relative to the blade.

First the velocity at which the blade moves due to time derivatives of the generalised coordinates  $\{\dot{q}\}$  is calculated. For this, the partial derivatives of the velocity of the hinges  $\frac{\partial \mathbf{v}_{hgk}}{\partial \dot{q}_j}$  are used. These have already been calculated in either ENERGY or NRGDTDQ.

As described in section 5.4.1 the local velocity can be calculated using equations 5.41 and 5.42. First the sum is taken of the derivatives for the element prior to the element for which the velocity is calculated:

$$\mathbf{v}_{h_{prior}(j)} = \sum_{i=1}^{j-1} \frac{\partial \mathbf{v}_{h_{prior}(j)}}{\partial \dot{q}_i} \dot{q}_i$$

The summation can be done without taking into consideration whether  $i$  is connected to  $prior(j)$  or not, because if there is no connection, the derivative will be zero. Of course this will cost extra calculation time. Once  $\mathbf{v}_{h_{prior}(j)}$  is known, the velocity of the endpoint of the previous element, this is transformed to the local reference frame of element  $j$  and the velocity at the beginning of element  $j$  is then known in its local reference frame. The distance between the hinge point and the point where the velocity should be calculated for the aerodynamic forces, is  $\mathbf{dr}$ . This distance still has to be taken into account. The velocity of this point is:

$$\mathbf{v} = \mathbf{v}_{h_j} + \boldsymbol{\omega}_j \times \mathbf{dr} \quad (6.8)$$

Therefore the rotational velocity of element  $j$  must be calculated first. This can be done similarly to the velocity:

$$\boldsymbol{\omega}_j = \sum_{i=1}^j \frac{\partial \boldsymbol{\omega}_j}{\partial \dot{q}_i} \dot{q}_i \quad (6.9)$$

again using the results already obtained in ENERGY or NRGDTDQ.

When applicable, the wind velocity vector is corrected by the induction factor and added to the negative of the local velocity of the element. Therefore it is first necessary to transform

the (corrected) wind velocity from the inertial reference frame to the local reference frame using WALK2. VELOC returns the velocity of the air relative to the blade element but without the tangential induction factor. This is added later on, because it is not constant along the rigid element.

### 6.2.18 WALKBK, walk.f

This subroutine determines the distance between a point on element  $i$  and the hinge of element  $j$ , given that element  $j$  is somewhere behind element  $i$ . This total distance is given in reference frame  $i$ .

Looking at figure 6.4 the distance between the hinge of element 1 (element  $i$ ) and point A on element 7 (element  $j$ ) can be calculated as follows. First the vector from hinge 7 to point A is transformed to reference frame 5:

$$\mathbf{R}_{7\mathbf{A}_5} = (r_{A_x}, r_{A_y}, r_{A_z})[R_7]\{\underline{\mathbf{E}}_5\} = (r_{A_{x5}}, r_{A_{y5}}, r_{A_{z5}})\{\underline{\mathbf{E}}_5\} \quad (6.10)$$

Then the hinge distance of element 5 is added and the result is transferred to reference frame 2:

$$\mathbf{R}_{5\mathbf{A}_2} = \left( (r_{A_{x5}}, r_{A_{y5}}, r_{A_{z5}}) + (r_{hg_{x5}}, r_{hg_{y5}}, r_{hg_{z5}}) \right) [R_5]\{\underline{\mathbf{E}}_2\} \quad (6.11)$$

This is repeated again, the total sum so far is added to the hinge distance of element 2 and transferred to reference frame 1. Finally the hinge distance of element 1 is added. These are the calculations that are performed by WALKBK.

### 6.2.19 CALCAPR, calcapr.f

CALCAPR calculates the tangential induced velocity according to rotor disc theory (see section 3.1.3). The tangential induced velocity depends on the radial distance, therefore it must be calculated for every subelement within every rigid body that generates lift. It needs the radial position of this subelement, the rotational velocity of the blades  $\Omega$ , the wind velocity as well as the current value of the axial induction factor. The tangential velocity can then be calculated for every subelement.

### 6.2.20 PRTIP, calcapr.f

The PRTIP subroutine calculates the tip correction according to Prandtl's formula (see 3.1.8). The angular velocity  $\Omega$ , the distance from the hinge to subelement, the wind velocity, the induction factor and the number of blades are needed as input into the subroutine. The correction factor is given as output. This subroutine must be called for every subelement separately.

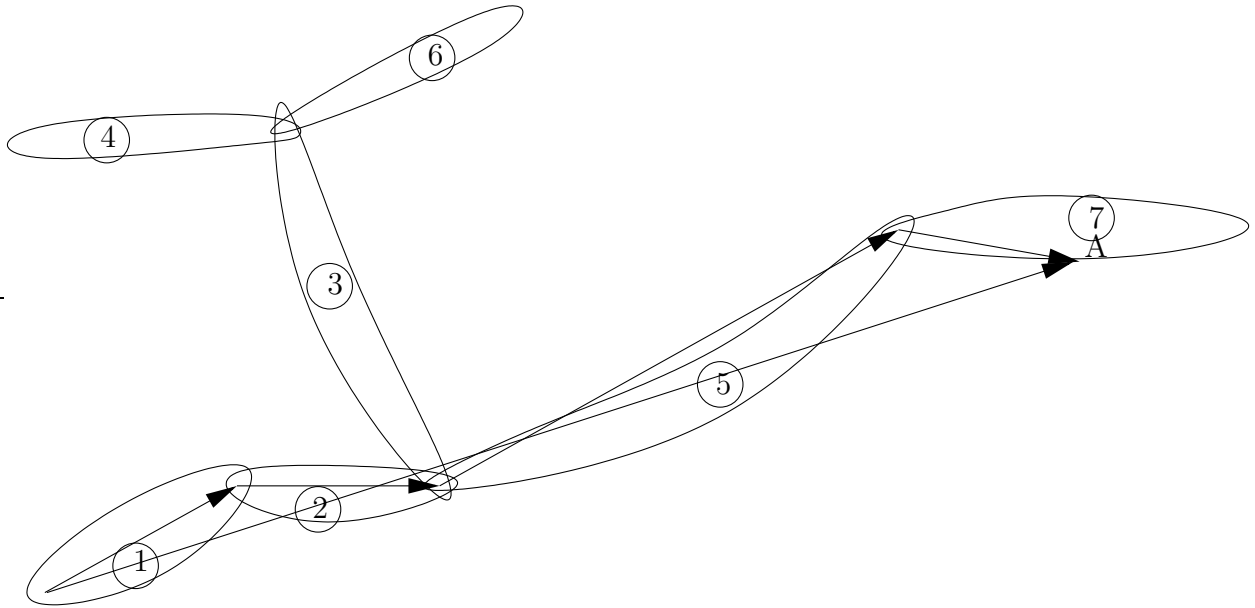


Figure 6.4: An example of the vector that can be calculated by WALKBK

### 6.2.21 WALK2, walk.f

This subroutine is used to transform the vector components from one reference frame to another, when there are an unknown number of matrices needed for this transformation. E.g.

$$(a, b, c)\{\mathbf{E}_i\} = (a, b, c)[R_i][R_{i-1}] \dots [R_j]\{\mathbf{E}_j\} = (d, e, f)\{\mathbf{E}_j\} \quad (6.12)$$

But it is also possible to go in the other direction, using transposed matrices:

$$(a, b, c)\{\mathbf{E}_j\} = (a, b, c)[R_{j+1}]^T[R_{j+2}]^T \dots [R_i]^T\{\mathbf{E}_i\} = (d, e, f)\{\mathbf{E}_i\} \quad (6.13)$$

The output of this subroutine is the vector components transformed to the new reference frame.

### 6.2.22 LINCL, Lincl.f

This function is used in the case the model assumes a constant  $c_{l_\alpha}$ . For the angle of attack  $\alpha$  a lift-coefficient is calculated using:

$$c_l = c_{l_\alpha}(\alpha - \alpha_0) \quad (6.14)$$

where  $\alpha_0$  is the angle of attack for which  $c_l = 0$ .

### 6.2.23 AERO, `aero.f`

The subroutine AERO is used to determine the lift-, drag- and moment-coefficients when the model is not assumed to have only a linear lift-coefficient for which the above described LINCL has been created. When using the AERO subroutine instead, the complete curves can be taken into account, including curves for the drag- and moment-coefficients. The AERO subroutine can calculate these coefficients based on quasi-steady aerodynamics or unsteady aerodynamics. In the latter case it is possible to use a first order model or a second order model of Snel's dynamic stall model [129] as described in 3.1.9 and appendix A. It is also possible to use quasi steady aerodynamics, in which case this subroutine is only used to call the CLCDCM subroutine.

When using unsteady aerodynamics, the results of the lift- drag- and moment- coefficients must be stored for the three most recent time steps, because the time derivatives of these coefficients must be calculated. Therefore subroutine HISTORY will ensure the storage of the three most recent values of the coefficients for every subelement.

The AERO subroutine is based on a subroutine from PHATAS [83], a programme from ECN, the Energy research Centre of the Netherlands. Due to the possibility of varying time steps in WOBBE, the PHATAS subroutine had to be altered to enable the calculation of the time derivatives of the coefficients with varying time steps [49].

The subroutine returns the new values for the dynamic or quasi-steady lift-, drag- and moment- coefficients for the subelement.

### 6.2.24 CLCDCM, `clcdcm.f`

Subroutines containing the lift- drag- and moment- coefficients for several aerofoils for certain Reynolds numbers are included in the program. The CLCDCM subroutine is used to call the subroutine that corresponds to the subelement's aerofoil, e.g. if the subelement is modeled using aerofoil 123, this subroutine will call CL123.

In WOBBE there is also the option to use linear interpolation between different thickness ratios;  $\frac{t}{c}$ . When this is used, the two subroutines corresponding to the two aerofoils between which the interpolation is used, are subsequently called from the CLCDCM subroutine and using linear interpolation the lift-, drag- and moment- coefficients are calculated in this subroutine. This is further illustrated in the flow diagram in figure F.10.

The results of this subroutine are a lift-, drag- and a moment- coefficient for the aerodynamic subelement,  $c_l$ ,  $c_d$  and  $c_m$ .

### 6.2.25 CLxxx, clxxx.f

Several aerofoils for different Reynolds numbers are included in the code. These are all stored in subroutines starting with CL followed by a code for the specific aerofoil, e.g. CL64618 for the NACA 64-618 aerofoil.

Each subroutine is based on a table containing values for the coefficients at different angles of attack. The subroutine will calculate the coefficient for the current angle of attack at the subelement using linear interpolation between the given points.

If a new table with coefficients and angle of attack is available, it is relatively simple to add this to the existing programme. A supporting programme has been created that will translate the table into FORTRAN code which can then be added to the programme. Next to this the properties of the new aerofoil must be added to the INITL subroutine and the call signs have to be added to the CLCDCM subroutine. The code must be recompiled after adding these alterations.

### 6.2.26 HISTORY history.f

The subroutine HISTORY is used when unsteady aerodynamics are included. In that case, the results obtained in the three most recent time steps, concerning the angle of attack and different lift coefficient terms (see appendix A) must be stored in order to be able to calculate the time derivatives of these variables, e.g.  $\frac{d\alpha}{dt}$ . For this reason the subroutine HISTORY has been created. It will store the variables for every subelement for the previous three time steps. It will also store the time itself, because it is possible to use integration routines with variable time steps and this must be taken into account when calculating the time derivatives of the coefficients.

### 6.2.27 DFRIDR, dfrid.f

In DFRIDR the partial derivatives  $\frac{\partial T}{\partial q_i}$  and  $\frac{\partial V}{\partial q_i}$  are calculated. This subroutine is called in combination with two different functions: T and V. T gives the kinetic energy while V results in the potential energy.

Originally Ridder's method [116, 103] was used to determine the partial derivatives. It is more accurate but it takes up a lot of calculation time. To save time, this method has been dropped from the programme and it is assumed that the input value  $h$  used in the numerical differentiation, currently one constant value for all DOF's, is well chosen. It is up to the user to check the correctness of this assumption.

The derivatives are calculated using:

$$\frac{\partial T}{\partial q_i} = \frac{T(q_i + h) - T(q_i - h)}{2} \quad (6.15)$$

and a similar equation is used for the potential energy.

The result of the DFRIDR subroutine is one partial derivative for either  $T$  or  $V$  to one of the generalised coordinates  $q_i$ .

### 6.2.28 V, v3c.f

The function V calculates the potential energy for a new value of  $q_i$  and is used to determine the derivative  $\frac{\partial V}{\partial q_i}$ . Gravitational acceleration and the elastic energy stored in the torsional springs result in potential energy. If the gravitational acceleration is not taken into account, the only calculation performed is:

$$V = \frac{1}{2}k_i q_i^2 \quad (6.16)$$

All other terms in the elastic energy will not change due to the new value of  $q_i$  and therefore do not need to be calculated.

When gravity is included, the calculations become a bit more complex. For every element behind element  $i$  the potential energy due to gravity must be calculated. The first step is to calculate the rotation transformation matrix for the new value of  $q_i$  by calling the TRAFI subroutine. Then, for every element behind  $i$ , the position of the c.g. relative to the hinge point of element 1 is determined. This expression is given in the local reference frame of the element. The gravitational acceleration  $\mathbf{g}$  is also transformed to the local reference frame. That part of the total gravitational potential energy that has changed due to the new value of  $q_i$  becomes:

$$V = \sum_{l=i}^N -m_l (g_{xl}, g_{yl}, g_{zl}) \{\mathbf{E}_i\} (\mathbf{E}_i) \begin{Bmatrix} r_{xl} \\ r_{yl} \\ r_{zl} \end{Bmatrix} \quad (6.17)$$

where the elements between  $i$  and  $N$  that are not in line with  $i$  can be skipped.

The gravitational term and the elastic term are summed and given as a result of this function.

### 6.2.29 T, t.f

The function T returns the value of that part of the kinetic energy that has changed due to the change in  $q_i$ . The function calls the subroutine NRGDTDQ, which returns the new values of those parts of the kinetic energy that have changed due to the new value of  $q_i$ .

### 6.2.30 JACOBN (jacobn.f), JCBNIMSL (jcbnimsl.f)

When using implicit integration routines, the Jacobian must be calculated:

$$[J] = \left[ \begin{array}{ccc|ccc} \frac{\partial^{ap} \dot{q}_1}{\partial q_1} & \dots & \frac{\partial^{ap} \dot{q}_N}{\partial q_1} & \frac{\partial^{ap} \dot{p}_1}{\partial q_1} & \dots & \frac{\partial^{ap} \dot{p}_N}{\partial q_1} \\ \vdots & \ddots & \vdots & \vdots & \ddots & \vdots \\ \frac{\partial^{ap} \dot{q}_N}{\partial q_N} & \dots & \frac{\partial^{ap} \dot{q}_N}{\partial q_N} & \frac{\partial^{ap} \dot{p}_N}{\partial q_N} & \dots & \frac{\partial^{ap} \dot{p}_N}{\partial q_N} \\ \hline \frac{\partial^{ap} \dot{q}_1}{\partial p_1} & \dots & \frac{\partial^{ap} \dot{q}_N}{\partial p_1} & \frac{\partial^{ap} \dot{p}_1}{\partial p_1} & \dots & \frac{\partial^{ap} \dot{p}_N}{\partial p_1} \\ \vdots & \ddots & \vdots & \vdots & \ddots & \vdots \\ \frac{\partial^{ap} \dot{q}_N}{\partial p_N} & \dots & \frac{\partial^{ap} \dot{q}_N}{\partial p_N} & \frac{\partial^{ap} \dot{p}_N}{\partial p_N} & \dots & \frac{\partial^{ap} \dot{p}_N}{\partial p_N} \end{array} \right] = \left[ \begin{array}{c|c} I & II \\ \hline III & IV \end{array} \right] \quad (6.18)$$

As discussed before, the partial differentiation with respect to  $q_i$  is defined differently here in the Jacobian than in all other calculations in WOBBE. For the Jacobian, the partial derivative with respect to  $q_i$  is taken by keeping all other generalised coordinates  $q_j$  as well as all generalised momenta  $p_l$  constant. The notation  $\frac{\partial^{*pq}}{\partial q_i}$  is used for this derivative.

There are two different subroutines in WOBBE that can calculate the Jacobian. The first one JACOBN is taken from numerical recipes for FORTRAN, [116]. It calculates the Jacobian by calculating  $\{\dot{q}\}$  and  $\{\dot{p}\}$  for  $q_i + h$ ,  $q_i - h$  as well as for  $p_i + h$  and  $p_i - h$ , where  $i = 1..N$ . This means that most calculations in WOBBE are repeated an extra  $4N$  times. This will cost a lot of calculation time, while it is not necessary to do the calculation this way. Similar to the calculations of  $\frac{\partial T}{\partial q_i}$  as described in appendix G, large reductions in calculation time are also possible in the calculation of the Jacobian. JCBNIMSL uses a quicker method to calculate the Jacobian by making use of results that have not changed due to the change in  $q_i$  or  $p_i$ . Therefore the JACOBN subroutine should only be used if there is any doubt about the correctness of the JCBNIMSL subroutine. For new complexities in models it is not unthinkable that some possibility has been overlooked in the JCBNIMSL routine resulting in an incorrect calculation of the Jacobian. One could for instance think of branching of already branched systems.

As mentioned before, the subroutine JCBNIMSL uses a lot less calculation time by calculating the Jacobian matrix more efficiently. The four different parts of the Jacobian as illustrated in equation 6.18 are calculated separately. All calculations that concern controlled rotations are not performed, the controlled rotations as well as the induced velocity will not be calculated using an implicit integration routine, it will be calculated using a simple Euler scheme.

First the subroutine DPDOTDP is called to calculate part IV in equation 6.18:  $\frac{\partial^{ap} \dot{p}_i}{\partial p_i}$ , where the  $\partial^{ap}$  notation is used to make a difference between the two different partial derivatives within the program.

Then part III in equation 6.18 is calculated using DERIVSN. This calculation uses equation 6.19:

$$\frac{\partial \dot{q}_i}{\partial p_j} = [A_{ij}^{-1}] \quad (6.19)$$

Using the results of the LU-decomposition, every element in the inverse matrix can simply be determined to find the derivatives, as described in the section dealing with DERIVSN.

Finally parts I and II are calculated using DERIVSN. This calculation does not need to be performed for  $i = 1$ , because changing  $q_1$  will not have any effect on the energy matrix, meaning that the velocities do not change due to a different value of  $q_1$ . To calculate  $\{\underline{\dot{q}}\}$  and  $\{\underline{\dot{p}}\}$  for a new value of  $q_i$ , DERIVSN is called for two different values of  $q_i$ . The derivatives in part I and II can then be calculated.

### 6.2.31 DPDOTDP, dpdotdp.f

This subroutine calculates  $\frac{\partial^{pq}\dot{p}_j}{\partial p_i}$ . Changing the value for  $p_i$  means that the velocities will all change, which will influence two terms in the calculation of  $\dot{p}_j$ :  $\frac{\partial T}{\partial q_j}$  and the generalised forces  $Q_i$ . The potential energy will not change. The energy matrix also remains the same. Therefore the LU decomposition of the energy matrix calculated before can be used again. The new values for the velocities  $\{\underline{\dot{q}}\}$  can be calculated using this. With these new velocities the generalised moments  $Q_i$  are calculated using GENFO3. The new velocities are also used to calculate the kinetic energy for all new values of  $p_i$ . Again, time can be saved here by using previous results.

Finally the derivative is calculated:

$$\frac{\partial^{pq}\dot{p}_j}{\partial p_i} = \frac{\frac{\partial T}{\partial q_j}|_{p_i+h} - \frac{\partial T}{\partial q_j}|_{p_i-h} + Q_j|_{p_i+h} - Q_j|_{p_i-h}}{2h} \quad (6.20)$$

Note that this equation entails both of the two defined partial derivatives with respect to  $q_i$  as explained in 6.2.30.

### 6.2.32 Linalg.f

In the file linalg.f all linear algebra routines are given. This is i.a. adding two rows, transforming a  $3 \times 3$  matrix, multiplication of row with a matrix etc. It also includes a special multiplication routine for multiplying a row with a transformation matrix, where the position of the row and columns with a 1 and two zeros is taken into account. This way a large reduction in calculation time has been obtained. The programme spends a lot of calculation time in these linear algebra subroutines, the multiplication of rows with transformation matrices is not a complex calculation, but it has to be performed many times during each time step.



# Chapter 7

## Multi-Body Modelling of Large Wind Turbines

*Models are to be used, not believed.*

- H. Theil 'Principles of Econometrics'

The method used to model a wind turbine is of vital importance for every simulation programme. Remember that "garbage in, garbage out": if the model is not representing the real turbine in a good way, the programme might be perfect, but the simulations will still give useless and incorrect results.

The basics of the modelling method used for simulations using the programme that has been described in chapter 6: WOBBE, will be explained in this chapter. Details of modelling are further investigated in chapter 9, here only the basics that are based on the available analysis for uniform beams are explained. For all simulations with WOBBE so-called superelements have been used. These superelements will be explained in the first section. The second section will describe the calculations performed to create an input file for WOBBE. Finally a short description of a complete wind turbine model is given in the third section.

### 7.1 Superelements

When WOBBE is used to simulate wind turbine blades, the so-called superelement modelling method is used to create the model [119, 120]. It has been found that using superelements is a good method to get correct natural frequencies using only a few degrees of freedom [91, 93, 94].

One superelement consists of three or four rigid bodies as shown in figure 7.1. The number of rigid bodies within one superelement depends on whether or not torsion is included in the model. To model torsional stiffness, the rigid body in the middle will be split into two equal

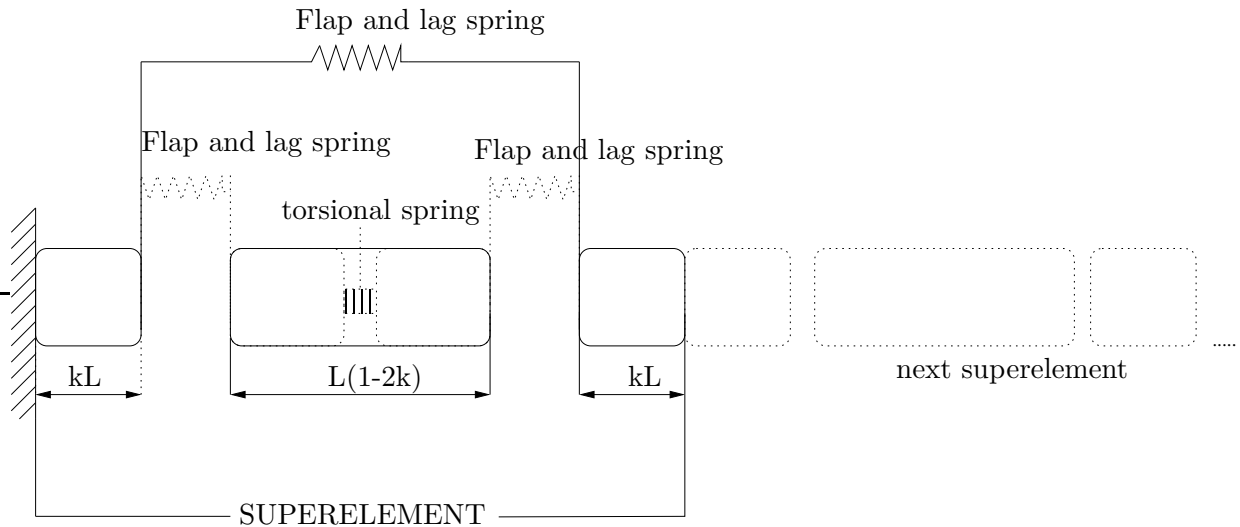


Figure 7.1: A superelement consisting of three or four rigid bodies, depending on the presence of torsion in the model. The last rigid body is rigidly combined with the first rigid body of the next superelement.

parts interconnected by a spring modelling the torsional stiffness. Therefore, when torsion is included, a superelement will consist of four elements with five degrees of freedom, while a model without torsion will be represented by superelements consisting of three elements with four degrees of freedom.

The different rigid bodies are connected by rotational springs. Using a partitioning coefficient  $k$ , the lengths of the first and last element are taken as  $kL$ , therefore the length of the centre rigid body (for three bodies, so no torsion) is  $(1 - 2k)L$ . This is also illustrated in figure 7.1. The first element of a superelement is assumed to be clamped. Therefore the last element of one superelement will form a rigid body with the first element of the following superelement. This results in an element with a length that is  $2kL$  as shown in figure 7.1. Rauh [119] concludes that the partitioning coefficient  $k$  should be chosen between  $k = \frac{1}{5}$  and  $k = \frac{1}{4}$ . For values of  $k$  in this range, the exact eigenfrequencies of the model are approximated using only a limited number of superelements.

The stiffnesses of the springs in a superelement are chosen such that, when loaded by a moment and a force, they will result in the same deflection as well as the same slope of the deflection at the tip of the superelement as the original beam. A uniform beam as shown in figure 7.2, is used to determine the equations for the spring stiffnesses. The analysis is done for one direction; only lag or only flap. For the model in figure 7.2: a uniform beam with stiffness  $EI$ , loaded by a force and moment at the tip, the equations for the deflection and the slope are [37] (see also figures B.8 and B.9):

$$\Delta v = \frac{FL^3}{3EI} + \frac{ML^2}{2EI} \quad (7.1)$$

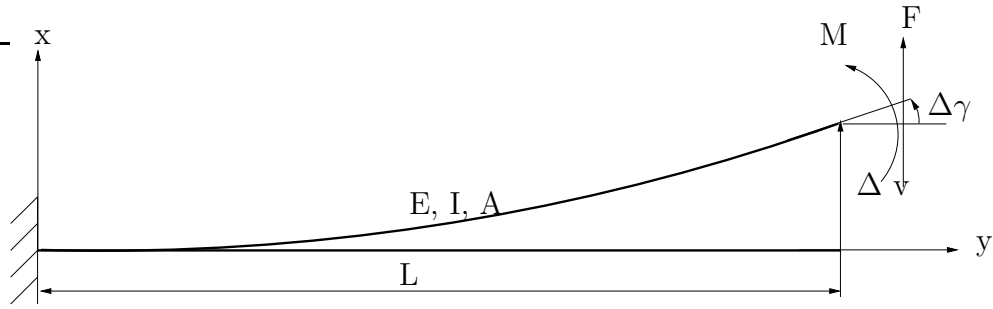


Figure 7.2: A clamped uniform beam under static loading, force  $F$  and moment  $M$  acting at the tip.

and

$$\Delta\gamma = \frac{FL^2}{2EI} + \frac{ML}{EI} \quad (7.2)$$

In matrix notation this becomes:

$$\begin{bmatrix} \Delta v \\ \Delta\gamma \end{bmatrix} = \frac{L}{6EI} \begin{bmatrix} 2L^2 & 3L \\ 3L & 6 \end{bmatrix} \begin{bmatrix} F \\ M \end{bmatrix} \quad (7.3)$$

Inverting this equation gives:

$$\begin{bmatrix} F \\ M \end{bmatrix} = \frac{EI}{L^3} \begin{bmatrix} 12 & -6L \\ -6L & 4L^2 \end{bmatrix} \begin{bmatrix} \Delta v \\ \Delta\gamma \end{bmatrix} \quad (7.4)$$

This results in an equation for a clamped uniform beam giving the force and moment that correspond to a given deflection and slope.

For the superelement illustrated in figure 7.3 the moments in the two hinges due to the external moment and force can be derived to be:

$$F(1-k)L + M = c_1q_1 + c_2(q_1 + q_2) \quad (7.5)$$

$$FkL + M = c_3q_2 + c_2(q_1 + q_2) \quad (7.6)$$

or in matrix notation:

$$\begin{bmatrix} c_1 + c_2 & c_2 \\ c_2 & c_2 + c_3 \end{bmatrix} \begin{bmatrix} q_1 \\ q_2 \end{bmatrix} = \begin{bmatrix} (1-k)L & 1 \\ kL & 1 \end{bmatrix} \begin{bmatrix} F \\ M \end{bmatrix} \quad (7.7)$$

For small deformations the deflection and slope of the superelement can be expressed as:

$$\begin{bmatrix} \Delta v \\ \Delta\gamma \end{bmatrix} = \begin{bmatrix} (1-k)L & kL \\ 1 & 1 \end{bmatrix} \begin{bmatrix} q_1 \\ q_2 \end{bmatrix} \quad (7.8)$$

Combining equations 7.4, 7.7 and 7.8 gives for the spring coefficients:

$$c_1 = c_3 = \frac{6EI}{L}(1 - 2k)^2 \quad (7.9)$$

and

$$c_2 = \frac{2EI}{L}(1 + 6k - 6k^2) \quad (7.10)$$

From equation 7.10 it can be concluded that for  $k = \frac{1}{2}(1 - \frac{1}{\sqrt{3}}) \approx 0.211$  the spring stiffness of the spring between the first and last element,  $c_2$ , becomes zero. For this value for the partitioning coefficient  $k$  the remaining two springs become:

$$c_1 = c_3 = \frac{2EI}{L} \quad (7.11)$$

For the torsional spring that can be included in the superelement, the stiffness is straightforward. Looking at equation B.9 and B.11 it is clear that the spring stiffness that will result in an equal twist in the model is:

$$c_{tors} = \frac{GI_p}{L} \quad (7.12)$$

For wind turbine blades, the values for  $EI$ ,  $GI_p$  and mass per unit length will not be constant, therefore it is necessary to further investigate what is a good method to calculate the spring stiffnesses and element properties. Some results on this can be found in section 9.1.

## 7.2 Calculation of the Superelement Properties

The superelements have been discussed in the previous section. The method that has been used to determine the properties of the superelements in a wind turbine blade model will be discussed here. There are many different options to calculate the properties of a model and in chapter 9 several different methods of calculating the stiffness and the structural pitch angles of the superelements are looked at. There are more properties for which the modelling method should be looked at in more detail as a continuation of this research, but in this section the discussion is limited to giving a general idea of how to calculate the properties of the superelements.

For the calculations presented in the next two chapters, a pre-processing programme has been created that generates the necessary input for WOBBE from tables containing the blade properties at different cross-sections. Between these cross-sections every property is linearly interpolated. The modelling method used in this supporting programme is described in this section.

To calculate the stiffnesses of the springs, several different options are possible, as described in section 9.1. The first part of a wind turbine blade is close to circular and much stiffer

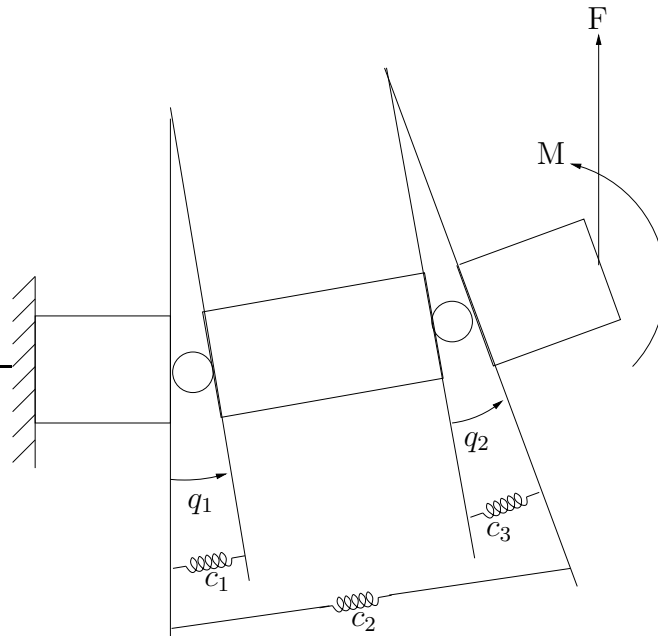


Figure 7.3: A superelement with rotational springs in one direction and without torsion, loaded by a force and a moment.

than the remainder of the blade. When the hub is included in the blade model, this will also be much stiffer than the remainder of the blade. If this is the case, it is important not to include this part in the calculation of the spring stiffnesses in a superelement that models the flexible part of the blade. Usually there will be a discontinuity in the table with stiffnesses at a certain radial position, as shown in figure 7.4. The stiff parts of the blade and the hub can be assumed to be rigid, or modelled by a separate superelement. The latter option is usually not very useful, the stiff part barely influences the results and it will strongly increase the calculation time of a simulation. In WOBBE it is best to combine the first rigid part with the first rigid body and these high values of stiffness are not used in the calculation of an average stiffness over part of the model. The calculation of the stiffnesses of the superelement springs will then start just outboard of this discontinuity.

When creating a blade model in WOBBE, first the length of the superelement will be calculated. It depends on the radius of the blade (without the hub and very stiff part of the blade) and on the number of superelements used in the blade model. All superelements are modelled as being of equal length:

$$L_{SE} = \frac{R - d_{disc}}{N_{SE}} \quad (7.13)$$

where  $L_{SE}$  is the length of one superelement,  $R$  is the radius of the turbine,  $d_{disc}$  is the length from the rotor centre to the flexible part of the blade and  $N_{SE}$  is the number of superelements in the model.

The directions of the springs must be determined before the spring stiffnesses can be cal-

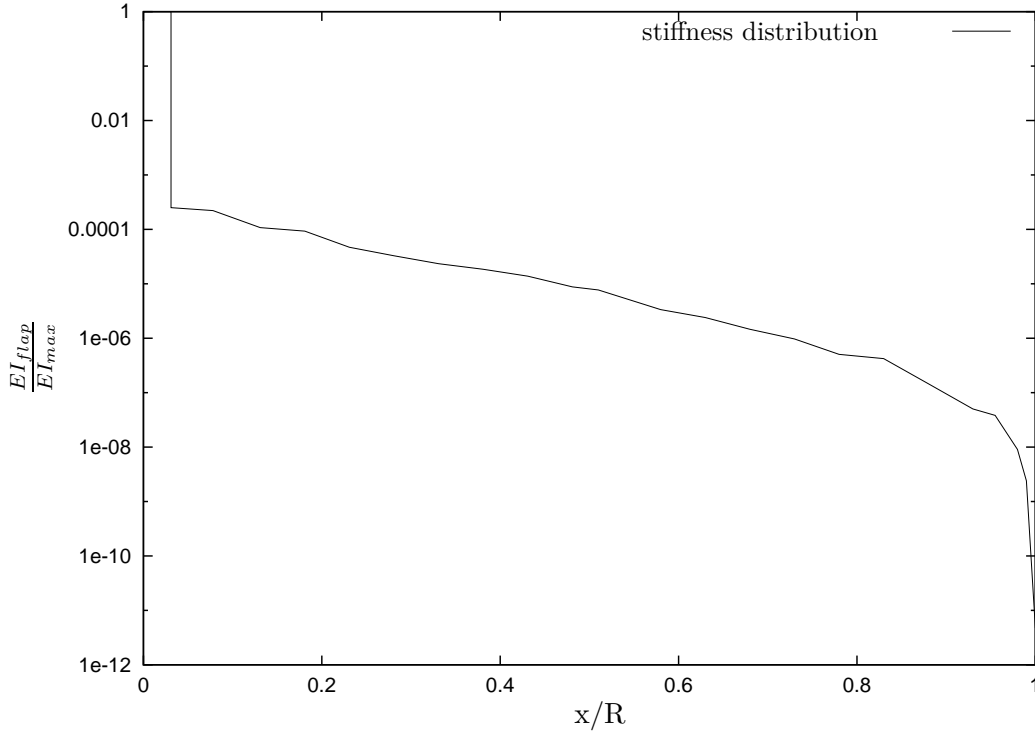


Figure 7.4: Sketch of a possible flap stiffness distribution along the radial position starting in the rotor centre. The first part in the graph therefore does not correspond to the blade, but to the model of the hub.

culated. As described in section 9.2, the structural pitch can be calculated using different methods, e.g. the value half way the rigid body or superelement or the average over the rigid body or each superelement.

Once the direction of the springs is known, the stiffness of the springs can be determined. The stiffness of the springs is calculated by determining the average stiffness  $EI_{x1}$  and  $EI_{y1}$  and the average stiffness  $GI_p$  for the torsional stiffness over a certain length, e.g. a superelement or half a superelement (see section 9.1). If the structural pitch angle in the different cross sections varies along (half) the length of a superelement, the stiffness must be corrected for the difference between the structural pitch in the model (that does not vary in the superelement or half the superelement) and the real structural pitch angle at each intersection. The equations to change the axes for the area moments of inertia are [37]:

$$I_{x1} = \frac{I_x + I_y}{2} + \frac{I_x - I_y}{2} \cos 2\theta - I_{xy} \sin 2\theta \quad (7.14)$$

and

$$I_{y1} = \frac{I_x + I_y}{2} - \frac{I_x - I_y}{2} \cos 2\theta + I_{xy} \sin 2\theta \quad (7.15)$$

where  $\theta$  is the angle between the old axes and the new axes. These expressions can easily be

derived using the method derived in section 6.2.3 for transforming the mass inertia matrix to another reference frame.

Equations 7.14 and 7.15 are valid when  $E$  has the same value in flatwise direction as in edgewise direction. When a material is isotropic, this will be true.

These two equations can be used to transform the values of  $EI_x$  and  $EI_y$  to the directions of the springs in the model. Due to these transformations the values for  $EI_{xy}$  will no longer be zero at one or more intersections. However, it is not possible for WOBBE to take this cross stiffness into account. The programme needs the springs in the model to be in the principal directions, therefore the resulting value of  $EI_{xy}$  is neglected. A more accurate method to model the blade would be an iteration to find the structural pitch directions of the model such that  $EI_{xy}$  is zero. However, the method described here, neglecting the resulting cross coupling, will only result in a small error. The structural pitch value will usually only change gradually along the blade, except for the part of the blade root, which is assumed rigid as discussed above, therefore there will be only a marginal difference between a model calculated using the method described above and a model calculated using an iteration.

Once the average values for the stiffnesses over the chosen length (half or whole superelement) are known, the springs can be calculated using equation 7.11. They should be located on the elastic axis.

The average value of  $GI_p$  has to be calculated over one superelement, if torsion is to be included in the model. The spring modelling torsion can be calculated from this average using equation 7.12. The torsion spring should be located at the shear centre.

The stiffnesses are not the only properties of the model that have to be calculated. The masses, mass moments of inertia, distance to hinges and centres of gravity and the aerodynamic properties must be determined.

To calculate the mass of the elements, the mass distribution of the actual blade is used and the actual mass of the part that is represented by one rigid body is calculated. Using the mass distribution, the distance to the local centre of gravity and the mass moments of inertia are also determined. The hinge distance is simply the length of the rigid body in one direction. The springs should be located on the elastic axis or in the shear centre, depending on the type of hinge (flap/lag or torsion). The hinge vector is therefore a vector that can have components in all three directions in order to point from one spring location to the next spring location.

The aerodynamic properties are also taken per rigid body and not per superelement. For the chord and thickness distribution there are two possibilities within WOBBE. It is possible to model each rigid body with a linear distribution of the chord and/or thickness where the value at the beginning and at the end of an element is calculated by linear interpolation between the given intersections. It is also possible to model the chord distribution and/or the thickness distribution along the entire blade using a 6<sup>th</sup> order polynomials in which case these polynomials are used to calculate thickness or chord at the subelement during the calculation of the aerodynamic forces. When compared to a linear distribution within

each rigid body, the polynomial approximation usually gives a much better representation of the chord and thickness distribution, especially when the model consists of only one or two superelements.

The aerodynamic twist can only be modelled by giving an aerodynamic twist angle at the root and at the tip of the rigid body. The values in the different subelements within the rigid body will be determined using linear interpolation between these two points on the rigid body. Note that the aerodynamic twist angle of a blade will be defined relative to the rotor swept area when the tip of the blade is set at zero aerodynamic pitch angle. In WOBBE however, it must be given relative to the local reference frame. Therefore aerodynamic twist must be corrected for the presence of structural pitch.

The aerodynamic centres (a.c.) at the root and at the tip of the rigid body must also be calculated. The programme will linearly interpolate to find the locations of the aerodynamic centre in the different subelements. The positions of the a.c.'s must be given relative to the hinge points and in the local reference frame of the rigid element. Therefore, it might be necessary to transform the coordinates of the a.c. position using the method discussed in section 2.1.2.

Once all properties are known, the first element of the first superelement and the part of the blade inboard of the discontinuity in stiffness will be added to the dummy element used for a constant rotation, this is sketched in figure 7.5. The inertia matrix of this dummy element will be determined from the inertia matrices of the different parts that are added together, their masses and the positions of their centres of gravity.

According to Steiner's rule the inertia can be determined:

$$I_{xx} = \sum_{i=1}^3 (I_{xxi} + m_i(dy_i^2 + dz_i^2)) \quad (7.16)$$

where  $dy_i$  and  $dz_i$  are the distances between the c.g. of part  $i$  and the c.g. of the complete element in the  $y$  and the  $z$  direction respectively. The mass of each part is  $m_i$ . The position of this c.g. can be determined by:

$$rx_{cg} = \frac{\sum_{i=1}^3 m_i x_{cgi}}{m_{tot}} \quad (7.17)$$

where  $rx_{cg}$  is the position of the c.g. in the  $x$  direction,  $x_{cgi}$  is the  $x$ -position of the c.g. of part  $i$ . This process is also illustrated in figure 7.5

By adding the first element of the superelement to the dummy element, the first element is indeed clamped as it should be according to the theory of the superelements. Often the hub is modelled as the first part of a blade. By dividing all properties of the hub properly over the two or three blades, this will result in a model with integrated hub.

From the description of WOBBE in chapters 5 and 6 it is clear that it is not possible to have more than one degree of freedom per rigid body in this programme. The rigid bodies of the superelements are therefore modelled by two elements in WOBBE. The first element will be

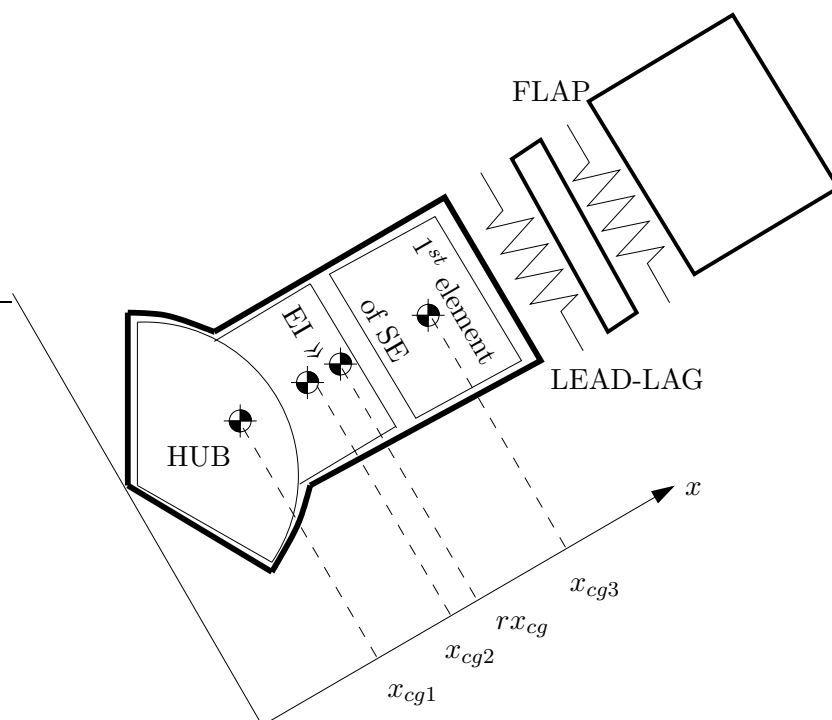


Figure 7.5: The hub, the very stiff first part of the blade and the first element of the first superelement are combined into one rigid body.

very small or zero and its degree of freedom and spring will model the lag stiffness in the principal direction. The second segment will have the total mass of the rigid body minus the mass of the very small first element. Its degree of freedom and spring will be in the most flexible direction of the blade, modelling the flap stiffness. This is also illustrated in figure 7.5. Note that this division into a small and larger rigid body does not introduce an artificial high frequency, because the inertia of both rigid elements will influence the frequency, not just the small element.

### 7.3 Elements used in a Model of a Wind Turbine

The method used to calculate the properties of the elements has been discussed in the previous section, but what elements should be used in a wind turbine or a wind turbine blade?

The tower can be modelled similarly to the blades, using superelements. The input for this can be generated by the same supporting programme as discussed in the previous section. The calculations for the tower are identical to those of the blades, only the aerodynamic properties are not needed. To model the flexibility of the foundation, there can be springs inserted that connect the inertial frame with the first tower element. The yaw and tilt

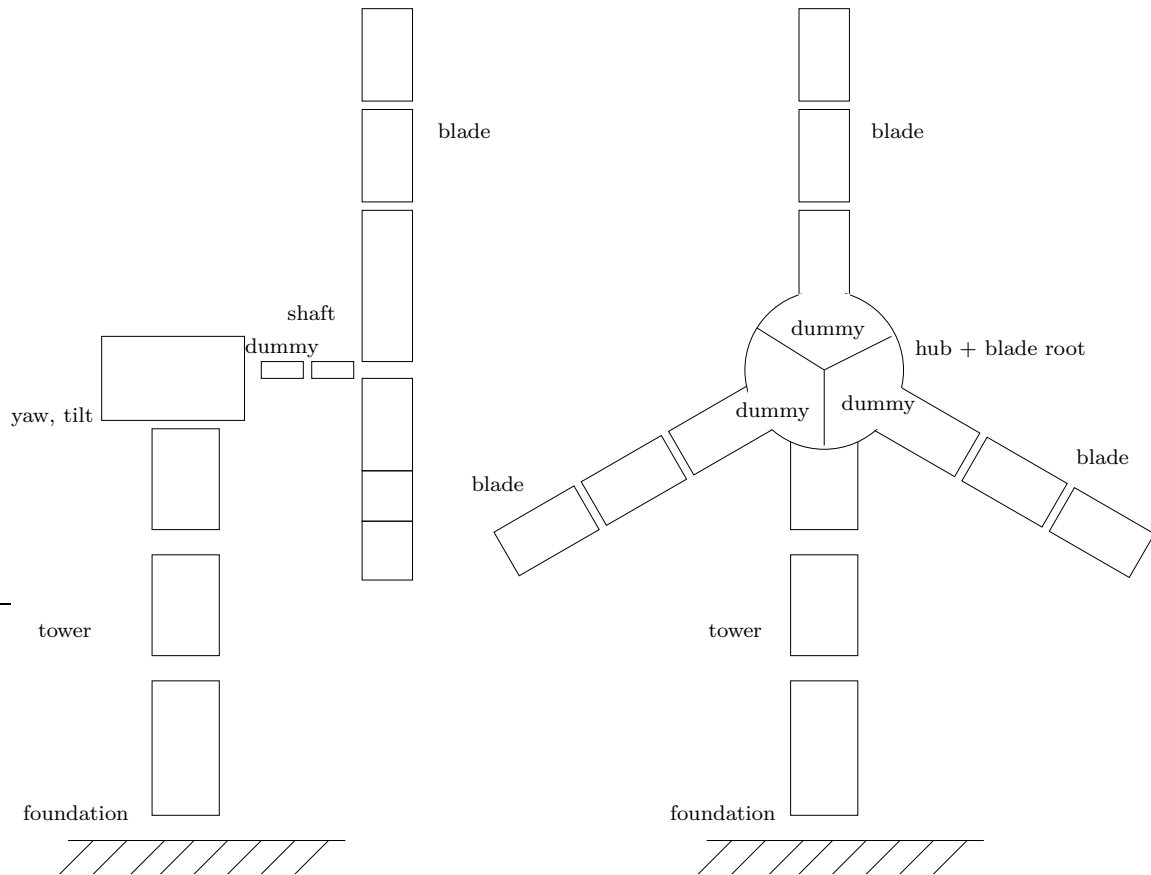


Figure 7.6: A model of a complete wind turbine

stiffnesses can be implemented at the top of the tower as illustrated in figure 7.6.

The shaft has an important effect on the natural frequencies mainly due to its torsional flexibility. Therefore this part of a turbine also needs to be modelled using superelements. The shaft will often have a varying stiffness along the shaft's length with discontinuities at one or more points. To enable the modelling of this shaft, the superelements approach should be used from discontinuity to discontinuity as illustrated in figure 7.8. If the bending of the shaft is of importance as well as the torsion, this can result in a rather large number of degrees of freedom for this one part of the turbine. If only torsion is needed, then one DOF per superelement can be used, the bending DOF's can be left out of the model. For the complex model including bending DOF's, model reduction is advised. It is possible to initially model the shaft using the superelements and add a rotating disc at the end with an inertia approximately the same as the three blades. This model can then be reduced by tuning a simpler shaft model with less degrees of freedom towards the same frequencies as the detailed shaft model's frequencies. This can reduce calculation time of the complete turbine model.

The generator in a wind turbine is also important, it has a strong influence on the natural



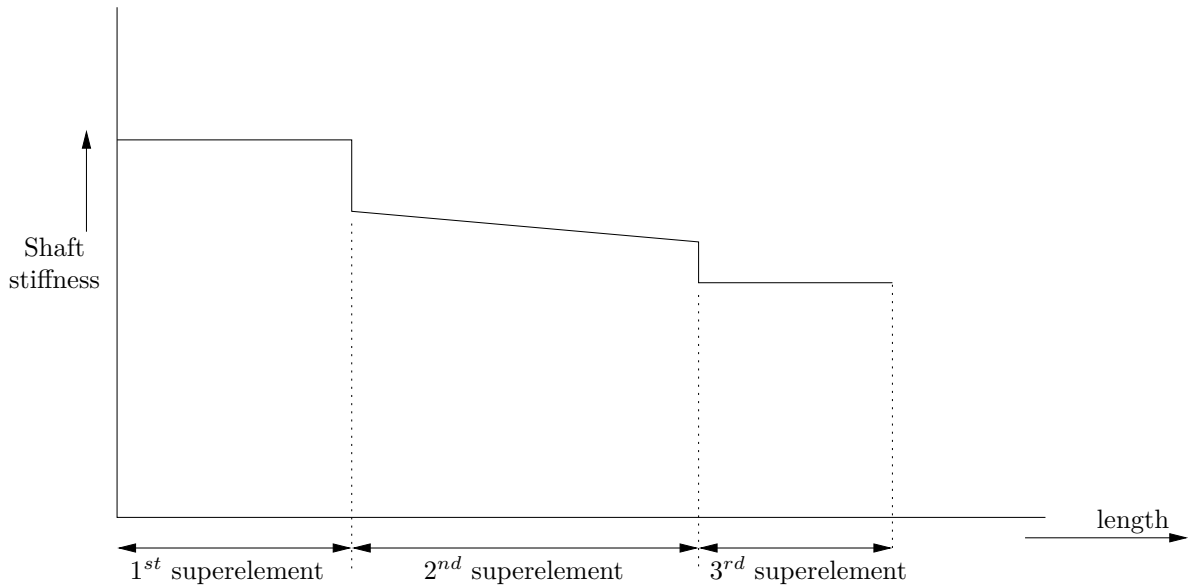


Figure 7.8: A possible distribution of stiffness of a shaft and the corresponding division into superelements

there are three elements needed that all start at the tip of the shaft, but have three different points for the next hinge, setting the three blades at  $120^\circ$  relative to each other. These three elements will all have a controlled velocity of 0 rad/s. After all, it is the shaft that rotates and for which the speed is controlled by the generator, the blades will be connected to this shaft. The control on the rotational speed of the blades is exerted on the shaft, using either the generator torque or a controlled rotation, and transferred to the blades. The blades are connected to the three dummy elements as illustrated in figure 7.6.

Using superelements, the number of degrees of freedom needed to model the frequencies correctly is relatively small. As shown in the next two chapters, two superelements in the blade suffices when looking at the first flap and first lead-lag frequencies of the blades. It is also possible to tune a model consisting of one superelement to the correct frequencies for the first flap and lead-lag mode by adjusting the stiffnesses of the springs. The correct frequencies may be known from measurements, from FEM calculations or estimated by using a detailed single blade model with three or more superelements. This way the total number of degrees of freedom in a complete wind turbine model can be kept relatively low, which appeared to be essential when using WOBBE to analyse the aeroelastic stability, as the programme takes a lot of calculation time even for relatively simple models. For example, a simulation of 50 seconds of an isolated blade with three superelements and including torsion can take about an hour on current PC's. This model has only 15 degrees of freedom, but already the calculation time is high. The time increases exponentially with the number of degrees of freedom, because not only does this entail more calculations for one time step, the time step also has to be taken smaller due to the higher frequencies present. Therefore when analysing a complete turbine, it is essential to try to limit the model to keep only the

necessary degrees of freedom.

The general idea of how to create a model in WOBBE has now been described. This method has been used in creating models of blades and turbines and the results are part of the validation of the code. This is discussed in the next chapter.



# Chapter 8

## Verification and Validation of WOBBE

*"Truth is more of a stranger than fiction."*

- Mark Twain

The purpose of creating the tool WOBBE, described in chapters 5 and 6, is to investigate and analyse the aeroelastic stability of wind turbines. When a wind turbine is designed, it is important that it is aeroelastically stable otherwise premature damage or even complete destruction can occur. As mentioned in the previous chapter, discussing the method to model a wind turbine, when the input model is incorrect, the results will also be nonsense. However, a good model alone is not enough, one must also make sure that the programme performs correctly and that the results resemble what genuinely happens. A wind turbine simulation tool is only useful if the results can be trusted. Theory is nice, but it must be compared to real life examples.

Two different aspects of testing of the code will be discussed in this chapter. First, discussed in section one of this chapter, there is the part that will be called verification of the code. Checks are performed to find out if the programme does indeed calculate what it was intended to calculate. This does not say anything about the validity of the assumed equations or simplifications, it only concerns the agreement between theory and implemented code.

The second aspect of investigating the validity of the results of WOBBE will be called the validation. This is described in the third section of the chapter. In the validation, the results of simulations using WOBBE will be compared to measurement results of a real turbine. This is therefore a check that can give a conclusion about the correctness of the assumptions and equations used, do they represent the real world well enough or not?

The second section in this chapter will discuss benchmark tests that have been performed. WOBBE has been used to simulate benchmark models and these results have been compared to results of several other codes. These different codes were mainly linear codes, with different

types of aerodynamic models and different methods to model the turbines and to derive the governing equations. This benchmark comparison, using a model based on a simplified real wind turbine, is neither real verification nor validation according to the above given distinction, it is somewhere in between, therefore the benchmark test and the results are discussed in the second section of this chapter.

Finally this chapter will end with a short summary of the main results of the verification and validation of WOBBE.

Confidentiality of many of the results, the blade properties, operational conditions etc. has made it impossible to show all results. A careful selection has been made in order to show the verification and validation of WOBBE to the largest extent possible without breaching the confidentiality.

## 8.1 Verification of WOBBE

WOBBE has been verified in several different ways. Firstly, as described in chapters 5 and 6, some parts of the calculations can be performed in different ways. The velocity determination as well as part of the determination of the generalised forces have, over time, been programmed in two different ways. Comparison of the results of both versions has been used as a verification of these parts of the code. Likewise, when adding new options to the programme the results using the new options (e.g. controlled rotations) were compared with the engineering solutions that were used before the addition (e.g. flywheel). This can also be seen as verification of parts of the programme. All these different verifications of the code by comparing results from different code versions are described in the first part of this section.

Secondly, a clamped homogeneous beam has been simulated, both non-rotating and rotating. The natural frequencies can be derived from the simulation results. These natural frequencies can also be determined analytically and the comparison between these analytical results and the frequencies found in the results of the simulations by WOBBE is another way of verifying the structural dynamics part of the code. As shown by Rauh and Schiehlen ([119, 120]) and by Molenaar ([92, 93]) the superelement models used should result in good approximations of the natural frequencies, therefore this comparison of analytical and calculated frequencies is another verification of the code. This part of the verification can be found in the second part of this section.

Finally the possibility of branching has been verified by analysing a model that, for the correct starting position, will result in the cancellation of one of its natural frequencies.

### 8.1.1 Verification by Results Comparison

The first version of WOBBE by van Overbeek [103] has been successfully verified by her, by comparing the analytical results of a simple helicopter blade model, with one flap, one

lag and one pitch hinge, to the results from WOBBE. This verification did not verify the possibility of branched systems, it did not include controlled rotations, fixed angles and the equations for the aerodynamic forces had to be derived and inputted by the user, but the basic calculations, such as the mass matrix calculation and the calculation of the derivatives needed in Lagrange's equations, were verified.

### Fixed Angles

After this initial verification, the first addition to the WOBBE code was the inclusion of the possibility of using fixed angles [48]. The engineering solution before the option of fixed angles was included, was to use a very stiff spring combined with a generalised force  $Q_i = -k_{stiff}(\theta_{cst} - \theta_{real})$ , where  $k_{stiff}$  is the very high stiffness,  $\theta_{cst}$  is the desired fixed angle and  $\theta_{real}$  is the real value of the degree of freedom that one tries to keep constant. When the possibility of fixed angles was added to the programme, the results of the new version and the old version using this engineering solution were compared for the baseline model illustrated in figure 8.1. Figure 8.2 shows the flap angle of the baseline model when the engineering solution is used to set the pitch angle at  $-3^\circ \approx 0.05235988$  radians. The result for the improved version of WOBBE is illustrated in figure 8.3. There is not a large difference visible. Figure 8.4 does show the difference between the two methods, when the engineering solution is used, a high frequency is added to the simulation. Therefore smaller time steps need to be taken during the simulation. This part of the programme has been verified by this test, the option of using fixed angles has been implemented correctly.

### Controlled Rotations

Similarly the addition of the controlled rotations has been verified. This is shown more extensively in appendix E. The new version of WOBBE has been compared with the engineering solution in the old version. In this case the engineering solution was to use a flywheel.

A clamped rotating Euler-Bernoulli beam (constant stiffness, constant cross-section), figure 8.5, was used to make a comparison between the results using a flywheel and the results using a controlled rotation. The constant rotation is acting on the first element. Aerodynamic forces have not been taken into account, therefore all generalised forces are equal to zero. Only in-plane bending is modelled. The beam is the same as discussed in 8.1.2, consisting of 4 super elements [119, 120]. Using 4 super elements the model consists of 9 rigid body elements in total.

Calculations have been performed using the controlled rotations option and compared to the results using a large flywheel as its first element. In this last case the actual model in WOBBE consists of 10 elements in total, 9 for the beam and one for the flywheel. In figure 8.6 both results for DOF  $q_5$  are printed in one figure and as can be seen the results are almost identical. However, using the flywheel will always introduce some small variations in the rotational velocity, while by using the controlled rotation the velocity is kept absolutely

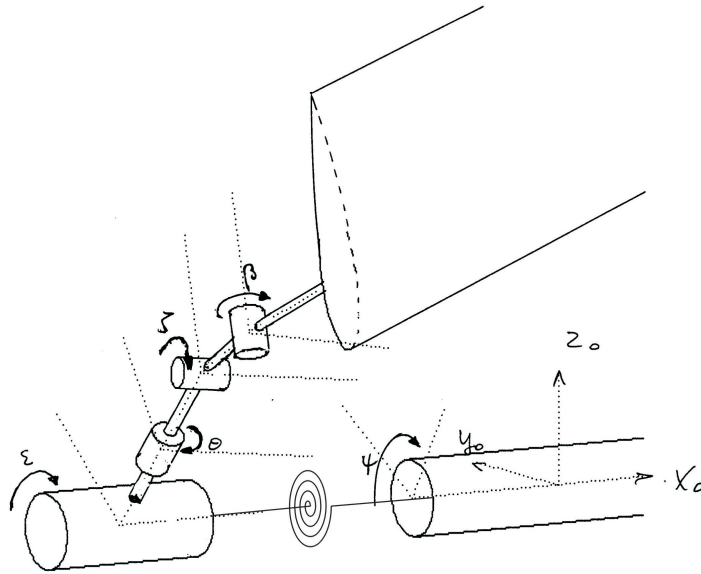


Figure 8.1: The baseline model, a model of an isolated blade. The model has three degrees of freedom:  $\varepsilon$ ,  $\zeta$  and  $\beta$ . The angle  $\theta$  is a constant angle. The shaft rotates with a constant rotational velocity  $\Omega$ .

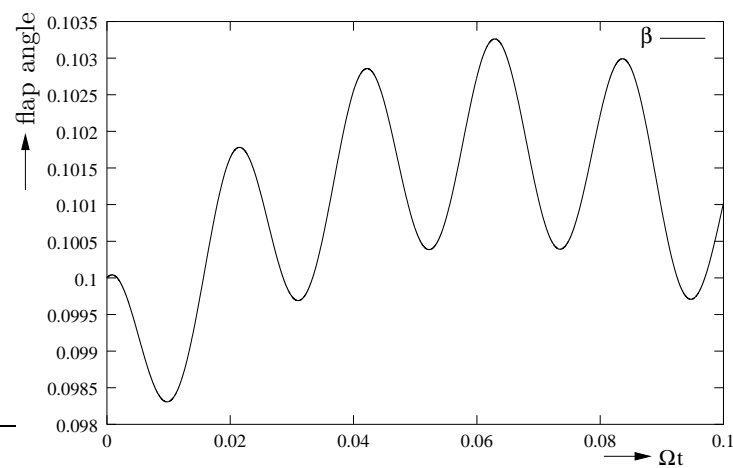


Figure 8.2: The flap angle for a simulation using the engineering solution for the needed fixed pitch angle.

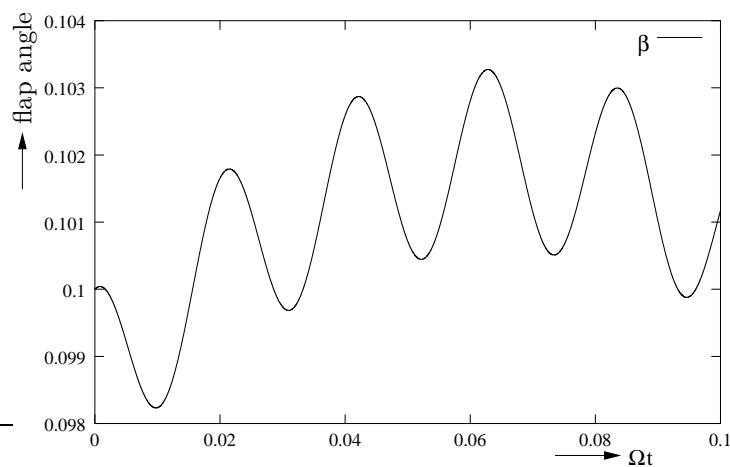


Figure 8.3: The flap angle for a simulation using the improved WOBBE code enabling the inclusion of a fixed pitch angle.

constant. This is shown in figure 8.7. Note that this figure zooms in on a small time frame.

As discussed in appendix E, the controlled rotations were also verified by simulating a very simple model for which the analytical result can easily be derived. The results of both methods were almost identical and the only differences can be explained to be due to the differences in the approach. The controlled rotations part of the programme has therefore also been verified.

### Automatic Calculation of Aerodynamic Forces

Another addition to the programme has been the automatic calculation of the aerodynamic forces. This way it is no longer necessary for the user to derive the equations for the aerodynamic forces. Adding the calculations of the aerodynamic forces resulted in two parts of the programme that were written in two different ways and for which the results could be compared.

First the calculation of the local velocities for the blade elements has been programmed using two different methods. The first method is described in 2.1.2, the second method uses equations 5.41 and 5.42. As both methods resulted in identical results, this part of the programme can also be considered to be verified.

Second the calculation of the generalised forces due to the aerodynamic forces has been implemented in two different ways: using the method described in 2.1.2 and using equations 5.48 and 5.49. Again both methods resulted in identical results and this part of the programme can also be considered to be verified.

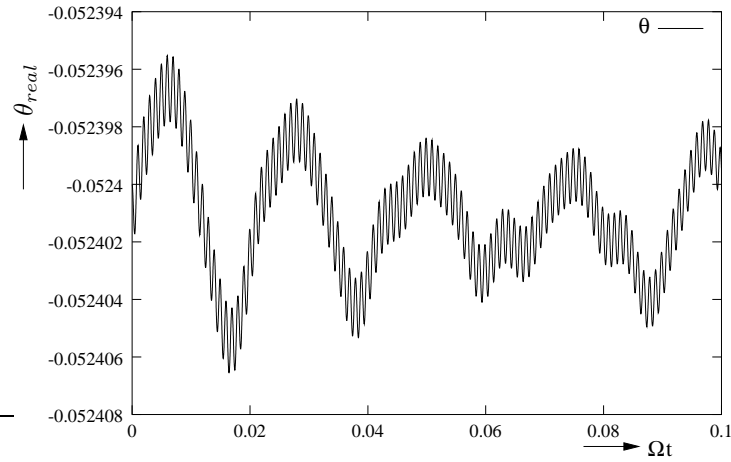


Figure 8.4: The pitch angle that is attempted to be kept constant using the engineering solution.

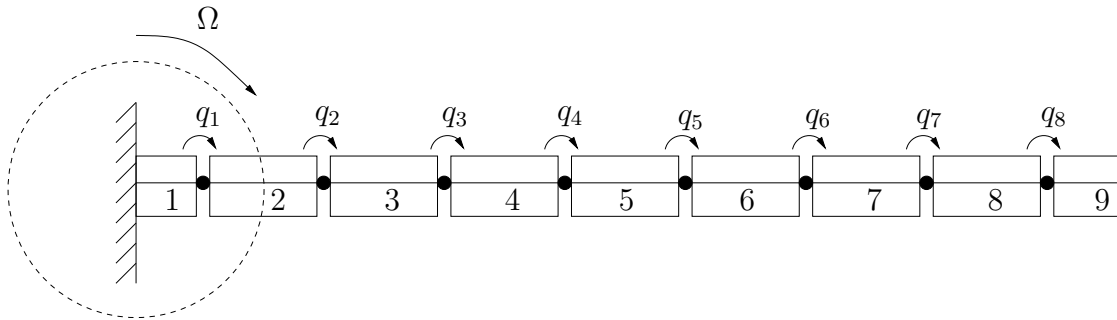


Figure 8.5: Euler-Bernoulli beam, with eight degrees of freedom. For the rotating beam calculations the root of the beam rotates with constant  $\Omega$

### 8.1.2 Euler-Bernoulli Beam

Small parts of the programme were verified during the development due to changing the methods of calculation, as discussed above. To verify the structural calculations of WOBBE, a model of an Euler-Bernoulli beam was used to determine its natural frequencies from the simulation results. The natural frequencies of this beam can also be determined analytically.

The beam is the same beam as analysed by Molenaar in [94]. It has a total length  $L = 50 \text{ m}$ , an area  $A = \pi \text{ m}^2$  and an area moment of inertia  $I = \frac{1}{4}\pi \text{ m}^4$ . The modulus of elasticity of the material of the beam is  $E = 21 \cdot 10^{10} \text{ N/m}^2$  and the density is  $\rho = 7850 \text{ kg/m}^3$ . The other properties of the beam are given in the first row of table 8.1.

To find the exact natural frequencies the following equation must be solved [145]:

$$\cos(kL) \cosh(kL) = -1 \quad (8.1)$$

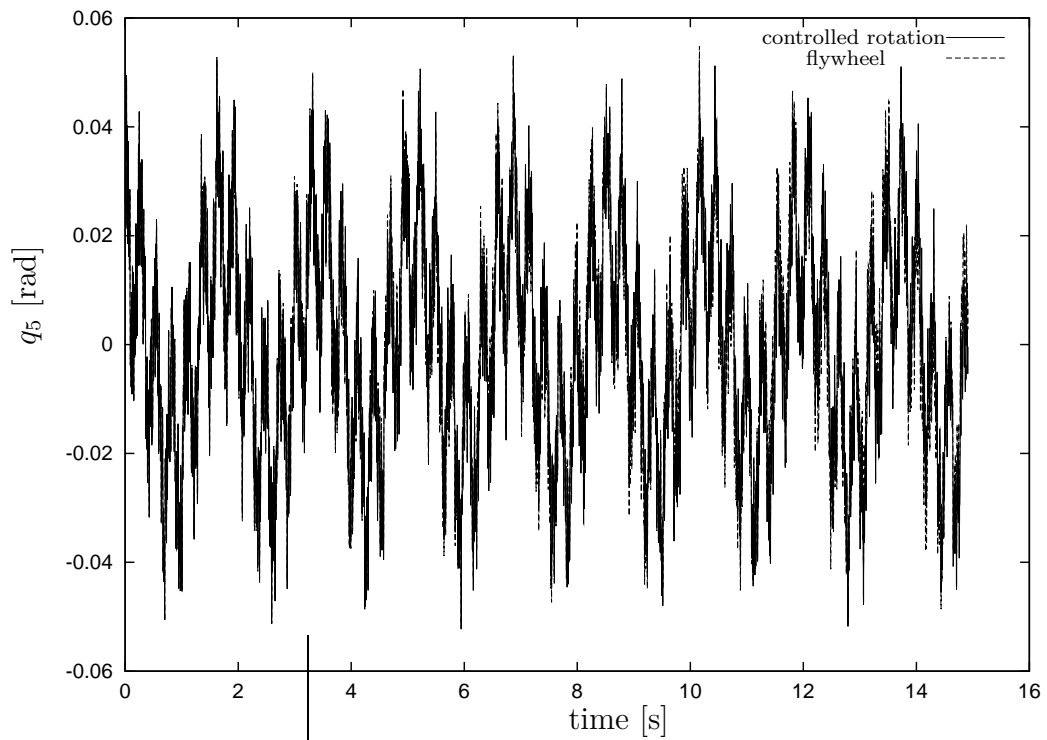


Figure 8.6: The output for DOF 5 for both methods.

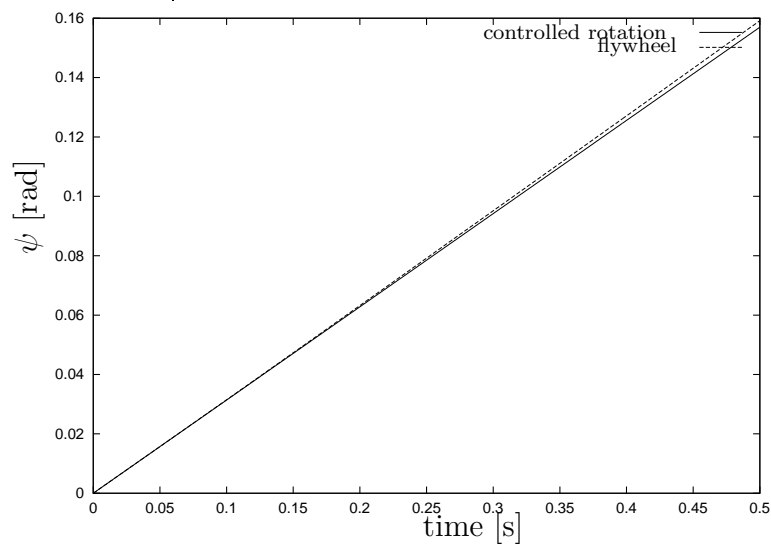


Figure 8.7: The angle corresponding to the constant rotation for both methods. This figure shows only 0.5 seconds in order to show the small difference.

element	length (m)	mass (kg)	$J_{xx} = J_{zz}$ (kg m <sup>2</sup> )	$J_{yy}$ (m <sup>4</sup> )	$c_{x1} = c_{x3}$ (Nm)
total beam	50	$1.23 \cdot 10^6$	$2.57 \cdot 10^8$	$6.17 \cdot 10^5$	—
1 and 9	2.64	$6.50 \cdot 10^4$	$5.40 \cdot 10^4$	$3.25 \cdot 10^4$	$2.64 \cdot 10^{10}$
2, 4, 6 and 8	7.23	$1.78 \cdot 10^5$	$8.20 \cdot 10^5$	$8.91 \cdot 10^4$	$2.64 \cdot 10^{10}$
3, 5 and 7	5.28	$1.30 \cdot 10^5$	$3.34 \cdot 10^5$	$6.50 \cdot 10^4$	$2.64 \cdot 10^{10}$

Table 8.1: Properties of the beam and the rigid bodies in the detailed superelement model

element	length (m)	mass (kg)	$J_{xx} = J_{zz}$ (kg m <sup>2</sup> )	$J_{yy}$ (m <sup>4</sup> )	$c_{x1} = c_{x3}$ (Nm)
total beam	50	$1.23 \cdot 10^6$	$2.57 \cdot 10^8$	$6.17 \cdot 10^5$	—
1 and 3	10.55	$2.60 \cdot 10^5$	$2.48 \cdot 10^6$	$1.30 \cdot 10^5$	$6.60 \cdot 10^9$
2	28.9	$7.11 \cdot 10^5$	$4.97 \cdot 10^7$	$3.55 \cdot 10^5$	$6.60 \cdot 10^9$

Table 8.2: Properties of the beam and the rigid bodies in the single superelement model

This equation holds for  $k_1, k_2, k_3, \dots$  and so on. Using

$$\omega_i = k_i^2 \sqrt{\frac{EI}{\rho A}} \quad (8.2)$$

the frequencies in radians per second can be calculated. For the chosen beam, the first four frequencies are given in table 8.3.

As described in 7.1, a good way to translate the Euler-Bernoulli beam into a rigid element model is using superelements. The Euler-Bernoulli beam has been simulated in WOBBE using a model with one superelement and a model consisting of four super elements. The single superelement model will entail three rigid bodies and have two degrees of freedom, the model with four superelements will consist of 9 rigid bodies and eight degrees of freedom as illustrated in figure 8.5. The properties of these rigid bodies are given in table 8.1. The properties of the rigid bodies in the model consisting of one superelement are given in table 8.2.

As discussed in chapter 6, WOBBE performs simulations in the time domain. These calculations are fully nonlinear and the results are the values of the different generalised coordinates ( $q_i$ ) at the calculated time steps. Therefore the natural frequencies are not readily available from the results, they need to be estimated by post-processing the results. The results for the simulations of this beam have been post-processed using a Fast Fourier Transform (FFT) (see appendix D). By determining the power spectral density (PSD) of the results using the FFT, it is possible to estimate the natural frequencies: the highest peaks in the PSD represent the natural frequencies. Note that when using an FFT, the highest frequency that can be analysed is the so-called Nyquist frequency which is equal to twice the sampling frequency, while the smallest possible difference between the discretely analysed frequencies is limited by the total time of the simulation  $T_{tot}$  as shown in D.1. The discrete steps that are taken in the FFT are equal to  $\frac{1}{T_{tot}}$ . The effect of leakage (nonzero values of the FFT at frequencies that are not present in the signal) will also be present in this post-processing

mode	exact [rad/s]	WOBBE ( $f_{i-1} \rightarrow f_{i+1}$ ) [rad/s]	error WOBBE
1	3.637	3.644 (3.519 $\rightarrow$ 3.770)	0.198 %
2	22.79	22.75 (22.62 $\rightarrow$ 22.87)	-0.197 %
3	63.82	63.08 (62.96 $\rightarrow$ 63.21)	-1.15 %
4	125.1	117.7 (117.6 $\rightarrow$ 117.9)	-5.88 %

Table 8.3: Exact frequencies and calculated frequencies by analysing the results of simulations with WOBBE using a model consisting of four superelements. The values of the frequencies analysed just above and just below the maximum are also given.

step. Therefore the natural frequencies determined from the simulations using the PSD will not perfectly coincide with the natural frequencies in the results, but will estimate these values with an accuracy that depends on the total simulation time. Consequently the determination of the natural frequencies using an FFT introduces an supplementary error in the results.

The results that were obtained from simulations of 50 seconds using 45000 time steps of the model illustrated in figure 8.5 are very close to the the analytical solutions as well as to the results obtained by Molenaar in [94] using another wind turbine simulation tool called DAWIDUM [93]. The high number of steps is needed because the highest frequency present in the simulations is above 180 Hz. This highest frequency comes from the high spring stiffness and the low inertia of the most outer rigid body, when using the detailed superelement model. When using Runge-Kutta's fourth order integration it is necessary to have time steps that are significantly smaller than this high frequency.

The frequencies that are found for the model consisting of four super elements and the exact natural frequencies for the uniform beam are shown in table 8.3. The results for the model that consists of one super element are shown in table 8.4. For both tables one must remember that there is possibly a supplementary error due to the size of the discrete steps in frequency taken when determining the PSD as described above. The values for the discrete frequencies just above and just below the value that has the maximum are also shown in the tables.

The tables show that WOBBE gives good results if four super elements are used, especially up to the third eigenfrequency. The results for one superelement illustrate that, by using one superelement, there is not enough detail in the model and it cannot be used in analysis if the second frequency is important, even the first frequency shows quite a large error. More information on the minimum number of superelements needed in a model can be found in chapter 9.

The same 50 meter long uniform beam has been simulated while rotating at different rotational velocities. This rotation, illustrated in figure 8.5, will result in centrifugal stiffening and therefore higher frequencies.

The natural frequencies of the rotating uniform beam can be estimated analytically and by analysing the PSD's of the output from WOBBE. The results of these analyses are shown in

mode	exact	WOBBE ( $f_{i-1} \rightarrow f_{i+1}$ )	error WOBBE
1	3.637	3.770 (3.644 $\rightarrow$ 3.896)	3.66 %
2	22.79	36.82 (36.69 $\rightarrow$ 36.95)	61.6 %

Table 8.4: Exact frequencies and calculated frequencies by analysing the results of simulations with WOBBE using a model consisting of one superelement. The values of the frequencies analysed just above and just below the maximum are also given.

figure 8.8. The calculation of the estimated eigenfrequencies [142] is described in appendix H. The results from the simulations in WOBBE are also shown in a table in this appendix.

Figure 8.8 gives a clear indication on the accuracy of the results from WOBBE. The natural frequencies found in the simulations are good up to the third natural frequency. This is a similar result as found before for the non-rotating beam. Chapter 9 further investigates the number of superelements that are needed in a model.

### 8.1.3 Structural Dynamics for Branched Systems

For branched systems, the structural dynamics part of the programme (so no aerodynamics included) has been verified using the model depicted in figure 8.9. When the simulation starts with the angle of the tower DOF equal to zero and the blades both at equal angles, one resulting in a deformation to the front and one to the rear, then the tower should not vibrate during the simulation. In other starting positions, the tower will take part in the vibration as it is excited by the imbalance in the blades.

The results of a simulation where the tower will take part in the vibration is given in figure 8.10. It is clearly visible that the blades excite the tower in this case. The results of a simulation where the blades are started such that the excitation on the tower of one blade will exactly be cancelled by the other blade are shown in figure 8.11. Zooming in on only the tower motion in figure 8.12 shows that the results for the tower are not exactly 0. This can be explained as numerical errors that will always be present in a programme due to the rounding off of numbers.

## 8.2 Benchmarking

A very useful test to investigate the reliability of a simulation tool such as WOBBE is to compare results with other programmes. This of course does not give any guarantee about the results, but it is a first step towards validation.

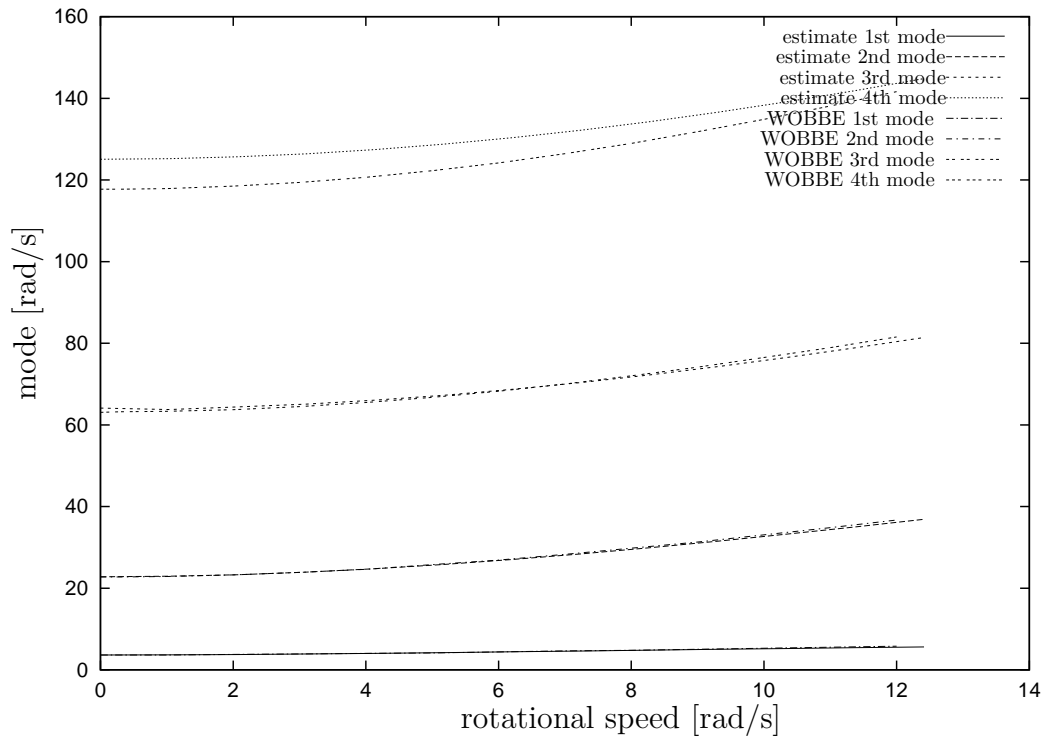


Figure 8.8: The first four frequencies of a rotating beam with in-plane flexibility; showing the calculated frequencies and the results from WOBBE using models consisting of four superelements.

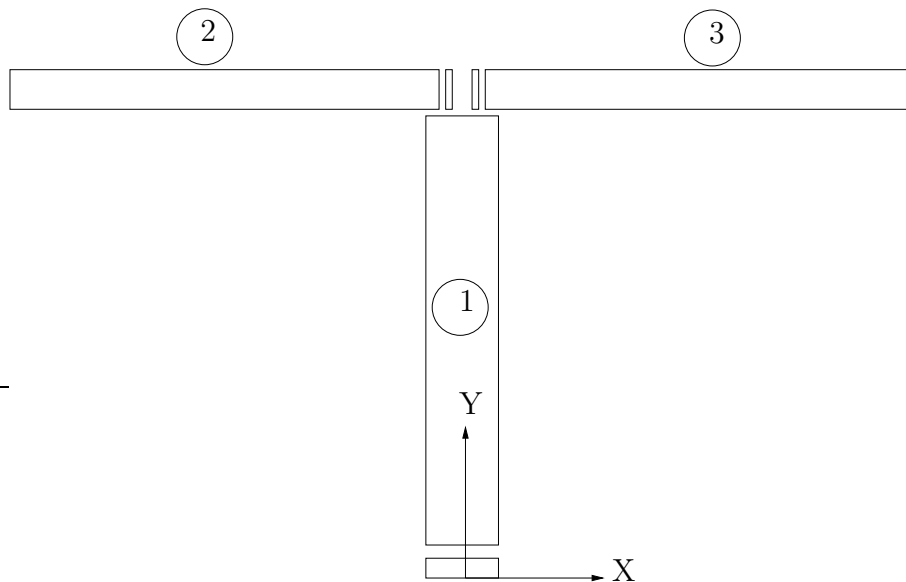


Figure 8.9: A tower (element 1) with a DOF about the x-axis and two blades (elements 2 and 3) with DOF's about the y-axis.

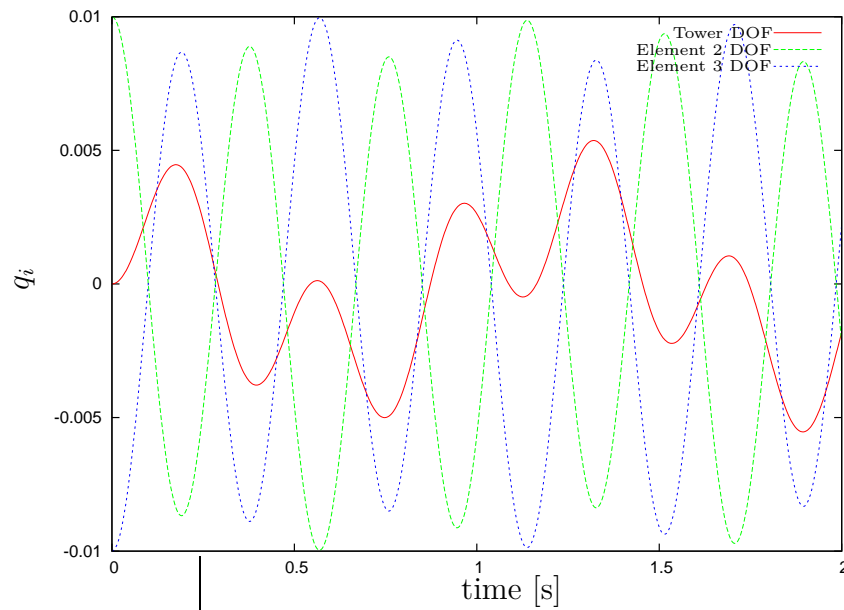


Figure 8.10: The response of the three DOFs in the test model, tower is excited by the blades.

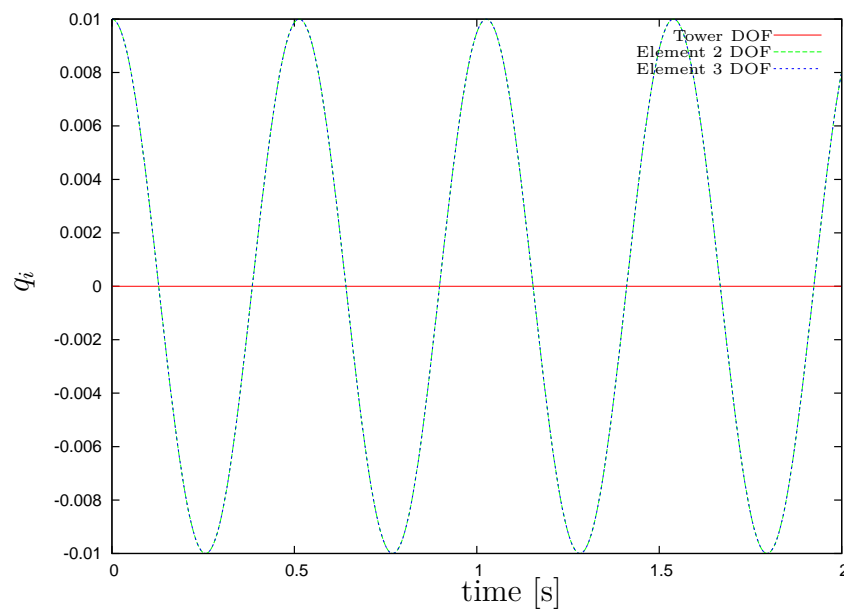


Figure 8.11: The response of the three DOFs in the test model, tower is not excited by the blades.

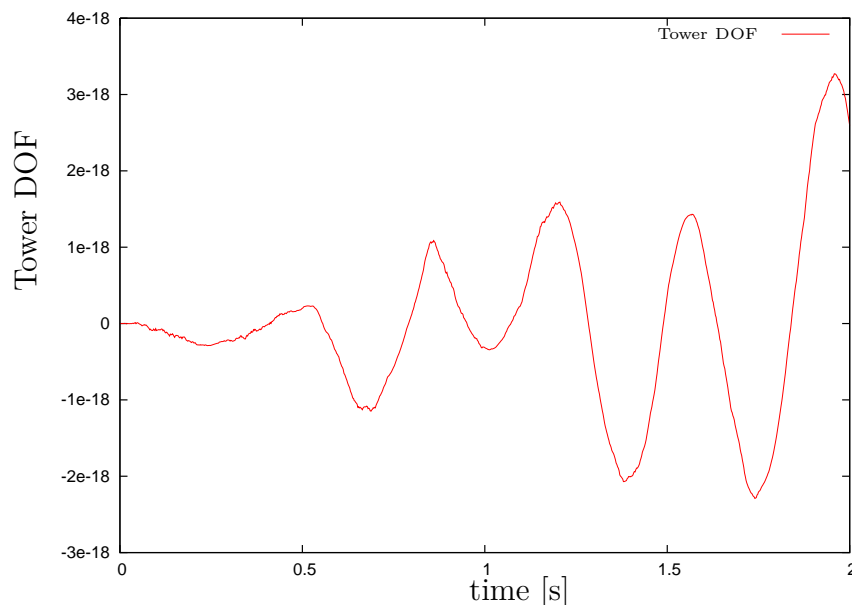


Figure 8.12: The response of the tower when the blades are started such that they should not excite the tower DOF.

### 8.2.1 LMH64-5

The first benchmark that was performed with WOBBE was the analysis of a new blade design during the DOWEC (Dutch Offshore Wind Energy Converter) project. This blade is part of a 6 MW turbine design with a diameter of 129 meters [27]. The main purpose for analysing the LMH64-5 blade was to judge its aeroelastic stability [50]. As the stability analysis was also performed using another tool and the frequencies were determined by several different tools, it can also be used as a sort of benchmark.

The model that was used in WOBBE for this investigation was a model of a single blade consisting of 14 elements with 14 degrees of freedom: 7 flap and 7 lead-lag. The model is based on using 3 superelements without torsion. The two extra degrees of freedom were at the root of the blade to model clamping stiffness.

The other tools that were used in this part of the DOWEC project were BLADMODE [82], PHATAS [74, 83] and FOCUS. The main result of the analysis was that the blade would be stable in the entire operational range, but the aerodynamic damping for low wind speeds (below rated) was minimal. The results from WOBBE compared well to the results from BLADMODE. Both WOBBE and BLADMODE did not show actual instabilities, both tools found less damping for the wind speeds below rated. The low damping is for example illustrated in figure 8.13, which shows the response of the blade for one of the flatwise degrees of freedom with an excitation at  $t=2$  s. The excitation is slowly damped out, while usually the flatwise modes are well damped for wind turbines. Only if the angle of attack gets too large, then the damping of the flatwise modes can become much smaller or even negative.

The small damping of the flatwise mode was caused by the large angle of attack.

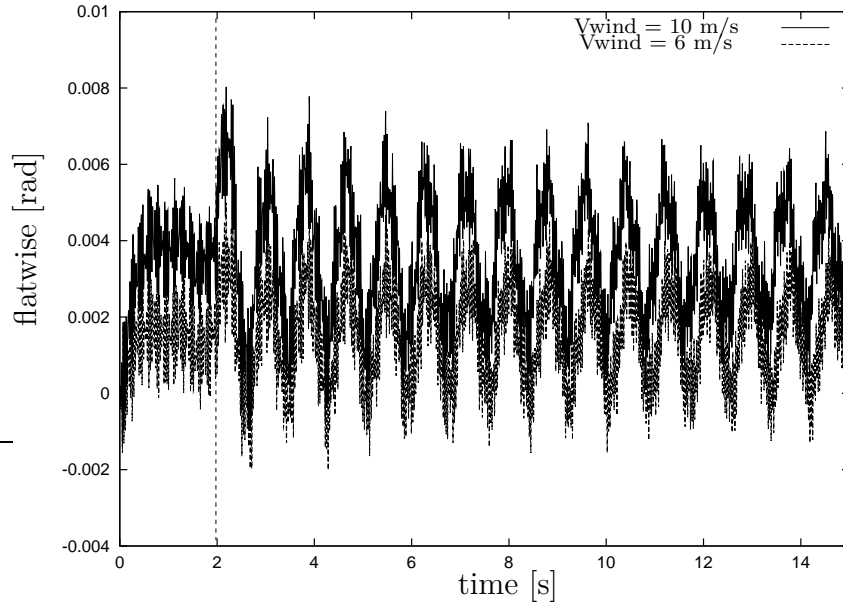


Figure 8.13: The response of the blade for a wind velocity of 6 m/s and 10 m/s

The frequencies that were determined by different tools also corresponded reasonably well to the frequencies calculated using WOBBE, as shown in table 8.5. The power was overestimated by WOBBE, but especially when taking into account the limitations at that stage in the development of WOBBE that can explain the differences in the power and frequency results, this benchmark can be considered successful. First, the power was overestimated due to the absence of the option of using Prandtl's tip correction in WOBBE at that time. Second, the calculation of the model properties was not yet very good. The root part of the blade has a much higher stiffness than the remainder of the blade and this high stiffness was included in the calculation of the average stiffness for the first superelement. As discussed in section 7.2, this is not the correct approach and it has a large impact on the frequencies. It will give a slight increase to the edgewise frequencies and increase the flap frequencies considerably. Third, the post-processing of the results was not yet done using system identification. Keeping this in mind, the comparison between the results of the different codes was satisfying.

## 8.2.2 STABCON Benchmark

During the European project STABCON [86], several aeroelastic programmes have taken part in a benchmark [115]. For this benchmark a model was used that is based on a wind turbine of NEG Micon, the NM80. The real wind turbine blade has been simplified by

	WOBBE	BLADMODE	PHATAS	FOCUS
rpm	11.844	11.8	11.8	11.0
Flat-1	0.76 Hz	0.683 Hz	0.675 Hz	0.702 Hz
Edge-1	1.18 Hz	- -	1.107 Hz	1.140 Hz

Table 8.5: Frequencies for different modes as analysed by different programmes. The analysis was performed for different rotational velocities  $\Omega$  by the different tools, as shown in the second row.

neglecting the structural pitch and assuming the c.g., a.c. and e.a. to be on the pitching axis. Different codes have been used to analyse this model in order to compare the results of the different programmes.

The model of this isolated blade used in WOBBE consists of 3 superelements. This results in a model that has 15 degrees of freedom. The blade has 3 torsional, 6 flap and 6 lag degrees of freedom, see figure 8.14. Looking at the results obtained for the uniform beam (see section 8.1.2), three superelements should result in good approximations of both the first and second flatwise and edgewise frequencies.

The simulations have been performed for several uniform horizontal constant wind velocities. Dynamic inflow is used; the induced velocity changes in time using the model described in section 3.1.7, but once the simulation is running, the induction factor will very quickly become almost constant. To calculate the induced velocity, the fact that it is a three bladed wind turbine is taken into account. This means that all forces on the blade are multiplied by three when calculating the induced velocities. Prandtl's tip correction (see section 3.1.8) has been used in WOBBE and in all other tools. The multi-blade effects have not been taken into account in the isolated blade analysis.

As described in the next section about the validation, comparing results to measurements is not an easy task. Comparing the nonlinear results of WOBBE to the results of other, linear programmes is neither straight forward. The results that have been compared are the power and thrust for different wind speeds, the axial and tangential induced velocity at different wind speeds, the natural frequencies and the corresponding damping coefficients at different wind speeds. These last two are the most important results for aeroelastic tools. They are also the most difficult results to distill from the time series produced by WOBBE.

The power and induced velocity are output from WOBBE. The only post-processing needed here before comparison is possible, is taking the average result of the last part of the simulation, where the turbine is operating around the steady state. The initial excitation given at the start of the simulation will influence the power and induced velocity in the first part of the simulation and therefore only the final part of the simulation should be used when determining the average power and induced velocity.

The power curves for all partners and the nominal power of the real turbine, the NM80, are shown in figure 8.15. This figure illustrates that the results obtained using WOBBE compared very well to the results of the other partners in the STABCON project. The same

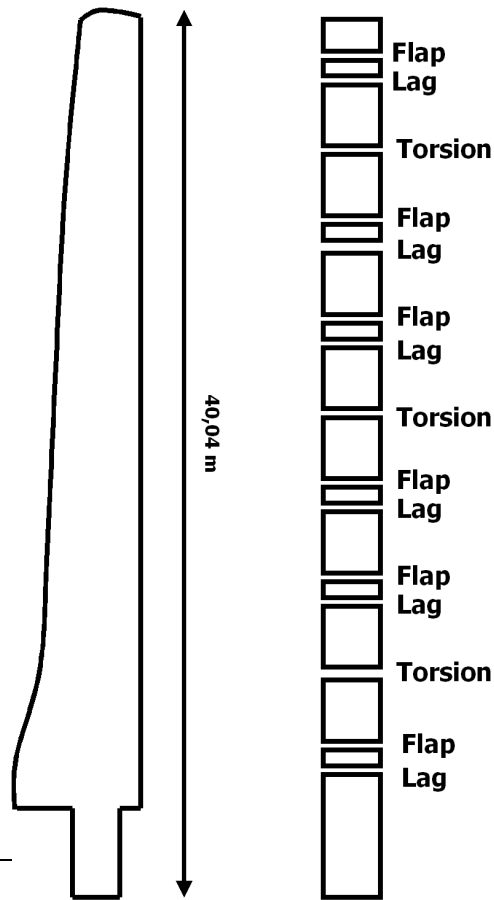


Figure 8.14: The model of the isolated blade. Three superelements are used. The elements between the lead-lag and flap hinges are kept very small.

goes for the thrust. As displayed in the figure, the results from WOBBE showed to be about the average of all partners for the whole wind speed range (5-20 m/s).

The assumption of constant axial induced velocity over the rotor plane as it is used in WOBBE, was not used by any other partner in the project. All other codes used the annulus approach for determining the induced velocity, as can be seen in figure 8.16. As discussed in 3.1.5, both methods are approximations. For the results of the induction factors of WOBBE to be judged as comparing well to the other results, it can be expected that the constant induced velocity of WOBBE is somewhere in the range of the average value along the radius calculated using the annulus approach. Figure 8.16 illustrates that this was indeed the case. It can be concluded that the induced velocity compared well to the other codes' results. The assumption of constant induced velocity over the rotor plane results in higher induced velocities near the root and tip when compared to the annulus approach and lower induced velocity for the middle section of the blade. Due to this difference, it can be expected that the tangential velocity will also differ from the results obtained by the other codes. The tangential velocity, as calculated by WOBBE, was somewhat lower for the middle part of

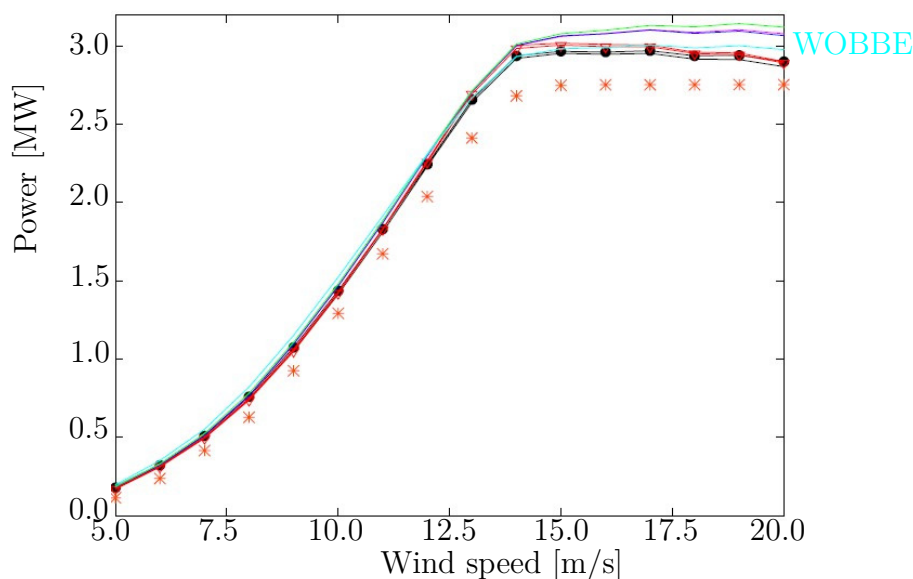


Figure 8.15: The power curves of the benchmark models calculated using isolated blade models. The results obtained using WOBBE are given in cyan, the red asterisks depict nominal power of the NM 80.

the blade and somewhat higher near the root, as was expected from the difference in axial induced velocity. This is illustrated on the right hand side of figure 8.16.

The difference in distribution of the induction factor will result in larger angles of attack in the mid part of the blade and smaller angles of attack near the root and tip. However, the forces near the root will be small compared to the forces on the remainder of the blade due to the small velocity in this part of the blade ( $V \approx \Omega r$ ) and the forces near the tip will be small due to Prandtl's tip correction. Therefore it can be expected that the assumption of constant induced velocity along the blade will have, as a main difference, slightly larger angles of attack in the mid of the blade which can result in smaller damping values as the effect of the smaller angles of attack near tip and root can be expected to be much less and not large enough to compensate for the difference at the mid part of the blade.

Damping can easily be determined from the results of the linearised programmes. As mentioned before, for nonlinear programmes like WOBBE, it is not so straight forward. For example figure 8.17 shows that vibrations of many different frequencies are combined forming the resulting output. Therefore the damping cannot be determined immediately. As discussed in section 8.1.2, it is possible to determine the natural frequencies using an FFT, but to determine the damping is a little bit more complicated. Several different methods have been investigated and are discussed in appendix D. When the simulation is performed for very small deflections about the equilibrium state, the results will be almost linear and the post-processing analysis to determine frequency and damping is best performed using a system identification tool (see appendix D.3). When the simulations are strongly nonlinear, there is in fact not one damping coefficient for every natural frequency, the damping will vary

in time and depend on the amplitude and it is not possible to distract one coefficient from the results. The frequencies will also not have constant values. In those cases it will only be possible to give a judgment on the stability. If the amplitude is decreasing quickly after the start of the simulation, the configuration seems stable. If the amplitude is increasing often only after quite a long simulation time, then the configuration is unstable. Note that it is possible that for example most modes are strongly damped, but one mode is negatively damped which might only show up if the simulation has run for a long enough time; the amplitudes of all positively damped modes will first show the large decrease due to the high damping and the effect of the negative damping is not visible in this first part of the simulation. It becomes visible much later on in the simulation. Therefore giving a judgement on the stability in these cases is also not straightforward.

The simulations of the isolated blade have been analysed using a system identification tool (see appendix D.3). By using system identification it was possible to determine the natural frequencies and corresponding damping coefficients in the simulation results. Compared to the results of the other partners in the STABCON project, the natural frequencies were within the range of the other partners, as shown in figure 8.18. The third mode found using WOBBE was however the lowest of all, with a difference of 0.1 Hz with the second lowest result.

The damping coefficients obtained by WOBBE showed the same trend in wind speed as the other partners. As an example the damping of the first flap mode is illustrated in figure 8.19. The damping of this mode is lowest around 6 m/s and 13 m/s, it is however always above a logarithmic decrement of 100%, often even above 200%. The damping values found by WOBBE for this mode are however substantially smaller than most other tools predict, though there is one other tool that predicts lower damping values for most wind speed values. As shown in figure 8.19, WOBBE predicts a 25% to 50% lower logarithmic decrement for the damping than most of the other codes. This difference might be due to the difference in approach in the calculation of the induction factors, a larger angle of attack can have a large effect on the damping of the flap mode.

For the first edgewise mode the results are similar. The first edgewise mode does not show large damping, but there is again a dip around 13 m/s, as shown in figure 8.20. All codes actually predict negative damping for this wind speed. Recall that these calculations were on a benchmark model where the structural pitch was assumed to be zero along the radius. As discussed in chapter 10, the structural pitch angle has an important stabilising effect on this mode. Next to this, the structural damping has not been taken into account, therefore it can be expected that for this benchmark model around rated (14 m/s) the damping of the first edgewise mode becomes small or even negative. The damping values found using WOBBE in the positive damping range are about the same as the other codes. The negative damping that is derived from the simulation results at 13 m/s is the most negative of all codes, but the logarithmic damping values are very small; they are all less than -2%. Note that when negative damping is present in the model, it becomes more difficult to estimate the damping value from the results from WOBBE, because the system identification will

only give good results if the signal is close to linear, meaning that the amplitudes must stay small. In case of negative damping the amplitudes will not remain small, they will increase in time, making it impossible to create a large enough data set that can be considered linear.

The results for the second and third flap mode were rather similar, the trend is well predicted by WOBBE, but the damping values are somewhat lower than predicted by the linear codes of the other partners. The results for the second flap mode are illustrated in figure 8.21.

Using the system identification tool it is also possible to determine the mode shapes. The first flapwise and the first edgewise structural mode shape (without the influence of aerodynamics) of the isolated blade have been determined using system identification. These structural mode shapes were compared to the mode shapes obtained by the other codes. For all partners in the STABCON project there was a very good correspondence in these mode shapes as can be seen in figures 8.22 and 8.24.

The complete results are given in the (confidential) task-1 report [115].

## 8.3 Validation of WOBBE

The previous sections in this chapter have dealt with verification of the programme WOBBE, although some results could also be considered as validation of the code. For example the aerodynamic power which can be compared to the real power of the turbine, but the main focus of those calculations was on the verification of the code.

This section will discuss the validation of WOBBE. The validation was performed by comparing the results of WOBBE to measurements on a real turbine, the NM-80. This validation process was also part of the STABCON project [86].

The wind turbine that has been used, the NM80 is a three bladed turbine with a diameter of 80 meters. It is a pitch regulated variable speed turbine that has a rated power of 2.75 MW.

### 8.3.1 Measurements for Validation

In order to validate the codes, a comparison between measurements and calculations is necessary. A full size NM80 wind turbine has been used for measurements [46]. The bending moments can be derived from measurements with strain gages at the root of the blades and on the tower. Two different methods have been used by Risø to measure the damping coefficients. First, different modes were excited in their natural frequency using pitch excitation or variation of the generator torque. Second, operational modal analysis based on stochastic subspace identification (SSI) has been used. SSI is a form of identification that can take into account the stochastic parts in the signal [105]. Using this method, a linear model of the turbine is estimated from which the natural frequencies and damping can be determined.

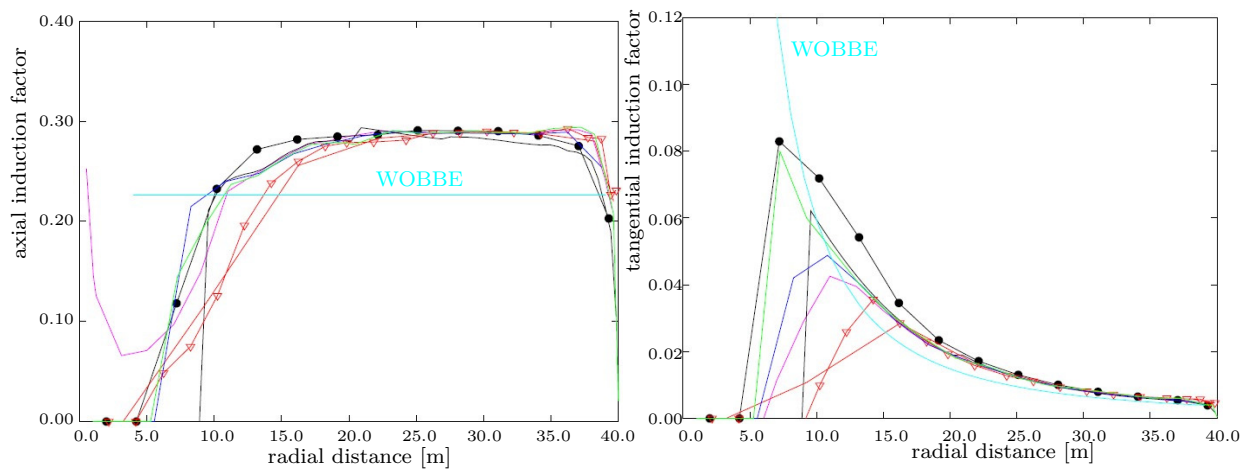


Figure 8.16: The axial and tangential induced velocity along the radius for a wind speed of 10 m/s for the benchmark models using isolated blade models. The results obtained using WOBBE are given in cyan.

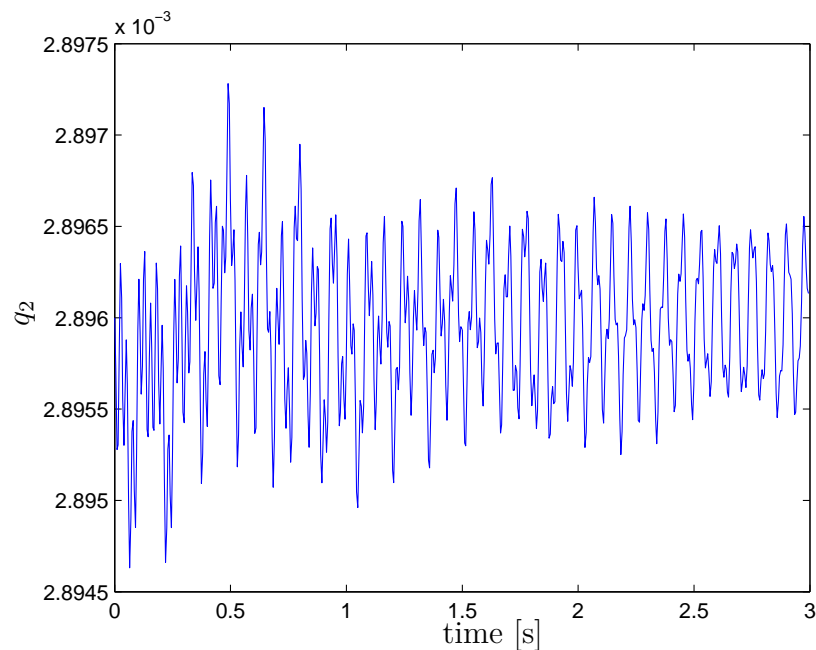


Figure 8.17: Example of a nonlinear vibration, the result in time for the first flap hinge in the blade model.

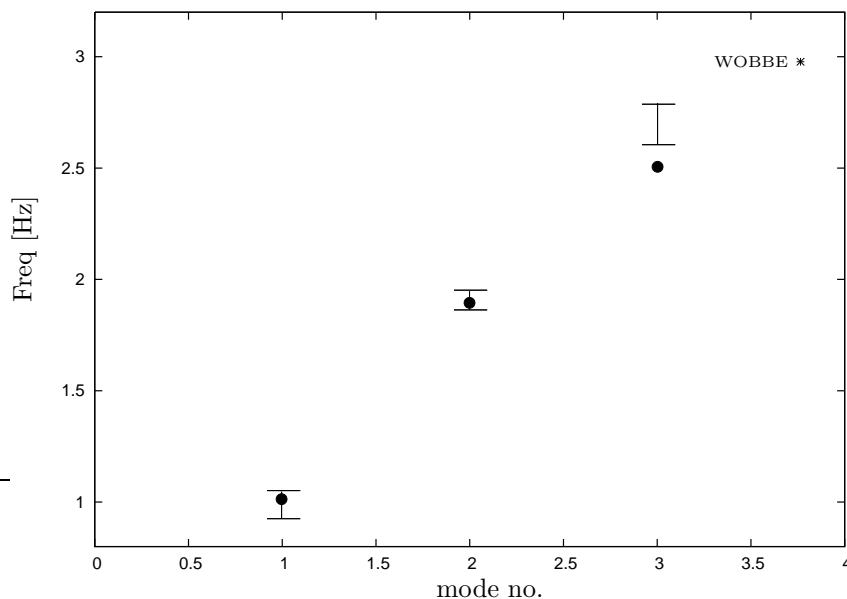


Figure 8.18: The frequencies of the first three modes of the blade. The range of the results obtained by the different partners is illustrated and the value as found using WOBBE is explicitly shown.

Exciting the eigen modes was found to be possible for only a few modes. Tower vibrations were excited using pitch excitation, however it was not possible to excite purely the longitudinal mode. As soon as the pitch excitation stopped, the motion would change from the well damped longitudinal mode towards the badly damped lateral mode, therefore the damping measured was not purely the damping of the longitudinal mode. This effect has not been attempted to be reproduced by the tools, but it can be expected that the linear tools will not predict this effect. Due to the limitation of the electrical pitch actuators, it was not possible to excite the flap modes or the edgewise whirling modes using the pitch, the pitching velocities needed for this excitation were higher than the actuators could deliver.

The electrical generator torque can also be varied in order to excite certain modes of the wind turbine. The lateral tower mode has been excited using this method and the damping was determined from the decaying response once the excitation halted.

Using the operational modal analysis based on stochastic subspace identification, it was possible to analyse more modes than with the excitations. The closeness of the different natural frequencies is not a problem when using this method. However, it is necessary to obtain long time series, therefore only closed loop operations can be analysed whereas the excitation methods only need short time series and therefore give the opportunity to analyse the damping in open loop operation [45, 46].

Next to this, the wind speed out in the open is not something which can be controlled. It will not be constant throughout the measurement and there will always be turbulence

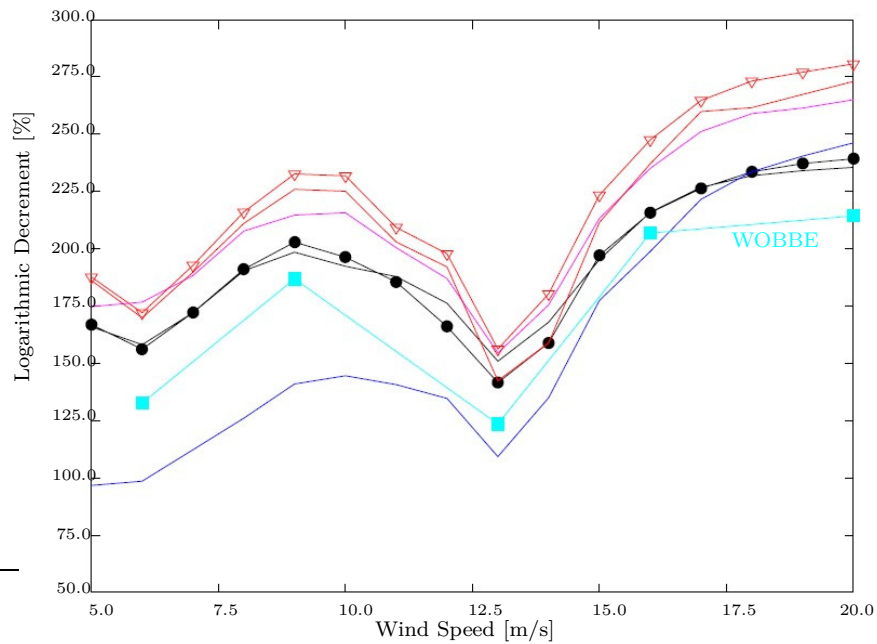


Figure 8.19: The damping of the first flap moment for different wind speeds for the benchmark models of an isolated blade. The results obtained using WOBBE are given in cyan.

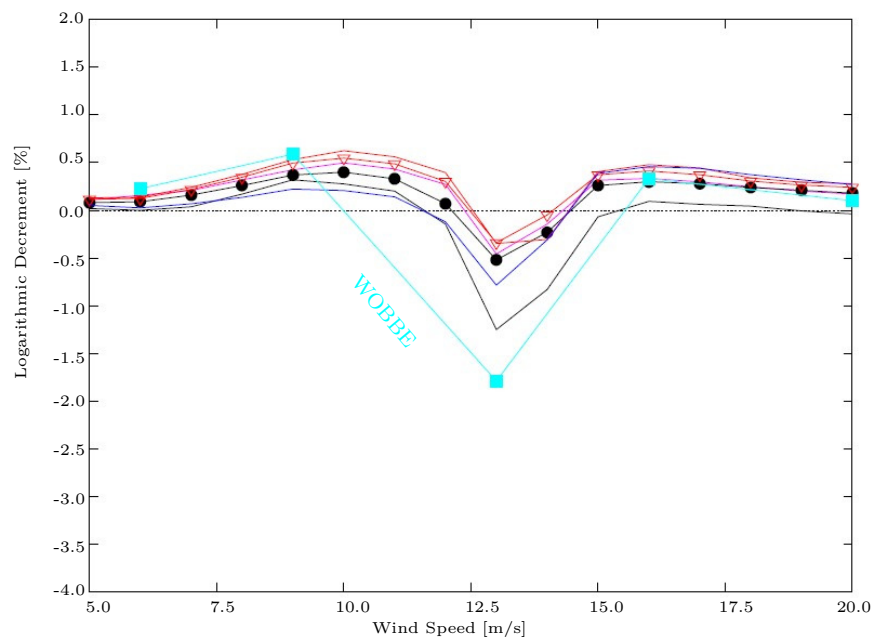


Figure 8.20: The damping of the first lead-lag moment for different wind speeds for the benchmark models of an isolated blade. The results obtained using WOBBE are given in cyan.

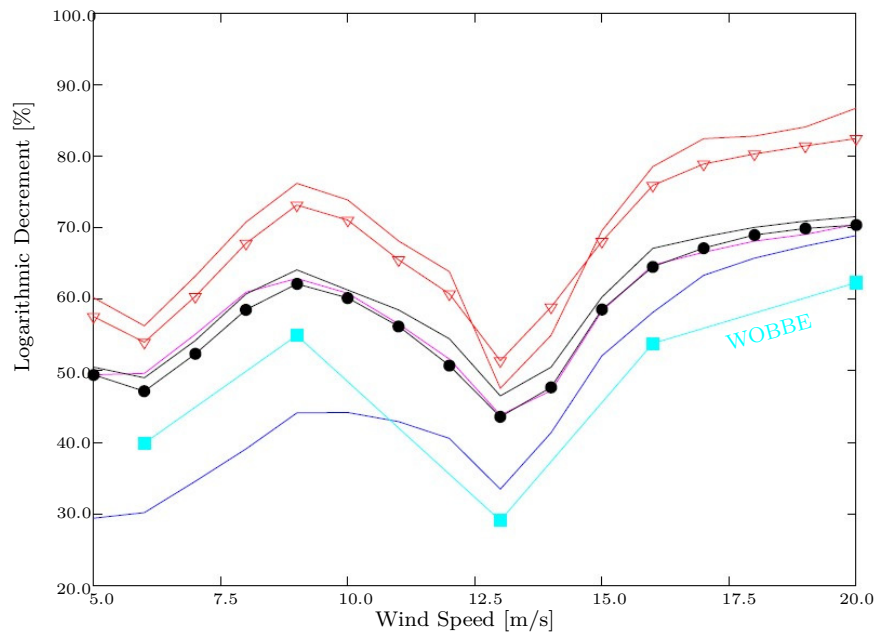


Figure 8.21: The damping of the second flap moment for different wind speeds for the benchmark models of an isolated blade. The results obtained using WOBBE are given in cyan.

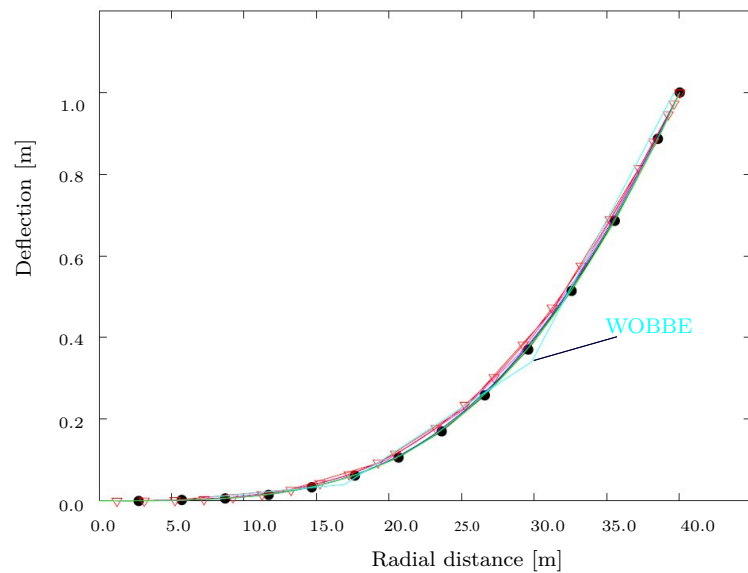


Figure 8.22: The first flap mode shape for the benchmark models of an isolated blade. The results obtained using WOBBE are given in cyan.

and shear flow. Within WOBBE these effects are not taken into account, therefore the comparison between the measurements and calculations is not performed for completely similar conditions and differences can be expected. It will be difficult to state how much difference there is in the results of the comparison due to the difference in conditions (non-uniform wind), the inaccuracy in the measurements, possible differences between the real turbine and the design properties and the inaccuracy in the programme and model. On the other hand, the programmes have been created in order to predict the aeroelastic stability of real wind turbines. Therefore the codes will only be useful, if the prediction gives some indication about the real stability situation.

### 8.3.2 Model of the NM80 in WOBBE

The complete NM80 turbine has been modelled and simulated. The model consists of foundation, tower, nacelle, shaft and blades. It has 27 degrees of freedom.

The foundation stiffness is modelled using two springs at the bottom of the tower, to enable the tower to bend sideways and fore/aft. The tower is modelled using one superelement without torsion. The yaw, tilt and roll of the nacelle are modelled with three springs, one in each direction. At the part of the shaft closes to the generator a constant velocity  $\Omega$  is inserted in the model, keeping the rotational velocity of this part of the shaft constant. This corresponds to an ideal generator that keeps the velocity of the shaft perfectly constant, possibly at a different constant velocity for each given operational setting in case of a variable speed wind turbine. The shaft itself has been modelled using two torsional degrees of freedom and two degrees of freedom for sideways bending and two for up/down bending of the shaft. The stiffnesses of the two torsion springs have been slightly adjusted in order to tune them towards the measured stand still natural frequencies.

The blades are modelled using one superelement without torsion. Using a model of the blade consisting of one superelement and comparing it to a more detailed blade model with 15 degrees of freedom, the springs have been tuned to get the correct first flap and first lag frequencies in the simplified blade model. The detailed blade model differs from the benchmark model discussed in section 8.2.2 only in the inclusion of structural pitch and not assuming the c.g., e.a. and a.c. to be on the pitch axis, but using their real positions. The blade model with four degrees of freedom that is tuned using the detailed model model also includes structural pitch and the positions of the c.g., e.a. and a.c.

In total the wind turbine model has 27 degrees of freedom: 2 in the foundation, 4 in the tower, 3 in the connection of the nacelle, 6 in the shaft and 4 in each of the three blades. The complete model is illustrated in figure 8.23.

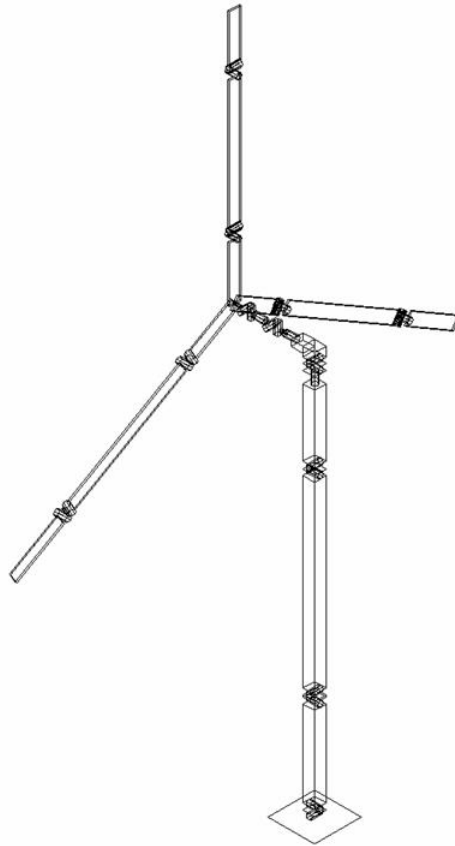


Figure 8.23: The model of the NM80 with 27 degrees of freedom

### 8.3.3 Comparison of Measurements and Simulation Results

The simulations of the 27 DOF model have resulted in different quantities that can be compared to measurements. First of all there is the power that can be compared to the real power obtained by the wind turbine for the different wind speeds. The power found in the simulations was somewhat higher than the measured values. This difference is expected because the turbulence in the flow will reduce the power and, more importantly, the losses between aerodynamic and electrical power were not taken into account in the simulations with WOBBE, but they are included in the measured power. The general trend and approximate values compared reasonably well to the measurements, similarly to the power results shown in the previous section discussing the benchmark model in STABCON.

The measured natural frequencies and damping coefficients have also been compared to the calculated values. To extract the natural frequencies and damping coefficients, the system identification tool AerID has been used. Because the steady state of a wind turbine is not a constant, but depends on the azimuth angle, AerID has been adjusted to handle this periodic steady state, as is explained in D.3. Due to the large computation time that was needed to first find the steady state and then complete a simulation that starts with a small deflection

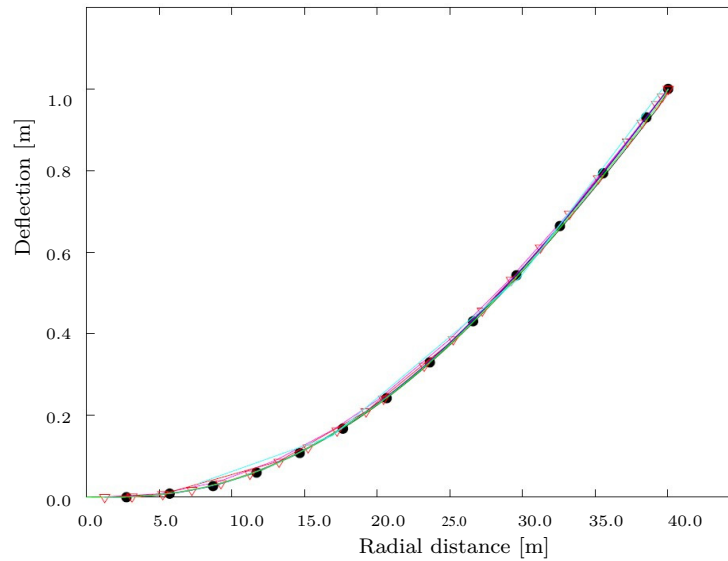


Figure 8.24: The first edgewise mode shape for the benchmark models of an isolated blade. The results obtained using WOBBE are given in cyan.

from the steady state, only at three wind velocities and corresponding operating conditions were analysed: 7 m/s, 9 m/s and 19 m/s. For these three wind speeds, it was possible to find some of the natural frequencies and their damping coefficients. Some modes were not found. These were probably not excited enough in the simulations to be identified from the results. For instance the backward and forward edgewise whirling modes could not be identified from the results of WOBBE and therefore these results could not be compared to the measurements.

The tower modes were predicted by WOBBE and some of the results of this are shown in figures 8.25 and 8.26. First figure 8.25 shows the frequencies of the first longitudinal tower mode. It shows the measurements, the results obtained using WOBBE as well as the results obtained by the other tools that were used during the STABCON project. Note that using WOBBE only 7 m/s, 9 m/s and 19 m/s wind speeds were analysed. The results show that WOBBE's results are actually for wind speeds for which no measurements are available. They also show that the differences between the different codes and the measurements are less than 0.08 Hz. Note that the dip around rated does not show up in WOBBE's results, as there was no simulation performed for wind speeds in that range.

Figure 8.26 shows the damping of the first lateral tower mode. Again the measurements and all STABCON results are shown in the picture. Almost every tool gives less damping than the measurements. The results from WOBBE correspond well to the results obtained by the other tools. If structural damping had been included, the damping values would be somewhat larger, but still less than the measured results. The damping of both the lateral and the longitudinal tower modes showed higher measured values than the calculated values by the different tools. In [52] several different possible explanations are given for this

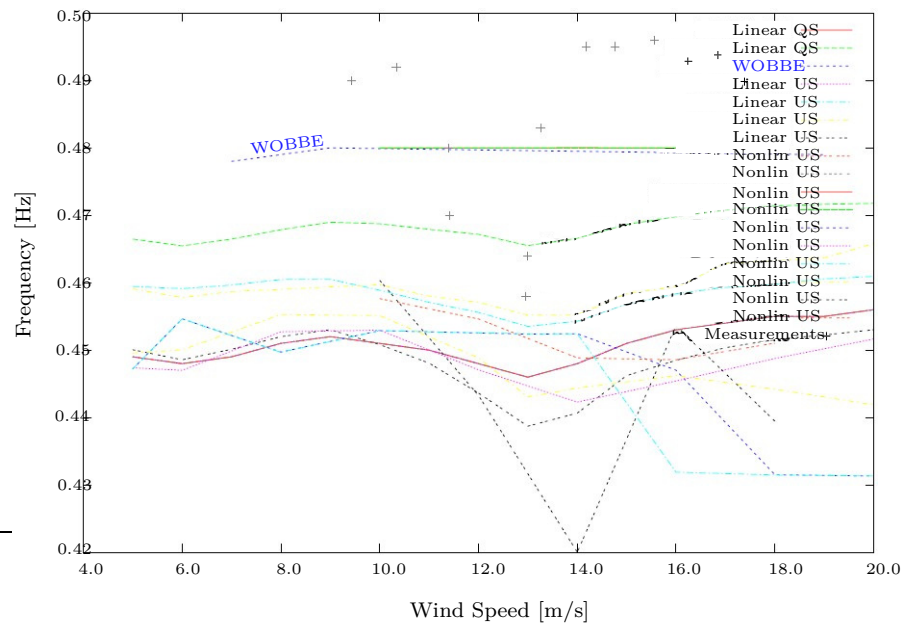


Figure 8.25: The frequency of the first longitudinal tower mode. The measurements are shown with +, WOBBE is the dashed dark blue line. For the other codes that were used in STABCON it is stated if it concerns a linear or nonlinear code and if the aerodynamics were modelled as quasi steady (QS) or unsteady (US).

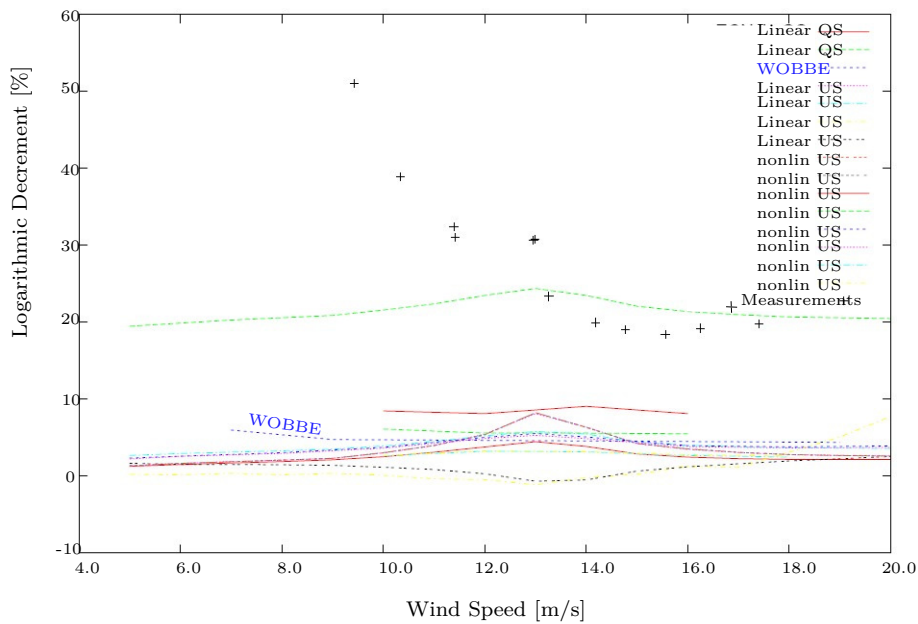


Figure 8.26: The damping of the first lateral tower mode. The measurements are shown with +, WOBBE is the dashed dark blue line. For the other codes that were used in STABCON it is stated if it concerns a linear or nonlinear code and if the aerodynamics were modelled as quasi steady (QS) or unsteady (US).

difference: it could be due to a damper in the tower top or due to the effect of the active controller that gives high damping.

The complete validation results are given in the (confidential) task report D4 [52].

## 8.4 Alterations to WOBBE due to Validation

The major problem for WOBBE during the STABCON project was the calculation time needed to simulate a complete wind turbine model. Therefore several improvements have been implemented that are already included in the discussion in chapter 6. Next to changing the programme to reduce calculation time, it was necessary to reduce the models complexity. The intended model with 51 degrees of freedom was reduced to a model with 27 degrees of freedom. In this new model the number of degrees of freedom for the tower and for the blades have been reduced, for each of these only four degrees of freedom were kept: 2 flap and 2 lead-lag or 2 sideways and 2 fore/aft in case of the tower. Due to the loss in detail in the blades and tower, these elements had to be tuned to the correct frequencies. For every configuration used (pitch angle and rotor velocity) the blades were first tuned to the correct frequencies by changing the stiffness. The rotational velocity of the blades has a large effect on the eigenfrequencies if only one superelement is used. For this reason simulations were run using a single blade model consisting of 3 superelements including the torsional degree of freedom. The results of these simulations resulted in the frequencies the simplified blade model consisting of one superelement was tuned to. To tune this model, the simplified blade has been simulated as a single blade as well, using different stiffnesses of the springs resulting in different eigenfrequencies. This way the model of a blade was tuned to the values obtained for the more detailed model consisting of three superelements. The tower has been tuned to the measured stand still frequencies. This has resulted in a model and a code combination that could simulate the complete turbine for 80 seconds in a few hours.

Before the refinement during the STABCON project were implemented, it was not possible to let the so-called dummy elements generate aerodynamic forces. Dummy elements are elements that can rotate at a given speed and therefore do not have a real degree of freedom. These dummy elements are among other used to keep the rotational speed constant. They are situated at the beginning of the blade, starting in the rotor centre. For the blade models, the length of these dummy elements is usually relatively small. However, for the reduced complexity of the blade model, these dummy elements become much larger than before. For a blade model consisting of three superelements, the dummy elements would have a length of close to 4 meters, measured from the rotor centre. While for the model using only one superelement, the length of the dummy element at the root of the blade becomes as large as 9.4 meters. For the detailed model, the dummy element of 4 meters would not generate aerodynamic forces, which is close to the truth. However for the simplified blade models, the dummy part becomes too large to be able to neglect the aerodynamic forces acting on this part of the blade. It will contribute considerably to the aerodynamic forces. Therefore, this

must be taken into account. WOBBE has been adjusted so that the dummy elements can be treated similar to the other elements in the blade during the calculation of the aerodynamic forces.

Using the reduced blade model also led to large differences between the real chord distribution and thickness distribution of the blade and the size used in WOBBE. This was caused by the fact that the chord and thickness were initially linearly interpolated between the beginning of the element and the end of the element. When using only one superelement this linear interpolation differs significantly from the real distribution of the chord and thickness. In order to reduce the differences between the values of the chord and thickness in WOBBE and of the actual wind turbine blade, an extra option has been implemented into WOBBE. The chord and/or thickness can now be either modelled as before by linear interpolation between values at the beginning and end of the element, or by a polynomial function up to the sixth order. For the model of the NM80 that produced the results in the previous section both the chord and the thickness have been modelled using sixth order polynomials.

These refinements have resulted in a programme that can be used to simulate a complete wind turbine with 27 degrees of freedom. The alterations to the aerodynamic model (aerodynamic forces on dummy elements and chord and thickness distribution) have had an influence on the results. It was clear from the power output of the model without aerodynamics acting on the dummy elements, that the power output was too low. This shows that the aerodynamic forces must be taken into account. This will increase the thrust on the wind turbine, therefore the induced velocity, which is taken constant over the rotor swept area, will increase. This will affect the angle of attack at the other elements. Compared to the original calculation, where the dummy elements did not generate aerodynamic forces, the angle of attack will have become smaller due to the larger induced velocity.

The results presented in the previous section are for the reduced model with the improvements to the aerodynamic possibilities included.

## 8.5 Summary of Verification and Validation

This chapter has described the different steps that have been taken in order to verify the code and validate the programmes results. After extensive verification of the code, the programme has also been validated by comparison with measurements.

It has been shown in this chapter that WOBBE gives results that do give a good indication for the aeroelastic stability of a wind turbine. However, to be able to fit a damping coefficient to the simulations it is necessary to perform some post-processing and only when the results are close to linear it is possible to fit a damping coefficient to the results. Of course, if the results are not linear, the damping coefficient as used in linear theory, does not really exist. So, if simulations are always performed in the linear area, one might think that there is no advantage in WOBBE being fully nonlinear. However, the linear tool for aeroelastic analysis which makes use of parameter identification as described combination of WOBBE

and the linear identification is completely different from the 'standard' linear tools. Linear tools are usually based on linearised equations of motion of a wind turbine model. But the linearisations are somewhat arbitrary. There are no guarantees that the terms that have been dropped during the linearisation cannot be of importance in some or all cases. If some terms are found to be of importance, adding these to the linearised tools can be a laborious process. The combination of WOBBE with the linear identification tool does not have this problem. The calculations in WOBBE are performed for small perturbations around the steady state. Then the identification tool is used to get a linear model from these responses. The linear model should be as close to the nonlinear results as possible. This way the linearisations are partially done by the nonlinear simulation tool and partially by the identification tool.

# Chapter 9

## Calculation of Model Properties

*The sciences do not try to explain, they hardly even try to interpret, they mainly make models. By a model is meant a mathematical construct which, with the addition of certain verbal interpretations, describes observed phenomena. The justification of such a mathematical construct is solely and precisely that it is expected to work.*

- Johann Von Neumann

To create a model of a wind turbine, the blade properties must be simplified. A few springs model the flexibility distribution of the blade. It is important that the frequencies of the blade are modelled correctly, but also the deformations must be comparable. For this reason it is important to use enough elements and calculate the stiffnesses of the springs and give them directions in the correct manner. This chapter describes the investigations that were done in order to try to find the correct methods for calculating the models. First the method used to calculate the stiffnesses of the springs is looked at. Different methods to calculate the stiffness in a tapered beam are compared to each other by simulating different models and analysing the results.

A similar investigation is performed for structural pitch for an isolated blade model. Different methods are used to calculate the model properties and the results of the simulations are then compared in the second part of this chapter.

Other model properties that have not been checked, but further analysis of these would be appropriate are the mass and mass moments of inertia distribution, the locations of the centres of gravity and the locations where the aerodynamic forces act on the system.

The results given in this chapter are obtained using WOBBE, but they are also valid for other multi-body codes.

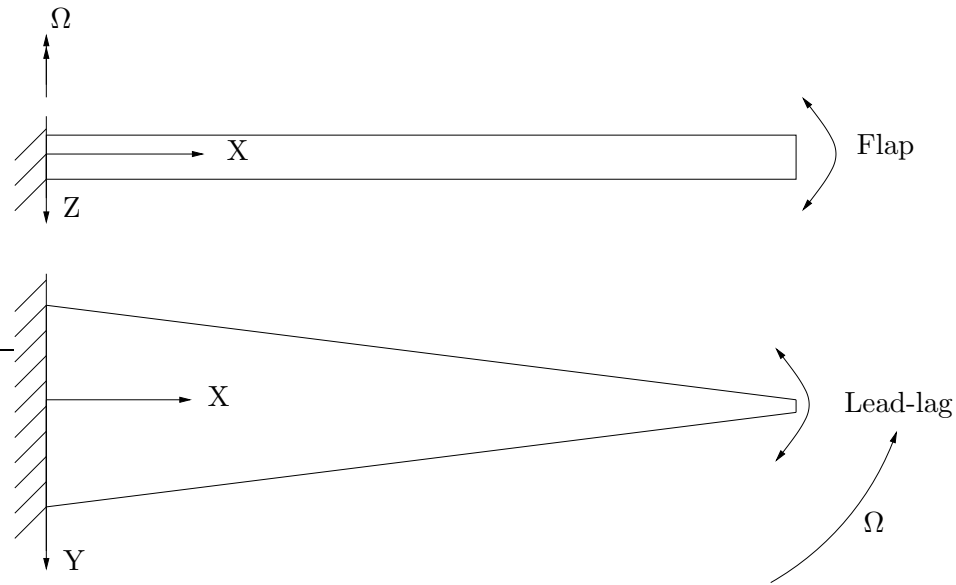


Figure 9.1: A tapered beam, side view and top view. The whole beam rotates with  $-\Omega$  rad/s about the  $z$ -axis.

## 9.1 Stiffness Calculation

To create a good model of a wind turbine, it is important to know how to calculate the properties of the rigid bodies and springs in the superelements. In [93] Molenaar uses the superelement method to model a uniform beam. Wind turbine blades are however, far from uniform. For this reason the calculation of the spring stiffnesses in the superelements modelling a 40 meter long rotating tapered beam has been investigated.

The tapered untwisted beam has a rectangular cross-section, a constant density, elastic modulus and thickness and a linearly varying width ("chord"), as shown in figure 9.1. This results in a linear stiffness variation in the out-of-plane direction. For a linear distribution it is possible to estimate the natural frequencies for the out-of-plane modes using a rather simple analysis as described by Yntema [143]. This estimation can serve as an extra verification of the results.

Figure 9.2 shows the stiffness in the out-of-plane direction of a realistic blade as well as the for the tapered beam. It clearly illustrates that a real wind turbine cannot be compared well to the tapered beam, the distribution of the stiffness in a wind turbine blade is nowhere near linear. In the in-plane direction, the stiffness variation of the tapered beam is nonlinear (see figure 9.3) and it is clear that in this direction the difference between a realistic blade and the tapered beam is significant. Torsion is not taken into account in these analysis. Details of the beam are given in table 9.1.

The discussed tapered beam has been simulated using 1 to 5 superelements. As shown in figure 7.1, one superelement has 4 degrees of freedom when torsion is not taken into account.

Length	40.04 <i>m</i>
thickness	0.5 <i>m</i>
$\rho$	400 <i>kg/m</i> <sup>3</sup>
E	1.80 10 <sup>11</sup> <i>N/m</i> <sup>2</sup>
mass	8.55 10 <sup>3</sup> <i>kg</i>
width at $X = 0$ <i>m</i>	2.1356 <i>m</i>
width at $X = 40.04$ <i>m</i>	1.06667 10 <sup>-4</sup> <i>m</i>

Table 9.1: Properties of the tapered beam.

Therefore the models used, range from 4 degrees of freedom to 20 degrees of freedom.

To calculate the stiffness of the springs, two different methods have been used. The first method calculates the average stiffness over the length of one superelement and calculates the stiffness for the two springs in the superelement in this direction from this average. This results in the two springs in one direction in a superelement to have the same stiffness. The same calculation is performed for the springs in the other direction.

The second method that has been used, calculates the average stiffness over half a superelement and uses this to determine the stiffness of one spring. This method will result in different spring stiffnesses for all springs. It can be expected that this second method will yield better results, as it is more detailed. Both methods are illustrated for a model consisting of two superelements in figure 9.4.

The stiffnesses of the springs are calculated from the average stiffness using the equations given in chapter 7. This corresponds to equal deflection and deformation at the end of the superelement when compared to a uniform beam of the same length and stiffness.

The tapered beam has been simulated rotating at 1.8 rad/s. These simulations ran for 100 s. The results were then analysed using the system identification tool AerID (see D.3). Memory limitations on the PC made it impossible to use the identification tool to analyse the entire simulation for the case of five superelements, therefore these simulations were limited to 50 seconds. By using the identification tool it is possible to determine the natural frequencies of the simulated models of the tapered beam, but this can only be done if the results remain close to linear, therefore only if the amplitudes of the vibrations remain small. For this reason only a relatively small excitation at the beginning of the simulation can be given to the beam's degrees of freedom (e.g.  $q_{i-flat} = 0.01$  *rad* and  $q_{i-lag} = 0.001$  *rad* with 1 superelement). As this is only a structural model, no damping is included in the results, except possibly for some numerical damping.

As mentioned above, the natural frequencies of the out-of-plane modes of the tapered beam can also be estimated using the method described by Yntema [143]. Yntema's method can also be found in [110]. Yntema assumes that the differences in the mode shape for the rotating beam and the non rotating beam are small enough to allow use of the non rotating

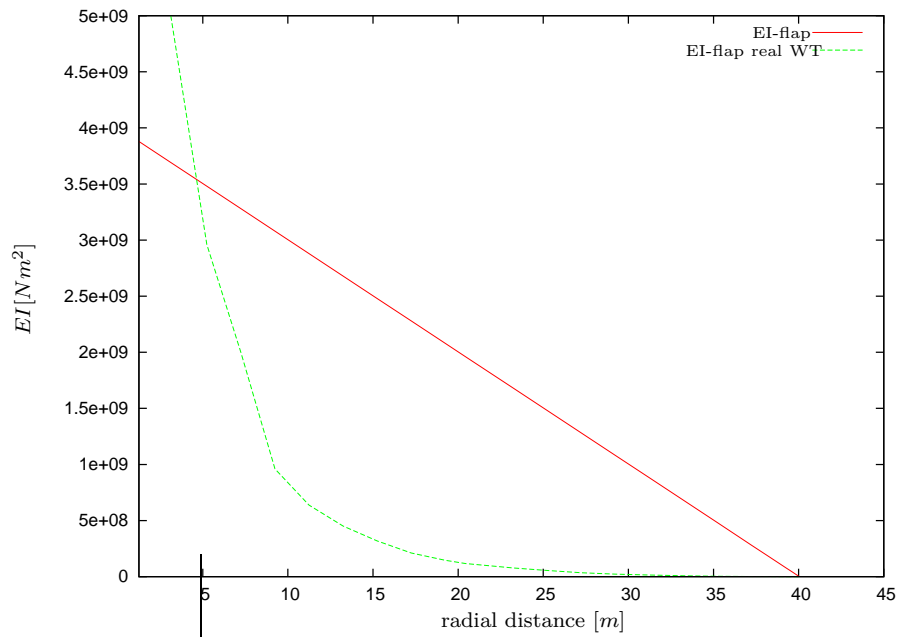


Figure 9.2: Stiffness in the out-of-plane direction of the tapered beam and the values of a realistic wind turbine blade model

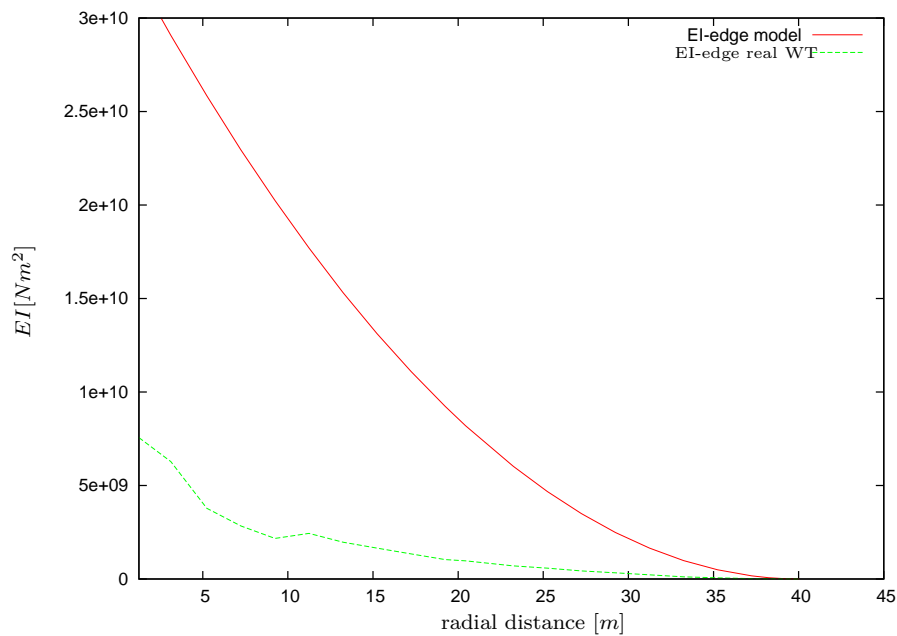


Figure 9.3: Stiffness in the in-plane direction of the tapered beam and the values of a realistic wind turbine blade model.

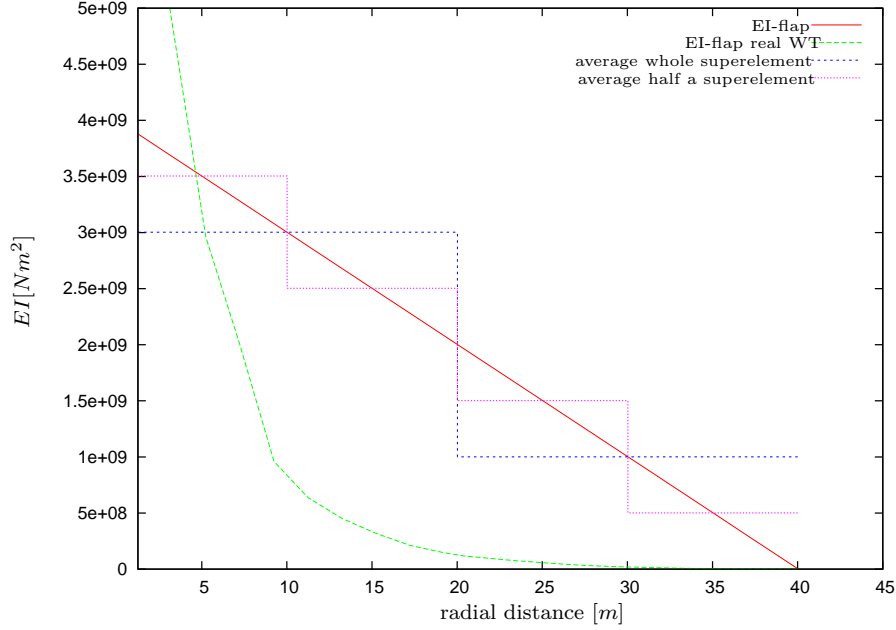


Figure 9.4: Illustration of the average values used to calculate the spring stiffnesses in flap direction for a model with two superelements. Both methods are illustrated: using the average over one superelement or the average over half a superelement.

modes in the analysis using the Rayleigh energy approach.

$$\Omega_{NR_n}^2 = a_n \frac{EI_R}{m_R L^4} \quad (9.1)$$

In this equation  $\Omega_{NR_n}$  is the  $n^{\text{th}}$  non-rotating eigenfrequency,  $a_n$  is the non-rotating beam bending frequency coefficient which can be determined from figures in [143],  $EI_R$  is the stiffness at the root and  $m_R$  is the mass/unit length at the root. This frequency can be corrected for the rotation:

$$\Omega_{R_n}^2 = a_n \frac{EI_R}{m_R L^4} + K_{0_n} \omega^2 \quad (9.2)$$

where  $K_{0_n}$  is the zero offset Southwell coefficient:

$$K_{0_n} = \frac{\int_0^L Y_n'^2 \left[ \int_x^L \eta m d\eta \right] dx}{\int_0^L m Y_n^2 dx} \quad (9.3)$$

With  $x$  the spanwise coordinate,  $\eta$  a dummy variable for the spanwise coordinate,  $Y_n$  the  $n^{\text{th}}$  mode shape,  $Y_n'$  the derivative of the mode shape with respect to  $x$  and  $m$  the mass distribution per unit length.

The bending frequency coefficients and the zero offset Southwell coefficients can be found in the graphs in [143]. For this tapered beam the coefficients for the first three flap frequencies

$a_1$	7.1	$K_{0_1}$	1.225
$a_2$	30.5	$K_{0_2}$	4.25
$a_3$	75	$K_{0_3}$	9.3

Table 9.2: The bending frequency coefficients ( $a_n$ ) and the zero offset Southwell coefficients ( $K_{0_n}$ ) for the first three flap frequencies as given by Yntema [143]

frequency	flap
1	2.22
2	9.34
3	22.8

Table 9.3: The first three flap frequency estimations using the method given by Yntema [143].

are given in table 9.2. The stiffness ratio of tip over root and the mass ratio are both very close to zero.

Substituting the properties of the beam into equation 9.2 results in the frequencies shown in table 9.3. They are also illustrated in the figures with the results. These results are shown in figures 9.5 to 9.10. From these results it can be concluded that, in this case, the approach to calculate the stiffness over half a superelement is a much better approach than taking the average over the length of one complete superelement and having two springs of equal stiffness. Figures 9.5 to 9.8 clearly illustrate this. The frequencies determined using a model consisting of 1 superelement with the springs calculated by using the average over half a superelement are much closer to the value that both methods seem to converge towards. The convergence also occurs significantly quicker.

The estimation for the out-of-plane frequencies as obtained using Yntema's method are also shown in the figures. Note that this is also just an estimation of the frequencies, the accuracy of these analytical results is limited and it is not expected that the results using superelement models in WOBBE will converge exactly toward these estimations. The estimated values for the flap frequencies as obtained using Yntema's method correspond rather well to the values obtained by the simulations with more detailed models, but there is a clear difference between the estimated values and the values toward which the simulation results are converging.

From this analysis it can be concluded that using the average stiffness over half a superelement to calculate the spring stiffnesses in the model is the best approach. Looking at the results, it can also be concluded that one in this case needs a minimum of one superelement above the number of frequencies in one direction that need to be included correctly in the analysis. Looking at figure 9.5 for the first out-of-plane frequency, the results do not differ much when two or more superelements are used in the model. The same goes for the first in-plane frequency illustrated in figure 9.6. The second in-plane and out-of-plane frequencies do not change much in value when using three or more superelements. The third out-of-plane frequency illustrated in figure 9.9 is calculated reasonably well using four superelements. For

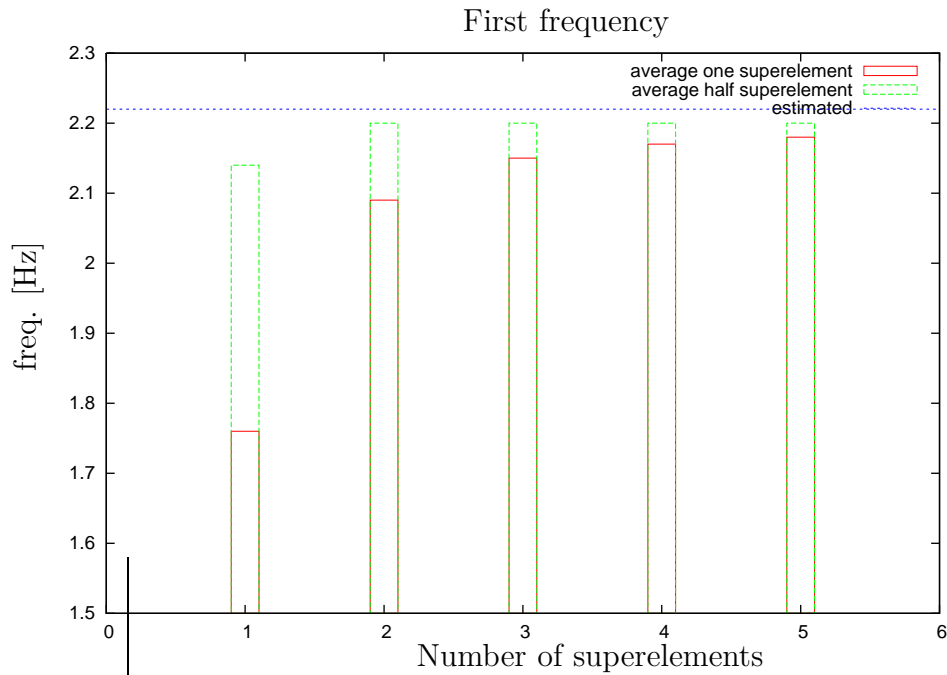


Figure 9.5: First bending (first flap) frequency of a tapered beam, using 1 - 5 superelements, for two different methods to calculate the springs. The estimated frequency is also illustrated.

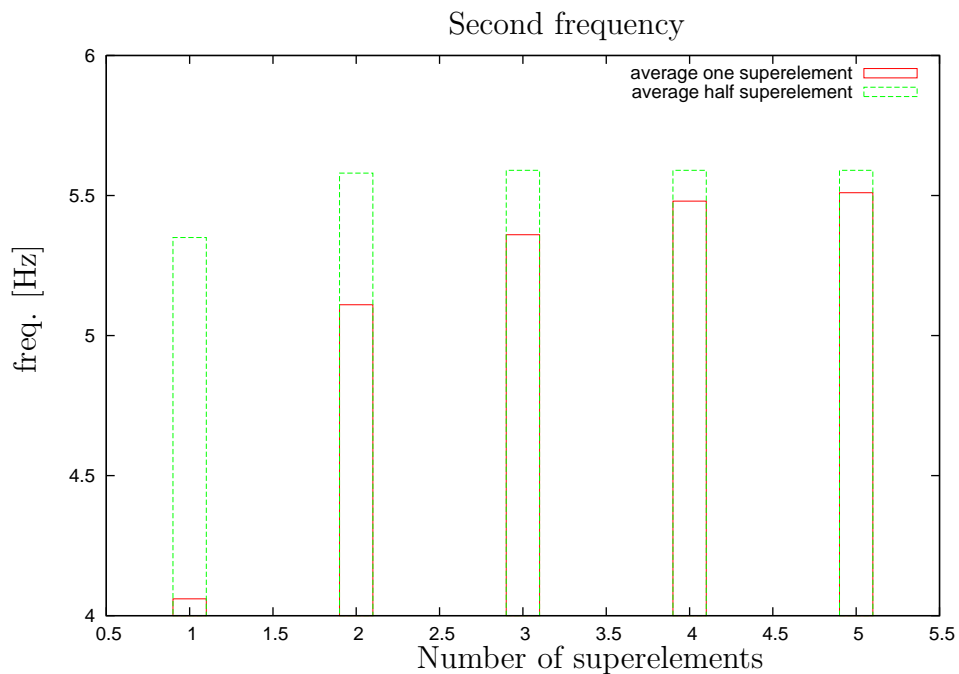


Figure 9.6: Second bending (first lead-lag) frequency of a tapered beam, using 1 - 5 superelements, for two different methods to calculate the springs.

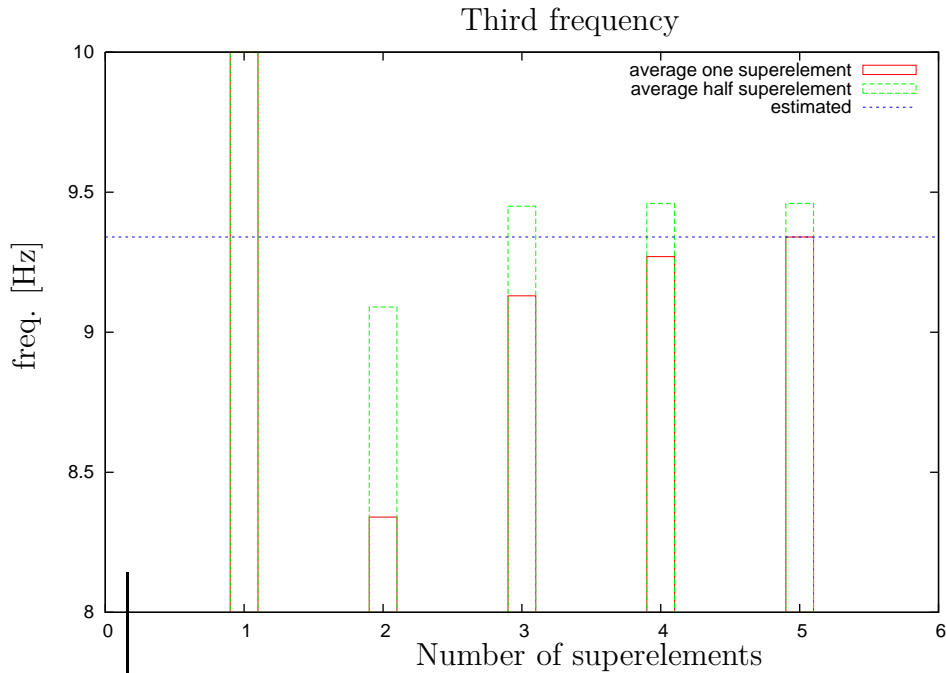


Figure 9.7: Third bending (second flap) frequency of a tapered beam, using 2 - 5 superelements, for two different methods to calculate the springs. The estimated frequency is also illustrated.

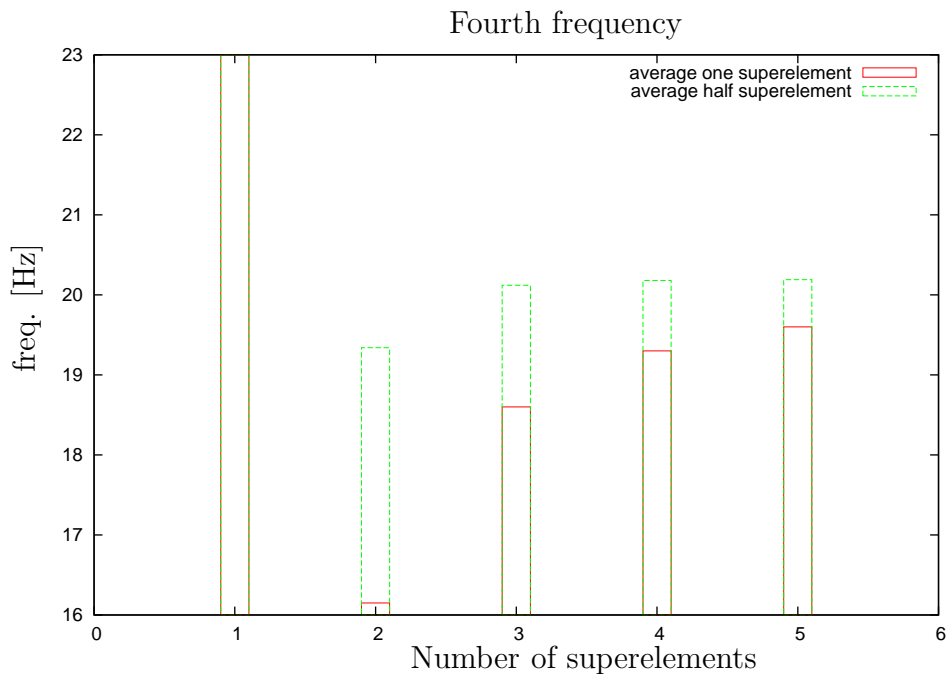


Figure 9.8: Fourth bending (second lead-lag) frequency of a tapered beam, using 2 - 5 superelements, for two different methods to calculate the springs.

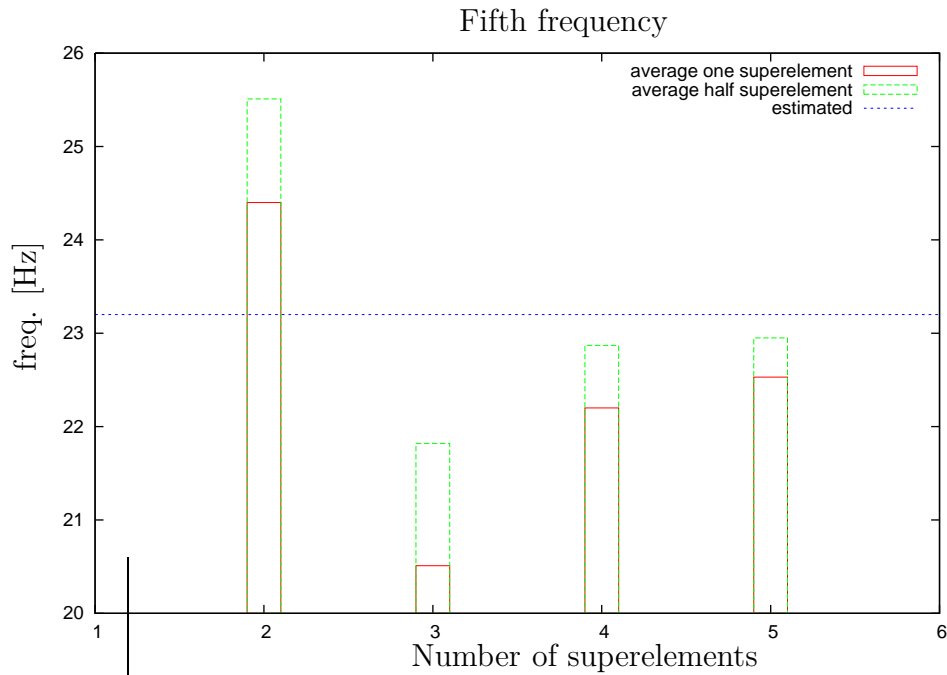


Figure 9.9: Fifth bending (third flap) frequency of a tapered beam, using 2 - 5 superelements, for two different methods to calculate the springs. The estimated frequency is also illustrated.

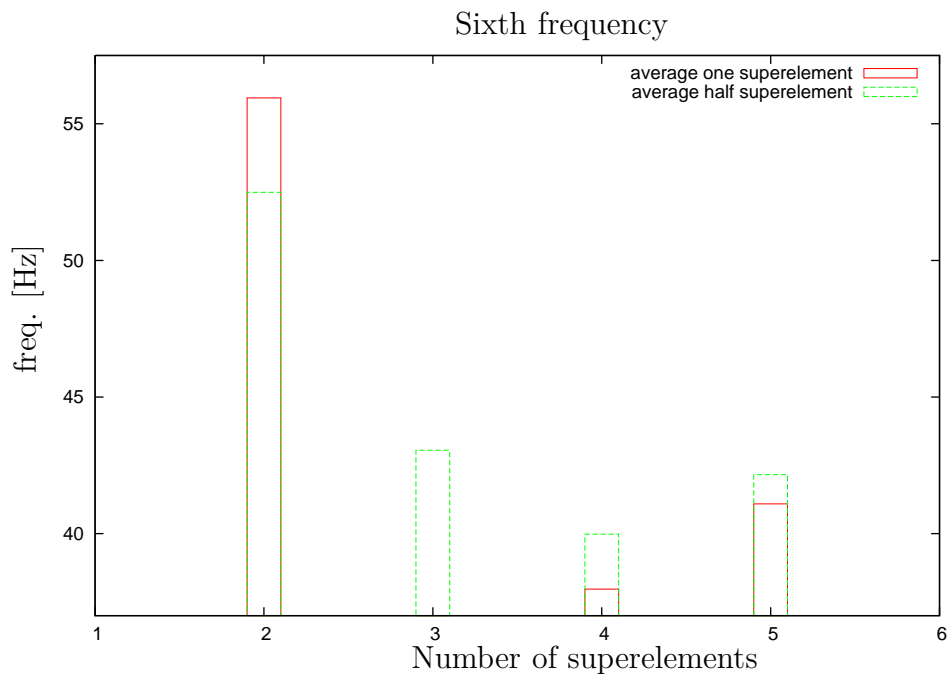


Figure 9.10: Sixth bending (third edgewise) frequency of a tapered beam, using 2 - 5 superelements, for two different methods to calculate the springs.

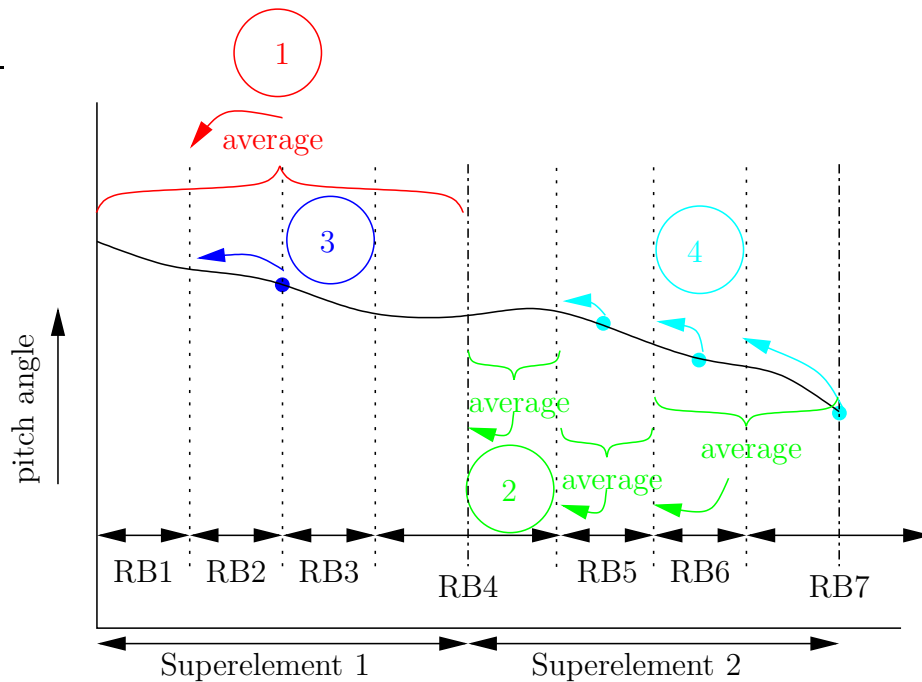


Figure 9.11: Illustration of four different methods that can be used to calculate the structural pitch in the model

the third in-plane frequency it is not so clear if the calculations are already converging using four or five superelements.

WOBBE has been used in this analysis, however the modelling issues discussed are not specific for WOBBE. The results are valid for other rigid body simulation tools as well.

## 9.2 Structural Pitch Calculation

Next to the stiffness, another important property of wind turbine blades is the direction of the principal axes. The angle describing this, the so-called structural pitch, will change along the blade. It has a large influence on the aeroelastic properties of the blade. The method used to model the structural pitch in rigid body models is therefore also important and is looked at in this section.

The simulation tool WOBBE has been used to investigate different methods to model structural pitch in rigid body modeling for wind turbines. WOBBE cannot handle any cross-coupling of the stiffnesses. By setting the springs in the model in the principal directions of the blade the cross-coupling terms become zero.

Many different methods can be thought of when looking at the modeling of the structural pitch. The following six methods have been investigated:

- 1: Average value over length of one superelement. Put this angle before the first springs (one lead-lag and one flap spring) in the superelement. The second set of springs will be in the same directions as the first set.
- 2: Average value over length of rigid body. Put this angle in front of the rigid element. The two sets of springs in one superelement will be in different directions.
- 3a: Value at  $\frac{1}{2}$  length of one superelement. Put this angle before the first springs in the superelement. The second set of springs will be in the same direction as the first set.
- 3b: Value at  $\frac{3}{4}$  length of one superelement, similar to 3a.
- 4a: Value at  $\frac{1}{2}$  length of one rigid body. Put this angle in front of the rigid element. The two sets of springs in one superelement will be in different directions.
- 4b: Value at  $\frac{3}{4}$  length of one rigid body, similar to 4a.

Four of these six methods are illustrated in figure 9.11. The a and b methods are similar, therefore only options 3a and 4a are illustrated in this figure. The methods that use a constant pitch setting in one superelement (methods 1, 3a and 3b) will be referred to as the "superelement methods". The other methods are referred to as the "rigid body methods".

The structural pitch has an important effect on the aerodynamic damping of wind turbine blades. Therefore an isolated wind turbine blade model has been chosen as a test object in this analysis. The out-of-plane motion is usually strongly damped, while the in-plane motion is commonly poorly damped. The lead-lag modes are therefore considerably better damped if they have some out-of-plane motion [111]. The flap mode will of course lose some of its damping in this case. The large influence on the damping due to the structural pitch angle makes it very important to model this property correctly when performing aeroelastic stability analysis.

The isolated blade has been modelled using one till five superelements combined with using the six different methods discussed above. The model using three superelements is illustrated in figure 8.14. As shown in this figure, torsion *is* included in the superelements. Therefore the models consisting of one superelement have 5 degrees of freedom: two flap, two lead-lag and one torsion. Two superelements will result in 10 degrees of freedom and so on, with the model consisting of five superelements entailing 25 degrees of freedom. All simulations were run for a wind speed of 5 m/s. The aerodynamic forces are modelled using blade element momentum method with quasi steady aerodynamics, including Prandtl's tip correction and dynamic inflow. The aerodynamic pitch angle at each point of the blade relative to the rotor swept area (in undeformed state) is the same for all methods, but not for different number of superelements. More superelements will result in a more detailed distribution of the aerodynamic twist angle, because the aerodynamic twist is linearly interpolated between the beginning and end of a rigid body. Since the aerodynamic twist distribution along a

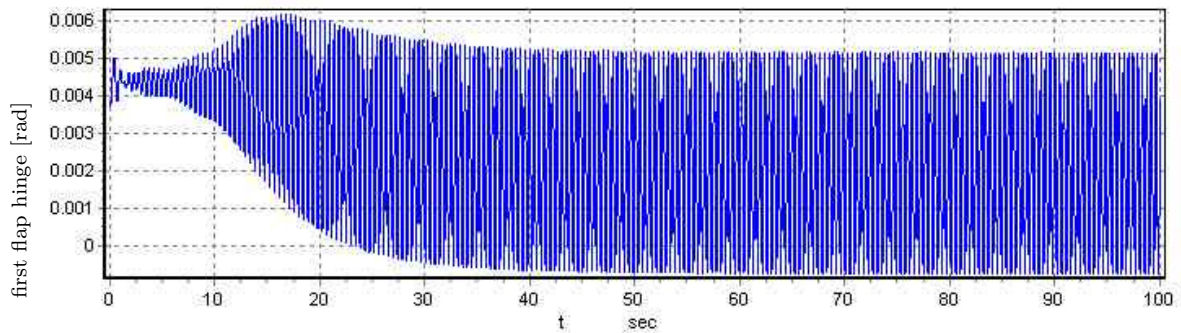


Figure 9.12: Example of limit cycle behaviour for models consisting of one superelement. This shows the angle of the first flap hinge as a function of time.

blade is usually far from linear, the models consisting of more rigid bodies will have a twist distribution that is closer to the distribution on the real blade. This will also have an influence on the results, however when looking at the models for one value of superelements, there is no difference in the distribution of the aerodynamic twist.

The structural damping is not included in the calculations.

The first flap and first lead-lag frequencies and their damping values have been investigated. In order to find the eigenfrequencies and damping coefficients from the nonlinear results, again system identification is used (see appendix D.3). The results from the identification are reliable as long as the nonlinearity is not too large. In some cases the results showed instabilities or limit cycle effects, as illustrated in figure 9.12. In these cases it is not possible to extract the frequency and damping from the results using the system identification tool, because the nonlinearities in the results are too large. The simulations of all "superelement methods" (1, 3a and 3b) as well as the method that uses the average pitch over a rigid body (2) gave unstable results for the models consisting of one superelement. Therefore these models are not included in the results.

The results for the first flap frequency for the different methods of calculating the structural pitch and the different number of superelements are illustrated in figure 9.13. This figure shows that the three "superelement methods" using constant pitch over a superelement (method 1, 3a and 3b) do not show much difference between them until three superelements, but the difference between these three methods and the "rigid body methods" is about 3%. When four or five superelements are used in the model, the method 50% of superelement results in another frequency than the other two "superelement methods", the 50% method does not seem to converge towards the same value as the other two "superelement methods". These last two seem to converge towards the same frequency as the "rigid body methods" or slightly higher. The difference between the three "rigid body methods" is very small, as can be seen in the figure. It can also be observed that the change in frequency from two superelements to more is relatively small for the "rigid body methods". Using two

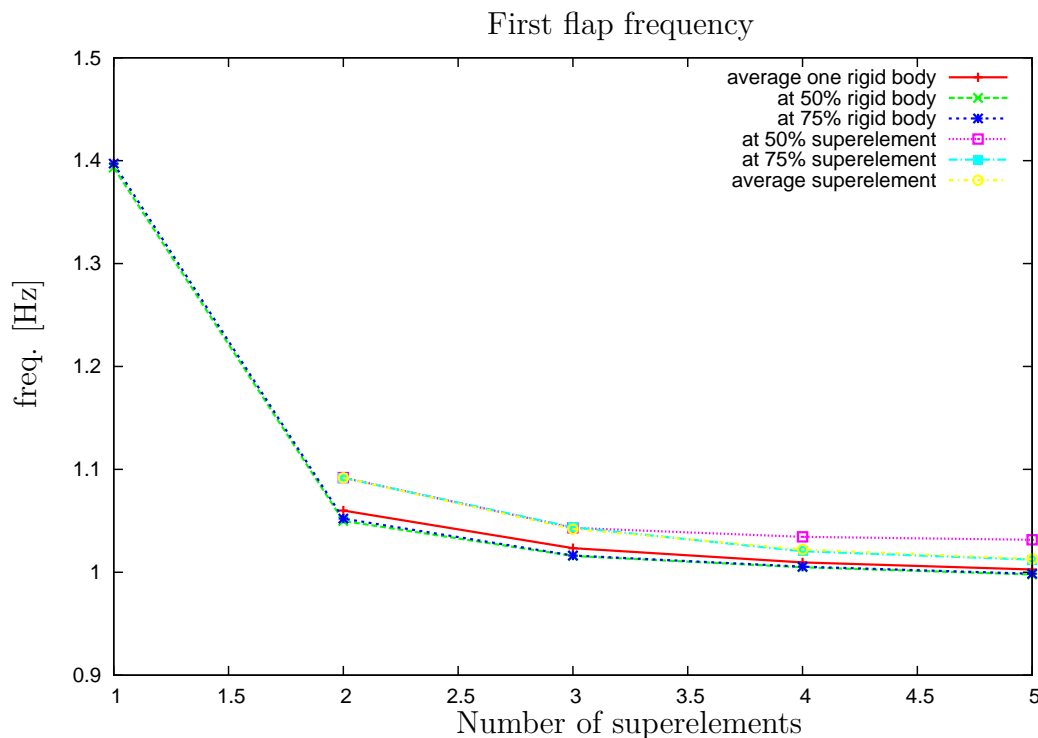


Figure 9.13: First flap frequency of an isolated blade using 1 - 5 superelements for different methods to calculate the structural pitch.

superelements seems to be enough for a good approximation of the first flap frequency.

The first lead-lag frequency is shown in figure 9.14. Here the results of two "superelement methods" (1, average and 3b, at 75%) show a considerable difference with the results of the other "superelement method", method 3a over the entire range of number of superelements. The figure also illustrates that there is again very little difference between the other methods, the three "rigid body methods". It can also be observed that the change in frequency from two superelements to more is relatively small for the rigid body methods. Using two superelements seems to be enough for a good approximation of the first lead-lag frequency.

Looking at these two figures (figure 9.13 and 9.14) it can be concluded that the different methods are converging. The different "rigid body methods" give almost identical results for the frequencies.

The damping of the first flap mode is illustrated in figure 9.15. Where the frequency results showed mainly a difference between the "superelement methods" and the "rigid body methods", the damping results show a different trend. The damping of the three "superelement methods" are close to each other, but method 2, using the average pitch angle of the rigid bodies, differs considerably from the other two "rigid body methods". The damping values of all methods get closer to each other for each increase in model complexity. Overall method 2 seems to give the best damping results for 2 or 3 superelements. However, it resulted in an

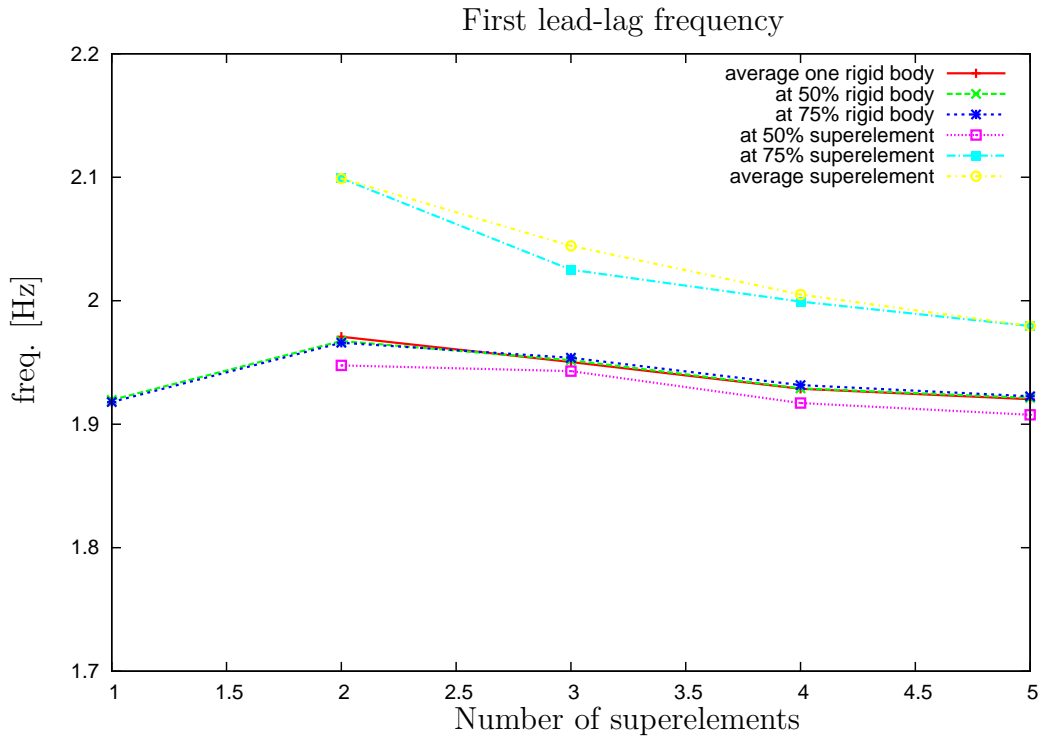


Figure 9.14: First lead-lag frequency of an isolated blade using 1 - 5 superelements for different methods to calculate the structural pitch.

unstable simulation when using 1 superelement, while the other two "rigid body methods" were stable and so were all simulations with more than one superelement.

The damping of the first lead-lag mode is illustrated in figure 9.16. This damping is much lower than the damping of the flap mode and this mode causes the instability in four of the six models using one superelement. The figure illustrates that the aerodynamic twist distribution has a large impact on the aerodynamic damping of this mode. As discussed above the aerodynamic twist distribution differs for different numbers of superelements in the model. The damping values for the different methods do not yet seem to converge, they are still increasing with an increase in model complexity. Noticeable is the difference between the three "superelement methods", their results show large differences, but the three "rigid body methods" also show relevant differences between them in the damping values found in the simulations.

It is difficult to draw conclusions from these results; it is not really possible to state that one method is better than all other methods. There is not one clear "winner". Overall the "rigid body methods" give better results than the "superelement methods". A better insight can be obtained by using models with even more superelements, but probably the best way to continue this analysis would be a better implementation of the aerodynamic twist. Similar to the chord and thickness distribution, the linear interpolation over each rigid body should be replaced by a polynomial function. This would eliminate the effect that is now present in

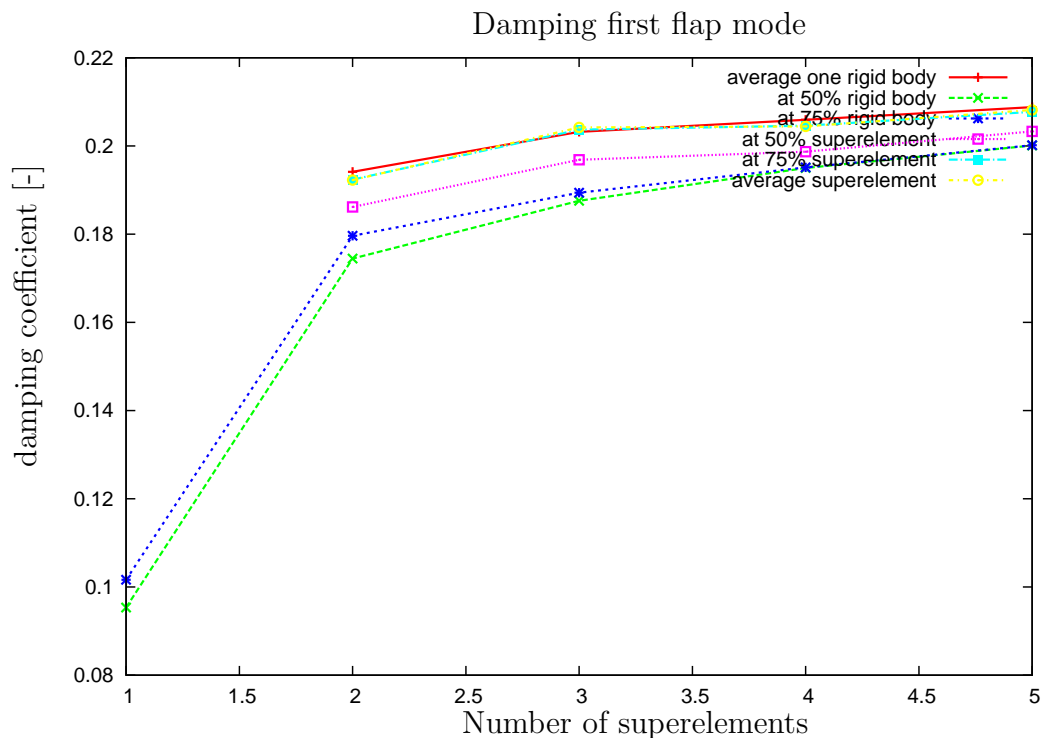


Figure 9.15: Damping of the first flap mode of an isolated blade using 1 - 5 superelements for different methods to calculate the structural pitch.

the simulations due to the differences in aerodynamic twist distribution for different number of superelements. Then it should become possible to draw conclusions that are valid for modelling in WOBBE, but also in other rigid body codes.

One thing that can be concluded from these calculations is that the minimum number of superelements that is needed in a wind turbine blade model when only the first flap and first lead-lag modes are important, is two. This agrees with the conclusion concerning number of superelements in a model drawn in the previous section: the minimum is one superelement more than the number of frequencies in each certain direction. This is in agreement with the conclusion drawn by Molenaar in [93].

The results also show the necessity of enough detail in the model and the importance of the structural pitch. Structural pitch is an important variable that can (de)stabilise the wind turbine. Most models with one superelement became unstable, while more detailed models showed that there was a small amount of damping present.

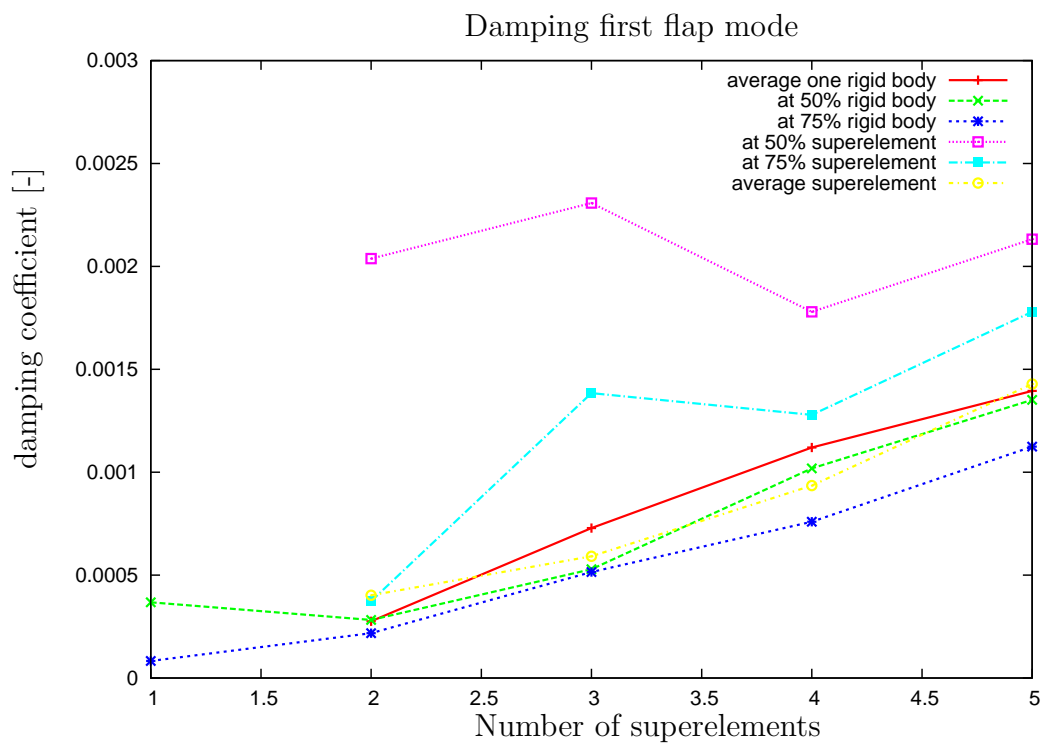


Figure 9.16: Damping of the first lead-lag mode of an isolated blade using 1 - 5 superelements for different methods to calculate the structural pitch.

## Chapter 10

# Investigation into the Possibility of Flap-Lag-Stall Flutter

Three possible blade instabilities for large wind turbines discussed in chapter 4 are the flap-lag flutter instability, the negative damping of the edgewise mode and the negative damping of the flapwise mode. In this chapter the possibility of flap-lag-stall flutter is investigated, a special case of flap-lag flutter. The negative damping of the edgewise mode and flapwise mode are also discussed in order to investigate if the flap-lag instability can occur while the other two modes are positively damped.

Several different methods are used to investigate the possibility of the flap-lag instability, for both stall and attached flow. The contradiction that appears to exist between the results obtained by different methods is looked at in more detail. The contradictions concern the limitations of flap-lag flutter occurring only at a certain interval for the non-dimensional flap frequency according to Ormiston and Hodges, while wind turbines will usually have flap frequencies that lie outside that interval. Second there are the results of other analyses showing that the negative damping of the edgewise mode that seems to occur much sooner than the so-called drag-stall.

In the first section of this chapter the derivation of the equations for the flap-lag instability as obtained by Ormiston and Hodges [102] is shown. The second section discusses the model used in the STABTOOL project and the main STABTOOL results. The third section shortly discusses the differences between these two models.

The fourth section shows the results obtained by adjusting the flap and lag frequencies of a realistic wind turbine blade to coincide. The effect of this coincidence on the damping is shown.

The fifth section gives a rather simplified derivation of the damping for motions in-plane and out-of-plane. This method can be used to give an indication when the flap-lag instability can occur and when the negative damping of the edgewise mode can occur. The possibility of flap-lag flutter for a wind turbine blade is investigated based on these equations.

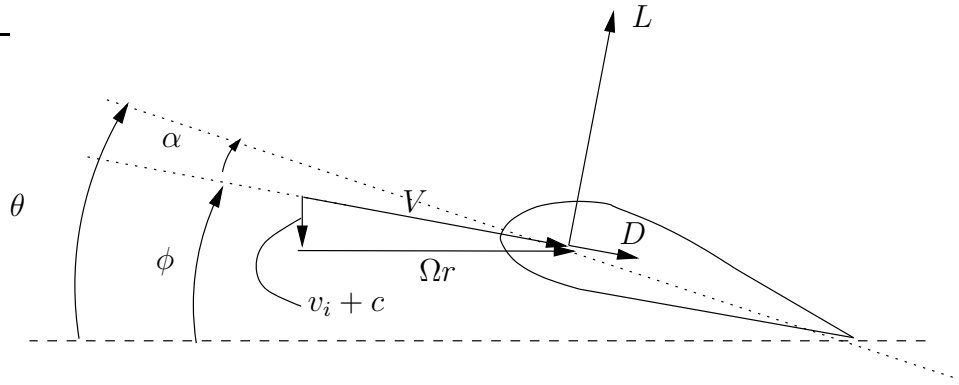


Figure 10.1: The flow angles, lift and drag on a helicopter blade element.

## 10.1 Classical Flap-Lag Equations

Ormiston and Hodges [102] have derived equations for a hingeless helicopter blade in order to investigate the flap-lag instability. In [63] it is assumed that the results of these equations, specifically the limitation on the flap frequency ( $\Omega < \omega_\beta < \sqrt{2}\Omega$ ), is not valid for wind turbines due to the fact that wind turbines often operate in stalled conditions. To be able to investigate this statement, the derivation used by Ormiston and Hodges must be looked at and the validity of their assumptions for wind turbines instead of helicopters must be analysed. The main question is whether the differences between helicopters and wind turbines can result in the limitation of the flap frequency to drop from the necessary conditions for the flap-lag instability.

### 10.1.1 Derivation of the Equations of Motion

#### Aerodynamic Forces

The aerodynamic forces on a blade element used in the classical helicopter flap-lag equations are derived as follows. First the forces in the in-plane and out-of plane direction are written as (see the aerodynamic forces acting on a helicopter blade element illustrated in figure 10.1):

$$dF_z = dL - \phi dD \quad (10.1)$$

and

$$dF_y = -dD - \phi dL \quad (10.2)$$

Notice that the aerodynamics are linearised assuming  $\phi$  to be small and that the definition of a positive value for  $\phi$  is different from the definition used in wind turbines.

Using:

$$\alpha = \theta - \phi ; \quad \phi \approx \frac{U_p}{U_t} \quad (10.3)$$

gives that the forces  $dL$  and  $dD$  are:

$$dL = \frac{1}{2} \rho c_{l_\alpha} c V^2 \left( \theta - \frac{U_p}{U_t} \right) dx \quad (10.4)$$

and

$$dD = \frac{1}{2} \rho c_{d_0} c V^2 dx \quad (10.5)$$

Notice that a linear correlation between the lift coefficient and the angle of attack  $\alpha$  is assumed. Substituting equations 10.4 and 10.5 into equations 10.1 and 10.2 and using  $\left(\frac{U_p}{U_t}\right)^2 \ll 1$ , therefore  $V^2 \approx U_t^2$  gives:

$$dF_z = \frac{1}{2} \rho c c_{l_\alpha} \left\{ \theta U_t^2 - \left(1 + \frac{c_{d_0}}{c_{l_\alpha}}\right) U_p U_t \right\} dx \quad (10.6)$$

and

$$dF_y = \frac{1}{2} \rho c c_{l_\alpha} \left\{ \frac{c_{d_0}}{c_{l_\alpha}} U_t^2 + \theta U_p U_t - U_p^2 \right\} dx \quad (10.7)$$

The tangential and perpendicular velocities must include the effect of the flap and lag motions. Ormiston and Hodges assume a centrally hinged rigid blade, with torsional springs in the hinges. For such a centrally hinged rigid blade the velocities become:

$$U_p = v_i + \dot{w} = v_i + x\dot{\beta} \quad (10.8)$$

and

$$U_T = \Omega x + \dot{v} = \Omega x + x\dot{\zeta} \quad (10.9)$$

with  $x$  the distance from the rotor centre. Discarding second order terms of small velocities, this gives:

$$dF_z = \frac{\rho c_{l_\alpha} c}{2} \left\{ \theta \Omega^2 x^2 - \left(1 + \frac{c_{d_0}}{a}\right) \Omega x v_i \left[ 2\Omega x \theta - v_i \left(1 + \frac{c_{d_0}}{c_{l_\alpha}}\right) \right] - \Omega x^2 \dot{\beta} \left(1 + \frac{c_{d_0}}{c_{l_\alpha}}\right) \right\} dx \quad (10.10)$$

and

$$dF_y = -\frac{\rho c_{l_\alpha} c}{2} \left\{ x^2 \Omega^2 \frac{c_{d_0}}{c_{l_\alpha}} + \theta x \Omega v_i - v_i^2 + x \dot{\zeta} \left( 2x \Omega \frac{c_{d_0}}{c_{l_\alpha}} + \theta v_i \right) + x \dot{\beta} (\theta \Omega x - 2v_i) \right\} dx \quad (10.11)$$

The moments about the flap and lead-lag hinges are:

$$M_{\beta_{aero}} = \int_0^R x dF_z \quad (10.12)$$

and

$$M_{\zeta_{aero}} = \int_0^R x dF_y \quad (10.13)$$

Now, assuming a constant chord distribution and blades without twist ( $\theta$ =constant along the radius), the results of the integrals are:

$$M_{\beta_{aero}} = \frac{\gamma I \Omega^2}{8} \left\{ \theta - \left( 1 + \frac{c_{d0}}{c_{l\alpha}} \right) A + \left[ 2\theta - \left( 1 + \frac{c_{d0}}{c_{l\alpha}} \right) A \right] \frac{\dot{\zeta}}{\Omega} - \left( 1 + \frac{c_{d0}}{c_{l\alpha}} \right) \frac{\dot{\beta}}{\Omega} \right\} \quad (10.14)$$

and

$$M_{\zeta_{aero}} = -\frac{\gamma I \Omega^2}{8} \left\{ \frac{c_{d0}}{c_{l\alpha}} + A\theta - C + \frac{\dot{\zeta}}{\Omega} \left( 2\frac{c_{d0}}{c_{l\alpha}} + A\theta \right) + \frac{\dot{\beta}}{\Omega} (\theta - 2A) \right\} \quad (10.15)$$

with

$$A = 4 \int_0^1 \xi^2 \left( \frac{v_i}{R\Omega} \right) d\xi \quad (10.16)$$

and

$$C = 4 \int_0^1 \xi \left( \frac{v_i}{R\Omega} \right)^2 d\xi \quad (10.17)$$

and  $\gamma$  is the Lock number:  $\gamma = \frac{\rho c_{l\alpha} c R^4}{I}$ .

Note that in these equations  $\beta$  is defined as the flapping angle purely out of plane (not at an angle  $\theta$ ) and that  $\zeta$  is used for the purely in-plane lead-lag angle.

### Rigid Blade Dynamic Equations

The linearised dynamics for a rigid blade rotating with  $\Omega$  and flapping out-of-plane with an angular velocity  $\dot{\beta}$  and an in-plane lead-lag angular velocity  $\dot{\zeta}$  can be derived to be:

$$M_{\beta_{dyn}} = -I(\ddot{\beta} + \Omega^2\beta + 2\Omega\beta\dot{\zeta}) \quad (10.18)$$

and

$$M_{\zeta_{dyn}} = -I(\ddot{\zeta} - 2\Omega\beta\dot{\beta}) + T \quad (10.19)$$

where  $T$  is the driving torque. The driving torque will drop from the equations when looking at small disturbances around the steady state.

### Rigid Blade Elastic Equations

To model the elastic coupling, two sets of springs are used, as illustrated in figure 10.2. The combined stiffnesses of two springs in one direction for the case  $\theta = 0$  are:

$$K_\beta = \frac{K_{\beta_H} K_{\beta_B}}{K_{\beta_H} + K_{\beta_B}} \quad (10.20)$$

and

$$K_\zeta = \frac{K_{\zeta_H} K_{\zeta_B}}{K_{\zeta_H} + K_{\zeta_B}} \quad (10.21)$$

Using these expressions, it is possible to set up the complete elastic moments:

$$M_{\beta_{elastic}} = -\frac{\beta}{\Delta} [K_\beta + R(K_\zeta - K_\beta) \sin^2 \theta] - \frac{\zeta R}{2\Delta} (K_\zeta - K_\beta) \sin 2\theta \quad (10.22)$$

$$M_{\zeta_{elastic}} = -\frac{\zeta}{\Delta} [K_\zeta - R(K_\zeta - K_\beta) \sin^2 \theta] - \frac{\beta R}{2\Delta} (K_\zeta - K_\beta) \sin 2\theta \quad (10.23)$$

with

$$\Delta = 1 + R(1 - R) \frac{(K_\zeta + K_\beta)^2}{k_\zeta K_\beta} \sin^2 \theta \quad (10.24)$$

and the elastic coupling term is defined as:

$$R = \frac{K_\beta}{K_{\beta_B}} = \frac{K_\zeta}{K_{\zeta_B}} \quad (10.25)$$

Therefore (using equations 10.20 and 10.21)

$$(1 - R) = \frac{K_\beta}{K_{\beta_H}} = \frac{K_\zeta}{K_{\zeta_H}} \quad (10.26)$$

Therefore if there is no elastic coupling ( $R = 0.0$ ), the flexibility is only present at the hub and the pitch angle has no effect on the stiffness. If there is full elastic coupling ( $R = 1.0$ ) then the flexibility is only present behind the pitch angle. The STABTOOL model that is discussed in the next section has some flexibility in the hub, but not in both directions. Therefore, in that case, it is not possible to use one elastic coupling parameter, the approach given in [101] would be more suitable for the STABTOOL model. Ormsiton and Bousman give another definition for the elastic coupling parameter.

Using:

$$R_\beta = \frac{K_\beta}{K_{\beta_B}} \quad (10.27)$$

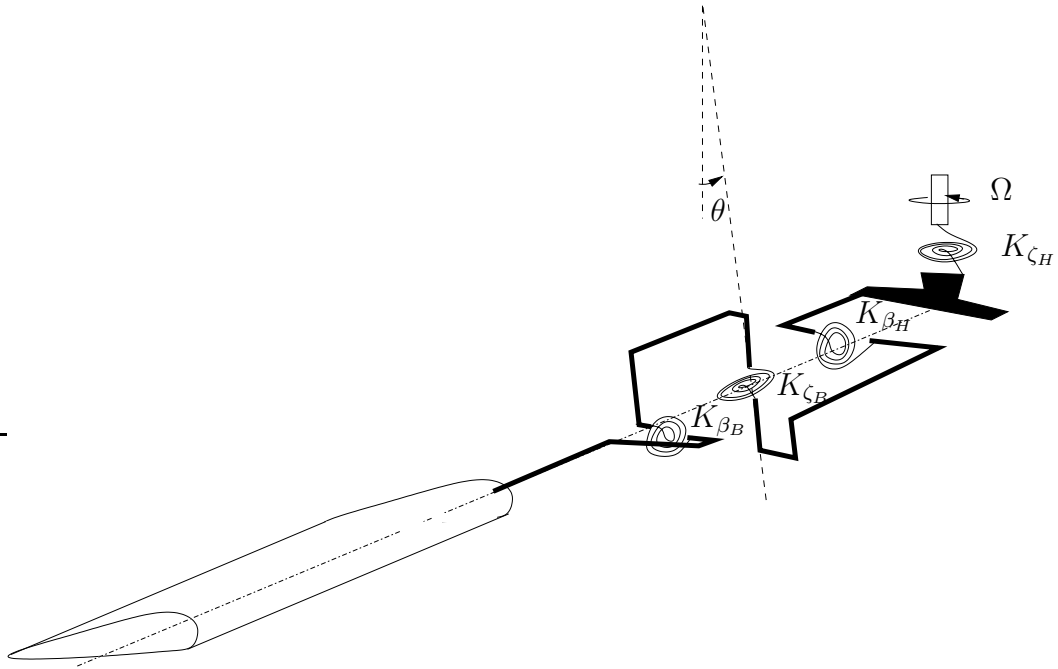


Figure 10.2: The springs that model elastic coupling. One set ( $K_{\zeta_H}$  and  $K_{\beta_H}$ ) is in the directions of the hub while the second set ( $K_{\zeta_B}$  and  $K_{\beta_B}$ ) is at an angle  $\theta$  in the blade directions.

and

$$R_\zeta = \frac{K_\zeta}{K_{\zeta_B}} \quad (10.28)$$

the elastic coupling parameter is defined as [101]:

$$R = \frac{\frac{K_\beta}{I\Omega^2} R_\beta - \frac{K_\zeta}{I\Omega^2} R_\zeta}{\frac{K_\beta}{I\Omega^2} - \frac{K_\zeta}{I\Omega^2}} \quad (10.29)$$

### Flap-Lag Equations

Combining the aerodynamic moments with the dynamic and elastic equations (for  $R = R_\beta = R_\zeta$ ) derived above, results in the flap-lag equations. Assuming small perturbations about the steady state values and neglecting the second order nonlinear products, the Laplace

transformed perturbation equations become [102]:

$$\begin{aligned} & \begin{bmatrix} s^2 + \frac{\gamma}{8}s + p^2 & -s \left[ \frac{\gamma}{8}(2\theta - A) - 2\beta_0 \right] + z^2 \\ -s \left[ 2\beta_0 - \frac{\gamma}{8}(\theta - 2A) \right] + z^2 & s^2 + s\frac{\gamma}{8} \left( 2\frac{c_{d_0}}{c_{l_\alpha}} + A\theta \right) q^2 \end{bmatrix} \begin{Bmatrix} \Delta\beta \\ \Delta\zeta \end{Bmatrix} = \\ \Delta\theta & \left[ \frac{\gamma}{8} \begin{Bmatrix} 1 \\ -A \end{Bmatrix} - R \frac{\frac{K_\zeta}{I\Omega^2} - \frac{K_\beta}{I\Omega^2}}{\Delta} \left\{ R_w \begin{bmatrix} \left[ \beta_0 - \frac{\gamma}{8}(\theta - A) \right] \\ \left[ \frac{\gamma}{8} \left( \frac{c_{d_0}}{c_{l_\alpha}} + A\theta - C \right) \right] \end{bmatrix} \right\} + \right. \\ & \left. + \left[ \beta_0 \begin{bmatrix} \sin 2\theta \\ \cos 2\theta \end{bmatrix} + \zeta_0 \begin{bmatrix} \cos 2\theta \\ -\sin 2\theta \end{bmatrix} \right] \right] \end{aligned} \quad (10.30)$$

with

$$R_w = (1 - R) \frac{\left( \frac{K_\zeta}{I\Omega^2} \right)^2 + \left( \frac{K_\beta}{I\Omega^2} \right)^2}{\frac{K_\zeta}{I\Omega^2} \frac{K_\beta}{I\Omega^2}} \sin 2\theta \quad (10.31)$$

$$p^2 = 1 + \frac{1}{\Delta} \left[ \frac{K_\beta}{I\Omega^2} + R \left( \frac{K_\zeta}{I\Omega^2} - \frac{K_\beta}{I\Omega^2} \sin^2 \theta \right) \right] \quad (10.32)$$

$$q^2 = \frac{1}{\Delta} \left[ \frac{K_\zeta}{I\Omega^2} - R \left( \frac{K_\zeta}{I\Omega^2} - \frac{K_\beta}{I\Omega^2} \sin^2 \theta \right) \right] \quad (10.33)$$

$$z^2 = \frac{R}{2\Delta} \left( \frac{K_\zeta}{I\Omega^2} - \frac{K_\beta}{I\Omega^2} \right) \sin 2\theta \quad (10.34)$$

The homogeneous flap-lag equation without elastic coupling and without pre-cone becomes:

$$\begin{bmatrix} s^2 + F_{\dot{\beta}} + F_\beta & -sF_{\dot{\zeta}} \\ -sC_{\dot{\beta}} & s^2 + C_{\dot{\zeta}}s + C_\zeta \end{bmatrix} \begin{Bmatrix} \Delta\beta \\ \Delta\zeta \end{Bmatrix} = 0 \quad (10.35)$$

with the coupling coefficients:

$$F_{\dot{\zeta}} = \frac{\gamma}{8}(2\theta - A) - 2\beta_0 \quad (10.36)$$

and

$$C_{\dot{\beta}} = 2\beta_0 - \frac{\gamma}{8}(\theta - 2A) \quad (10.37)$$

The steady state flap angle is:

$$\beta_0 = \frac{\gamma(\theta - A)}{8p^2} \quad (10.38)$$

with  $p^2 = \frac{K_\beta}{I\Omega^2} + 1$ .

The term  $F_{\dot{\zeta}}$  is a combination of the aerodynamic moment in flap direction due to the lead-lag velocity and the centrifugal flap moment due to the flap angle which acts in the opposite direction. The Coriolis lead moment due to the flapping velocity is included in  $C_{\dot{\beta}}$

combined with a small aerodynamic moment. The potentially destabilising flap-lag coupling is represented by  $F_{\zeta}C_{\dot{\beta}}$ . In [102] the induced inflow parameter  $A$  is approximated using  $\frac{\theta}{2}$ , which results in:

$$F_{\zeta}C_{\dot{\beta}} = \frac{\left[\frac{\gamma}{8}\right]^2 \left[\frac{3}{2} - \frac{1}{p^2}\right]}{p^2} \quad (10.39)$$

The destabilising part in this expression ( $\frac{3}{2}$ ) is caused by the product of aerodynamic and Coriolis moments. The stabilising term is caused by the product of the Coriolis moments with the centrifugal moment. The maximum flap-lag coupling occurs for  $p = \sqrt{\frac{4}{3}}$ .

The validity of  $A = \frac{\theta}{2}$  is limited, the influence of the solidity on the induction is not taken into account, while it has a significant effect. Therefore Ormiston and Hodges [102] use another approximation in the calculations:

$$A_{approx} = \frac{\pi\sigma}{6} \left[ \sqrt{1 + \frac{12\theta}{\pi\sigma}} - 1 \right] \quad (10.40)$$

where a representative section at  $\frac{3}{4}R$  has been used and  $c_{l_{\alpha}} = 2\pi$ .

### 10.1.2 Stability Calculations

Using the equations derived in the previous section, one can determine the damping values for different flap and lead-lag frequencies, as described by Ormiston and Hodges [102]. They show that in case of a rigid blade without pre-cone or elastic coupling, the flap mode is well damped for all calculated configurations, but that the lead-lag mode shows weak instabilities for in-plane frequencies that are close to the flap frequency, when the collective pitch angle is increased. The equation for the collective pitch angle for neutral stability in case of a rigid blade without pre-cone or elastic coupling is derived to be:

$$(\theta - A)^2 = \frac{P^2}{2(P-1)(2-P)} \cdot \left\{ D + \frac{[D + A\theta][P - W]^2}{\eta^2[W + P(D + A\theta)][1 + D + A\theta]} \right\} \quad (10.41)$$

with  $D = \frac{2c_{d0}}{c_{l_{\alpha}}}$ ;  $P = p^2$ ;  $W = \frac{K_{\zeta}}{I\Omega^2}$  and  $\eta = \frac{\gamma}{8}$ . From equation 10.41 it can be concluded that the instability can only occur if  $1 < p^2 < 2$ . This is because  $c_{d0} > 0$  and  $A\theta > 0$ , therefore the term between curly brackets in the equation is positive and, as the left hand side of the equation is also positive, the term  $\frac{P^2}{2(P-1)(2-P)}$  must also be positive for the neutral stability to exist, only then can there be unstable situations. For wind turbines the flap frequency will be higher than this range, as will be discussed in 10.2.3.

The case of a rigid blade without elastic coupling but with pre-cone shows that instabilities can also occur for other values of  $p$ , not only within the above derived interval of  $1 < p^2 < 2$ . The worst condition occurs if the pre-cone angle is:

$$\beta_{pre-cone_{worst}} = \frac{\eta}{4} \frac{3p^2 - 4}{p^2 - 1} (\theta - A) \quad (10.42)$$

In this case the least stability again occurs when the rotating flap frequency is equal to the lead-lag frequency. The stability boundary is now even independent of  $p$ :

$$(\theta_{min} - A) = 2\sqrt{\frac{2c_{d0}}{c_{l\alpha}}} \quad (10.43)$$

However, for "ideal" pre-cone (exact balance between aerodynamic and inertial flap moments when the hinge spring gives no flap moment), it is derived that no instability can occur in hover. This makes clear that the pre-cone angle can be both stabilising or destabilising.

When looking at a rigid blade with elastic coupling but without pre-cone, it can be concluded that the elastic coupling can be either stabilising or destabilising, depending on whether it is a soft inplane (stabilising) or a stiff inplane (destabilising) configuration.

The equation for the collective pitch angle for neutral stability now becomes [102]:

$$(\theta - A)^2 = \frac{P^2}{2(P - 1)(2 - P)} \cdot \left\{ D + \frac{d(W - P)^2 - Z(\theta + A)(W - P)[1 - d] + Z^2[(d + 1)^2 - (\theta + A)^2]}{\eta^2(d + 1)[W + Pd + Z(\theta + A)]} \right\} \quad (10.44)$$

with  $Z = z^2$ ,  $d = D + A\theta$ .

Ormiston and Hodges also show that for partial elastic coupling the neutral stability boundary for  $p = \sqrt{\frac{4}{3}}$  will occur for the same pitch angle as the was the case without elastic coupling, but the inplane frequencies can have other values than  $p$  and result in instabilities at the same pitch angle, while without elastic coupling this was not the case. Full elastic coupling almost completely eliminates the instability, while partial elastic coupling can be strongly destabilising for stiff in-plane blades.

So far only constant values for  $c_{l\alpha}$  were assumed in the analysis. Ormiston and Bousman [101] investigate the effect of stall on a rigid blade model with elastic coupling. The effect of stall is largest for the stiff inplane configuration. If there is no elastic coupling, stall stabilises the lead-lag mode, but when the elastic coupling is not zero, a strong destabilisation of the lead-lag mode is caused by stall. For the fully coupled configuration, the elastic coupling combined with stall results in instabilities, where in linear theory it was concluded that full coupling would result in a stable configuration. In [101] it is also concluded that  $c_{d\alpha}$  is usually destabilising while  $c_{d0}$  is stabilising. The effect on the stability of the slope of the lift curve  $c_{l\alpha}$  depends on the configuration, in some cases it was stabilising, in others destabilising. It must be noted however that these analyses were only performed for  $p = \sqrt{\frac{4}{3}}$ , while for large wind turbines the flap frequency will be significantly higher.

## 10.2 Flap-Lag-Stall Instability as Derived in STABTOOL

As mentioned before, during the STABTOOL project, it was concluded that the increase in size of the wind turbines has resulted in the flap and lead-lag frequency coming closer together and that this, combined with the operation in stall can result in instabilities [67]. In this section the model used for this analysis and the results are discussed.

### 10.2.1 Equations of Motion for Three DOF Model in Stall

During the Dutch STABTOOL project it was concluded that the flap-lag instability could occur on wind turbines when these were operating in stall, even though the flap frequency is much higher than the limit found by Ormiston and Hodges described in the previous section [54, 55, 56, 64, 65].

To check the aeroelastic stability of large wind turbine blades a model of a single blade has been used during the STABTOOL project. This model has been kept rather simple and its main purpose was to get a first insight into the possible instabilities of large blades [53]. This baseline model has only three degrees of freedom and is sketched in figure 10.3.

The model is an isolated blade model, i.e. only one blade is considered, the tower, foundation, other blades etc. are not included in the model. The shaft of the model rotates at a constant speed  $\Omega$ . The first degree of freedom is about the same axis as this rotation and it is called  $\varepsilon$ . It is used to model the clamping stiffness and the multi-blade effects (see 10.2.2) and can also be used to model the influence of the generator. The blade is set at a constant angle  $\theta$ . This angle is the so-called structural pitch angle. It is assumed to have a fixed setting when operating, so it is not one of the degrees of freedom in the model. This structural pitch angle will align the blade flap- and lag hinge with the principal stiffness directions. By choosing the hinges to be in the principal directions, the cross-coupling between flap and lag becomes zero.

Behind the constant structural pitch angle  $\theta$ , the second degree of freedom is situated: the lead-lag angle ( $\zeta$ ). The final degree of freedom is the flap angle ( $\beta$ ). The structural pitch setting causes the flap hinge to be in the most flexible direction of the blade and the lag hinge to be in the stiffest direction of the blade. There are no hinge offsets assumed, but there is a definite hinge order as described: first  $\varepsilon$ , then  $\zeta$  and finally  $\beta$ .

A line distribution of mass along the  $Z$ -axis is assumed for the blade. Therefore the inertia matrix of the blade relative to the local blade reference frame is:

$$[J_{cg}] = \begin{bmatrix} I_x & 0 & 0 \\ 0 & I_y & 0 \\ 0 & 0 & 0 \end{bmatrix} \quad (10.45)$$

As this model is to be used in aeroelastic analysis, the aerodynamic forces must be deter-

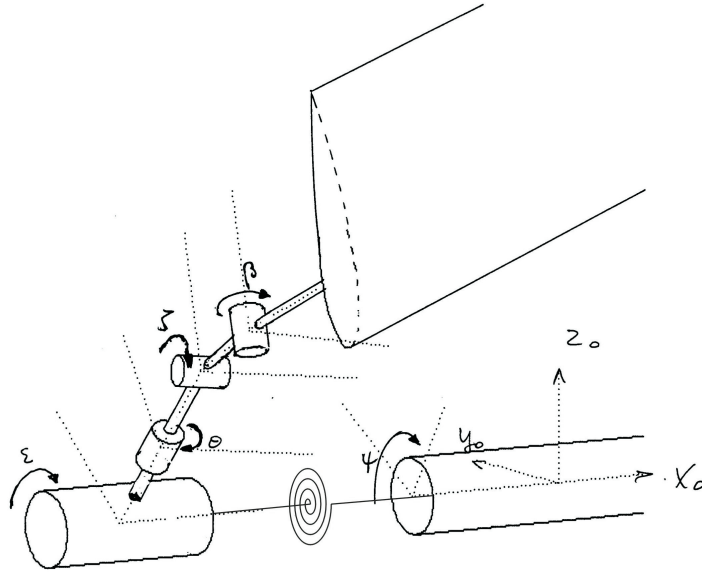


Figure 10.3: The baseline model, a model of an isolated blade. The model has three degrees of freedom:  $\varepsilon$ ,  $\zeta$  and  $\beta$ . The angle  $\theta$  is a constant angle. The shaft rotates with a constant rotational velocity  $\Omega$ .

mined as well. To keep the calculations simple, blade element theory is used to determine the aerodynamic forces acting on the blade. The complete derivation of the partially linearised equations of motion, including the aerodynamic forces is discussed in appendix I. The derivation makes use of the method discussed in section 2.1.2. The equations are not linearised for  $\theta$ , because this resulted in false instabilities.

The equations of motion for small perturbations are derived in appendix I. Simplifying the notation by using  $\beta$ ,  $\zeta$  and  $\varepsilon$  now for the small perturbations instead of  $\Delta\beta$ ,  $\Delta\zeta$  and  $\Delta\varepsilon$ , the equations of motion become:

$$\begin{aligned} & \beta'' \sin \theta - 2\beta_0 \beta' + \frac{\gamma}{8c_{l_\alpha}} (c_{l_0} - c_{d_\alpha}^*) \beta' + \varepsilon'' + \frac{\gamma}{8c_{l_\alpha}} 2c_{d_0} \varepsilon' \\ & + \nu_\varepsilon^2 \varepsilon + \zeta'' \cos \theta + \frac{\gamma}{8c_{l_\alpha}} \cos \theta + \frac{\gamma}{8c_{l_\alpha}} 2c_{d_0} \zeta' = 0 \end{aligned} \quad (10.46)$$

$$\begin{aligned} & -2\beta_0 \beta' + \frac{\gamma}{8c_{l_\alpha}} (c_{l_0} - c_{d_\alpha}^*) \beta' + \varepsilon'' \cos \theta \\ & + \frac{\gamma}{8c_{l_\alpha}} c_{d_0} 2\varepsilon + \zeta'' + \frac{\gamma}{8c_{l_\alpha}} c_{d_0} 2\zeta' + \nu_\zeta^2 \zeta = 0 \end{aligned} \quad (10.47)$$

$$\begin{aligned} & \beta'' + \frac{\gamma}{8c_{l_\alpha}} c_{l_\alpha}^* \beta' + \beta(1 + \nu_\beta^2) + \varepsilon'' \sin \theta \\ & + \varepsilon' [2\beta_0 - \frac{\gamma}{8c_{l_\alpha}} 2c_{l_0}] + \zeta' [2\beta_0 - \frac{\gamma}{8c_{l_\alpha}} 2c_{l_0}] = 0 \end{aligned} \quad (10.48)$$

where  $(\ )' = \frac{\partial}{\partial \psi}$ ;  $(\ )'' = \frac{\partial^2}{\partial \psi^2}$ ;  $(\ )^* =$  value at representative section ( $\frac{3}{4}R$ );  $c_{l_0}$  the lift coefficient in the equilibrium position;  $\gamma$  the Lock number ( $\gamma = \frac{\rho c_{l_0}^* c R^4}{I}$ );  $\nu_\beta, \nu_\varepsilon, \nu_\zeta$  the non-dimensional natural frequencies;  $\beta_0$  the flap angle for the equilibrium position and all degrees of freedom are expressed as small variations relative to the equilibrium values.

These equations can be used to perform stability calculations. Root locus calculations can result in the stability boundaries as will be discussed in section 10.2.3.

## 10.2.2 Multi-blade Effects

When a new blade is designed, the natural frequencies of the blade are calculated in order to ensure prevention of aeroelastic instabilities. This calculation is usually performed with the clamping to the hub assumed to be infinitely stiff. Likewise, when blade frequencies of a blade are measured, the blade is clamped as stiff as possible. In practice however, some of the multi-blade effects [96] result in a much lower stiffness in the lead-lag direction. The multi-blade modes can result in a rotation of the hub, thus resulting in a significantly lower clamping stiffness. This can be modelled as a lower edgewise stiffness. For a two bladed rotor, the multi-blade modes are shown in figures 10.4 and 10.5. In the case of a symmetrical lead-lag vibration (figure 10.4), the hub does not take part in the motion. The eigenfrequency of each blade is solely determined by the mass and stiffness characteristics of the blade itself. In the case of an anti-symmetric vibration mode (figure 10.5), the situation is different. The hub rotates and each blade separately experiences a reduced clamping stiffness. This results in a decrease of its eigenfrequency.

For a three bladed wind turbine four different natural modes can be distinguished that all concern multi-blade effects. These four modes are shown in figures 10.6 until figure 10.9. The two scissor modes (figures 10.6 and 10.7) do not result in hub motion. However, the two asymmetric coning modes (figures 10.8 and 10.9) do result in hub motion. Depending on the relative values of the blade mass and the equivalent hub inertia, the hub motion may be in phase or in anti-phase with the blade motion. This will lead to either reduced or increased values of the lead-lag eigenfrequency.

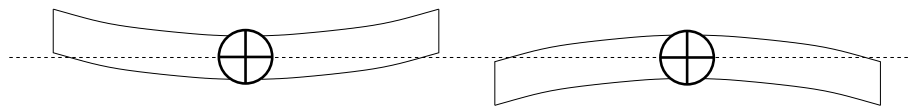


Figure 10.4: Symmetric lead-lag mode for a two bladed turbine

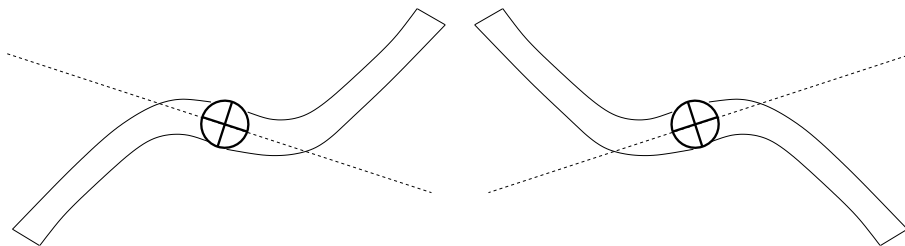


Figure 10.5: Anti-symmetric lead-lag mode a for two bladed turbine

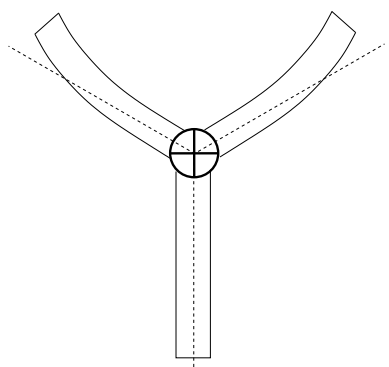


Figure 10.6: Scissors or reactionless mode, there is no hub motion.

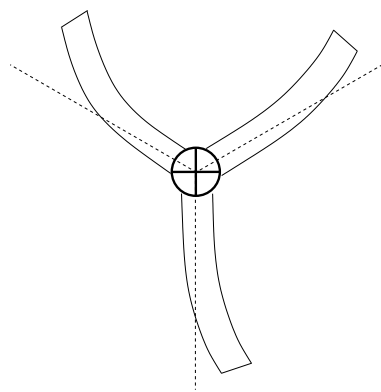


Figure 10.7: Modified scissors or modified reactionless mode, there is no hub motion.

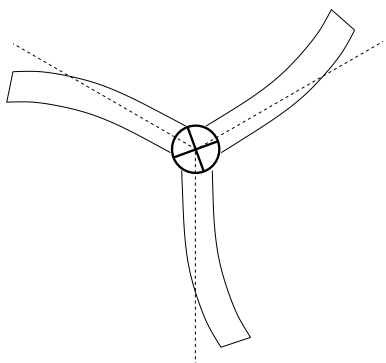


Figure 10.8: Symmetrical in-phase coning mode, there is hub motion.

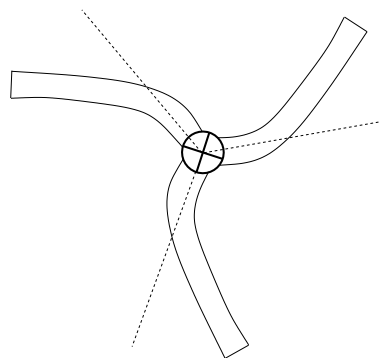


Figure 10.9: Symmetrical anti-phase coning mode, there is hub motion.

Multi-blade effects do not only influence the frequencies. Those modes that did not have any effect on the frequencies, will have an effect on the tower excitation. It is shown in the literature [97] that, in the case of the modes that do exert forces on the tower, the resulting effect will always be a combination of a fast rotating force in the same direction as the rotor

speed, and a slow counter rotating force. Therefore it is always possible to replace the multi-blade rotor by an equivalent single-blade model. In order to represent the magnitude of the forces on the tower correctly in such a single-blade model, one should use an appropriate "equivalent" mass. To represent the effect of the extra flexibility due to the hub motion, the stiffness should be altered to find an appropriate representation [64].

### 10.2.3 Stability of the Isolated Blade

Once the partially linearised equations of motion are known, it is possible to determine the stability boundary. By substituting assumed exponential functions for the degrees of freedom:

$$\beta = Ae^{\lambda t} \quad (10.49)$$

and similarly for the other two degrees of freedom, it is possible to derive a system of second order polynomial equations that determine the stability. If any of the eigenvalues has a positive real part, the configuration is unstable.

The Routh-Hurwitz method can then be used to determine the stability boundary. For example for a fourth order polynomial such as:

$$a_4x^4 + a_3x^3 + a_2x^2 + a_1x + a_0 = 0 \quad (10.50)$$

with  $a_i$  are all real coefficients. If this polynomial is the expression for the equations of motion with  $\lambda$  as the variable, the solution will only be stable if all real parts of the roots are negative. According to Routh all roots can only be negative if all coefficients  $a_0, a_1, \dots, a_4$  and the discriminant  $R = a_1a_2a_3 - a_0a_3^2 - a_4a_1^2$  are of the same sign [124]. Hurwitz determined a criterion for polynomial equations of  $n^{\text{th}}$  degree in terms of a series of determinants [35]. For a fourth degree polynomial the real parts of the roots are all negative if the following four determinants are all positive and  $a_0 > 0$ .

$$|a_1| ; \begin{vmatrix} a_1 & a_0 \\ a_3 & a_2 \end{vmatrix} ; \begin{vmatrix} a_1 & a_0 & 0 \\ a_3 & a_2 & a_1 \\ 0 & a_4 & a_3 \end{vmatrix} ; \begin{vmatrix} a_1 & a_0 & 0 & 0 \\ a_3 & a_2 & a_1 & a_0 \\ 0 & a_4 & a_3 & a_2 \\ 0 & 0 & 0 & a_4 \end{vmatrix} \quad (10.51)$$

These matrices can be extended to higher degree polynomials. In order to find the stability boundary Routh's determinant must be set equal to zero.

For the equations derived in section 10.2.1, the substitution as given in equation 10.49 results in three second order polynomials for which the stability can be analysed using the Routh-Hurwitz method. Several instabilities have been found by using this method [56]. First there are two different possibilities for the case where drag is neglected. If the rotating flap frequency lies between  $1 - P$  and  $1.4 P$  ( $0 < \nu_\beta^2 < 1$ ), instability is possible. This is the "classical" flap-lag instability discussed in section 10.1. In view of their much higher flapping

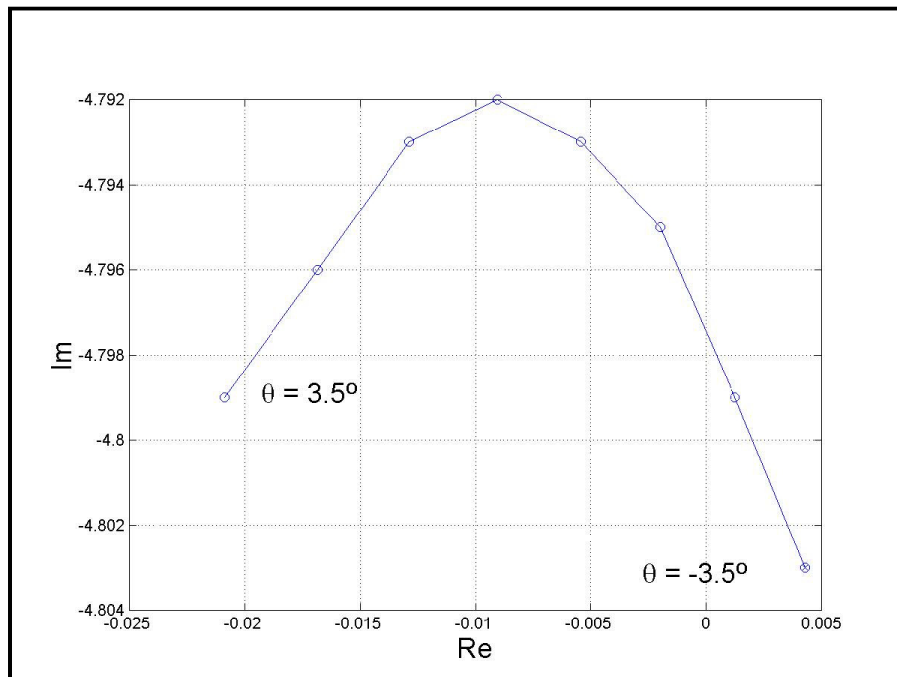


Figure 10.10: The root locus plot for varying structural pitch angle  $\theta$ , without drag.

frequency, this type of instability is irrelevant for wind turbines. However, the variant flap-lag coupling in combination with stalled conditions could be relevant.

Another potential instability is found from the Routh-Hurwitz criterion when  $\beta_0 < 0$  or when  $\theta < 0$ , where the latter is more relevant and may occur in the case of fine pitch setting of a wind turbine blade with large built in twist.

The root-locus plot given in figure 10.10 shows that this instability appears to be a mild instability. An energy-flow consideration [62] shows that it is essential that the hub takes part in the motion.

The second limiting case that has been investigated is the so-called drag-stall case, where drag-stall is defined as the situation where the  $c_{l_0} - c_{d_\alpha}$  term is strongly decreased. This results in the destabilising Coriolis forces on the blade no longer being counteracted by the stabilising tilting of the lift vector due to flapping. Therefore this can result in an instability.

Figure 10.11 shows a root-locus plot, where along the locus the parameter  $\theta$  (associated with blade pitch and twist) is varied. Increasing  $\theta$  acts stabilising. This suggests that blade twist might actually be used as a remedy.

The isolated blade also shows an instability when  $\gamma < 0$ , this is simply a case of negative damping of the flap mode. This will occur in stall, when the lift coefficient becomes smaller for larger angle of attack. The instability can however also occur when  $c_{l_\alpha}$  is still positive, but small. This is illustrated in the root-locus plot in figure 10.12.

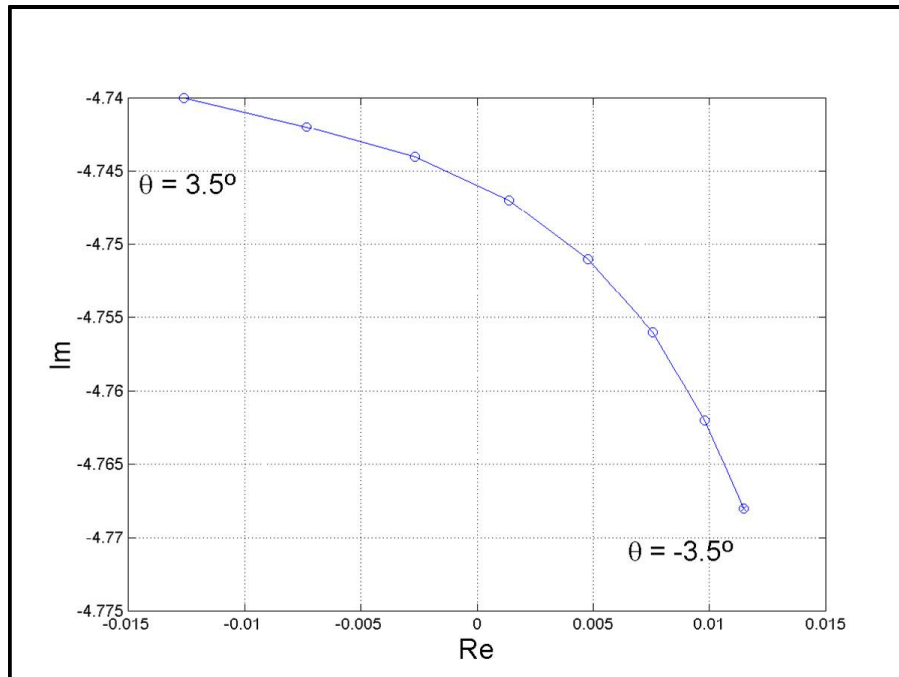


Figure 10.11: The root locus plot for varying structural pitch angle  $\theta$ , in case of drag-stall.

#### 10.2.4 Effect of Linearisations

As mentioned before, linearising for  $\theta$  led to false instabilities. This is one example that shows that linearising is a complicated task. Another example are the Coriolis terms, these cannot be dropped in the linearisation, they can have a large impact on the stability. If linearisation is not done correctly, the results of the calculations will be useless.

During the STABTOOL project, the baseline model has also been simulated using the tool WOBBE which was described in chapters 5 and 6. The results of these nonlinear simulations of the baseline model are compared to the results shown above obtained by solving the partially linearised equations of motion in the previous section. The differences in these results are also discussed in this section.

The three degrees of freedom model described in section 10.2.1 has been implemented in the aeroelastic tool WOBBE. The aerodynamic forces have been implemented in exactly the same way as for the linear model; the derived equations for the generalised forces in appendix I.1 are implemented as the generalised forces acting on the single blade model. This means that, unlike the description in chapter 6, the aerodynamic forces are not calculated using small subelements and determining the angle of attack for each subelement. The generalised forces are therefore linearised, only the dynamics are fully nonlinear in the WOBBE calculations for the baseline model.

The main distinction between the linear calculations and the simulations using WOBBE that can lead to differences in results is the linearisation. The equations are solved fully nonlinear

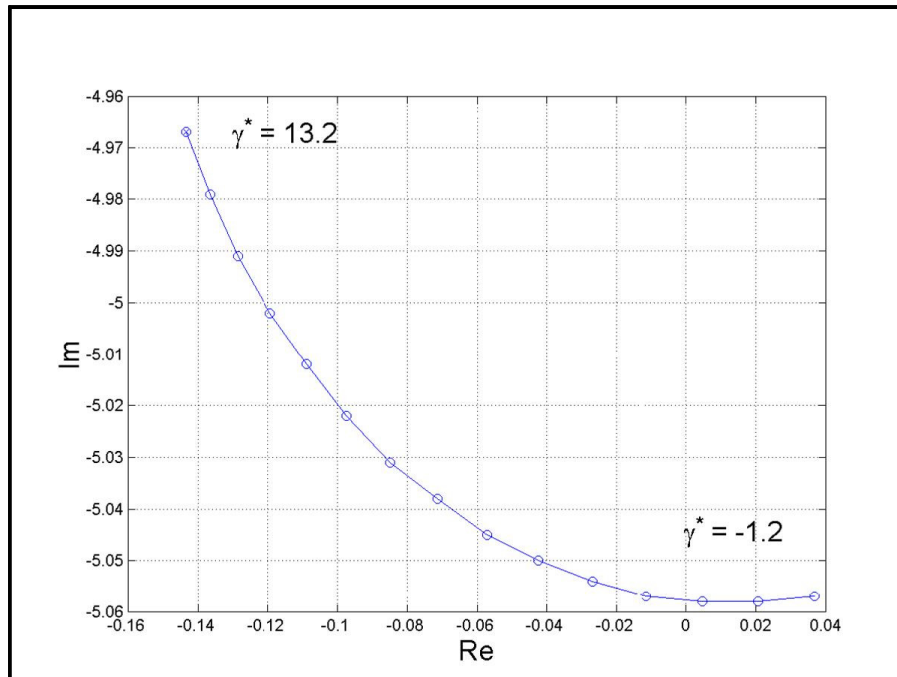


Figure 10.12: The root locus plot for lift-stall.

by WOBBE, while the partially linearised equations have been simplified by dropping higher order terms. Therefore the differences in results between the two methods say something about the linearisations of the dynamics (note that the aerodynamics are linearised for both calculation methods). However there are other things to take into account, such as possible numerical damping present in the simulation as well as the problem of identifying the instabilities from the time simulations. On this last problem: the time simulations result in the response in time. With different frequencies present, it is not always possible to see the difference between very slightly damped, undamped or a very small negative damping. Also, the linearised equations can be used to immediately determine the stability boundary, while the simulations must be run for specifically chosen configurations. From each simulation the stability can then be investigated. E.g. where the linearised equations can result in a stability boundary at a wind speed of 14.395 m/s, the nonlinear method will only state that the system is stable for a wind speed of 14 m/s and unstable for a wind speed of 15 m/s, assuming steps of 1 m/s were used in the chosen configurations.

The results of WOBBE have been compared to the results of the linearised method discussed above. As can be expected, there were some differences between the results of the linear and nonlinear tool. The results for the nonlinear tool WOBBE were more stable than expected from the linearised equations, but the general trend was the same. The results of both tools are shown in figure 10.13.

The fact that the linearised equations result in an absolute boundary, one might overlook the "strength" of the instability. When looking at the non-linear result, it is immediately

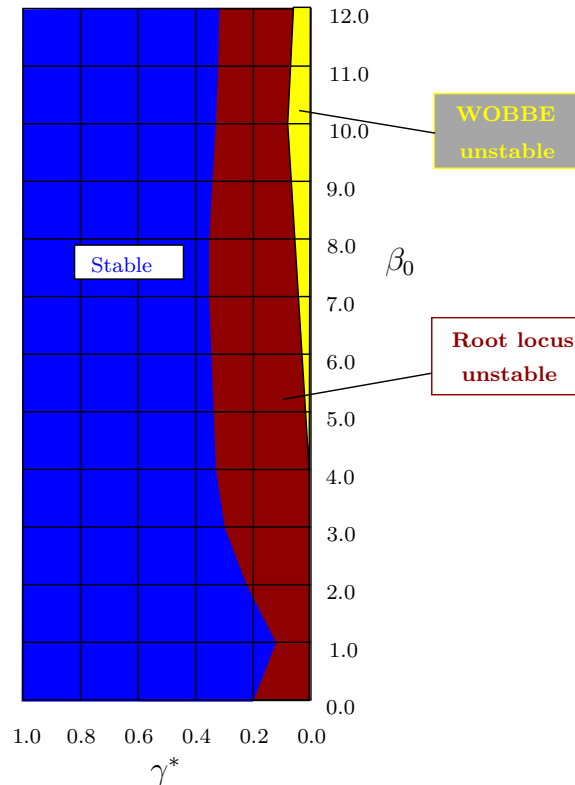


Figure 10.13: Differences in stability boundary for linear and non-linear method.

clear if there is a strong instability or only a mild instability. When structural damping is not taken into account, one can expect that a calculated unstable configuration will actually be stable, if the instability is mild. The structural damping can be enough to result in a stable system as described in [55].

Next to the limitation of not taking into account the structural damping, another limitation is the fact that this is a rather simplified analysis, especially the aerodynamics can show important nonlinearities that have not been taken into account. Furthermore the assumption of the so-called drag-stall occurring on a wind turbine blade, where  $c_{l_0} - c_{d_\alpha} \approx 0$  is not realistic. Figure 10.14 shows the lift coefficient  $c_l$  and the  $c_{d_\alpha}$  for different aerofoils. The figure shows ten different aerofoils, the aerofoils with larger values for  $c_{l_0} - c_{d_\alpha}$  have not been included in the graph. The lift and drag coefficients were generated by ATG [11, 12]. The aerofoil coefficients have not been corrected for 3D effects nor has the laminar drag bucket been removed in order to show the most critical cases, but it is clear that the assumption used in the equations to set  $c_{l_0} - c_{d_\alpha} = 0$  is far from realistic in the common aerofoils used on wind turbines. For some aerofoils there is a very strong increase visible in  $c_{d_\alpha}$  for angles of attack of around  $10^\circ$ , but the values are not larger than the lift coefficient. Besides, the increase does not take place before stall, in most cases the strong increase occurs for the same angles of attack as lift stall.

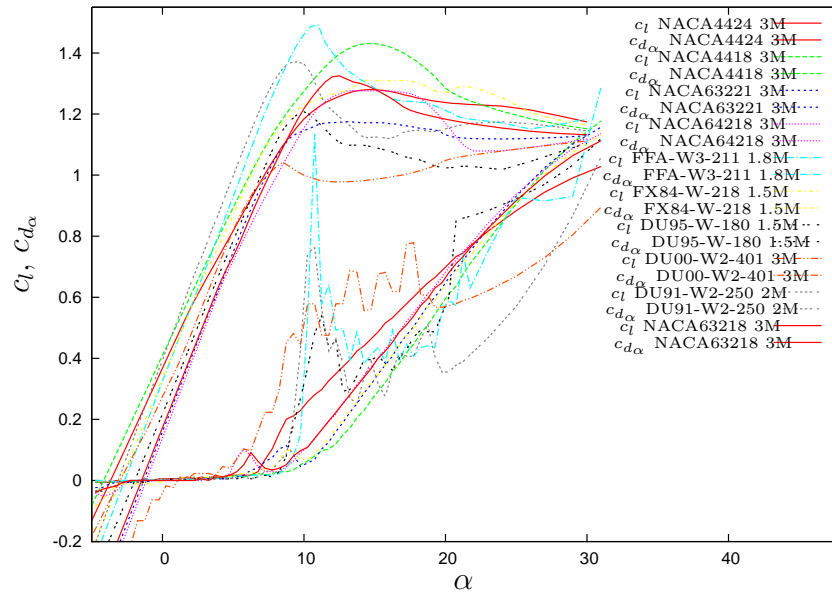


Figure 10.14: The lift coefficients and the  $c_{d\alpha}$  values against angle of attack for different wind turbine aerofoils.

During wind tunnel tests the flap-lag-stall instability could not be reproduced [55]. The most likely cause for this was the mild character of the calculated instability that was changed into a stable situation due to structural damping. The lift-stall instability measured and calculated did show a good correspondence.

### 10.3 Helicopter Flap-Lag Instability and Wind Turbine Flap-Lag-Stall Instability

The previous sections have dealt with the flap-lag instability as known in helicopter blades and the flap-lag-stall instability in wind turbine blades. In section 10.2.3 it was already mentioned that the flap frequency of large wind turbines is nowhere near the interval for instabilities ( $1 < p^2 < 2$ ) that was found by Ormiston and Hodges [102]. However, section 10.1 has also shown that this limit is not always valid. For example, in case of pre-cone, the interval can even completely disappear and the instability can become independent of the flap frequency, if the flap frequency is equal to the lag frequency.

A wind turbine blade will differ from the defined helicopter blade in the definition of positive pitch and the local out of plane velocity of the air. Both will be in the opposite direction compared to the helicopter blade. Therefore the above derived equations will hold for a wind turbine when both  $\theta$  and  $A$  are assumed to be negative. Looking at equation 10.41, this does not change the interval for instabilities. In this equation the  $\theta$  and  $A$  only occur in combined multiplication, which results in the same situation as for helicopters. When elastic coupling

is included, equation 10.44 is valid. In this case the effect of the change in sign of  $\theta$ ,  $A$  and  $Z$  is also cancelled. The values for these three properties can possibly differ significantly, resulting in differences in the stability boundaries for wind turbines compared to helicopter blades. When elastic coupling is included, the interval for the flap frequency is no longer a limit for possible instabilities.

The inclusion of stall effects in the calculations by Ormiston and Bousman has shown to have significant effect on the stability. Unfortunately the analysis in [101] is limited to values of  $p$  that are within the given interval for instabilities.

All in all it is clear that the conditions that lead to the limiting frequency interval for possible flap-lag instabilities in helicopters ( $\Omega < \omega_\beta < \sqrt{2}\Omega$ ) is not valid for wind turbines. The elastic coupling that is present in a wind turbine blade, changes the equations for neutral stability and the interval is no longer valid, instabilities can also occur outside of this flap frequency interval. The elastic coupling assumed in the baseline model for STABTOOL differs from the elastic coupling used by Ormiston and Hodges [102]. According to their definition, there is full elastic coupling in the flap direction;  $R_\beta = 1$ , because all flexibility is in the directions of the blade, no flap flexibility in the hub directions. But in the lead-lag direction the coupling is half:  $R_\zeta = 0.5$ , because the springs stiffnesses were assumed to be equal:  $k_\varepsilon = k_\zeta$  and  $\varepsilon$  was defined as the degree of freedom in the directions of the hub while  $\zeta$  was a degree of freedom that was defined in the directions of the blade.

## 10.4 Flap-Lag Coincidence

As a first investigation, the wind turbine blade model discussed in section 8.2.2 has been altered such that the flap- and lead-lag frequency come closer together and coincidence has also been looked at. The configuration for an active stall regulated (ASR) turbine has been used. This configuration has been created during the STABCON project and it means that the blade of the benchmark is used (see section 8.2.2), but the pitch setting and rotational velocity have been chosen such that the power of the turbine is limited not by pitching towards smaller angles of attack, but by the effect of stall.

To investigate the effect of changing the difference between the first flap and first lead lag frequency of the blade, the simulations were run with five different blade models [51]. These are summarised in table 10.1. First model A is the original blade. A reduction of the lag stiffness reducing the difference between lag and flap stiffness by 75% is called blade B. Blade C is the blade where the lag stiffness has been reduced to equalise the flap stiffness. Blade D is the blade where the difference between flap and lag stiffness has been reduced by 75 % but now by increasing the flap stiffness. The last blade model is model E where the flap and lag stiffness are equalised to both be the original lag stiffness.

The equation used to calculate the stiffnesses in blade model B is:

$$k_{\zeta_{75}} = k_\zeta - (k_\zeta - k_\beta) \cdot 0.75 \quad (10.52)$$

Model	Description, relative to original blade
A	Original blade
B	Reduction of lag stiffness, difference between flap and lag reduced by 75%
C	Reduced lag stiffness to equal flap stiffness
D	Increased flap stiffness, difference between flap and lag reduced by 75%
E	Increased flap stiffness to equal lag stiffness

Table 10.1: Different models simulated using WOBBE

and similar to this for blade model D:

$$k_{\beta_{75}} = k_{\beta} - (k_{\beta} - k_{\zeta}) \cdot 0.75 \quad (10.53)$$

The simulations were run for configurations for 5 m/s, 8 m/s, 12 m/s, 15 m/s and 18 m/s. For each wind speed a certain pitch setting and rotational velocity is used. As mentioned before, these settings are not the actual settings of the wind turbine, but of a model of an active stall regulated wind turbine that results in the same power for the different wind speeds as the actual wind turbine.

Similar to section 8.2.2, the identification tool is used to find the damping coefficients (see appendix D). Small perturbations around the steady state are used, but because the flap vibration will be strongly damped, the initial amplitudes given to the flap angles are larger than the other angles. If these angles are taken too small, the flap vibration will not be identified correctly, because the flap vibration will then hardly be present in the simulation results.

The simulations were all successfully run and identified. The lead-lag frequency changed due to the change in the stiffness of the springs for configurations B and C. For configurations D and E the flap eigenfrequency changed. The frequencies for the different configurations at the different wind speeds were determined using the identification tool [87] and are shown in table 10.2 and table 10.3. The frequencies are also illustrated in figure 10.15 and 10.16. The tables show that the flap and lead-lag frequencies do not exactly coincide for blades C and E. For these blades the stiffness in lead-lag direction and flap direction have been equalised. The difference in the frequencies is due to the difference in centrifugal stiffening for the flap and the lead-lag mode. There is also a difference in the moments of inertia about the flap and lead-lag axis, which will also result in a difference between the frequencies if springs of equal stiffness are chosen.

Changing the lead-lag or flap stiffness does not only change the eigenfrequencies. It also results in changes in among other the steady state. The effect of changing the stiffness on the angle of attack is rather small. The average value of the angle of attack does not show a change, as illustrated in figure 10.17. The amount of variation in angle of attack does show differences. These differences can be expected, because the damping values for the flap modes of the different blades will be different and a reduction in the damping of the flap mode will result in larger fluctuations of the angle of attack during the simulation. Another

Model \ wind speed	5	8	12	15	18
A	0.99	1.04	1.04	1.04	1.03
B	0.98	1.04	1.04	1.03	1.03
C	0.98	1.03	1.03	1.04	1.03
D	1.75	1.78	1.77	1.76	1.76
E	1.91	1.93	1.93	1.95	1.94

Table 10.2: Identified first flap frequencies for the different models at the different wind speeds.

Model \ wind speed	5	8	12	15	18
A	1.89	1.89	1.89	1.89	1.89
B	1.37	1.38	1.38	1.38	1.38
C	0.96	0.98	0.98	0.97	0.98
D	1.89	1.90	1.90	1.91	1.90
E	1.89	1.90	1.90	1.88	1.89

Table 10.3: First lead-lag frequencies for the different models at the different wind speeds.

effect due to the differences in stiffness is the change of the Coriolis moments. As shown in section 10.2, the steady state value of the flap angle plays an important role in the stability of a blade.

The identified damping for the first flap mode is shown in figure 10.18 and for the first lead-lag mode the damping is shown in figure 10.19. Figure 10.18 shows that the damping of the first flap mode is unchanged in the cases where the lead-lag stiffness is changed and it shows a decrease for the cases where the blade's flap stiffness has been increased. Figure 10.19 shows that the wind turbine blade suffers from instabilities in its base model. As discussed before, the configuration of the stall regulated turbine has been chosen to result in the same power as the original pitch regulated variable speed turbine. This has resulted in a model that becomes unstable for some wind speeds in the first lead-lag mode. For the cases calculated in this section the highest two wind speeds (15 m/s and 18 m/s) show the blade to be unstable. However, if the structural damping would be taken into account, this instability will probably disappear. Figure 10.19 also shows a very small decrease in stability for all blades compared to the baseline blade (A) for 5 and 8 m/s, but an increase for 12 and 15 m/s. The difference for the low wind speeds is however very small, this cannot be really seen as an explicit difference in damping. It seems that the difference in stiffness has no influence on the damping of the first lead-lag mode for the low wind speeds. The effect on the higher wind speeds is however significant. Figure 10.19 also shows that the stabilising effect is greatest for blades C and E, these are the blades where the stiffnesses in flap and lead-lag direction have been set equal to each other and therefore the eigenfrequencies of the first two modes are very close.

The time histories resulting from the simulations show the instabilities at the higher wind

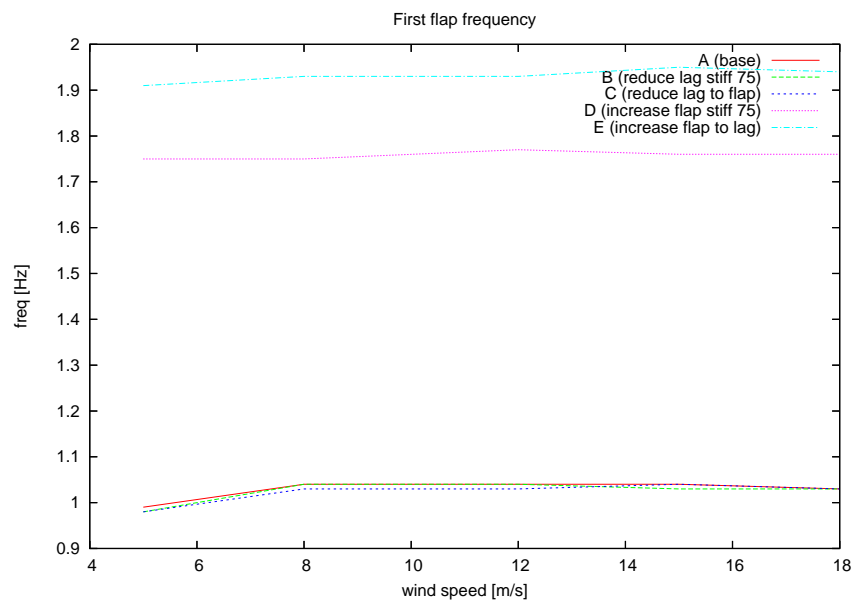


Figure 10.15: First flap frequencies of the different blades

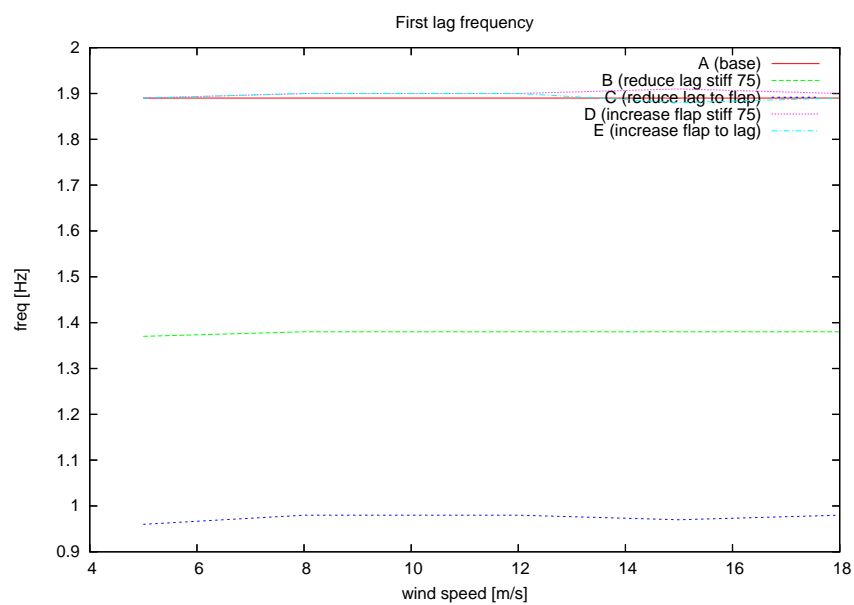


Figure 10.16: First lead-lag frequencies of the different blades

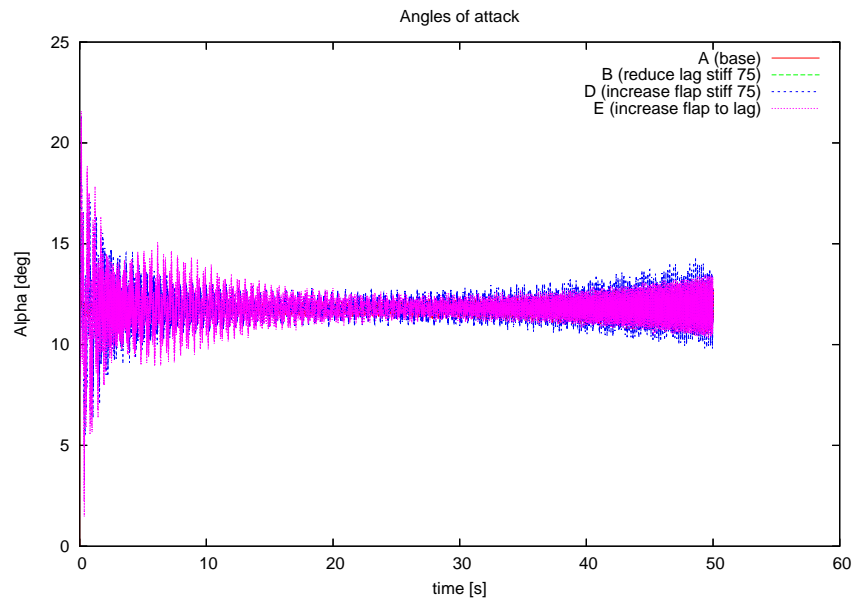


Figure 10.17: The behaviour in time of the angles of attack at a point on the blade, for three different blades, all at 15 m/s.

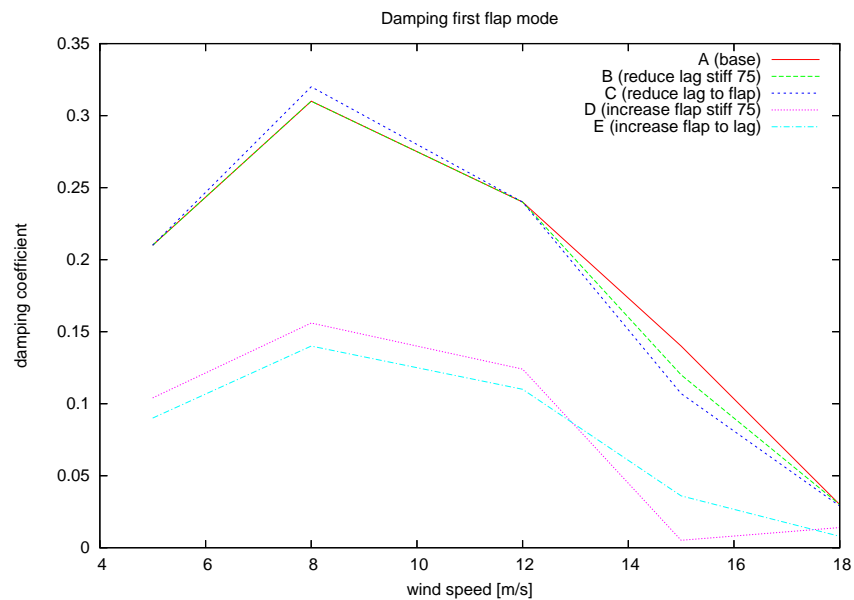


Figure 10.18: Damping of the first flap mode for different wind speeds and different blades

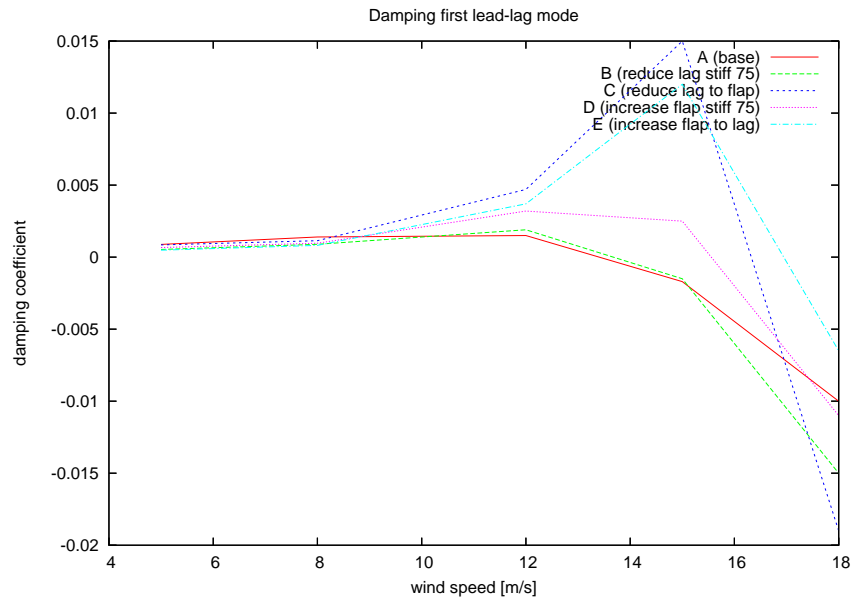


Figure 10.19: Damping of the first lead-lag mode for different wind speeds and different blades

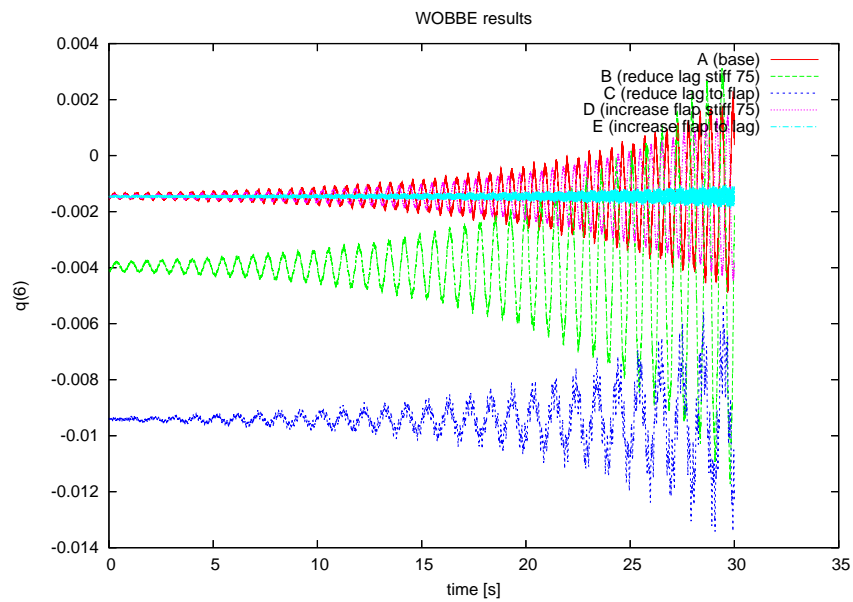


Figure 10.20: Time response resulting from WOBBE for the 6th degree of freedom (lead-lag) for the different blades at 18 m/s. The starting amplitude was not exactly the same for all blades.

speeds very clearly. The difference between the different models also appears very clearly in these results. This is illustrated in figure 10.20. This figure shows the time histories of the lag hinge, that is the 6<sup>th</sup> generalised coordinate, for simulations at 18 m/s. Note that the different simulations were not all run starting from the exact same amplitudes relative to the steady state. The difference in steady state is clearly visible and the difference between blade C (weakest instability) and blade E (strongest instability) is also clearly illustrated.

The simulations of the wind turbine blade showed that changing the lead-lag stiffness while keeping the flap stiffness the same does not influence the damping of the first flap mode. Only for a wind speed of 15 m/s a small difference shows up.

The damping of the first lead-lag mode becomes slightly smaller for the low wind speeds, but it improves for higher wind speeds (up to 15 m/s), where the baseline blade has become unstable. The altered blades are also unstable, but the damping is less negative than the damping of the baseline blade. This effect is greatest for the two blades where the first flap and first lag frequency almost coincide. These results are similar to those found by Buhl e.a. [17, 16].

All in all changing the blade stiffness which results in frequencies coming closer together did not result in a clear trend that was expected. The possibility of flap-lag-stall occurring on large wind turbines will be investigated further in the next section.

## 10.5 Simplified Blade Damping Model

For further investigation of the possibility of flap-lag-stall on wind turbines, a simplified blade model has been used to determine the damping coefficients for motions of the blade in-plane or out-of-plane. With this model it is possible to estimate the configurations for which the edgewise mode will be negatively damped and for which configurations flap-lag-stall flutter would be possible.

### 10.5.1 Derivation of the Damping Coefficients

The damping of a wind turbine blade due to aerodynamics can be approximated using a simple model as illustrated in figure 10.21. The figure shows a blade element with the wind velocity  $V$  and the velocity due to the rotation  $r\Omega$ . These two velocities will change when the blade moves in either direction, in-plane or out-of-plane. Petersen [111] *et al.* describe that the influence of these motions on the aerodynamic forces can be derived. The forces are linearised using:

$$F_x^R(\Delta V, \Delta(r\Omega)) \simeq F_x^R(V_0, r\Omega_0) + \frac{\partial F_x^R(V_0, r\Omega_0)}{\partial V} \Delta V + \frac{\partial F_x^R(V_0, r\Omega_0)}{\partial(r\Omega)} \Delta(r\Omega) \quad (10.54)$$

and a similar equation can be derived for the force in the  $y$ -direction. The superscript  $( )^R$  is used to indicate that the  $x$  and  $y$  coordinates are defined in the directions parallel to the

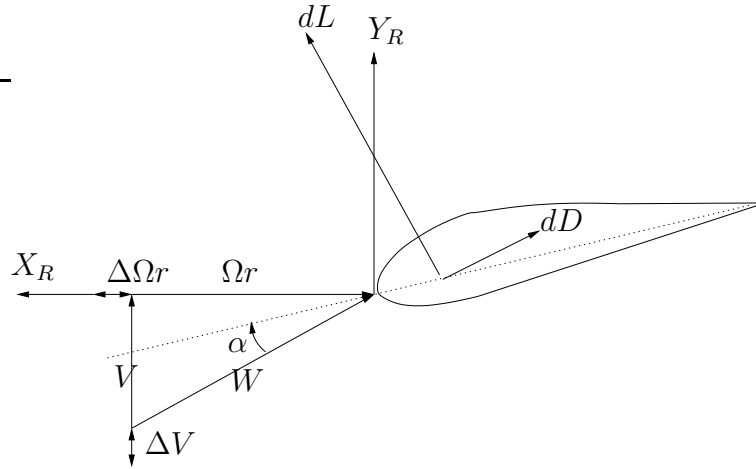


Figure 10.21: The aerodynamic forces acting on an element due to the local wind velocity. By looking at changes of the wind speed and rotational speed of the rotor, the damping matrix can be derived.

rotor plane and perpendicular to the rotor plane. Combined this gives:

$$\begin{Bmatrix} F_x^R \\ F_y^R \end{Bmatrix} \simeq \begin{Bmatrix} F_{x0}^R \\ F_{y0}^R \end{Bmatrix} + \begin{bmatrix} \frac{\partial F_x^R}{\partial(r\Omega)} & \frac{\partial F_x^R}{\partial V} \\ \frac{\partial F_y^R}{\partial(r\Omega)} & \frac{\partial F_y^R}{\partial V} \end{bmatrix} \begin{Bmatrix} \Delta(r\Omega) \\ \Delta V \end{Bmatrix} \quad (10.55)$$

Notice that an increase in  $r\Omega$  results in a negative  $\Delta y_R$ . Using the velocities  $\dot{x}_R$  and  $\dot{y}_R$  the aerodynamic damping matrix can be defined as:

$$[c^R] = \begin{bmatrix} c_{xx} & c_{xy} \\ c_{yx} & c_{yy} \end{bmatrix} = \begin{bmatrix} -\frac{\partial F_x^R}{\partial(r\Omega)} & \frac{\partial F_x^R}{\partial V} \\ -\frac{\partial F_y^R}{\partial(r\Omega)} & \frac{\partial F_y^R}{\partial V} \end{bmatrix} \begin{Bmatrix} \dot{x}_R \\ \dot{y}_R \end{Bmatrix} \quad (10.56)$$

The lift- and drag force per unit length of the blade can be determined using blade element theory:

$$dL = \frac{1}{2} \rho c W^2 c_l \quad (10.57)$$

and

$$dD = \frac{1}{2} \rho c W^2 c_d \quad (10.58)$$

The resulting wind speed  $W$  in these equations is:

$$W = \sqrt{V^2 + r^2 \Omega^2} \quad (10.59)$$

The resulting forces in the  $x_R$  and  $y_R$  directions are:

$$\begin{Bmatrix} F_x^R \\ F_y^R \end{Bmatrix} = \begin{bmatrix} \sin \phi & -\cos \phi \\ \cos \phi & \sin \phi \end{bmatrix} \begin{Bmatrix} dL \\ dD \end{Bmatrix} \quad (10.60)$$

with

$$\phi = \theta + \alpha \quad (10.61)$$

and

$$\cos \phi = \frac{r\Omega}{W}; \quad \sin \phi = \frac{V}{W} \quad (10.62)$$

Using these expressions the resulting forces can be written as:

$$F_x^R = \frac{1}{2}\rho c V W c_l - \frac{1}{2}\rho c r \Omega W c_d \quad (10.63)$$

and

$$F_y^R = \frac{1}{2}\rho c r \Omega W c_l + \frac{1}{2}\rho c V W c_d \quad (10.64)$$

The terms in the damping matrix can be determined by calculating the derivatives of the resulting forces. Taking the derivative of the force in  $x$ -direction relative to the change in velocity in  $x$ -direction gives  $c_{xx}^R$ :

$$\begin{aligned} c_{xx}^R &= -\frac{\partial F_x^R}{\partial(r\Omega)} \\ &= -\frac{1}{2}\rho c \left[ V \frac{\partial W}{\partial(r\Omega)} c_l + V W c_{l\alpha} \frac{\partial \alpha}{\partial(r\Omega)} + W c_d + r\Omega \frac{\partial W}{\partial(r\Omega)} c_d + r\Omega W c_{d\alpha} \frac{\partial \alpha}{\partial(r\Omega)} \right] \end{aligned} \quad (10.65)$$

The derivatives of the resulting wind speed and the angle of attack are:

$$\frac{\partial W}{\partial(r\Omega)} = \frac{\partial \sqrt{V^2 + r^2\Omega^2}}{\partial(r\Omega)} = \frac{r\Omega}{\sqrt{V^2 + r^2\Omega^2}} = \frac{r\Omega}{W} \quad (10.66)$$

$$\frac{\partial \alpha}{\partial(r\Omega)} = \frac{\partial \arcsin \frac{V}{W}}{\partial(r\Omega)} = -\frac{V}{W^2} \quad (10.67)$$

With these expressions the damping coefficient  $c_{xx}^R$  can be written as:

$$c_{xx}^R(r\Omega, V) = \frac{1}{2}c\rho \frac{r\Omega}{W} \left[ \left( \frac{2r^2\Omega^2 + V^2}{r\Omega} \right) C_d - V C_{d\alpha} - V C_l + \frac{V^2}{r\Omega} C_{l\alpha} \right] \quad (10.68)$$

Using

$$\frac{\partial W}{\partial V} = \frac{V}{W}; \quad \frac{\partial \alpha}{\partial V} = \frac{r\Omega}{W^2} \quad (10.69)$$

the other three damping coefficients can also be derived in a similar manner resulting in:

$$\begin{aligned} c_{xx}^R(r\Omega, V) &= \frac{1}{2}c\rho \frac{r\Omega}{W} \left[ \left( \frac{2r^2\Omega^2 + V^2}{r\Omega} \right) C_d - V C_{d\alpha} - V C_l + \frac{V^2}{r\Omega} C_{l\alpha} \right] \\ c_{xy}^R(r\Omega, V) &= \frac{1}{2}c\rho \frac{r\Omega}{W} \left[ -V C_d - r\Omega C_{d\alpha} + \left( \frac{2V^2 + r^2\Omega^2}{r\Omega} \right) C_l + V C_{l\alpha} \right] \\ c_{yx}^R(r\Omega, V) &= \frac{1}{2}c\rho \frac{r\Omega}{W} \left[ -V C_d + \frac{V^2}{r\Omega} C_{d\alpha} - \left( \frac{2r^2\Omega^2 + V^2}{r\Omega} \right) C_l + V C_{l\alpha} \right] \\ c_{yy}^R(r\Omega, V) &= \frac{1}{2}c\rho \frac{r\Omega}{W} \left[ \left( \frac{2V^2 + r^2\Omega^2}{r\Omega} \right) C_d + V C_{d\alpha} + V C_l + r\Omega C_{l\alpha} \right] \end{aligned} \quad (10.70)$$

The damping matrix can now be calculated for different values of the wind velocity and the velocity due to the rotation of the blade. Looking at the term  $c_{xx}^R$  it is clear that this value can easily become negative, which could lead to an instability. However, the damping matrix derived here is for purely in-plane and purely out-of-plane motions only. Usually the first lead-lag mode will have an out-of-plane component in it, as will the first flap mode have an in-plane component. The damping coefficients of the eigenmodes are the ones determining the stability, therefore these must be calculated. Transforming the damping matrix from equation 10.70 to the local reference frame in the directions of the modes gives[111]:

$$[c^B] = -[T_{RB}][c^R][T_{RB}]^T = \begin{bmatrix} \cos \theta_{RB} & \sin \theta_{RB} \\ -\sin \theta_{RB} & \cos \theta_{RB} \end{bmatrix} \begin{bmatrix} c_{xx}^R & c_{xy}^R \\ c_{yx}^R & c_{yy}^R \end{bmatrix} \begin{bmatrix} \cos \theta_{RB} & -\sin \theta_{RB} \\ \sin \theta_{RB} & \cos \theta_{RB} \end{bmatrix} \quad (10.71)$$

This gives:

$$\begin{aligned} c_{xx}^B &= \cos^2 \theta_{RB} c_{xx}^R + \sin^2 \theta_{RB} c_{yy}^R + \sin \theta_{RB} \cos \theta_{RB} (c_{xy}^R + c_{yx}^R) \\ c_{xy}^B &= -\sin^2 \theta_{RB} c_{yx}^R + \cos^2 \theta_{RB} c_{xy}^R + \sin \theta_{RB} \cos \theta_{RB} (c_{yy}^R - c_{xx}^R) \\ c_{yx}^B &= \cos^2 \theta_{RB} c_{xy}^R - \sin^2 \theta_{RB} c_{yx}^R + \sin \theta_{RB} \cos \theta_{RB} (c_{yy}^R - c_{xx}^R) \\ c_{yy}^B &= \sin^2 \theta_{RB} c_{xx}^R + \cos^2 \theta_{RB} c_{yy}^R - \sin \theta_{RB} \cos \theta_{RB} (c_{xy}^R + c_{yx}^R) \end{aligned} \quad (10.72)$$

From these equations it is clear that:

$$c_{yy}^B(\theta_{RB}) = c_{xx}^B(\theta_{RB} - 90^\circ) \quad (10.73)$$

and

$$c_{yx}^B(\theta_{RB}) = -c_{yx}^B(-\theta_{RB}) \quad (10.74)$$

Typical values for the structural pitch of wind turbine blades will be angles of  $0^\circ$  till  $-20^\circ$  for the lead-lag mode for zero pitch setting. Therefore the values for the corresponding damping in the flap mode can be found as  $c_{xx}^B$  for values of  $\theta_{RB}$  between  $70^\circ$  and  $90^\circ$ .

The effect of the structural pitch angle on the damping coefficients will be looked at in more detail in section 10.5.3.

## 10.5.2 Difference Between Two Instabilities: Flap-Lag Flutter and Negative Damping of Edgewise Mode

In this chapter, equations have now been derived for two different instabilities. How do the two instabilities described above compare to each other? The first instability, negative damping in edgewise direction is caused by a negative value for the damping in the direction of this mode. Usually this direction will not be only in the in-plane direction, the mode will also have an out-of-plane contribution. To calculate the damping for this case, it is necessary

to transform the damping values from section 4.3.1, equation 10.70 to the directions of the first flap and first lead-lag mode.

The second instability that is described, the flap-lag-stall instability, will only occur when the frequencies (first flap and first lead-lag) are close to each other and one might expect that it is purely caused by the coupling terms in the damping matrix. The flap motion will lead to an increase in the lead-lag motion and/or vice-versa. However, these damping coefficients derived in the previous section are based on a rather simple and purely aerodynamic analysis, while the dynamics of the system, in particular the Coriolis accelerations, are also of importance for the flap-lag-stall instability. Therefore looking only at  $c_{xy}^B$  is not sufficient.

The values of  $c_{xx}^B$  and  $c_{xy}^B$  can be calculated for different directions of the modes and for different angles of attack.

### 10.5.3 Flap-Lag Coincidence and the Possibility of Flap-Lag-Stall

Recall that using simple aerodynamics, equations were derived for the damping coefficients in the directions of the flap and lead-lag motion (Eq. 10.72):

$$\begin{aligned} c_{xx}^B &= \cos^2 \theta_{RB} c_{xx}^R + \sin^2 \theta_{RB} c_{yy}^R + \sin \theta_{RB} \cos \theta_{RB} (c_{xy}^R + c_{yx}^R) \\ c_{xy}^B &= -\sin^2 \theta_{RB} c_{yx}^R + \cos^2 \theta_{RB} c_{xy}^R + \sin \theta_{RB} \cos \theta_{RB} (c_{yy}^R - c_{xx}^R) \\ c_{yx}^B &= \cos^2 \theta_{RB} c_{xy}^R - \sin^2 \theta_{RB} c_{yx}^R + \sin \theta_{RB} \cos \theta_{RB} (c_{yy}^R - c_{xx}^R) \\ c_{yy}^B &= \sin^2 \theta_{RB} c_{xx}^R + \cos^2 \theta_{RB} c_{yy}^R - \sin \theta_{RB} \cos \theta_{RB} (c_{xy}^R + c_{yx}^R) \end{aligned}$$

where  $\theta$  is the angle for the structural pitch.

The values of  $c_{xx}^B$  and  $c_{xy}^B$  can be calculated for different directions of the modes and for different angles of attack.

Looking at a model of a real wind turbine blade, it is possible to calculate the values of these coefficients for different wind speeds and corresponding pitch setting and rotational velocity and as a function of the structural pitch angle  $\theta_{RB}$ . This analysis has been performed for several points along the blade. From this analysis it is possible to determine the values of the pitch and angle of attack for which the flap-lag-stall instability can occur, while the negative damping in edgewise direction is not occurring.

The blade that has been used in this analysis is the same blade as discussed in section 8.2.2. The results for the original pitch regulated variable speed turbine for 5, 10, 13 and 16 m/s at four different points along the blade are shown in figures 10.22 until figure 10.25. These figures show the different damping coefficients made non dimensional by dividing  $c_{ij}^B$  by  $\frac{1}{2}\rho\Omega r$ .

Assuming an active stall regulated wind turbine, calculations have also been performed for the same points along the blade and the same wind speeds. The results for 5 m/s, 10 m/s and 13 m/s do not differ from the results of the variable speed turbine, because the setting in these cases is rather similar. The results for 16 m/s are shown in figure 10.26.

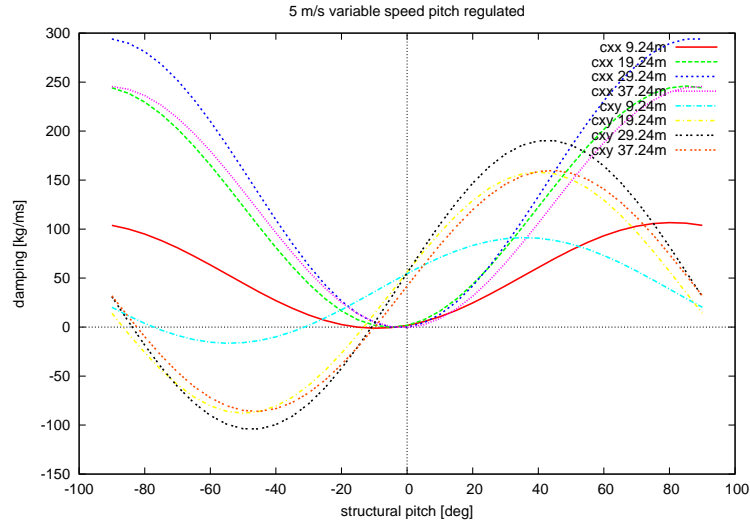


Figure 10.22: Non dimensional values for the damping  $c_{xx}^B$  and  $c_{xy}^B$  as functions of the structural pitch angle for 5 m/s at four different points along the blade.

To investigate the effect of stall, another situation has been analysed where the blade is operating under conditions that result in such large angles of attack that the slope of the lift curve is negative. This situation is for 16 m/s with an aerodynamic pitch setting (this has no influence on the structural pitch angle  $\theta_{RB}$ ) of -10 degrees. In this case the angle of attack for the four illustrated points along the blade radius vary from 42 degrees to 22 degrees.

The values for  $c_{xx}^B$  give an indication for the areas where negative damping of the first lead-lag mode can take place. If these values are negative, this instability is likely to occur. The flap-lag-stall instability will occur on its own for circumstances that results in a (small) positive value for  $c_{xx}^B$  combined with a negative value for  $c_{xy}^B$  and  $c_{yx}^B$ . Of course the damping of the flap mode must also be positive,  $c_{yy} > 0$ . However, note that as discussed before, this analysis is based on a strong oversimplification, the aerodynamics are treated separately without taking into account any coupling to dynamics or aeroelastics, while the Coriolis acceleration can also play an important destabilising role. Therefore this analysis is too simplistic to be able to completely analyse the possibility of flap-lag-stall flutter. It does however give a reasonably good idea about the damping of the edgewise mode.

If flap-lag-stall is actually occurring, this should be illustrated by a clear effect on the stability of the blade when reducing the difference in frequency. If there is a case where flap-lag-stall will occur, this will only happen when the frequencies are close to each other and therefore reducing the difference between the flap and the lead-lag frequency will reduce the stability or increase the instability.

The results for 5 m/s in figure 10.22 show the possibility of flap-lag flutter to occur for very large structural pitch angles (  $-40^\circ$  till  $-60^\circ$ ). For these pitch angles  $c_{yx}^B$  will also be negative, while at the same time the damping of the lead-lag mode is very large. Of course for this low wind speed the blade will not be stalled. The combination of these damping

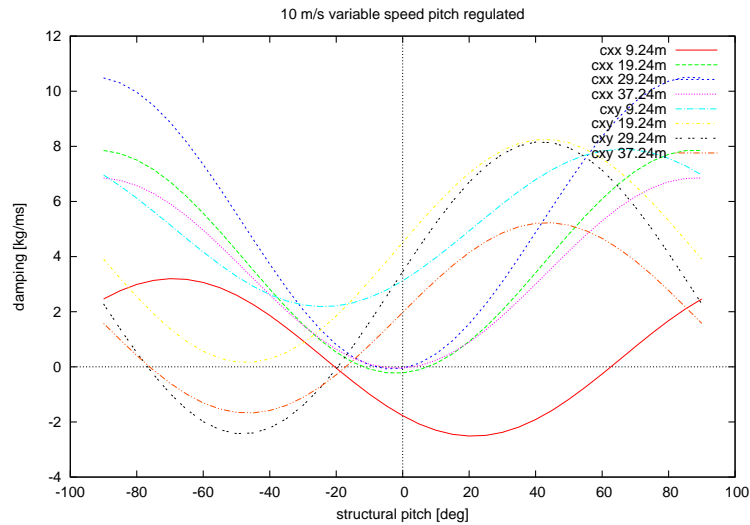


Figure 10.23: Non dimensional values for the damping  $c_{xx}^B$  and  $c_{xy}^B$  as functions of the structural pitch angle for 10 m/s at four different points along the blade.

values could result in a flap-lag instability.

The results for 10 m/s in figure 10.23 show the possibility of flap-lag flutter for the same range as the results for 5 m/s, but the negative damping is smaller and for the two points closest to the hub the damping is positive. The instability of the lead-lag mode due to negative damping is also not to be expected for any value of  $\theta_{RB}$ .

The results for 13 m/s in figure 10.24 show a range for the structural pitch where one can expect negative damping of the lead-lag mode, but the values for  $c_{xy}^B$  remain positive. However, the values for  $c_{yx}^B$  will have a range where they are negative.

The results for 16 m/s in figure 10.25 are rather similar to the results for 10 m/s. There is no range of structural pitch angles for which either instability can be expected.

The results for 16 m/s for a stall regulated configuration in figure 10.26 shows a large range of structural pitch angles for which the negative damping of the lead-lag mode can be expected. The flap-lag-stall instability however, does not seem a possibility.

The results for 16 m/s with an aerodynamic pitch setting that has increased the angle of attack such that the lift slope is negative, are illustrated in figure 10.27. This shows that there is a small range for the structural pitch angle, just before  $0^\circ$  where all the damping values are negative. For the common values of the structural pitch ( $-20^\circ$  till  $0^\circ$ ) this configuration could show the flap-lag-stall instability, however, when looking to figure 10.27 and recalling that the damping of the flap mode is given by looking at  $\theta_{RB} + 90^\circ$  then it shows that the flap mode will now be negatively damped. Again, there is no possibility for the flap-lag stall instability occurring on its own.

In an attempt to find out when flap-lag-stall instabilities will actually occur, simulations

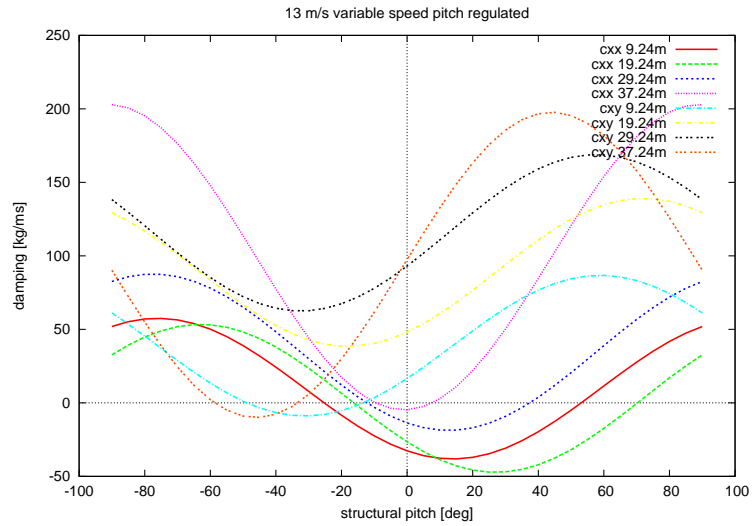


Figure 10.24: Non dimensional values for the damping  $c_{xx}^B$  and  $c_{xy}^B$  as functions of the structural pitch angle for 13 m/s at four different points along the blade.

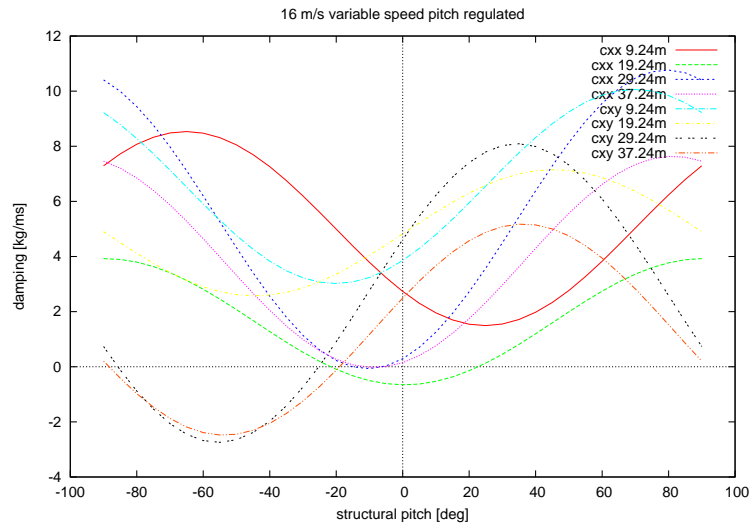


Figure 10.25: Non dimensional values for the damping  $c_{xx}^B$  and  $c_{xy}^B$  as functions of the structural pitch angle for 16 m/s at four different points along the blade.

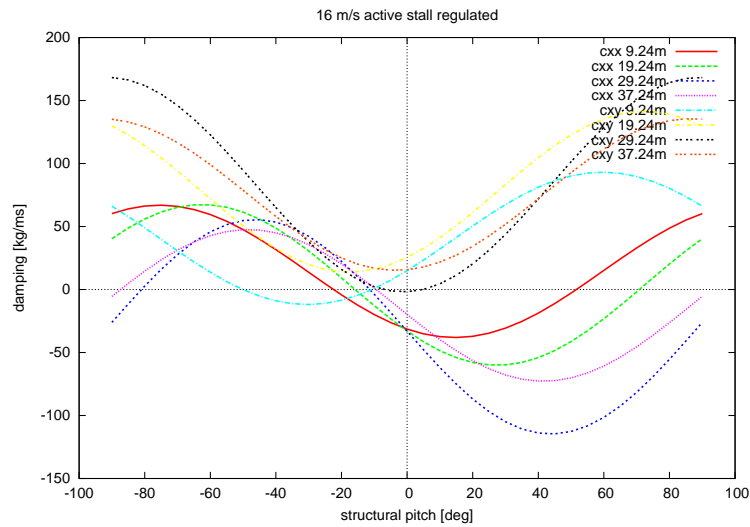


Figure 10.26: Non dimensional values for the damping  $c_{xx}^B$  and  $c_{xy}^B$  as functions of the structural pitch angle for 16 m/s at four different points along the blade. The pitch setting of a stall regulated turbine has been used.

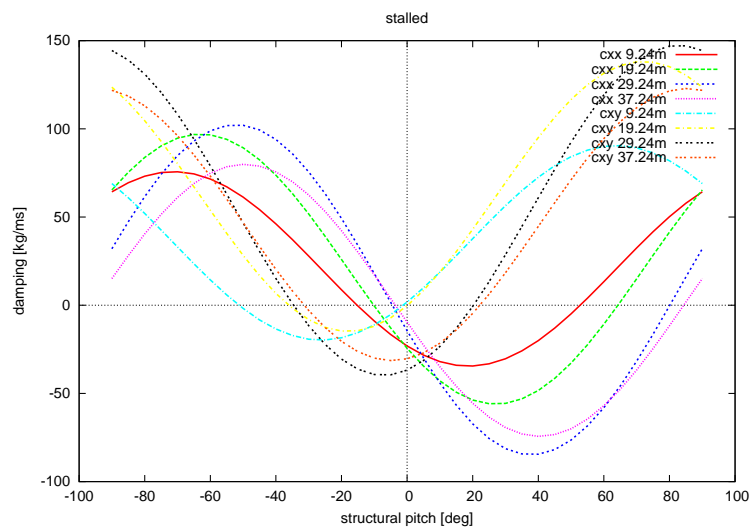


Figure 10.27: Non dimensional values for the damping  $c_{xx}^B$  and  $c_{xy}^B$  as a function of the structural pitch angle for 16 m/s at four different points along the blade. By changing the aerodynamic pitch setting, the angle of attack of the blade is so large that the lift slope is negative.

were run, using the fully non-linear rigid body simulation tool described in chapters 5 and 6, on blade models that according to the results given above should show this instability.

The model used is based on the results for the calculations for the variable speed wind turbine at  $5m/s$ . From figure 10.22 it can be seen that for a pitch angle of  $-40^\circ$  it is possible for a flap-lag instability to occur without the negative damping of the lead-lag occurring. However, the flow is nowhere near stall in this case, the angles of attack are very small.

To investigate the possible instability, a model based on a real wind turbine blade with 15 degrees of freedom (6 flap, 6 lead-lag and 3 torsion, figure 8.14) has been simulated. The stiffness in lead-lag direction has been reduced towards the value of the flap stiffness. The resulting frequencies are shown in figure 10.28. As shown in section 10.4, the reduction in lead-lag stiffness did not have much effect on the damping coefficients. Of course this was for a blade with a more normal structural pitch setting. For the blade used in that case, according to figure 10.22, the flap-lag instability should not occur. For the new model with the large structural pitch angle, the results are different, as illustrated by figure 10.29. The damping of the flap mode is strongly increased, but the damping in the lead-lag mode shows a large reduction, but it does not become unstable.

These results show the possibility of flap-lag flutter, but the blade is not stalled. Also, the results remain positively damped, although only just. The structural pitch angle of  $40^\circ$  is not realistic, resulting in a conclusion that there can be a destabilising effect from the frequency coincidence, but it will not easily lead to instabilities. The negative damping of the edgewise mode is much more critical as it is more likely to occur.

It must be noted that in the STABTOOL project, it was concluded that the destabilising Coriolis moments would result in the instability, therefore small positive values of the coupling damping terms could also result in an instability. The large structural pitch used in the previously discussed calculations will also have an effect on the Coriolis terms, it will significantly reduce the out-of-plane position of the blade for a given flap angle in the most flexible direction

Another situation that has been simulated is a case from figure 10.27, where the angle of attack is so large that the lift slope has become negative. For a structural pitch angle of  $-20^\circ$  the flap motion is negatively damped, but there should also be an influence of frequency coincidence. Using the simulation tool gives fully non-linear time results, but for instabilities it is not possible to extract a damping coefficient from the results by using the identification tool. This is because the identification tool is only reliable when the results are close to linear, while the instability will make it impossible to keep the deformations small enough to stay close to linear results. Therefore the only indication that can be given is the resulting time series themselves.

In figure 10.30 one of the flap angles in the model is shown as a function of time for both the original blade as well as a blade where the stiffness of the lag springs has been reduced to the values of the flap springs. This figure illustrates that there was a clear instability of the flap mode. Figure 10.31 shows one of the lead-lag angles in the model as a function of

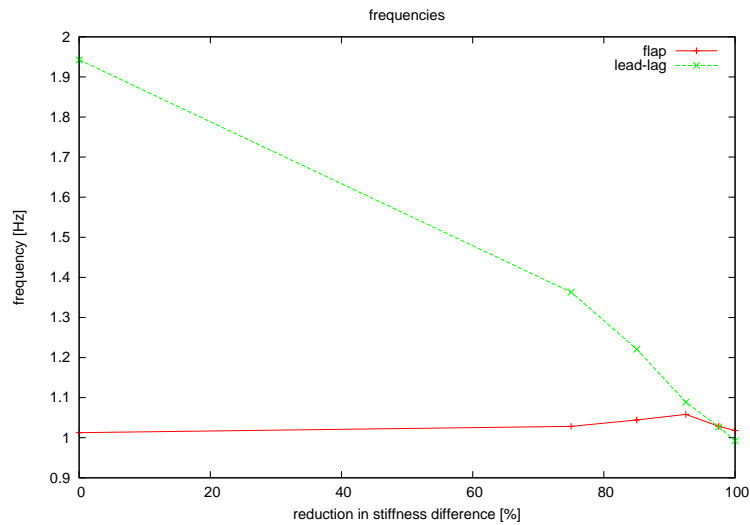


Figure 10.28: The first flap and first lead-lag frequency of a blade with a very large structural pitch for different values of the original difference between the stiffnesses in these two directions. The original values (0%), a reductions of the difference by 75%, 85%, 92.5% and 97.5% and setting the stiffness in both directions equal.

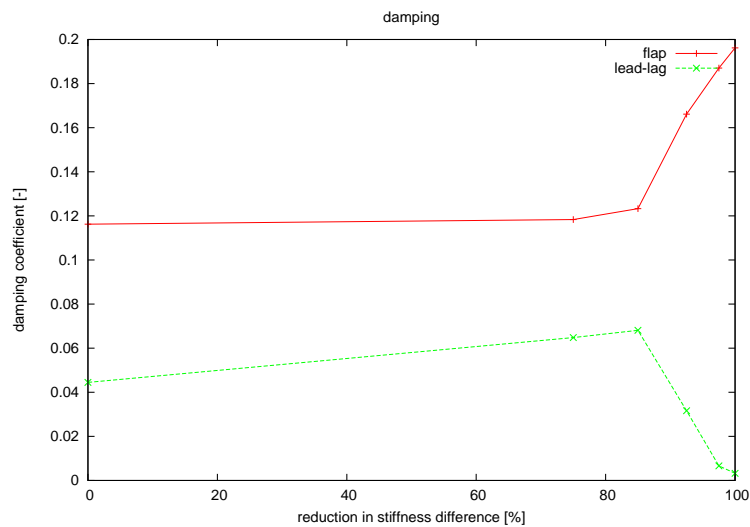


Figure 10.29: Damping of the first flap and first lead-lag mode of a blade with a very large structural pitch for different values of the original difference between the stiffnesses in these two directions. The original values (0%), a reductions of the difference by 75% , 85%, 92.5% and 97.5% and setting the stiffness in both directions equal.

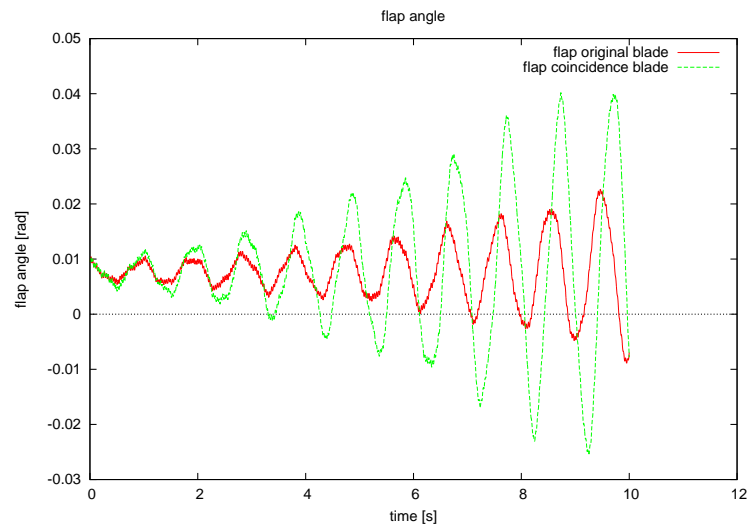


Figure 10.30: Time response of second flap angle, for both the original blade as for a blade with reduced lead-lag stiffness.

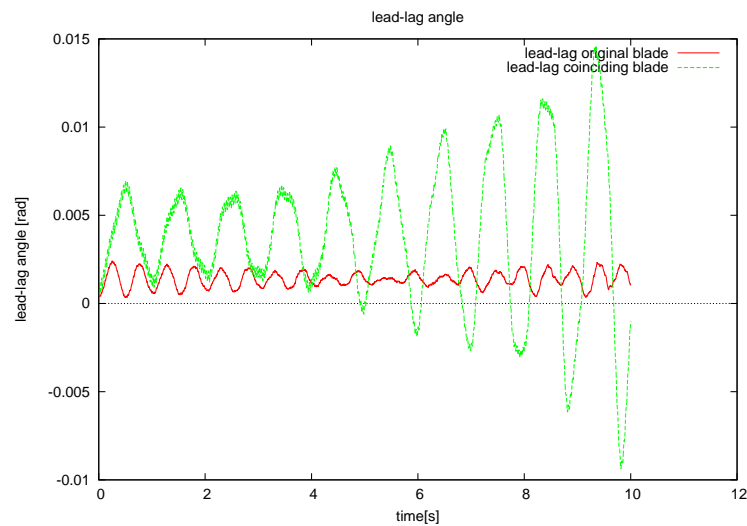


Figure 10.31: Time response of second lead-lag angle, for both the original blade as for a blade with reduced lead-lag stiffness.

time, again for both blade models. This figure illustrates that there is an extra destabilising effect due to the frequency coincidence. Of course due to the reduction in the stiffness, the angles become larger in lead-lag direction, but for the modified blade the lead-lag angle is also clearly unstable. This is not the case for the original blade. This example shows the possibility of the flap-lag-stall instability, but as it is occurring while the blade is already suffering from negative damping in the flap direction, it is not a critical factor for the blade designer.

# Chapter 11

## Conclusions and Recommendations

*Never discourage anyone...who continually makes progress, no matter how slow.*

- Plato

This chapter first gives the main conclusions. In the second section the recommendations are given for further development of the tool described in this dissertation.

### 11.1 Conclusions

Aeroelasticity has become an important subject when developing large wind turbines. The aeroelastic analysis must play an important role in the design process. Over the years, there have been some examples of wind turbines that were not designed well and which suffered from problems due to aeroelasticity. Those examples illustrate the necessity of aeroelastic analysis of wind turbines.

In an effort to further improve the possible aeroelastic analysis of wind turbines, this dissertation has investigated developing a new simulation tool. It is expected that nonlinearities will play an important role in large wind turbines, therefore the tool has to be able to handle nonlinearities. As a result, the fully nonlinear simulation tool WOBBE has been extended, verified and validated. WOBBE simulates rigid body models of wind turbines or isolated wind turbine blades in the time domain. It is a tool that can be used during the wind turbine design process, but due to the long calculation time that is needed for each simulation, it should only be used for some final checks, where the nonlinearity is expected to be of importance. The time it takes to run one simulation using WOBBE is clearly a drawback.

The validation of an aeroelastic simulation tool is not a simple task. Measurements have been used in the validation process, but of course the wind conditions out in the field are not exactly known and very different from what is used in the programme. Next to this, the results that are compared are the damping coefficients and frequencies, while the real wind

turbine will be a nonlinear system that does not actually respond according to the linear vibration theory. Extracting the linear results from the measurements is therefore always somewhat arbitrary. For these reasons an exact match can never be expected, but as it is the goal of this tool to enable designers to evaluate the stability of their design, the results must be representable for the real life situation. Differences will always be there, but the tool must give an idea if the design is safe enough or not in the real world, not if the design would be stable under ideal uniform wind conditions.

Next to investigating the stability of a new wind turbine design, the tool WOBBE can also be used to investigate the modelling method. The tool can handle all kinds of details in the model in a fully nonlinear way, e.g. the position of the aerodynamic centre, the position of the elastic axis or the shear centre, making it useful for this type of investigations. In this dissertation the stiffness calculation as well as the structural pitch calculation used in the modelling procedure have both been investigated. The investigations of the modelling methods can be performed by comparing the results obtained using different models, that are calculated using different methods. By increasing the number of superelements used in the model, the results for the different methods should converge to the same values, but it can be seen which method converges quicker. Such an analysis has been successfully performed for the method to calculate the spring stiffnesses in the superelement models. It can be concluded that the stiffnesses of the springs in flap- and edgewise directions in the model should be calculated using the average stiffness over each half of the superelements. For the structural pitch, it is not clear which method is best to be used. This was due to the fact that the aerodynamic angle of twist was linearly interpolated from root to tip of each rigid body, which led to differences in the distribution of the aerodynamic angle of twist for models with more rigid bodies compared to the less detailed models. Therefore not only the structural pitch effect was included in the results, but also this difference in aerodynamic twist distribution.

Especially as the calculation time is a drawback of WOBBE, it is essential to have an idea of the minimum number of degrees of freedom that need to be included in the model and not put unnecessary extra degrees of freedom in the model. From different calculations, it became clear that the minimum number of superelements needed for reliable analysis is one more than the number of frequencies in each direction that one wants to include with enough accuracy. For example, if the first and second blade flap frequencies are expected to be of importance for the analysis, using three superelements in the blade model would suffice. When a complete turbine model is to be simulated, it is possible to tune the blades and tower individually and reduce the number of superelements needed by one superelement.

An investigation into the possibility of flap-lag-stall flutter on large wind turbines has also been discussed in this dissertation. From this investigation, it can be concluded that the occurrence of flap-lag-stall flutter on large wind turbines is not likely, the turbines are much more susceptible to negative damping of the edgewise mode. The calculations showed that, before flap-lag flutter would occur, the blade would suffer from negative damping of the edgewise mode, unless the structural pitch angle was unrealistically large, in which case the

instability occurring then was not at all related to stall.

## 11.2 Recommendations

Further development of WOBBE can be almost ever ongoing. There are still many things that could be improved. Clearly the most important and urgent improvements are those that can reduce the calculation time that is needed for one simulation. There are several recommendations to be given that can reduce the calculation time:

- The programme spends most of its calculation time in the vector times matrix multiplication routine, therefore the largest reduction can be obtained here. Currently all transformations are performed in the following order:

$$(a, b, c) = \left\{ \left( (d, e, f) [R_{j-(j-1)}]^T \right) [R_{(j+1)-j}]^T \right\} \quad (11.1)$$

Time can be saved by calculating transformation matrices between the different reference frames, e.g.  $[R_{(j+1)-(j-1)}]$ :

$$(a, b, c) = \left\{ (d, e, f) \left( [R_{j-(j-1)}]^T [R_{(j+1)-j}]^T \right) \right\} = (d, e, f) [R_{(j+1)-(j-1)}] \quad (11.2)$$

To determine  $(a, b, c)$ , this new method (equation 11.2) will take more calculations than the current method (equation 11.1), but by reusing this matrix, the total number of calculations during one time step can be reduced, but *only* during the calculation of the aerodynamic forces. Only in those calculations the transformation matrices over several reference frames in one go, can be used several times.

- The calculation of the potential energy due to gravitational acceleration should be adjusted similar to the aerodynamic forces, so that it uses the interim results obtained during the calculation of the energy matrix, as described by equation 5.31:

$$\frac{\partial V_{grav}}{\partial q_i} = \frac{\sum_{i=1}^N -m_i \mathbf{g} \cdot \mathbf{r}_{cg_i}}{\partial q_i} = \sum_{i=1}^N -m_i \mathbf{g} \cdot \frac{\partial \mathbf{r}_{cg_i}}{\partial q_i} = \sum_{i=1}^N -m_i \mathbf{g} \cdot \frac{\partial \mathbf{v}_{cg_i}}{\partial \dot{q}_i}$$

- Investigate if it is possible to simplify the calculations when using RK4 by assuming the aerodynamic forces to remain constant within the four interim steps. If calculating the aerodynamic forces only in the first step within one time step and use this for the other three interim steps within one time step, leads to acceptable results, the calculation time can be reduced by implementing this option.
- Use the analytical method to determine the derivative of the kinetic energy as described in section 5.2.2.
- Investigate if further simplifications by neglecting terms with little influence on the end results within the calculation of the Jacobian are possible.

There are also other points where further improvements are recommended that will increase the quality of the calculations, not reduce the calculation time. These are:

- The aerodynamics can be further improved. Several different models should still be included, such as models for tower shadow, wind shear, yawed flow, turbulence etc.
- The use of splines for the chord, thickness and aerodynamic twist distribution would improve the modelling possibilities.
- The calculations of the aerodynamic coefficients can also be improved by using splines instead of linear interpolation between the different angles of attack.
- Translational degrees of freedom can be added. So far the programme has been limited to systems consisting of rigid bodies that are interconnected by hinges, therefore only rotational degrees of freedom exist. Adding translations means that the elongations due to the forces can be taken into account. For helicopters it would mean that the translational accelerations of a helicopter can be simulated. The theory discussed in chapter 5 can easily be extended to include translational velocities. This would mainly influence the calculation of the energy matrix.
- Adjust the momentum theory equations to enable it to handle the different states in which a helicopter operates. Currently only the wind mill state and turbulent wake state are included in the calculations.

With these improvements implemented, WOBBE would become a very useful fully nonlinear simulation tool that can be used for aeroelastic analysis of wind turbines and helicopters. The proposed improvements that can reduce the time of a simulation are expected to result in significant reductions of the calculation time, thereby reducing the major drawback of WOBBE. The advantages of WOBBE are the nonlinearity of the dynamics and aerodynamics as well as the possibilities for different models, details and configurations to be used in the simulations, making it a more flexible tool than most aeroelastic tools currently used in the wind energy world.

# Bibliography

- [1] C. W. Acree, R. J. Peyran, and W. Johnson. Rotor design for whirl flutter: An examination of options for improving tiltrotor aeroelastic stability margins. In *Proceedings of the 55th Annual Forum of the American Helicopter Society*, 1999.
- [2] C. Anderson, H. Heerkes, and R. Yemm. The use of blade-mounted dampers to eliminate edgewise stall vibration. In *EWEA 1999*, Nice, France, 1999.
- [3] J. D. Anderson Jr. *Fundamentals of Aerodynamics*. Mc Graw Hill, third edition edition, 2001.
- [4] A. Bedford and W. T. Fowler. *Engineering Mechanics Dynamics*. Prentice Hall, New Jersey, 2002.
- [5] K. H. Bergey. The lanchester-betz limit. *Journal of Energy*, 3:382–384, 1979.
- [6] A. Betz. *Schraubenpropeller mit geringstem Energieverlust*. Gottinger Nachr., 1919.
- [7] A. Betz. 'Applied Airfoil Theory' Volume IV, Division J in Durand, W.F. 'Aerodynamic Theory, A General Review of Progress'. 1935.
- [8] R. L. Bielawa. *Rotary Wing Structural Dynamics and Aeroelasticity*. AIAA Education Series, Washington DC, USA, 1992.
- [9] R. L. Bisplinghoff, H. Ashley, and R. L. Halfman. *Aeroelasticity*. Dover Publications, Inc., New York, USA, 1996.
- [10] P. Bongers, W. Bierbooms, S. Dijkstra, and Th. van Holten. An Integrated Dynamic Model of a Flexible Wind Turbine. Technical Report memt 6, Faculty of Mechanical Engineering and Marine Technology, Delft, 1990.
- [11] E. Bot. Aërodynamische tabel generator : handleiding. Technical Report ECN-C-01-077, ECN, Petten, 2001.
- [12] E. Bot. Aërodynamische tabel generator : technische beschrijving. Technical Report ECN-C-01-130, ECN, Petten, 2001.

- 
- [13] A. R. S. Bramwell, G. Done, and D. Balmford. *Bramwell's Helicopter Dynamics*. Butterworth-Heinemann, Oxford, 2nd edition edition, 2001.
- [14] A. J. Brand, C. Lindenburg, J. W. M. Dekker, B. Visser, and G. A. M. van Kuik. Stall flexteeter - computations. Technical Report ECN-C-95-010, ECN, Petten, 1995.
- [15] E. O. Brigham. *The Fast Fourier Transform and its applications*. Prentice Hall, 1988.
- [16] T. Buhl and et al. Parameter variations for active-stall and pitch-regulated turbine, task 6 report. Technical Report Technical Report Risø-I-2413(EN), Risø National Laboratory, Roskilde, Denmark, 2005.
- [17] T. Buhl, H. Markou, M. H. Hansen, K. Thomsen, and F. Rasmussen. Aeroelastic stability analysis and passive instability suppression. In *European Wind Energy Conference*, Athens, 2006.
- [18] T. Burton, D. Sharpe, N. Jenkins, and E. Bossanyi. *Wind energy handbook*. Wiley, 2001.
- [19] G. J. W. van Bussel. *The aerodynamics of horizontal axis wind turbine rotors explored with asymptotic expansion methods*. PhD thesis, Delft University of Technology, 1995.
- [20] S. J. Chapman. *Fortran 90/95 for Scientists and Engineers*. McGraw-Hill Science/Engineering/Math, 2 nd edition, 2003.
- [21] M. Chasles. Note sur les propriétés générales du système de deux corps semblables entr'eux et placés d'une manière quelconque dans l'espace; et sur le déplacement fini ou infiniment petit d'un corps solide libre. *Bulletin des Sciences Mathematiques, Astronomiques, Physiques et Chimiques*, 14:321–326, 1830.
- [22] P. K. Chaviaropoulos. Flap/lead-lag aeroelastic stability of wind turbine blade sections. *Wind Energy*, 2:99–112, 1999.
- [23] R. P. Coleman and A. M. Feingold. Theory of self-excited mechanical oscillations of helicopter rotors with hinged blades. Technical Report TN 3844, NACA, 1957.
- [24] A. R. Collar. The expanding domain of aeroelasticity. *Journal of the Royal Aeronautical Society*, L:613–636, 1946.
- [25] S. T. Crews, K. H. Hohenemeser, and R. A. Ormiston. An unsteady wake model for a hingeless rotor. *Journal of Aircraft*, 10:758–759, 1973.
- [26] J. W. M. Dekker, C. M. de Groot, and M. Spath. Mechanical measurements on vsh 20-wpx-thr rotor blades at the '25 hawt' rotor test facility - part 1. Technical Report ECN-89-35, ECN, Petten, 1989.
- [27] DOWEC Steering committee. Offshore wind energy: 'the road to maturity'. Technical report, ECN, Petten, the Netherlands, 2004.

- 
- [28] E. H. Dowell (editor), H. C. C. Jr., R. H. Scanlan, and F. Sisto. *A Modern Course in Aeroelasticity, Third Revised and Enlarged Edition*. Kluwer Academic Publishers, Dordrecht, 1995.
- [29] S. Drzewiecki. Sur une méthode pour la détermination des éléments mécaniques des propulseurs hélicoidaux. *Compte rendu de l'Académie des Science, Paris*, 114:820–822, 1892.
- [30] W. F. Durand, editor. *Aerodynamic Theory*, volume IV (J-M). Springer, Berlin, 1935.
- [31] D. M. Eggleston and F. S. Stoddard. *Wind Turbine Engineering Design*. Van Nostrand Reinhold Company, New York, USA, 1987.
- [32] T. G. van Engelen. Frequency domain load calculation for offshore wind turbines (turbu offshore). In *European Wind Energy Conference*, London, UK, 2004.
- [33] R. E. Froude. *Transactions, Institution of Naval Architects*, 30:390, 1889.
- [34] W. Froude. On the elementary relation between pitch, slip, and propulsive efficiency. *Transactions, Institution of Naval Architects*, 19:47–57, 1878.
- [35] Y. C. Fung. *An Introduction to the Theory of Aeroelasticity*. Dover Publications, Inc., New York, USA, 1969.
- [36] A. van Garrel. Development of a wind turbine aerodynamics simulation module. Technical Report ECN-C-03-079, ECN, Petten, 2003.
- [37] Gere and Timoshenko. *Mechanics of materials*. Chapman & Hall, third SI edition, 1991.
- [38] J. H. Ginsberg. *Advanced Engineering Dynamics*. Cambridge University Press, second edition, 1995.
- [39] H. Glauert. The analysis of experimental results in the windmill brake and vortex ring states of an airscrew. Technical Report Reports and Memoranda, No. 1026, Aeronautical Research Committee, London, 1926.
- [40] H. Glauert. *Airplane propellers in Aerodynamic theory (ed. Durand W.F.)*. Julius Springer, Berlin, Germany, 1935.
- [41] H. Glauert. *Windmills and fans in Aerodynamic theory (ed. Durand W.F.)*. Julius Springer, Berlin, Germany, 1935.
- [42] C. E. Hammond and R. V. Doggett Jr. Determination of subcritical damping by moving-block/randomdec applications. In *NASA Symp. Flutter Testing Techniques*, number NASA CP-415, pages 59–76, 1975.

- 
- [43] A. C. Hansen and C. P. Butterfield. Aerodynamics of horizontal-axis wind turbines. *Annual Review of Fluid Mechanics*, 25:115–149, 1993.
- [44] M. H. Hansen. Aeroelastic stability analysis of wind turbines using an eigenvalue approach. *Wind Energy*, 7:133–143, 2004.
- [45] M. H. Hansen, T. Knudsen, K. Thomsen, and P. Fuglsang. Measurement of modal damping for the nm80/2750 prototype in tjaereborg, task 3 report. Technical Report Technical Report Risø-I-2258(EN), Risø National Laboratory, Roskilde, Denmark, 2004.
- [46] M. H. Hansen, K. Thomsen, P. Fuglsang, and T. Knudsen. Two methods for estimating aeroelastic damping of operational wind turbine modes from experiments. *Wind Energy*, 9:179–191, 2006.
- [47] M. O. L. Hansen. *Aerodynamics of Wind Turbines*. James and James, London, UK, 2000.
- [48] J. G. Holierhoek. Alterations to WOBBE to Include the Possibility of Fixed Rotations. Technical Report FM&P-00.010, Faculty of Aerospace Engineering, Delft, 2000.
- [49] J. G. Holierhoek. Alterations to WOBBE to include the effects of unsteady aerodynamics. Technical Report FM&P-02.015, Faculty of Aerospace Engineering, Delft, 2002.
- [50] J. G. Holierhoek. Non-linear simulations of the Im64-5 blade using wobbe. Technical Report FM&P-03.004, Faculty of Aerospace Engineering, Delft, 2003.
- [51] J. G. Holierhoek. The effect of changing the blade stiffness on the flap-lag-stall instability of large wind turbines. In *31st European Rotorcraft Forum*, number 57, Florence, Italy, 2005.
- [52] J. G. Holierhoek, B. A. H. Marrant, P. Lisandrin, and T. J. Mulder. Theoretical analysis and comparison to experiments. Technical Report STABCON D4, Faculty of Aerospace Engineering, Delft, 2005.
- [53] J. G. Holierhoek and Th. van Holten. Equations of Motion of Flap-Lag Model, Including a Stability Analysis. Technical Report FM&P-00.012, Faculty of Aerospace Engineering, Delft, 2000.
- [54] J. G. Holierhoek and Th. van Holten. Flap-lag instability of large wind turbines. In *European Wind Energy Conference*, number PG2.2, Copenhagen, Denmark, 2001.
- [55] J. G. Holierhoek, Th. van Holten, and H. Mulder. Aeroelastic stability of large wind turbines (with emphasis on flap-lag flutter). In *4<sup>th</sup> GRACM Congress on Computational Mechanics*, Patras, Greece, 2002.

- 
- [56] J. G. Holierhoek, Th. van Holten, and T. J. Mulder. Automatic simulation to determine the aeroelastic stability of large scale wind turbine rotors (with emphasis on flap-lag-stall flutter). In *26th European Rotorcraft Forum in conjunction with 15th European Helicopter Association Symposium Proceedings*, number 69, The Hague, the Netherlands, 2000.
- [57] Th. van Holten. Some notes on unsteady lifting-line theory. *Journal of Fluid Mechanics*, 77(3):561–579, 1976.
- [58] Th. van Holten. On the validity of lifting line concepts in rotor analysis. *Vertica*, 1:239–254, 1977.
- [59] Th. van Holten. Analysis of the vibrations of the kewt wind turbine. Technical Report intern report, SPE, Amsterdam, December 1987. in Dutch.
- [60] Th. van Holten. Hamiltonian mechanics as a possible alternative for deriving aeroelastic equations. In *13th European Rotorcraft Forum Proceedings*, number 6-8, 1987.
- [61] Th. van Holten. On the use of hamiltonian concepts in rotordynamics. In *16th European Rotorcraft Forum Proceedings*, number II.3.5.1-6, 1990.
- [62] Th. van Holten. Energy flow considerations, an educational tool to clarify aeroelastic phenomena. In *26th European Rotorcraft Forum in conjunction with 15th European Helicopter Association Symposium Proceedings*, number 66, The Hague, the Netherlands, 2000.
- [63] Th. van Holten. Final report STABTOOL phase II, aeroelastic tools to asses the stability of large wind turbines. Technical Report FM&P00.016, Faculty of Aerospace Engineering, Delft, 2000.
- [64] Th. van Holten and J. G. Holierhoek. The influence of scale effects on the aeroelastic stability of large wind turbines. In *International Forum on Aeroelasticity and Structural Dynamics 2001*, number 054, 2001.
- [65] Th. van Holten and J. G. Holierhoek. The influence of scale effects on the aeroelastic stability of large wind turbines. In *European Wind Energy Conference*, number OC4.1, Copenhagen, Denmark, 2001.
- [66] Th. van Holten and J. G. Holierhoek. Advanced dynamics. Technical Report AE4-216, Faculty of Aerospace Engineering, Delft, 2005.
- [67] Th. van Holten, M. D. Pavel, and G. N. Smits. Aeroelastic stability of modern wind-turbines, final report phase 1. Technical Report Memorandum M-880, Faculty of Aerospace Engineering, Delft, 1999.

- [68] G. Horvay and W. Yuan. Stability of rotor blade flapping motion when the hinges are tilted. generalization of the "rectangular ripple" method of solutions. *Journal of Aeronautical Sciences*, pages 583–593, 1947.
- [69] W. H. Hui and J. J. Hu. Space-marching gridless computation of steady supersonic/hypersonic flow. *International Journal of Computational Fluid Dynamics*, 20-1:55–59, 2006.
- [70] S. A. Huyer, D. A. Simms, and M. C. Robinson. Unsteady aerodynamics associated with a horizontal-axis wind turbine. *AIAA Journal*, 34:1410–1419, 1996.
- [71] D. J. Inman. *Engineering Vibration*. Prentice Hall, 1994.
- [72] W. Johnson. Dynamics of tilting proprotor aircraft in cruise flight. Technical Report TN D-7677, NASA, 1974.
- [73] W. Johnson. *Helicopter Theory*. Princeton University Press, 1980.
- [74] H. J. T. Kooijman, C. Lindenburg, D. Winkelaar, and E. L. van der Hooft. DOWEC 6 MW PRE-DESIGN, Aero-elastic modelling of the DOWEC 6 MW pre-design in PHATAS. Technical Report DOWEC-F1W2-HJK-01-046/9, ECN, Petten, 2003.
- [75] G. A. M. van Kuik. *On the Limitations of Froude's Actuator Disc Concept*. PhD thesis, Technische Universiteit Eindhoven, 1991.
- [76] G. A. M. van Kuik. Are wind turbines growing too fast? In *2001 European Wind Conference*, 2001.
- [77] G. A. M. van Kuik. The lanchester-betz-joukowsky limit. *wind energy*, in press:–, 2007.
- [78] J. L. Lagrange. *Mécanique Analytique*. L'Académie Royal des Sciences, Paris, 1788.
- [79] F. W. Lanchester. A contribution to the theory of propulsion and the screw propeller. *Transactions of the Institution of Naval Architects*, 57:98–116, 1915.
- [80] J. G. Leishman. *Principles of Helicopter Aerodynamics*. Cambridge Aerospace Series, Cambridge, UK, 2000.
- [81] J. G. Leishman. Challenges in modelling the unsteady aerodynamics of wind turbines. *Wind Energy*, 5:85–132, 2002.
- [82] C. Lindenburg. Bladmode; program for rotor blade mode analysis . Technical Report ECN-C-02-050, ECN, Petten, 2003.
- [83] C. Lindenburg. Phatas release "nov-2003" and "apr-2005" user's manual; program for horizontal axis wind turbine analysis and simulation. Technical Report ECN-I-05-005, ECN, Petten, 2005.

- 
- [84] C. N. H. Lock, H. Bateman, and H. C. H. Townsend. An extension of the vortex theory of airscrews with applications to airscrews of small pitch, including experimental results. Technical Report Aeronautical Research Committee Reports and Memoranda, No. 1014, Her Majesty's Stationery Office, London, 1926.
- [85] P. Lundsager, H. Petersen, and S. Frandsen. The dynamic behavior of the stall-regulated nibe a wind turbine measurements and a model for stall-induced vibrations. Technical Report Technical Report Risø-M-2253, Risø National Laboratory, Roskilde, Denmark, 1981.
- [86] H. Markoe, M. H. Hansen, T. Buhl, T. van Engelen, E. S. Politis, V. Riziotis, N. K. Poulsen, A. J. Larsen, T. S. Mogensen, and J. G. Holierhoek. Aeroelastic stability and control of large wind turbines - main results. In *European Wind Energy Conference*, number BT4.1, Milan, Italy, 2007.
- [87] B. Marrant, P. Lisandrin, and Th. van Holten. Aero-elastic analysis of wind turbines using system identification techniques. In *31st European Rotorcraft Forum*, number 58, Florence, Italy, 2005.
- [88] B. Marrant and Th. van Holten. System identification for the analysis of aeroelastic stability of wind turbine blades. In *European Wind Energy Conference*, London, UK, 2004.
- [89] B. A. H. Marrant and Th. van Holten. Investigation of rotor weaving on a helicopter with a hiller-system and the influence of high coning angles on rotor-fuselage coupling. In *27th European Rotorcraft Forum Symposium Proceedings*, number 12, 2001.
- [90] J. L. Meriam and L. G. Kraige. *Engineering Mechanics volume 2 Dynamics*. John Wiley and Sons, New York, 1987.
- [91] D.-P. Molenaar. Modeling the structural dynamics of the lagerwey lw-50/750 turbine. Technical Report N-522, Mechanical Engineering, Systems and Control, Delft, 1998.
- [92] D.-P. Molenaar. State-of-the-art of wind turbine design codes. Technical Report N-523, Mechanical Engineering, Systems and Control, Delft, 1999.
- [93] D. P. Molenaar. *Cost effective design and operation of variable speed wind turbines*. DUP Science, Delft, The Netherlands, 2003.
- [94] D.-P. Molenaar and S. Dijkstra. Modeling the structural dynamics of a flexible wind turbine: The Lagerwey LW-50/750. *Selected topics in Identification Modelling and Control*, 11:51–59, 1998.
- [95] T. Møller. Blade cracks signal new stress problem. *WindPower Monthly*, May, 1997.
- [96] T. J. Mulder and Th. van Holten. Hub stiffness influenced by multi-blade effects. Technical Report FM&P-00.002, Faculty of Aerospace Engineering, Delft, 2000.

- [97] S. Newman. *The Foundations of Helicopter Flight*. Halsted Press, New York, 1994.
- [98] S. I. Newton. *Philosophiae Naturalis Principia Mathematica*. Royal Society, London, 1687.
- [99] R. A. Ormiston. Application of simplified inflow models to rotorcraft dynamic analysis. *Journal of the American Helicopter Society*, 21:34–37, 1976.
- [100] R. A. Ormiston. Investigations of hingeless rotor stability. *Vertica*, 7:2:143–181, 1983.
- [101] R. A. Ormiston and W. G. Bousman. A study of stall-induced flap-lag instability of hingeless rotors. In *Presented at the 29th Annual National Forum of the American Helicopter Society*, Washington D.C., May 1973. American Helicopter Society.
- [102] R. A. Ormiston and D. H. Hodges. Linear Flap-Lag Dynamics of Hingeless Rotor Blades in Hover. *Journal of the American Helicopter Society*, 17:2:2–14, 1972.
- [103] K. van Overbeek and Th. van Holten. WOBBE Automatic Simulation of Complex Non-Linear Dynamic Systems. Technical Report FM&P-99.027, Faculty of Aerospace Engineering, Delft, 1999.
- [104] K. van Overbeek and Th. van Holten. Automatic Simulation of Complex Non-Linear Dynamic Systems. In *26th European Rotorcraft Forum in conjunction with 15th European Helicopter Association Symposium Proceedings*, number 65, 2000.
- [105] P. van Overschee and B. D. Moor. *Subspace identification for linear systems  $\dot{U}$  Theory, Implementation, Applications*. Kluwer academic Publishers, 1996.
- [106] S. Øye. Unsteady effects caused by pitch-angle changes. In *IEA Symposium - joint action on aerodynamics of wind turbines*, London, 1986.
- [107] M. D. Pavel. An investigation of the rotor - tower instability of the kewt wind turbine. Technical Report Memorandum M-879, Faculty of Aerospace Engineering, Delft, 1999.
- [108] M. D. Pavel and M. M. J. Schoones. Literature survey on aeromechanical instabilities for helicopters and wind turbines. Technical Report Memorandum M-877, Faculty of Aerospace Engineering, Delft, 1999.
- [109] M. D. Pavel and Th. van Holten. A rotor-tower instability associated with the advancing lead-lag mode. In *19th ASME Wind Energy Symposium*, number AIAA-2000-0068, Reno, January 2000. AIAA.
- [110] P. R. Payne. *Helicopter Dynamics and Aerodynamics*. Sir Isaac Pitman and Sons. Ltd., London, 1959.
- [111] J. T. Petersen and et al. Prediction of dynamic loads and induced vibrations in stall. Technical Report Technical Report Risø-R-1045(EN), Risø National Laboratory, Roskilde, Denmark, 1998.

- 
- [112] J. T. Petersen, K. Thomson, and H. A. Madsen. Local blade whirl and global rotor whirl interaction. Technical Report Technical Report Risø-R-1067(EN), Risø National Laboratory, Roskilde, Denmark, 1998.
- [113] D. Petot. Progress in the semi-empirical prediction of aerodynamic forces due to large amplitude oscillations of an airfoil in attached or separated flow. In *9th European Rotorcraft Forum*, Stresa, Italy, September 1983.
- [114] D. M. Pitt and D. A. Peters. Rotor dynamic inflow derivatives and time constants from various inflow models. In *9th European Rotorcraft Forum*, Stresa, Italy, September 1983.
- [115] E. Politis, P. Chaviaropoulos, M. Hansen, D. Winkelaar, T. van Engelen, V. Riziotis, S. Voutsinas, K. Braun, S. Steiner, and J. G. Holierhoek. Benchmark calculations on the nm80 wind turbine, STABCON task-1 technical report. Technical report, Centre for Renewable Energy Sources, Pikermi, Greece, November 2003.
- [116] W. H. Press and et al. *Numerical Recipes in FORTRAN, The Art of Scientific Computing*. Cambridge University Press, Cambridge, second edition edition, 1992.
- [117] R. W. Prouty. *Helicopter Performance, Stability and Control*. PWS Publishers, Boston, Massachusetts, USA, 1986.
- [118] W. J. M. Rankine. On the mechanical principles of the action of propellers. *Transactions, Institution of Naval Architects*, 6:13–30, 1865.
- [119] J. Rauh. Ein Beitrag zur Modellierung elastischer Balkensysteme. *Fortschritt-Berichte VDI, VDI-Verlag GmbH, Düsseldorf, Reihe 18: Mechanik/Bruchmechanik*, 37, 1989.
- [120] J. Rauh and W. Schiehlen. Various approaches for the modeling of flexible robot arms. In *Proceedings of the Euromech-Colloquium 219 on Refined Dynamical Theories of Beams, Plates, and Shells and their Applications*, pages 420–429, 1986.
- [121] W. H. Reed III. Review of propeller-rotor whirl flutter. Technical Report TR 4-264, NASA, 1968.
- [122] V. A. Riziotis and S. G. Voutsinas. Advanced aeroelastic modeling of complete wind turbine configurations in view of assessing stability characteristics. In *European Wind Energy Conference*, Athens, 2006.
- [123] V. A. Riziotis, S. G. Voutsinas, E. S. Politis, and P. K. Chaviaropoulos. Aeroelastic stability of wind turbines: the problem, the methods and the issues. *Wind Energy*, 7:373–392, 2004.
- [124] E. J. Routh. *Advanced Rigid Dynamics*, volume 2. Macmillan Co., London, 1930.

- [125] W. Rulka and A. Eichberger. Simpack an analysis and design tool for mechanical systems. *Vehicle System Dynamics*, pages 122–126, 1993.
- [126] W. Z. Shen, R. Mikkelsen, and J. N. Sørensen. Tip loss corrections for wind turbine computations. *Wind Energy*, 8, 2005.
- [127] W. Z. Shen, J. N. Sørensen, and R. Mikkelsen. Tip loss correction for actuator/navier-stokes computations. *Journal of Solar Energy Engineering*, 127:209–215, 2005.
- [128] C. B. Smith and N. M. Wereley. Transient analysis for damping identification in rotating composite beams with integral damping layers. *Smart Mater. Struct.*, 5:540–550, 1996.
- [129] H. Snel. Heuristic modelling of dynamic stall characteristics. In *European Wind Energy conference, October 1997, Dublin Castle, Ireland*, pages 429–433, 1997.
- [130] H. Snel. Review of the present status of rotor aerodynamics. *Wind Energy*, 1, 1998.
- [131] H. Snel. Review of aerodynamics for wind turbines. *Wind Energy*, 6, 2003.
- [132] J. N. Sørensen. *Three level viscous-inviscid interaction technique for the prediction of separated flow past rotating wing*. PhD thesis, Technical University of Denmark, 1986.
- [133] D. A. Spera. *Wind Turbine Technology, fundamental concepts of wind turbine engineering*. ASME, New York, USA, 1994.
- [134] W. Z. Stepniewski and C. N. Keys. *Rotary-Wing Aerodynamics*. Dover Publications Inc., New York, USA, 1984.
- [135] H. Stiesdal. Extreme wind loads on stall regulated wind turbines. In *BWEA 16*, Stirling, UK, June 1997. Mechanical Engineering Publications Ltd.
- [136] T. L. Sullivan. A review of resonance response in large, horizontal-axis wind turbines. In R. Thresher, editor, *Proceedings Wind Turbine Dynamics Workshop*, number CONF - 810226 in NASA Conference Publication 2185, pages 237–244, Cleveland Ohio, 1981. NASA Lewis Research Center, DOE Publication.
- [137] E. S. Taylor and K. A. Browne. Vibration isolation of aircraft power plants. *Journal of Aeronautical Sciences*, 6(2):43–49, 1938.
- [138] R. Thakoer, G. A. M. van Kuik, and H. L. van Leeuwen. Classification of future 5 mw turbines, by extrapolation of current trends. Technical Report Ivw 99160R, Faculty of Civil Engineering and Geosciences, Delft, 1999.
- [139] V. K. Truong. A 2-d dynamic stall model based on a hopf bifurcation. In *19th European Rotorcraft Forum Proceedings*, number C23, 1993.
- [140] F. M. White. *Viscous fluid flow*. McGraw-Hill Book Company, New York, USA, 1974.

- 
- [141] R. E. Wilson, P. B. S. Lissaman, and S. N. Walker. Aerodynamic performance of wind turbines. Technical Report ERDA/NSF/04014-76/1, U.S. Department of Energy, Washington, USA, 1976.
- [142] A. D. Wright, C. E. Smith, R. W. Thresher, and J. L. C. Wang. Vibration modes of centrifugally stiffened beams. *Journal of Applied Mechanics*, 49:197–202, 1982.
- [143] R. T. Yntema. Simplified procedures and charts for the rapid estimation of bending frequencies of rotating beams. Technical Report Technical Note 3459, NACA, Langley Field, VA, 1955.
- [144] R. J. Zwaan. Aeroelasticity of aircraft. Technical Report Dictaat 30, Faculty of Aerospace Engineering, Delft, 1990.
- [145] R. J. Zwaan. Trillingen van vliegtuigen. Technical Report LR31, Faculty of Aerospace Engineering, Delft, 1990.



# Appendix A

## Unsteady Aerodynamics

In 3.1.9 the phenomenon of dynamic stall is discussed. The model that has been included in the simulation tool WOBBE (as discussed in chapters 5 and 6) is explained in that same section. In this appendix the details of this method can be found. As mentioned in chapter 3 the code is based on the model described by Snel in [129]. It had already been implemented in PHATAS [83]. The code from PHATAS concerning the dynamic stall model has been implemented in WOBBE using some slight adjustments that were necessary due to differences between the two programmes.

The model by Snel is an adapted model from Truong [139], which was based on a Hopf bifurcation. The dynamic lift coefficient is written as:

$$c_{l,dyn} = c_{l,steady} + \Delta c_{l1} + \Delta c_{l2} \quad (\text{A.1})$$

where  $c_{l,steady}$  is the lift coefficient without dynamic stall model. The following first order ordinary differential equation is used for  $\Delta c_{l1}$ :

$$\tau \frac{d\Delta c_{l1}}{dt} + cf_{10}\Delta c_{l1} = ft_1 \quad (\text{A.2})$$

Where  $\tau = \frac{c}{2U}$ . Using this differential equation  $\Delta c_{l1}$  will follow the frequency of the forcing terms. A derived aerofoil specific quantity is used as a forcing term. It is chosen to be equal to the non-dimensional time derivative of  $\Delta c_{l,pot}$ .

$$ft_1 = \tau \frac{d\Delta c_{l,pot}}{dt} \quad (\text{A.3})$$

Where  $\Delta c_{l,pot}$  is defined as the difference between the potential flow lift coefficient and the aerofoil steady lift coefficient:

$$\Delta c_{l,pot} = c_{l,pot} - c_{l,steady} = 2\pi \sin(\alpha - \alpha_0) - c_{l,steady} \quad (\text{A.4})$$

where  $c_{l,steady}$  is the value of the lift coefficient at the angle of attack  $\alpha$  without any dynamic stall effects. And

$$cf_{10} = \frac{1 + 0.5\Delta c_{l,pot}}{1 + 60\tau(d\alpha/dt)} \quad (\text{A.5})$$

The differential equation for  $\Delta c_{l2}$  must be of second order as it must introduce the higher frequency dynamics:

$$\tau^2 \frac{d^2 \Delta c_{l2}}{dt^2} + cf_{21} \frac{d\Delta c_{l2}}{dt} + cf_{20} \Delta c_{l2} = ft_2 \quad (\text{A.6})$$

Where

$$cf_{20} = k_s^2 [1 + 3(\Delta c_{l2})^2] [1 + 3(d\alpha/dt)^2] \quad (\text{A.7})$$

and

$$cf_{21} = \begin{cases} 60\tau k_s [-0.01(\Delta c_{l,pot} - 0.5) + 2(\Delta c_{l2})^2] & \text{if } \frac{d\alpha}{dt} \geq 0, \\ 2\tau k_s & \text{if } \frac{d\alpha}{dt} \leq 0 \end{cases} \quad (\text{A.8})$$

In these equations  $k_s$  is the Strouhal frequency which has been given a value of 0.2 by Truong [139]. The forcing function is chosen as:

$$ft_2 = 0.12 * (-0.15\Delta c_{l,pot} + 0.05 \frac{d\Delta c_{l,pot}}{dt}) \quad (\text{A.9})$$

The above mentioned formulas have been used in WOBBE.

A first order model has also been implemented in WOBBE. This is a linearised version from the model discussed above. The dynamic lift is then solved from the following equation:

$$\tau \frac{dc_l}{dt} + cf_{10}(c_l - c_{l,steady}) = \tau \frac{dc_{l,pot}}{dt} \quad (\text{A.10})$$

The effect of including this dynamic stall model will be that the lift curve will show different loops during a simulation of a wind turbine or wind turbine blade. These loops can have considerable effect on the damping to the system and it is therefore important to include the dynamic stall effect in the simulations.

# Appendix B

## Introduction to Elasticity

This appendix gives a very short introduction into elasticity. Only beams for which the Euler-Bernoulli equations are valid are discussed.

In chapters 2 and 3 the dynamics and the aerodynamics have been explained. When treating aeroelasticity, next to the aerodynamic and inertia forces, the elastic forces play an important role. This section of the appendix will give a very short summary of some of the important aspects of elasticity, focussing on the elastic theory used in the analysis. The interested reader is referred to some of the numerous books dealing with engineering mechanics, e.g. [37] The books dealing with aeroelasticity also give good descriptions of elasticity, e.g. [9, 28, 35]

When a bar or a beam is subjected to a tensile force, as illustrated in figure B.1, it will elongate. This elongation mainly depends on the force, the material and the surface area of the cross-section. A typical result for the measured force against the elongation diagram, when a bar is tested on a tensile test machine, is shown in figure B.2.

When a bar is elongated due to the forces, at first the elongation will be an elastic elongation, i.e. when the force is removed the bar will return to its original length. Most beams made from structural materials will, up to a certain force, show a linear relation between the force and the elongation. This is also the case for the diagram shown in figure B.2.

For a given beam and force, the elongation will depend on the cross-sectional area. For this

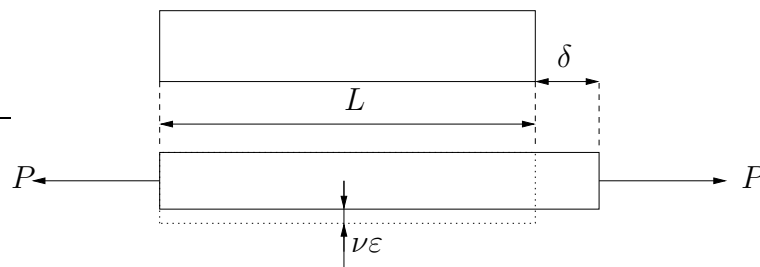


Figure B.1: A bar elongates when subjected to a tensile force

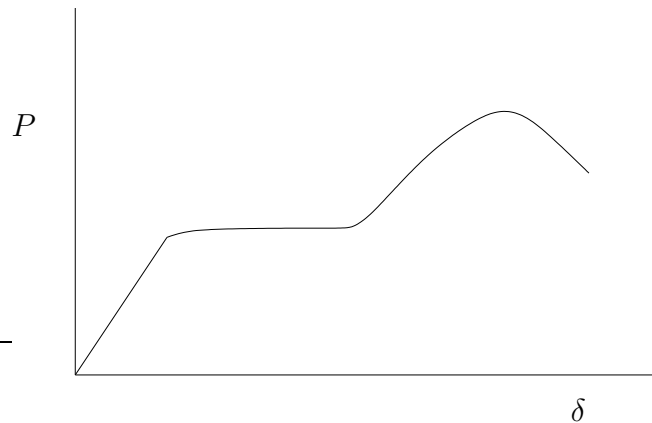


Figure B.2: The elongation of a beam against the tensile force acting on the beam during a tensile test until breakage

reason the stress ( $\sigma$ ) is defined as the force per unit area:

$$\sigma = \frac{P}{A} \quad (\text{B.1})$$

The stress signifies the intensity of the force. The strain ( $\varepsilon$ ) is defined as the elongation per unit length of the beam:

$$\varepsilon = \frac{\delta}{L} \quad (\text{B.2})$$

Using these expressions it is possible to express the linear relationship between stress and strain in a bar as:

$$\sigma = E\varepsilon \quad (\text{B.3})$$

where  $E$  is the modulus of elasticity or Young's modulus for the material. Equation B.3 is commonly known as Hooke's law. Using equations B.1, B.2 and B.3, one can find an expression for the elongation of a beam subjected to a tensile force  $P$ :

$$\delta = \frac{PL}{EA} \quad (\text{B.4})$$

If a beam is elongated, it can be expected that it will also contract laterally. This is also illustrated in figure B.1. The ratio of strain in lateral direction to strain in longitudinal direction is called Poisson's ratio  $\nu$ . It is a material property.

So far the discussion has been limited to normal stress. Another type of stress is shear stress which is a stress that acts parallel or tangential to the surface of the material. An example of shear stresses is given in figure B.3. The connection between two plates subjected to tension, results in a bolt that is under shear stress as illustrated in the figure.

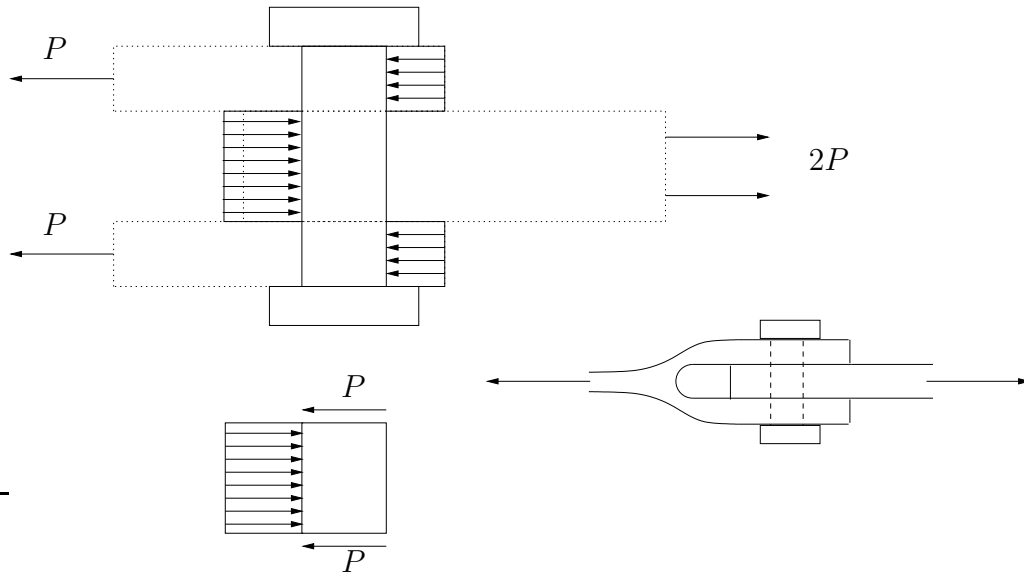


Figure B.3: A bolt connecting two plates. The bolt is subjected to shear stress.

The average shear stress on the cross section of the bolt is:

$$\tau_{aver} = \frac{P}{A} \quad (\text{B.5})$$

Shear stress results in a change in shape of the bolt. The angle  $\gamma$  measuring the distortion due to shear stress is called the shear strain. Similar to the normal stress-strain relationship, many materials will, up to a certain stress, have a linear relation between shear stress and shear strain resulting in Hooke's law in shear:

$$\tau = G\gamma \quad (\text{B.6})$$

where  $G$  is the shear modulus of elasticity. The modulus of elasticity in tension and the shear modulus are related by:

$$G = \frac{E}{2(1 + \nu)} \quad (\text{B.7})$$

where  $\nu$  is Poisson's ratio. The derivation of this relationship can be found in e.g. [37].

Another example of shear stress is a circular bar under pure torsion as illustrated in figure B.4. The bar is twisted through an angle  $\phi$ . The angle of twist per unit length is called  $\theta$ . Using this, the shear strain is  $\gamma = \frac{r d\phi}{dx} = r\theta$ . In the case of pure torsion of a uniform bar,  $\theta$  is constant.

$$\gamma = r\theta = \frac{r\phi}{L} \quad (\text{B.8})$$

For linearly elastic material the shear stress at the surface of the bar is:

$$\tau = G\gamma = G\rho\theta \quad (\text{B.9})$$

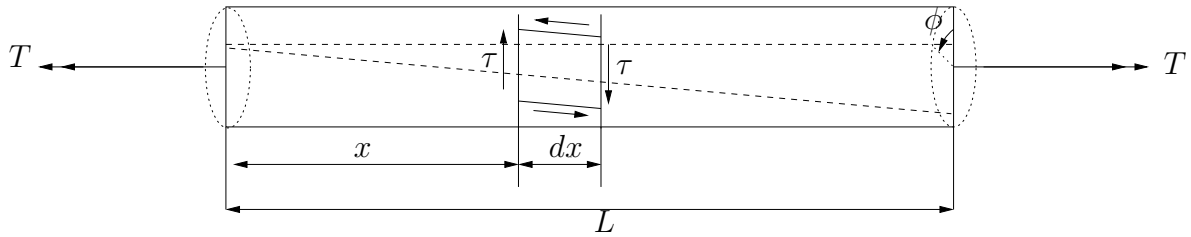


Figure B.4: A bar with circular cross section subjected to torsion.

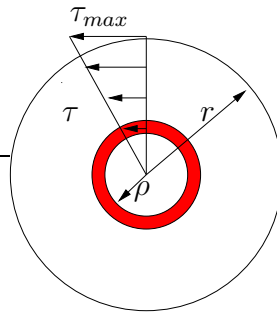


Figure B.5: The shear stress in the cross section of a circular bar.

The shear stress in a ring at distance  $\rho$  from the centre will be:

$$\tau = G\rho\theta \quad (\text{B.10})$$

The shear stress in this ring gives a moment about this centre of  $\tau\rho dA$ . Therefore the total torque must be equal to:

$$T = \int G\theta\rho^2 dA = G\theta \int \rho^2 dA = G\theta I_p \quad (\text{B.11})$$

with

$$I_p = \int \rho^2 dA \quad (\text{B.12})$$

is the polar moment of inertia.

Another important case in which the stress can easily be determined is a beam under pure bending. The beam will deflect as shown in figure B.6. The curvature  $\kappa$  is defined as the reciprocal of the radius of curvature,  $\rho$ :

$$\kappa = \frac{1}{\rho} = \frac{d\theta}{dx} \quad (\text{B.13})$$

Looking at the normal stresses in a cross section of the beam under pure bending, they will vary over the cross section. This is illustrated in figure B.7. It is clear that part of the cross section will be under tensile stress and elongating, while another part will be under pressure

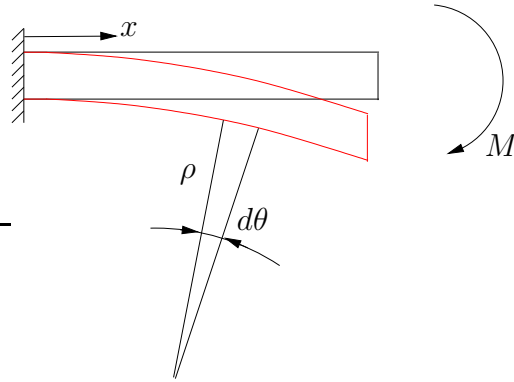


Figure B.6: The deformation of a beam under pure bending.

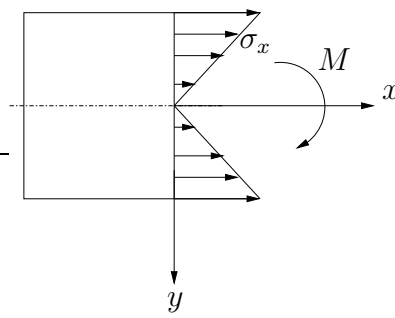


Figure B.7: The normal stresses in a beam due to an external moment.

and reduced in length. There must also be a surface where the original length remains, this is called the neutral surface. The elongation at a point in the cross section  $\varepsilon_x$  is equal to the curvature  $\kappa$  times the distance from the neutral surface:

$$\sigma_x = E\varepsilon_x = -E\kappa y \quad (\text{B.14})$$

The stresses must result in the same moment as the external moment  $M$ . The moment due to the stress acting on a small surface area within the cross section is:

$$dM = -\sigma_x y dA = -E\kappa y^2 dA \quad (\text{B.15})$$

The integral over the surface gives:

$$M = -\kappa \int y^2 dA = -\kappa EI_x \quad (\text{B.16})$$

where  $I_x = \int y^2 dA$  is the area moment of inertia. Using equation B.16, it is possible to determine the deflection of beams due to moments and/or forces when the beam is under pure bending.

For cantilever beams it is not complicated to derive equations for the vertical deflection and the slope of the deflection curve using the above derived equations. The derivation can be found in many books, e.g. [37]. Here only the resulting equations are given. Looking at cantilever beams subjected to a force at the tip, a moment at the tip or a constant distributed force along the entire beam, it is possible to derive equations for cantilever beams subjected to forces or moments at other point on the beam or to distributed forces that are not along the entire beam. Therefore only the first three cases are shown in figures B.8 till B.10. In these figures the vertical deflection  $v$  and the slope of the deflection curve  $v'$  are given as a function of the position along the beam. The value at the tip for the deflection and the slope are also given in these figures.

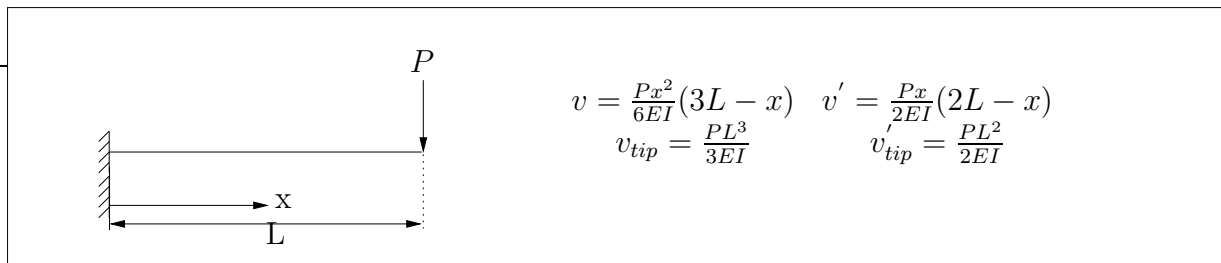


Figure B.8: A cantilever beam subjected to a force at the tip.

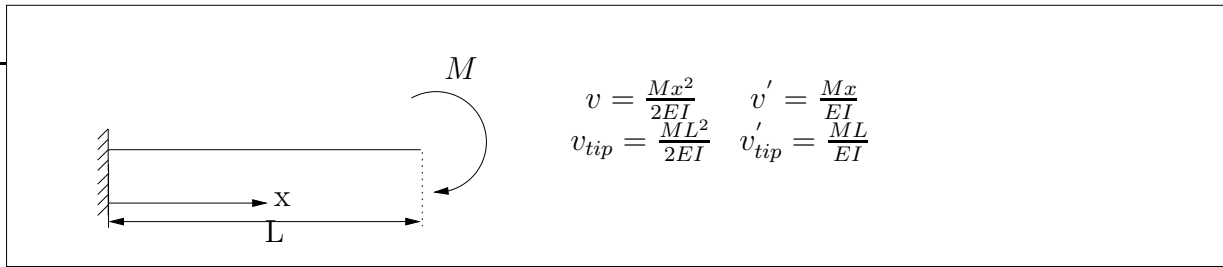


Figure B.9: A cantilever beam subjected to a moment at the tip

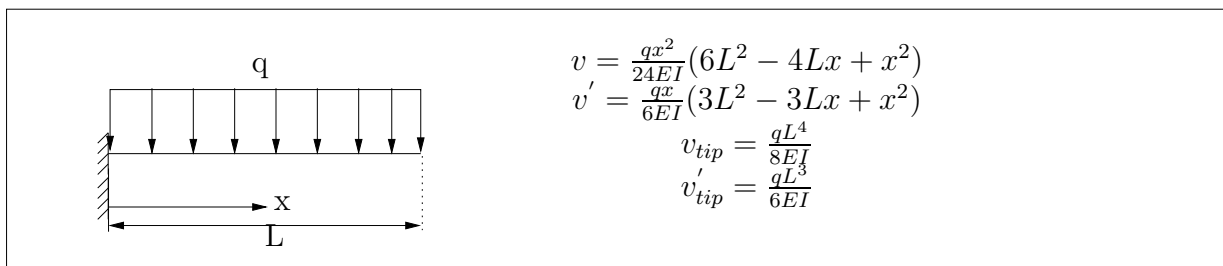


Figure B.10: A cantilever beam subjected to a constant distributed force

It should again be stressed that the discussion in this section about elasticity is a very limited discussion. Only that part of elasticity that was necessary to derive the equations for the superelements discussed in chapter 7 has been discussed.



# Appendix C

## Introduction to Linear Vibrations

In this appendix a short introduction will be given into the analysis of linear vibrations.

Vibrations can be divided into two different types: there is the free vibration, where a mechanical system has some initial input and is then left to vibrate freely. In this case the system will vibrate in its own natural frequency or frequencies. The other type of vibration is the forced vibration, where a system is driven to vibrate by an alternating force acting on the system. The frequency of the vibration is in this case, apart from transients, the frequency of the forcing function, but the amplitude of the vibration is strongly dependent on the natural frequencies of the system itself [71].

A system is linear if the state variables and their derivatives in the equation are only present to the zeroth or first power (e.g.  $x_1^0 = c$  and  $x_1^1 = x$ ) and are not multiplied by any other state variable. All other systems are nonlinear.

A very simple example of a linear vibration is a one degree of freedom system with a spring and a damper as shown in figure C.1. A point mass is connected to both a spring and a damper and it can vibrate in the  $x$ -direction.

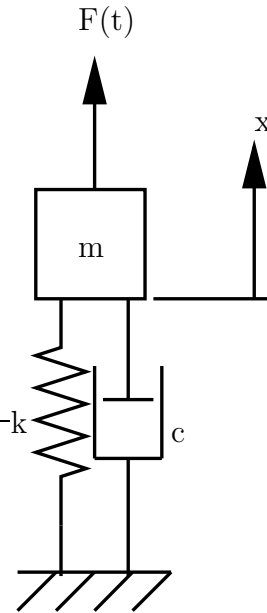


Figure C.1: A spring damper system with one degree of freedom

The general equation for vibrations of such systems can be derived using a force balance, resulting in:

$$m\ddot{x} - c\dot{x} + kx = F(t) \quad (\text{C.1})$$

where  $F(t)$  can be an external force acting on the point mass. If there is no external force acting on the system the equation becomes:

$$m\ddot{x} - c\dot{x} + kx = 0 \quad (\text{C.2})$$

Equation C.2 can be solved by substituting

$$x(t) = a_1 e^{\lambda_1 t} + a_2 e^{\lambda_2 t} \quad (\text{C.3})$$

The equation must hold for every value of  $t$ , therefore  $a e^{\lambda t} \neq 0$ . This results in:

$$m\lambda^2 + c\lambda + k = 0 \quad (\text{C.4})$$

Giving two solutions for  $\lambda$ :

$$\lambda_{1,2} = -\frac{c}{2m} \pm \frac{1}{2m} \sqrt{c^2 - 4km} \quad (\text{C.5})$$

The solutions for  $\lambda$  can be real or complex numbers, depending on the sign of  $c^2 - 4km$ . There are three possibilities to be distinguished.

First  $c^2 - 4km$  can be greater than zero. In that case both  $\lambda_1$  and  $\lambda_2$  will be negative real numbers. Second, there is the case where  $c^2 = 4km$ . This will result in equal values for  $\lambda_1$

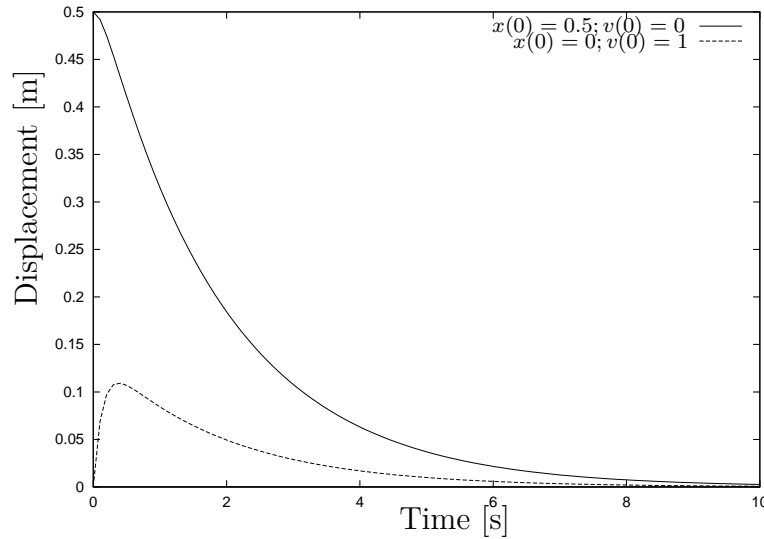


Figure C.2: An example of an overdamped system, for two different initial conditions: one with an initial velocity and one with an initial displacement.

and  $\lambda_2$ , both the same negative real number. If, on the other hand the square root results in a complex number, this is the case if  $c^2 < 4km$ , the resulting values for  $\lambda_1$  and  $\lambda_2$  will be a complex conjugate pair.

These three cases are best examined using the critical damping ratio defined by:

$$\zeta = \frac{c}{c_r} = \frac{c}{2m\omega} \quad (\text{C.6})$$

where  $\omega$  is the undamped natural frequency :  $\omega = \sqrt{\frac{k}{m}}$  and  $c_r$  is the critical damping coefficient.

Using this notation the solutions for  $\lambda$  can be written as:

$$\lambda_{1,2} = -\zeta\omega \pm \omega\sqrt{\zeta^2 - 1} \quad (\text{C.7})$$

The three different cases distinguished above can now easily be categorised. The first case corresponds to a value for  $\zeta$  that is greater than 1. This is the overdamped case (figure C.2). The motion corresponding to this solution will not show any oscillation. The system will return to its equilibrium position exponentially. The second case corresponds to  $\zeta = 1$  (figure C.3). This is called a critically damped motion . This case separates the nonoscillation from the oscillation. The third and final case results in a value for the damping ratio that is less than one. This is called the underdamped motion (figure C.4). This will result in a motion that is oscillating, but with a decreasing amplitude.

The solution of the underdamped motion will be:

$$x(t) = Ae^{\zeta\omega t} \sin(\omega_d t + \theta) \quad (\text{C.8})$$

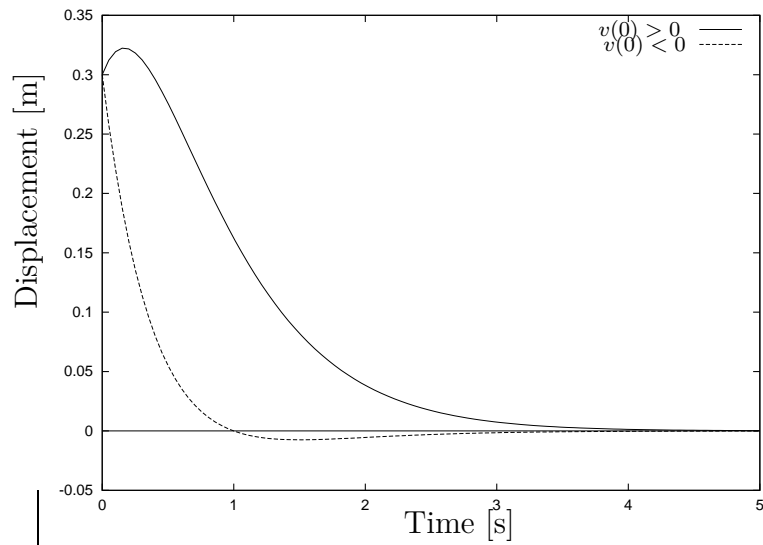


Figure C.3: An example of a critically damped system, for two different velocities at the start, one positive and one negative.

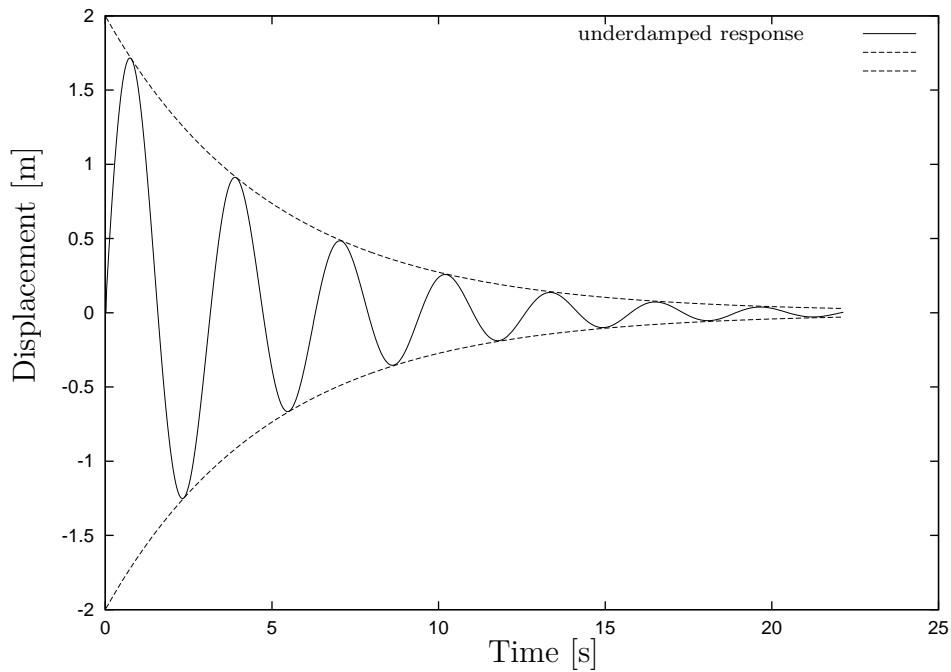


Figure C.4: An example of an underdamped system for a damping ratio  $\zeta = 0.1$  and a frequency  $\omega = 2$ .

where  $\omega_d = \omega\sqrt{1 - \zeta^2}$ .  $A$  and  $\theta$  are determined by the initial conditions.

As mentioned before, vibrations can be split into free vibrations and forced vibrations. The previous equations were for a free vibrating system. Many systems however will vibrate due to an alternating forcing function. The solution for the forced vibration with harmonic excitation can be determined once the solution of the homogeneous equation is known. Thus if

$$m\ddot{x} - c\dot{x} + kx = F(t) \quad (\text{C.9})$$

with  $F(t)$  some harmonic function, first

$$m\ddot{x} - c\dot{x} + kx = 0 \quad (\text{C.10})$$

must be solved as shown above. Then a particular solution must be found which, since the system is linear, must be added to the solution of the free vibration.

For example if the external force is:

$$F(t) = F_0 \cos \omega_f t \quad (\text{C.11})$$

the particular solution for the undamped case ( $c = 0$ ) would be:

$$x_p = A_0 \cos(\omega_f t) \quad (\text{C.12})$$

with

$$A_0 = \frac{f_0}{\omega^2 - \omega_f^2} \quad (\text{C.13})$$

provided that  $\omega \neq \omega_f$  and using  $f_0 = \frac{F_0}{m}$ . This particular solution must then be added to the previously discussed solution of the free vibration. If the difference between  $\omega$  and  $\omega_f$  is small and the free vibration is undamped, the response will show so-called beats, as shown in figure C.5. There will be a vibration with a slowly varying amplitude.

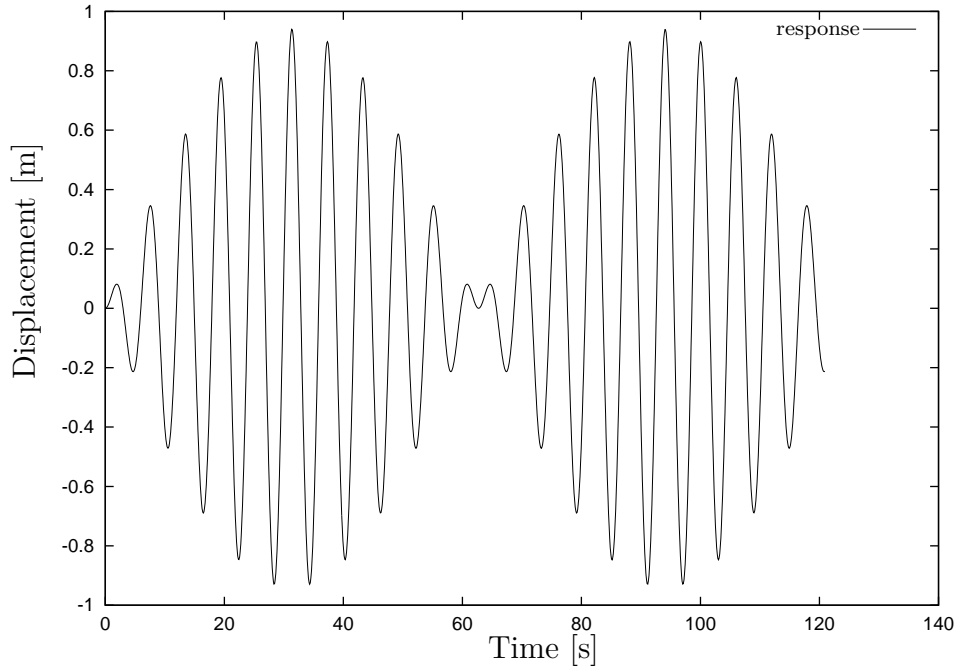


Figure C.5: An example of the response of an undamped system that clearly shows beats. The driving frequency is 1 rad/s and the system's natural frequency is 1.1 rad/s.

For the limit case, if  $\omega = \omega_f$ , resonance will occur and the solution found above is no longer valid. The particular solution must then have the following form:

$$x_p(t) = tA_0 \sin \omega_f t \quad (\text{C.14})$$

This will result in:

$$x_p(t) = \frac{f_0}{2\omega} t \sin \omega_f t \quad (\text{C.15})$$

giving the total solution as:

$$x(t) = A_1 \sin \omega t + A_2 \cos \omega t + \frac{f_0}{2\omega} t \sin \omega_f t \quad (\text{C.16})$$

In the case of resonance the response will grow without bound, as shown in figure C.6.

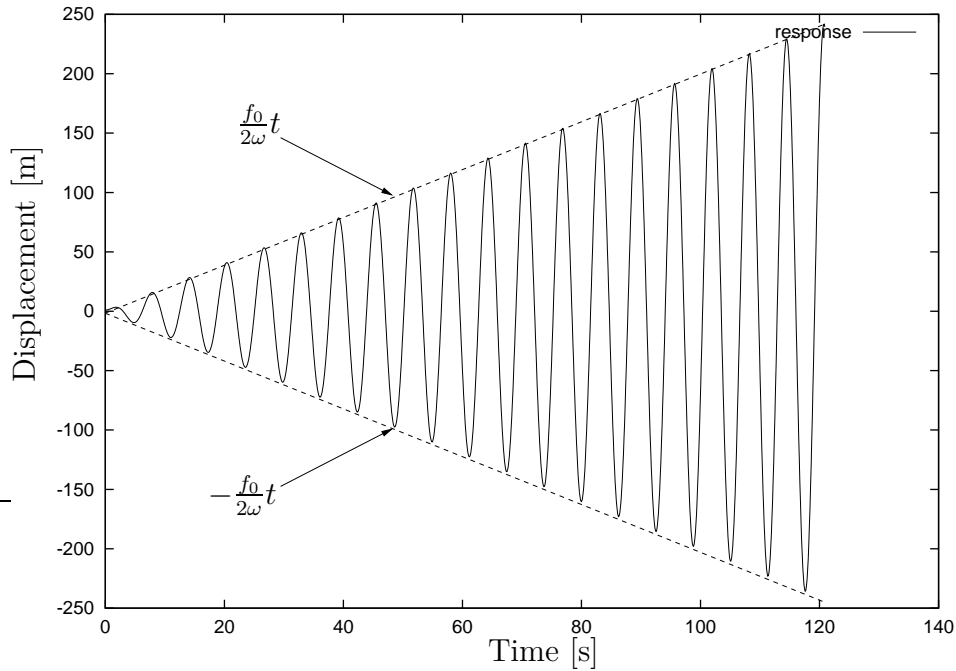


Figure C.6: The response of a system that is driven at exactly its own natural frequency, showing resonance.

Forced vibrations that include a damping term will satisfy the following equation of motion:

$$\ddot{x} + 2\zeta\omega\dot{x} + \omega^2x = f_0 \cos \omega_f t \quad (\text{C.17})$$

The particular solution for a damped equation will be a harmonic function that has the same frequency as the force, but has a different phase and amplitude:

$$x_p(t) = A_0 \cos(\omega_f t - \phi) \quad (\text{C.18})$$

which can also be written as:

$$x_p(t) = A \cos \omega_f t + B \sin \omega_f t \quad (\text{C.19})$$

provided that the following two equations hold:  $A_0 = \sqrt{A^2 + B^2}$  and  $\phi = \arctan \frac{B}{A}$ .

Substituting this particular solution into the equation of motion will give the following solution [71]:

$$x_p(t) = \frac{f_0}{\sqrt{(\omega^2 - \omega_f^2)^2 + (2\zeta\omega\omega_f)^2}} \cos\left(\omega_f t - \arctan \frac{2\zeta\omega\omega_f}{\omega^2 - \omega_f^2}\right) \quad (\text{C.20})$$

This particular solution must be added to the solution for the homogeneous equation of motion.

The steady state solution can be written as:

$$x(t) = A_f \cos(\omega_f t - \phi) \quad (\text{C.21})$$

With the amplitude  $A_f$ :

$$A_f = \frac{f_0}{\omega^2} \frac{1}{\sqrt{(1 - (\frac{\omega_f}{\omega})^2)^2 + (2\zeta \frac{\omega_f}{\omega})^2}} \quad (\text{C.22})$$

And the phase angle  $\phi$ :

$$\phi = \arctan \frac{2\zeta \frac{\omega_f}{\omega}}{1 - (\frac{\omega_f}{\omega})^2} \quad (\text{C.23})$$

The normalised amplitude of the response can be plotted for different forcing frequency over natural frequency ratios and different damping ratios as shown in figure C.7. This figure shows that the amplitude will become larger if the forcing frequency is closer to the systems natural frequency, especially if the damping value is low. The case of resonance with zero damping is also shown.

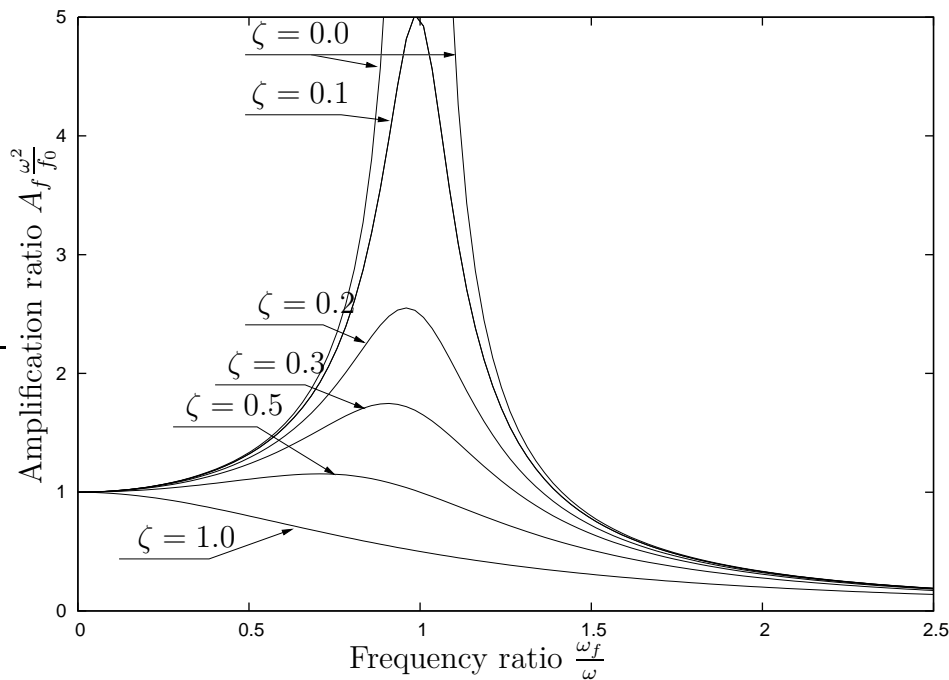


Figure C.7: The frequency response of a forced system.

This has been a very short introduction into linear vibrations. Many good extensive books exist that deal with this subject, e.g. [71].

# Appendix D

## Post-Processing Methods

The simulation tool WOBBE returns time series that are fully nonlinear, therefore the damping values and eigenfrequencies, as used in the linear vibration theory, are not actually present as such in the nonlinear results; the damping and frequencies will change during the simulation. However, to be able to judge if a vibration is stable or not and to be able to make some comparison with other results and measurements, one has to try to somehow fit frequencies and damping values to the results. This appendix will discuss the post-processing methods that have been used to obtain damping and frequency results that are discussed throughout this dissertation. The first section discusses the Fast Fourier Transform, it describes the method and the possible applications to find frequencies and damping values. The second section discusses the identification tools that have been used for post-processing.

### D.1 Fast Fourier Transform

One option to analyse the results from a simulation is to use the Fast Fourier Transform (FFT). The discussion of FFT is limited to the aspects that are of importance for the analysis described in this dissertation. First a definition of the Fourier transform will be given and the method used to determine the Fast Fourier Transform will be explained. The last section in this appendix will show the possibilities and problems with using FFT to determine the damping.

#### D.1.1 Fourier Transformation

The Fourier transform is defined by (see for example: [15]):

$$H(f) = \int_{-\infty}^{\infty} h(t)e^{-j2\pi ft} dt \tag{D.1}$$

where  $j = \sqrt{-1}$  and  $H(f)$  is the Fourier transform of  $h(t)$ , provided that the integral exists for every value of  $f$ . The Fourier transform  $H(f)$  is a function of the variable: frequency,  $h(t)$  is a function of the variable: time.

The inverse Fourier transform is defined as:

$$h(t) = \int_{-\infty}^{\infty} H(f)e^{j2\pi ft}df \quad (\text{D.2})$$

The Fourier series for a periodic function  $h(t)$  with period  $T_0$  is:

$$h(t) = \frac{a_0}{2} + \sum_{n=1}^{\infty} [a_n \cos(2\pi n f_0 t) + b_n \sin(2\pi n f_0 t)] \quad (\text{D.3})$$

where  $f_0 = \frac{1}{T_0}$ . The coefficients  $a_n$  and  $b_n$  are calculated using the following formula:

$$a_n = \frac{2}{T_0} \int_{-\frac{T_0}{2}}^{\frac{T_0}{2}} h(t) \cos(2\pi n f_0 t) dt \quad n = 0, 1, 2, 3, \dots \quad (\text{D.4})$$

$$b_n = \frac{2}{T_0} \int_{-\frac{T_0}{2}}^{\frac{T_0}{2}} h(t) \sin(2\pi n f_0 t) dt \quad n = 1, 2, 3, \dots \quad (\text{D.5})$$

The discrete Fourier transform is a special form of the continuous Fourier transform (see [15]):

$$G\left(\frac{n}{NT}\right) = \sum_{k=0}^{N-1} g(kT)e^{-j2\pi nk/N} \quad n = 0, 1, 2, 3, \dots, N-1 \quad (\text{D.6})$$

with  $g(kT)$  the sampled signal,  $T$  the sampling interval and  $N$  the total number of samples used.

The FFT is a quick way to calculate the Fourier transform, the number of calculations needed compared to direct calculation of the discrete Fourier transform is strongly reduced. For the direct calculation one would need  $O(N^2)$  operations, while FFT formulations reduce this to  $O(N \log(N))$  operations. A widely used example is the Cooley-Tukey algorithm that recursively breaks down the discrete Fourier transform into smaller discrete Fourier transforms, but more algorithms exist that work similarly [15]. Many programs have FFT algorithms included, for example when using Matlab or Maple the FFT can easily be determined, because the algorithms are part of the program.

### D.1.2 Determination of Natural Frequencies using FFT

Linear vibrations are combinations of a certain number of sines or cosines for different frequencies. These frequencies are called the natural frequencies or eigenfrequencies of the system. When linear time series are available, the determination of the natural frequencies

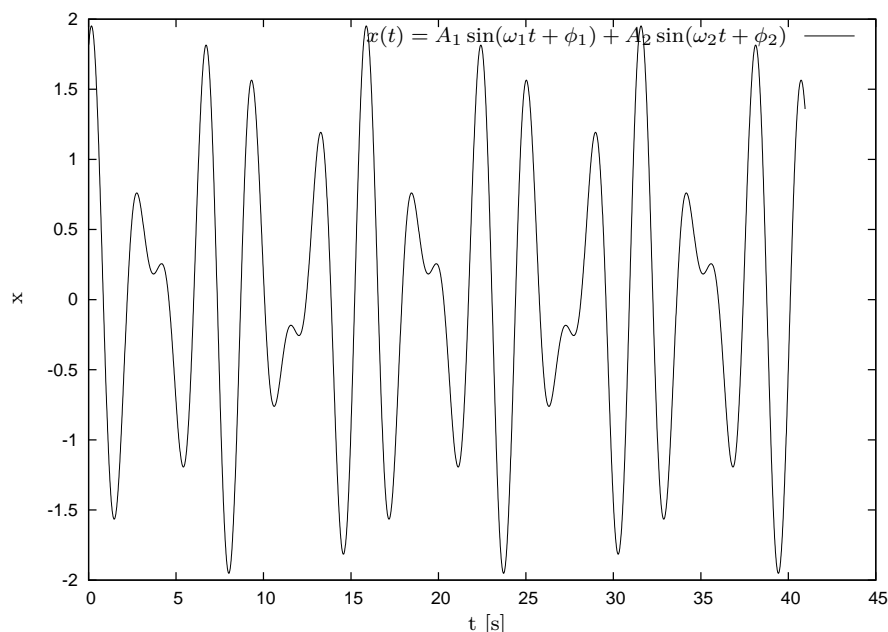


Figure D.1: An example linear vibration:  $x(t) = \frac{1}{2}\sqrt{5} \sin(2.0 * t + 1.107) + 0.84949 \sin(2.8 * t + 1.228)$

can be done using FFT. When a continuous function is known, the Fourier transform will be distinct impulses at zero and at the natural frequencies and their negatives. When the discrete Fourier transform is determined, so when a sampled signal is available, the DFT will not be exactly predicting the natural frequencies. For example figure D.1 shows a linear vibration consisting of two sine functions:

$$x(t) = \frac{1}{2}\sqrt{5} \sin(2.0 * t + 1.107) + 0.84949 \sin(2.8 * t + 1.228) \quad (\text{D.7})$$

This is a vibration with  $\omega_1 = 2.0$  rad/s, a starting position  $x_1(0) = 1.0$  and a starting velocity  $\dot{x}_1(0) = 1.0$  combined with a vibration with  $\omega_2 = 2.8$  rad/s, a starting position  $x_2(0) = 0.8$  and a starting velocity  $\dot{x}_2(0) = 0.8$ . This vibration has been sampled with a time step of 0.01 seconds.

It is possible to determine the power spectral density (PSD) using fast Fourier transforms (FFT). The PSD will show the presence of different frequencies in the signal; peaks for the natural frequencies will show up in the graph. The PSD as determined using the DFT is illustrated in figure D.2. The frequencies that are in the vibration are  $\omega_1 = 2$  rad/s = 0.31830989 Hz and  $\omega_2 = 2.8$  rad/s = 0.44563384 Hz. Figure D.2 illustrates however that these frequencies have not been the discrete frequencies that were analysed and that other frequencies also have non-zero values in the PSD. For this particular case the frequencies that were analysed using the DFT, were multiples of 0.048851978505122.

Increasing the number of samples without changing the time step, gives better results. Figure D.3 shows the PSD for twice as many samples. This shows the smaller steps taken in the

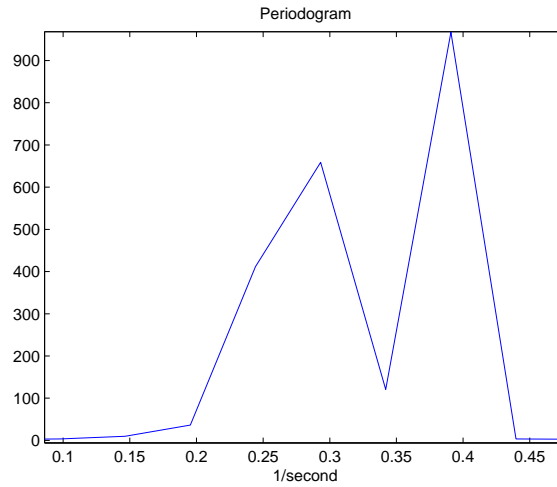


Figure D.2: The PSD of the vibration.

discrete frequencies and improved results. There is however still so-called leakage visible; frequencies that are not present in the signal do get non-zero values. This leakage can be reduced by using for example a Hanning window [15].

When there is a large difference in amplitude between the two vibrations with different frequency, the frequency with the small amplitude can become invisible in the PSD, this is illustrated in figure D.4. This figure shows the PSD for the vibration given before, but now with a starting position  $x_1(0) = 10.0$  and a starting velocity  $\dot{x}_1(0) = 10.0$ , the other values have remained the same. The resulting PSD does not show a peak at the highest of the two frequencies anymore, the leakage of the lower frequency is larger than the power of the higher frequency.

As mentioned in the previous section, there are many programs available to determine the Fast Fourier Transform of series of variables, e.g. Matlab (used in the previous example), Maple, Fortran IMSL and Windap. Windap is a programme by Kenneth Thomsen from Risø National Laboratory in Denmark. This program has been used to create figures D.5 and D.6. Figure D.5 shows the position in the out of plane  $z$ -direction of the last hinge of the benchmark model of the isolated blade (see figure 8.14) for a wind velocity of  $15 \text{ m/s}$ . This  $z$ -direction is given relative to the rotor centre and in the rotating reference frame; this reference frame follows the motion of the root of the blade.

The PSD of this position is given in figure D.6. This shows the first flap frequency to be around 1 Hz. Figure D.5 shows that this frequency is strongly damped.

This example in figure D.6 shows that the FFT can be used to determine the natural frequencies from nonlinear results, the value corresponds well to measured frequencies for the blade that was modelled. However, due to leakage and the steps taken in the discrete frequency values, there will always be errors and when there are large differences in the amplitudes of the vibrations, it can become harder to find the natural frequencies. These large differences

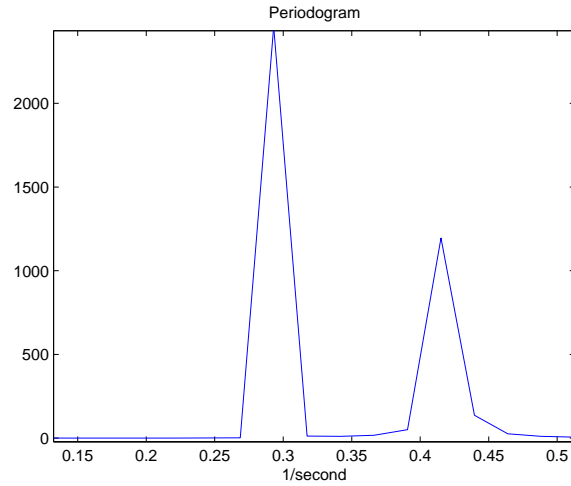


Figure D.3: The PSD of the vibration, using a two times longer time series.

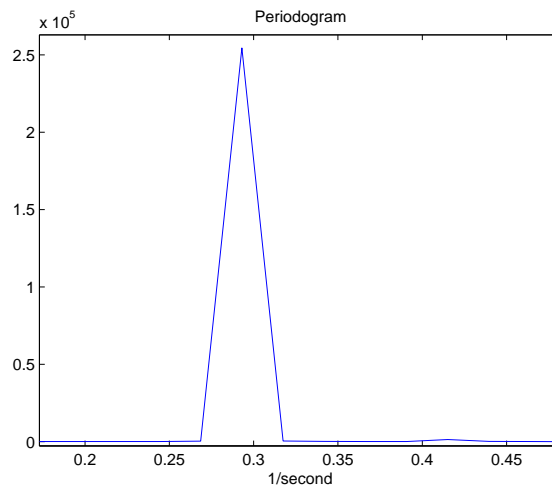


Figure D.4: The PSD of the vibration (with log scale) with large amplitude for one frequency and small amplitude for other frequency.

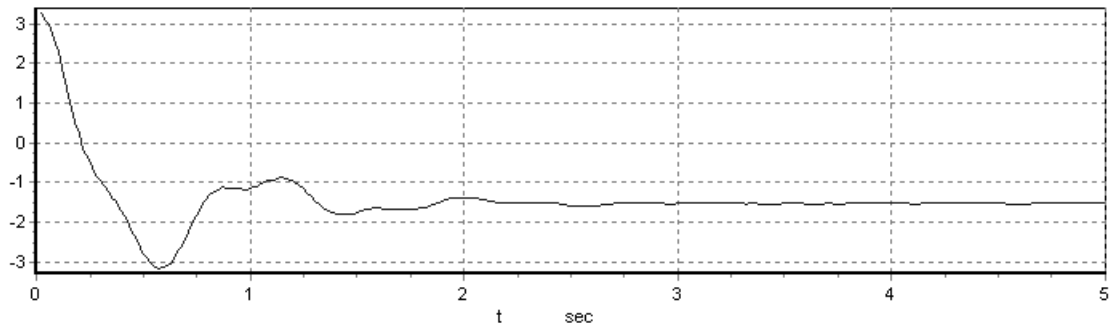


Figure D.5: Position in  $z$ -direction of the final hinge of a 15 DOF isolated blade model.

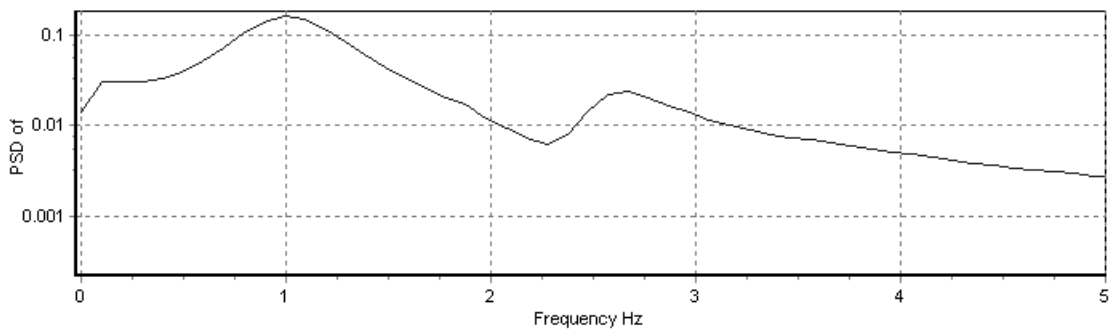


Figure D.6: Spectrum of the position in  $z$ -direction of the final hinge of the isolated blade model, determined using FFT

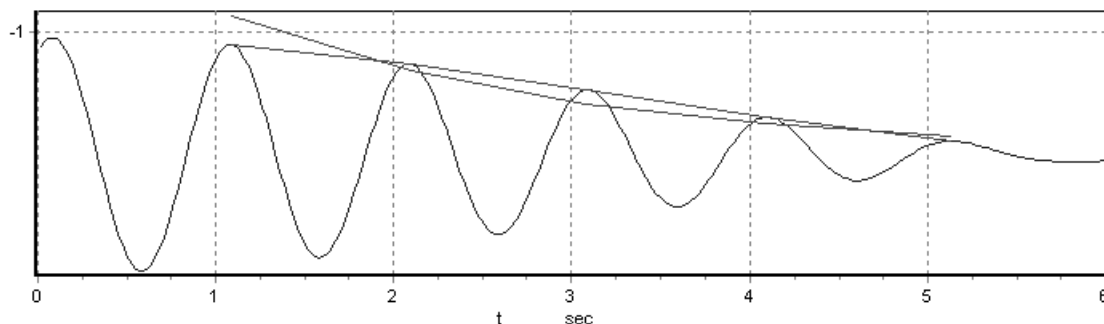


Figure D.7: The result of filtering the  $z$ -coordinate of the final hinge of the blade. Damping estimate 0.5 in logarithmic decrement

can easily occur due to differences in damping, some frequencies are well damped, while other frequency have very little damping, this combined with a small difference in frequency can result in some frequencies that cannot be determined using FFT.

### D.1.3 Determination of Damping using FFT

The most important results when investigating the aero-elastic stability are the damping coefficients for the different modes. To be able to compare results from WOBBE with linear programmes and to be able to fully analyse the results, damping coefficients must be estimated from the output of WOBBE.

Knowing the eigenfrequencies of the system it is possible to use an FFT-filter to limit the resulting plot to only the response in a small frequency band around a given eigenfrequency.

Looking back at figure D.5, this signal can be filtered around the first flap frequency of approximately 1 Hz. This filtering results in figure D.7. From this plot a damping coefficient can be determined. For the filtering and the determination of the damping, the programme called Windap has been used. As shown in figure D.7 an exponential function can be drawn as close to the peaks as possible and from this the damping is determined. In this case the logarithmic damping decrement was found to be 0.5.

Due to the non-linearity of the results and the errors that are always present when using FFT and FFT filters, the accuracy in the answers that are obtained using this method is not high. Next to this, the damping for a non-linear vibration is not constant and can depend on the amplitude. The inaccuracy of the method is illustrated by comparing figure D.8, which shows a different interval of the plot, to figure D.7. This new interval results in a significantly different damping coefficient for exactly the same simulation, it now has almost half the value of the previous analysis.

Another way of determining the damping using FFT is to calculate the PSD over changing time intervals; the moving block method [128]. This method is widely used in the rotorcraft

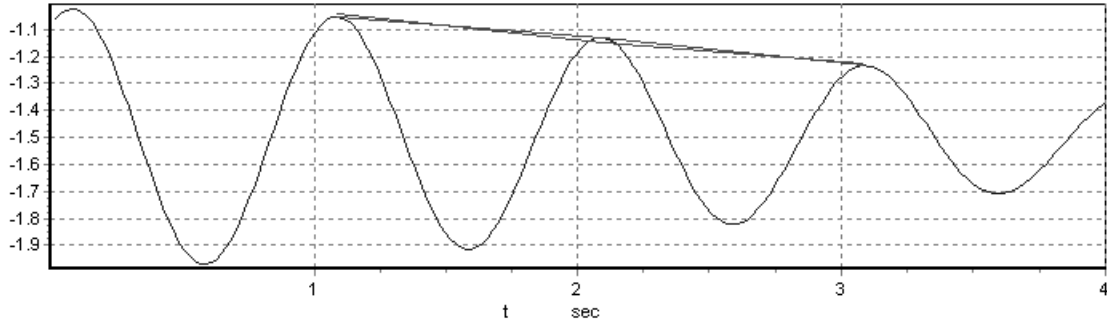


Figure D.8: The result of filtering the  $z$ -coordinate of the final hinge of the blade. Damping estimate 0.26 in logarithmic decrement

industry. By determining the PSD over different time intervals, it is possible to analyse the damping for the different frequencies. This is illustrated in figures D.9 till D.11.

First figure D.9 shows the response of a linear damped vibration:

$$x(t) = Ae^{-\zeta\omega t} \sin(\omega_d t + \phi) \quad (\text{D.8})$$

with  $\zeta = 0.1$ ,  $\omega = 2.0$ ,  $V(0) = 5$ ,  $x(0) = 1$ ,  $\omega_d = \omega\sqrt{1 - \zeta^2} = 1.98997$ ,

$A = \sqrt{\frac{(V(0) + 2\zeta x(0))^2 + (x(0)\omega_d)^2}{\omega_d^2}} = 2.7979$  and  $\phi = \arctan\left(\frac{x(0)\omega_d}{V(0) + \zeta\omega x}\right) = 0.3655$ . FFT's have been determined using the different time intervals illustrated in figure D.9 by the green rectangles. In this example, a Hann window has been used to obtain better results and resolve some of the leakage:

$$x^*(n) = x(n) \frac{1}{2} \left(1 - \cos\left(\frac{2\pi n}{N-1}\right)\right) \quad (\text{D.9})$$

The PSD is then determined for each time interval:

$$S_{yy} = G * \overline{G} \quad (\text{D.10})$$

with  $G$  the discrete Fourier transform of  $x(t)$ . The different PSD's can be plotted in a 3D plot, as shown in figure D.10. This figure shows that the peaks change in value due to the damping. As discussed in [128], it is possible to determine the damping from these peaks. Figure D.11 shows the peaks in a PSD against time. As derived in [42] the natural logarithm of the Fourier transform is approximately equal to the damping coefficient times the frequency:

$$\ln|F(\omega, t)| = \ln \sqrt{S_{yy}} \approx -\zeta\omega t_{block} + C \quad (\text{D.11})$$

The peaks in the PSD in figure D.10 are plotted in figure D.11 and  $\ln(\sqrt{S_{yy}})$  is shown in figure D.12. This last figure shows the linear function that is almost identical to the peaks. From

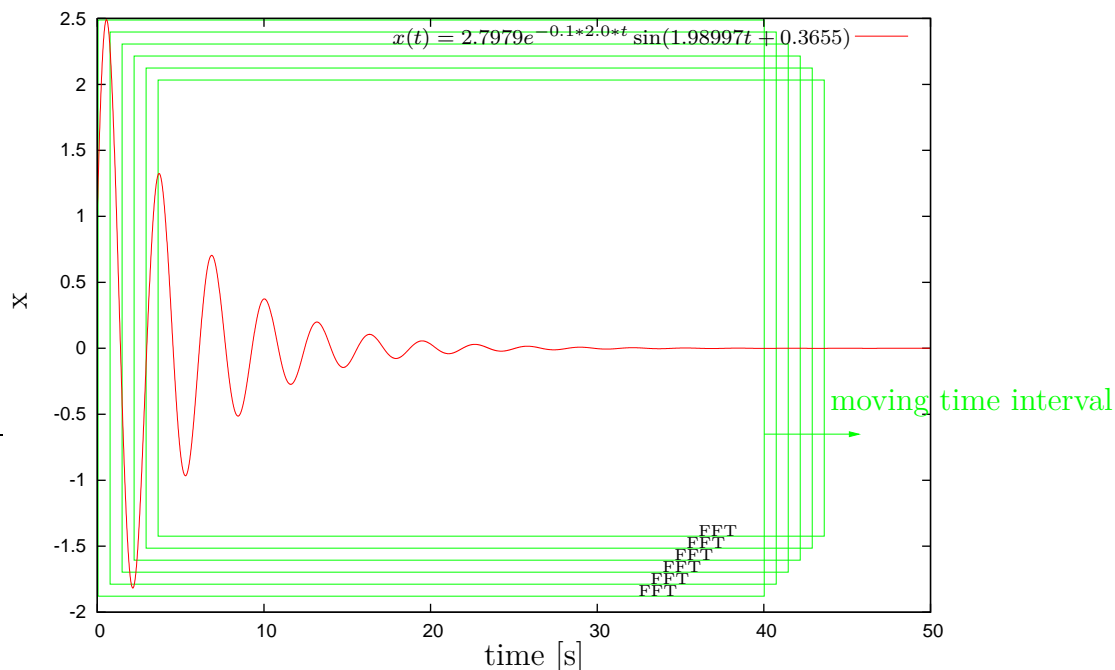


Figure D.9: An example of a damped vibration analysed using moving block FFT. The PSD is determined using different intervals, the length of the interval is kept the same, but it is shifted in time.

this equation it can be seen that  $-\zeta\omega = 0.2$ , which returns the correct damping coefficient:  $\zeta = 0.1$ . Often the resulting line will not be such a straight line, a variation with a frequency of  $2\omega$  is actually superimposed on the linear line [128], which is not visible in this case. This variation makes it important to use enough results and take the average straight line through the peaks.

This method is successful in this example and can be used in many cases. However, when the frequencies are close, while the damping shows large differences, e.g. one badly damped mode relatively close to a strongly damped mode, the leakage can make it impossible to produce reliable results. This was the reason why it was unsuccessful in the analysis of the results obtained using WOBBE.

## D.2 Logarithmic Decrement

To estimate the damping of a nonlinear vibration, the logarithmic decrement can be used. This technique is the classical damping identification method. The logarithmic decrement is defined as:

$$\delta = \frac{1}{n} \ln \frac{x_1}{x_2} \quad (\text{D.12})$$

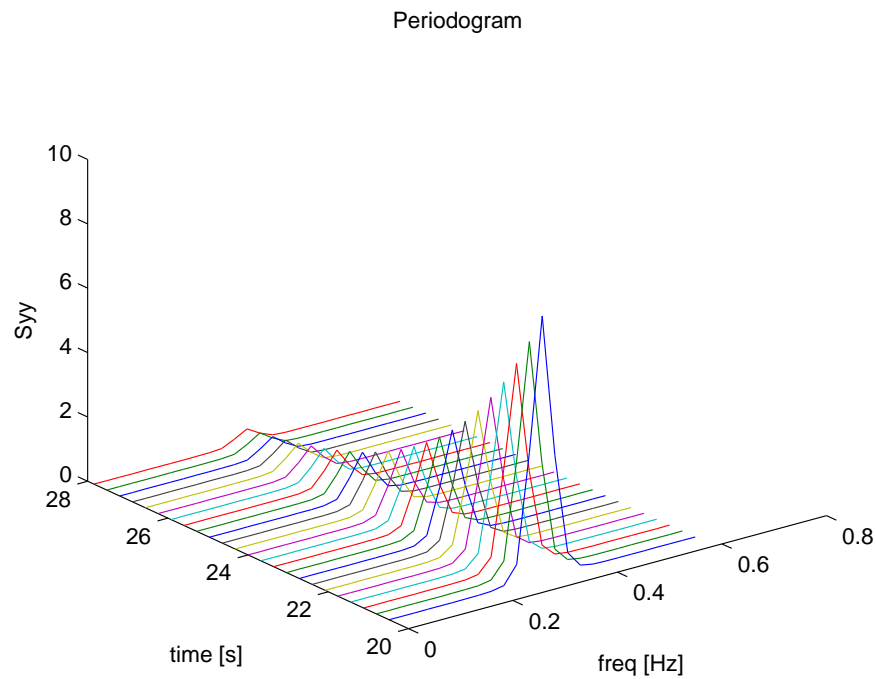


Figure D.10: A 3D plot of the moving block FFT analysis. The PSD over different time intervals is shown. The average time in the interval is plotted against the frequency and against  $S_{yy}$

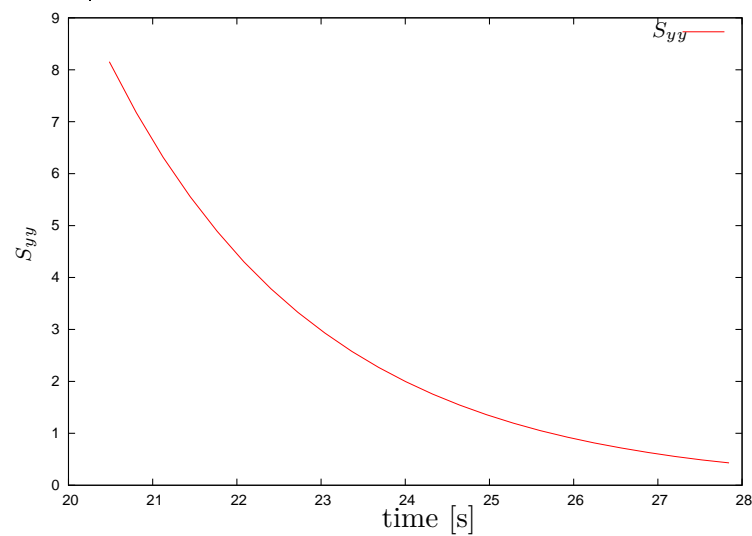


Figure D.11: The peaks in the PSD,  $S_{yy}$ , against time

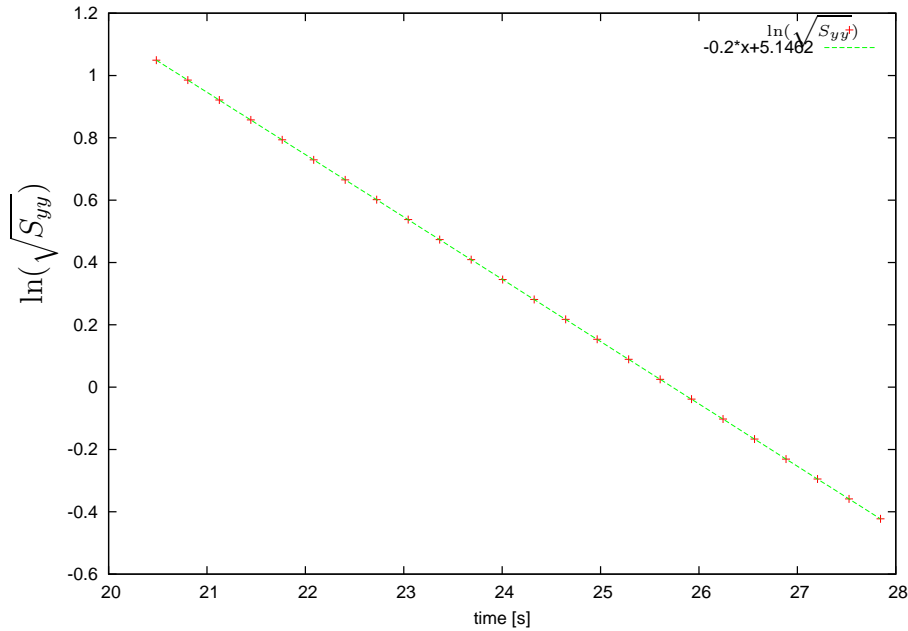


Figure D.12: The linear reduction in  $\ln(\sqrt{S_{yy}})$ , against time

where  $x_1$  is a peak amplitude and  $x_2$  is the peak amplitude  $n$  cycles further. The damping ratio is then given by:

$$\zeta = \frac{\delta}{\sqrt{(2\pi)^2 + \delta^2}} \quad (\text{D.13})$$

If  $\delta$  is small ( $\delta \ll 2\pi$ ), then this equation can be estimated using:

$$\zeta \simeq \frac{\delta}{2\pi} \quad (\text{D.14})$$

## D.3 System Identification

As discussed above, the methods described in the previous section are not always very accurate. Another option is to use an identification method that will identify a linear model from the results.

System identification can be used to find the natural frequencies and corresponding damping values as well as the mode shapes of nonlinear results from WOBBE. As a linear response is identified that corresponds as good as possible with the nonlinear results, it is only possible to get good results if the nonlinearity is relatively small. The simulation has to be started with a small excitation relative to the steady state, otherwise the identification process will not lead to acceptable results. This excitation however cannot be too small, the different modes must be excited, otherwise they will not be identified.

The identification tool AerID, developed by Delft University of Technology, is based on black box identification [52, 87] and is programmed in the Matlab-Simulink environment. It is specifically created for the post-processing of WOBBE output. Originally it was attempted to create a grey box identification tool, but that was without success [88]. Therefore it is completely black box identification and it cannot be used to predict any stability boundaries or trends in the stability, it is only useful to analyse the results obtained using the simulation tool WOBBE.

To analyse isolated blade simulations, the identification is rather straight forward. This is discussed in the first section. The complete wind turbine needs a slightly different approach, due to the periodicity in the steady state: the steady state will depend on the azimuth angle. The identification technique used for the complete turbine models is discussed in the second section.

### D.3.1 Constant Steady State

A linear system of equations can be identified from the results from WOBBE using the least squares technique. The state-space equation is:

$$\dot{\underline{x}}(t) = A(t)\underline{x}(t) \quad (\text{D.15})$$

where the state vector  $\underline{x}$  is:

$$\underline{x} = \left\{ \begin{array}{c} \underline{q} \\ \underline{\dot{q}} \end{array} \right\} \quad (\text{D.16})$$

The state variables are defined relative to their steady state value. Using the generalised coordinates and their time derivatives as state variables gives reasonable results when the simulation results are close to linear. Better results can be obtained when the induction factor  $a$  is added to the state vector:

$$\underline{x} = \left\{ \begin{array}{c} \underline{q} \\ a \\ \underline{\dot{q}} \end{array} \right\} \quad (\text{D.17})$$

The dynamic inflow model in WOBBE has a significant effect on the results, due to the excitation at the start of the simulation, the induction factor will also be excited at the start of the simulation and it will take some time for the induction to return to the steady state value. For this reason it has been included in the state variable.

Using the identification tool to find the frequencies and damping values, the calculations performed in WOBBE must be close to linear, but the modes must be excited. When the simulation starts too close to the steady state, one or more modes will not be identified as they are hardly present in the results. Therefore it can be necessary that several simulations must be performed. First a simulation is needed to determine the steady state. Then

a second simulation must be performed and analysed using the identification tool. If the results are not satisfying, it can be necessary to perform another simulation with smaller or larger excitations at the start of the simulation. It can be necessary to repeat this process until the results obtained are accurate enough and the identified signal fits the original time series with a high percentage. If the simulation has an instability, it can become impossible to obtain good results, the amplitude of the vibrations will increase in time and it becomes impossible to stay close to a linear model.

As an example illustrating the results, figure D.13 shows the original and identified signal of several generalised coordinates for a blade model consisting of 5 superelements (=25 degrees of freedom). The added state is shown in figure D.14. The fit of the induced velocity is not as good as of the generalised coordinates, clearly nonlinearities play an important role here, but adding this to the state vector has improved the fit of the generalised coordinates by a few percent. Note that the state variables are all plotted relative to the steady state value.

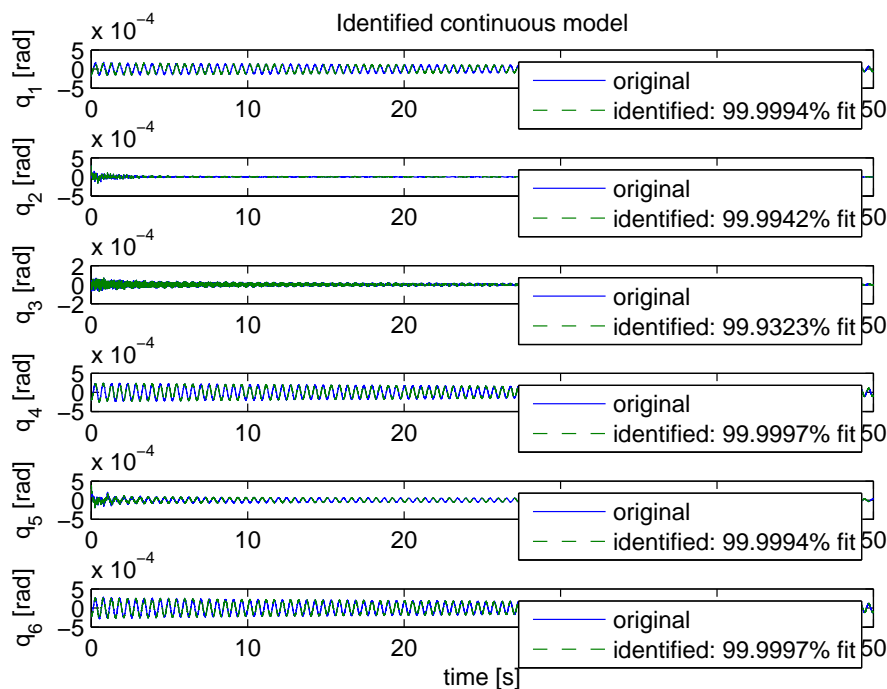


Figure D.13: The original and identified signals for the first six dof's in an isolated blade model consisting of 5 superelements, as used in section 9.2.

### D.3.2 Periodic Steady State

For the identification of a linear wind turbine model the states are considered to be known since they can all be retrieved from the non-linear code WOBBE. Moreover the system is

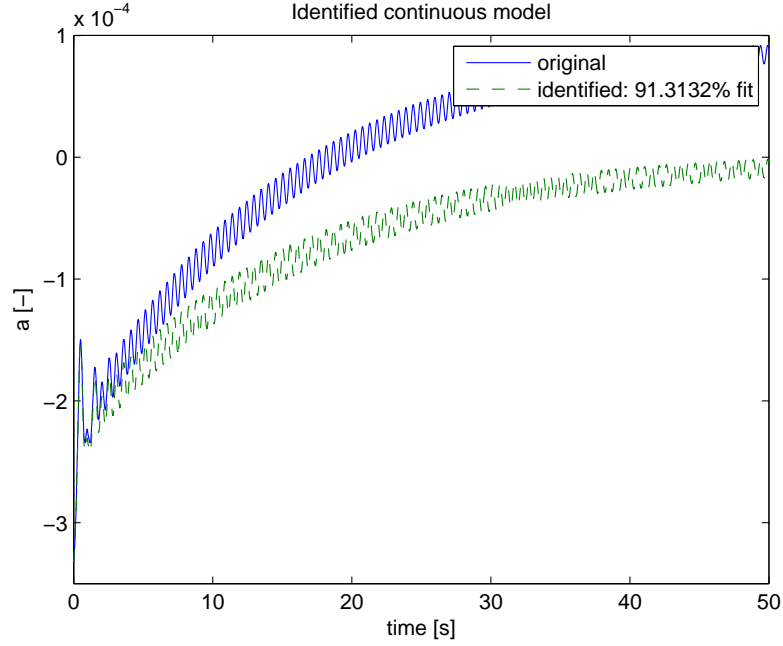


Figure D.14: The original and identified induction factor w.r.t. its steady state for an isolated blade model consisting of 5 superelements, as used in section 9.2.

also considered to be autonomous (i.e. no inputs) and periodic. The state space equation again looks as follows:

$$\dot{\underline{x}}(t) = A(t)\underline{x}(t) \quad (\text{D.18})$$

where  $\underline{x}$  is the state vector and  $A(t)$  is periodic matrix of the system that still has to be determined. It is possible to determine the matrix by analysing different azimuth angles separately. Divide the  $360^\circ$  azimuth range into  $n$  discrete values for the azimuth angle and for each of these set up the datasets. If for each azimuth angle  $N$  data sets are available, these can be used to estimate the each  $A_i$  matrix:

$$[\dot{\underline{x}}_i(1) + \dot{\underline{x}}_i(2) + \dots + \dot{\underline{x}}_i(N)] = A_i(t) [\underline{x}_i(1) + \underline{x}_i(2) + \dots + \underline{x}_i(N)] \quad (\text{D.19})$$

where  $i$  will correspond to angles running from 0 till  $2\pi$ . This equation can be written as:

$$\underline{Y}_i = A_i \underline{X}_i \quad (\text{D.20})$$

with  $\underline{X}_i = [\underline{x}_i(1) + \underline{x}_i(2) + \dots + \underline{x}_i(N)]$  and  $\underline{Y}_i = [\dot{\underline{x}}_i(1) + \dot{\underline{x}}_i(2) + \dots + \dot{\underline{x}}_i(N)]$ . This system can be solved using the least squares technique. This gives:

$$A_i = \underline{Y}_i \underline{X}_i^T (\underline{X}_i \underline{X}_i^T)^{-1} \quad (\text{D.21})$$

Solving these equations for each  $i$  will result in the identification of  $n$  different  $A$  matrices for a periodic system from which the damping and frequencies can be determined [87].

# Appendix E

## Controlled Rotations vs the Flywheel Approach

As described in section 5.3.2 the first version of WOBBE used a flywheel to keep the rotational velocity  $\Omega$  of the blade constant. This appendix will show why this engineering solution does not suffice in the case of a wind turbine where the tower motions are included in the model. It will also show the differences between the results using the flywheel and a controlled rotation added to the code.

### E.1 Shortcomings of the Flywheel approach

Looking at a wind turbine model, including the tower, as drawn in figure E.1 the problem of using a flywheel is illustrated. The kinetic energy of the tower and the rotor blades would be:

$$T = \frac{1}{2}I_{tower}\dot{q}^2 + \frac{1}{2}I_{rotor}(\dot{q} + \Omega)^2 + \frac{1}{2}(\dot{q}l)^2m_{rotor} \quad (\text{E.1})$$

In this equation  $I_{tower}$  is the inertia of the top half of the tower and  $I_{rotor}$  is the total inertia of the blades. The mass of the blades is  $m_{rotor}$ . The generalised momentum would become:

$$p = \frac{\partial T}{\partial \dot{q}} = I_{tower}\dot{q} + I_{rotor}(\dot{q} + \Omega) + \dot{q}l^2m_{rotor} \quad (\text{E.2})$$

If the model including a flywheel to simulate the constant rotation  $\Omega$  is used, this would result in a different kinetic energy:

$$T = \frac{1}{2}I_{tower}\dot{q}^2 + \frac{1}{2}(I_{flywheel} + I_{rotor})(\dot{q} + \Omega)^2 + \frac{1}{2}(\dot{q}l)^2m_{rotor} \quad (\text{E.3})$$

In this equation  $I_{flywheel}$  is the inertia of the flywheel about its rotating axis. It must be large relative to the other inertias to keep the rotational velocity  $\Omega$  approximately constant.

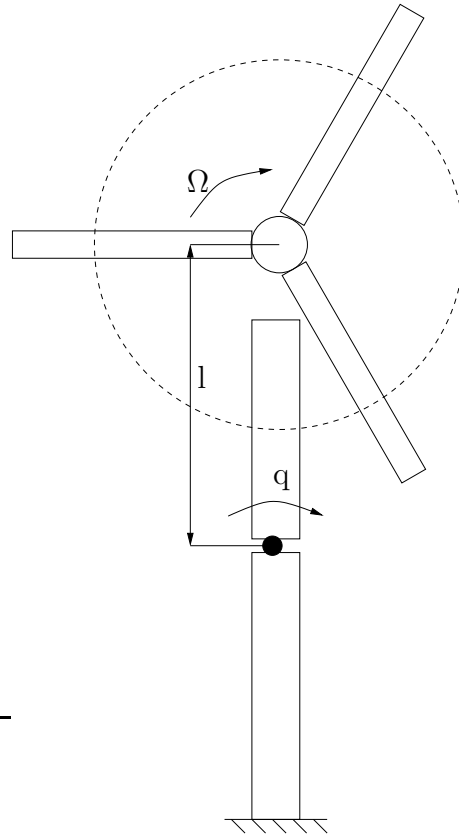


Figure E.1: Wind turbine model with a tower bending degree of freedom and flywheel.

The generalised momentum would in this case be:

$$p = \frac{\partial T}{\partial \dot{q}} = I_{tower}\dot{q} + (I_{rotor} + I_{flywheel})(\dot{q} + \Omega) + \dot{q}l^2m_{rotor} \quad (\text{E.4})$$

These different kinetic energies result in completely different values for the generalised momentum as introduced by Hamilton:  $p = \frac{\partial T}{\partial \dot{q}}$ . Thus using the flywheel for this model leads to incorrect answers. Therefore some other way must be found to model the controlled rotation.

## E.2 Verification of the Controlled Rotations

The method described in section 5.3.2 has been implemented into WOBBE. To investigate the correctness of this implementation as well as to investigate the differences between the flywheel and the controlled rotations, several calculations were performed. Two different calculations were done to check the adjusted code. The first is an Euler-Bernoulli beam. The results of the calculations on the beam are compared to the results obtained by using a flywheel to generate the constant rotational velocity. This is discussed in section 8.1.1.

A second calculation that has been performed uses a very simple model of a helicopter. For this model the results from WOBBE are compared to its analytical solution. This simple model can very easily be validated by hand. The model consists of two elements: the body of the helicopter and the blades as drawn in figure E.2. The blades are assumed to form one rigid blade. The body element is free to rotate about the axis through the c.g.'s of the

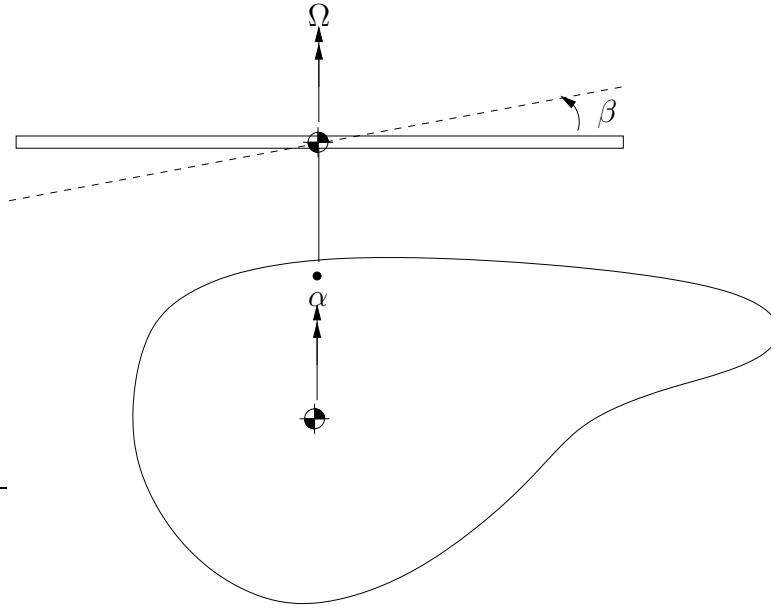


Figure E.2: The helicopter model,  $\beta$  will remain zero

body and the blade. Between the body and the rotor the controlled rotation is added. The function of the rotation of the blades relative to the body is:

$$\Omega = 12 + 2t \quad (\text{E.5})$$

This means that:

$$\dot{\Omega} = 2 \quad (\text{E.6})$$

To keep the model as simple as possible in order to be able to easily check it with the exact solution no extra degree of freedom is wished for. However, in WOBBE it is necessary to give the blades an actual degree of freedom. Therefore the single element representing both blades has a flapping degree of freedom, but the initial angle and rotational velocity are set to zero. And as the aerodynamic forces are neglected the flapping angle will remain zero. Therefore this flapping angle is also neglected in the following equations.

The rotating axis is assumed to be a principal axis of the body and of the rotor. With this assumption the kinetic energy of the system is:

$$T = I_{body}\dot{\alpha}^2 + I_{blade}(\dot{\alpha} + \Omega)^2 \quad (\text{E.7})$$

Where  $I_{body}$  is the moment of inertia about the rotation axis of the helicopter body,  $I_{blade}$  is the moment of inertia of the blade and  $\alpha$  is the angle that corresponds to the degree of freedom of the helicopter body. Using Lagrange's equations the equation of motion can be found for the only generalised coordinate  $\alpha$ :

$$2(I_{body} + I_{blade})\ddot{\alpha} + 2I_{blade}\dot{\Omega} = M_{ext} \quad (\text{E.8})$$

Supposing that there are no external non-conservative forces on the model and substituting the assumed function for  $\Omega$  gives:

$$\ddot{\alpha} = -\frac{2I_{blade}}{I_{body} + I_{blade}} \quad (\text{E.9})$$

The following values were used for the moments of inertia:  $I_{blade} = 100$  and  $I_{body} = 800$ . With these values the angular acceleration of the helicopter body becomes  $\frac{2}{9}$ . The rotational velocity at the start of the simulation was set at 0.4 radians per second. The angle is assumed to be equal to zero at the start. Using these starting values and the calculated acceleration of the body the angle at every time instant can be calculated. The function for  $\alpha$  is:

$$\alpha = \alpha_0 + \dot{\alpha}_0 t + \frac{1}{2}\ddot{\alpha}t^2 = 0 + 0.4 \cdot t - \frac{1}{2} \cdot \frac{2}{9} \cdot t^2 \quad (\text{E.10})$$

This function is plotted together with the output of WOBBE in figure E.3 This figure clearly shows that both graphs are exactly equal.

This simulation could not have been performed by using a flywheel, not even if  $\Omega$  was assumed to be constant. This is because the inertia of the flywheel will be about the same axis as the rotation of an element placed before this flywheel, in this case the body, similar to the example of the wind turbine given in section E.1.

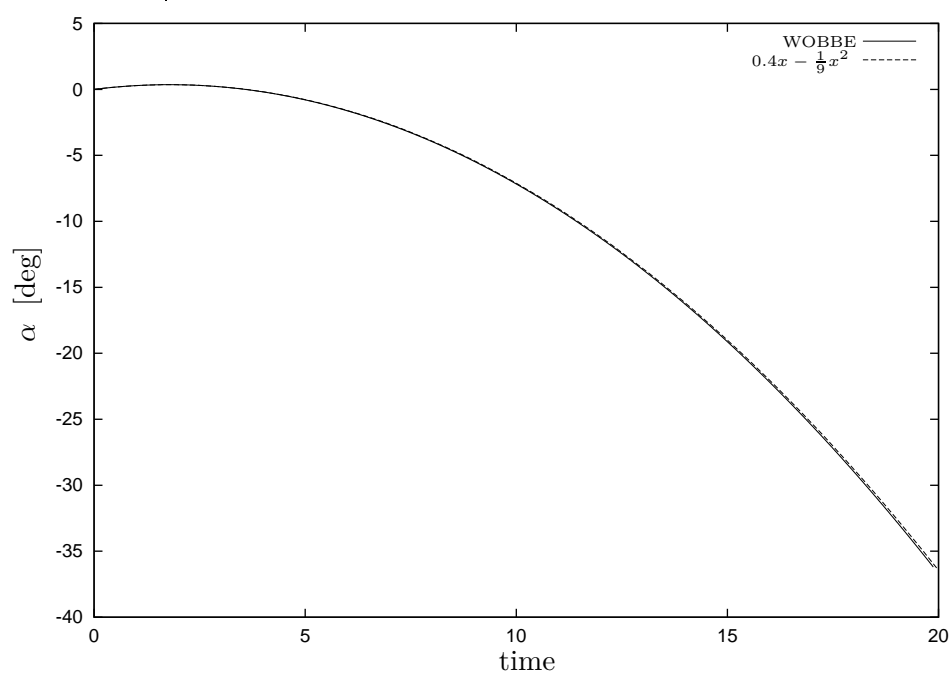


Figure E.3: Result WOBBE and exact analytical solution



# Appendix F

## WOBBE Flow Diagrams

This appendix shows several flow diagrams of WOBBE and gives a more extensive description of some of the subroutines. First an explanation is given of terms used in several flow diagrams. Terms that are specific for one subroutine are explained in the subsection of that subroutine. In the second section the flow diagrams are shown for a selection of subroutines, showing the calculations in much more detail.

### F.1 Explanation of Terms Used in Flow Diagrams

The following sections will show several different flow diagrams. To keep them as compact as possible, terms are used that need some explanation. Therefore table F.1 will give a clearer description of the meaning of the different terms. Terms that are only used in one flow diagram are described in the sections belonging to the flow diagrams. The table here only shows terms that are used in the flow diagrams of several subroutines.

### F.2 Subroutines

This section gives the flow diagrams of a selection of subroutines in WOBBE. For some subroutine a more detailed description than can be found in chapter 6 is also given.

#### F.2.1 Main Program

The main program WOBBEB is where the calculation starts and ends. The actions taken in this part of the programme are described in section 6.2.1. The flow diagram is shown in figure F.1

term	explanation
$A_{changed}$	Elements of the energy matrix $[A]$ that have changed in value due to a change in $q_{index}$
$A_{unchanged}$	Elements of the energy matrix $[A]$ that have not changed in value due to a change in $q_{index}$
DOFDIR(I)	Direction of the degree of freedom
DUMMY	Element with controlled rotation
FLNTFL(I,J,K)	For $K = 0$ the total number of elements that are not in line with J and are at the same time behind I is given and for $K = 1$ to $K = FLNTFL(I, J, 0)$ these elements are given.
FOLLOW(I,K)	A table with all elements that are behind element I, for $K = 0$ the total number of elements behind element I is given and for $K = 1$ to $K = FOLLOW(I, 0)$ these elements are given.
INDEX	The ID of the DOF that is changed in order to calculate a partial derivative with respect to this DOF, such as $\frac{\partial T}{\partial q_{index}}$ or $\frac{\partial \underline{q}}{\partial q_{index}}$
IOM	Number of controlled rotations
new	Value not taken from memory, it has changed due to the change in $q_{index}$ and has been recalculated.
N	Number of degrees of freedom
NOTFOLLOW(I,K)	A table with all elements that are not in line with element I, for $K = 0$ the total number of elements not in line with element I is given and for $K = 1$ to $K = NOTFOLLOW(I, 0)$ these elements are given.
NT	Total number of rigid elements, equal to the number of degrees of freedom plus the controlled rotations.
old	Value taken from memory, it has not changed due to the change in $q_{index}$ .
PRIOR(I)	Element to which element I is connected as a following element, therefore PRIOR(I) is the element that is before element (I).
$Q_i$	Generalised moments due to aerodynamic forces and structural damping
RESTART	If RESTART = 1 the simulation is a continuation of a previous simulation, the state variables at the start of the simulation are not read from the input file, but taken from the restart file.
SOLVE	If solve=1, the induction factor has to be calculated by iteration.
Y	A row with all generalised coordinates ( $\underline{q}$ ) followed by all generalised momenta ( $\underline{p}$ ) and when applicable followed by the induction factor.

Table F.1: Explanation of terms used in the flow diagrams

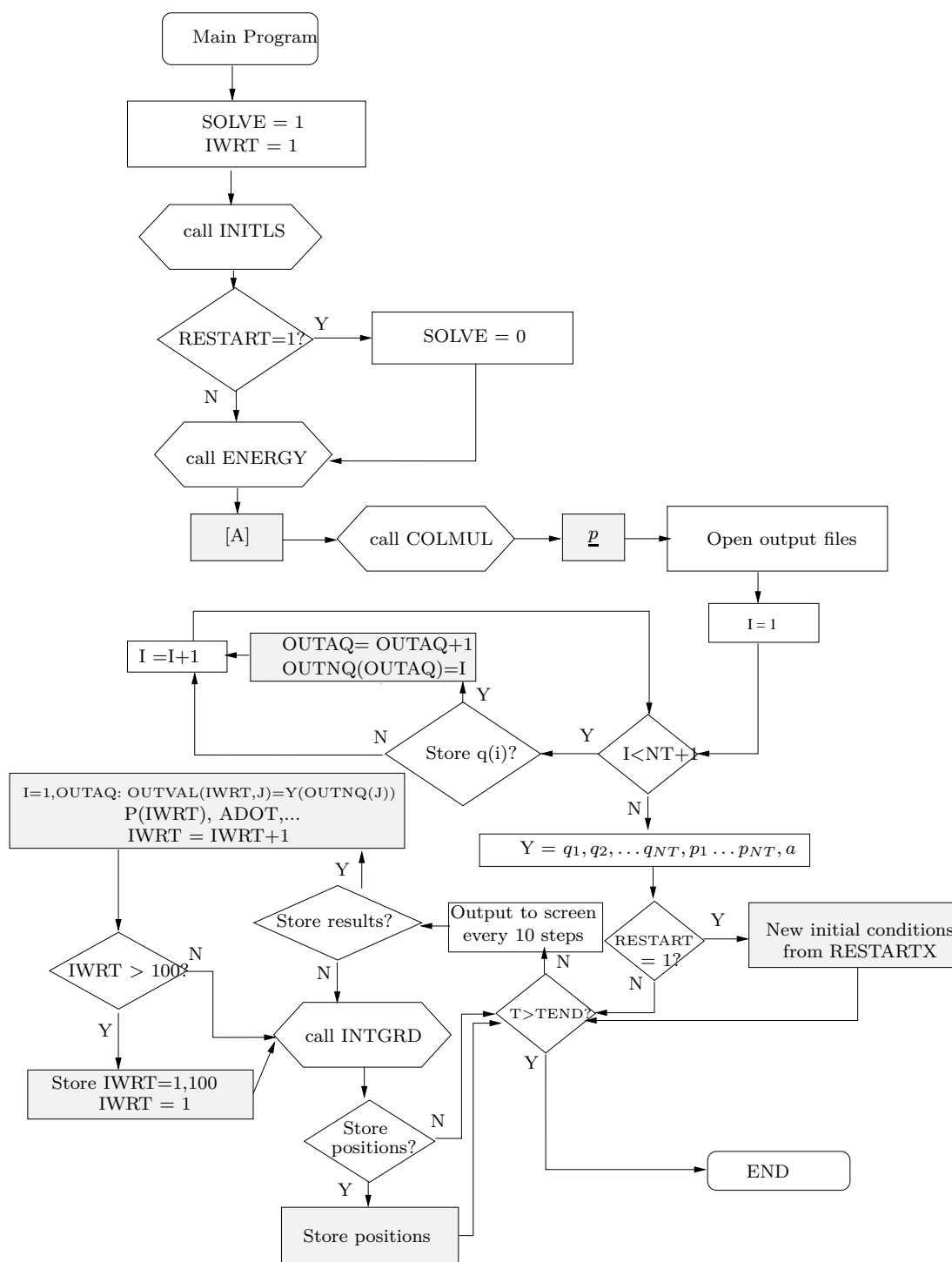


Figure F.1: Flow diagram of the main program routine. First INITLS is called to perform the model set-up. Then the energy matrix  $[A]$  is calculated and the generalised momenta  $\{p\}$  are determined. The integration routine is called and when necessary the results are stored in the output files.

The flow diagram shows the actions taken in the main part of the programme. First INITL is called, then the generalised momenta are calculated using the energy matrix.

Which generalised coordinates and velocities should be stored in an output file is indicated by the user in the input file. Therefore a row is set up that defines the coordinates that are stored. In the diagram the term OUTAQ is used to calculate the number of generalised coordinates and their derivatives that are to be stored in the output file. The ID's of these coordinates are stored in the row OUTNQ. Once the row OUTNQ has been set up, the integration is started. To save some time, the results are first stored in memory, until 100 time steps are in memory. They are then all written to the output file at the same time. IWRT is the variable that is used to count the number of steps stored in memory.

Once the end time step has been reached, the program finishes.

## F.2.2 INITL

In section 6.2.2 a short description is given of the INITL subroutine. This current section gives a more detailed description of the calculations that take place in this subroutine.

The subroutine INITL reads the data of the namelist input file and does any necessary work on this data, e.g. adding the dummy elements that model the controlled rotations as elements between the other elements. The subroutine is also used for calculating coefficients that remain constant during the simulation.

First the default settings are loaded, most variables will get a default value. The input data is then read from the namelist overwriting the default values. The input file gives the start and end time of the simulation as well as the number of steps taken. In INITL the size of the step ( $\delta t$ ) is calculated once the input is known. Then the output files are opened. If there are any controlled rotations in the model, the corresponding dummy elements are added to the model. As described in section 5.3.2, the elements behind the controlled rotation(s) need to be renumbered. The method used for this renumbering is illustrated in the flow diagram in figure F.2. The dummy elements corresponding to the controlled rotations can have a length, an inertia, a mass etc. This is defined in the input.

The renumbering that takes place in this subroutine for the PRIOR variable is rather complex. PRIOR defines which element is in front of the current element. Therefore not only the index of PRIOR must be renumbered, e.g. PRIOR(INDEX), the value it is given must also be corrected for the added dummy. For example assume that a controlled rotation is added as the first element in an isolated blade model. In that case element "A" that used to have an index 4 will get index 5. At the same time the PRIOR of element A had an index 3, but after adding the dummy element this will become index 4: PRIOR(4) = 3 becomes PRIOR(5)=4.

Once the renumbering due to the controlled rotations has finished, the VECMAT subroutine is called. The VECMAT routine (see 6.2.3) creates the operator matrix that corresponds

to a vector. This way the cross product of two vectors can be changed into a product of the second vector with an operator matrix of the first vector, as discussed in chapter 2. In WOBBE matrices are created for the position of the c.g. and the hinge, relative to the local reference frame. These matrices can then be used when the velocities need to be calculated.

Once these matrices are set up, the subroutine DIRECT is called, see 6.2.4. This subroutine creates a table with vectors that define the direction of the DOF in the local reference frame. These vectors will be unit vectors written as  $(c_{x_k}, c_{y_k}, c_{z_k})\{\underline{\mathbf{E}}_k\}$ , where two  $c$ 's will be zero, and one will be equal to one.

The next calculation concerns the PATH variable. This variable has been introduced in order to handle branched systems [103]. If element  $I$  and  $J$  are in line and  $I > J$ , then the PATH(I,J,K) will give the elements that connect  $J$  to element  $I$ .

For every element the variable  $DUMMY(I)$  will be given a value, depending on the kind of element. If the element is a dummy element, this value will be equal to 1. However, if it is a dummy element that models the shaft and should be used to calculate the power, this value is changed to  $DUMMY(I) = 2$ . If the shaft is modeled by an element with a DOF, this element will also get a nonzero value:  $DUMMY(I) = -2$ . All other elements will have a value of zero for this variable. This way it is possible to easily distinguish between dummy elements and DOF's; if the value of  $DUMMY(I) < 1$ , the element has a DOF. And if  $ABS(DUMMY(I)) = 2$ , the element is the shaft of the wind turbine and the generalised forces about this shaft can be used to calculate the power and induced velocity.

The INITL subroutine also performs many calculations that need to be performed only once during a simulation. This means i.a. the rotation transformation matrices of the fixed angles. These matrices are determined in the same way as described in section 6.2.6, but they will remain constant throughout the simulation. For this reason they will be calculated once and stored in a common block to be used throughout the simulation. The INITL subroutine also calculates the thickness ratios of the different aerodynamic subelements, if this is defined by a polynomial expression. It will save the thickness ratios. The angle for zero lift (needed for the unsteady aerodynamics) for each aerofoil data set that is included in the code is stored. It will also calculate the interpolation factor for each subelement, TOCFAC, see also table F.2. The angle of attack for zero lift for each subelement is linearly interpolated in the same way. There are also other variables that do not change during a simulation that are calculated in INITL, such as the rotor swept area, rotor radius etc.

The subroutine will also set up a matrix FOLLOW that stores all element indices that are behind a certain element. The total number of elements that are behind a certain element are calculated as well. E.g. for a system as shown in figure 6.4, the variable FOLLOW will give for element 1 a total number of elements behind it of 6,  $FOLLOW(1,0) = 6$ . And the row containing all these elements will be:  $FOLLOW(1,1..6) = (2, 3, 4, 5, 6, 7)$ . This variable is very useful in WOBBE as it specifies the elements to be looked at when calculating the generalised forces and the derivatives of the kinetic and potential energy. The matrix NOTFOLLOW will, for each element, store all elements that are not behind that element. Finally there is also a three dimensional matrix FLNTFL(I,J,K) set up that

CPOL	Defines the chord input: 0: a linear chord distribution within each rigid body or 1: a fifth order polynomial distributed over the entire blade
CHORDSUB	The chords of every subelement as determined by a polynomial input given in the input file.
KSPRNG	Spring stiffness
NMBPRF	Total number of aerofoil data sets or CLxxx subroutines to be used
PLACE	This gives an induction of the positions of controlled rotations
PRFINT	Gives the two aerofoils between which the thickness ratio of the subelement is defined, these two aerofoils are used in the interpolation based on the thickness ratio.
RPRANDTL	Distance from rotor centre, to be used in Prandtl's tip correction
TBLRCG	Table with operator matrices for the vectors from hinge to c.g.
TBLHNG	Table with operator matrices for the vectors from hinge to next hinge
TOCFAC	The factor for the interpolation: $c_l = c_{l_{aerofoil1}} * TOCFAC + c_{l_{aerofoil2}} * (1 - TOCFAC)$
TOCLX	Thickness ratio calculated using a polynomial distribution.

Table F.2: Explanation of terms used in the flow diagram for initl

gives all elements that are in line with J but are not behind I.

### F.2.3 ENERGY

The energy or mass matrix  $[A]$  is calculated in the ENERGY subroutine using the equations given in section 5.2.1. A description of the subroutine is given in section 6.2.5.

As illustrated in the flow diagram in figure F.3, first the rotation transformation matrices for the complete system are determined. For this the subroutine TRAFOT is called. Next the different components of the energy matrix can be calculated, starting with the values of  $\frac{\partial \omega_k}{\partial \dot{q}_j}$ ,  $\frac{\partial v_{hgk}}{\partial \dot{q}_j}$  and  $\frac{\partial v_{hgk}}{\partial \dot{q}_j}$ . As described in section 5.2.1 each of these can be split into three different calculations, depending on the connection between  $k$  and  $j$ . The calculations start for  $k = j$  and then the derivatives for other values of  $k$  can be calculated as shown in the flow diagram.

The result from this subroutine is the energy matrix  $[A]$  as well as some of the intermediate results that are used again elsewhere in the programme: in VELOC to calculate the velocities and in NRGDTDQ to limit the calculation to only those parts that have changed at that point of the calculation.

In the ENERGY subroutine, there is also a call to TRNSLAT, the subroutine that will calculate the positions of the hinges relative to a chosen hinge and expressed in the local

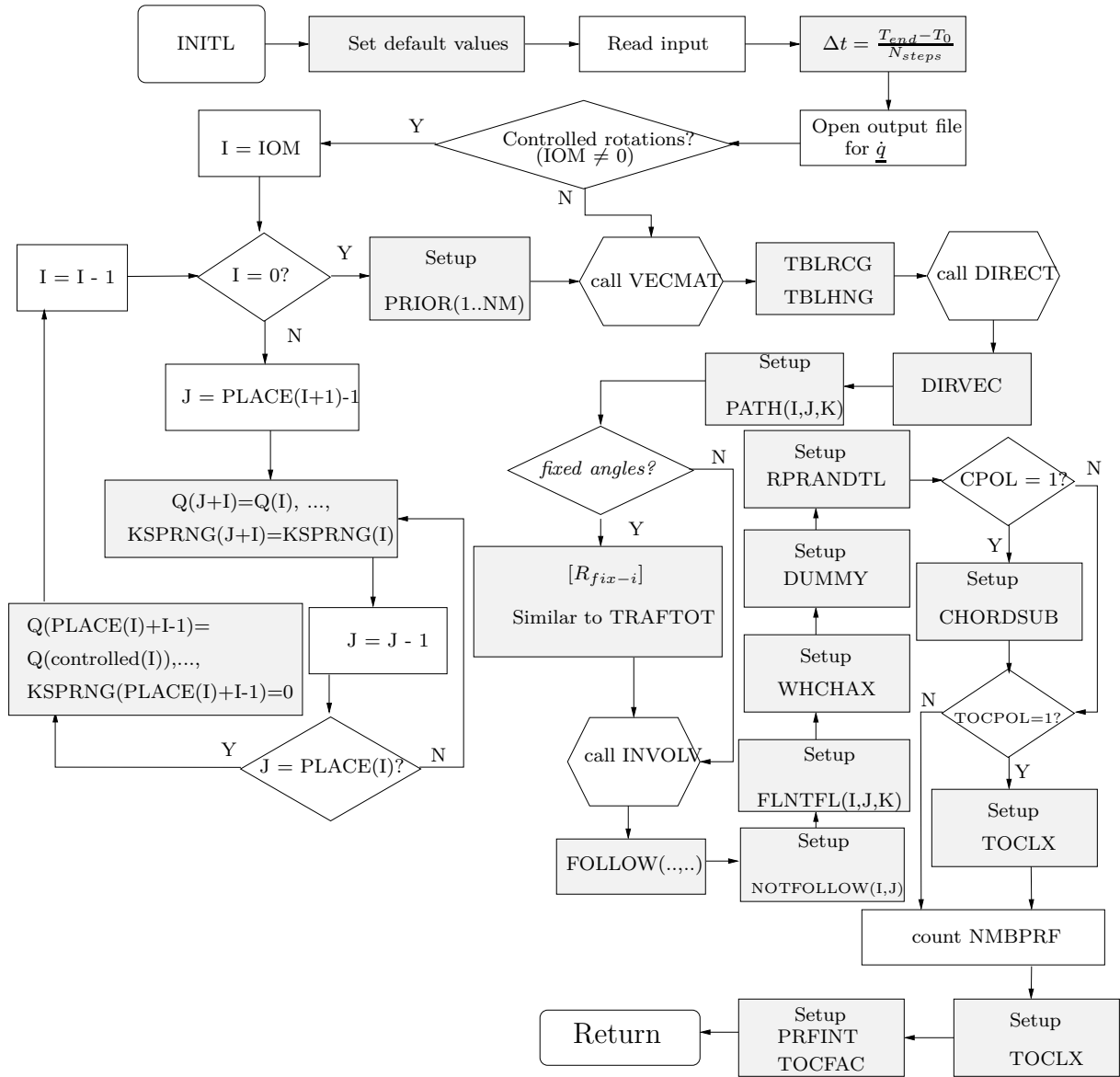


Figure F.2: Flow diagram of INITL. This subroutine performs all initial calculations. The input is read, any controlled rotations are added to the model, several variables corresponding to the model are calculated. Most results are stored in common blocks and can be used where necessary in the program.

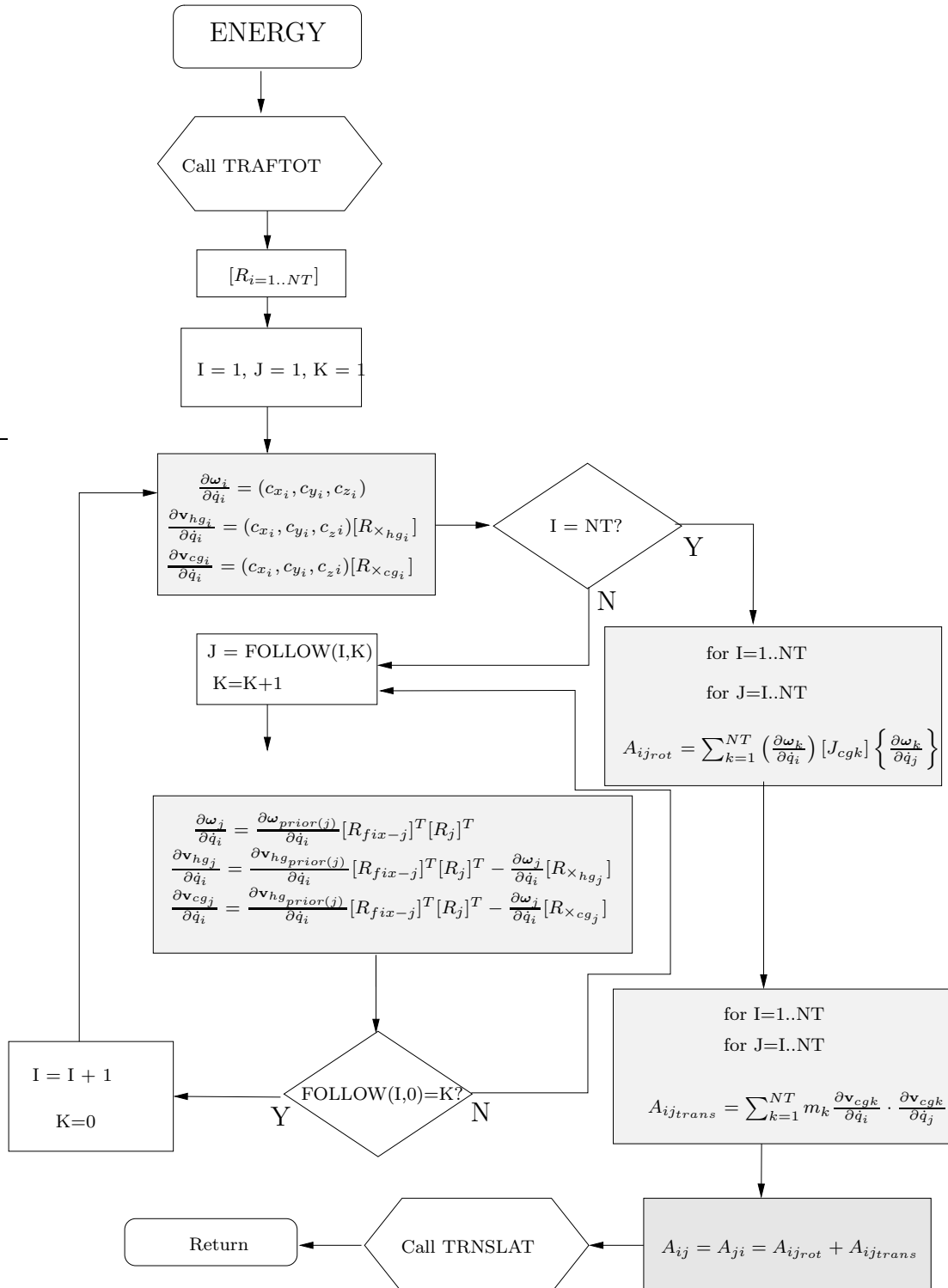


Figure F.3: Flow diagram of ENERGY. This subroutine determines the energy or mass matrix  $[A]$

AS	The energy matrix, without terms corresponding to controlled rotations.
AT	The complete energy matrix, including terms corresponding to controlled rotations.
DVDQ(I)	The partial derivative of the potential energy with respect to $q_i$ .
DTDQ(I)	The partial derivative of the kinetic energy with respect to $q_i$ .
PS	The generalised momenta, with corrected terms due to controlled rotations.
QS	The generalised coordinates, without those corresponding to controlled rotations.

Table F.3: Explanation of terms used in the flow diagram for derivs/derivsn

reference frame of that hinge. If the energy routine is entered at a time step at which the user has specified the position output is wished for, this subroutine will be called and the positions will be calculated.

#### F.2.4 TRAFOT

The subroutine TRAFOT is called to calculate all rotation transformation matrices for the current time step as illustrated in the flow diagram in figure F.4.

In 6.2.6 the equations are described for the three different rotation transformation types. Which one of these matrices is used, is determined by the variable  $DOFDIR(J)$ . The value of this variable corresponds to the axis about which the rotation can take place: 1 for the  $x$  axis, 2 for the  $y$  axis and 3 for the  $z$  axis. The transposed rotation transformation matrices that correspond to these rotations are given in the flow diagram.

#### F.2.5 DERIVS/DERIVSN

The subroutine DERIVS or DERIVSN performs the main calculations in WOBBE. It calculates the time derivatives of the generalised coordinates and the time derivatives of the generalised momenta as described in section 6.2.10. Figure F.5 shows the corresponding flow diagram, table F.3 explains the terms used in the flow diagram.

The input into these subroutines is a row Y containing all current values of  $(\underline{p})$  and  $(\underline{q})$ . This is first split up into a row for  $(\underline{p})$  and a row for  $(\underline{q})$ . If induced velocity (see section 5.4.1) is calculated during the simulation, the induction factor  $a$  will also be in the same row and taken out of this row. The output is the time derivative of the row Y: YFLUX.

Section 6.2.10 gives a complete description of the calculations involved in the remainder of this subroutine.

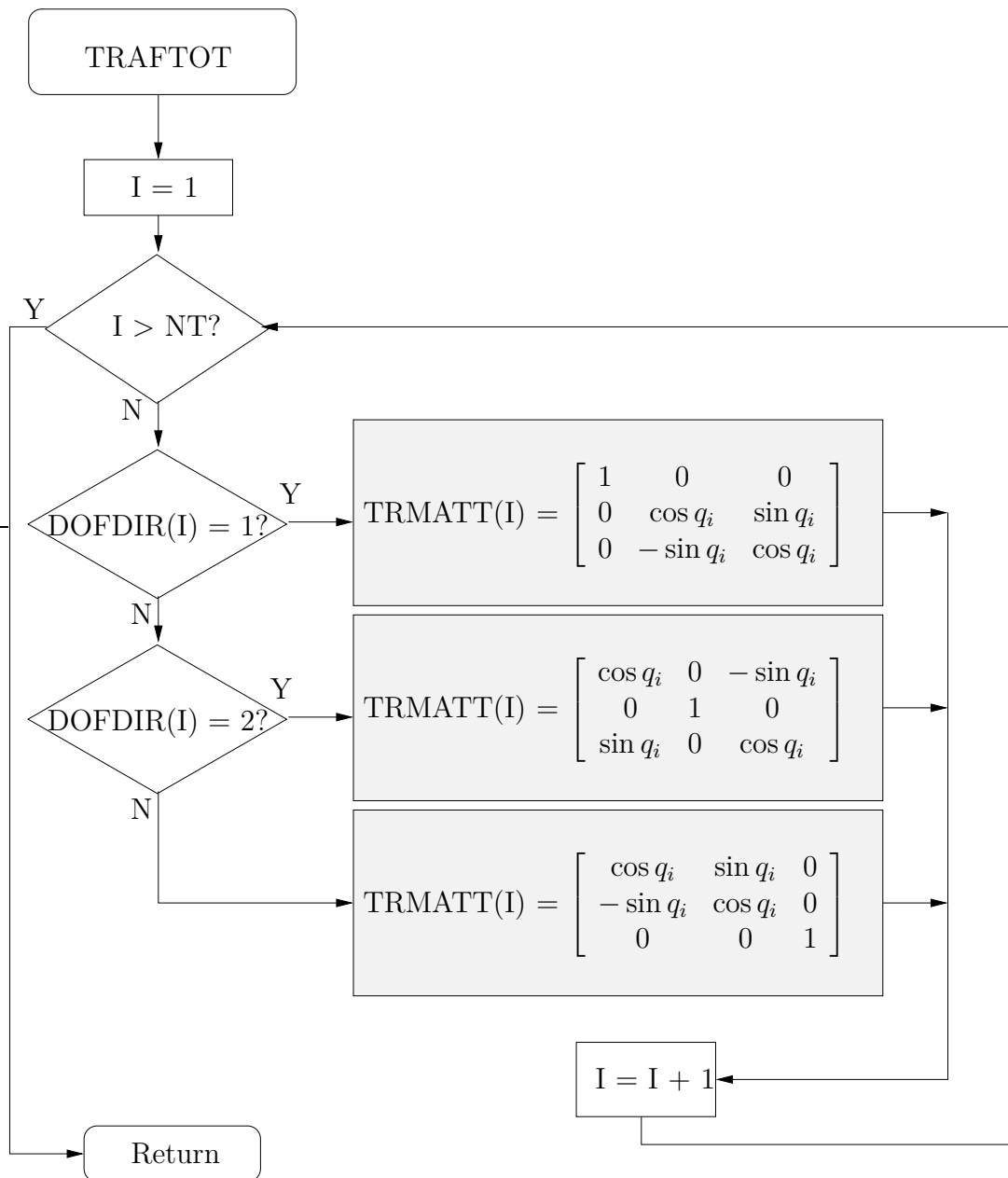


Figure F.4: Flow diagram of TRAFOT. This subroutine determines all rotation transformation matrices:  $\{\mathbf{E}_{prior(i)}\} = [R_i]\{\mathbf{E}_i\}$

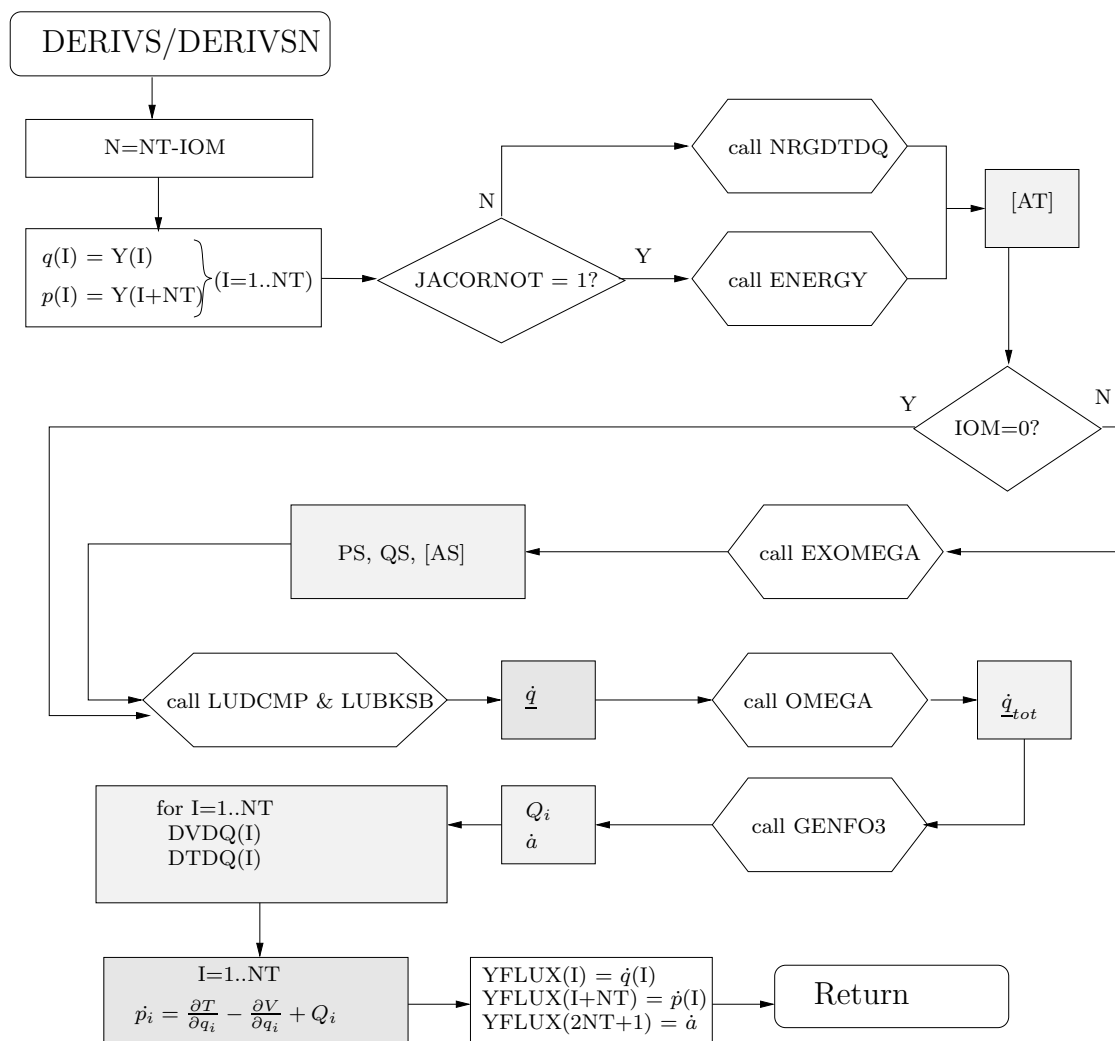


Figure F.5: Flow diagram of DERIVS and DERIVSN. When necessary the energy matrix  $[A]$  is first calculated. The controlled rotations are taken out and  $(\dot{q})$  is calculated. The generalised forces are computed and the derivatives of the kinetic and potential energy. Then  $(\dot{p})$  can be calculated.

## F.2.6 NRGDTDQ

The NRGDTDQ subroutine shows many similarities with the ENERGY subroutine. The differences are due to the time saving elements in NRGDTDQ by not calculating previously obtained results, as described in 6.2.11. The parts of the calculations that have changed are relatively simple to determine. This is also described in more detail in appendix G.

However, for the calculation of the Jacobian, the complete matrix is needed in order to determine new values for  $\{\dot{q}\}$  for a given changed value of  $q_{INDEX}$ . In that case the process is more complicated. It is illustrated in figures F.6 and F.7. From these figures the selection process for the other calculations in NRGDTDQ can also be derived by neglecting the unchanged parts.

## F.2.7 EXOMEGA

The EXOMEGA subroutine, illustrated in figure F.8, is used to perform the reduction to the energy matrix and the corrections to the generalised momenta when calculating the velocities in a model that contains controlled rotations. The subroutine is described in section 5.3.2.

If one or more of the controlled rotations are not constant, this subroutine is where the functions defining the controlled rotation(s) are given as source code. Note that this brings about that the programme must be recompiled if a function for a controlled rotation is changed. To use different values for constant rotational velocities in different simulations, it is not necessary to recompile the code.

## F.2.8 GENFO3

The GENFO3 subroutine, as described in section 6.2.15, calculates the generalised forces. Its flow diagram is shown in figure F.9. Some of the terms used in the flow diagram are explained in table F.4.

This subroutine calls FRCAIR for every lift generating rigid body element (HASAIR=1). FRCAIR gives the forces acting on the different elements that generate lift as well as the bending moments. Actually, the result of FRCAIR is already split up into a term that has to be multiplied with the derivative of the  $\frac{\partial \mathbf{v}_j}{\partial \dot{q}_i}$  at the beginning of the rigid body and a term that has to be multiplied with the derivative for the end of the rigid body (see equation 5.48). It returns also a term for the generalised moment due to the aerodynamic moment. This term has to be multiplied with  $\frac{\partial \omega_j}{\partial \dot{q}_i}$  (see equation 5.49).

The axial force has to be calculated to find the induction factor. The force is determined by transforming all aerodynamic forces to the reference frame connected to the hub, using the WALK2 subroutine. All components in the direction of the shaft are summed which gives the total axial force. This force can be multiplied by a factor two or three, if a single

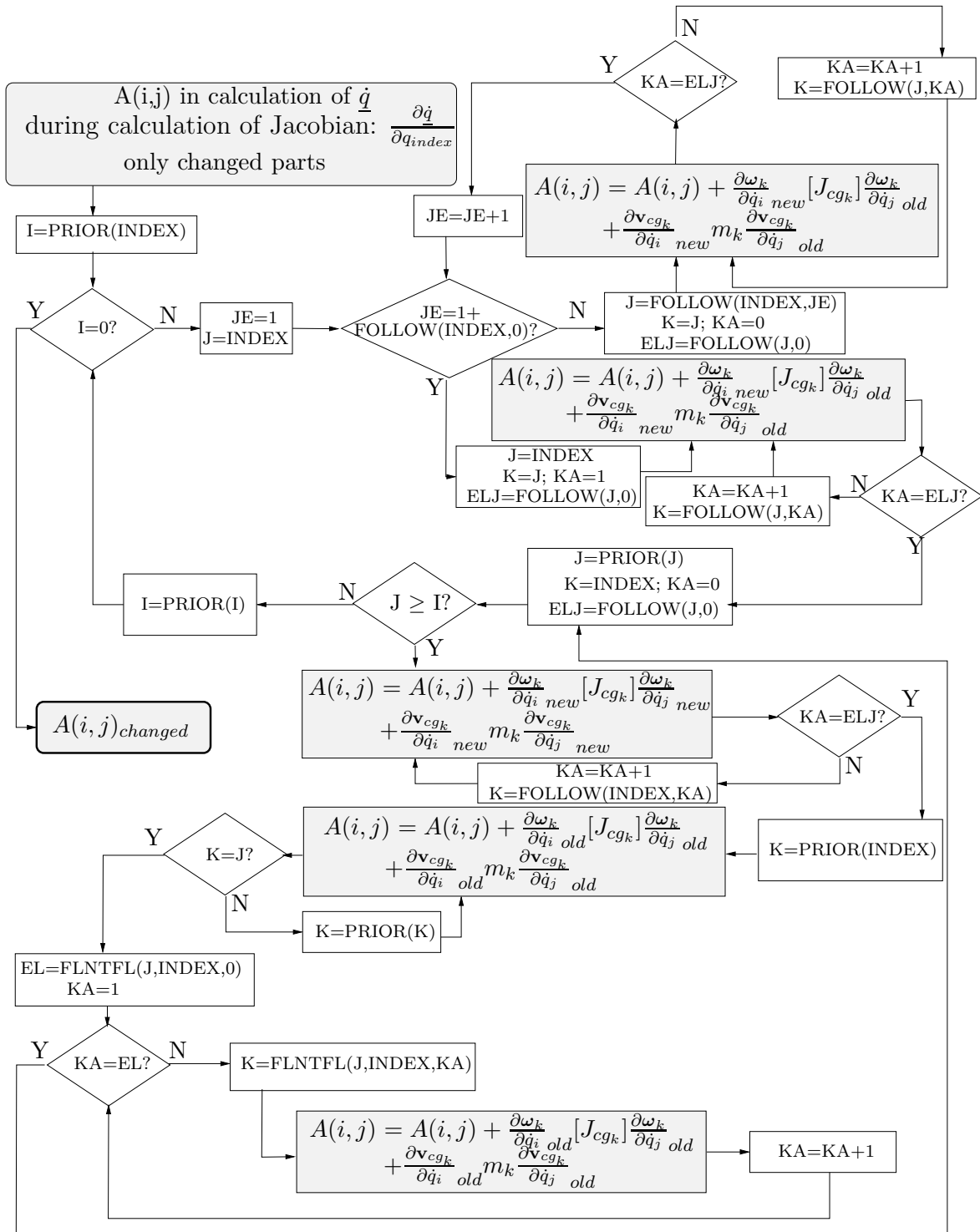


Figure F.6: The calculations needed in NRGDTDQ to find the changed elements of the  $[A]$  matrix to calculate  $\{\dot{q}\}$  in the Jacobian.



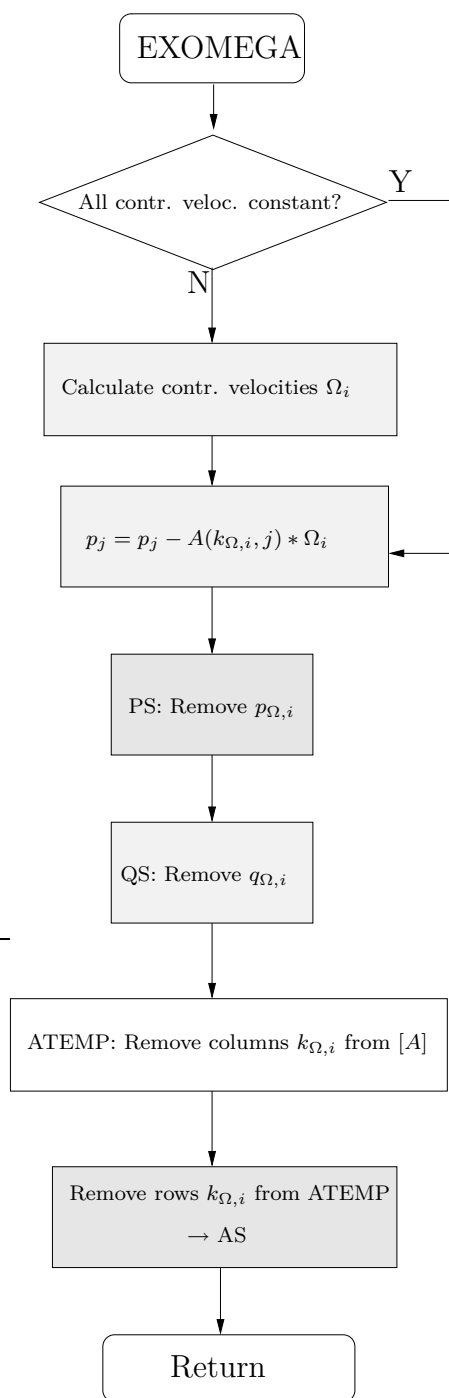


Figure F.8: Flow diagram of EXOMEGA. This subroutine calculates the energy matrix and generalised momenta that are to be used in the calculation of the time derivatives of the generalised coordinates. The controlled rotations must therefore be taken out of the matrix and generalised momenta.

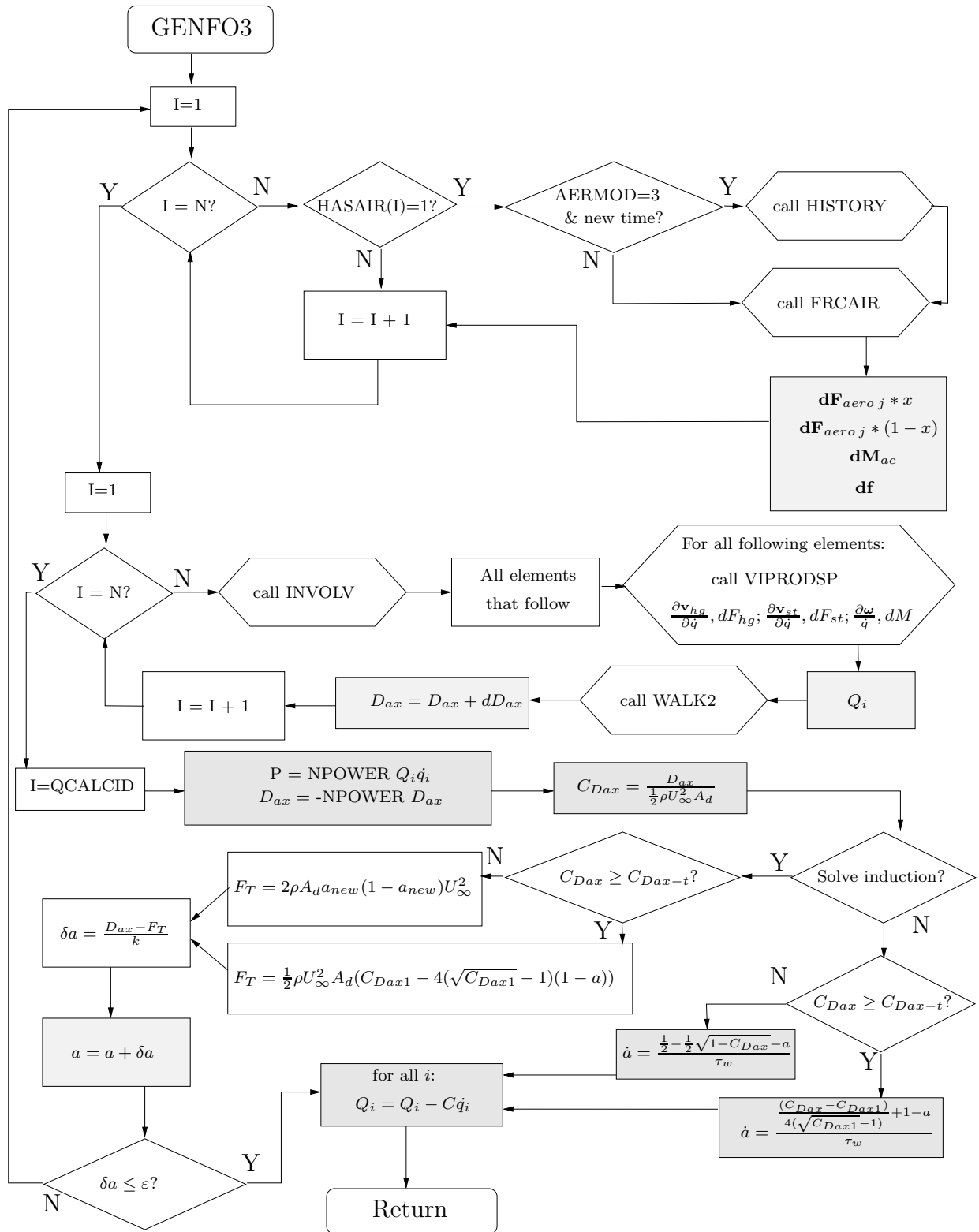


Figure F.9: Flow diagram of GENFO3.

AERMOD	Defines the aerodynamic model used, only if AERMOD = 3 dynamic stall can be used
INVOLV	A subroutine that determines the elements that are behind the current element
NPOWER	Number of blades in turbine divided by number of blades in model
QCALCID	Defines axis about which $D_{ax}$ is calculated
VIPRODSP	Subroutine that calculates the dot product of two vectors that are stored in a 3 and a 2 dimensional matrix

Table F.4: Explanation of terms used in the flow diagram for GENFO3

blade model is used for a two-bladed or three-bladed wind turbine respectively. This way the induction factor is calculated as if two or three blades are connected to the hub.

The first time the the axial force is calculated, the induction factor is not yet known, while it will have a large influence on the axial force. An iteration is therefore needed at the start of a simulation to find the induction factor. This iteration is done by comparing the axial force that comes from the aerodynamics with the axial force that corresponds to the calculated induction factor (equation 3.23). The difference between these two forces divided by  $8\rho A_d U_\infty^2$  is added to the induction factor and used as a new estimate for the induction. This way the calculation will iterate to a correct induction factor.

Dynamic inflow, as described in section 3.1.7, will be used during the remainder of the simulation. This is a more realistic representation of the actual situation and it saves a lot of calculation time, because the iteration can be skipped, except for the first time step. The time derivative of the induction factor is calculated and the induction factor for the next time step will be calculated by integration using this derivative, not by iteration.

For both the iteration as the dynamic inflow, the effect of turbulent wake flow (section 3.1.6) is taken into account as illustrated in the flow diagram.

When applicable the generalised moments  $Q_i$  are corrected for the damping coefficients representing structural damping after the aerodynamic calculations.

Generator control can be added to this part of the programme. It is possible to add the torque from the generator as a generalised moment acting on the shaft. In this case, the shaft will not have a controlled rotation, it will be a degree of freedom in the system. The controller can also set a new pitch angle to increase or reduce the delivered power, similar to a real turbine.

Note that a small reduction in calculation time can still be obtained by removing the call to the INVOLV subroutine (see table F.4), as the FOLLOW variable is stored in memory and can be used as a quicker replacement.

TOCINT	If TOCINT=1: interpolation between two aerofoils based on thickness ratios, if TOCINT=0 one aerofoil is used, no interpolation.
PRFLTMP	The codes corresponding to the two aerofoils used in the interpolation
PRFINT	A table with the codes corresponding to the two aerofoils used in the interpolation for each subelement in each rigid body

Table F.5: Explanation of terms used in the flow diagram for CLCDCM

### F.2.9 CLCDCM

The subroutine CLCDCM calls the correct subroutines for the different aerofoils in order to determine the lift-, drag- and moment- coefficient as described in 6.2.24. The possible interpolation between different aerofoil thicknesses also takes place in this subroutine. The flow diagram of this subroutine is shown in figure F.10. Some terms in the flow diagram are explained in table F.5.

### F.2.10 V

The flow diagram for the function V is shown in figure F.11. The subroutine is described in section 6.2.28.

V calculates the potential energy, first the elastic energy that has changed with  $q_{INDEX}$  is calculated. When gravity is taken into account, the changed rotation transformation matrix  $[R_{index}]$  is calculated. Then the gravitational acceleration is expressed in the different local reference frames. The distances from start point to each c.g. is calculated in the local reference frames and the gravitational potential energy is determined. Finally this is added to the changed elastic energy.

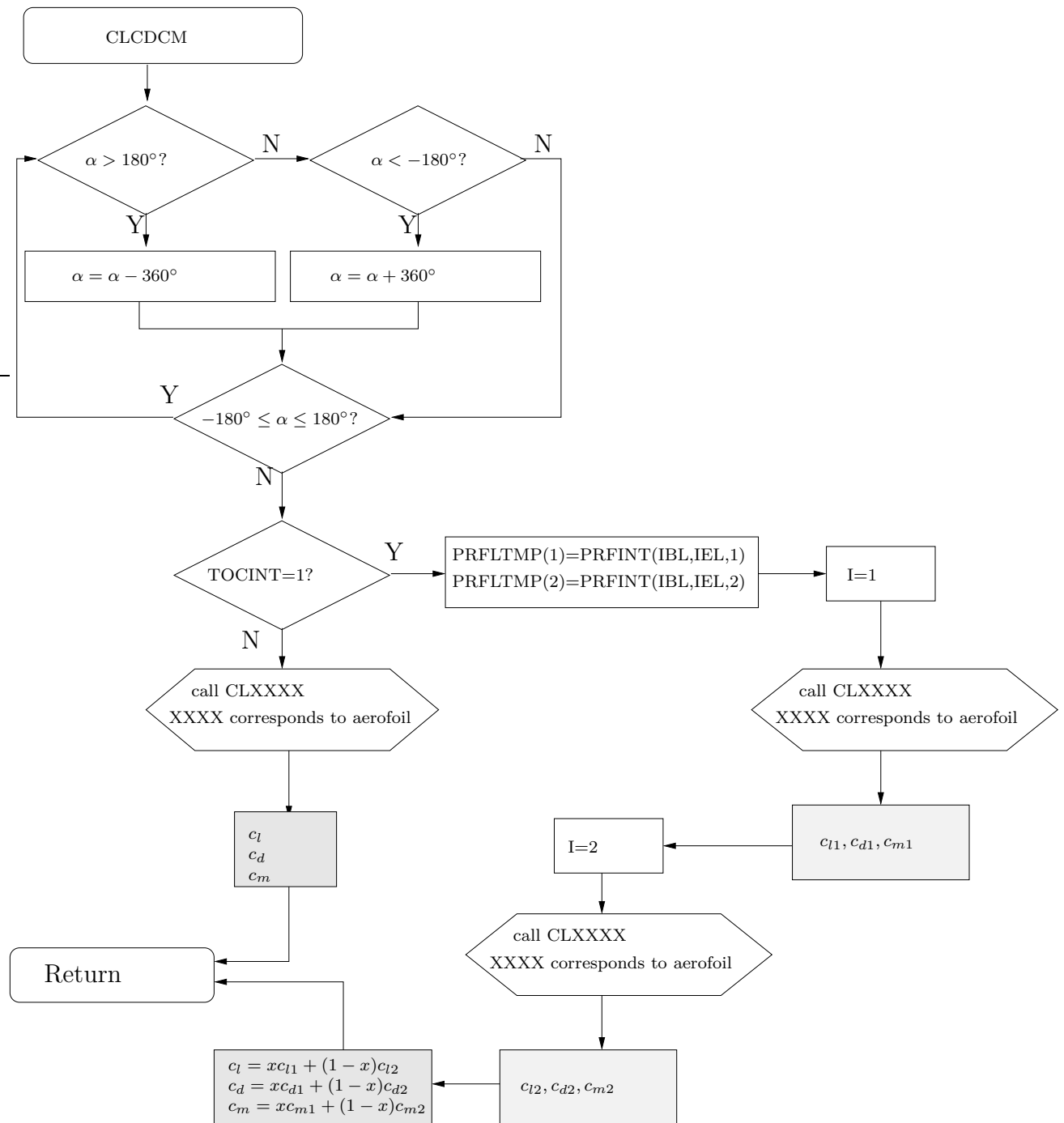


Figure F.10: Flow diagram of CLCDCM. First the angle of attack is corrected if the value is not given as an angle between  $-180^\circ$  and  $+180^\circ$ . Next the subroutines containing the coefficients are called. If linear interpolation is used, the coefficients are calculated from the results given by the CLxxx subroutines.

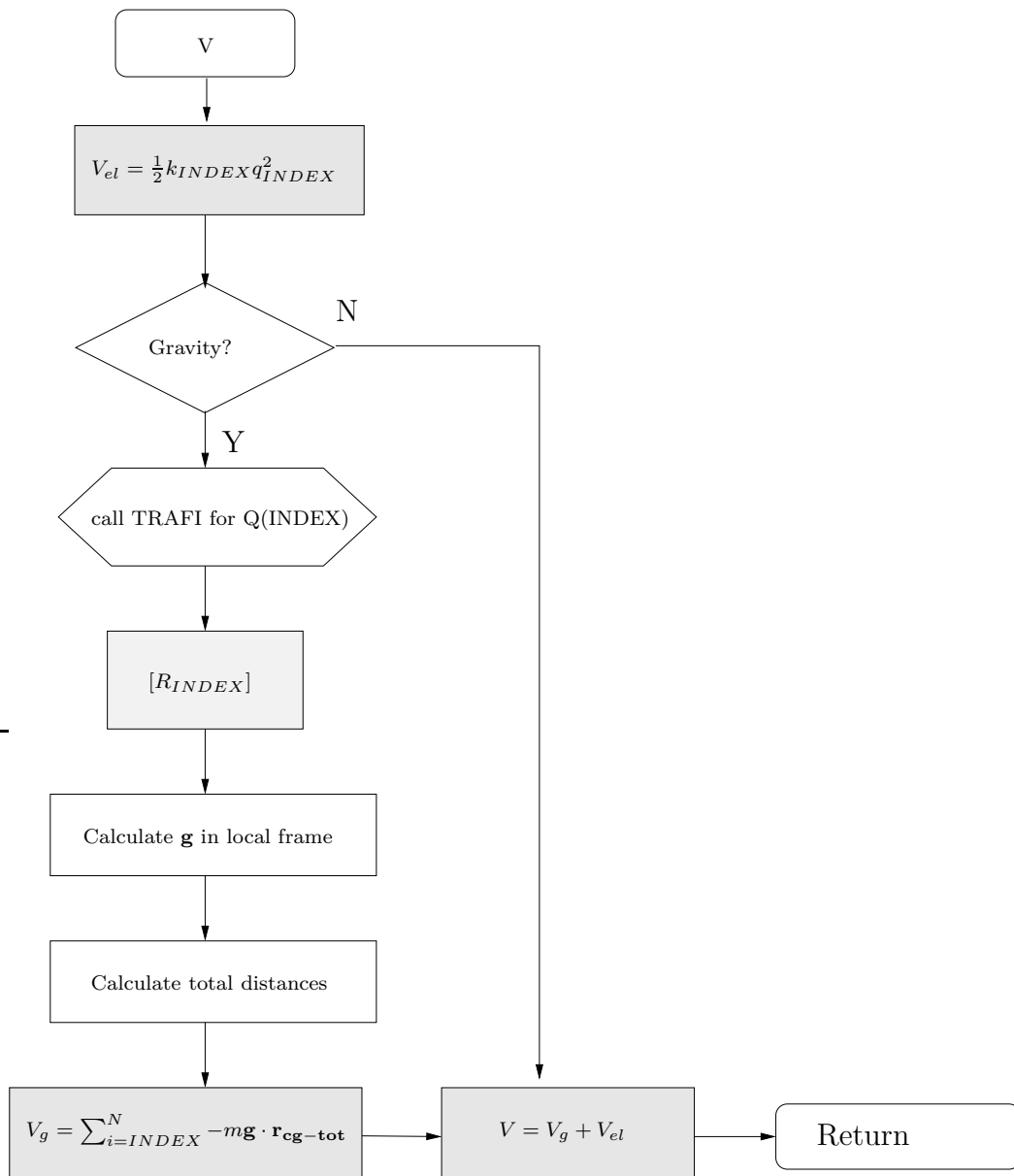


Figure F.11: Flow diagram of function V.

# Appendix G

## Energy Matrix Calculations

The subroutine that determines the energy or mass matrix  $[A]$  is used at least  $2N + 1$  times each time step: once to determine the time derivatives of the generalised coordinates and  $2N$  times to numerically determine the partial derivatives of the kinetic energy. As it is also a relatively complicated calculation, a large reduction in the calculation time can be accomplished by increasing the efficiency of the calculations in this subroutine.

In this appendix the reduction in the number of calculations needed to determine the energy matrix is first described after which the results will be discussed.

### G.1 Reduction in Number of Calculations

The energy or mass matrix (see section 5.2.1) is used in for two different parts of the calculation in WOBBE, first it is used to determine the time derivatives of the generalised coordinates:

$$\underline{\dot{q}} = [A]^{-1}\underline{p} \tag{G.1}$$

The second part in which it is used, is the part in which the partial derivatives of the kinetic energy  $\frac{\partial T}{\partial q_i}$  are determined. These derivatives are calculated numerically by determining the kinetic energy for two different values of  $q_i$ :  $q_i^+ = q_i + h$  and  $q_i^- = q_i - h$  (see section 5.2.2). The change in  $q_i$  changes the energy matrix, therefore this needs to be determined for each new value of  $q_i$ . Once the new energy matrix is known, the kinetic energy can be calculated using:

$$T = \frac{1}{2}\underline{\dot{q}}[A]\underline{\dot{q}} \tag{G.2}$$

A reduction in the number of calculations needed to determine the energy matrix is achieved for these calculations of the derivatives of the kinetic energy. As the energy matrix has already been calculated to determine the velocities, before the derivatives of the kinetic energy

are determined, some calculations to determine the new  $A$  have already been performed. It is possible to save a lot of valuable calculation time by using the interim results of the first determination of  $A$  to determine the change in kinetic energy.

When determining  $\frac{\partial T}{\partial q_i}$ , it is not necessary to calculate the total kinetic energy of the system. Only those terms that actually depend on  $q_i$  are relevant. Only these terms of the kinetic energy will change and therefore have an effect on the derivative. Looking at the basic calculations to determine the kinetic energy, it is clear that for this partial derivative, the time derivatives of the generalised coordinates will not change, but the energy matrix  $[A]$  will change. Assigning a new value to  $q_i$  will change the rotation transformation matrix  $[R_i]$  which is used in several terms in the energy matrix. Every term that has been calculated using the rotation transformation matrix  $[R_i]$  must be calculated again for the new value of  $q_i$ . All other terms remain the same and previously obtained results can be used.

Recall the equations for the elements of the energy matrix:

$$A_{mn_{rot}} = \left( \frac{\partial \omega_1}{\partial \dot{q}_m} \right) [J_{cg1}] \left\{ \frac{\partial \omega_1}{\partial \dot{q}_n} \right\} + \left( \frac{\partial \omega_2}{\partial \dot{q}_m} \right) [J_{cg2}] \left\{ \frac{\partial \omega_2}{\partial \dot{q}_n} \right\} + \dots + \left( \frac{\partial \omega_N}{\partial \dot{q}_m} \right) [J_{cgN}] \left\{ \frac{\partial \omega_N}{\partial \dot{q}_n} \right\} \quad (\text{G.3})$$

and

$$A_{mn_{trans}} = m_1 \frac{\partial \mathbf{v}_{cg1}}{\partial \dot{q}_m} \cdot \frac{\partial \mathbf{v}_{cg1}}{\partial \dot{q}_n} + m_2 \frac{\partial \mathbf{v}_{cg2}}{\partial \dot{q}_m} \cdot \frac{\partial \mathbf{v}_{cg2}}{\partial \dot{q}_n} + \dots + m_N \frac{\partial \mathbf{v}_{cgN}}{\partial \dot{q}_m} \cdot \frac{\partial \mathbf{v}_{cgN}}{\partial \dot{q}_n} \quad (\text{G.4})$$

The rotation transformation matrices are used in the calculations of  $\frac{\partial \omega_k}{\partial q_i}$  and  $\frac{\partial \mathbf{v}_{cgk}}{\partial q_i}$ .

To illustrate which terms involve a multiplication with the new rotation transformation matrix  $[R_i]$ , an example is given for an unbranched system. This example deals with a system with 5 degrees of freedom for which the calculation to determine  $\frac{\partial T}{\partial q_3}$  is illustrated.

This means that  $[R_3]$  changes. The following equation shows the matrix of  $\frac{\partial \omega_k}{\partial q_i}$  (all given in local reference frame  $k$ ) in the following where the elements of this matrix that will change if  $q_3$  gets a new value are shown in **bold**. All other terms remain unchanged and results obtained during the calculation of the energy matrix can be reused.

$$\left[ \begin{array}{ccccc} \frac{\partial \omega_1}{\partial q_1} = (c_{x1}, c_{y1}, c_{z1}) & \frac{\partial \omega_1}{\partial q_2} = 0 & \frac{\partial \omega_1}{\partial q_3} = 0 & \frac{\partial \omega_1}{\partial q_4} = 0 & \frac{\partial \omega_1}{\partial q_5} = 0 \\ \frac{\partial \omega_2}{\partial q_1} = \frac{\partial \omega_1}{\partial q_1} [R_2]^T & \frac{\partial \omega_2}{\partial q_2} = (c_{x2}, c_{y2}, c_{z2}) & \frac{\partial \omega_2}{\partial q_3} = 0 & \frac{\partial \omega_2}{\partial q_4} = 0 & \frac{\partial \omega_2}{\partial q_5} = 0 \\ \frac{\partial \omega_3}{\partial q_1} = \frac{\partial \omega_2}{\partial q_1} [R_3]^T & \frac{\partial \omega_3}{\partial q_2} = \frac{\partial \omega_2}{\partial q_2} [R_3]^T & \frac{\partial \omega_3}{\partial q_3} = (c_{x3}, c_{y3}, c_{z3}) & \frac{\partial \omega_3}{\partial q_4} = 0 & \frac{\partial \omega_3}{\partial q_5} = 0 \\ \frac{\partial \omega_4}{\partial q_1} = \frac{\partial \omega_3}{\partial q_1} [R_4]^T & \frac{\partial \omega_4}{\partial q_2} = \frac{\partial \omega_3}{\partial q_2} [R_4]^T & \frac{\partial \omega_4}{\partial q_3} = \frac{\partial \omega_3}{\partial q_3} [R_4]^T & \frac{\partial \omega_4}{\partial q_4} = (c_{x4}, c_{y4}, c_{z4}) & \frac{\partial \omega_4}{\partial q_5} = 0 \\ \frac{\partial \omega_5}{\partial q_1} = \frac{\partial \omega_4}{\partial q_1} [R_5]^T & \frac{\partial \omega_5}{\partial q_2} = \frac{\partial \omega_4}{\partial q_2} [R_5]^T & \frac{\partial \omega_5}{\partial q_3} = \frac{\partial \omega_4}{\partial q_3} [R_5]^T & \frac{\partial \omega_5}{\partial q_4} = \frac{\partial \omega_4}{\partial q_4} [R_5]^T & \frac{\partial \omega_5}{\partial q_5} = (c_{x5}, c_{y5}, c_{z5}) \end{array} \right] \quad (\text{G.5})$$

This example illustrates that the derivatives  $\frac{\partial \omega_k}{\partial q_i}$  for  $k$  smaller than  $i$  or for  $l$  equal or larger than  $i$  do not change. But for  $k$  equal or higher than  $i$  combined with  $l$  smaller than  $i$ , the components for  $\frac{\partial \omega_k}{\partial q_i}$  must be recalculated for the new value of  $q_i$ . Similarly, it can be shown that the elements corresponding to the same  $k$  and  $l$  values must be recalculated for the translational velocity terms (see also section 5.2.1). This example also shows that the

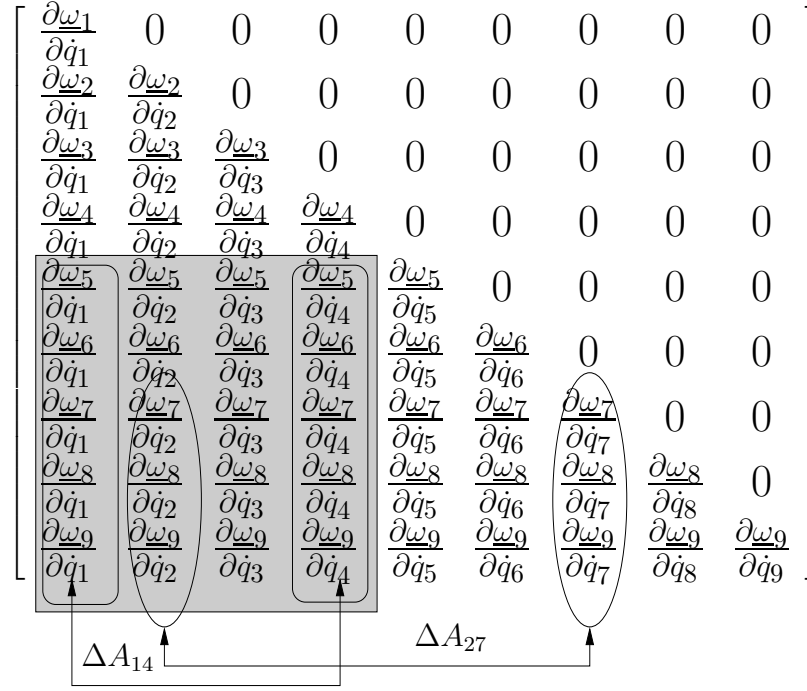


Figure G.1: Determination of the changed elements of the energy matrix for a chain system in order to determine  $\frac{\partial T}{\partial q_5}$ , the calculations for the rotational part are shown here.

derivative of the kinetic energy with respect to the first generalised coordinate ( $\frac{\partial T}{\partial q_1}$ ), will always be equal to zero. The first angle in the system will not influence the kinetic energy.

Equation G.5 illustrates that only certain partial derivatives of the velocity and rotational velocities change due to the new value for  $q_i$  for example  $\frac{\partial \omega_4}{\partial q_1}$ . In the example discussed  $\frac{\partial \omega_4}{\partial q_1}$  has changed and  $\frac{\partial \omega_4}{\partial q_3}$  has not, but the multiplication  $\frac{\partial \omega_4}{\partial q_1} [J_{cg4}] \frac{\partial \omega_4}{\partial q_3}$  must be determined to find the changed part of  $A_{13}$ .

Figure G.1 illustrates the multiplications that must be done for an unbranched system. This time a system with 9 degrees of freedom has been used as an example. The part of the  $\frac{\partial \omega_k}{\partial q_i}$  matrix that has changed due to the new value assigned to  $q_5$ , is illustrated in gray in the figure. The multiplications that are needed to determine the changed parts of two elements of the energy matrix ( $\Delta A_{kl}$ ) are illustrated in the figure:

$$\Delta A_{14} = \sum_{k=5}^9 \frac{\partial \omega_k}{\partial q_1} [J_{cgk}] \frac{\partial \omega_k}{\partial q_4} \quad (\text{G.6})$$

and

$$\Delta A_{27} = \sum_{k=7}^9 \frac{\partial \omega_k}{\partial q_2} [J_{cgk}] \frac{\partial \omega_k}{\partial q_7} \quad (\text{G.7})$$

Similarly, all other terms can be calculated for the rotational parts as well as for the translational parts of the energy matrix. These can then be used to calculate only that part of the kinetic energy that has changed using:

$$T = \frac{1}{2} \dot{q} [\Delta A] \dot{q} \quad (\text{G.8})$$

Only those terms that will give a non-zero result need to be calculated. For an unbranched system this means that only the terms  $A_{kl}$  where at least one of  $k$  and  $l$  is less than  $i - 1$  need to be used, as can be concluded from figure G.1; the terms  $A_{kl}$  where both  $k$  and  $l$  are above  $i - 1$  do not change in value and do not need to be calculated.

Calculating only the changed parts of the kinetic energy will not only result in a faster running programme, but also in a more accurate calculation of  $\frac{\partial T}{\partial q_i}$ , because large terms that remain constant can cause the smaller differences to disappear due to a limited number of digits used for each variable. This is especially the case when a constant rotational velocity  $\Omega$  is included in the model.

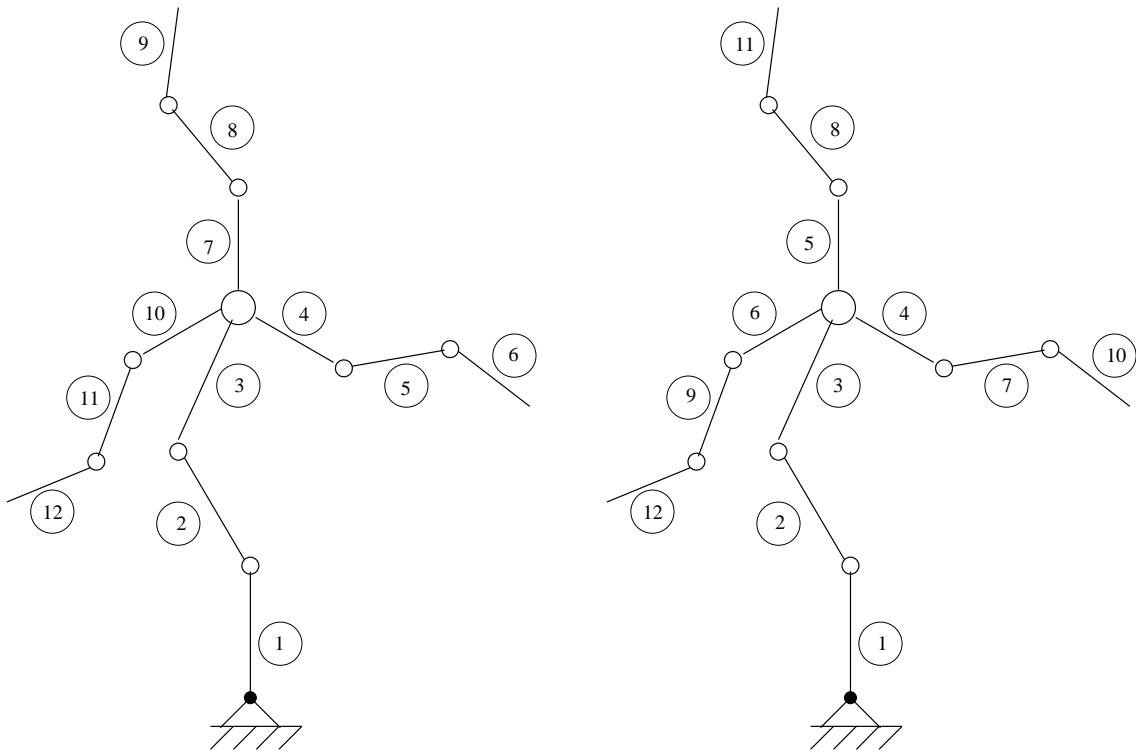


Figure G.2: Different options for numbering the elements in a branched system

The possibility of branching makes the calculation slightly more complicated. For instance looking at the branched systems in figure G.2 it is clear that the change of for instance  $q_4$  will not affect the kinetic energy of elements on other branches in the system, while a change in  $q_2$  will influence the energy of all elements except for element 1. Both methods of numbering

the elements shown in this figure are allowed in WOBBE. The only limitation given to the numbering process is that the element prior to element  $k$  must have a lower number than element  $k$ . In order to efficiently and correctly determine the changed kinetic energy of a branched system, it is necessary to determine the elements influenced by a change in  $q_i$  as well as the order of the elements prior to it, because this will determine the calculation of, for example  $\frac{\partial \omega_k}{\partial q_i}$ . For this reason there is a variable that will contain all elements connected after an element. It will also give the number of elements after a certain element.

More details about the actual implementation in WOBBE of the discussed calculations can be found in appendix F.2.6.

## G.2 Results

As mentioned in the previous section, the described method will not only result in a faster programme, but also in a more accurate calculation of the derivatives of the kinetic energy. The kinetic energy might change due to the new value for  $q_i$ , but relative to the total kinetic energy, it is a very small change, in which case the result of the numerical differentiation can become zero. For example using double precision an incorrect answer will be found if the total kinetic energy is  $1.0 \cdot 10^8$  and the change due to the difference in  $q_i$  is  $1.0 \cdot 10^{-6}$ :

$$\frac{\partial T}{\partial q_i} = \frac{(1.0 \cdot 10^8 + 1.0 \cdot 10^{-6}) - 1.0 \cdot 10^8}{2h} \Rightarrow 0.0 \quad (\text{G.9})$$

While if only the changed part of the kinetic energy is determined, the small value for  $\frac{\partial T}{\partial q_i}$  will be calculated correctly.

To further illustrate this, the results of a simulation of a complete benchmark wind turbine can be used. It is a model consisting of a tower, three blades and three DOF's for the nacelle and rotor shaft. Each blade and the tower are modelled using 2 superelements including torsion, resulting in 10 DOF's per blade/tower.

At the start of the simulation the tower is not deformed, but every blade has a deformation in flap and in lead-lag direction. This starting position means that the change in kinetic energy due to a change in one of the degree of freedoms in the tower is relatively small. Before the implementation of the method described above, determining the derivative of the kinetic energy w.r.t. a DOF in the tower resulted in the answer 0.0D0 while the newly implemented code gives very small values for  $\frac{\partial T}{\partial q_i}$  for the DOF's in the tower.

The effect of this difference is also shown in figure G.3. This figure shows the deformation of the hinge in yaw direction at the nacelle in the full wind turbine bench mark model. A small difference is visible between the two results. This is caused by the better calculations of  $\frac{\partial T}{\partial q_i}$  in the new and faster code, resulting in small terms that would previously have been lost as illustrated above. This difference will mainly show up in the torsional degrees of freedom. As shown in figure G.4, the difference in the bending hinge is negligible.

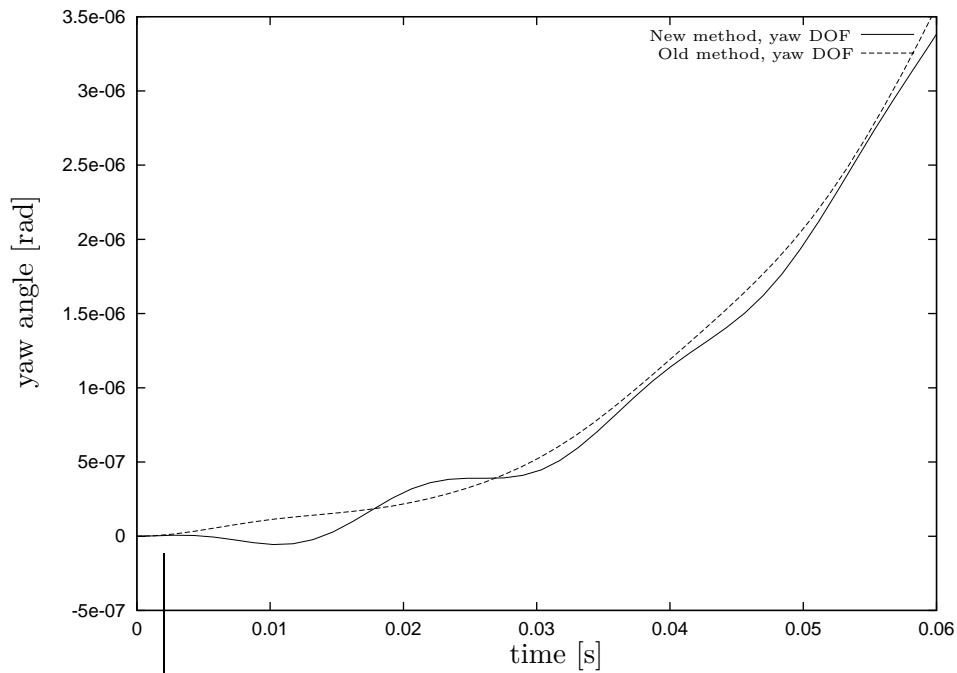


Figure G.3: The deformation angle in the hinge in yaw direction at the nacelle for the method that calculates only the changes in the kinetic energy and the method that calculates the total kinetic energy.

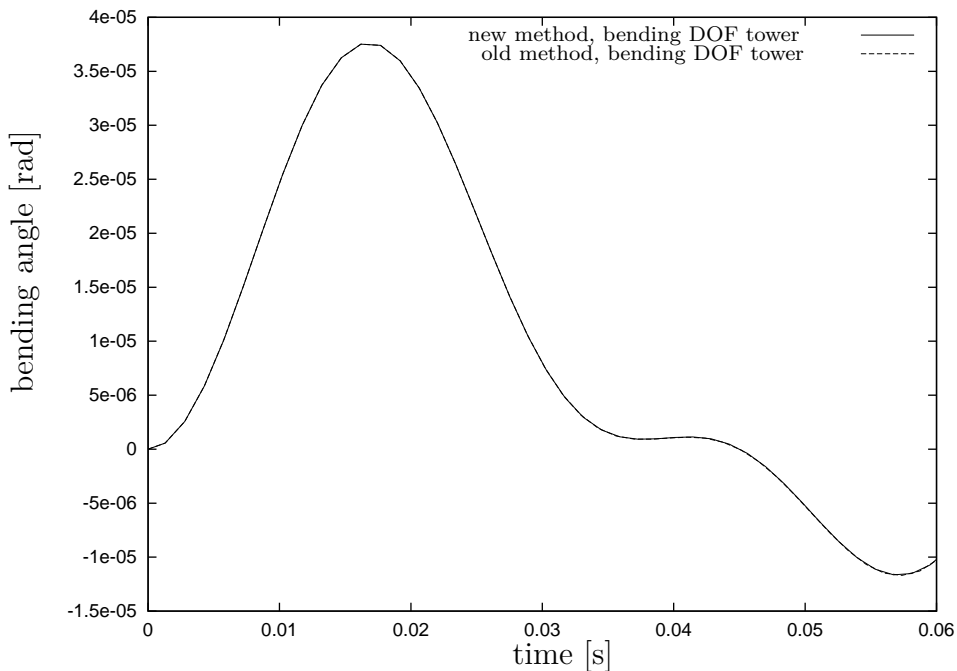


Figure G.4: The deformation angle in the highest fore/aft hinge in the tower for the method that calculates only the changes in the kinetic energy and the method that calculates the total kinetic energy.

Subroutine	Time excl. child	Time incl. child	Function of subroutine
ENERGY	34.7%	88.8%	Calculate $[A]$
VT3X3	48.9%	48.9%	Multiplication of $r(3) * D(i, 3, 3)$
T	1.0%	86.7%	Calculate kinetic energy

Table G.1: Time consumption for several subroutines, excluding and including subroutines called from this subroutine, for the code before implementation of the reduction in calculations

Subroutine	Time excl. child	Time incl. child	Function of subroutine
NRGDTDQ	40.8%	67.9%	Determine the changed parts of the kinetic energy
ENERGY	3.7%	8.8%	Calculate $[A]$
VT3X3	25%	25%	Multiplication of $r(3) * D(i, 3, 3)$
T	0.0%	68%	Calculate kinetic energy

Table G.2: Time consumption for several subroutines, excluding and including subroutines called from this subroutine, for the code after implementation of the reduction in calculations

The most important reason to implement the described new method to calculate the derivatives of the kinetic energy was to reduce the calculation time of WOBBE. Using Visual Fortran it is possible to determine the amount of time spent in each subroutine including or excluding the subroutines called from the subroutine considered. From this time consumption analysis for the same model of the complete benchmark wind turbine it can be concluded that the determination of the energy matrix takes up almost 90% of the total calculation time in the old code. Table G.1 shows the percentages for the most important subroutines and describes shortly what each subroutine does. For the new code, use is made of two subroutines. First there is the original energy subroutine that has hardly changed. This will be used only once for every time step during the determination of  $\dot{q}$  from  $\underline{p} = [A]\dot{q}$ . The results for several intermediate results, such as  $\frac{\partial \omega_k}{\partial q_i}$ , will be saved and used in the new subroutine "NRGDTDQ". This last subroutine will be used for all calculations of  $\frac{\partial T}{\partial q_i}$  and its output is the changed part of the kinetic energy. The time consumption for the new version of WOBBE is shown in table G.2. This table shows that instead of almost 87 % of the time being spend on the calculation of  $\frac{\partial T}{\partial q_i}$ , only 68 % of the time is spend on this calculation. In total the time has been reduced significantly. The profiling function in Visual Fortran also gives a total calculation time. For the benchmark model with 15 DOF's that was discussed in section 8.2.2, the time to simulate has been reduced by more than 50% by implementing this quicker method to determine the partial derivatives of the kinetic energy.

Table G.2 shows that the new subroutine takes up a large proportion of the reduced calculation time. Therefore this subroutine must be programmed as efficiently as possible.



# Appendix H

## Rotating beam

In section 8.1.2 the verification performed by simulating a beam has been discussed. More detailed results are presented in this appendix.

The beam has a total length  $L = 50 \text{ m}$ , an area  $A = \pi \text{ m}^2$  and an area moment of inertia  $I = \frac{1}{4}\pi \text{ m}^4$ . The modulus of elasticity of the material of the beam is  $E = 21 \cdot 10^{10} \text{ N/m}^2$  and the density is  $\rho = 7850 \text{ kg/m}^3$ . The other properties of the beam and the properties of the rigid elements are given in table 8.1.

The rotating frequencies for this beam were determined. To calculate the frequency of the rotating beam [94] table H.1 can be used in combination with the following equations:

$$\omega_i = \frac{1}{p} \sqrt{(\omega_i^*)^2 - (\eta)^2} \quad \text{for } i = 1, 2, 3, 4 \quad (\text{H.1})$$

where  $\omega_i^*$  is the non dimensional frequency,  $\eta$  the non dimensional rotation rate:

$$\eta = \Omega p \quad (\text{H.2})$$

and

$$p = \sqrt{\frac{\rho A L^4}{EI}} \quad (\text{H.3})$$

In tptable H.2 the calculated frequencies are given for the beam that was modelled. In table H.3 the results from the simulations for different rotational velocities using WOBBE are given. In figure 8.8 these frequencies for the rotating beam calculated in WOBBE and the calculated frequencies are shown .

$\eta$	$\omega_1^*$	$\omega_2^*$	$\omega_3^*$	$\omega_4^*$
0.0	3.5160	22.0345	61.6972	120.9020
1.0	3.6817	22.1810	61.6418	121.0510
2.0	4.1373	22.6149	62.2732	121.4970
3.0	4.7973	23.3203	62.9850	122.2360
4.0	5.5850	24.2734	63.9668	123.2610
5.0	6.4495	25.4461	65.2050	124.5660
6.0	7.3604	26.8091	66.6840	126.1400
7.0	8.2996	28.3341	68.3860	127.9720
8.0	9.2568	29.9954	70.2930	130.0490
9.0	10.2257	31.7705	72.3867	132.3580
10.0	11.2023	33.6404	74.6493	134.8840
11.0	12.1843	35.5890	77.0638	137.6140
12.0	13.1702	37.6031	79.6145	140.5340

Table H.1: Non-dimensional frequencies as a function of the dimensionless rotation rate  $\eta$ 

$\Omega$	$\omega_1$	$\omega_2$	$\omega_3$	$\omega_4$
0.0	3.6371	22.7933	64.1013	125.0657
1.0344	3.6653	22.9216	63.7563	125.2156
2.0689	3.7465	23.3021	64.3846	125.6642
3.1033	3.8725	23.9230	65.0802	126.4076
4.1387	4.0320	24.7661	66.0402	127.4388
5.1722	4.2141	25.8093	67.2520	128.7521
6.2066	4.4101	27.0289	68.7007	130.3364
7.2411	4.6126	28.4014	70.3696	132.1810
8.2755	4.8175	29.9045	72.2414	134.2730
9.3099	5.0216	31.5184	74.2986	136.5994
10.3444	5.2228	33.2259	76.5241	139.1453
11.3788	5.4204	35.0120	78.9015	141.8978
12.4133	5.6141	36.8643	81.4155	144.8429

Table H.2: Calculated frequencies of the beam rotating at  $\Omega$  rad/s

---

$\Omega$	$\omega_1$	$\omega_2$	$\omega_3$	$\omega_4$
0.0	3.644	22.75	63.08	117.7
1.0	3.644	22.87	63.33	117.9
2.0	3.770	23.25	63.71	118.5
3.0	3.896	23.88	64.47	119.4
4.0	4.021	24.63	65.47	120.6
5.0	4.147	25.76	66.73	122.3
6.0	4.398	26.89	68.24	124.2
7.0	4.650	28.27	69.99	126.4
8.0	4.775	29.78	72.01	128.9
9.0	5.027	31.29	74.14	131.8
10.0	5.278	33.05	76.53	134.8
11.0	5.529	34.81	78.92	138.1
12.0	5.781	36.69	81.56	141.6

Table H.3: Calculated frequencies by WOBBE of the beam rotating at  $\Omega$  *rad/s*



# Appendix I

## Derivation of the Equations Governing the Flap-Lag Instability

For the single blade model with three degrees of freedom as used in the STABTOOL project, the partially linearised equations of motion were derived in order to investigate the possibility of the flap-lag-stall instability. In this appendix the derivation of the partially linearised equations, including the aerodynamic moments is given.

Using this derivation of the equations of motion as an example, it is also a good way to illustrate the method described in 2.1.2.

In the first section, the model is described first, followed by the derivation of the governing equations of motion. The other two sections show the results for two limiting cases: neglecting drag forces and the so-called drag-stall, where drag-stall is defined as the case where the  $c_{l_0} - c_{d_\alpha}$  term is strongly decreased.

### I.1 Governing Equations for an Isolated Blade with 3 Degrees of Freedom

The method described in section 2.1.2 is illustrated in this section by deriving the equations of motion for the isolated blade model. First the model is described, after which a complete description of the derivation of the equations of motion for the model is given.

#### I.1.1 Model Description

The model is illustrated in figure 10.3 and described in section 10.2.1. The single blade model contains three degrees of freedom, one for the hub motion, one for the lead-lag motion and one for the flap motion of the blade. The lead-lag and flap hinges are aligned with the

principal directions of the stiffness of the blade.

As described in section 10.2.1, the blade is assumed to have a line distribution of mass. The hinges are all in the hub centre, so there are no hinge off-sets. There is however a definite hinge order: hub ( $\varepsilon$ ), lead-lag ( $\zeta$ ) and finally flap ( $\beta$ ). The fixed structural pitch angle ( $\theta$ ) is situated behind the first degree of freedom: the hub motion.

The gravitational forces are not taken into account in this baseline model. For the specific aeroelastic instability that is investigated using this model, the flap-lag-stall instability, the gravitational acceleration does not have an important effect on the stability.

### 1.1.2 Using Vector and Matrix Notations to Determine the Equations of Motion

When using computers to derive equations of motion of a system it is very useful to use vector and matrix notations, especially since the symbolic manipulation software has become available. Using the method described in section 2.1.2, will lead to a rather simple outline that can be followed by a programme such as the simulation tool that is discussed in chapters 5 and 6. In this part of this appendix the method is illustrated. The method is used to derive the equations of motion for the single blade model with three degrees of freedom.

For every element, a reference frame is defined that will rotate with the element. This is useful as it enables all element properties to be given in this local reference frame. First notice that the notation used throughout this dissertation is once again used here: **Vectors** are given as **bold symbols**: **a**. **underlined** symbols are used for **rows** (a) and **columns**: {a}. This last category therefore does not have a physical meaning, as a vector does, it is simply an enumeration of numbers.

The rotation transformation matrices for the baseline model are determined using figures (a) to (e) in figure I.1. Looking at (a) in figure I.1 the unit vectors of reference frame  $\psi$  can be written as the following combinations of the unit vectors of reference frame  $H$ :

$$\begin{aligned} \mathbf{i}_\psi &= \mathbf{i}_H \\ \mathbf{j}_\psi &= \mathbf{j}_H \cos \psi + \mathbf{k}_H \sin \psi \\ \mathbf{k}_\psi &= -\mathbf{j}_H \sin \psi + \mathbf{k}_H \cos \psi \end{aligned} \tag{I.1}$$

This results in the rotation transformation matrix:

$$\{\underline{\mathbf{E}}_\psi\} = [R_\psi]\{\underline{\mathbf{E}}_H\} = \begin{bmatrix} 1 & 0 & 0 \\ 0 & \cos \psi & \sin \psi \\ 0 & -\sin \psi & \cos \psi \end{bmatrix} \{\underline{\mathbf{E}}_H\} \tag{I.2}$$

Similarly for the other rotations present in the model, the matrices can be determined to be:

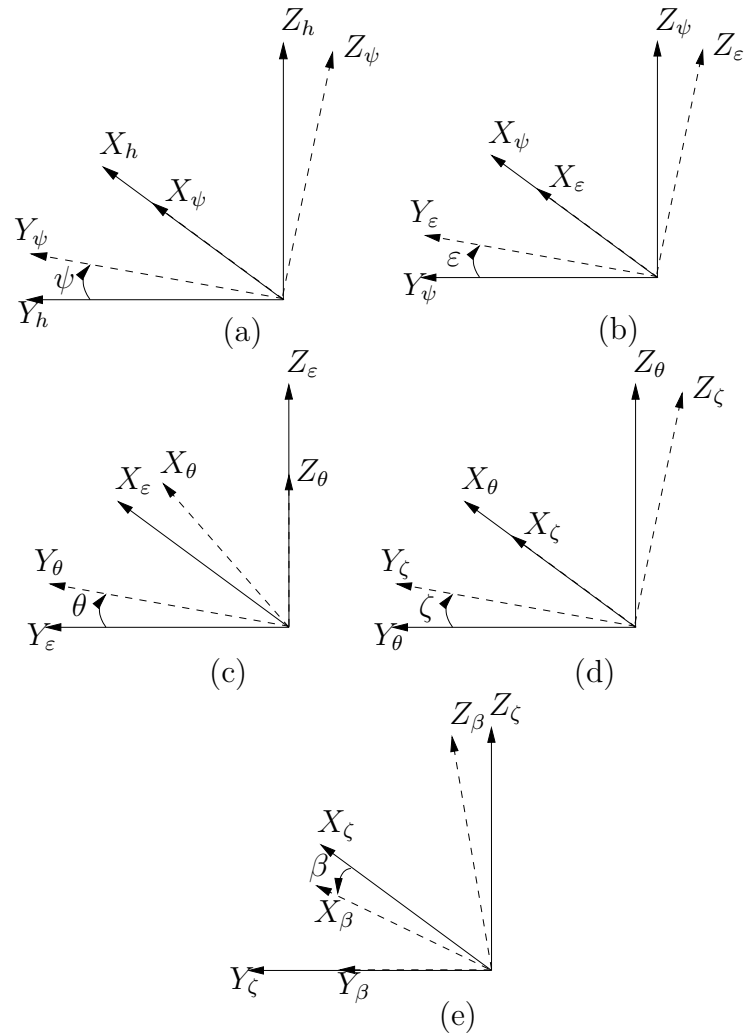


Figure I.1: The different reference frames: a. The non-rotating (inertial) and rotating reference frames, b. The rotating reference frame and the hub reference frame, c. The hub reference frame and the fixed pitch reference frame, d. The fixed pitch and the lag reference frames, e. The lag reference frame and the blade reference frame.

$$\{\underline{\mathbf{E}}_\varepsilon\} = [R_\varepsilon]\{\underline{\mathbf{E}}_\psi\} = \begin{bmatrix} 1 & 0 & 0 \\ 0 & \cos \varepsilon & \sin \varepsilon \\ 0 & -\sin \varepsilon & \cos \varepsilon \end{bmatrix} \{\underline{\mathbf{E}}_\psi\} \quad (\text{I.3})$$

$$\{\underline{\mathbf{E}}_\theta\} = [R_\theta]\{\underline{\mathbf{E}}_\varepsilon\} = \begin{bmatrix} \cos \theta & -\sin \theta & 0 \\ \sin \theta & \cos \theta & 0 \\ 0 & 0 & 1 \end{bmatrix} \{\underline{\mathbf{E}}_\varepsilon\} \quad (\text{I.4})$$

$$\{\underline{\mathbf{E}}_\zeta\} = [R_\zeta]\{\underline{\mathbf{E}}_\theta\} = \begin{bmatrix} 1 & 0 & 0 \\ 0 & \cos \zeta & \sin \zeta \\ 0 & -\sin \zeta & \cos \zeta \end{bmatrix} \{\underline{\mathbf{E}}_\theta\} \quad (\text{I.5})$$

$$\{\underline{\mathbf{E}}_\beta\} = [R_\beta]\{\underline{\mathbf{E}}_\zeta\} = \begin{bmatrix} \cos \beta & 0 & -\sin \beta \\ 0 & 1 & 0 \\ \sin \beta & 0 & \cos \beta \end{bmatrix} \{\underline{\mathbf{E}}_\zeta\} \quad (\text{I.6})$$

where  $\{\underline{\mathbf{E}}_\beta\}$  is the reference frame for which the inertia matrix  $[J_{cg}]$  can easily be defined as it is the local blade reference frame.

Using these different reference frames, it is possible to give the position vector  $\mathbf{R}_P$  of any point on the blade:

$$\mathbf{r}_P = (r_\varepsilon)\{\underline{\mathbf{E}}_\psi\} + (r_\theta)\{\underline{\mathbf{E}}_\varepsilon\} + (r_\zeta)\{\underline{\mathbf{E}}_\theta\} + (r_\beta)\{\underline{\mathbf{E}}_\zeta\} + (r_P)\{\underline{\mathbf{E}}_\beta\} \quad (\text{I.7})$$

The hinge off-sets in the baseline model are all zero, therefore this equation becomes:

$$\mathbf{r}_P = (r_P)\{\underline{\mathbf{E}}_\beta\} \quad (\text{I.8})$$

The velocity of a point can be found by differentiating the position vector:

$$\dot{\mathbf{r}}_P = (r_{\dot{P}x}, r_{\dot{P}y}, r_{\dot{P}z})\{\underline{\mathbf{E}}_\beta\} + (r_{Px}, r_{Py}, r_{Pz})(\dot{\underline{\mathbf{E}}}_\beta) \quad (\text{I.9})$$

with

$$(\dot{\underline{\mathbf{E}}}_\beta) = [\Omega_{\times\beta}]\{\underline{\mathbf{E}}_\beta\} = \begin{bmatrix} 0 & r_\beta & -q_\beta \\ -r_\beta & 0 & p_\beta \\ q_\beta & -p_\beta & 0 \end{bmatrix} \{\underline{\mathbf{E}}_\beta\} \quad (\text{I.10})$$

To be able to determine the generalised forces, the velocity of the air relative to the blade must be determined. The situation at  $\frac{3}{4}$ -radius will be used as typical for the entire blade.

This means that the angle of attack at this point is assumed to be the angle of attack for the entire blade. The lift- and drag coefficients are assumed to be representative for the entire blade, but the force and moment acting on the blade will also depend on the absolute velocity ( $|\mathbf{V}| \approx \Omega r$ ). The differences in the absolute velocity value along the blade will be taken into account, as described at the end of this section. To determine the velocity of the blade at the representative point, the position vector should be differentiated:

$$\mathbf{r}_{3/4} = (0, 0, \frac{3}{4}R)\{\mathbf{E}_\beta\} \quad (\text{I.11})$$

which gives:

$$\mathbf{V}_{3/4} = (0, 0, \frac{3}{4}R)[\Omega_{\times\beta}]\{\mathbf{E}_\beta\} \quad (\text{I.12})$$

The total angular velocity of the blade can be written as:

$$\boldsymbol{\omega}_\beta = (\Omega, 0, 0)\{\mathbf{E}_\psi\} + (\dot{\varepsilon}, 0, 0)\{\mathbf{E}_\varepsilon\} + (\dot{\zeta}, 0, 0)\{\mathbf{E}_\zeta\} + (0, \dot{\beta}, 0)\{\mathbf{E}_\beta\} \quad (\text{I.13})$$

Using the transformation matrices one finds:

$$\boldsymbol{\omega}_\beta = \left( [(\Omega, 0, 0)[R_\varepsilon]^T + (\dot{\varepsilon}, 0, 0)] [R_\theta]^T + (\dot{\zeta}, 0, 0) \right) [R_\zeta]^T + (0, \dot{\beta}, 0)\{\mathbf{E}_\beta\} \quad (\text{I.14})$$

Substituting the rotation transformation matrices results in the following expression for the total rotation:

$$\begin{aligned} \boldsymbol{\omega}_\beta &= \left( [(\Omega + \dot{\varepsilon}) \cos \theta + \dot{\zeta}] \cos \beta + (\Omega + \dot{\varepsilon}) \sin \theta \sin \zeta \sin \beta, \right. \\ &\quad \left. (\Omega + \dot{\varepsilon}) \sin \theta \cos \zeta + \dot{\beta}, ((\Omega + \dot{\varepsilon}) \cos \theta + \dot{\zeta}) \sin \beta - (\Omega + \dot{\varepsilon}) \sin \theta \sin \zeta \cos \beta \right) \{\mathbf{E}_\beta\} \\ &= (p_\beta, q_\beta, r_\beta)\{\mathbf{E}_\beta\} \end{aligned} \quad (\text{I.15})$$

Using this expression the velocity can be written as:

$$\mathbf{V}_{3/4} = (\frac{3}{4}Rq_\beta, -\frac{3}{4}Rp_\beta, 0)\{\mathbf{E}_\beta\} \quad (\text{I.16})$$

To investigate the stability of the isolated blade, the equations of motion must be determined. These can then be (partially) linearised and the stability boundary can be determined. To find the equations of motion, Lagrange's equations are used (see equation 2.143) [78]:

$$\frac{d}{dt} \left( \frac{\partial T}{\partial \dot{q}_j} \right) - \frac{\partial T}{\partial q_j} + \frac{\partial V}{\partial q_j} = Q_j, \quad j = 1, 2, \dots, n$$

where  $Q_j$  is the generalised force corresponding to the generalised coordinate  $q_i$ ,  $T$  is the kinetic energy and  $V$  is the potential energy.

The kinetic energy  $T$  for a system consisting of  $N$  elements can be calculated using equation 2.51 and taking the sum over all elements:

$$T = \sum_{i=1}^N \left( \frac{1}{2} m_i \mathbf{V}_{cgi} \cdot \mathbf{V}_{cgi} + \frac{1}{2} \boldsymbol{\omega}_i [J_{cgi}] \boldsymbol{\omega}_i \right) \quad (\text{I.17})$$

The velocity can be expressed in any reference frame, but most of the time the local reference frame will be used.

As discussed in chapter 2, if an element is rotating about a point A and this point has no velocity, the kinetic energy can be calculated by using:

$$T = \frac{1}{2} \boldsymbol{\omega}_i [J_{i,A}] \boldsymbol{\omega}_i \quad (\text{I.18})$$

For the baseline model all masses except the blade mass are assumed to be zero. The length of every element, except for the blade itself, is also assumed to be zero. Therefore the velocity of the centre of gravity of the blade does not need to be calculated as the velocity of the hinge point will be zero and equation I.18 can be used to calculate the kinetic energy.

The inertia matrix about the hinge point relative to the reference frame that rotates with the blade is:

$$[J_{\beta,A}] = \begin{bmatrix} I_{xx,A} & 0 & 0 \\ 0 & I_{yy,A} & 0 \\ 0 & 0 & 0 \end{bmatrix} \quad (\text{I.19})$$

For a line distribution of mass, a mass  $m$  and a length  $R$ , the inertia becomes  $I_{xx,A} = I_{yy,A} = \frac{1}{3} m R^2$ .

Substituting equation I.15 into equation I.18 and using equation I.19, results in the kinetic energy:

$$T_{rot} = \frac{1}{2} \boldsymbol{\omega}_\beta [J_H] \boldsymbol{\omega}_\beta = \frac{1}{2} \left[ \left( ((\Omega + \dot{\varepsilon}) \cos \theta + \dot{\zeta}) \cos \beta + ((\Omega + \dot{\varepsilon}) \sin \theta \sin \zeta \sin \beta) \right)^2 I_{xxA} + \left( (\Omega + \dot{\varepsilon}) \sin \theta \cos \zeta + \dot{\beta} \right)^2 I_{yyA} \right] \quad (\text{I.20})$$

To be able to use Lagrange's equations to find the governing equations of motion, the potential energy must be determined. For the baseline model of the isolated blade the gravitational forces are not taken into account, resulting in a potential energy that is only in the form of elastic spring energy. The potential energy of the system is:

$$V = V_e = \frac{1}{2} k_\varepsilon \varepsilon^2 + \frac{1}{2} k_\zeta \zeta^2 + \frac{1}{2} k_\beta \beta^2 \quad (\text{I.21})$$

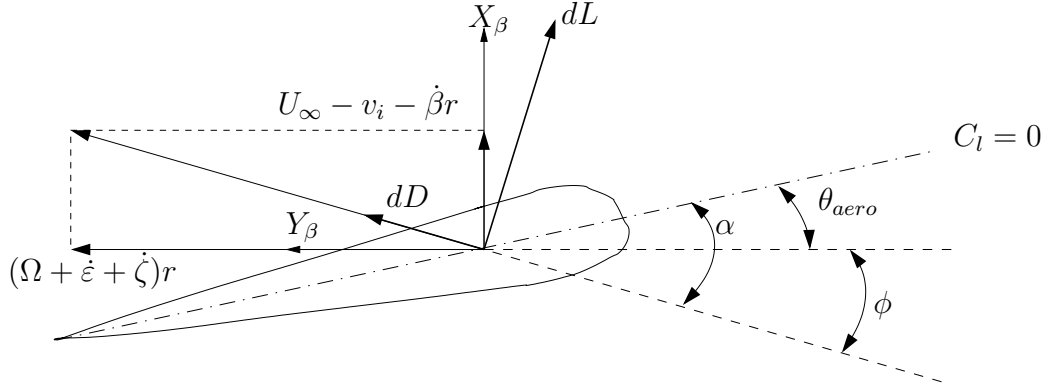


Figure I.2: The aerodynamic forces on the model

The left hand sides of Lagrange's equations can now be determined for all three degrees of freedom in the model. From this, the three equations of motions can be determined, but the generalised forces  $Q_i$  in the equations must still be calculated. For the single blade model discussed in this appendix, all degrees of freedom are angles. Therefore the generalised forces in Lagrange's equations are actually moments and not forces.

Assuming the tangent velocity to be much larger than the perpendicular velocity, the force of a blade element becomes:

$$d\mathbf{F} = \frac{1}{2}u_t^2(\Omega r)^2 cdr(c_l \cos \phi + c_d \sin \phi, -c_l \sin \phi + c_d \cos \phi, 0)\{\mathbf{E}_\beta\} \quad (\text{I.22})$$

Where  $u_t$  is the tangent velocity divided by  $\Omega r$ , making it non-dimensional, and  $\phi = \arctan\left(\frac{u_p}{u_t}\right) \approx \frac{u_p}{u_t}$ , as shown in figure I.2, where the perpendicular velocity divided by  $\Omega r$  is written as  $u_p$ . The corresponding moment is:

$$\begin{aligned} d\mathbf{M} &= \mathbf{r} \times d\mathbf{F} \\ &= (0, 0, r)\{\mathbf{E}_\beta\} \times \frac{1}{2}u_t^2(\Omega r)^2 cdr(c_l \cos \phi + c_d \sin \phi, -c_l \sin \phi + c_d \cos \phi, 0)\{\mathbf{E}_\beta\} \\ &= \frac{1}{2}\rho u_t^2(\Omega r)^2 cr dr(c_l \cos \phi + c_d \sin \phi, -c_l \sin \phi + c_d \cos \phi, 0)[A]\{\mathbf{E}_\beta\} \end{aligned} \quad (\text{I.23})$$

where

$$[A] = \begin{bmatrix} 0 & 1 & 0 \\ -1 & 0 & 0 \\ 0 & 0 & 0 \end{bmatrix} \quad (\text{I.24})$$

As mentioned before, a representative section at  $\frac{3}{4}$  of the radius is used. The values for  $u_t$ ,  $u_p$ ,  $c_l$  and  $c_d$  at  $\frac{3}{4}$ -radius are assumed to be representative for the entire blade. This simplification is noted by using a superscript \*. Now one can integrate the expression for the moment, using the locknumber:

$$\gamma = \frac{\rho c_{l\alpha} c^* R^4}{I} \quad (\text{I.25})$$

The linearised moment becomes:

$$\mathbf{M} = \frac{\gamma \Omega^2 I}{8 c_{l_\alpha}} u_t^2 (c_l^* \phi - c_d^*, c_l^*, 0) \{ \underline{\mathbf{E}}_\beta \} \quad (\text{I.26})$$

The generalised momenta become:

$$M_\beta = \mathbf{M} \cdot (\underline{\mathbf{E}}_\beta) \cdot \begin{Bmatrix} 0 \\ 1 \\ 0 \end{Bmatrix} = \frac{\gamma \Omega^2 I}{8 c_{l_\alpha}} c_l u_t^2 \quad (\text{I.27})$$

$$\begin{aligned} M_\zeta &= \mathbf{M} \cdot (\underline{\mathbf{E}}_\zeta) \begin{Bmatrix} 1 \\ 0 \\ 0 \end{Bmatrix} = \frac{\gamma \Omega^2 I}{8 c_{l_\alpha}} u_t^2 (c_l \phi - c_d, c_l, 0) [R_\beta] \begin{Bmatrix} 1 \\ 0 \\ 0 \end{Bmatrix} \\ &= \frac{\gamma \Omega^2 I}{8 c_{l_\alpha}} (c_l u_p u_t - c_d u_t^2) \end{aligned} \quad (\text{I.28})$$

and

$$\begin{aligned} M_\varepsilon &= \mathbf{M} \cdot (\underline{\mathbf{E}}_\varepsilon) \begin{Bmatrix} 1 \\ 0 \\ 0 \end{Bmatrix} = \frac{\gamma \Omega^2 I}{8 c_{l_\alpha}} u_t^2 (c_l \phi - c_d, c_l, 0) [R_\beta] [R_\zeta] [R_\theta] \begin{Bmatrix} 1 \\ 0 \\ 0 \end{Bmatrix} \\ &= \frac{\gamma \Omega^2 I}{8 c_{l_\alpha}} (c_l (u_p u_t + \theta u_t^2) - c_d u_t^2) \end{aligned} \quad (\text{I.29})$$

For the lift- and the drag-coefficients the following simplification is used:

$$c_l^* = c_{l_0}^* + c_{l_\alpha}^* (\alpha^* - \alpha_0^*) \quad (\text{I.30})$$

$$c_d = c_{d_0} + c_{d_\alpha}^* (\alpha^* - \alpha_0^*) \quad (\text{I.31})$$

where

$$\alpha = \theta_{aero} + \frac{u_p^*}{u_t^*} \quad (\text{I.32})$$

The angular velocities can be written as dimensionless velocities using:

$$\dot{\beta} = \Omega \frac{d\beta}{d\psi} = \Omega \beta' \quad (\text{I.33})$$

Similar for the angular accelerations.

Looking at figure I.2 one can write for the velocities:

$$u_p^* = \frac{\mu - \lambda_i}{x} - (\theta + \beta') \quad (\text{I.34})$$

and

$$u_t^* = 1 + \varepsilon' + \zeta' \quad (\text{I.35})$$

Where

$$\mu = \frac{U}{\Omega r}; \quad \lambda_i = \frac{u_i}{\Omega r} \quad (\text{I.36})$$

Assuming that  $\varepsilon', \zeta' \ll 1$ , one can write for the angle of attack:

$$\alpha^* = \theta_{aero} + \frac{\mu - \lambda_i}{x} - (\theta + \beta') \quad (\text{I.37})$$

Using this one can write:

$$\alpha^* - \alpha_0^* = -\beta' \quad (\text{I.38})$$

This leads to the following expressions for the lift- and drag-coefficient:

$$c_l^* = c_{l_0}^* - c_{l_\alpha}^* \beta' \quad (\text{I.39})$$

$$c_d^* = c_{d_0}^* - c_{d_\alpha}^* \beta' \quad (\text{I.40})$$

Therefore the linearised generalised moments become:

$$M_\beta = \frac{\gamma \Omega^2 I}{8 c_{l_\alpha}} [c_{l_0}^* + 2c_{l_0}^* \varepsilon' + 2c_{l_0}^* \zeta' - c_{l_\alpha}^* \beta'] \quad (\text{I.41})$$

$$M_\zeta = \frac{\gamma \Omega^2 I}{8 c_{l_\alpha}} [c_{l_0}^* \frac{\mu - \lambda_i}{x} - c_{l_0}^* (\theta + \beta') - c_{d_0}^* (1 + 2\varepsilon' + 2\zeta') + c_{d_\alpha}^* \beta'] \quad (\text{I.42})$$

$$M_\varepsilon = \frac{\gamma \Omega^2 I}{8 c_{l_\alpha}} [c_{l_0}^* \frac{\mu - \lambda_i}{x} - c_{l_0}^* \beta' - c_{d_0}^* (1 + 2\varepsilon' + 2\zeta') + c_{d_\alpha}^* \beta'] \quad (\text{I.43})$$

For the stability investigation the equations of motion can be split up into equations about the equilibrium state and the equations for the small perturbations. To enable this split, the angles are written as:

$$\beta = \beta_0 + \Delta\beta \quad (\text{I.44})$$

Similar for all other degrees of freedom. The same is done for the moments. This gives three equations about the equilibrium state, first for the hub:

$$\nu_\varepsilon^2 \varepsilon_0 = \frac{\gamma}{8c_{l_\alpha}} [c_{l_0}^* \frac{\mu - \lambda_i}{x} - c_{d_0}^*] \quad (\text{I.45})$$

for the lag:

$$\nu_\zeta^2 \zeta_0 = \frac{\gamma}{8c_{l_\alpha}} [c_{l_0}^* \frac{\mu - \lambda_i}{x} - c_{l_0}^* \theta - c_{d_0}^*] \quad (\text{I.46})$$

and finally for the flap:

$$\beta_0(1 + \nu_\beta^2) = \frac{\gamma}{8c_{l_\alpha}} c_{l_0} \quad (\text{I.47})$$

Dropping the  $\Delta$  from the notation for the small perturbations the following three equations of motion are derived:

$$\begin{aligned} \beta'' \sin \theta - 2\beta_0\beta' + \frac{\gamma}{8c_{l_\alpha}}(c_{l_0} - c_{d_\alpha}^*)\beta' + \varepsilon'' + \frac{\gamma}{8c_{l_\alpha}}2c_{d_0}\varepsilon' \\ + \nu_\varepsilon^2\varepsilon + \zeta'' \cos \theta + \frac{\gamma}{8c_{l_\alpha}} \cos \theta + \frac{\gamma}{8c_{l_\alpha}}2c_{d_0}\zeta' = 0 \end{aligned} \quad (\text{I.48})$$

$$\begin{aligned} -2\beta_0\beta' + \frac{\gamma}{8c_{l_\alpha}}(c_{l_0} - c_{d_\alpha}^*)\beta' + \varepsilon'' \cos \theta \\ + \frac{\gamma}{8c_{l_\alpha}}c_{d_0}2\varepsilon + \zeta'' + \frac{\gamma}{8c_{l_\alpha}}c_{d_0}2\zeta' + \nu_\zeta^2\zeta = 0 \end{aligned} \quad (\text{I.49})$$

$$\begin{aligned} \beta'' + \frac{\gamma}{8c_{l_\alpha}}c_{l_\alpha}^*\beta' + \beta(1 + \nu_\beta^2) + \varepsilon'' \sin \theta \\ + \varepsilon'[2\beta_0 - \frac{\gamma}{8c_{l_\alpha}}2c_{l_0}] + \zeta'[2\beta_0 - \frac{\gamma}{8c_{l_\alpha}}2c_{l_0}] = 0 \end{aligned} \quad (\text{I.50})$$

These equations can be used to perform the stability analysis.

## I.2 Neglecting Drag Forces

A limiting case that has been investigated [56] is the case where the drag forces are neglected. This is achieved by setting  $c_{d_\alpha} = c_{d_0} = 0$  in the above derived equations of motion, resulting in the following equations:

$$\beta'' \sin \theta - 2\beta_0\beta' + \frac{\gamma}{8c_{l_\alpha}}c_{l_0}\beta' + \varepsilon'' + \nu_\varepsilon^2\varepsilon + \zeta'' \cos \theta + \frac{\gamma}{8c_{l_\alpha}} \cos \theta = 0 \quad (\text{I.51})$$

$$-2\beta_0\beta' + \frac{\gamma}{8c_{l_\alpha}}c_{l_0}\beta' + \varepsilon'' \cos \theta + \zeta'' + \nu_\zeta^2\zeta = 0 \quad (\text{I.52})$$

$$\beta'' + \frac{\gamma}{8c_{l_\alpha}}c_{l_\alpha}^*\beta' + \beta(1 + \nu_\beta^2) + \varepsilon'' \sin \theta + \varepsilon'[2\beta_0 - \frac{\gamma}{8c_{l_\alpha}}2c_{l_0}] + \zeta'[2\beta_0 - \frac{\gamma}{8c_{l_\alpha}}2c_{l_0}] = 0 \quad (\text{I.53})$$

## I.3 Drag-stall

The second limiting case looked at is the so-called drag-stall [56]. This is the case that  $c_{d_\alpha}$  increases so much that the term  $c_{l_0} - c_{d_\alpha}$  in the equations of motion becomes small. In

this case the destabilising Coriolis forces on the blade are no longer counteracted by the stabilising tilting of the lift vector due to flapping, which can result in an instability. The equations derived for drag-stall assume that the term  $c_{l_0} - c_{d_\alpha}$  is equal to zero, resulting in the following equations of motion:

$$\beta'' \sin \theta - 2\beta_0\beta' + \varepsilon'' + \frac{\gamma}{8c_{l_\alpha}}2c_{d_0}\varepsilon' + \nu_\varepsilon^2\varepsilon + \zeta'' \cos \theta + \frac{\gamma}{8c_{l_\alpha}} \cos \theta + \frac{\gamma}{8c_{l_\alpha}}2c_{d_0}\zeta' = 0 \quad (\text{I.54})$$

$$-2\beta_0\beta' + \varepsilon'' \cos \theta + \frac{\gamma}{8c_{l_\alpha}}c_{d_0}2\varepsilon + \zeta'' + \frac{\gamma}{8c_{l_\alpha}}c_{d_0}2\zeta' + \nu_\zeta^2\zeta = 0 \quad (\text{I.55})$$

$$\beta'' + \frac{\gamma}{8c_{l_\alpha}}c_{l_\alpha}^*\beta' + \beta(1 + \nu_\beta^2) + \varepsilon'' \sin \theta + \varepsilon'[2\beta_0 - \frac{\gamma}{8c_{l_\alpha}}2c_{l_0}] + \zeta'[2\beta_0 - \frac{\gamma}{8c_{l_\alpha}}2c_{l_0}] = 0 \quad (\text{I.56})$$



# Curriculum Vitae

Jessica Holierhoek was born on April 14, 1974 in Leiderdorp, the Netherlands. She fulfilled her VWO at dr. W.A. Visser 't Hooft Lyceum in Leiden between 1986 and 1992. In 1992 she started her studies; Aerospace Engineering at Delft Univeristy of Technology. In January 2000 she obtained her master of science degree. The title of the thesis: "The Effect of Variable Wall Thickness on the Buckling Load of Imperfect Anisotropic Cylindrical Shells". After graduating she started to work as a researcher and teacher and from 2005 as a PhD student at the same institution. Since August 2007 she works as a researcher in wind energy at ECN, Energy research Centre of the Netherlands.

During her studies she was an active fencer, competing in many international tournaments and became dutch champion in women's sabre in 1999.

She is happily married and mother of one daughter.

# Index

- 20-WPX-THR blades, 74
- Acceleration, 8, 12, 13, 24
- Action integral, 31
- Actuator disc, 38
- Aerodynamic moment, 317
- Aeroelastic stability, 4
- Angle of attack, 48
- Angular momentum, 9, 12–14, 24, 26, 45
- APX40T, 72
- BEM, 4, 38–50
- Bernoulli, 39, 40
- Betz limit, 44
- Blade element momentum method, 4, 38–50, 103
- Blade flow, 38
- Centre of gravity, 12, 13, 15, 25, 80
- Centre of mass, 12
- Chasles' theorem, 15, 16
- Configuration space, 28
- Conservation of mass, 39
- Conservative forces, 16, 30, 32
- Controlled rotations, 100, 113
- Critical damping ratio, 259
- Critically damped, 259
- Damper, 257
- Damping ratio, 259
- Drag, 47
- Drag-stall, 193, 210
- Dynamics, 7
- Edgewise instability, 72
- Edgewise mode, 72
- Edgewise vibration, 3
- Eigen frequency, 259
- Eigenfrequency, 152
- Eigenfrequency, rotating, 156, 313
- Elastic coupling, 197, 201
- Elongation, 16
- Energy consumption, 2
- Energy matrix, 91, 112, 117
- Equations of motion, 7, 24, 33, 34
- External forces, 11, 16, 17, 258
- External moments, 14
- Fast Fourier Transform, 154, 265
- FFT, 154, 265
- Fixed point of rotation, 14, 26
- Flap mode, 74
- Flap-lag flutter, 193, 194
- Flap-lag-flutter, 76
- Flap-lag-stall flutter, 5, 193, 202
- Flapwise instability, 75
- Flutter, 70, 193
- Flutter -flap-lag-stall, 193
- Generalised coordinates, 4, 31, 32
- Generalised force, 32, 33, 103, 113, 122
- Generalised momentum, 112
- Generator, 106
- Glauert, 52
- Global flow, 38
- Gravitational forces, 16
- Hamilton's generalised momentum, 28, 35
- Hamilton's principle, 28, 30, 31
- Hingeless, 70
- Holonomic, 30
- Incompressible, 40
- Induced velocity, 123

- Induction factor, 41, 42, 123  
Inertia matrix, 14, 25, 26  
Instability, 3, 67, 193  
Internal force, 28
- Jacobian, 130
- KEWT wind turbine, 85  
Kinetic energy, 8, 14, 15, 25, 26, 29, 32, 34
- Lagrange's equations, 28, 32–34, 321  
Lagrangian, 31  
Lift, 47  
Lifting line, 49  
limit cycle, 75  
Linear impulse-momentum principle, 9  
Linear vibration, 257  
Linearisation, 4  
LMH64-5, 159  
Local speed ratio, 45  
LU-decomposition, 112
- Mach-number, 40  
Mass matrix, 91, 117  
Maximum power coefficient, 44  
Modelling, 133  
Moment, 11, 12, 24  
Moment of inertia, 14  
Momentum, 9, 10, 12  
Momentum theory, 38–44  
Multi-blade effects, 204  
Multi-body, 4, 94, 133
- Natural frequency, 152, 259  
Natural frequency, rotating, 156, 313  
Newton, 7, 30, 33  
Nibe turbines, 74  
NM-80, 5  
Nonconservative force, 33  
Nonconservative forces, 17, 32  
Nonlinear tool, 4, 87, 109
- Orthonormal, 20  
Overdamped, 259
- Pitch-flap flutter, 80  
Pitch-lag instability, 79  
Potential energy, 16, 27, 30, 32, 34  
Potential function, 30  
Power, 42, 45  
Power coefficient, 44  
Prandtl's lifting line, 49  
Prandtl's tip loss, 54  
Pre-cone, 200  
Product of inertia, 14
- Quasi steady aerodynamics, 127
- Reference frame, 17, 18, 20–22, 24, 25  
Reynolds number, 48  
Rigid body, 133  
Rotation operator, 22  
Rotation operator matrix, 23  
Rotation transformation matrix, 18, 20, 24, 112  
Rotation vector, 22  
Rotational part of the kinetic energy, 15  
Rotational velocity, 13, 17, 21, 23  
Rotor disc theory, 44
- Scale effect, 77  
Scaling, 3  
Spring forces, 16  
Stall, 70  
Stall flutter, 75  
Stiffness variation, 212  
Strouhal, 60, 248  
Superelement, 4, 133, 154, 161  
Symbolic manipulation, 24
- Tangential induced velocity, 125  
Tangential induction, 45  
Thrust, 42  
Tip loss, 54  
Torque, 45  
Torsion, 133  
Total rotation, 25  
Tower instability, 81, 85  
Transform, 25

- Translational part of the kinetic energy, 15
- Transpose, 20
- Turbulent wake state, 51
  
- Underdamped, 259
- Unsteady aerodynamics, 247
  
- Velocity, 21, 23, 25
- Vibration, 257
- Virtual displacement, 29, 30
- Virtual work, 30, 32
  
- Whirl flutter, 81
- WOBBE, 4, 87–107, 109–131, 285–302
- Work done, 8, 16, 17, 33
- Work-energy principle, 8, 15, 17



